



Numerical modeling and analysis of the active magnetic regenerator

Nielsen, Kaspar Kirstein

Publication date:
2010

Document Version
Publisher's PDF, also known as Version of record

[Link back to DTU Orbit](#)

Citation (APA):
Nielsen, K. K. (2010). *Numerical modeling and analysis of the active magnetic regenerator*. Technical University of Denmark.

General rights

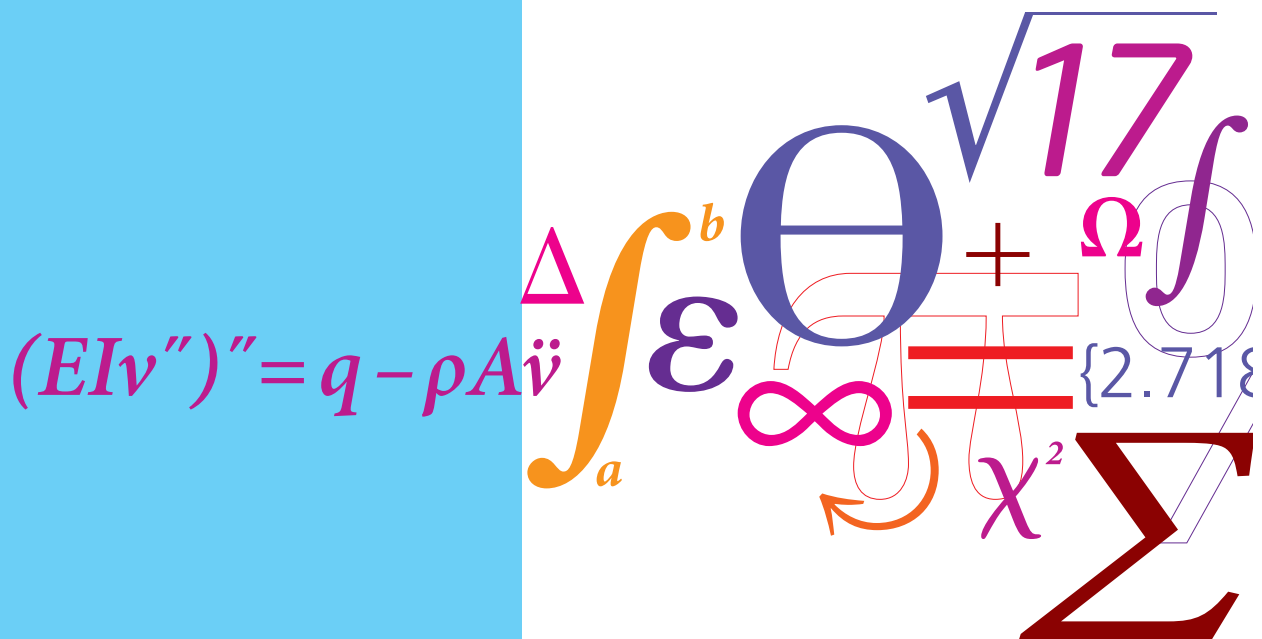
Copyright and moral rights for the publications made accessible in the public portal are retained by the authors and/or other copyright owners and it is a condition of accessing publications that users recognise and abide by the legal requirements associated with these rights.

- Users may download and print one copy of any publication from the public portal for the purpose of private study or research.
- You may not further distribute the material or use it for any profit-making activity or commercial gain
- You may freely distribute the URL identifying the publication in the public portal

If you believe that this document breaches copyright please contact us providing details, and we will remove access to the work immediately and investigate your claim.

Numerical modeling and analysis of the active magnetic regenerator

PhD Thesis



Kaspar Kirstein Nielsen
August 2010

Preface

This thesis represents the work I did as a part of my PhD, the Magcool project and the general magnetic refrigeration effort at Risø DTU from 1 September 2007 until 20 August 2010. The main purpose of my PhD has been to further develop an existing 2-dimensional numerical model of the active magnetic regenerator (AMR) that was first developed by Dr. Thomas Frank Petersen at Risø DTU from 2004 to 2007 and which has been published in Petersen et al. (2008b). The model was originally developed in the commercial finite element software package Comsol and was therefore not optimal in terms of computational speed¹. I therefore completely re-implemented the model using finite differences, a different temporal integration scheme and wrote it in Fortran. In this way a factor of 100 was gained in computational speed. This has enabled rather large parametric studies. Such have been performed and are presented in the thesis.

As my journey into the magnetic refrigeration research continued I was amazed by at least two very important issues. One, the fact that the magnetocaloric properties of candidate magnetic materials are usually not published in a usable way from a modeller's point of view; typically, the magnetic entropy change is the only property available. Therefore, I set the task of enhancing this rather weak point in the research area and have tried to encourage researchers to publish more relevant details as well as I have learned how to measure both the magnetic entropy change, the adiabatic temperature change and the specific heat of magnetic materials as a function of both magnetic field and temperature experimentally. This has certainly opened my eyes to a very interesting area and I daresay that interesting scientific results have come out of it.

The other big issue that I believe is not taken care of properly in the magnetic refrigeration community is the concept of the internal magnetic field, \mathbf{H} , and the magnetic flux density, \mathbf{B} . These two fields are regularly debated among physicists – which is the “right” one or the more physically correct. This particular question is certainly interesting. The internal field may be quite far from the applied field both in terms of magnitude and topology within the magnetic material. This has to do with the concept of geometric demagnetization, which is a consequence of the accumulation of magnetic “charges” on surfaces perpendicular to the applied field. This is all very interesting, however, in the thesis I show that the impact on magnetic refrigeration may be severe and that the problem is strongly coupled not only to the geometry of the magnetic material used but certainly also the composition

¹The pioneering work of Dr. Petersen is most appreciated and his model was the very first to take the rather big step into the 2-dimensional modeling of the AMR. I consider myself rather lucky to have been able to continue his work and this is a beautiful example of the way of science: that we stand on the shoulders of other people in order to obtain even more detailed knowledge.

of the material(s) and the temperature distribution inside the material. These are all relevant configurations for a magnetic refrigerator and this thesis has an entire chapter devoted to the investigation of these effects.

I have worked and am working in close collaboration with experimentalists building, developing and running AMR test machines. In this way I have been able to compare the numerical AMR model with actual experiments. At Risø DTU an experimental test machine is situated and this is described in detail in the thesis. I visited the University of Victoria, Canada (UVic) research group doing magnetic refrigeration lead by Dr. Andrew Rowe during a period of a total of five months in 2009. This has provided quite close collaborations and scientific papers have come out of our work together, but more importantly the joint work has inspired many new ways of considering magnetic refrigeration from my perspective at least. The permanent magnetic refrigerator situated at UVic is the world leading in terms of produced temperature span and cooling power considering the applied magnetic field etc.

I also visited the magnetic refrigeration research group at University of Santa Catarina in Florianopolis, Brazil lead by Dr. Jader Barbosa Jr. and the group at the University of Ljubljana, Slovenia lead by Dr. Alojz Poredos. During these two stays I believe quite solid friendships and partnerships for common research within magnetic refrigeration were established. I have also been able to visit Astronautics Corp. of America in Madison, Wisconsin in the USA. This private company has been doing research within magnetic refrigeration for several decades and their experience has been most inspiring and I must say that I have learned quite a lot from all these visits. The knowledge I have gained and collected during my stays at various research institutions during my PhD is obviously quite defining for my thesis. I have aimed at writing this thesis such that my own personal opinions are clearly marked and the results obtained either in collaboration with other researchers or solemnly by others are completely apparent too. I wish you, the reader, a hopefully enjoyable experience while reading my thesis. Furthermore, any comments, corrections, subjects for debate and the like are more than welcome.

Kaspar Kirstein Nielsen, Risø 20 August 2010.

Acknowledgements

I wish to express my gratitude to a number of people and institutions for support during the work of my PhD. My supervisors, Dr. Jesper Hattel, Dr. Nini Pryds, Dr. Christian Bahl and Dr. Anders Smith have been quite helpful and very supportive. It is my experience that you believed in me and my way of working. I know that I have strong opinions on how things should be done in terms of the work and you gave me plenty of room to exploit this. I thank you for that.

I would also like to express a special gratitude to Dr. Thomas Frank Petersen for his pioneering work in the numerical modeling of magnetic refrigeration. You certainly boosted my knowledge in the field in a very short time and I can say without a doubt that the PhD thesis I have read the second most is yours.

My close colleagues, Dr. Rasmus Bjørk, Dr. Kurt Engelbrecht, Dr. Stinus Jeppesen, Mr. Jesper Jensen and Mr. Dan Eriksen have all been a great part of the joy of going to work every day. You guys are great to work with – both professionally, but certainly also on a personal level. I enjoy our time together like, e.g., all the times we had cake and told jokes etc.

For their great technical support I thank Mr. Jørgen Geity and Mr. Finn Saxild. The more I work with you two the more I realize how exceptionally little I know about the real world in terms of mechanics and craftsmanship. I dare say that you two are invaluable to a place like Risø DTU with your technical experience and expertise. Without you many things simply would not work or be done.

The students I have had the pleasure of co-supervising are also thanked. Mr. Dennis Christensen, Mr. Kasper Lipsø and Miss Anne-Sofie Lautrup Sørensen I thank you all for the great work we did together (and are still doing). I hope that your patience have not been tested too much having me as a co-supervisor, but I believe that you all did great jobs while working here at Risø DTU and I hope that you will continue with your promising science careers.

During my visits at University of Victoria I got a few very good friends. I would therefore like to thank Mr. Armando Tura, Mr. Sandro Schopfer, Mr. Daniel Arnold and Mr. Anton Kiddess for the work we did and the time we spent together. The amount of good food in our Italian-Swiss-German-Danish fusion kitchen was awesome as were the results of our joint work. I learned a great deal from staying with you guys at UVic. To Dr. Andrew Rowe I wish also to express my most sincere gratitude. That you welcomed me to your research group, taught me several things about experimental magnetic refrigeration and introduced me to the guys just mentioned is simply cool. I really appreciate that and I hope that our continued collaboration will provide even more interesting findings.

To Dr. Jader Barbosa Jr, Mr. Jaime Lozano, Mr. Paolo Trevizoli and Mr. Pablo Oliveira I wish to thank you for your kindness during my stay at University of

Santa Catarina, Florianopolis, Brazil. I thoroughly enjoyed working with you guys and I expect that we will get even more collaboration in the future.

To Mr. Jaka Tusek I wish to express my deepest gratitude of your hospitality during my visit in Ljubljana working with you. I think that we can greatly improve the level of AMR modeling currently present together. I really enjoyed visiting you and Slovenia and I am sure that our future collaboration will be significant.

All these journeys visiting other universities had not been possible were it not for the travel grant I received from the Danish Ministry for Science, Technology and Innovation. I great appreciate that I received this grant and I must say that it has certainly improved the work of my PhD in many ways.

Finally, I would like to acknowledge the financing of my PhD. I therefore thank the support of the Programme Commission on Energy and Environment (EnMi) (Contract no. 2104-06-0032) which is part of the Danish Council for Strategic Research.

Abstract, English

In this thesis the active magnetic regenerator (AMR) is analyzed using various numerical tools and experimental devices. A 2-dimensional transient numerical model of the AMR is developed and implemented and it is used to investigate the influence of a range of parameters on the performance of the AMR. The model simulates a regenerator made of parallel plates. The operating parameters, such as fluid flow rates, thermal utilization, magnetocaloric properties etc. are varied as are geometric properties such as plate and channel thickness, regenerator length and porosity. In this way the performance expressed as temperature span versus cooling power is mapped as a function of the central parameters.

Since regenerators built of several magnetic materials distinguished by their respective magnetic transition temperatures are reported to perform better than single-material AMRs this concept has been investigated using the numerical AMR model. The results show indeed that the performance may be enhanced significantly and it may thus be concluded that the performance of the AMR is dependent on a vast number of parameters (material composition, magnetic field source, regenerator geometry, regenerator efficiency, operating conditions etc.). The results presented in this thesis thus provide an overview of the influence of many of these parameters on the AMR performance.

It is also concluded that the internal field of an AMR is far from homogeneous. Indeed, it does depend on both regenerator geometry, orientation of the applied field, the temperature distribution in the material and the material composition. A magnetostatic 3-dimensional model is developed (by the author of this thesis in close collaboration with Mr. D.V. Christensen, Risø DTU). The results from this show that the resulting internal field in an active regenerator may vary so significantly that clearly preferable configurations exist and in particular that certain configurations should not be considered. The combination of the model for the internal field and the transient AMR model has not been fully implemented and the performance impact of the internal field model remains thus to be investigated.

Finally, suggestions for future work are provided based on the knowledge presented here. These include alternative regenerator geometries, a list of physical effects that have not been investigated in terms of their impact on the AMR performance yet etc. Several ready-to-go projects are thus suggested for future work.

Resumé, dansk

Den aktive magnetiske regenerator (AMR) er undersøgt ved brug af forskellige numeriske værktøjer og eksperimentelt apparatur i denne afhandling. En 2-dimensionel tidsafhængig numerisk AMR model er udviklet og implementeret og den bliver brugt til at undersøge indflydelsen af en række parametre på ydeevnen af en AMR. Modellen simulerer en regenerator baseret på parallelle plader. Operationsparametre, såsom væske massestrømme, termisk udnyttelse, de magnetokaloriske egenskaber etc. bliver varieret og ligeså gør geometriske parametre såsom plade og kanal tykkelse, længden af regeneratoren samt porøsitet. På denne måde bliver ydeevnen udtrykt som temperatur forskel overfor køleeffekt kortlagt som funktion af de centrale parametre.

I og med at regenerators bygget af flere magnetiske materialer, adskilt af deres magnetiske overgangstemperaturer, kan opnå bedre effektivitet end enkelt-materiale regenerators er dette koncept undersøgt ved hjælp af AMR modellen. Resultaterne viser, at ydeevnen bestemt kan forstærkes betragteligt med flere materialer og man kan dermed konkludere, at AMR ydeevnen er afhængig af en lang række af parametre såsom materiale sammensætning, magnetfelt, regenerators geometri, dens effektivitet, operations parametrene osv. Resultaterne der er givet i denne afhandling udgør dermed et overblik over de forskellige parametres indflydelse på ydeevnen af en AMR.

Det bliver også fundet, at det interne magnetfelt i en AMR er langt fra homogent. Det afhænger rent faktisk af både regenerators geometri, orientering af det eksterne magnetfelt, temperaturen i regeneratoren samt sammensætningen af materialet. En 3-dimensional magnetostatisk model er udviklet af forfatteren i tæt samarbejde med D.V. Christensen ved Risø DTU. Ved hjælp af denne model viser det sig, at det interne felt i en AMR varierer så betydeligt afhængigt af de givne parametre, at klart foretrukne konfigurationer eksisterer og navnlig ikke-foretrukne. Indbygning af den magnetostatiske model i AMR modellen er ikke færdigudviklet endnu og dermed kan den direkte indflydelse på AMR ydeevnen ikke estimeres endnu. Dette er derfor arbejde, som bør fortsættes.

Endelig opstilles en række forslag baseret på den viden, som er præsenteret her. Disse er bl.a. alternative regenerator geometrier, en række fysiske effekter som ikke er modelleret endnu med hensyn til deres betydning for AMR ydeevnen osv. Der er derfor opstillet en række projekter, som er lige til at gå til for den foretagsomme.

List of publications

Papers published in peer-reviewed international scientific journals

K.K. Nielsen, C.R.H. Bahl, A. Smith, N. Pryds and J. Hattel, *A comprehensive parameter study of an active magnetic regenerator using a 2D numerical model*, 2010 International Journal of Refrigeration 33, 753-764

K.K. Nielsen, C.R.H. Bahl and A. Smith, *Constraints on the adiabatic temperature change in magnetocaloric materials*, 2010, Physical Review B 81, 054423

A. Smith, K.K. Nielsen, D.V. Christensen, C.R.H. Bahl, R. Bjørk and J. Hattel, *The demagnetizing field of a nonuniform rectangular prism*, 2010, Journal of Applied Physics 107, 103910

D.V. Christensen, R. Bjørk, K.K. Nielsen, C.R.H. Bahl, A. Smith and S. Clausen *Spatially resolved measurements of the magnetocaloric effect and the local magnetic field using thermography*, 2010, Journal of Applied Physics 108, 063913.

C.R.H. Bahl and K.K. Nielsen, *The effect of demagnetization on the magnetocaloric properties of gadolinium*, 2009, Journal of Applied Physics 105, 013916

K.K. Nielsen, C.R.H. Bahl, A. Smith, R. Bjørk, N. Pryds, J. Hattel, *Detailed numerical modeling of a linear parallel-plate active magnetic regenerator*, 2009, International Journal of Refrigeration 32, 1478-1486

K.K. Nielsen, J. Tusek, K. Engelbrecht, S. Schopfer, A. Kitanovski, C.R.H. Bahl, A. Smith, N. Pryds and A. Poredos, *Review on numerical modeling of active magnetic regenerators*, 2010 accepted for publication in International Journal of Refrigeration

K. Engelbrecht, K.K. Nielsen, C.R.H. Bahl, *Experimental results for a magnetic refrigerator using three different types of magnetocaloric material regenerators*, 2010, accepted for publication in International Journal of Refrigeration

N. Pryds, F. Celemens, M. Menon, P.H. Nielsen, K. Brodersen, R. Bjørk, C.R.H. Bahl, K. Engelbrecht, K.K. Nielsen, A. Smith, *Monolithic Perovskite for magnetic regenerator*, 2010, accepted for publication in Journal of American Ceramic Society

Papers submitted to peer-reviewed international scientific journals

D.V. Christensen, K.K. Nielsen, C.R.H. Bahl, A. Smith, *Demagnetizing field of a stack of nonuniform rectangular prisms*, 2010, submitted to Journal of Applied Physics.

K.W. Lipsø, K.K. Nielsen, D.V. Christensen, C.R.H. Bahl, K. Engelbrecht, A. Smith, *Measuring the effect of demagnetization in stacks of rectangular gadolinium prisms using the magnetocaloric effect*, 2010, submitted to Journal of Magnetism and Magnetic Materials.

Papers published in conference proceedings

K.K. Nielsen, R. Bjørk, J.B. Jensen, C.R.H. Bahl, N. Pryds, A. Smith, A. Nordentoft, J. Hattel, *Magnetic cooling at Risø DTU*, 2008, in the proceedings of the 7th Gustav Lorentzen Conference

K.K. Nielsen, N. Pryds, A. Smith, C.R.H. Bahl, J. Hattel, *2-dimensional numerical modeling of Active Magnetic Regeneration*, 2010, in the proceedings of the 3rd International Conference on Magnetic Refrigeration at room temperature

K.K. Nielsen, K. Engelbrecht, C.R.H. Bahl, A. Smith, N. Pryds, J. Hattel, *Numerical modeling of multi-material active magnetic regeneration*, 2009, in the proceedings of the 7th World Conference on Experimental heat transfer, fluid mechanics and thermodynamics

R. Bjørk, K.K. Nielsen, C.R.H. Bahl, A. Smith, N. Pryds, J. Hattel, *Numerical modeling in magnetic refrigeration*, 2009, in the proceedings of the 50th International Conference of Scandinavian Simulation Society, Modelling and Simulation of Energy Technology (SIMS 50)

K.K. Nielsen, C.R.H. Bahl, K. Engelbrecht, A. Smith, N. Pryds, J. Hattel, *Numerical modeling of graded active magnetic regenerators*, 2010, in the proceedings of the 4th International Conference on Magnetic Refrigeration at room temperature

K.K. Nielsen, J.R. Barbosa, Jr, P.V. Trevizoli, *Numerical analysis of a linear reciprocating active magnetic regenerator*, 2010, in the proceedings of the 4th International Conference on Magnetic Refrigeration at Room Temperature

K. Engelbrecht, K.K. Nielsen, N. Pryds, *An experimental study of passive regenerator geometries*, 2010, in the proceedings of the 4th International Conference on Magnetic Refrigeration at Room Temperature

Papers in preparation for submission

J. Lozano, K.K. Nielsen, J. Barbosa, Jr, *The magnetocaloric properties of $MnFeP_{0.46}As_{0.54}$* , 2010, in prep.

A. Tura, K.K. Nielsen, A. Rowe, *Experimental an modeling results of a parallel-plate based Active Magnetic Regenerator*, 2010, in prep.

Contents

1	Introduction	1
1.1	Overview of magnetic refrigeration	2
1.1.1	Numerical AMR modeling	4
2	Fundamentals of the magnetocaloric effect	5
2.1	Thermodynamics of the magnetocaloric effect	5
2.2	Curie and peak temperatures	7
2.2.1	Determination of the Curie temperature	8
2.2.2	1 st and 2 nd order transitions	9
2.3	Mean field model	9
2.4	Constraints on the adiabatic temperature change	11
2.4.1	Irreversible, first order materials	13
2.5	Experimental determination of the MCE	16
2.6	Summary	18
3	The active magnetic regenerator	23
3.1	The AMR cycle	23
3.2	Development of a numerical AMR model	25
3.2.1	Numerical implementation	28
3.2.2	The convective term	31
3.2.3	Boundary conditions	32
3.2.4	Moving boundaries	33
3.2.5	Thermal parasitic losses (“2.5D” model)	34
3.2.6	Summary and input parameters of the model	35
3.3	Validation	37
3.3.1	Energy conservation	37
3.3.2	Analytical solution	37
3.3.3	Standard experiment	38
3.4	Summary	39
4	Parameter study of the AMR	41
4.1	Design and parameters	41
4.1.1	Non-dimensionalizing the parameters	42
4.1.2	Obtaining the cooling capacity	43
4.2	Results and discussion	44
4.2.1	Dependence on porosity	45
4.2.2	Dependence on NTU	47

4.2.3	Dependence on the utilization	47
4.2.4	Influence of the cycle timing	49
4.2.5	Influence of pressure drop	53
4.3	Summary	53
5	Multi-material regenerators	55
5.1	Introducing multi-material AMRs	55
5.1.1	The utilization of a multi-material regenerator	56
5.2	Two-material Gd-like regenerators	57
5.2.1	Variation of the parameters	57
5.2.2	Results	58
5.3	n -material Gd-like regenerators	60
5.3.1	Cooling power versus temperature span	61
5.3.2	Maximum cooling power and temperature span	62
5.3.3	Realistic assessment of multi-material regenerators	63
5.3.4	Influence of a larger distance between materials	66
5.4	n -material LCSM-like regenerators	68
5.5	Multi-material LCSM with experimental data	72
5.6	Summary	74
6	Model predictions of an experimental AMR device	75
6.1	The Risø DTU test device	75
6.1.1	Regenerators	76
6.1.2	Single material experiments	77
6.1.3	Multi-material experiments	81
6.2	Summary	83
7	Modeling the demagnetizing field	85
7.1	Magnetic fields	86
7.2	A single rectangular prism	87
7.2.1	Results relevant to magnetic refrigeration	88
7.3	A stack of rectangular prisms	95
7.3.1	Single material results	95
7.3.2	Multi-material results	98
7.3.3	The effect of demagnetization in selected materials	100
7.4	Demagnetizing effects in generalized stacks of parallel plates	103
7.4.1	Influence of the number of plates	103
7.4.2	Spacing of the plates	104
7.4.3	Porosity of the stack	105
7.5	Experimental predictions	106
7.5.1	The single prism case	106
7.6	Summary	107
8	Perspectives and future challenges	111
8.1	Suggestions for candidate regenerator geometries	111
8.2	Demagnetization	114
8.3	Impact of other physical effects	114
8.3.1	Hysteresis	115

8.3.2	Specific heat and asymmetrical flow periods	115
8.3.3	Channeling effects	115
9	Conclusion	117
A	Papers	123
A.1	Papers published in peer-reviewed international scientific journals . .	123
A.1.1	The effect of demagnetization on the magnetocaloric properties of gadolinium; published in Journal of Applied Physics .	123
A.1.2	Constraints on the adiabatic temperature change in magnetocaloric materials; published in Physical Review B	129
A.1.3	The demagnetizing field of a nonuniform rectangular prism; published in Journal of Applied Physics	135
A.1.4	Spatially resolved measurement of the magnetocaloric effect and the local magnetic field using thermography; published in Journal of Applied Physics	144
A.1.5	A comprehensive parameter study of an active magnetic regenerator using a 2D numerical model; published in International Journal of Refrigeration	149
A.1.6	Detailed numerical modeling of a linear parallel-plate active magnetic regenerator; published in International Journal of Refrigeration	162
A.1.7	Review on numerical modeling of active magnetic regenerators; accepted for publication in International Journal of Refrigeration	172
A.1.8	Experimental results for a magnetic refrigerator using three different types of magnetocaloric material regenerators; accepted for publication in International Journal of Refrigeration	228
A.1.9	Monolithic Perovskite for magnetic regenerator; accepted for publication in Journal of American Ceramic Society	258
A.2	Papers submitted to peer-reviewed international scientific journals .	278
A.2.1	Demagnetizing effects in stacked, rectangular prisms; submitted to Journal of Applied Physics	278
A.2.2	Measuring the effect of demagnetization in stacks of rectangular gadolinium plates using the magnetocaloric effect; submitted to Journal of Magnetism and Magnetic Materials . . .	294
A.3	Papers published in conference proceedings	310
A.3.1	Magnetic cooling at Risø DTU; published in the proceedings of the 7 th Gustav Lorentzen Conference	310
A.3.2	2-dimensional numerical modeling of Active Magnetic Regeneration; published in the proceedings of the 3 rd International Conference on Magnetic Refrigeration at room temperature .	319
A.3.3	Numerical modeling of graded active magnetic regenerators; published in the proceedings of the 4 th International Conference on Magnetic Refrigeration at room temperature	328

A.3.4	Numerical modeling of multi-material active magnetic regeneration; published in the proceedings of the 7 th World Conference on Experimental heat transfer, fluid mechanics and thermodynamics	337
A.3.5	Numerical analysis of a linear reciprocating active magnetic regenerator; published in the proceedings of the 4 th International Conference on Magnetic Refrigeration at Room Temperature	346
A.3.6	Numerical modeling in magnetic refrigeration; published in the proceedings of the 50 th International Conference of Scandinavian Simulation Society, Modelling and Simulation of Energy Technology (SIMS 50)	354
A.3.7	An experimental study of passive regenerator geometries; published in the proceedings of the 4 th International Conference on Magnetic Refrigeration at Room Temperature	363
	References	372

Chapter 1

Introduction

The content of this thesis reflects the work performed by the author during the three years from September 2007 till August 2010. The outline is not chronological, but rather subject based. After the introduction, this chapter, the fundamentals of the magnetocaloric effect and a numerical model of an active magnetic regenerator (AMR) are presented in Chapters 2 and 3, respectively. In the former chapter a thermodynamic constraint on the derivative of the adiabatic temperature change with respect to temperature is derived. This is a fundamental new result and the interested reader may enjoy this part even though a thorough knowledge and understanding of the magnetocaloric effect is already possessed. In the latter a numerical model describing the active magnetic regenerator based on parallel plates is developed and validated. This chapter is strictly of a technical nature.

In Chapters 4–6 the numerical AMR model is applied to a range of modeling cases. First, in Chap. 4 a comprehensive survey consisting of 27,216 simulations in total is presented. The configuration is for a single material regenerator and the geometric and operating parameters have been varied. The results are presented in terms of the cooling power and temperature span of the magnetic refrigeration system. Second, in Chap. 5 the model is applied to different cases where the number of materials comprising the regenerator is varied. It has been experimentally proven that such multi-material regenerators may increase cooling power and temperature span of the system, e.g. Rowe & Tura (2006). Finally, in Chap. 6 the AMR model is used to simulate the experimental AMR device located at Risø DTU.

In Chapter 7 a numerical so-called “demagnetization model” able to calculate the internal magnetic field of a rectangular prism and a stack of such prisms is described in detail. This is a natural extension of the AMR model considered in the previous four chapters. It is found that the internal magnetic field may vary greatly with temperature and geometry of the regenerator. This is a topic that has been discussed only very little in the literature concerned with magnetic refrigeration. However, in this chapter it is shown that the effect of demagnetization on a single rectangular prism and a stack of such prisms may be of significant importance.

Chapter 8 provides both a reflection of what could have been done and what should be considered in the future in order to make magnetic refrigeration come closer to a commercially viable level. Here, a range of alternative regenerator geometries are considered and an approach as how to incorporate the demagnetization model into the AMR model is suggested.

Finally, Chap. 9 provides a summary of the overall conclusions of this thesis.

Scientific publications

This thesis is based on a range of scientific papers. These are provided in Appendix A. The papers are all results of close collaboration between the author and a range of other scientists, mainly situated at Risø DTU. In order to give a somewhat fair overview of the responsibilities of each co-author on the papers a co-author statement has been made for each paper and signed by all co-authors. These are submitted to the Technical University of Denmark as per the regulations concerned with the submission of a PhD thesis. They are available upon request.

The thesis has been written such that it is self-contained. It is thus not imperative to read the papers in order to understand the thesis. However, the topics and results presented in the thesis are in close conjunction with the published papers and these have thus been cited appropriately and at the beginning of each chapter the papers relevant to the chapter are listed for convenience. The papers are divided into four groups. First are the papers published in international scientific journals, second those submitted to such journals. Thirdly, papers published in various conference proceedings are given and finally, a few relevant papers in preparation are given. The latter group is merely included since some of the results presented in the thesis are going to be published in these papers.

The remainder of this chapter is devoted to a mini-review of the magnetic refrigeration research during the past 40 years in general and the numerical AMR modeling in particular. Sec. 1.1 is partially based on Paper A.1.7 (Nielsen et al., 2010e).

1.1 Overview of magnetic refrigeration

The magnetocaloric effect (MCE) has been known for more than a century. It is an inherent effect of all magnetic materials, however, its magnitude varies significantly from material to material. The effect is conventionally expressed as an adiabatic temperature change when the magnetic field applied to a magnetic material is changed. In this way it is possible to induce a temperature change and for many magnetocaloric materials¹ the effect is reversible. It thus seems obvious that this effect might be used for refrigeration due to the reversibility and thus small intrinsic entropy losses. In the 1920s and 30s the MCE was realized to be usable for reaching temperatures close to the absolute zero (Giauque & MacDougall, 1933) when adiabatically demagnetizing a magnetic salt.

For room temperature refrigeration, which this work is concerned with, the first experimental device performing magnetic refrigeration based on the MCE was presented by Brown (1976). This device used a superconducting magnet with a resulting field of 7 T and a maximum temperature span of 47 K using gadolinium (Gd) as a refrigerant. Now, the active magnetic regenerative (AMR) cycle was not invented as a topic in 1976, however, Brown investigated different cycles applied

¹The term magnetocaloric material is simply used to describe that a material exhibits the magnetocaloric effect.

to his apparatus and concluded that the “constant magnetization” or “magnetic Stirling” cycle produced the optimal results.

Later, in Barclay (1983) the AMR cycle was suggested. It was realized early on that the usability of the MCE in a single blow machine would be limited due to the fact that the MCE is no more than a few degrees in a one tesla magnetic field. The AMR cycle is thus a combination of 1) a classical regenerative cycle where a porous regenerator made of solid material is used to store a thermal gradient between a hot and a cold reservoir and 2) by using the MCE as work input. Through making the regenerator of one or more magnetocaloric materials it was demonstrated by Barclay (1983) that large temperature spans could be achieved.

In papers like, e.g., Matsumoto & Hashimoto (1990); DeGregoria (1991); Yan & Chen (1992); Chen et al. (1994) the numerical modeling of the AMR was developed using 1-dimensional models and it was shown that cooling powers and usable temperature spans could be achieved. This development led to the design and construction of several AMR test devices. Reviews of these AMR devices are given in Gschneidner & Pecharsky (2008); Yu et al. (2010). The perhaps most remarkable devices may include those designed and built at Astronautics Corp. of America (Zimm et al., 1998, 2006), those from University of Victoria, Canada (Rowe & Barclay, 2002; Tura & Rowe, 2007) and that of Tokyo Institute of Technology, Japan (Okamura et al., 2006). The test device located at Risø DTU (Bahl et al., 2008; Engelbrecht et al., 2009) does not provide temperature spans of more than 10 K, however, it is an extremely versatile device where, e.g., the regenerator geometry may be changed rapidly such that testing of a range of parameters may be performed quickly.

The devices briefly mentioned are different in many ways such as the magnetic field source, the magnetocaloric material refrigerant, regenerator geometry, operating AMR cycle frequency etc. Now, it is generally accepted that in order to develop commercially viable magnetic refrigeration technology for room temperature applications permanent magnet magnetic field sources must be used (Rowe, 2009; Bjørk, 2010). Considering permanent magnet based AMR devices the Permanent Magnet Magnetic Refrigerator (PMMR) located at University of Victoria (UVic) may be the best performing device built so far. A temperature span of 30 K and a cooling power of 50 Watts are achievable using 110 grams of Gd spheres with a maximum applied field strength of 1.46 T and running the AMR cycle at 4 Hz (Tura & Rowe, 2009). However, the pressure drop in the heat transfer fluid across the regenerator reaches up to almost 10 bar and this puts tight constraints on the further improvement of the performance. This geometry provides superior heat transfer characteristics, however, the pressure drop across the regenerator bed is inherently large. It is therefore necessary to develop new regenerator geometries or change the overall device design in order to minimize the pressure drop. Parallel plate-based regenerators are expected to provide an alternative to the packed sphere-based regenerators. In this thesis the focus is thus entirely on the performance of such regenerators. The analysis consists of three approaches:

- The theoretical AMR performance is analyzed using a 2D numerical model
- The experimental AMR performance is analyzed using several different AMR experiments
- A detailed analysis of the magnetic field of the stack of parallel plates is pro-

vided

1.1.1 Numerical AMR modeling

Since this thesis is mainly concerned with the more theoretical aspects of the overall AMR in general and the numerical modeling of the coupled heat transfer and fluid dynamics problem of the magnetic regenerator in particular, it seems prudent to dwell on the development of AMR modeling through the past 30 years.

The problem of modeling an AMR system has been considered from many sides. A range of “simplified” models, sometimes referred to as steady-state or zero-period models, have been presented. These are models where the details of the heat transfer in the regenerator are not really considered, but rather overall energy or entropy balances are analyzed in order to gain information of the overall performance of the system. Such models have been presented by, e.g., Yan & Chen (1991, 1992); Zhang et al. (1993, 2000); He et al. (2003); Rowe & Barclay (2003); Jacobs (2009).

Another approach to the AMR modeling is through using a detailed transient model that takes into account the local heat transfer between the solid and the fluid throughout the regenerator bed and has a periodic variation of the fluid movement and magnetic field, includes detailed magnetocaloric properties such as the specific heat and the adiabatic temperature change, which are both functions of the magnetic field and temperature etc. Such models are based on the well-known passive regenerator energy equations with the addition of the magnetic properties and the magnetocaloric effect. Such a transient AMR model thus simulates the actual physics of an AMR experiment to some extent. Most such models are 1-dimensional, which means that they resolve the direction of the fluid and not any transverse directions. In such a situation a Nusselt-Reynolds correlation is needed in order to calculate the local heat transfer coefficient throughout the regenerator. Such models have been published widely and examples may be found in Smailli & Chahine (1998); Dikeos et al. (2006); Engelbrecht (2008); for a review of the transient AMR models see Nielsen et al. (2010e) (paper A.1.7).

For some regenerator geometries it is fairly straightforward to make a 2-dimensional (or, perhaps, even 3-dimensional) AMR model. If the geometry is, e.g., parallel plates the computational domain is rather simple. Transient AMR models of such kind have been published in Petersen et al. (2008b); Nielsen et al. (2009a); Oliveira et al. (2009). Using such a model it is possible to resolve the transverse thermal gradient with respect to the flow direction. In this way it may be argued that the physical situation is more well represented by a 2D model that actually resolves the boundary between the solid and fluid and does thus not rely on correlations for heat transfer coefficients etc.

Finally, 3-dimensional modeling of the AMR has been initiated by Bouchard et al. (2009). Their model resolves a cell with a few magnetocaloric particles (spherical and elliptically shaped) and the fluid flow and heat transfer is solved with certain imposed boundary conditions. The results are of a limited nature so far, however, more results are expected.

Chapter 2

Fundamentals of the magnetocaloric effect

This chapter presents the basic thermodynamics of the magnetocaloric effect (MCE) in general and describes the complete material characterization of magnetic materials needed for usage in magnetic refrigeration in particular. The chapter is meant to be an introduction for researchers to the topic and to go into particular details on the MCE highly relevant for magnetic refrigeration as such. The scientific content of this chapter is a combination of established, well-known research and a few new findings contributed to some degree by the author of this thesis. Thus, some of the results in this chapter are based on papers A.1.1 (Bahl & Nielsen, 2009) and A.1.2 (Nielsen et al., 2010b).

This chapter is outlined in the following way. In Sec. 2.1 the basic thermodynamics of the MCE are discussed. In Sec. 2.2 the Curie temperature is introduced and its rôle in magnetic refrigeration is outlined. In Sec. 2.3 the mean field model for a ferromagnet is presented. This model enables the calculation of the basic magnetocaloric properties needed for modeling a magnetocaloric material in, e.g., a magnetic refrigerator. In Sec. 2.4 a fundamental constraint on the adiabatic temperature change is derived and discussed. In Sec. 2.5 the experimental determination of the MCE is considered. Finally, in Sec. 2.6 this chapter is summarized.

2.1 Thermodynamics of the magnetocaloric effect

The MCE is the result of a rather complex interaction between the change in internal magnetic field strength, H , in a magnetic material, the spin system of the material and any contributors to entropy inside the material. Considering a soft ferromagnet, which is almost always the case in the regime of magnetic refrigeration, the increase in magnitude of the internal magnetic field tends to align the electronic spins. This ordering is inevitably associated with a lowering of the magnetic entropy, S_{mag} . Now, depending on whether the internal magnetic field was changed under adiabatic or isothermal circumstances the total entropy of the material, S , will either remain constant or decrease. Writing the total entropy as a sum of the three main contributors, namely the magnetic, electronic (S_{ele}) and lattice entropies (S_{lat}) the following expression is obtained (Pecharsky et al., 2001)

$$S = S_{\text{mag}} + S_{\text{lat}} + S_{\text{ele}}. \quad (2.1)$$

Considering the total entropy to be a function of temperature, T , and H only – i.e. assuming constant volume and pressure – the total derivative of the entropy may be found

$$dS = \frac{\partial S}{\partial T}dT + \frac{\partial S}{\partial H}dH. \quad (2.2)$$

Now, returning to the case of changing the magnetic field adiabatically the following may be found

$$dT = -\frac{T}{c_H} \frac{\partial S}{\partial H}dH, \quad (2.3)$$

where the definition of the specific heat (at constant field), c_H , has been used:

$$c_H = T \frac{\partial S}{\partial T}. \quad (2.4)$$

Equation 2.3 is usually integrated from initial to final magnetic field, H_i and H_f , respectively, to obtain the adiabatic temperature change

$$\Delta T_{\text{ad}}(T_i, H_i, H_f) = T_f - T_i = - \int_{H_i}^{H_f} \frac{T}{c_H} \frac{\partial S}{\partial H}dH, \quad (2.5)$$

where the initial and final temperatures, T_i , T_f , were introduced. However, some care should be applied in this case. The derivative of the entropy with respect to magnetic field and the specific heat are both functions of T and H in general. The temperature, T , is usually considered an independent variable. However, in this case it should be considered an implicit function of the magnetic field and the initial temperature. This implies that the integral in Eq. 2.5 cannot be written fully explicitly, even in the case where the specific heat and the derivative of the entropy are known analytical functions.

When considering a 2nd order transition¹ the magnitude of the magnetization, M , is linked to the entropy through a Maxwell relation

$$\mu_0 \frac{\partial M}{\partial T} = \frac{\partial S}{\partial H}, \quad (2.6)$$

casting Eq. 2.5 into its perhaps most well-known form

$$\Delta T_{\text{ad}} = -\mu_0 \int_{H_i}^{H_f} \frac{T}{c_H} \frac{\partial M}{\partial T}dH, \quad (2.7)$$

where the vacuum permeability, μ_0 , has been introduced. Since the Maxwell relations are only valid under the assumption of thermodynamic equilibrium care should be taken when applying Eq. 2.6. In the case of a 1st order transition this assumption is not valid due to the release of latent heat. In such a case the formalism developed in, e.g., Tocado et al. (2009) should be applied.

Considering the case of isothermally changing the internal magnetic field Eq. 2.3 becomes

$$dS = \frac{\partial S}{\partial H}dH, \quad (2.8)$$

¹1st and 2nd order transitions are introduced in Sec. 2.2.2.

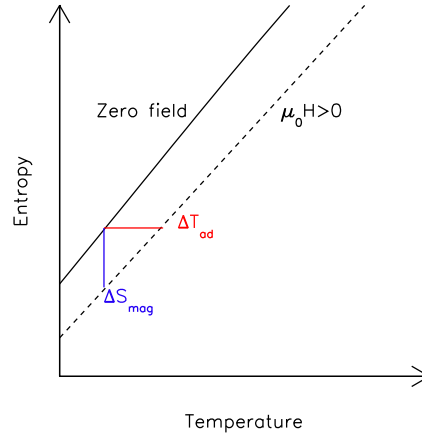


Figure 2.1: The $T - S$ diagram showing the MCE. The full line is the entropy in zero field and the dashed line in a non-zero field. The adiabatic temperature change is defined as the difference in temperature between two points with the same entropy but in different fields. The isothermal entropy change is defined as the entropy difference between two curves in two different fields at the same temperature.

and utilizing the Maxwell relation from Eq. 2.6 the magnetic entropy change may be found

$$\Delta S_{\text{mag}} = \mu_0 \int_{H_i}^{H_f} \frac{\partial M}{\partial T} dH. \quad (2.9)$$

Equations 2.7 and 2.9 may both be viewed as expressions for the magnetocaloric effect (MCE). From a fundamental thermodynamic view point understanding the adiabatic temperature change and the isothermal magnetic entropy change may be done by considering the total entropy. This is found through

$$S(T_f, H = H_0) = \int_0^{T_f} \frac{c_H(T, H_0)}{T} dT, \quad (2.10)$$

where the magnetic field is kept constant at H_0 . From an $T - S$ diagram as shown in Fig. 2.1 the MCE can be deduced. Considering a starting temperature of T_i the adiabatic temperature change upon changing the magnetic field from H_i to H_f is defined as

$$S(T_i, H_i) = S(T_i + \Delta T_{\text{ad}}(T_i, H_i, H_f), H_f). \quad (2.11)$$

Similarly, the isothermal magnetic entropy change is given by

$$\Delta S_{\text{mag}}(T_i, H_i, H_f) = S(T_i, H_f) - S(T_i, H_i). \quad (2.12)$$

This quantity is thus usually negative when the change in field is positive.

2.2 Curie and peak temperatures

Having considered the basic thermodynamics of the MCE it is relevant to dwell a moment at the magnitude of the effect. As was mentioned in the previous section

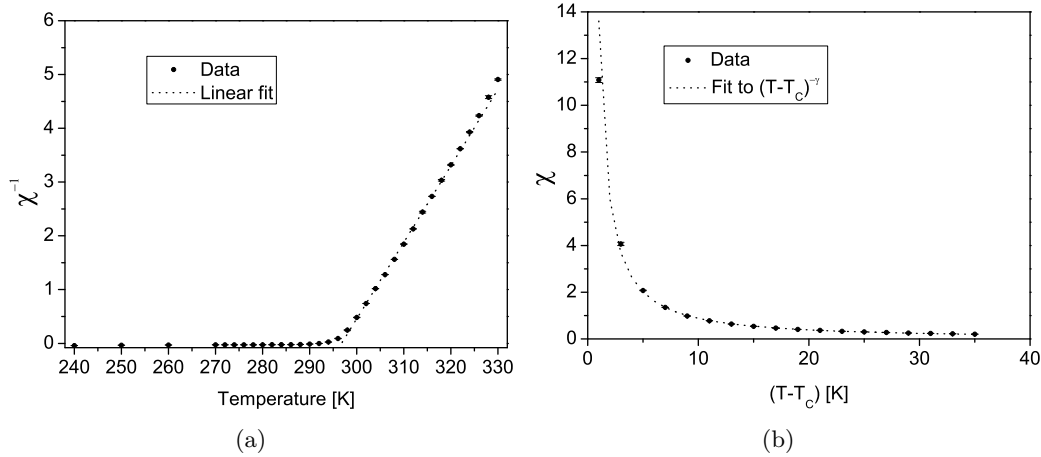


Figure 2.2: Examples of two methods for determining the Curie temperature. In this case magnetization data of Gd have been used. In (a) the inverse susceptibility method is shown. Above T_C the inverse susceptibility is proportional to $T - T_C$ (the Curie-Weiss law). In (b) an example of the critical exponent method is shown. The expression $\chi \propto (T - T_C)^{-\gamma}$ is fitted to the data and T_C is found. In these cases the values found are 297(2) and 295(2) K, respectively, which is in fine accordance with other published values (Hargraves et al., 1988). The figure is reproduced from paper A.1.1 (Bahl & Nielsen, 2009).

the MCE is generally a function of both temperature and magnetic field strength. As it turns out the effect is usually largest around a specific temperature where the material undergoes a magnetic phase change between being ferromagnetic and paramagnetic. When considering a magnetic material in zero applied field the transition temperature is usually denoted the Curie temperature or T_C and it is defined as the temperature at which the spontaneous magnetization becomes zero (Kittel, 1996).

2.2.1 Determination of the Curie temperature

Now, the definition of T_C is often not very practical for several reasons. First, soft ferromagnets have in principle zero *total* magnetization due to their domain structure in zero or low applied fields². This means that measuring, e.g., the magnetization, which would seem quite obvious due to the definition of T_C , will not provide a useful result as long as a macroscopic sample is used (i.e. one with domains). Second, the peak temperature of the MCE is often a function of the magnetic field (Pecharsky et al., 2001; Tocado et al., 2006; Palacios et al., 2010; Nielsen et al., 2010d). This means that T_C is insufficient in characterizing the MCE of a given magnetic material.

There are other experimental definitions of T_C . These include the following:

- 1) The temperature at which the derivative of the magnetization with respect to temperature at constant magnetic field is minimal (it is negative for ferromagnets).
- 2) The inverse susceptibility method. The inverse susceptibility is found from magnetization measurements at a range of constant temperatures and extrapolating the

²This is true when the size of the body considered is significantly greater than the typical domain size as is always the case in this context.

linear part of this expression to intersect with the temperature axis gives T_C (see Fig. 2.2(a)). 3) Through fitting the susceptibility, χ , to the expression $\chi \propto (T - T_C)^{-\gamma}$ (see Fig. 2.2(b)).

Other, more crude ways of defining T_C include the peak temperatures of the specific heat, the isothermal entropy change and the adiabatic temperature change. These three quantities all certainly have peak temperatures, which may even vary as a function of magnetic field (Pecharsky et al., 2001; Tocado et al., 2006; Palacios et al., 2010; Nielsen et al., 2010d). Considering, e.g., Eqs. 2.7 and 2.9 (the expressions for the adiabatic temperature change and isothermal entropy change, respectively) it is observed that their integrands contain different functions of both T and H and it may thus be concluded that the peak temperatures should not, a priori, coincide.

2.2.2 1st and 2nd order transitions

The phase transition at the Curie temperature of a ferromagnet is 2nd order. However, in the case where, e.g., a structural transition co-exists with the magnetic transition, the phase transition may become 1st order. The definition of such a phase transition is the presence of latent heat. The characteristic properties are furthermore

- Sharp and narrow peak in the magnetocaloric properties
- $\frac{\partial S}{\partial T}$ and $\frac{\partial M}{\partial T}$ are infinite at the transition temperature
- Consequently the specific heat is also, theoretically, infinite at the transition temperature
- Hysteresis

Considering 2nd order transitions, there is no latent heat present and the peak of the magnetocaloric properties is wide and more smooth. The derivatives $\frac{\partial S}{\partial T}$ and $\frac{\partial M}{\partial T}$ are discontinuous rather than infinite and consequently the specific heat is also discontinuous at the transition temperature (in zero applied field).

It is often argued that the materials exhibiting a 1st order transition are the most promising candidates for a magnetic refrigeration application due to their large MCE, though usually only around a narrow temperature interval (Pecharsky & Gschneidner, 2006). However, to this date detailed numerical modeling or experimental investigation have not been conducted, to the knowledge of the author, in order to actually evaluate the potential performance of materials exhibiting a 1st order transition. It is at this time thus unclear how the hysteretic losses, the quite sharp shape of the specific heat as a function of temperature and the fact that the specific heat peak temperature may change rather significantly with field will impact the AMR cycle (introduced in Chap. 3).

2.3 Mean field model

The Weiss mean field theory for a ferromagnet can be used to obtain the theoretical magnetization and the magnetic contribution to the specific heat capacity as described in, e.g., Morrish (1965). The specific magnetization can be written as

$$m = N_s g J \mu_B B_J(\chi). \quad (2.13)$$

Table 2.1: The mean field model parameters for gadolinium. Taken from Lide (2004); Tishin & Spichkin (2003).

N_s [kg^{-1}]	g [-]	J [\hbar]	N [kg^{-1}]	θ_D [K]	γ_e [$\text{Jkg}^{-1}\text{K}^{-2}$]
3.83×10^{24}	2	3.5	3.83×10^{24}	169	6.93×10^{-2}

Here N_s is the number of magnetic spins per unit mass, g is the Landé factor, J is the total angular momentum in units of \hbar and the Bohr magneton is denoted μ_B . The Brillouin function is defined as

$$B_J(\chi) = \frac{2J+1}{2J} \coth\left(\frac{2J+1}{2J}\chi\right) - \frac{1}{2J} \coth\left(\frac{1}{2J}\chi\right) \quad (2.14)$$

$$\chi = \frac{gJ\mu_B\mu_0 H}{k_B T} + \frac{3T_C J}{T(J+1)} B_J(\chi).$$

Here the Boltzmann constant k_B was introduced. Naturally, Eq. 2.14 must be iterated to obtain a self-consistent solution.

The magnetic contribution to the specific heat is

$$c_m = -\mu_0 H \frac{\partial M}{\partial T} - 1/2 N_{\text{int}} \frac{\partial m^2}{\partial T}, \quad (2.15)$$

where the mean field constant N_{int} is defined as

$$N_{\text{int}} = \frac{3k_B T_C}{N_s g^2 \mu_B^2 (J+1)}. \quad (2.16)$$

The Debye model can be used to obtain the lattice contribution to the specific heat (Ashcroft & Mermin, 1976)

$$c_l = 9Nk_B \left(\frac{T}{\theta_D}\right)^3 \int_0^{\theta_D/T} \frac{x^4 e^x}{(e^x - 1)^2} dx. \quad (2.17)$$

Here the number of atoms per unit mass, N , and the Debye temperature, θ_D , have been introduced.

Finally, the Sommerfeld model for the free electron contribution to the specific heat is (Ashcroft & Mermin, 1976)

$$c_e = \gamma_e T, \quad (2.18)$$

introducing the Sommerfeld constant γ_e . The mean field model values for Gd are given in Tab. 2.1. It should also be noted that T_C is an input parameter to the mean field model. When deriving magnetization, specific heat, the magnetic entropy change and the adiabatic temperature change using this model these properties will have certain characteristics at T_C . The isothermal entropy change and the adiabatic temperature change both peak at T_C whereas $\frac{\partial M}{\partial T}$ has a global minimum here. In Fig. 2.3 the adiabatic temperature change and the specific heat calculated using the mean field, Debye and Sommerfeld models are plotted.

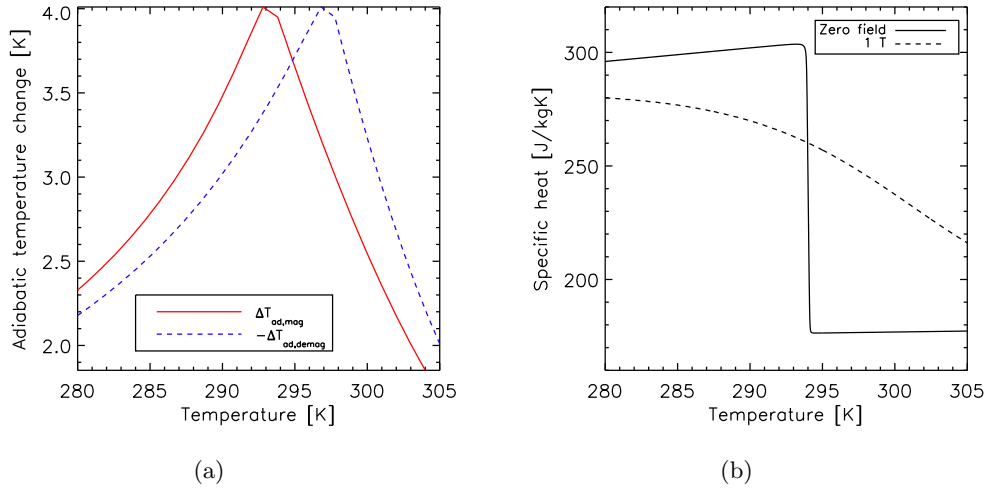


Figure 2.3: The adiabatic temperature change of Gd calculated using the mean field theory (a). The magnetic field change is from 0 to 1 T. The solid (red) curve shows the adiabatic temperature change when magnetizing and the blue dashed line shows it when demagnetizing. In (b) the specific heat calculated using the mean field model is shown.

2.4 Constraints on the adiabatic temperature change

One of the main reasons the MCE is considered as a potential high efficiency way of producing refrigeration is the inherent reversibility of the effect. Magnetocaloric materials exhibiting second-order (continuous) phase transitions have a reversible magnetocaloric effect. It is therefore worthwhile to investigate how the reversibility of the effect influences the fundamental magnetocaloric properties. In this case the adiabatic temperature change is considered.

Consider a ferromagnet in a state where the temperature is T_i and the magnetic field is H_i . When the field is changed adiabatically from H_i to H_f the temperature changes from T_i to T_f . The relation between these four variables is

$$T_f = T_i + \Delta T_{\text{ad,mag}}(T_i, H_i, H_f), \quad (2.19)$$

when $H_f > H_i$ and $\Delta T_{\text{ad,mag}}$ is some function³. Demagnetizing from H_f to H_i at T_f gives

$$T^* = T_f + \Delta T_{\text{ad,demag}}(T_f, H_f, H_i), \quad (2.20)$$

where $\Delta T_{\text{ad,demag}}$ is also *some* function. If the MCE is reversible, then $T^* = T_i$ or

$$\Delta T_{\text{ad,mag}}(T_i, H_i, H_f) = -\Delta T_{\text{ad,demag}}(T_f, H_f, H_i). \quad (2.21)$$

Now, due to the reversibility of the MCE Eq. 2.21 must apply for all temperatures, T , or

$$\Delta T_{\text{ad,mag}}(T, H_i, H_f) = -\Delta T_{\text{ad,demag}}(T + \Delta T_{\text{ad,mag}}(T, H_i, H_f), H_f, H_i). \quad (2.22)$$

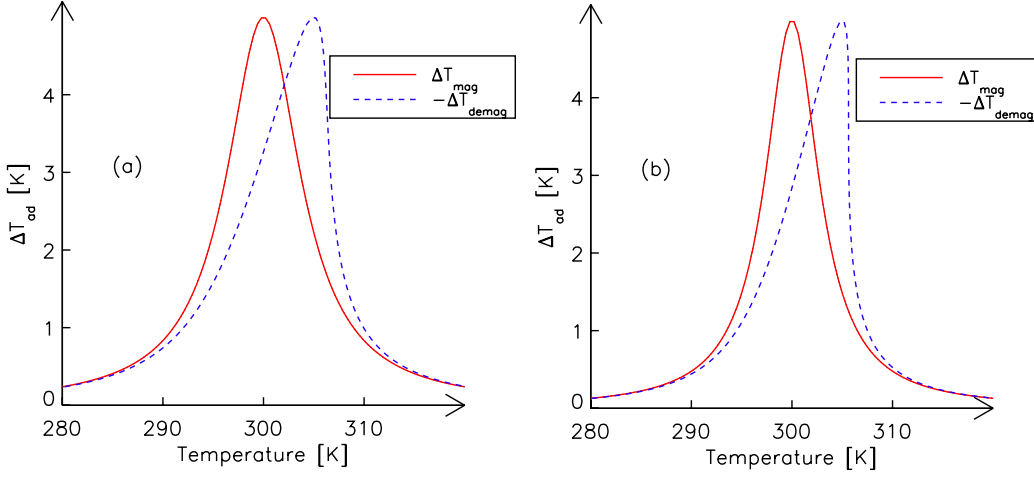


Figure 2.4: The adiabatic temperature change of a model magnetocaloric material both when magnetizing (full red line) and demagnetizing (dashed blue). (a) the slope of the $\Delta T_{\text{ad,mag}}$ is greater than -1 for all temperatures. (b) The slope of the $\Delta T_{\text{ad,mag}}$ curve is exactly -1 at a single temperature above T_* . This results in a demagnetization curve with a vertical tangent at the corresponding temperature. Reproduced from paper A.1.2 (Nielsen et al., 2010b).

Note that $\Delta T_{\text{ad,demag}}$ is negative (if $\Delta T_{\text{ad,mag}}$ is positive).

In the following all H dependence is suppressed, and to emphasize the fact that $\Delta T_{\text{ad,mag}}$ and $\Delta T_{\text{ad,demag}}$ are different functions of temperature the following notation is introduced:

$$f(T) \equiv \Delta T_{\text{ad,mag}}(T, H_i, H_f) \quad (2.23)$$

$$g(T) \equiv \Delta T_{\text{ad,demag}}(T, H_f, H_i). \quad (2.24)$$

In terms of f and g the condition of reversibility becomes:

$$f(T) = -g(T + f(T)). \quad (2.25)$$

This equation allows the determination of g given the measurement of f (and vice versa). In Figure 2.4 are shown corresponding f and g curves. It is clearly apparent that the shape and maximum point of the two curves differ. The general shape of the curves is one appropriate for pure materials (i.e. not containing grains of different composition and Curie temperature) where the adiabatic temperature change upon magnetization for a given set of H_i and H_f has a single maximum at $T = T_*$, and no other local extrema. This maximum will be close to the Curie temperature T_C but will in general not coincide with it (Pecharsky et al., 2001); indeed, it will often depend on H as discussed in Sec. 2.2.

Read from right to left equation (2.25) states that a material in field at a temperature $T + f(T)$ will, when demagnetized, cool to T . A magnetized material demagnetized from a starting temperature T_s will cool to a unique temperature T_e which obeys $T_s = T_e + f(T_e)$. The uniqueness implies that $T + f(T)$ is one-to-one

³Assumptions about this function will be provided shortly.

considered as a function of temperature. Furthermore, the magnetized material may obviously be demagnetized from any starting temperature T_s by connecting it to a heat bath at an appropriate temperature while in field; isolating it thermally; and then removing the field. This means that $T + f(T)$ must also map the entire temperature range $[0, T_s]$ onto itself. Taken together with the fact that it is one-to-one this implies that $T + f(T)$ is an invertible function. If $f(T)$ is continuous a necessary and sufficient condition for this to be the case is that $T + f(T)$ is monotonically increasing in the entire range $[0, T_s]$ (*increasing*, given that $f(T)$ approaches 0 for $T \rightarrow 0$ and $T \rightarrow T_s$), i.e. that the derivative is greater than zero for all T : $d(T + f(T))/dT > 0$, or

$$\frac{d(\Delta T_{\text{mag}}(T, H_i, H_f))}{dT} > -1. \quad (2.26)$$

It is noted that assuming that f and g are differentiable — which is a reasonable assumption for real materials, at most excepting a finite number of temperatures — the following is obtained:

$$f'(T) = -\frac{1}{1 + g'(T + f(T))^{-1}}. \quad (2.27)$$

From this it is seen that if $f'(T)$ approaches -1 at a given temperature T_1 , the demagnetization curve g becomes steeper and steeper, and when $f'(T_1)$ reaches -1 the derivative of g becomes infinite at the corresponding temperature $T_1 + f(T_1)$, i.e. the curve becomes vertical at this point. This is shown on Figure 2.4b. It is stressed, however, that differentiability is not a *necessary* condition for the constraint in Eq. 2.26 to be valid, albeit it is a sufficient condition when assuming reversibility. The two necessary conditions are continuity and reversibility. In the following these two conditions are discussed in terms of their impact on the adiabatic temperature change in conjunction with the constraint in Eq. 2.26.

2.4.1 Irreversible, first order materials

For magnetocaloric materials exhibiting a first-order phase transition, the magnetocaloric effect can be irreversible due to hysteretic losses (Morrison et al., 2009). In such cases, the equality Eq. 2.22 is changed into an inequality:

$$\Delta T_{\text{mag}}(T_0, H_i, H_f) > -\Delta T_{\text{demag}}(T_0 + \Delta T_{\text{mag}}(T_0, H_i, H_f), H_f, H_i). \quad (2.28)$$

It is important to note that this irreversibility is limited to a temperature interval in the vicinity of the phase transition (Morrison et al., 2009). Outside this temperature interval, the magnetocaloric effect is still reversible and the arguments of the previous section still apply, and in particular the constraint Eq. (2.26) applies.

Inside the irreversibility region it is possible to use the general shape of the $T - S$ -diagram for a first-order material to place limits on the variation of ΔT_{mag} . Pecharsky et al. (2001) consider such a material having a first order phase-transition from a low temperature phase to a high temperature phase at a temperature $T_{\text{pt},1}$ in zero field. At a field H the transition temperature will be $T_{\text{pt},2} > T_{\text{pt},1}$. Such a material will in the vicinity of the phase transition have an $T - S$ -diagram as shown schematically in Figure 2.5. For an ideal first-order transition, the entropy will be

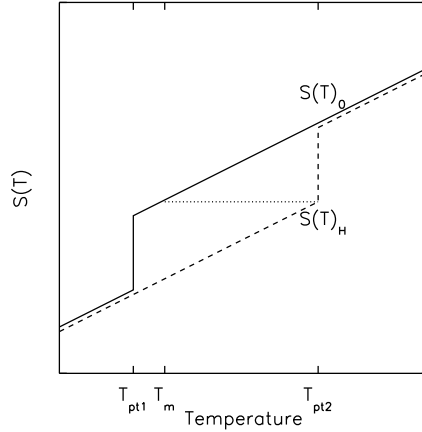


Figure 2.5: Schematic $T - S$ -diagram for a first-order material (after Pecharsky et al. (2001)). Horizontal lines between the two curves with field 0 (full line) and H (dashed line) correspond to the adiabatic temperature change ΔT_{mag} . The adiabatic temperature change has its maximum in the temperature interval between $T_{\text{pt},1}$ and T_m (defined geometrically as shown). For $T_m < T < T_{\text{pt},2}$ the adiabatic temperature change decreases as $\Delta T_{\text{mag}} = T_{\text{pt},2} - T$ due to the vertical entropy curve at $T_{\text{pt},2}$. If the transition is not strictly first order, the entropy curve will have a finite, positive slope at $T_{\text{pt},2}$ and the decrease of ΔT_{mag} will be slower. Reproduced from paper A.1.2 (Nielsen et al., 2010b).

discontinuous, i.e. the entropy curves will be vertical at $T_{\text{pt},1}$ and $T_{\text{pt},2}$, respectively. The temperature T_m is defined by the following equation

$$S(T_m, 0) = S(T_{\text{pt},2}, H), \quad (2.29)$$

Above T_m , ΔT_{mag} will decrease linearly with T until $T_{\text{pt},2}$ is reached, as can be seen geometrically from the figure, i.e. $\Delta T_{\text{ad,mag}} = T_{\text{pt},2} - T$. This means that for $T_m < T < T_{\text{pt},2}$ the following equality applies:

$$\frac{d(\Delta T_{\text{mag}}(T, H))}{dT} = -1. \quad (2.30)$$

In the interval $T_{\text{pt},1} < T < T_m$ the slope of the adiabatic temperature change is strictly greater than -1 . In this interval the adiabatic temperature change attains its maximum value, which may be at more than one temperature. Indeed, direct measurements show plateau-like maximum adiabatic temperature changes (Burriel et al., 2005).

Thus, for first order materials the strict inequality Eq. (2.26) is replaced by:

$$\frac{d(\Delta T_{\text{mag}}(T, H))}{dT} \geq -1, \quad (2.31)$$

valid for all T . Fig. 2.6 shows an example of the MCE in a material exhibiting a 1st order transition and it is seen that the constraint in Eq. 2.31 is indeed not violated.

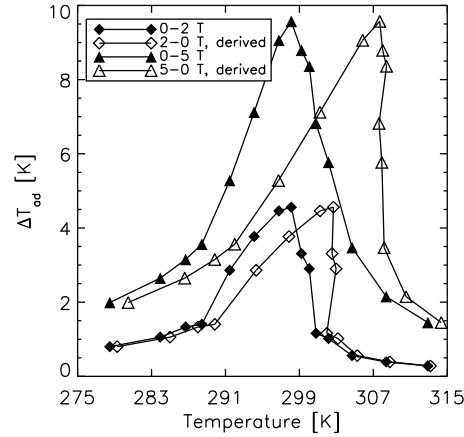


Figure 2.6: The adiabatic temperature change of $\text{Mn}_{1.03}\text{As}_{0.7}\text{Sb}_{0.3}$ as a function of temperature and for applied magnetic fields of 2 and 5 T. The data used is from Wada et al. (2007) with permission from Dr. H. Wada (private communication). The “derived” data are calculated using Eq. 2.22 and the experimentally observed adiabatic temperature change data. Reproduced from paper A.1.2 (Nielsen et al., 2010b).

“Discontinuous materials”

As shown above, a sufficient condition for the validity of the constraint, Eq. (2.26) (reversible materials) or Eq. (2.31) (irreversible materials), is that $f(T) = \Delta T_{\text{mag}}$ should be a continuous function of temperature. In this section it is shown that a discontinuous, reversible ΔT_{mag} can indeed violate the inequality. To do this a model shape of a discontinuous $f(T)$ with $df/dT < -1$ in a given interval is constructed. For simplicity a constant slope $\alpha < -1$ is chosen:

$$f(T) = \begin{cases} \beta_1(T) & \text{for } T < T_1 \\ \Delta T_0 + \alpha(T - T_1) & \text{for } T_1 < T < T_2 \\ \beta_2(T) & \text{for } T > T_2 \end{cases} \quad (2.32)$$

Here T_1 , T_2 and ΔT_0 are constants, while β_1 and β_2 are arbitrary functions obeying $d\beta_1/dT > -1$ and $d\beta_2/dT > -1$, with the limiting values of $\beta_1(T_1) = \Delta T_0 + (1 + \alpha)(T_2 - T_1)$ and $\beta_2(T_2) = \Delta T_0 - (T_2 - T_1)$. These values are chosen to make $T + f(T)$ invertible and thus ensure that Eq. (2.25) can be fulfilled for all temperatures. In Fig. 2.7 an example of such a discontinuous f and the corresponding $g(T) = \Delta T_{\text{demag}}$ are shown.

It may be asked if such discontinuous materials actually exist. While the author is not aware of any direct reports in the literature of such magnetocaloric materials it is not completely inconceivable that they could exist. Consider, e.g. a material with competing structural and magnetic transitions. A low-temperature magnetic state with a Curie temperature $T_{C1} > T_0$ (or indeed a non-magnetic state) is destabilized by a structural phase transition at $T = T_0$ in favor of a second magnetic state with a Curie temperature $T_{C2} \leq T_0$. This second phase does not manifest itself at the low-temperature side of T_0 due to the structural phase transition. At $T = T_1$ the

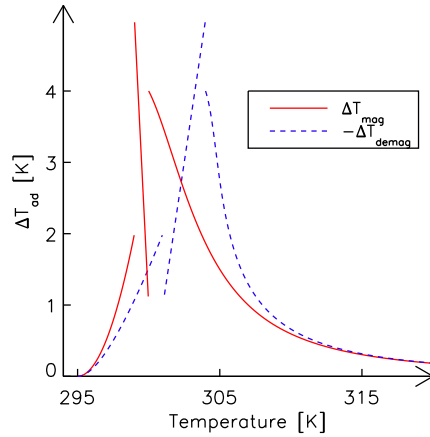


Figure 2.7: The adiabatic temperature change of a fictitious reversible magnetocaloric material with a discontinuous magnetocaloric effect. The full red line is the magnetization curve whereas the dashed blue line is the demagnetization curve. It is observed that such a material fulfils the reversibility criterion in Eq. 2.22 even though the slope of ΔT_{mag} is less than -1 over an entire temperature interval. Note that discontinuity is a necessity for the constraint in Eq. 2.26 to be invalid. Reproduced from paper A.1.2 (Nielsen et al., 2010b).

second phase is destroyed due to another structural instability in favor of a third phase with a Curie temperature T_{C3} .

While such an interplay of phases may seem unlikely, the example at least shows that there are no obvious theoretical reasons forbidding a discontinuous variation of ΔT_{mag} with temperature.

2.5 Experimental determination of the MCE

At the Fuel Cells and Solid State Chemistry Division at Risø DTU three experimental setups for measuring the MCE and related properties are located. These are a Vibrating Sample Magnetometer (VSM), a Differential Scanning Calorimeter (DSC) and a device for measuring the adiabatic temperature change.

The VSM (LakeShore 7407) measures the bulk magnetization of a sample in a homogeneous applied field and as a function of temperature. The maximum field is 1.6 T and the temperature may be varied from 85 to 450 K using a liquid nitrogen cryostat. The equipment allows for either temperature sweeping at constant field or field sweeping at constant temperature. Using this equipment the magnetization may thus be measured as a function of the magnitude of the applied field, H_{appl} , and T .

The DSC (built in-house) measures the heat flux through a sample when a fixed temperature ramp rate is applied (using a feedback loop). In this way the specific heat may be obtained. The device operates from around 235 to 320 K and an applied field of up to 1.5 T using a variable permanent magnet may be applied, such that the specific heat can be measured as a function of both H_{appl} and T similar

Table 2.2: Relevant properties of selected magnetocaloric materials. The values of LCSM and LaFeCoSi are estimates since the exact data for each specific composition has not been measured. The data in this table are from Jacobsson & Sundqvist (1989); Visser et al. (1997); Fujieda et al. (2004); Fukamichi et al. (2006). k is the thermal conductivity and ρ is the mass density.

	k [W/mK]	ρ [kg/m ³]
LCSM	1	6000
LaFeCoSi	9	7100
Gd	10.5	7900

to the magnetization. In Jeppesen et al. (2008) the DSC is outlined in detail.

The device for measuring the adiabatic temperature change (the so-called $\Delta T_{\text{ad-ometer}}$ ⁴) is able to move a sample in and out of a magnetic field region (which may be adjusted from 0 to 1.5 T) rather fast (< 200ms) using compressed air. The ambient temperature may be controlled from 255 to 320 K and in this way it is thus possible to measure $\Delta T_{\text{ad,mag}}(T, H_{\text{appl}})$ and $\Delta T_{\text{ad,demag}}(T, H_{\text{appl}})$. In Bjørk et al. (2010) this device is described in details.

These devices enable the characterization of magnetocaloric materials around room temperature, so that such materials may be evaluated, compared and the data used in, e.g., a numerical AMR model.

In the following the magnetocaloric properties of various magnetocaloric materials are presented. This is done for two reasons: first, the data is scientifically interesting in itself and thus serves to provide an overview for the reader. Secondly, the data is used in both the AMR model (presented in Chapters 3–6) and the demagnetization model (presented in Chapter 7).

Two material series are presented. First the $\text{La}_{0.67}\text{Ca}_{0.33-x}\text{Sr}_x\text{Mn}_{1.05}\text{O}_3$ ⁵ has been characterized.⁶ This material, abbreviated LCSM, is a ceramic material with magnetocaloric properties. The Curie temperature may be tuned by adjusting the parameter x , i.e. the ratio between the Ca and the Sr content. When the material is pure LCM, i.e. $x = 0$, the Curie temperature is around 267 K and the material exhibits a 1st order transition (Dinesen, 2004). When the material is pure LSM, i.e. $x = 0.33$, the material exhibits a second order transition with a Curie temperature of 367 K (Dinesen, 2004).

The other material series considered is $\text{LaFe}_{13-x-y}\text{Co}_x\text{Si}_y$, which has been provided by Vacuumschmelze GmbH, Germany. The material is abbreviated LaFeCoSi. By adjusting the ratio between x and y the Curie temperature of the material may be adjusted. It is noted that the experimental data was obtained and the post processing was performed by Dr. R. Bjørk at Risø DTU. A few other relevant properties

⁴A quite irrelevant note for the work of this thesis: This device is actually named “The dunker” due to its very characteristic sound when moving the sample in and out of field. A more proper English translation is not available at this time, unfortunately.

⁵Note that the manganese is over-stoichiometric, which has been experimentally found to yield better sintering properties.

⁶It is emphasized that the actual experiments were performed by Dr. Carlos Eugenio Ancona-Torres and Dr. Radha Krishnan Venkatesh, both at Risø DTU, and that the data are subject for future publication. The post-processing of the experimental data was performed by the author of this thesis.

of these materials are given in Tab. 2.2.

Properties of LCSM

Figure 2.8(a) shows the adiabatic temperature change when applying a field of 1 T and Fig. 2.8(b) the specific heat in zero field and for an applied field of 1 T of the LCSM when x is varied from 0.0375 to 0.09. It is apparent from the figure that the peak value of both the adiabatic temperature change and the specific heat decreases with increasing peak temperature and that the peak temperatures of both the adiabatic temperature change and the specific heat increase as x increases, which is in close resemblance with the results of Dinesen (2004).

The magnetization and the derivative of the magnetization with respect to temperature are plotted in Figs. 2.8(c)–(d). An interesting observation from the figure is that the minima of $\frac{\partial M}{\partial T}$ are at lower temperatures than the peak temperatures of the adiabatic temperature change and the specific heat. This simple observation serves to show that considering the Curie temperature as a sufficiently characterizing property for a specific material composition may be inadequate.

Now, these magnetocaloric properties are important in many aspects and in Chapters 5, 6 and 7 they will be applied in an AMR and a magnetostatic model, respectively. In this way a deeper analysis of the behavior of the LCSM material series, when applied to a magnetic refrigeration scenario, can be mapped.

Properties of LaFeCoSi

The magnetization and $\frac{\partial M}{\partial T}$ of the LaFeCoSi series are given in Fig. 2.9. The data of three different compositions are plotted. In the figure legend each individual curve is indicated by a “ T_C ”, which is the temperature at the inflection point of the magnetization or the minimum value of its derivative with respect to temperature. These data will be applied in the AMR modeling of experimental AMRs in Chap. 6 and in the demagnetization model presented in Chap. 7.

2.6 Summary

In this chapter the magnetocaloric effect was introduced from a basic thermodynamic point of view by considering the entropy of a magnetic material. This led to the derivation of the adiabatic temperature change and the isothermal entropy change as a function of temperature and magnetic field. It was emphasized that the magnetic field considered is the internal field of the sample. This is a most important point and Chap. 7 is devoted entirely to the calculation of this quantity in a range of different configurations including magnetic materials, temperature profiles, material compositions etc.

As a natural consequence of discussing the MCE from a thermodynamic point of view the Curie temperature was introduced and defined. It was concluded that the T_C itself is insufficient for fully characterizing an MCM and that the peak temperatures of the various properties (adiabatic temperature change, isothermal entropy change and specific heat) should be reported when considering the magnetocaloric characterization of MCMs. The two types of phase transitions, 1st and 2nd order,

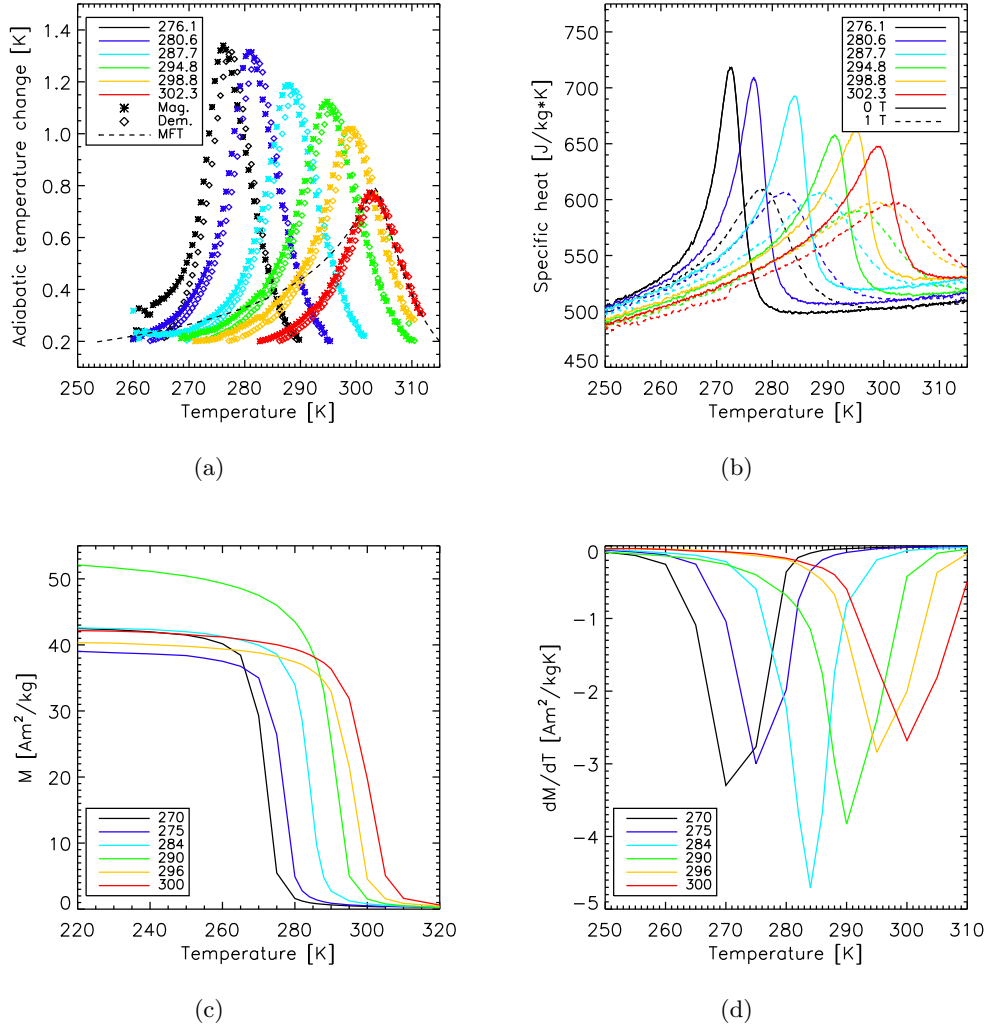


Figure 2.8: The adiabatic temperature change (a) of LCSM when applying a magnetic field of 1 T and the specific heat (b) in zero field and for an applied field of 1 T. The legend indicates the peak temperature of the adiabatic temperature change. The MFT-calculated adiabatic temperature change of LCSM with a $T_C = 302$ K is added for comparison. In (c) the magnetization of the samples is plotted and in (d) $\frac{\partial M}{\partial T}$ is plotted. In both cases the indicated temperatures in the legend represent the inflection points of the magnetization. The colors correspond to the same materials in the figures.

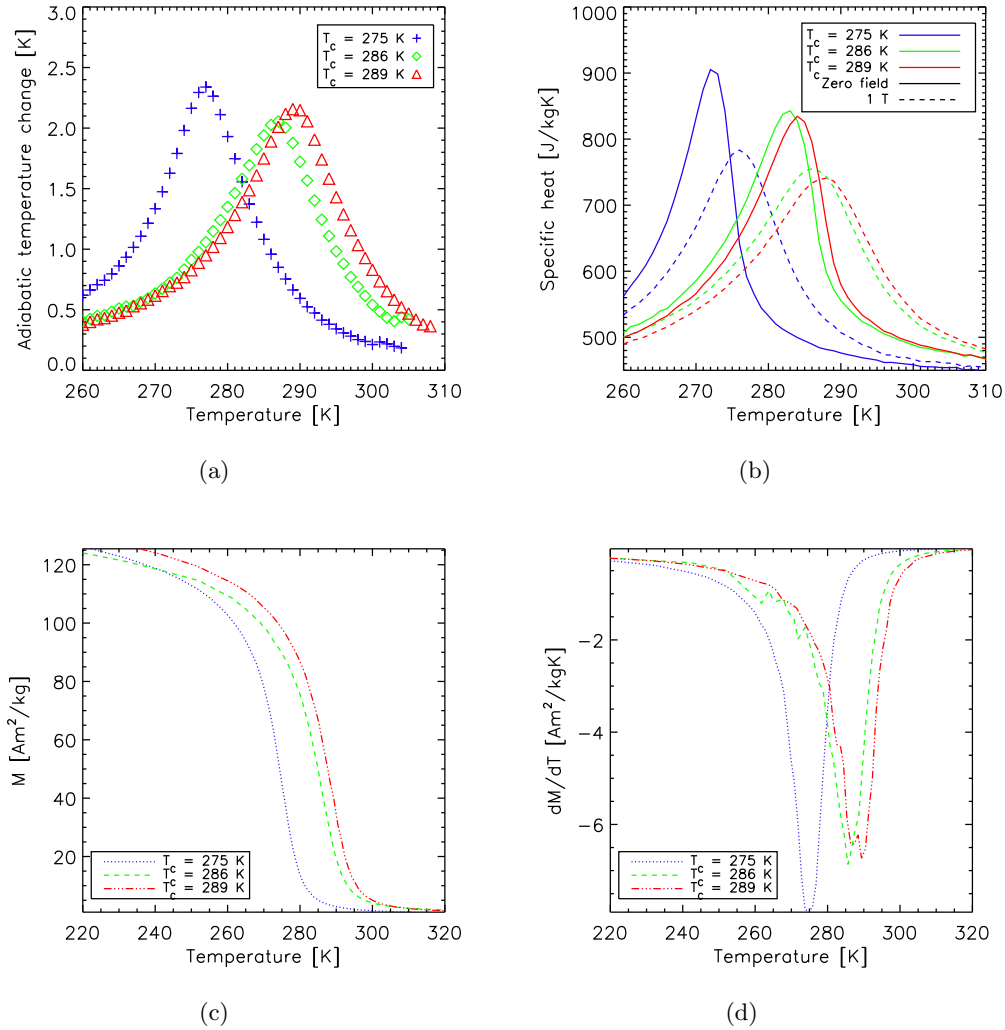


Figure 2.9: The adiabatic temperature change when magnetizing from zero to 1.0 T (internal field) is given in (a), the specific heat in (b), the magnetization (c) (in an internal field of 0.1 T) and the derivative of the magnetization (d) of the three samples of LaFeCoSi. Their respective inflection points are indicated in the figure legend, i.e. the minima of $\frac{\partial M}{\partial T}$. The data was obtained by Dr. R. Bjørk and is published in a slightly different form in Bjørk et al. (2010).

were introduced, defined and discussed. These may have a significant impact on the performance of a magnetic refrigerator. This will be further discussed in Chapter 8.

In order to calculate the magnetocaloric properties the mean field model for a ferromagnet was introduced. This model enables the full theoretical characterization of a 2nd order magnetocaloric material.

Having introduced the basics of the MCE a constraint on the adiabatic temperature change was introduced. This was derived from the most fundamental assumption of reversibility and continuity of the MCE expressed as the adiabatic temperature change.

Finally, the experimental determination of the magnetocaloric properties was

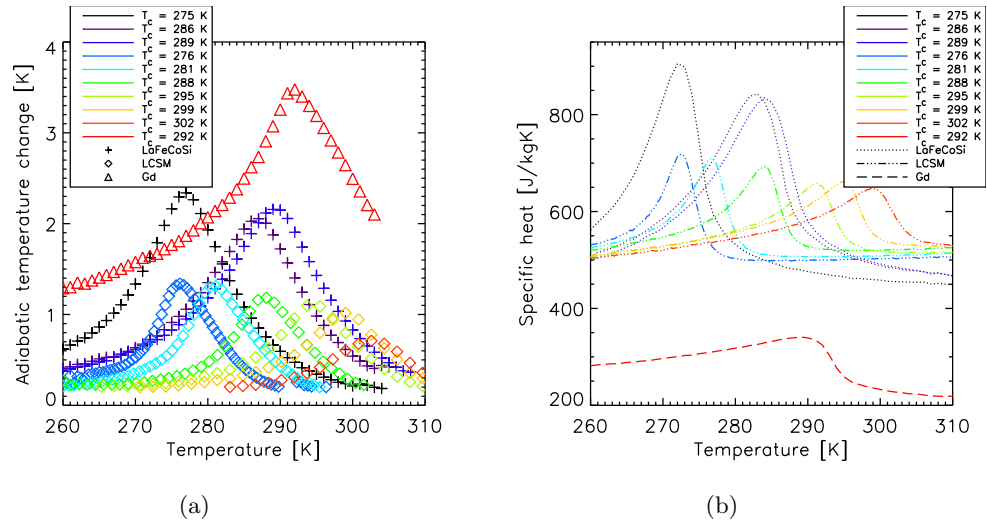


Figure 2.10: The adiabatic temperature change of all materials considered here ((a). Gadolinium data has been added to the figure for comparison (data from Bjørk et al. (2010)). The internal field is 1.0 T. In (b) the specific heat of the same materials (in zero field) has been added. The data was obtained by various people including Dr. R. Bjørk, Dr. C. Ancona-Torres and Dr. R.K. Venkatesh all at Risø DTU.

introduced and a range of such properties was given for several different kinds of magnetocaloric materials. These properties will, to some extent, be used in the remainder of this thesis as input parameters to both the AMR model, which is considered in Chapters 3–6 and the demagnetization model introduced and discussed in Chap. 7. In this way the presentation of the experimental data is not only interesting in itself but serves as very important input information for the numerical models. Fig. 2.10 provides an overview of the magnetocaloric data used in the remainder of this thesis.

Chapter 3

The active magnetic regenerator

The following chapter is devoted to the development, numerical implementation and validation of a 2-dimensional AMR model. The model was previously implemented in the commercial finite-element based software package Comsol (Comsol, 2005) by Petersen et al. (2008b). The new implementation of the model has been done using Fortran and a different numerical scheme. This has yielded a performance gain of a factor of 100 compared to the previous model, which has enabled rather large parameter studies to be feasible in terms of computational time. The chapter is outlined in the following way. First, the active magnetic regenerator cycle is presented in Sec. 3.1. Second, the development of a numerical AMR model is discussed in Sec. 3.2. The model is validated against certain known cases and previous established models in Sec. 3.3. Finally, in Sec. 3.4 the chapter is summarized. This chapter is based partially on paper A.1.6 (Nielsen et al., 2009a).

3.1 The AMR cycle

The MCE in a realistic scenario involving permanent magnets producing a flux density of 1.5 T maximum is only a few degrees. This means that in order to generate usable refrigeration, with a temperature span significantly greater than a few degrees, the MCE must be used as the active component in a regenerator cycle as suggested by Barclay (1983).

The thermodynamic cycle utilized in most magnetic refrigeration devices is denoted the active magnetic regenerator (AMR) cycle. This is a composite thermodynamic cycle consisting of four independent thermodynamic processes, namely two iso-field and two that are adiabatic. In close conjunction with the thermal storage in the regenerator matrix, which is made of the magnetocaloric material, the MCE is enhanced from the few K a single-blow technique would yield to several times this temperature span. Care should be taken when considering the AMR cycle. It cannot be described as a conventional thermodynamic cycle, but should rather be considered as an infinite series of infinitesimal thermodynamic processes experienced locally in the regenerator (Rowe & Barclay, 2003). In Fig. 3.1 an illustration of the analogy between a conventional vapor-compression based refrigeration cycle and the AMR cycle is given.

Figure 3.2 shows the $T - S$ -diagram of the AMR cycle at a given point in the regenerator. The entropy should thus be considered as the total entropy of

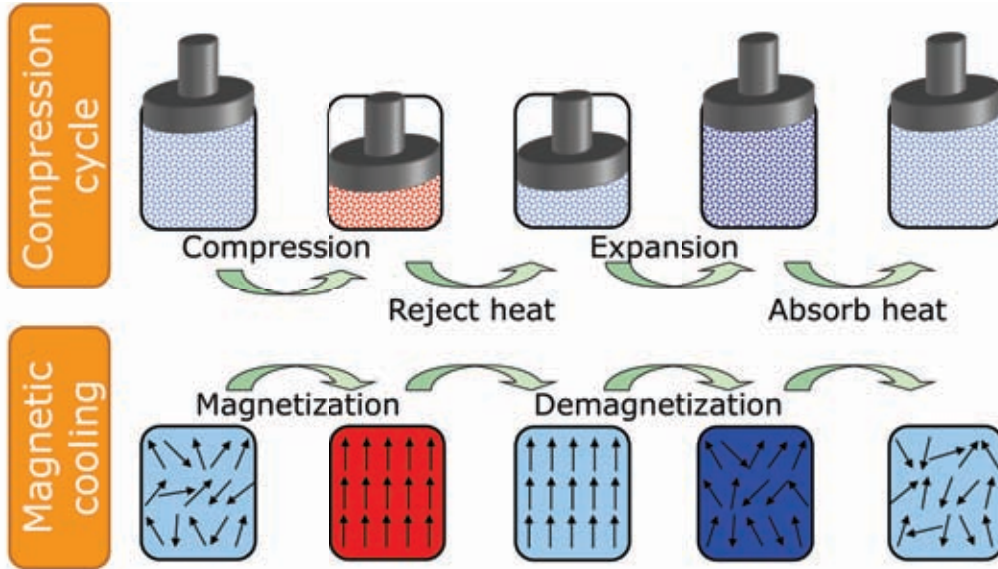


Figure 3.1: Illustration of the analogy between a conventional vapor-compression based refrigeration cycle and the AMR cycle. It is important to note that the AMR cycle takes place at a localized point in the regenerator since a temperature gradient is present along the flow direction of the regenerator and the whole system may therefore not be described a unique thermodynamic cycle. When the magnetic material is magnetized the temperature increases, which corresponds to the compression of a gas. Heat is then rejected to the ambient bringing the system back to the temperature it had before magnetization / compression. The magnetic material is then demagnetized corresponding to the expanding of a gas. In this way a temperature below the initial temperature is reached. Finally, a heat load is absorbed and the cycle restarts.

such a “unit cell” including both the solid and the fluid. Starting in point A and moving clockwise around in the diagram the cycle is described as follows. First, the magnetocaloric material (MCM) is adiabatically exposed to a positive change in magnetic field thus increasing its temperature (Fig. 3.3(a)). Secondly (from B to C in the diagram (Fig. 3.2) and Fig. 3.3(b)), the heat transfer fluid is moved from the cold end to the hot end (the so-called “hot blow”) thus absorbing heat from the regenerator and rejecting it to the surroundings via the hot heat exchanger (HHEX). Third, (from C to D in Fig. 3.2; see also Fig. 3.3(c)) the magnetic field is removed and the MCM cools adiabatically. Finally, the heat transfer fluid is moved from the hot to the cold end (the so-called “cold blow”) thus absorbing heat from the cold heat exchanger (CHEX) (D to A in Fig. 3.2; see also Fig. 3.3(d)). Thus, the physical problem of the AMR cycle includes an interaction between a temporally (and potentially spatially) changing magnetic field, a regenerator matrix made of one or several magnetocaloric materials and an oscillating flow of a heat transfer fluid. The following section describes this interaction mathematically.

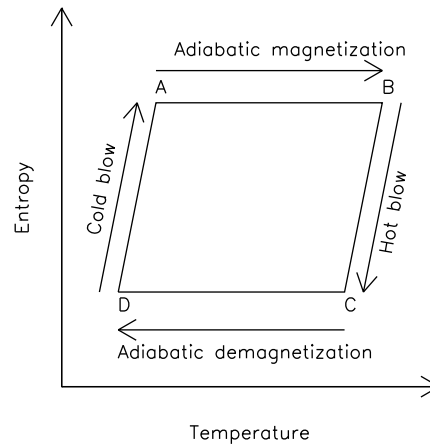


Figure 3.2: The AMR cycle is split in four individual processes including two adiabatic and two isofield processes. The schematic in this figure shows the $T-S$ -diagram of this process for an infinitesimal part of the regenerator. It is important to stress that the AMR cycle cannot be described solely by this diagram; the regenerator physics are not described here but rather in the transient and spatial partial differential equations given in Eqs. 3.1-3.2.

3.2 Development of a numerical AMR model

The numerical model is two-dimensional and simulates half a replicating cell, i.e. half a plate of MCM and half a fluid channel. The x -direction is parallel to the plates and is also the direction of the flow. The y -direction is perpendicular to the plates and the z -direction is not represented by the model, i.e. the flow channels and plates are assumed to have infinite width. This is a good approximation in terms of the flow, but maybe insufficient in the long run in terms of the thermal coupling to the ambient via the boundary conditions. This means that losses are not assumed in the original model.

Next to the plates are two flow-guides assumed to be made of a perfect insulation material (one on each side) and next to these are two heat exchangers; a cold (CHEX) and a hot (HHEX) corresponding to inside and outside of the refrigerator, respectively. The virtual flow guides are assumed to work as a passive extension of the regenerator material such that a constant channel thickness may be maintained throughout the whole domain. In Fig. 3.4 a schematic shows the geometry. The solid materials, i.e. heat exchangers, insulating material and MCM, are fixed with respect to each other at all times during the simulations. However, they are allowed to move with respect to the fluid channel thus modeling a fluid movement.

This leaves the boundary conditions to be either adiabatic (every symmetry and outer boundary except the upper boundaries of both heat exchangers) or thermally coupled inner boundaries (between the solids and the fluid). The governing

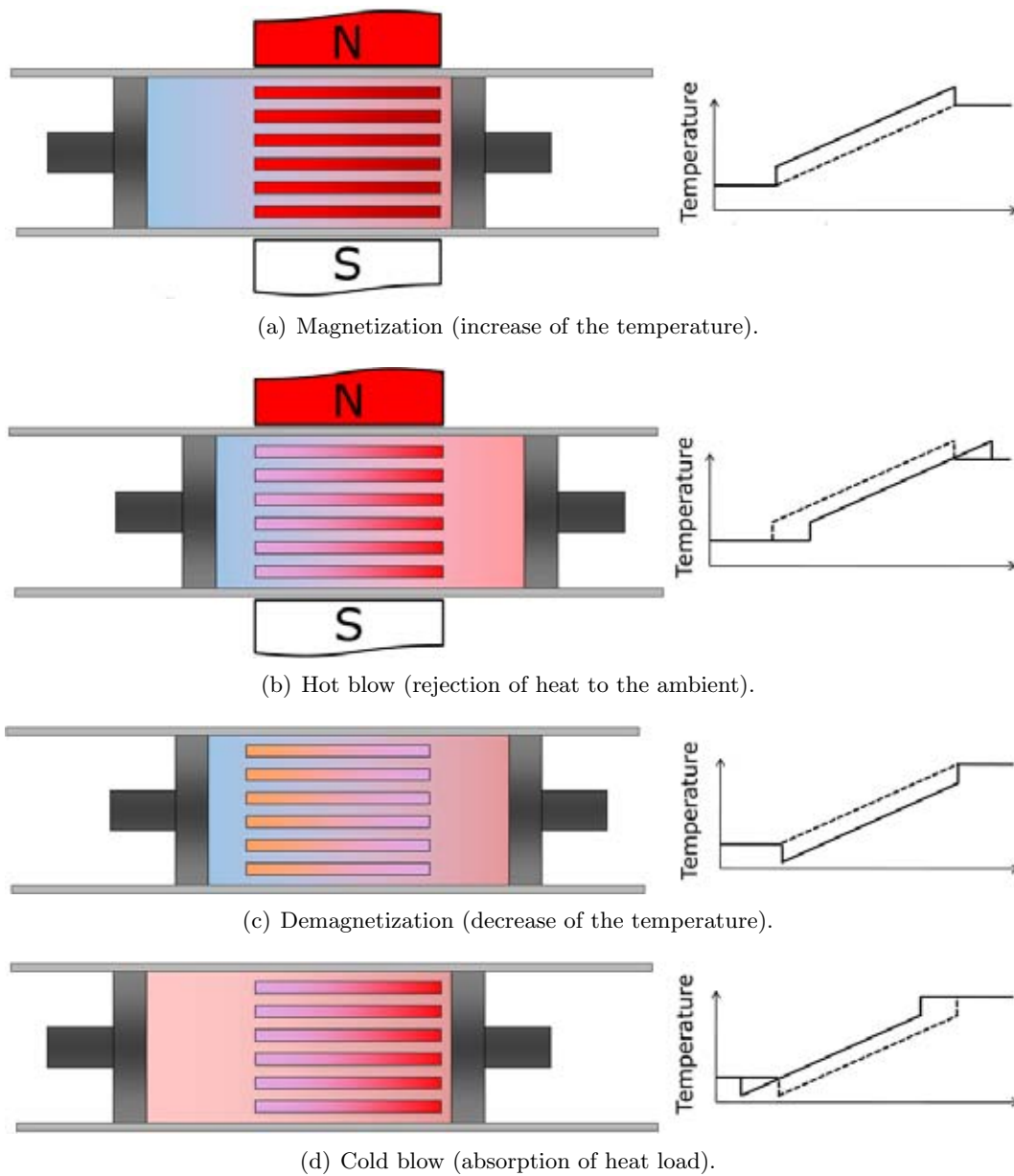


Figure 3.3: Schematic of the four processes, which the AMR cycle consists of.

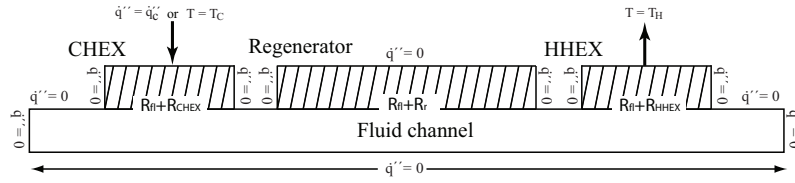


Figure 3.4: The computational domain of the numerical AMR model. The heat exchangers (HEX) are indicated as are the fluid channel and the regenerator solid. The boundary conditions are indicated and all symmetry and outer boundaries are seen to have zero heat flux ($\dot{q}'' = 0$) except the two heat exchangers. Here, either a boundary flux (\dot{q}'') or a temperature can be set. The internal boundaries are indicated with their respective thermal resistance. The figure is from Petersen (2007) and has been slightly modified.

equations of the thermal system are:

$$\frac{\partial T_f}{\partial t} = \frac{k_f}{\rho_f c_f} \left(\frac{\partial^2 T_f}{\partial x^2} + \frac{\partial^2 T_f}{\partial y^2} \right) - (\mathbf{u} \cdot \nabla) T_f, \quad (3.1)$$

$$\frac{\partial T_s}{\partial t} = \frac{k_s}{\rho_s c_s} \left(\frac{\partial^2 T_s}{\partial x^2} + \frac{\partial^2 T_s}{\partial y^2} \right). \quad (3.2)$$

With subscripts s and f denoting solid and fluid, respectively. In fact, since three solid domains are present the subscript s describes each of these. Equation 3.1 consists of the diffusion term and the convective term, which is induced by the movement of the fluid. The velocity field, \mathbf{u} , is obtained from solving the Navier-Stokes equations for the flow problem. Equation 3.2 only contains the diffusion term (and obviously the transient term). The thermal conductivity is denoted by k , the mass density is ρ and the specific heat capacity is c ; all with the appropriate subscripts. All thermal and material properties are assumed constant except the heat capacity of the MCM. In Table 3.1 the values of the thermal properties assumed are given.

This formulation of the thermal equation system is done also under the assumption that the change in magnetic field (both up and down) is done instantaneously so that the temperature change in the regenerator can be assumed to be adiabatic and thus Eq. 2.5 can be used to calculate the temperature change. This

Material/property	k [W/m · K]	ρ [kg/m ³]	c_p [J/kg · K]
HEX (copper)	401	8933	385
Fluid (water)	0.595	997	4183
MCM (Gd)	10.5	7900	170-300 (approx.)
Housing (plastic)	0.2	800	1250

Table 3.1: The table shows the thermal and material properties of relevant materials around room temperature. In general, all the properties are assumed to be constant except the heat capacity of Gd, which varies strongly both as a function of temperature and magnetic field. The values are obtained from Lide (2004); Tishin & Spichkin (2003).

is, however, a short-coming of the original model. Formulating the MCE as a source term in Eq. 3.2 for the regenerator material (subscript r, which underlines that the solid domain considered here is the active regenerator material only) gives the following

$$\rho_r c_r \frac{\partial T_r}{\partial t} = k_r \left(\frac{\partial^2 T_r}{\partial x^2} + \frac{\partial^2 T_r}{\partial y^2} \right) + Q_{\text{MCE}}. \quad (3.3)$$

The term Q_{MCE} can be derived fairly easy by considering the change in entropy of an MCM when subjected to a magnetic field given by

$$\frac{ds}{dt} = \frac{c_H}{T} \frac{dT}{dt} + \mu_0 \frac{\partial m}{\partial T} \frac{dH}{dt}. \quad (3.4)$$

Assuming the change is adiabatic, the temperature change is found by setting $\frac{ds}{dt} = 0$:

$$\left. \frac{dT}{dt} \right|_{\text{MCE}} = -\mu_0 \frac{T}{c_H} \frac{\partial m}{\partial T} \frac{dH}{dt} \quad (3.5)$$

$$Q_{\text{MCE}} = -\rho T \mu_0 \frac{\partial m}{\partial T} \frac{dH}{dt}. \quad (3.6)$$

Finally, in order to model the fluid flow period the solid domains are moved with respect to the fluid domain¹. In Sec. 3.2.4 the implementation details of the moving boundaries are outlined.

3.2.1 Numerical implementation

How the numerical discretization is done spatially and temporally is equally important. However, the two different parts of the numerical model are completely separated in the sense that either one can be exchanged with whatever scheme one would like. For the spatial discretization finite differences of first and second order (also known as the classical centered difference scheme) are used and for the temporal integration of the PDEs an Alternate Direction Implicit (ADI) solver is used. Several fully explicit schemes (i.e. 2nd and 4th order Runge-Kutta and 1st order forward Euler) were also tried for the temporal integration, but it turned out that the timestep criterion was too conservative in the sense that the highly thermally conductive copper heat exchangers required an unrealistically low timestep (of the order $10^{-6} - 10^{-7}$ seconds). Thus, the ADI solver was preferred since it is unconditionally stable numerically. This has, however, turned out to be not entirely true due to the moving boundary conditions (see Section 3.2.3).

To solve equations like 3.1 and 3.2 numerically one can choose between many different approaches once the numerical scheme has been decided. Here an actual numerical derivation is chosen (as opposed to using an operator formulation). The discretized energy equation is:

$$\Delta x \Delta y \Delta z \rho c_H \frac{T^* - T^0}{\Delta t} = \sum_{\text{bd}} q_{\text{bd}} + Q_{\text{source}}, \quad (3.7)$$

¹This is of a technical nature. Since the solid domains are smaller than the fluid domain it is more efficient to move these.

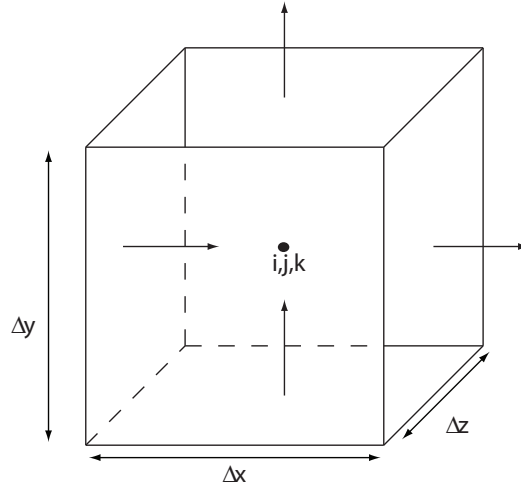


Figure 3.5: An example numerical grid cell is shown. At the centre, i, j, k , the temperature is defined for the entire cell and at each face a boundary flux is specified dependent on how the spatial discretization is defined.

where the lefthand side is the transient term including the timestep Δt , the new temperature $T^* = T(x, y, t + \Delta t)$ (i.e. the temperature at time $t + \Delta t$) and the old temperature $T^0 = T(x, y, t)$, i.e. the temperature at time t . The righthand side of the equation consists of the sum of the boundary fluxes, q_{bd} , and any given source terms (in this formulation also including the convective term since only well-behaving fully developed, steady and laminar flows are assumed). Now, the formulation given in Eq. 3.7 is the fundamental description of energy conservation for a virtual numerical grid cell with dimensions Δx , Δy and Δz (see Fig. 3.5). The formulation simply dictates that whatever temporal change there is in energy of a defined volume is given only by what the volume contained at time t , what came and left through the boundaries and what somehow evolved during the timestep (e.g. in the case of the MCE an adiabatic temperature change due to an external change in magnetic field). Thus, and this should be emphasized, this formulation dictates *strict* energy conservation as opposed to the finite element method (FEM) which works with fluxes in node-points and not on entire boundaries and therefore must rely on the precision of interpolation methods.

The boundary fluxes are given, for a completely internal cell, directly by Fourier's law of heat conduction for a material with constant thermal conductivity:

$$q_{bd} = -k_m A \frac{\Delta T}{L}, \quad (3.8)$$

where k_m is the given material's thermal conductivity, A is the area of the boundary face, L is the center distance between the cell and its neighbor (the one with which the boundary is shared) and ΔT is the temperature difference between the two cells (obviously calculated with the proper sign). Now, the boundary flux between two cells in the x -direction where the central cell is the rightmost (in terms of physical

coordinates in the conventional righthand system) is given by:

$$q_{\text{bd}} = -\frac{k_{\text{m}}\Delta y\Delta z}{\Delta x}(T_{i,j,k} - T_{i-1,j,k}), \quad (3.9)$$

where i, j, k have been introduced in the same manner as in Fig. 3.5 where i is the running index in the x -direction and j and k are the corresponding indices in the y - and z -directions respectively.

Now, by convention the flux across the leftmost boundary (i.e. the boundary face between the central cell and the previous cell in the particular direction) is calculated as a positive flux if heat enters the central cell and the opposite is obviously valid for the rightmost boundary (i.e. the boundary between the central cell and the next cell in the particular direction). This leads to the following by combining Eqs. 3.7 and 3.9 and omitting any source terms for simplicity:

$$\begin{aligned} \Delta x\Delta y\Delta z\rho_{\text{m}}c_{\text{m}}\frac{T^* - T^0}{\Delta t} &= -\frac{k_{\text{m}}\Delta y\Delta z}{\Delta x}(T_{i,j,k} - T_{i-1,j,k}) \\ &+ \frac{k_{\text{m}}\Delta y\Delta z}{\Delta x}(T_{i+1,j,k} - T_{i,j,k}) \\ &- \frac{k_{\text{m}}\Delta x\Delta z}{\Delta y}(T_{i,j,k} - T_{i,j-1,k}) \\ &+ \frac{k_{\text{m}}\Delta x\Delta z}{\Delta y}(T_{i,j+1,k} - T_{i,j,k}) \\ &- \frac{k_{\text{m}}\Delta x\Delta y}{\Delta z}(T_{i,j,k} - T_{i,j,k-1}) \\ &+ \frac{k_{\text{m}}\Delta x\Delta y}{\Delta z}(T_{i,j,k+1} - T_{i,j,k}) \end{aligned} \quad (3.10)$$

$$\begin{aligned} \rho_{\text{m}}c_{\text{m}}\frac{T^* - T^0}{\Delta t} &= \frac{k_{\text{m}}}{\Delta x^2}(T_{i+1,j,k} + T_{i-1,j,k} - 2T_{i,j,k}) \\ &+ \frac{k_{\text{m}}}{\Delta y^2}(T_{i,j+1,k} + T_{i,j-1,k} - 2T_{i,j,k}) \\ &+ \frac{k_{\text{m}}}{\Delta z^2}(T_{i,j,k+1} + T_{i,j,k-1} - 2T_{i,j,k}). \end{aligned} \quad (3.11)$$

It is seen from the last equation (3.11) that the well known centered difference scheme comes out of the choice of discretization automatically. In the derivation it was assumed that the thermal conductivity is spatially constant for simplicity; the derivation assuming a spatially dependent conductivity is trivially straightforward, however, slightly more tedious.

The righthand side temperature variables have not been flagged in terms of whether they are explicitly known (i.e. at time t) or if they are implicitly determined (i.e. if they are solved for at time $t + \Delta t$). This is so because it depends on the type of integration method. One has the choice of using fully explicit, fully implicit or something in-between. In this work there will only be focus on the in-between situation, which is also known as the ADI method.

From now on in this work we will only deal with the two-dimensional situation. The general three-dimensional setup was shown in order to give an overview on how and from where the different parts of the numerical discretization come. However, in the model this work is concerned about only two dimensions are used.

The ADI method is a two-step integration in time when working with two spatial dimensions. The idea is to split the timestep in two symmetric parts and in one part to consider the x -direction as being implicit and the y -direction to be explicitly determined and then reverse the situation in the other part of the timestep. Denoting the temperature at time t as T^0 , at time $t + \Delta t/2$ as T^* and at time $t + \Delta t$ as T^{**} and choosing arbitrarily the x -direction to be implicit in the first part of the timestep the following is obtained:

$$\begin{aligned} \rho_m c_m \frac{T_{i,j}^* - T_{i,j}^0}{1/2\Delta t} &= \frac{k_m}{\Delta x^2} (T_{i+1,j}^* + T_{i-1,j}^* - 2T_{i,j}^*) \\ &+ \frac{k_m}{\Delta y^2} (T_{i,j+1}^0 + T_{i,j-1}^0 - 2T_{i,j}^0), \end{aligned} \quad (3.12)$$

$$\begin{aligned} \rho_m c_m \frac{T_{i,j}^{**} - T_{i,j}^*}{1/2\Delta t} &= \frac{k_m}{\Delta x^2} (T_{i+1,j}^* + T_{i-1,j}^* - 2T_{i,j}^*) \\ &+ \frac{k_m}{\Delta y^2} (T_{i,j+1}^{**} + T_{i,j-1}^{**} - 2T_{i,j}^{**}). \end{aligned} \quad (3.13)$$

The only remaining issue for the ADI method is to solve the system of linear equations given by Eqs. 3.12 and 3.13. Re-arranging these equations to their final form yields:

$$\begin{aligned} T_{i,j}^* \left(1 + \frac{k_m \Delta t}{\rho_m c_m \Delta x^2} \right) &- \frac{k_m \Delta t}{2\rho_m c_m \Delta x^2} (T_{i-1,j}^* + T_{i+1,j}^*) \\ &= \frac{k_m \Delta t}{2\rho_m c_m \Delta y^2} (T_{i,j-1}^0 + T_{i,j+1}^0) + T_{i,j}^0, \end{aligned} \quad (3.14)$$

$$\begin{aligned} T_{i,j}^{**} \left(1 + \frac{k_m \Delta t}{\rho_m c_m \Delta y^2} \right) &- \frac{k_m \Delta t}{2\rho_m c_m \Delta y^2} (T_{i,j-1}^{**} + T_{i,j+1}^{**}) \\ &= \frac{k_m \Delta t}{2\rho_m c_m \Delta x^2} (T_{i-1,j}^* + T_{i+1,j}^*) + T_{i,j}^*. \end{aligned} \quad (3.15)$$

It should be noted that in the second part of the timestep the temperatures with super script $*$ are explicit (namely determined from the previous half-timestep where they were implicit). Now the equations are on a form that can be solved linearly in time because the equation system is tri-diagonal. The righthand side of the equation system consists of the explicit terms. For the matrix inversion of a tri-diagonal matrix one can use the Tri-Diagonal Matrix Algorithm (TDMA) method given in e.g. Patankar (1980) or Hattel (2005).

3.2.2 The convective term

The convective term, $-(\mathbf{u} \cdot \nabla)T$, in the energy equation (3.1) for the (moving) fluid is discretized by using the following analytical expression for the velocity field (derived in e.g. Nielsen et al., 2009a) for the steady, laminar fluid motion between to infinitely wide parallel plates:

$$u(y) = \tilde{u} \left(\frac{6y^2}{H_f^2} - 1/2 \right). \quad (3.16)$$

where H_f is the height of the fluid channel and \tilde{u} the mean fluid velocity. There is assumed to be no velocity component in the y -direction (i.e. $v = 0$).

The fluid flow may be assumed to be either instantaneous in which case the movement is either on or off. This is a rather idealized assumption, however, a temporally changing profile for the mean fluid velocity may also be applied. In experiments such a profile may, e.g., be a sinusoidal curve.

The numerical implementation is done using the up-wind scheme discussed in detail in e.g. Patankar (1980). Following this scheme means that the convective flux is determined by the central temperature ($T_{i,j}$) and either the lefthand temperature ($T_{i-1,j}$) if the fluid velocity is positive or the righthand temperature ($T_{i+1,j}$) if the fluid velocity is negative. The discretization equations (3.14) and (3.15) now become:

$$\begin{aligned} T_{i,j}^* \left(1 + \frac{k_m \Delta t}{\rho_m c_m \Delta x^2} \right) &= \frac{k_m \Delta t}{2\rho_m c_m \Delta x^2} (T_{i-1,j}^* + T_{i+1,j}^*) \\ &+ \frac{k_m \Delta t}{2\rho_m c_m \Delta y^2} (T_{i,j-1}^0 + T_{i,j+1}^0) + T_{i,j}^0 \\ &- \frac{u_{i,j} \Delta t}{2\Delta x} F, \end{aligned} \quad (3.17)$$

$$\begin{aligned} T_{i,j}^{**} \left(1 + \frac{k_m \Delta t}{\rho_m c_m \Delta y^2} \right) &= \frac{k_m \Delta t}{2\rho_m c_m \Delta x^2} (T_{i-1,j}^* + T_{i+1,j}^*) \\ &+ \frac{k_m \Delta t}{2\rho_m c_m \Delta y^2} (T_{i,j-1}^{**} + T_{i,j+1}^{**}) + T_{i,j}^* \\ &- \frac{u_{i,j} \Delta t}{2\Delta x} F. \end{aligned} \quad (3.18)$$

where F is defined as

$$F = \begin{cases} T_{i,j}^* - T_{i-1,j}^* & \text{if } u_{i,j} > 0 \\ T_{i+1,j}^* - T_{i,j}^* & \text{if } u_{i,j} < 0. \end{cases}$$

3.2.3 Boundary conditions

Numerical grid cells with one or more boundaries to the ambient or e.g. between two different materials have special versions of the above mentioned discretized equations (3.14 and 3.15 or 3.17 and 3.18 depending on the physics of the particular subdomain). The simplest is when the grid cell experiences an adiabatic boundary meaning that the flux across that boundary face is zero. The discretization equation is then trivial.

It becomes a bit more difficult when the boundary condition is either a prescribed temperature or a given boundary flux (which could easily be time- and / or spatially dependent). The first case has several different situations where it appears in various formulations. The simplest is when the ambient has a specified constant temperature T_∞ . Then the equation is simply the convective or Newton cooling law:

$$\begin{aligned} q_{\text{bd,conv}} &= \frac{T_\infty - T_{\text{cell}}}{R_{\text{cell}} + R_\infty} \\ &= \frac{T_\infty - T_{\text{cell}}}{\frac{1/2\Delta x_i}{k_m \Delta x_j \Delta x_k} + \frac{1}{h_{\text{conv}}}}. \end{aligned} \quad (3.19)$$

Here the thermal resistances, R_{cell} and R_∞ , have the meaning of the thermal resistance between the grid cell's centre and its boundary (prescribed by Fourier's law)

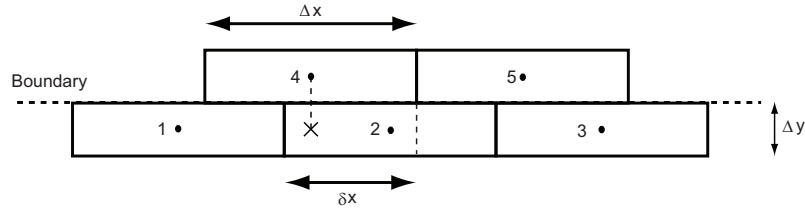


Figure 3.6: The upper grid cells belong to domain number one and the lower grid cells belong to domain number two.

and between the boundary and the ambient (prescribed by convective cooling with the parameter h_{conv}) respectively. The finite size of the cell has been denoted by Δx , Δy and Δz .

It is very important to treat the unknown cell temperature in Eq. 3.19 correctly, i.e. it should be implicitly determined in one half of the timestep and explicit in the other — just like the ADI solver dictates. If one were to use the cell's temperature explicitly throughout the entire timestep and the convective heat loss through h_{conv} were large then the solver would most definitely break down due to *too* much explicitness in the formulation and thus a strong dependence of the choice of timestep would dominate the solution. Since explicit solvers are only conditionally stable and one therefore has to strictly follow timestepping criteria (like e.g. the well-known Courant conditions), this could be critical for the solution time with no physical gain. These criteria are usually much more conservative than need be in most situations meaning that they dictate a much too fine timestep compared to the physics one wishes to model.

3.2.4 Moving boundaries

The choice of using finite differences as the discretization makes it straightforward to ensure energy conservation across the moving boundaries between the domains.

At the beginning of each timestep the heat flux across the domain boundaries is calculated and distributed through the timestep in the boundary cells. Considering Fig. 3.6 a part of the boundary between two neighboring domains is visualized. Cell number four shares its boundary with both cells one and two. The temperature at the virtual point marked with an \times is interpolated linearly between the two nearest neighbors, i.e. the central temperatures of cells one and two. This temperature, denoted by T_{interp} , is then used in the following expression

$$q_{\text{bd,internal}} = -\frac{T_4 - T_{\text{interp}}}{1/2 \left(\frac{\Delta y_1}{k_1 \Delta x} + \frac{\Delta y_2}{k_2 \Delta x} \right)}. \quad (3.20)$$

The indices indicate the domain (1 for the domain including cells four and five and 2 for the domain including cells one, two and three). The length, Δx , is the same for each cell. The heat flux $q_{\text{bd,internal}}$ is used directly in the heat equation for cell four whereas one part of it is used in cell one and the other part in cell two. How much of the flux that goes into which cell is determined by the amount of shared area with cell number four. In this way energy conservation is ensured across the boundary at all times.

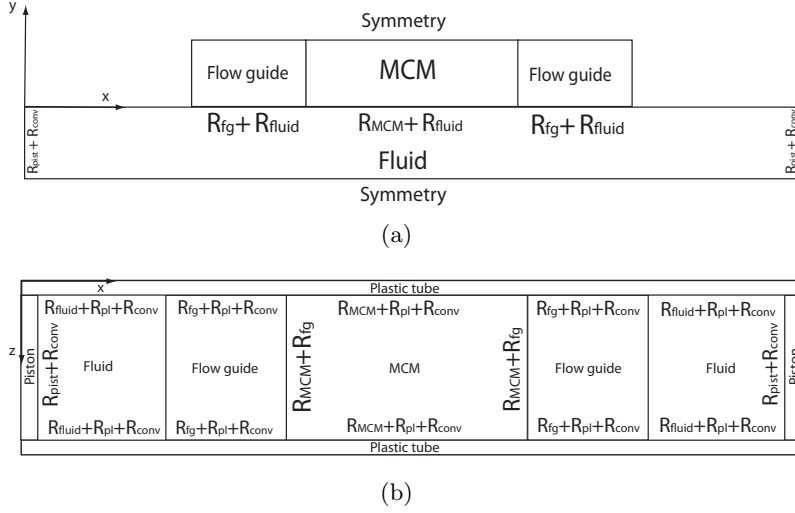


Figure 3.7: (a) The xy -plane of the system including the internal boundaries. (b) The xz -plane of the model. The z -direction is not resolved, however, the 2.5D model takes the distance from the center of the control volumes to the ambient into account when calculating the thermal losses, as indicated on the figure. The subscripts have the following meaning: pist = piston, conv = convection, pl = plastic and MCM = magnetocaloric material.

The timestepping is sensitive to the amount of heat flux across the boundary since it is assumed as a fully explicit determined part of the energy equation for the grid cell. This is unavoidable if the ADI-solver is to be used and thus the benefit of the tri-diagonal matrix formulation is to be utilized. It is possible to formulate the problem fully implicit but that would generate an asymmetric matrix representing the equations to solve for the cells. To invert such a matrix is at least of the order N^2 in time as opposed to the order N using the TDMA algorithm on a tri-diagonal matrix (where N is the number of grid cells).

3.2.5 Thermal parasitic losses (“2.5D” model)

It is expected that the performance in general will be over-estimated by the model since it may be considered ideal without losses to the ambient and that the trends in performance (both in load and no-load situations) will be reproduced fairly well by the model. However, in order to improve the model, heat losses have been implemented. This is done through a lumped analysis and under the assumption that the replicating cell under consideration loses most of its heat in the not-resolved z -direction. The loss can then be implemented as an additional term in Eqs. 3.17 and 3.18 using the formalism of thermal resistance

$$Q_{\text{loss}} = \frac{T_{\infty} - T_{i,j}}{\sum_l R_l}, \quad (3.21)$$

where the total thermal resistance from the center of the cell (in terms of the z -direction) to the ambient is denoted by $\sum_l R_l$. There are three terms in this

sum. First the thermal resistance through the material within the regenerator R_m (fluid or solid). Second, the housing of the regenerator block R_{pl} (made of a plastic material) and finally loss via natural convection to the ambient R_{conv}

$$\begin{aligned} \sum_l R_l &= R_m + R_{pl} + R_{conv} \\ &= \frac{1/2\Delta z}{k_m \Delta x \Delta y} + \frac{1/2\Delta z}{k_{pl} \Delta x \Delta y} + \frac{1}{h_{conv} \Delta x \Delta y}. \end{aligned} \quad (3.22)$$

This 2.5D thermal loss formulation is schematically visualized in Fig. 3.7. The loss to the ambient through natural convection is characterized by the parameter h_{conv} and the thickness of the housing, Δz . Textbook values suggest that h_{conv} lies in the range 5 – 20 W/K · m² (Holman, 1987). The thermal properties of the plastic housing are given in Table 3.1.

3.2.6 Summary and input parameters of the model

In the previous sections (3.2.1—3.2.5) it was described in detail how a basic numerical AMR model was implemented on a rather technical level. In this subsection the various input parameters to the model are defined and described for further usage in later chapters.

Timings

The AMR cycle may be characterized with a total of four timings each corresponding to the four processes illustrated in Fig. 3.2. The timings are denoted τ_{1-4} and cover the periods of the magnetization, hot blow, demagnetization and cold blow, respectively. These timings are in general not equal since the various processes are not fundamentally bound to last an equal amount of time. However, it is conventional that the magnetization and demagnetization processes last the same time, thus $\tau_1 = \tau_3$, and the same is usually true for the blow periods, i.e. $\tau_2 = \tau_4$. The duration of τ_1 and τ_3 is usually minimized and even in some cases neglected (Kuz'min, 2007).

The second set of timings, concerning the blow periods, is more difficult to imagine being asymmetrical since that could induce an imbalance in the flow system dependent on the specific experiment. However, since the specific heat of MCMs usually is rather dependent on the current magnetic field and the two blow periods are performed in field and zero-field, respectively, one could imagine that asymmetrical blow periods could be favorable. However, that is not considered further in this thesis and is thus of interest for future work only.

The total cycle time of one AMR cycle is denoted τ_{tot} and is thus given by $\tau_{tot} = \sum_{i=1}^4 \tau_i$. Assuming the AMR cycle to be symmetric with respect to time the dimensionless variable $\tau_{rel} = \tau_1/\tau_2 = \tau_3/\tau_4$ is introduced.

It is further noted that the division into four separate timings is of a more theoretical nature than practical. One could easily imagine the regenerator to be magnetized during the hot blow period etc. Experimental AMR devices have been published where this is, in fact, the case (Tura & Rowe, 2009).

Steady-state

The AMR model is initialized from some state, which is typically a constant temperature throughout the entire domain. The boundary conditions combined with the input parameters then dictate the eventual steady-state solution. A number of AMR cycles are simulated until a cyclic steady-state is reached. This state is defined such that the maximum relative change between two consecutive AMR cycles of the cooling load, q_c , and the heat rejection, q_h , is less than 10^{-4} .

Geometric parameters

A parallel plate regenerator may be defined geometrically using three quantities, namely the length of the regenerator L_s , the thickness of the solid magnetocaloric plate, H_s , and the thickness of the flow channel, H_f . The porosity, ϵ ,², and the specific surface area, a_s of the regenerator may then be found

$$\epsilon = \frac{H_f}{H_f + H_s} \quad a_s = \frac{2}{H_f + H_s}. \quad (3.23)$$

This also leads to the hydraulic diameter, defined as four times the flow cross section divided by the wetted perimeter:

$$D_H = 2H_f. \quad (3.24)$$

The hydraulic diameter is an important parameter since the pressure drop across the regenerator is determined by it. Thus, two different regenerators with the same hydraulic diameter will have (approximately) the same pressure drop across them. In Chapter 8 D_H is used in an analysis of the performance of more generalized regenerator geometries.

Flow parameters

The flow is characterized through the duration of a flow period (τ_2 or τ_4), the fluid inlet velocity (\tilde{u} ; as defined in Eq. 3.16), the hydraulic diameter and, of course, the properties of the heat transfer fluid, i.e. the mass density, specific heat and viscosity. In this work the fluid is generally assumed to be water with various additives such as glycol. In terms of the model geometry, see Fig. 3.4, a relation may be found between the length of a blow, δx , and the inlet velocity:

$$\delta x = \tilde{u}\tau_2. \quad (3.25)$$

In this context it is relevant to consider the utilization, φ , of the regenerator. This is defined as the ratio between the total thermal mass of the fluid moved and the thermal mass of the regenerator material, i.e.

$$\varphi = \frac{\dot{m}_f c_f \tau_2}{m_s c_s}, \quad (3.26)$$

²It is yet again stressed that by porosity is meant the overall void volume to total volume fraction; on the local scale the porosity is anisotropic in a parallel-plate regenerator.

where the mass flow rate during a blow period is denoted \dot{m}_f . The utilization may be re-written for the specific case of a parallel-plate regenerator:

$$\varphi = \frac{\rho_f c_f H_f \delta x}{\rho_s c_s H_s L_s}. \quad (3.27)$$

Now, this parameter is quite useful when comparing experimental and modeling results. However, the specific heat of the solid is included in the denominator of the expression for the utilization. As discussed in Chapter 2 this value is a strong function of both temperature and magnetic field. In order to keep things simple, it is therefore semi-conventionally decided to use the specific heat at the Curie temperature in zero field, i.e. $c_s(T = T_C, \mu_0 H = 0)$, which is in line with the definition of e.g. Tura & Rowe (2009). This is, however, only a good approach when the regenerator is made of a single magnetocaloric material. When considering regenerators made of multiple materials the assumption of a single value of the specific heat breaks down and, e.g., a weighted average would be more appropriate. This is further discussed in Sec. 5.1.1.

3.3 Validation

The validation is divided into several parts which include

- Energy conservation with adiabatic boundaries
- Analytical calculation of the magnetic work has to be equal to the heat output from the HHEX in steady-state and no-load conditions
- Standard case test validated against the same configuration in Petersen (2007)
- Grid and timestep sensitivity analysis

3.3.1 Energy conservation

The standard case with $\Delta x = 2$ cm, $\tau_{\text{tot}} = 6$ s, $\tau_{\text{rel}} = 2$, $H_f = 0.5$ mm and $H_r = 0.5$ mm was used with adiabatic boundaries (also on the hot heat exchanger). The total energy of the system is shown as a function of time over one cycle in Fig. 3.8.

It is seen that no energy escapes the system. Any numerical noise should only manifest itself in the last one or two digits and since double precision is used throughout the entire code this has no significant effect on the result.

3.3.2 Analytical solution

The MCE is highly non-linear (as shown in Chapter 2). Thus it is impossible to analytically calculate the behaviour of the AMR (hence, the reason to do it numerically). However, if the regenerator is simplified to have constant c_s and a constant (artificial) adiabatic temperature change is used, the magnetic work in steady-state can be calculated³. Under no-load conditions the magnetic work over an entire cycle must be equal to the amount of heat leaving the HHEX. The expression for

³It is strongly emphasized that this is *not* thermodynamically self-consistent but serves only as a simplified test case.

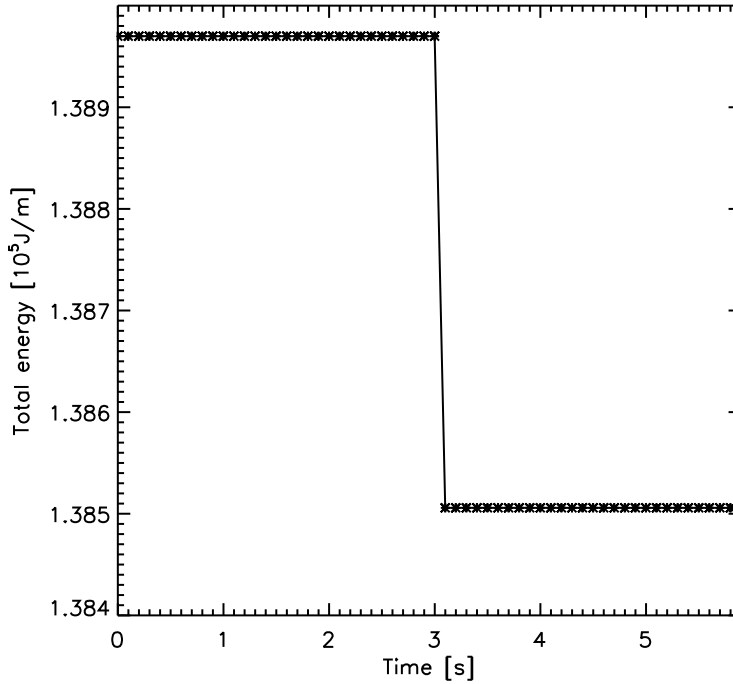


Figure 3.8: The unit on the y -axis is in J/m since the model is 2-dimensional. The change after three seconds is simply there to show that the code handles changes (like the adiabatic temperature change) without any difficulties.

calculating the magnetic work per unit length is:

$$w_{\text{mag}} = c_s \rho_s (\Delta T_{\text{ad,mag}} + \Delta T_{\text{ad,demag}}) L_s H_s, \quad (3.28)$$

where L_s and H_s denote the length and half height of the regenerator⁴. If c_s is chosen to be $235 \text{ Jkg}^{-1}\text{K}^{-1}$ (a value representing the mean of the span of c_r around the Curie temperature), using the standard value for ρ_s , letting $\Delta T_{\text{ad,mag}} = 5 \text{ K}$ and $\Delta T_{\text{ad,demag}} = -4 \text{ K}$ and set $L_s = 5 \text{ cm}$ and $H_s = 0.5 \text{ mm}$ the result is $w_{\text{mag}} = 46.4125 \text{ Jm}^{-1}$.

Table 3.2 gives the results of various numerical simulations of the analytical experiment at different grid and timestep resolutions. The definition of low, normal and high resolution is given in Table 3.3. The results are seen to be very close to the analytical solution. Since the normal and high resolution configurations agree on a converged temperature span (292.5 K), the normal resolution is considered sufficient.

3.3.3 Standard experiment

The parameter-setup known as the “standard”-experiment is the same as in the setup for the comparison to the analytical expression with the only difference that the mean field model is used for calculating the highly non-linear $\Delta T_{\text{ad}}(T, H)$ and

⁴Note that the half height is used here since only a symmetry-replicating cell is considered — not the entire cooling device.

Resolution	dt	w_{\max} [Jm^{-1}]	Deviation [%]	T_{cold} [K]
Low	Low	46.4177	0.012	292.16
Low	Normal	46.4175	0.011	292.15
Low	High	46.4175	0.011	292.17
Normal	Normal	46.4163	0.008	292.50
Normal	High	46.4162	0.008	292.50
High	Normal	46.4157	0.007	292.50
High	High	46.4157	0.007	292.51

Table 3.2: The analytical value is found through Eq. 3.28 to be 46.4125 Jm^{-1} . This table shows the model results and the deviation from the analytical. The normal resolution is seen to be sufficient. T_{cold} denotes the cold side temperature. The ambient temperature is set to 298 K.

Label	Spatial resolution (fluid, regenerator, HEX)	Timestep [s]
Low	80x5,25x5,10x5	0.01
Normal	160x10,50x10,20x10	0.001
High	320x20,100x20,40x20	0.0001

Table 3.3: The spatial and temporal resolution is given. The normal spatial resolution corresponds to cells of $1 \times 0.05 \text{ mm}^2$ in x, y coordinates.

Resolution	dt	ΔT [K]
Low	Low	287.18
Low	Normal	287.22
Low	High	287.25
Normal	Normal	287.16
Normal	High	287.18
High	Normal	287.15
High	High	287.18

Table 3.4: Standard no-load experiment.

$c(T, H)$. The result from the corresponding experiment in Petersen et al. (2008b) are that $\Delta T = 287.1 \text{ K}$. In Table 3.4 the corresponding results from the numerical model are given. It is concluded that the normal-normal resolution is sufficient.

3.4 Summary

In this chapter the active magnetic regenerator cycle was introduced. The AMR cycle was discussed from a thermodynamic point of view. This led to the development of a 2-dimensional numerical model of the AMR system. This model was derived from basic heat transfer equations and the numerical details were thoroughly discussed. The model enables the usage of various magnetocaloric materials, spatially changing magnetic field, thermal parasitic losses etc. Relevant parameters such as

the utilization, porosity, hydraulic diameter etc. were introduced for later reference.

In this way a powerful tool has been developed that enables investigations of the vast parameter space of parallel-plate based AMRs. In the following chapters this model will be applied first to the case of a single material regenerator under ideal conditions (Chap. 4). Then the case of multiple material AMRs is considered (Chap. 5). Finally, in Chap. 6 the model is applied to cases that have been investigated experimentally in various AMR experimental test machines.

Chapter 4

Parameter study of the AMR

In the present chapter a parameter study of the AMR performance is presented. A range of operational and geometric parameters are varied and the resulting cooling power versus temperature span curves are analyzed. The results provide a mapping of the influence of the various parameters and draw general conclusions on the range of the parameters of the optimal operation of the AMR. The results are presented as a function of comparable parameters such as the exergetic cooling power, thermal utilization of the regenerator and the number of transfer units, NTU. This chapter is extensively based on paper A.1.5 (Nielsen et al., 2010c) and to some extent also paper A.3.1 (Nielsen et al., 2008), which was presented at the 8th IIR Gustav Lorentzen Conference on Natural Working Fluids in Copenhagen, September 2008.

4.1 Design and parameters

The theoretical cooling power of an AMR device based on a regenerator with parallel plates of gadolinium (Gd) modeled via the mean field theory (MFT) (see Chapter 2) is mapped as a function of a range of operational and geometric parameters in the following. The magnetic field change has been set to be from 0 to 1 tesla (T) and the input parameters for the MFT are equivalent to those for Gd given in Table 2.1. The thermal properties of the heat transfer fluid are assumed constant.

The reason for choosing Gd is that it can be well described via the MFT and Gd is the material of choice for many AMR test devices (Zimm et al., 2006; Bahl et al., 2008; Tura & Rowe, 2009). However, it is not claimed that the MFT perfectly reproduces the magnetocaloric effect of Gd but it does provide a good basis for comparison and does not lack the typically insufficient parameter coverage of MCE datasets found through experiments. The reason why the magnetic field change is chosen to be from 0 to 1 T is that this is roughly what is expected to be feasible for permanent magnets in large scale devices to produce. Permanent magnets may be designed to produce up to 2 T in field change, however, the cost of such magnets and the rather small volume available for the regenerator make this unrealistic in a large scale device (Bjørk et al., 2008).

The length of the regenerator solid, L_s , is kept constant at 0.05 m. The parameters varied are the regenerator plate thickness H_s , the fluid channel thickness H_f , the fluid stroke length δx expressed as a fraction of regenerator length L_s , the total cycle time τ_{tot} and the ratio τ_{rel} between the duration of the magnetization

Table 4.1: The system-specific parameters covered in this survey. The total number of AMR simulations amount to all combinations of this table, i.e. 27,216.

Parameter	Values
δx [%]	40, 50, 60, 70, 80, 90
τ_{tot} [s]	0.25, 0.5, 1.0, 2.0, 3.0, 4.0, 5.0, 6.0, 7.0
τ_{rel} [-]	0.25, 0.5
H_f [mm]	0.2, 0.3, 0.4, 0.5, 0.6, 0.7, 0.8, 0.9, 1.0
H_s [mm]	0.25, 0.5, 0.75, 1.0
ΔT [K]	0,5,10,15,20,25,30

period and the duration of the blow period. The cycle frequency is $f = 1/\tau_{\text{tot}}$. Finally, the temperature span of the regenerator, ΔT , is varied from zero to 30 K and the ambient temperature is fixed at 298 K. Table 4.1 provides an overview of the parameter space covered.

This parameter space is based on estimates of realistic geometrical and operating conditions for a parallel plate AMR. The minimum flow channel and plate thicknesses are estimated from realistic manufacturability. The timings, or frequencies, are chosen from a practical viewpoint. The stroke lengths are chosen from experimental experience (e.g. Bahl et al., 2008).

4.1.1 Non-dimensionalizing the parameters

The process and geometrical parameters are to a certain extent fixed in terms of the specific regenerator system modeled. Therefore they are cast into a non-dimensional form through the three parameters utilization, φ , porosity, ϵ , and number of transfer units, NTU, to be defined below. The ranges of the non-dimensional parameters included in this study are given in Table 4.2. The utilization and the porosity were introduced and defined in Sec. 3.2.6.

An expression for the number of transfer units for laminar flow between parallel plates found in Nickolay & Martin (2002) is

$$\text{NTU} = 4 \frac{\text{Nu}_m}{\text{Gz}_L}, \quad (4.1)$$

where also the mean Nusselt number, $\text{Nu}_m \equiv \frac{hD_H}{k_f}$ for a blow of length L is found. The convective heat transfer coefficient, h , and the hydraulic diameter, $D_H = 2H_f$ have been introduced. The NTU expresses how fast the temperature in the fluid and the solid equalize during a blow period (this goes as $\exp(-\text{NTU})$). A correlation for

Table 4.2: The range of the three non-dimensional units used to plot the results in a meaningful and generic way.

Non-dimensional unit	Range
φ	0.14-6.4
ϵ	0.17-0.8
NTU	0.16-74.8

Table 4.3: The thermal properties of the MCM and the heat transfer fluid (water).

Parameter	Value
ρ_f	1000 kg/m ³
ρ_s	7900 kg/m ³
c_f	4200 J/kgK
$c_s(\mu_0 H = 0, T = T_C)$	300 J/kgK

the mean Nusselt number for a parallel-plate regenerator is found in (Nickolay & Martin, 2002)

$$\begin{aligned} \text{Nu}_m &= (\text{Nu}_1^n + \text{Nu}_2^n)^{1/n} \\ \text{Nu}_1 &= 7.541 \quad \text{Nu}_2 = 1.841 \text{Gz}_L^{1/3} \quad n = 3.592 \\ \text{Gz}_L &= 4 \frac{H_i^2}{\alpha_f \tau_2}. \end{aligned} \quad (4.2)$$

The expression for the Graetz number, Gz_L , has been rewritten to the form given in Petersen et al. (2008a); $\alpha_f = k_f/c_f\rho_f$ is the thermal diffusivity of the fluid and k is the thermal conductivity. The diffusivity is constant for this case and thus the NTU is a function of blow period timing and channel thickness only. In Fig. 4.1 the NTU is plotted as a function of fluid channel thickness for each cycle frequency simulated. As expected it is observed that the faster an AMR cycle is, the thinner the fluid channel should be in order to keep a high value of the NTU. In Li et al. (2006) it is found that the value of the NTU should be above 10 for obtaining the maximum possible efficiency of the regenerator (dependent on the utilization). Therefore it may be expected from Fig. 4.1 that the simulation results obtained with total cycle frequencies of 1.0 Hz or greater are significantly less optimal than those at smaller frequencies for the otherwise same operating parameters.

The Biot number can be written as

$$\text{Bi} \equiv \frac{hH_s}{k_s} = \text{Nu}_m \frac{k_f}{k_s} \frac{H_s}{2H_f}, \quad (4.3)$$

where the definition of the Nusselt number has been used.

If the Biot number is less than one the heat transfer from the interior of the regenerator plate to the boundary interface between the plate and the fluid is faster than the heat transfer across the boundary. Thus, in this case, the plate is essentially able to supply the heat transfer fluid with heat at all times. In the opposite case, if the Biot number is greater than one, the heat transfer within the plate is too slow and the performance may therefore be expected to decrease. The range of the Biot numbers in the present modeled parameter survey is 0.05 to 1.11.

4.1.2 Obtaining the cooling capacity

For each parameter configuration the following expression was fitted to obtain the cooling power

$$Q_c = -\alpha\Delta T + \beta, \quad (4.4)$$

assuming a linear relation between the cooling power and the temperature span ΔT . The assumption of linearity is justified through both the modeling results and

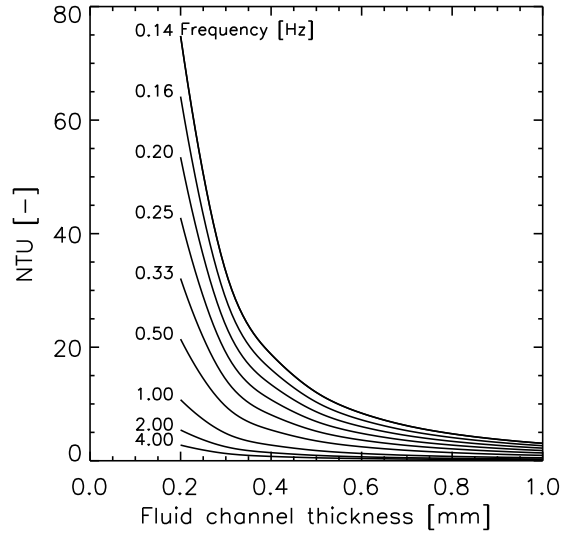


Figure 4.1: The number of transfer units (NTU) as a function of fluid channel thickness for the operating frequencies covered.

experimental experience (Zimm et al., 2006; Nielsen et al., 2008; Oliveira et al., 2009; Tura & Rowe, 2009). The standard error on the fitted values of α and β are all within 5 %. The offset of the cooling curve, β , expresses the zero temperature span cooling power Q_{\max} and the ratio between the offset and the slope, β/α , expresses the zero cooling load temperature span ΔT_{\max} . It should be noted that in the case of a negative temperature span or negative cooling power, Eq. 4.4 is also valid. This is seen both from the model results (not all configurations included in this survey can sustain temperature spans up to 30 K) and through experiments (e.g. Nielsen et al., 2008) .

4.2 Results and discussion

Considering the slope of the cooling curve, α , and the offset, β , it is somewhat complicated to define what their optimal values are. The two parameters are tightly connected and together they provide information on the cooling capacity and obtainable temperature span. It is expected that the maximum temperature span is a function of regenerator efficiency only (obviously at a fixed magnetic field change) whereas the cooling power is expected also to be proportional to the operating frequency and the amount of active material in the regenerator. The parameters have therefore been normalized in units of mass of magnetocaloric material.

In order to evaluate the performance of the individual configuration a third parameter, the exergetic equivalent cooling power, is introduced. The task of a refrigeration device is to move a load from the cold end to the hot end in order to release it to the ambient. This can be formulated as moving an amount of entropy,

ΔS , from the cold to the hot end, which may be expressed as

$$\Delta S = \frac{Q_c}{T_{\text{cold}}} - \frac{Q_c}{T_{\infty}}. \quad (4.5)$$

The exergetic equivalent at a certain cooling power and ambient temperature is then

$$\text{Ex}_Q(Q_c) = T_{\infty} \Delta S = Q_c \left(\frac{T_{\infty}}{T_{\text{cold}}} - 1 \right). \quad (4.6)$$

This result may also be found in Rowe (2009) and re-casting Eq. 4.6 in terms of the maximum cooling power and maximum temperature span assuming that Eq. 4.4 is valid gives

$$\begin{aligned} \text{Ex}_Q(Q_c) &= \frac{Q_c(Q_{\text{max}} - Q_c)}{Q_{\text{max}} \frac{T_{\infty}}{\Delta T_{\text{max}}} - (Q_{\text{max}} - Q_c)} \\ &= \frac{Q_c(\beta - Q_c)}{\alpha T_{\infty} - (\beta - Q_c)} \end{aligned} \quad (4.7)$$

as found in Rowe (2009). The maximum cooling capacity, Q_{max} , and the maximum temperature span, ΔT_{max} , have been expressed in terms of α and β . It is further noted that the hot side temperature is assumed to be equal to the ambient temperature.

Considering Eq. 4.7 it is seen that when the temperature span or cooling power is zero then the exergy is also zero. These two states thus represent useless modes of the refrigeration system, or modes where no more useful cooling power may be extracted from them (Bejan, 2006; Rowe, 2009).

In the case of a refrigeration system the exergy should be viewed as a potential of the ability of the refrigerator to transport a cooling load from one reservoir to the other. The maximization of the exergy should thus be sought. When the cooling power versus temperature span curve is assumed linear, i.e. Eq. 4.4 is valid, then the maximum exergy may be obtained at approximately $Q_c = Q_{\text{max}}/2$ (Rowe, 2009), thus

$$\text{Ex}_{\text{max}} = \text{Ex}_Q(Q_{\text{max}}/2) = \frac{\beta/4}{\alpha T_{\infty}/\beta - 1/2}. \quad (4.8)$$

4.2.1 Dependence on porosity

In Fig. 4.2 the porosity is mapped as a function of α and β . From the plots it is evident that the porosity should be minimized in order to get the best values of ΔT_{max} . Higher values generally seem to yield too low temperature spans to be usable. The general trend seems to be that a lower porosity is better. It is noted, however, that not all configurations with a low porosity are automatically optimal. As can be seen from Fig. 4.2 some of these configurations are quite far from optimal, which only confirms that the porosity is not the only important parameter for the performance of the AMR.

Fig. 4.3(a) shows the maximum temperature span as a function of porosity for each plate thickness included in this survey. From the figure the trend seems to be a monotonical decrease in the maximum temperature span as a function of porosity.

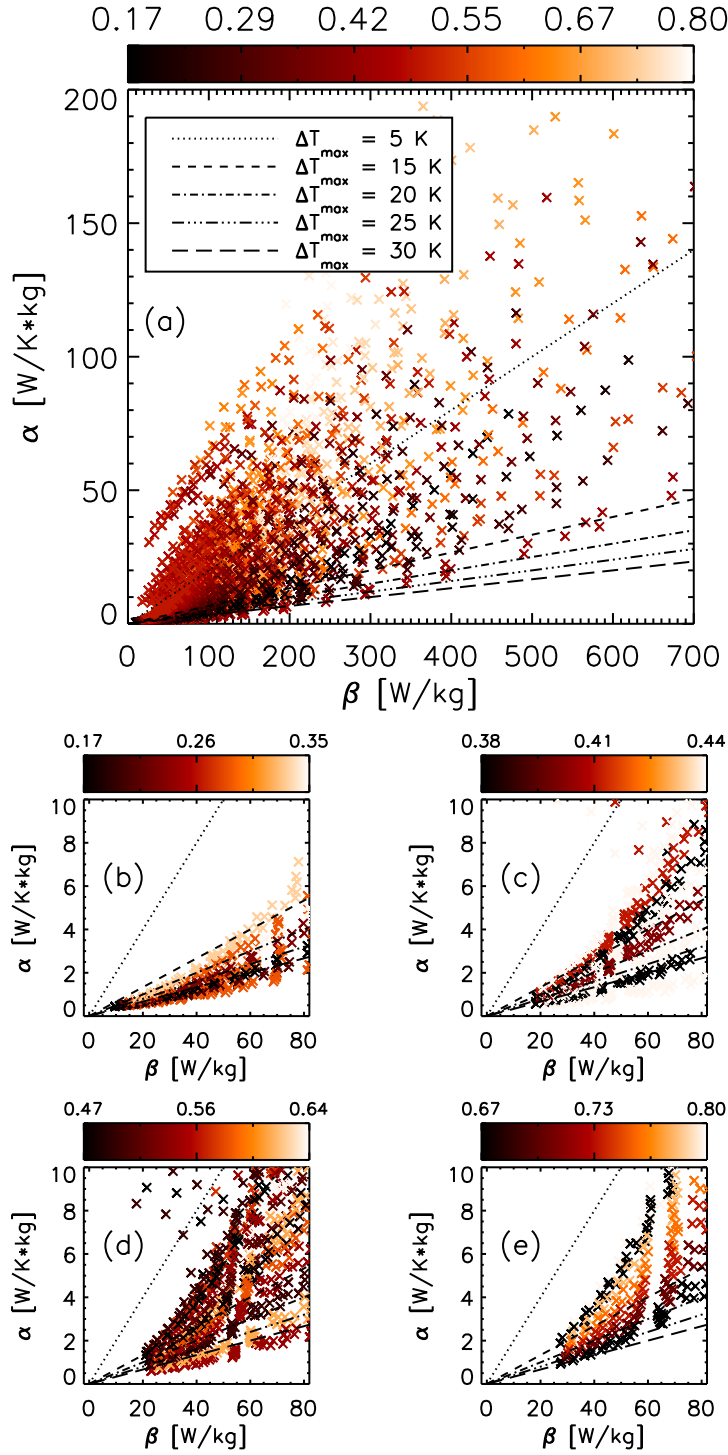


Figure 4.2: The slope of the cooling capacity versus temperature span curve (α) as a function of zero temperature span cooling power (β). The color mapping indicates the porosity, ϵ . The straight lines indicate curves with the same maximum temperature span. Points below a given line are configurations able to yield a higher temperature span than indicated. (a) shows the total parameter space covered. (b)-(e) show a magnified area of the most data-point dense region divided into four ranges of values of the porosity for clarity.

Furthermore, the thinner the plate the higher the maximum temperature span can be achieved, which is due to the lower Biot number.

The plot of the maximum exergy (Fig. 4.3(b)) as defined in Eq. 4.8 as a function of porosity is seen to have the same trends as for the maximum temperature span. Nevertheless, the decrease in maximum exergy as a function of porosity is somewhat more steep than the decrease in maximum temperature span (as seen in Fig. 4.3(a)).

It is concluded that the porosity and the plate thickness should be minimized when considering the maximization of exergy and temperature span. Furthermore, the present survey is limited to a minimum porosity of 0.17 and it can therefore not be determined whether an optimum porosity value exists at or below a value of 0.17.

4.2.2 Dependence on NTU

Figure 4.4 maps the number of transfer units as a function of α and β . A clear trend is observed, namely that the larger the value of the NTU the higher the maximum achievable temperature span. The color scale of Fig. 4.4 shows that the configuration with a value of the NTU between 5 and 10 are mostly situated between the lines denoting maximum temperature spans of 15 K and 20 K, respectively. Between the lines denoting maximum temperature spans of 20 K and 25 K respectively the value of the NTU lie in the range of approximately 10 and 15. The trend continues for higher maximum temperature spans.

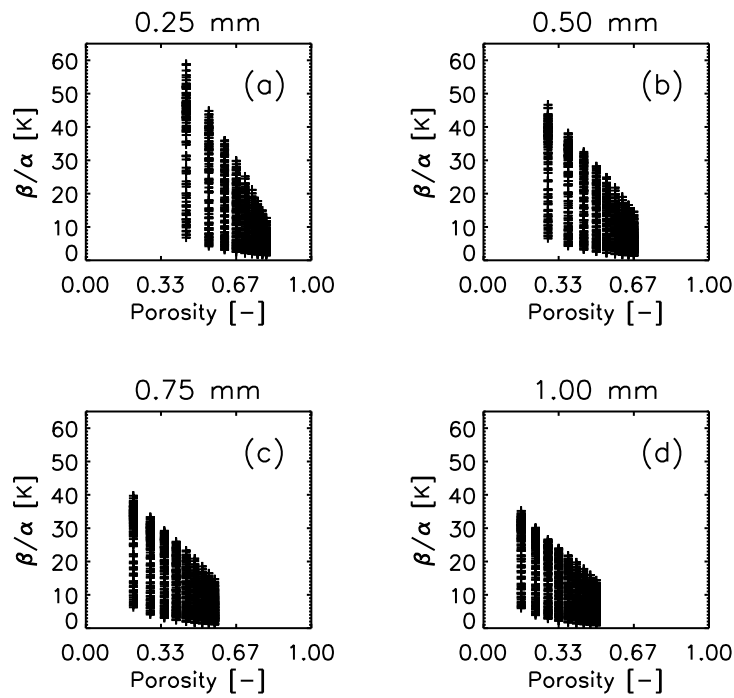
Considering Fig. 4.5 it is seen that within the parameter space covered here the high values of NTU are at the lowest frequency. This was expected from Fig. 4.1 as well. However, the largest temperature span is obtained at values of the NTU less than half the maximum spanned by the present parameter space, i.e. between 20 and 50 but at higher cycle frequencies (in the range 0.3-0.5 Hz).

Figure 4.6 shows that for a given frequency the higher the value of the NTU the higher the maximum exergy. However, the frequency of the cycle has a significant impact. It is evident from the figure that a higher frequency yields a higher maximum exergy at a lower value of the NTU. Therefore the cycle frequency may compensate somewhat for a lower value of the NTU.

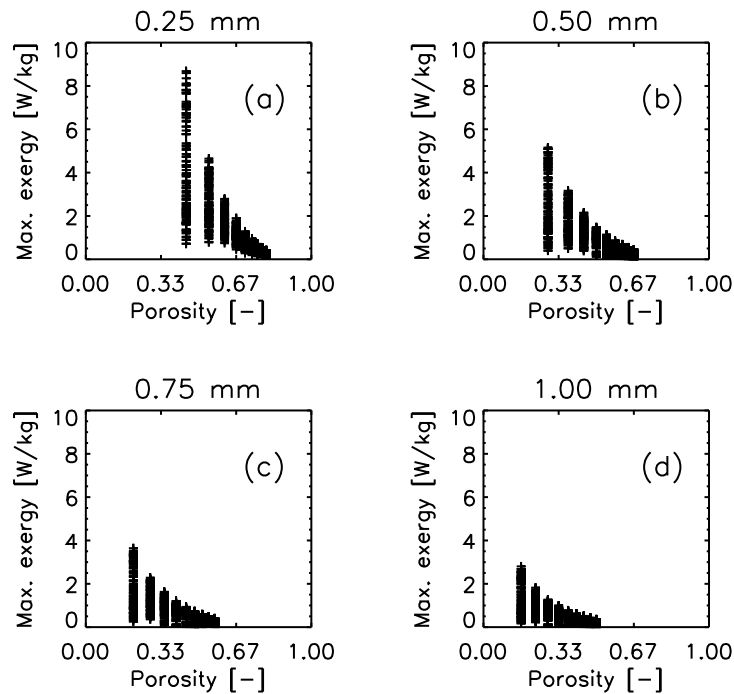
Combining the results from Figs. 4.5 and 4.6 it is concluded that the geometrical constraints on the regenerator pose quite a firm upper limit in terms of the NTU, namely a value of roughly 50. This leaves room for operating at higher frequencies, which evidently yields the most optimal performance considering the maximization of the exergy.

4.2.3 Dependence on the utilization

The utilization is mapped as a function of α and β in Fig. 4.7. Not surprisingly, the largest temperature spans are obtained for the smallest values of the utilization. More interestingly, it is observed that values of the utilization up to about 1 seem feasible in terms of obtaining a high maximum temperature span and at the same time maintaining a reasonable cooling power. This is in good accordance with the results of e.g. Li et al. (2006); Tura & Rowe (2009).



(a) The maximum temperature span, β/α , as a function of porosity. Each subfigure, (a)-(d), shows the results for a specific plate thickness (0.25–1.0 mm respectively).



(b) The maximum exergy as defined in Eq. 4.8 as a function of porosity. Each subfigure, (a)-(d), shows the results for a specific plate thickness (0.25–1.0 mm respectively).

Figure 4.3: The maximum temperature span and maximum exergy.

Fig. 4.8 shows that the maximum temperature span is obtained at the lowest values of the utilization independently of the cycle frequency. Fig. 4.9 shows that the maximum exergy is optimized at values of the utilization around one independent of the frequency. However, the figure also shows that the utilization is not the only parameter characterizing the optimal maximum exergy.

4.2.4 Influence of the cycle timing

The total cycle time, τ_{tot} , should generally be minimized in order to increase the cooling capacity and maximize the exergy. This poses a problem since the regenerator geometry puts a tight constraint on how fast the AMR device can be operated. The NTU should be in the range 10-50 as previously mentioned and since the NTU decreases with increasing frequency (Fig. 4.1), a faster operating AMR device demands a smaller geometry, i.e. thinner plates and closer spacing.

At the same time the fraction τ_{rel} between the time of magnetization (τ_1) and the blow period (τ_2) should be minimized. This can be argued for in the following way: the time used for magnetization / demagnetization is a period where no cooling power is generated (the fluid is stationary) and is thus practically wasted time. An AMR cycle with overlapping timings could possibly be more beneficial (see, e.g., Chap. 6).

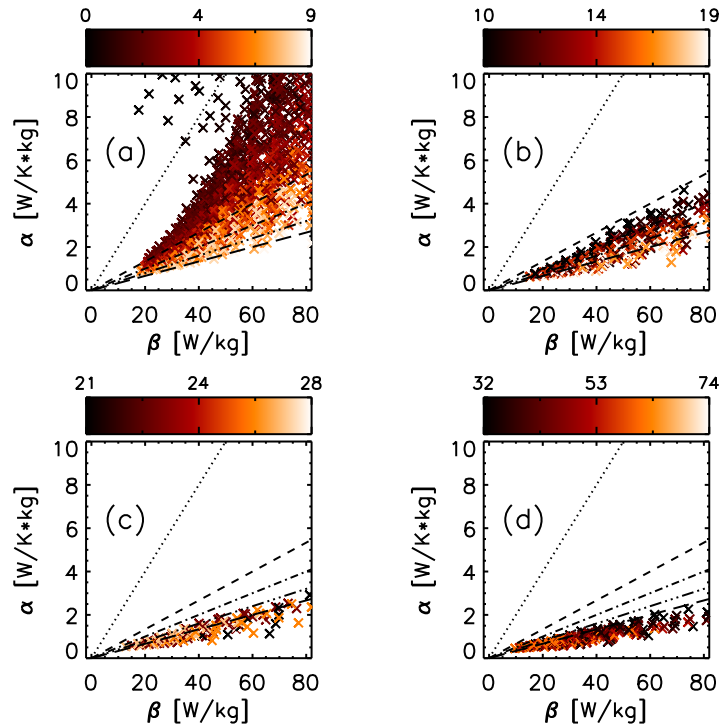


Figure 4.4: The slopes of the cooling curves (α) as a function of maximum cooling power (β) color mapped with NTU divided into four ranges in subfigures (a)-(d). The lines indicate, as in Fig. 4.2, curves with the same maximum temperature span.

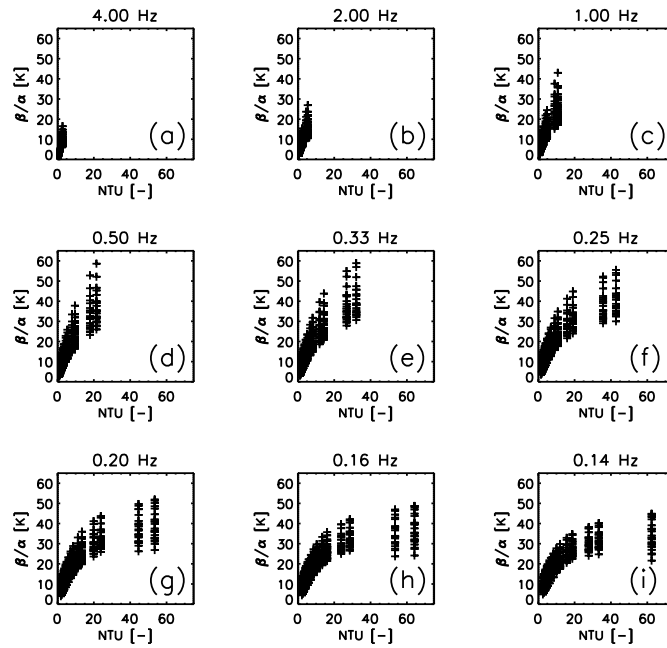


Figure 4.5: The maximum temperature span, β/α , as a function of NTU. Each subfigure, (a)-(i), shows a specific operating frequency, 4-0.14 Hz respectively.

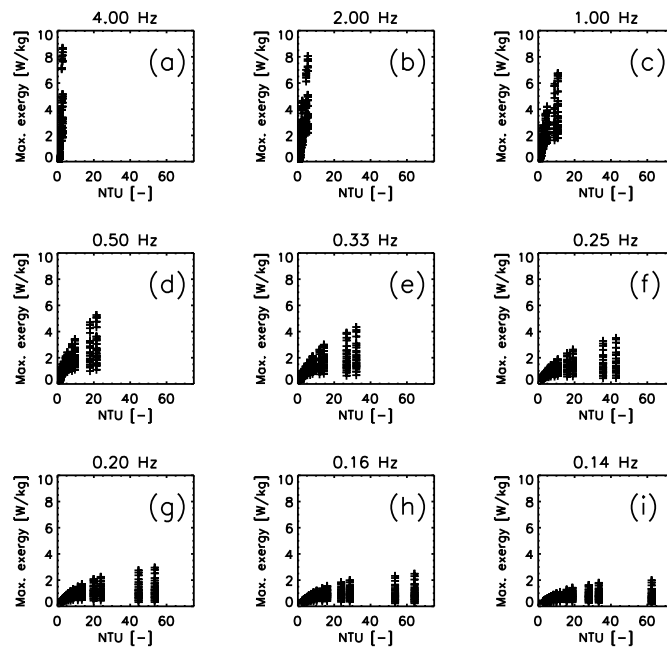


Figure 4.6: The maximum exergy as defined in Eq. 4.8 as a function of NTU. The subfigures (a)-(i) each show the results for a specific frequency, 4-0.14 Hz respectively.

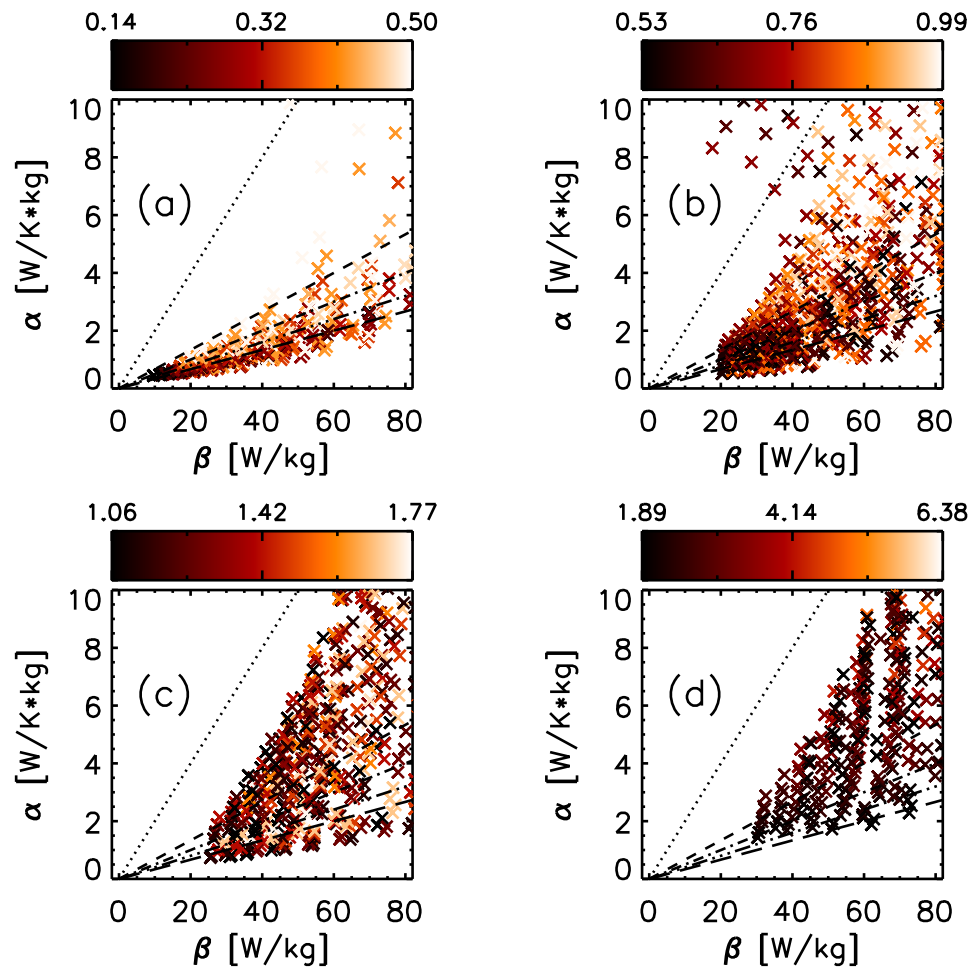


Figure 4.7: The cooling curve slope, α , as a function of the zero temperature span cooling capacity, β , color mapped with utilization. The straight lines indicate the same as in Fig. 4.2. The utilization has been divided into four intervals as indicated in subfigures (a)-(d) for clarity.

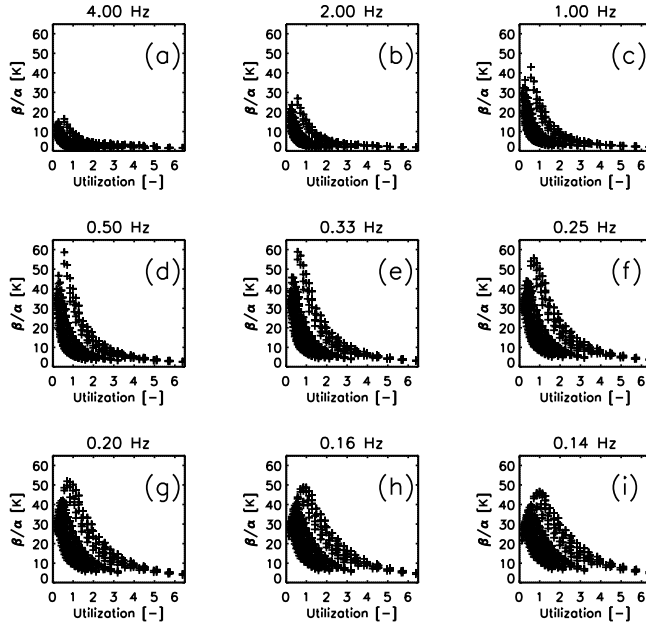


Figure 4.8: The maximum temperature span, β/α , as a function of utilization. The nine subfigures (a)-(i) each show a specific operating frequency, 4-0.14 Hz respectively.

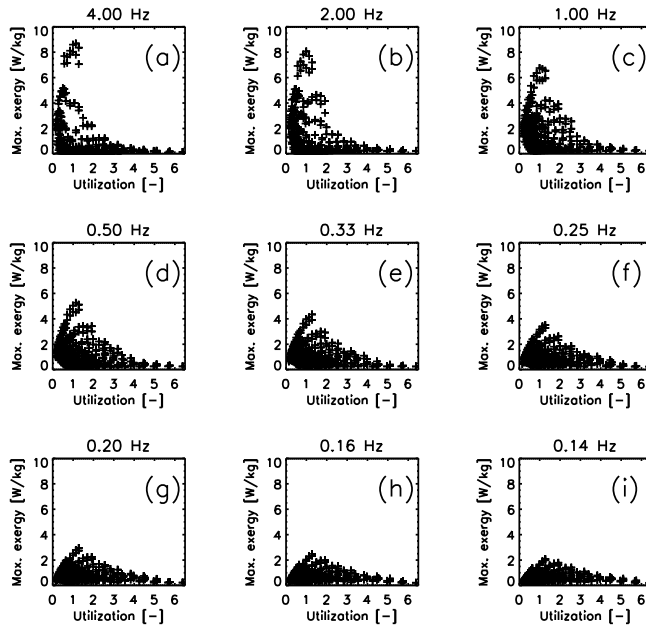


Figure 4.9: The maximum exergy as defined in Eq. 4.8 as a function of utilization. Each subfigure, (a)-(i), shows a specific frequency, 4-0.14 Hz respectively.

4.2.5 Influence of pressure drop

Even though the model does not take pressure drop into account in terms of viscous dissipation – it is, of course, implicitly included through the flow profile – it is possible to estimate the pressure drop and pumping power required. The pressure drop for a channel pipe may be expressed as (Incropera & Dewitt, 1996)

$$\Delta p = \frac{96}{\text{Re}} \rho_f \frac{L_f}{D_H} \frac{\tilde{u}^2}{2}, \quad (4.9)$$

where \tilde{u} is the mean fluid velocity and the Reynolds' number is $\text{Re} = \frac{\rho_f \tilde{u} D_H}{\mu_f}$ with μ_f denoting the dynamic viscosity of the fluid. The pump work per mass and unit width of the regenerator, \dot{w}_{pump} , is then expressed as the pressure drop multiplied with the volume flow

$$\begin{aligned} \dot{w}_{\text{pump}} &= 2 \frac{\Delta p \tilde{u}}{\rho_f L_f} \frac{H_f}{H_s} \\ &= 24 \frac{\mu_f}{\rho_f} u^2 \frac{1}{H_f H_s}. \end{aligned} \quad (4.10)$$

Now, from Table 4.1 the two parameter configurations with the largest and smallest pressure drops and pump works can be found. The smallest pressure drop is found when the fluid channel is thickest and the flow velocity minimal, i.e. at the shortest stroke length and the lowest cycle frequency. The greatest value of the pressure drop when the situation is reversed, i.e. when the flow channel height is minimal, the stroke length and frequency are maximal.

The pump work is maximized when the flow velocity is maximum and the flow and plate heights are minimal. In the reverse situation, when the flow velocity is minimum and the flow and plate heights are maximized, the pump work is minimized.

The respective values are

$$\begin{aligned} \Delta p_{\min} &= 3.7 \text{ Pa} \\ \Delta p_{\max} &= 6014 \text{ Pa} \\ \Delta \dot{w}_{\text{pump},\min} &= 0.001 \text{ W/kg} \\ \Delta \dot{w}_{\text{pump},\max} &= 87 \text{ W/kg} \end{aligned} \quad (4.11)$$

It is seen that the span of values is large and care must therefore be taken when designing a device. However, these values are, as expected, all significantly lower than those found in spherical particle beds (e.g. Tura & Rowe, 2009). Here the pressure drop may be as large as 10 bar and the pumping power more than 200 W/kg.

4.3 Summary

Through an extensive coverage of the relevant parameter space (consisting of 27,216 simulations) of parallel-plate based active magnetic regenerative refrigeration utilizing a 2-dimensional numerical model the key parameters for the optimal design and

operation of an AMR device have been investigated. It was shown that the optimal range of the utilization is roughly constant when maximization of the exergy and temperature span are sought. The values should be in the range 0.2-1.

The maximum exergy and temperature span were seen to decrease with increasing porosity and generally increase with decreasing plate thickness.

It was also shown that the maximum exergy is linearly increasing with cycle frequency, which leads to the conclusion that higher frequency will generally increase the available cooling power. This conclusion is by itself neither surprising nor new, but combined with the results of the maximum temperature span obtainable, an optimized compromise (for a given geometry) was found to be possible.

The primary reason for the peak in maximum temperature span at fairly low frequencies (0.3-0.5 Hz) was seen to be too low values of the NTU at higher frequencies. It is concluded that the value of the NTU should be in the region 10-50. Lower values will yield too small temperature spans and higher values achieved by smaller values of H_f and H_s will result in enhanced heat transfer but at the cost of increased pressure drops, thus increasing losses and cost unnecessarily.

It is concluded that the success of parallel-plate based AMR refrigerators depends partially on whether sufficiently thin channels and plates can be manufactured. At least 0.2 mm channel spacing, and thus plates of thickness 0.3 mm are needed to obtain reasonable performance compared to packed sphere regenerators with sphere diameter of 0.6 mm. To further improve the parallel plates either even thinner channels and plates or more than one MCM (i.e. a multi-material regenerator) are needed. The thinner the plates and fluid channels the more costly the system will be both in terms of manufacturing and assembly but also in terms of increased pressure drop (which scales quadratically with the inverse fluid channel thickness). Alternatively, modified parallel plates may be considered, e.g. dimpled or perforated plates. The main reason why parallel plates are interesting, even though they have obvious obstacles to overcome, is their inherent low pressure drops in operation. The problem inherent to too high pressure drops, as seen in particle beds, is an increase in the work input to the fluid pump and thus a lowering of the coefficient of performance (COP). This also adds unwanted heating in the system due to viscous dissipation in the regenerator.

Chapter 5

Multi-material regenerators

In this chapter modeling active magnetic regenerators composed of more than one material, i.e. graded AMRs, is considered. This is an important issue that is not well-understood in literature both from a theoretical and an experimental point of view. Rowe & Barclay provided a simplified analytical approach to this problem in 2003. Later, experimental and modeling results were given by Rowe & Tura (2006) and Jacobs (2009), which showed an increase in performance as the number of materials used was increased. The grading of the regenerator, i.e. splitting the regenerator material in sections each having an individual Curie temperature, is often viewed as a necessity if the realization of magnetic refrigeration as a competing technology is to be realized.

This chapter is outlined such that in Sec. 5.1 a few concepts about multi-material AMRs are discussed for clarity. In Sec. 5.2 a two-material regenerator is studied using the mean field model of Gd. The results presented in Sec. 5.2 are partially based on paper A.3.3 (Nielsen et al., 2010a), which was presented at the 4th International Conference on Magnetic Refrigeration at Room Temperature, 23-28 August 2010 in Baotou, Inner Mongolia, China. In Sec. 5.3 the case of n -material regenerators is investigated. This part of the work has not been published yet, however, a paper is in preparation on this topic. In Sec. 5.4 modeling of multi-material regenerators made of various compositions of the LCSM ceramic material series is presented. This work has also not been published yet and is thus in preparation for publication. In Sec. 5.5 experimental LCSM magnetocaloric data is applied in the model such that regenerator configurations with actual material data may be probed. Finally, in Sec. 5.6 the multi-material modeling results are summarized and concluded.

5.1 Introducing multi-material AMRs

A standard terminology considering multi-material AMRs has not been established yet. It therefore seems prudent to define a few terms that are quite useful when discussing graded AMRs.

First of all it is noted that the grading of an AMR means that the regenerator solid is made of more than one magnetocaloric material and that this division of the solid is done *along* the flow direction (consider the schematic in Fig. 5.1). The

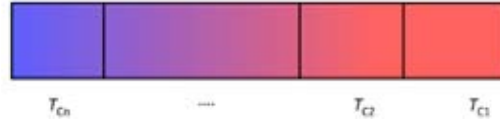


Figure 5.1: A schematic of the grading of an AMR. The color map shows the cold end (blue) and the hot end (red) as well as n different materials comprising the regenerator.

main difference between the magnetocaloric materials is their difference in T_C ¹. The reason for doing this grading is that when a temperature span is present along the flow direction each individual material will operate around its own Curie temperature and thus in this way a maximization of the overall MCE may be obtained. It is thus a concept to apply for both extending the temperature span and the cooling power of the AMR.

Now, the central variables to consider are the number of materials used, n , and the difference in Curie temperature between each consecutive material

$$\delta T_{C,i} = T_{C,i+1} - T_{C,i}, \quad (5.1)$$

where $T_{C,i}$ is the Curie temperature of the i th material and $1 \leq i < n$. In a similar way the volume fraction of each individual material may be defined as f_i such that

$$1 = \sum_i^n f_i. \quad (5.2)$$

5.1.1 The utilization of a multi-material regenerator

The thermal utilization of the regenerator for the single-material case was defined in Eq. 3.26. Here it was defined that the specific heat of the solid, which varies strongly with both temperature and magnetic field, should be evaluated at the peak temperature in zero field. This definition may, of course, be disputed in the sense that the specific heat might just as well be, e.g., an average value over the temperature range of the given regenerator (as well as operating and geometric parameters) and perhaps even taking into account the inherently different specific heat values when in zero or non-zero fields. However, it is the belief of the author of this thesis that the peak temperature, zero-field definition is the simplest and most easy to use for comparison. It does not include any influence of the given parameter configuration etc., however, on the other side it may not capture the physically most realistic utilization. It is also worthwhile to consider asymmetry in the AMR process. This topic is discussed further in Chapter 8.

Now, for the case of multiple materials, which may very well have quite different values of their peak specific heats, the definition in Eq. 3.26 is definitely inadequate. Sticking to the concept of using the peak values of the respective specific heats a weighting of each individual material could be employed (private communication

¹Here, for simplicity, considered as the peak temperature of the adiabatic temperature change when magnetizing.

with Dr. A. Rowe, and Arnold et al. (2010)):

$$c_{\text{multi,ref}} = \frac{V_s}{m_s} \sum_{i=1}^n f_i \rho_i c_{\text{peak},i} \quad (5.3)$$

where the total volume of the regenerator solid is denoted V_s , the total mass of the solid is m_s , the fraction, mass density and peak specific heat of the i th material are f_i , ρ_i and $c_{\text{peak},i}$, respectively, and the number of materials is denoted n . This definition is actually just a generalization of the definition for a single material regenerator (Eq. 3.26).

5.2 Two-material Gd-like regenerators

Property	Value
L_s [m]	0.05
H_s [mm]	0.5
H_f [mm]	0.2
δx [%]	25-75
τ_{tot} [s]	2
τ_{rel} [-]	0.25
φ [-]	0.14-0.43
$\mu_0 H_{\text{max}}$ [T]	1.0
$\mu_0 H_{\text{min}}$ [T]	0.01
T_∞ [K]	298

Table 5.1: *Input parameters for the 2-material modeling. The values of the utilization are estimated using Eqs. 3.26 and 5.3.*

The model presented in Chapter 3 accepts a range of n different magnetocaloric data sets (adiabatic temperature change and specific heat both as functions of magnetic field and temperature). Each material may have an individual length in terms of fraction of the total length of the regenerator and thus a multi-material regenerator may be modeled. In the following Gd modeled using the mean field theory (MFT), as presented in Sec. 2.3, is used as magnetocaloric material and in order to achieve various, although hypothetical, materials the Curie temperature has been varied — this is possible as a direct input parameter in the MFT; see Sec. 2.3. In this way a thermodynamically self-consistent data set is constructed and the focus may be put on how varying the material composition of the regenerator affects performance without considering (potential) problems like e.g. purity of the samples, insufficient data sets etc.

5.2.1 Variation of the parameters

The Curie temperatures of the two individual materials comprising the regenerator were varied from 275 to 301 K in steps of 2 K. For each pair of Curie temperatures, i.e. $T_{\text{C,cold}}$, $T_{\text{C,hot}}$ denoting the cold and hot side materials, respectively, a range of simulations were performed. The two parts of the regenerator are of equal size.

The operational and geometric parameters were fixed at the values given in Tab. 5.1, with the exemption of the stroke length, which was varied to obtain different values of the utilization (see Sec. 5.1.1 for a discussion of how to define this parameter for multi-material regenerators). This parameter configuration was chosen such that the regenerator would be sufficiently effective to obtain at least a temperature span of 20 K and still maintain a cooling power (in the single-material case where $T_{\text{C}} = 293$ K). Finally, the ambient temperature was kept fixed at 298 K.

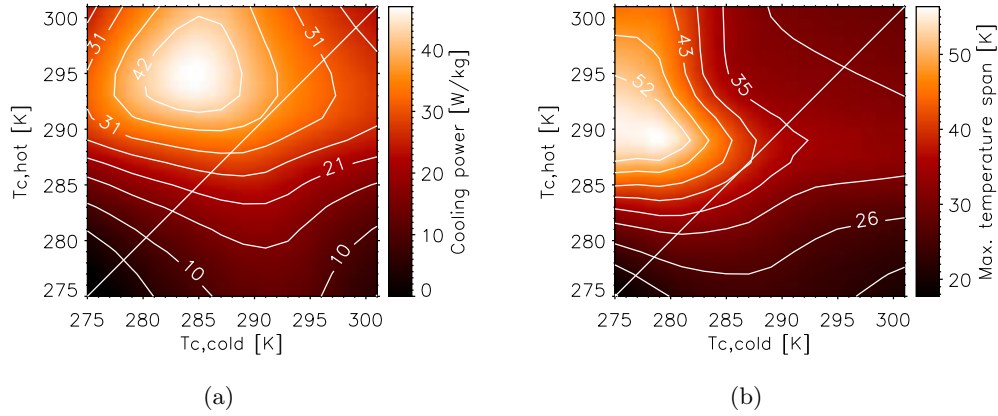


Figure 5.2: The cooling power at a temperature span of 20 K (a) and the maximum temperature span (b) both as a function of the cold and hot Curie temperatures (abscissa and ordinate, respectively). The diagonal line, present in both plots, shows where in the diagram the two Curie temperatures are equal, i.e. the regenerator is made of a single material.

5.2.2 Results

Cooling power and temperature span

For the parameter configuration given in Tab. 5.1 and, of course, the variation of the two Curie temperatures, a range of temperature spans were imposed in order to obtain the cooling power versus temperature span curves. In Fig. 5.2 the resulting cooling power, at a fixed span of 20 K, and the maximum obtainable temperature span are plotted as a function of the two Curie temperatures. The single maxima in both plots are located at $(T_{C,cold}, T_{C,hot}) = (285, 295)$ K and $(280, 289)$ K, respectively. That serves to show that multi-material regenerators may indeed increase the performance of the regenerator.

The increase from the maximum performance when considering a single-material regenerator, i.e. on the diagonal line in the plots in Fig. 5.2, to the global maximum is of the order 25 percent in terms of the cooling power. This increase should be viewed as proof of the fact that the performance may increase when grading the regenerator, however, the increment may indeed be dependent on other circumstances such as geometry, operating parameters etc.

Maximum exergy and COP

Considering Fig. 5.3 the maximum exergy and the coefficient of performance are plotted as functions of the two Curie temperatures. Since the regenerator is comprised of more than one material the cooling power as a function of temperature span may not a priori be assumed to be linear as was the case in Chapter 4. Thus, the exergy as a function of cooling power and temperature span (and ambient tem-

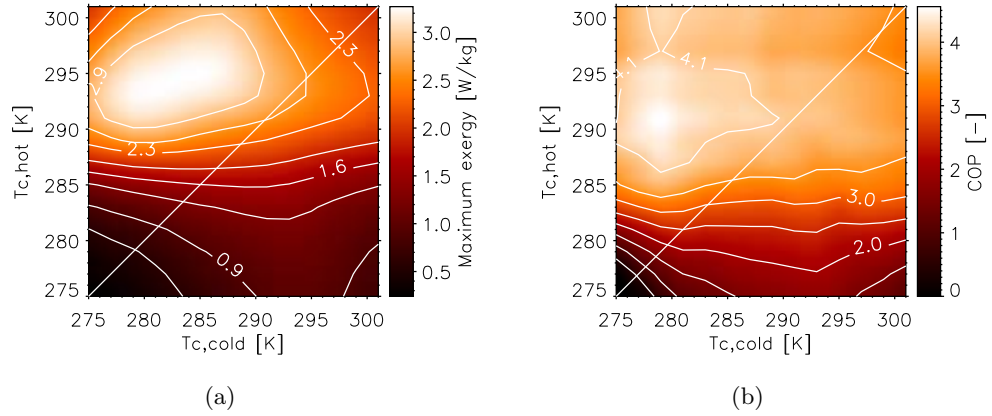


Figure 5.3: The maximum exergetic cooling power (a) and the coefficient of performance (b) both as a function of the cold and hot Curie temperatures.

perature, of course) should be found through the fundamental equation

$$\text{Ex}_Q = Q_c \left(\frac{T_\infty}{T_{\text{cold}}} - 1 \right) \quad (5.4)$$

rather than the derived expression in Eq. 4.7, which was based on an assumption of linearity between the cooling power and the temperature span (Rowe, 2009). The maximum exergy, or available cooling power, is then found as the maximum of Eq. 5.4 as a function of the temperature span. The COP is found through the equation

$$\text{COP} = \frac{Q_c}{W}, \quad (5.5)$$

where W is the total work of the regenerator, here assumed to be equal to the magnetic work, i.e. $W = Q_c + Q_h$.

The maxima of the exergy and the COP are located around (284,295) K and (280, 291) K, respectively (see Fig. 5.3). The same conclusion as for the cooling power and maximum temperature span is thus valid — the multi-material regenerator may certainly perform better than the single-material. The performance gain between a single and a two-material regenerator, in terms of the maximum exergy, is around 25 percent (from approximately 2.6 to 3.2 W/kg; see Fig. 5.3), which is very similar to the result from the cooling power (Fig. 5.2).

Varying the ratio between the two materials

The previous results were all found using the same amount of each material of the two different Curie points. However, it is non-trivial to decide whether a different ratio between the fractions of the two materials will improve performance. Thus, for the configurations given in Tab. 5.1 the ratio was varied from 1/10 to 8/10 in terms of the cold-end material's fraction of the entire length of the regenerator. Fig. 5.4 shows the maximum cooling power and the COP for each fraction.

The results show that there is a single maximum, which is present at the fraction where there is an equal amount of the two materials. Although the change between fractions of 40, 50 and 60 percent, respectively, is rather small, it is clear that there should be an equal amount of the two materials. However, this may only hold for two material regenerators where the MCE is roughly the same, albeit with varying Curie temperatures.

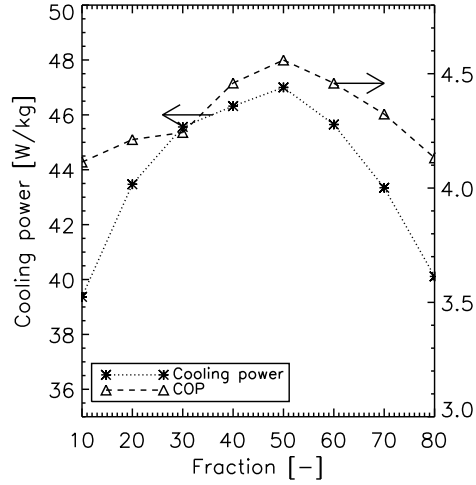


Figure 5.4: For each fraction between the two materials the maximum of the cooling power and the COP at a temperature span of 20 K are found as a function of cold and hot Curie temperature.

5.3 n -material Gd-like regenerators

The more generalized case of multi-material AMRs is now considered. The setup is similar to that of the previous section, 5.2, however, the length of the regenerator is set to be 0.2 m rather than 0.05 m. This is due to the fact that as many as eight materials are considered simultaneously and thus in order to have a realistic length of each individual material a rather long regenerator is needed.

The distance between two consecutive Curie temperatures is set to be 4 K, i.e. $\delta T_C = 4$ K. The number of materials in the regenerator is varied from two to eight and in all cases the amount of each material is the same, such that, e.g., in the case of six materials each material will have a spatial extension in the flow-direction (which is, of course, also the direction of the grading of the regenerator) of $0.2\text{m}/6 = 0.033$ m. This is done in order to keep at least some parameters fixed such that the results are more easily interpreted. Later work should definitely consider varying the volume fraction of each individual material. The input parameters to the model are given in Tab. 5.2.

In the following sections the cooling power versus temperature span is investigated as a function of number of materials and utilization. First, in Sec. 5.3.1 the actual cooling power versus temperature span curves are presented. Second, in Sec. 5.3.2, the functional dependency of the maximum cooling power and temperature span, respectively, as a function of the number of materials is investigated. Finally, in Sec. 5.3.3, the COP, maximum exergy and realistic operating temperature spans and cooling powers are probed.

Property	Value
L_s [m]	0.2
H_s [mm]	0.3
H_f [mm]	0.3
δx [%]	20-70
τ_{tot} [s]	2
τ_{rel} [-]	0.125
φ [-]	0.28-1.0
$\mu_0 H_{\text{max}}$ [T]	1.0
$\mu_0 H_{\text{min}}$ [T]	0.01
T_∞ [K]	298

Table 5.2: Input parameters for the n -material modeling. The values of the utilization are estimated using Eqs. 3.26 and 5.3.

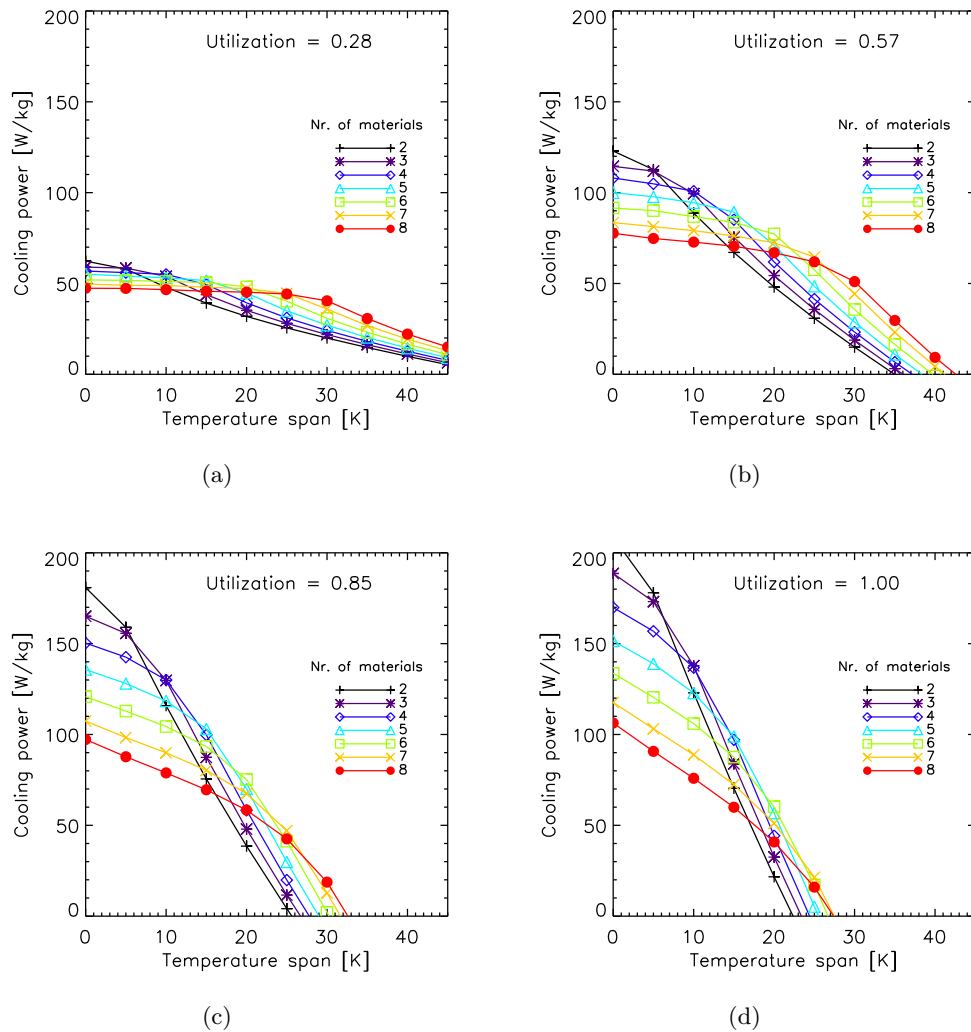


Figure 5.5: The cooling power versus temperature span at different utilizations. The cooling power has been normalized in terms of mass of the regenerator material.

5.3.1 Cooling power versus temperature span

In Chapter 4 it was argued that the cooling power versus temperature span is linear (based on both modeling and experimental results as well as results reported in literature) for single material regenerators. However, any a priori expectation of the shape of the cooling power versus temperature span curve when grading the regenerator with several different materials is difficult to provide. It is therefore quite reasonable to explicitly consider the cooling power versus temperature span curves for this case.

Figure 5.5 shows the cooling power (normalized in terms of the mass of the regenerator solid material) versus temperature span for several values of the utilization and for regenerators made of two to eight materials. First, it is noted that for small values of the utilization all the curves are quite flat and that the temperature span at which the cooling power begins to drop increases with the number of materials. The

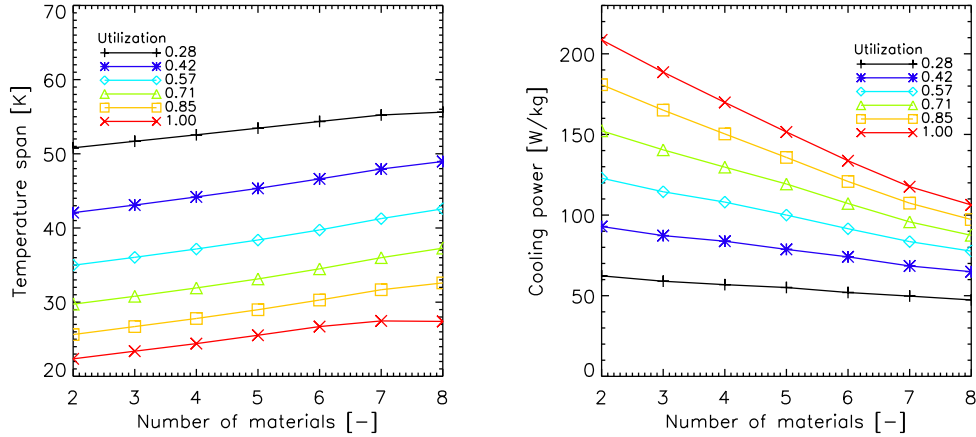


Figure 5.6: The maximum temperature span (left) and the maximum cooling power (right) as a function of number of materials and utilization.

curves become steeper when the utilization is increased. The trend that the cooling power remains fairly constant until a certain temperature span and then decreases linearly becomes more vague as the utilization increases and at a utilization of 1 the cooling power curves are virtually linear as a function of the temperature span. Since a relatively large amount of heat transfer fluid is moved the temperature span will decrease due to the less efficient regenerator; see also Chap. 4. In this case the addition of more materials will not improve the performance of the AMR since one or more of the materials, which the regenerator is made of, are not operating at their respective optimal temperatures. This point certainly also serves to show that the choice of which materials, and how much of each, should be used is highly dependent on the application both in terms of temperature span and ambient temperature.

If, e.g., the cooling curve for the 8-material regenerator in Fig. 5.5(a) is considered it is observed that the cooling power is virtually constant until a temperature span of 30 K is reached whereafter the curve falls linearly eventually to zero cooling power. The same trend is apparent when considering the utilizations of 0.57 and 0.85 (Figs. 5.5(b)-(c)). In fact, it may be concluded that adding materials to the regenerator, in the fashion investigated here and described at the beginning of this section, “pushes” the temperature span at which the cooling power versus temperature span starts dropping linearly.

5.3.2 Maximum cooling power and temperature span

Many experimental results are reported in the form of the maximum cooling power or the ditto temperature span. The maximum cooling power is the cooling power at zero temperature span whereas the maximum temperature span is the span at zero cooling power. Both numbers are irrelevant for the application as such since they both represent non-useful states of the AMR. If no temperature span is present no lowering of the temperature of the object that needs refrigeration is done. On the other hand, if no cooling power is available there will be no net refrigeration at the

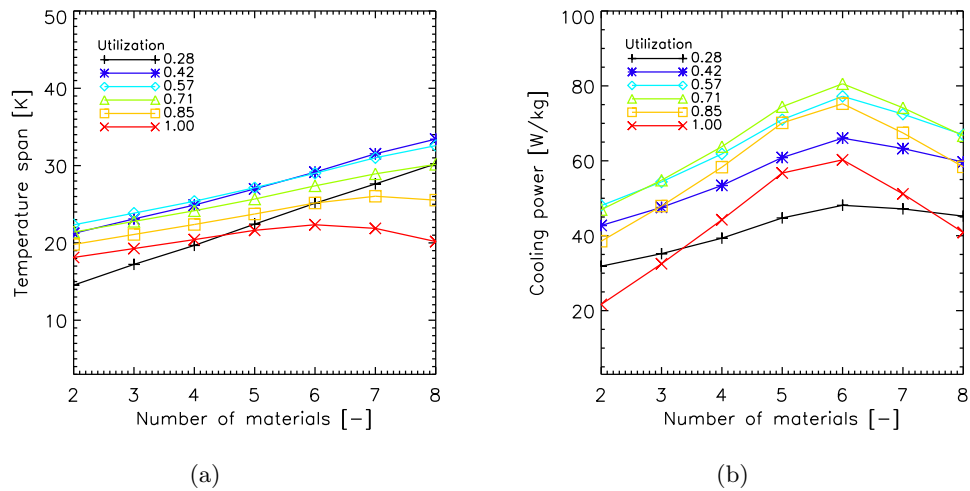


Figure 5.7: The temperature span at a cooling power of 40 W/kg (a) and the cooling power at a temperature span of 20 K (b) both as a function of the number of materials and the utilization.

given temperature span. It is thus of limited interest to consider these parameters. However, they may serve to illustrate the trend as a function of the number of materials used.

In Fig. 5.6 the maximum temperature span and cooling power are plotted. It is evident from the figure that the temperature span increases as a function of the number of materials in the regenerator, albeit no more than ten degrees going from two to eight materials. It is clear that the lower utilization yields the largest temperature span, which may be expected with, e.g., the results of Chap. 4 in mind. The maximum cooling load decreases as a function of the number of materials, which is quite reasonable. This is so since increasing the number of materials will increase the amount of the regenerator solid that has an optimal operating temperature range away from the ambient and thus reduce the overall magnetocaloric effect. The trend due to the utilization, that the higher utilization yields a larger cooling power, is also expected again as per the results of Chap. 4.

5.3.3 Realistic assessment of multi-material regenerators

As it was argued in the previous section, 5.3.2, assessing the performance of the AMR in general and multi-material AMRs in particular is non-trivial. However, considering the temperature span at a non-zero cooling power, or the cooling power at a non-zero temperature span, provides a relevant platform for assessing the AMR performance.

In Fig. 5.7 the temperature span at a cooling power of 40 W/kg and the cooling power at a temperature span of 20 K are plotted as a function of the number of materials. It is observed that the temperature span increases linearly as a function of the number of materials until a utilization of about 0.7 is reached. Hereafter the regeneration is too affected by the rather large movement of the heat transfer fluid to uphold the temperature span and the optimal number of materials seems to be

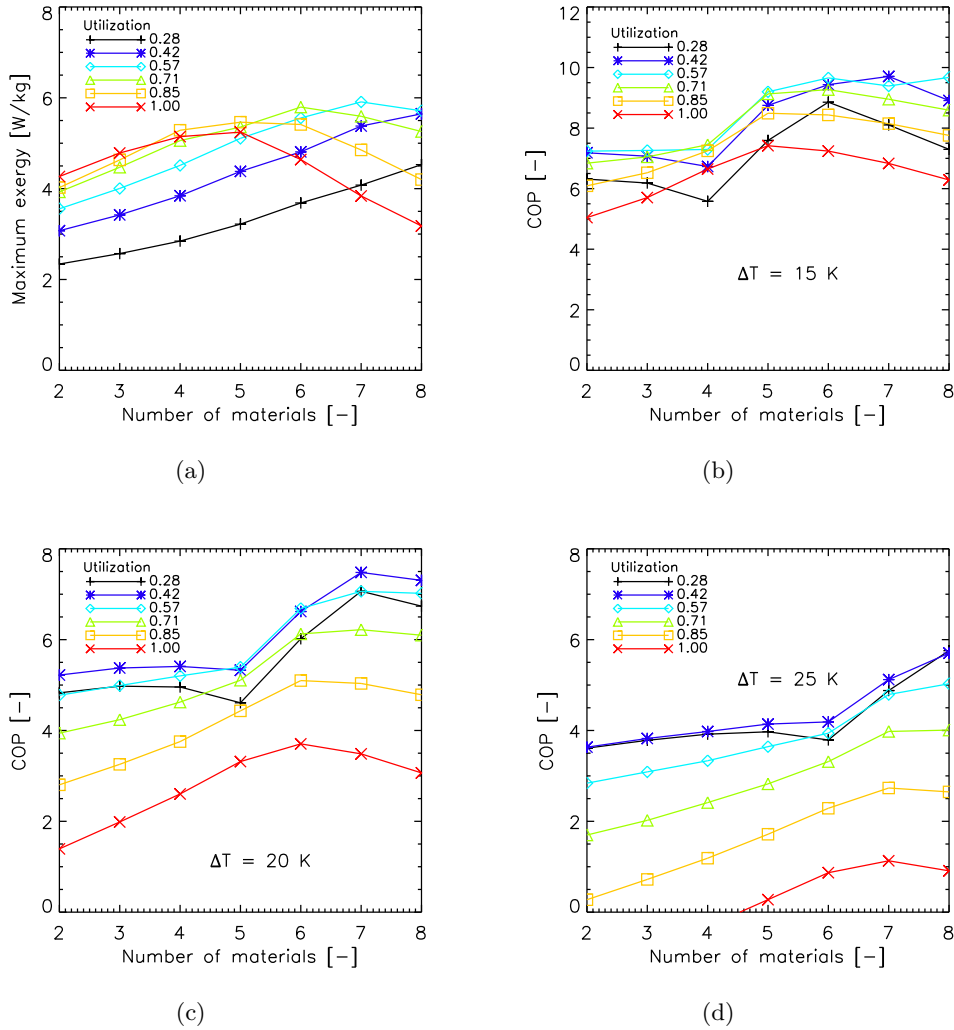


Figure 5.8: The maximum exergy (a) and the COP (b)–(d) as a function of the number of materials and utilization. The COP has been evaluated at the temperature spans 15, 20 and 25 K, respectively.

less than eight (in terms of maximizing the temperature span). However, the figure 5.7(a) clearly shows that increasing the number of materials certainly increases the performance in terms of the temperature span for smaller values of the utilization.

In Fig. 5.7(b) the cooling power at a temperature span of 20 K is plotted as a function of the number of materials in the regenerator. It is evident from the figure that there is an optimum for all the utilizations considered at a number of materials less than eight. This is, of course, biased somewhat from the choice of a temperature span of 20 K. However, it certainly shows that increasing the number of materials indefinitely is not a priori optimal as it likewise shows that more than one material is certainly advantageous.

Another set of resulting parameters for probing the performance are the maximum exergetic cooling power, i.e. the maximum of the curve defined in Eq. 5.4, and the coefficient of performance (COP). These parameters are plotted in Fig. 5.8.

It is apparent from Fig. 5.7(a) that the maximum exergy is a function of both the utilization (as shown previously; see Chapter 4) and the number of materials. This may be understood from the fact that the exergy is a function of both the cooling power and the temperature span and thus since the optima for these two parameters, respectively, in terms of the number of materials are not generally coinciding, the maximum exergy should not be expected to be present at, e.g., a fixed number of materials. The trend is, in fact, that the lower the utilization the larger the number of materials should be in order to maximize the maximum exergy.

The coefficient of performance (COP) at the two temperature spans 15 and 20 K, respectively, (see Figs. 5.8(b)–5.8(c)) has a maximum value at a number of materials between six and seven depending on the utilization. At a temperature span of 25 K (Fig. 5.8(d)) the COP increases roughly monotonically as a function of the number of materials and a maximum is thus not observed. Since the temperature span is rather large it is expected that at a larger number of materials the COP will maximize.

The exergy as a function of cooling power

In Fig. 5.8 the maximum exergy was considered as a function of the number of materials and utilization. Now, this parameter was argued to be useful when evaluating the performance of an AMR in Sec. 4.2. In this analysis, however, the shape of the exergy as a function of cooling power was assumed to be a parabola for the case of a single-material regenerator and it was noted that for the multi-material case this shape might not be true. It is therefore relevant to consider the exergy as a function of cooling power for the multi-material case. In Fig. 5.9 the exergy is plotted as a function of the cooling power for different number of materials and values of the utilization.

The curves have a single maximum. However, for the two low values of the utilization the shapes are quite assymetrical. This is in fine accordance with the cooling power versus temperature span curves given in Fig. 5.5 where the curves are quite flat for low values of the utilization. It may thus be concluded that the shape of the exergy versus cooling power curve for multi-material regenerators cannot a priori be assumed to be parabolic. The rather steep decline of the exergy as a function of cooling power at a larger number of materials right after the maximum indicates that the AMR is sensitive to the operating conditions when several materials are used. This behavior seems to be present for all the utilizations considered in Fig. 5.9. It is also noted that the cooling power at which the exergy is maximized is identical to the cooling power at which the corresponding cooling power versus temperature span curve “breaks” (for the cases where this break in the curve is present).

It may thus be concluded that a multi-material regenerator may certainly enhance the temperature span and cooling power of the AMR, however, it is important to operate the device within the cooling power / temperature span range where the exergy is increasing or maximized; when the exergy is decreasing as a function of cooling power (i.e. the cooling power is large and so the temperature span is small) the operating mode of the AMR may be considered far from the optimal and unstable in the sense that the change in, e.g., the exergy per cooling power is relatively large.

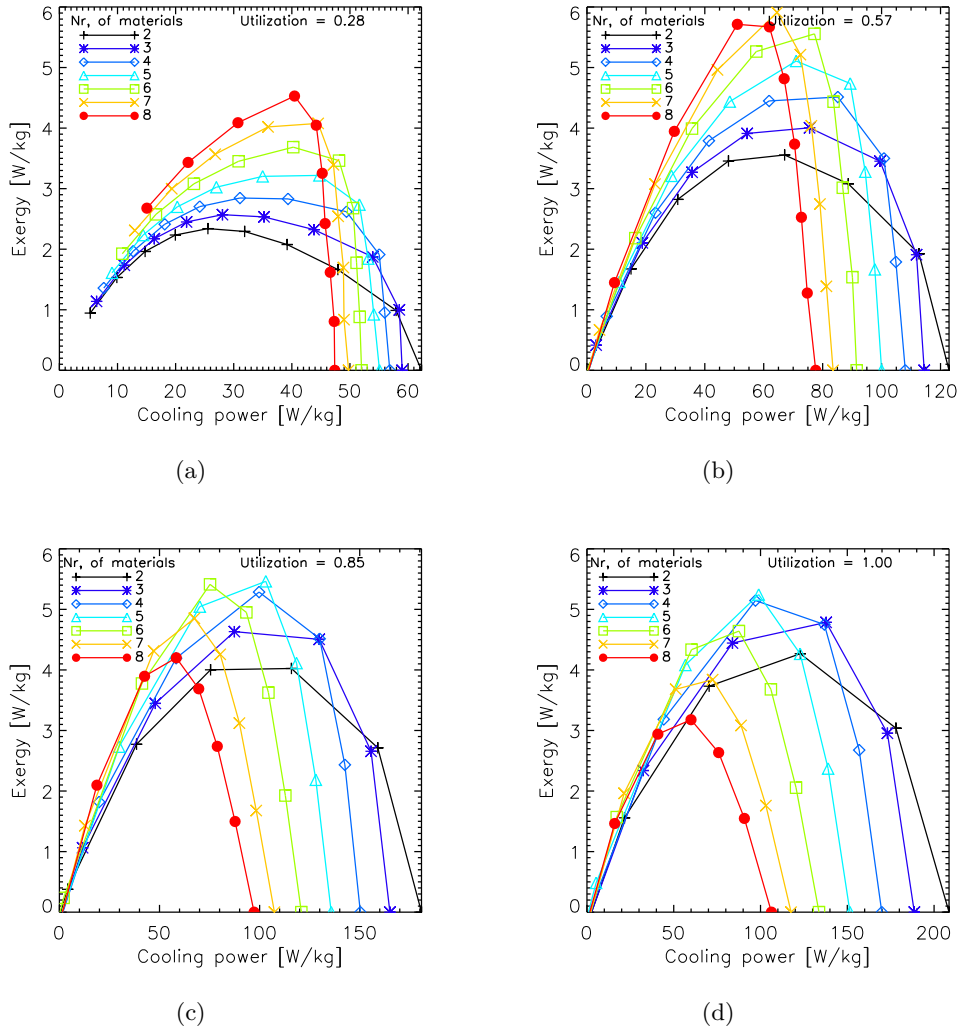


Figure 5.9: The exergy as a function of cooling power for different number of materials and values of the utilization as indicated in the figures.

5.3.4 Influence of a larger distance between materials

The results presented so far in Sec. 5.3 have been concerned with a spacing of 4 K between each material's Curie temperature ($\delta T_C = 4\text{K}$). An investigation of the influence of a different spacing is thus needed.

Spacings of 8 and 12 K between the Curie temperatures of consecutive materials were used as the basis of a range of simulations otherwise completely identical to those with a spacing of 4 K. In Fig. 5.10 an ensemble of cooling power versus temperature span curves are shown. The number of materials in the 8 K spaced cases has been limited to five since the largest difference in Curie temperature is then very similar to that of the 4 K spaced cases and the 12 K spaced cases have been limited to a maximum of four materials for the same reason.

The results shown in Fig. 5.10 reveal that using, e.g., seven materials spaced evenly in Curie temperature with 4 K or four materials with a spacing of 8 K

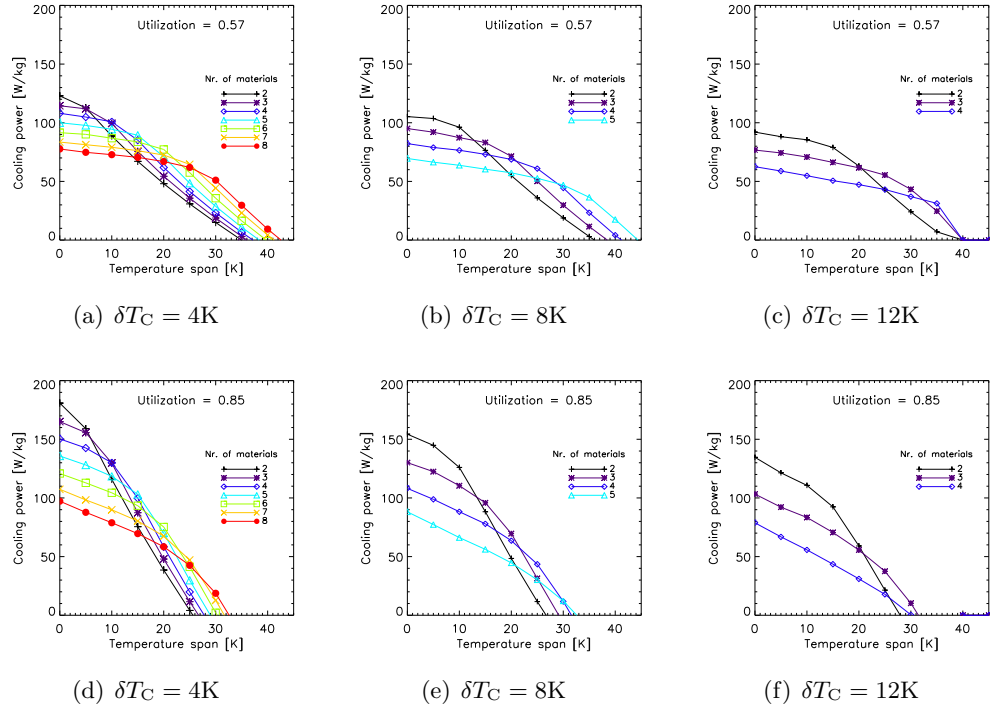


Figure 5.10: The cooling power versus temperature span curves for two different values of the utilization (0.57 and 0.85, respectively) for the cases of a difference in consecutive Curie temperatures of 4 K ((a) and (d)), 8 K ((b) and (e)) and 12 K ((c) and (f)), respectively. Comparing, e.g., curves with a Curie temperature difference of 4 K and seven materials with the corresponding 8 K in difference and four materials reveal that the performance is virtually identical if the cold end Curie temperatures are identical (compare, e.g., the yellow lines in (a) and (d) with the blue lines in (b) and (e)).

performs virtually identically. The cold end Curie temperatures are in both cases 274 K. This is quite interesting since the number of materials is then proven not to be the only dominating factor in terms of performance increment when considering graded AMRs.

Consider the 4 K and 12 K spaced cases (Figs. 5.10(a)-(d) and 5.10(c)-(f)) and focusing on, e.g., the 4 K spaced, 7-material regenerator and the 12 K spaced, 3-material regenerator, both having a difference between the two end-material Curie temperatures of 24 K. It is seen that the 7-material configuration shows a slightly higher performance in terms of cooling power as a function of temperature span. However, this difference is rather small.

It may thus be concluded that for case of using Gd-like compounds (with the Curie temperature tuned somehow, which could in reality be done using GdTb or GdEr alloys (Gschneidner & Pecharsky, 2000)) and fixing the difference in Curie temperatures between the end-materials that fewer materials are sufficient. This is, of course, quite dependent on the temperature span wanted and the adiabatic temperature change as a function of temperature for the involved materials. The width of such curves differs significantly from material to material and the optimum

Table 5.3: The mean field model parameters for $\text{La}_{0.67}\text{Ca}_{0.26}\text{Sr}_{0.07}\text{Mn}_{1.05}\text{O}_3$. Data from Dinesen (2004).

N_s [kg^{-1}]	g [-]	J [\hbar]	N [kg^{-1}]	θ_D [K]	γ_e [$\text{Jkg}^{-1}\text{K}^{-2}$]
2.8×10^{24}	2	1.83	1.44×10^{25}	353	2.5×10^{-2}

number of materials may vary significantly dependent on the used material series.

5.4 n -material LCSM-like regenerators

The ceramic material LCSM, which was introduced in Section 2.5 in terms of its magnetocaloric properties, is in the following considered as a gradable magnetocaloric material for the AMR. The MFT describes, to some degree, the properties of LCSM fairly well. Thus, MFT-based data are used to produce results, which are directly comparable with the MFT Gd from the previous sections in this chapter. The input parameters to the MFT are given in Tab. 5.3. The Curie temperature is changed in the same fashion as done for the Gd-like results. This is done in order to make the results directly comparable. It is noted that this approach is a significant simplification that serves to provide a base for comparing multi-material regenerators comprised of MCMs of a different nature. As it was seen in Fig. 2.8, the width and height of both the adiabatic temperature change and specific heat change as a function of the Curie temperature. This effect is not captured here and that is not the intent either. In the next section, 5.5, the experimental LCSM data are used for modeling a real-world application of this material.

The operating and geometric parameters are kept the same as those used for the Gd modeling (see Tab. 5.2). The density and thermal conductivity are 6000 kg/m^3 and 1 W/mK (Visser et al., 1997), respectively. Since the operating conditions are kept the same as for the Gd-like modeling, the utilization becomes somewhat different due to the difference in peak specific heat in zero field (see Fig. 2.8). However, the general trends are certainly comparable. Now, Fig. 5.11 presents a sample of cooling power versus temperature span curves. In Fig. 5.11(a) and (c) the spacing between Curie temperatures is 4 K and in Fig. 5.11(b) and (d) the spacing is 6 K. This means that, e.g., using a spacing of 4 K and seven materials gives a difference between the hot- and cold-side T_C of 24 K. Similar conditions are present when using a spacing of 6 K and five materials. Thus, comparing these graphs (yellow in (a) and (c) and turquoise in (b) and (d)) it is seen that the curves are virtually identical. This trend seems to follow for all the comparable curves. It may thus be concluded that the conclusion from the previous section, i.e. that as long as the hot and cold Curie temperature difference is the same (when considering a constant difference in consecutive Curie temperatures) the performance is quite similar also holds for the LCSM-based modeling. However, this conclusion will have a limited range in terms of the Curie temperature spacing between two materials due to the limited width of the adiabatic temperature change curves.

A more general understanding of the relation between the number of materials, δT_C , cooling power and temperature span may be obtained from Fig. 5.12. Here, the trend seems to be same as that observed in Fig. 5.11. The physical explanation for

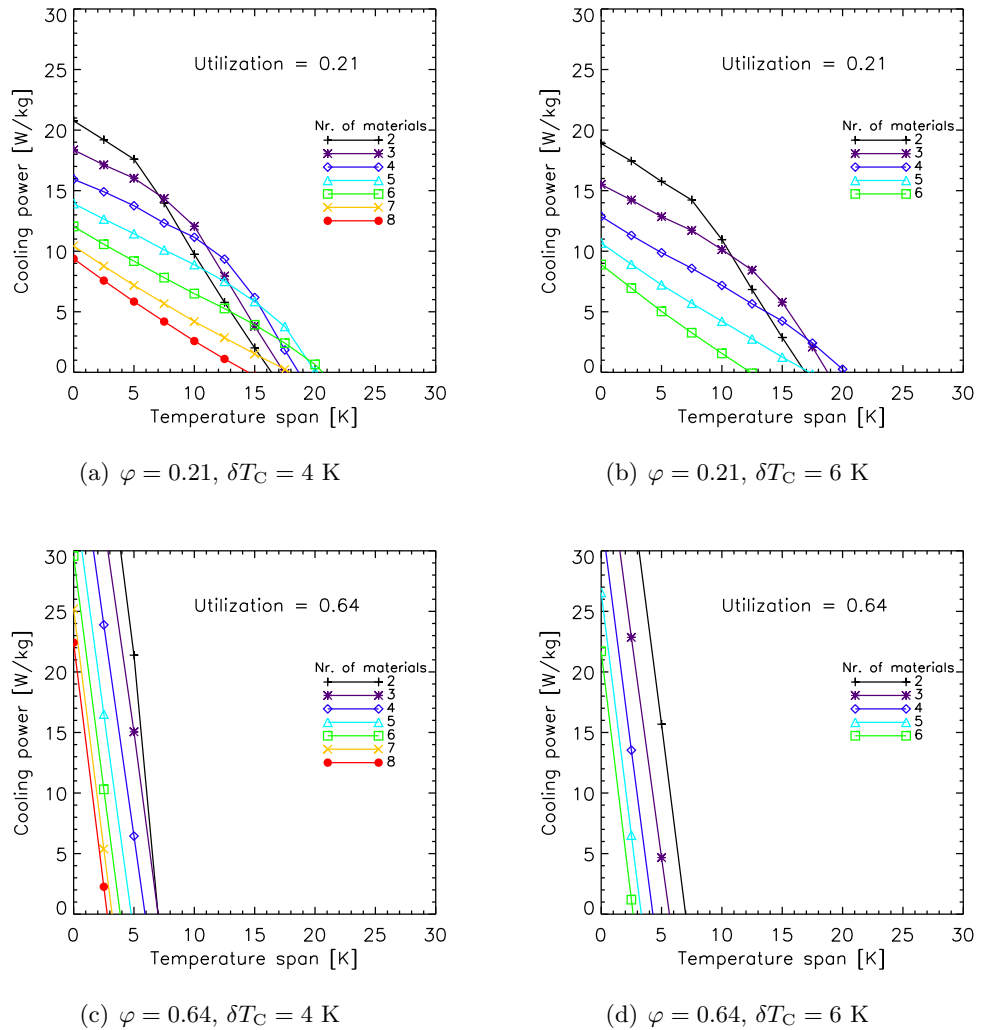


Figure 5.11: The cooling power versus temperature span for the MFT modeled LCSM regenerators. Left: the spacing between two adjacent materials is 4 K ($\delta T_C = 4 \text{ K}$). Right: the spacing is 6 K.

this may, at least partially, be that when increasing the number of materials each individual material becomes small (the total length of the regenerator is kept fixed). In this way each individual material may operate only around its Curie temperature, in which case the exploitation of the MCE would seem maximized. However, it does not take a big change in the overall temperature profile of the entire regenerator for the individual materials to operate relatively far from the temperature range where their MCE is maximized. Another effect is the “local” utilization for each material. The fluid is moved a certain amount in relation to the total length of the regenerator. However, when that is comprised of many materials each of these will experience a larger local utilization.²

²This is also an argument against considering a multi-material regenerator as being analogue to a series of single-material regenerators. If one were to create such a system heat exchangers would have to be in between each sub-regenerator.

Another interesting observation from Fig. 5.12 is that for a given cooling power (e.g. 7 W/kg in Fig. 5.12(a)) the maximum temperature span is obtained at $(n - 1) \times \delta T_C$ (in this case 16 K with $n = 9$). It is, of course, noted that this rule of thumb assumes the ambient temperature to be appropriate such that the materials are operating close to the temperature region where their MCE is maximized. In this fashion the physical reason for this is the global maximization of the MCE of the entire regenerator.

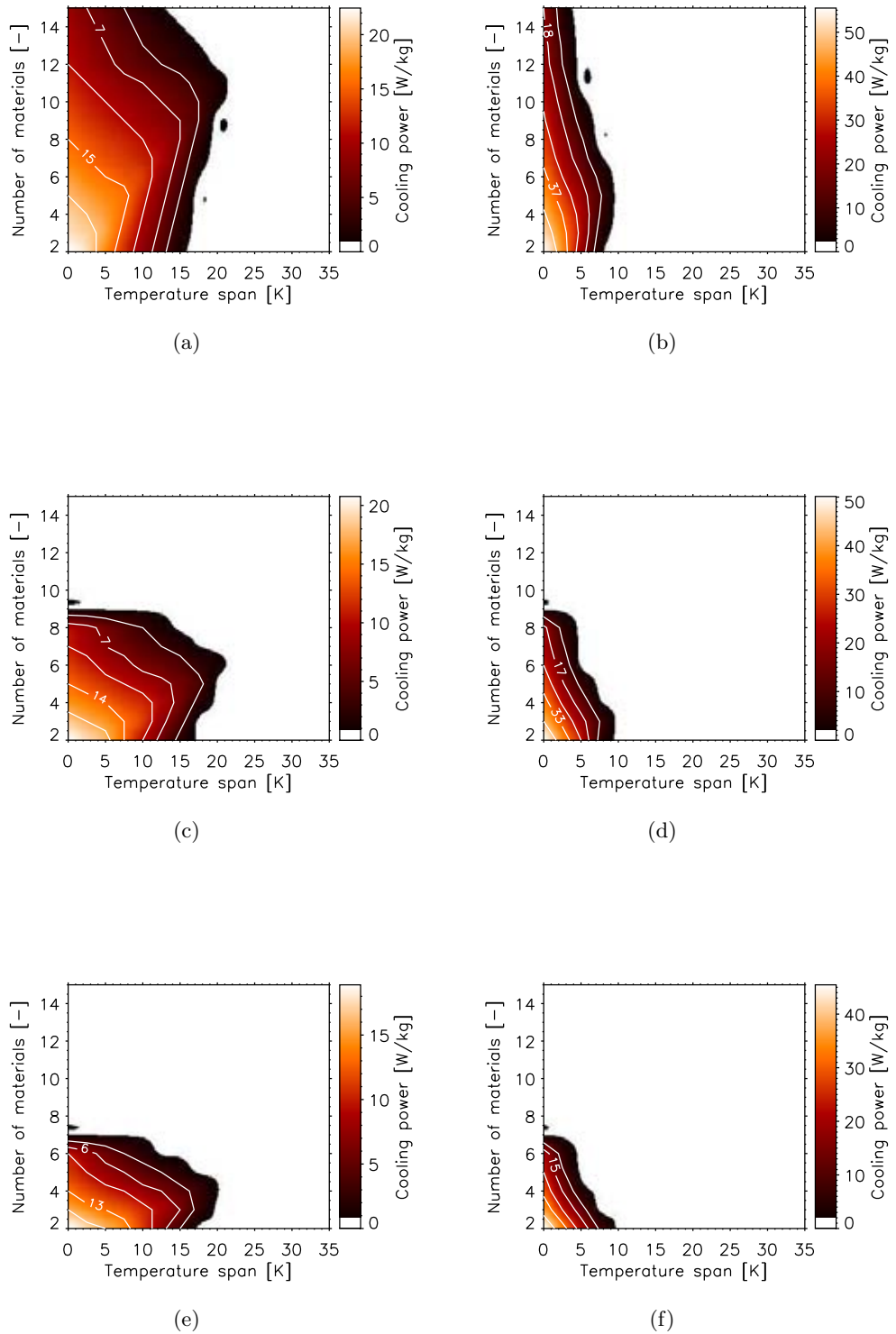


Figure 5.12: Cooling power mapped as a function of temperature span and number of materials at a utilization of 0.21 (left figures) and 0.53 (right figures). In (a)-(b) $\delta T_C = 2$ K, in (c)-(d) $\delta T_C = 4$ K and in (e)-(f) $\delta T_C = 6$ K.

Table 5.4: The four LCSM configurations using measured magnetocaloric properties. The temperatures given in the “Materials” column indicate the adiabatic temperature change peak temperatures; see Fig. 2.8 for reference. The ambient temperature is indicated in the column labeled T_∞ . The “ideal” temperature span column indicates the difference between the hot and cold side Curie temperatures.

Config.	Materials	T_∞ [K]	“Ideal” temperature span [K]
4 mat	276.1, 280.6, 287.7, 294.8	296	19
5 mat	276.1, 280.6, 284.1, 287.7, 294.8	296	19
6 mat	276.1, 280.6, 284.1, 287.7, 294.8, 298.8	300	23
7 mat	276.1, 280.6, 284.1, 287.7, 294.8, 298.8, 302.3	304	27

5.5 Multi-material LCSM with experimental data

The previous section focused on the MFT-based modeling of the LCSM material series. However, as it was argued, this was aimed at gaining an understanding of the theoretical performance of multi-material AMRs and especially for comparing with the MFT-based Gd modeling presented in Sec. 5.3. The conclusions of the comparison were quite easy to comprehend: the general trends are much the same, however, the significantly smaller MCE of the LCSM and the 10 times smaller thermal conductivity of the LCSM compared to Gd means that the Gd-graded AMRs perform significantly better in terms of cooling power and temperature span than those based on LCSM.

Now, it is of great interest to actually probe a real-world material. For this purpose the LCSM is an excellent choice of material since it is, in fact, fairly easy to tune the Curie temperature and such a material series with varying Curie temperature has actually been manufactured and characterized in terms of the relevant magnetocaloric properties; see, e.g., Fig. 2.8. Of the materials given in Fig. 2.8 four configurations were selected for simplicity. Some of these include an “artificial” material with an adiabatic temperature change peak temperature right inbetween the two materials with peak temperatures 280.6 and 287.7 K, respectively. In this way this material is simply designed as a linear interpolation of these two materials. The reason for having this material is the fact that an equal spacing of about 4 K between each material can then be achieved. The configurations are given in Table 5.4. The reference specific heat used in the calculation of the utilization of each configuration is found to be approximately 700 J/kgK using Eq. 5.3.

The AMR model was configured to use the dataset given in Fig. 2.8, the thermal conductivity was kept at 1 W/mK, however, the mass density was set to 4500 kg/m³. This value is not the atomic mass density, i.e. the value the material would have if it were completely solid. During the manufacturing process of the plates of the LCSM material, which is done by tapecasting followed by sintering, a porosity is introduced into the structure. Measurements have shown a resulting effective mass density of about 4500 kg/m³, which is then some 25 percent less than the nominal value.

The resulting cooling power versus temperature span is given in Fig. 5.13. It seems, in general, that the four material configuration is slightly better than the

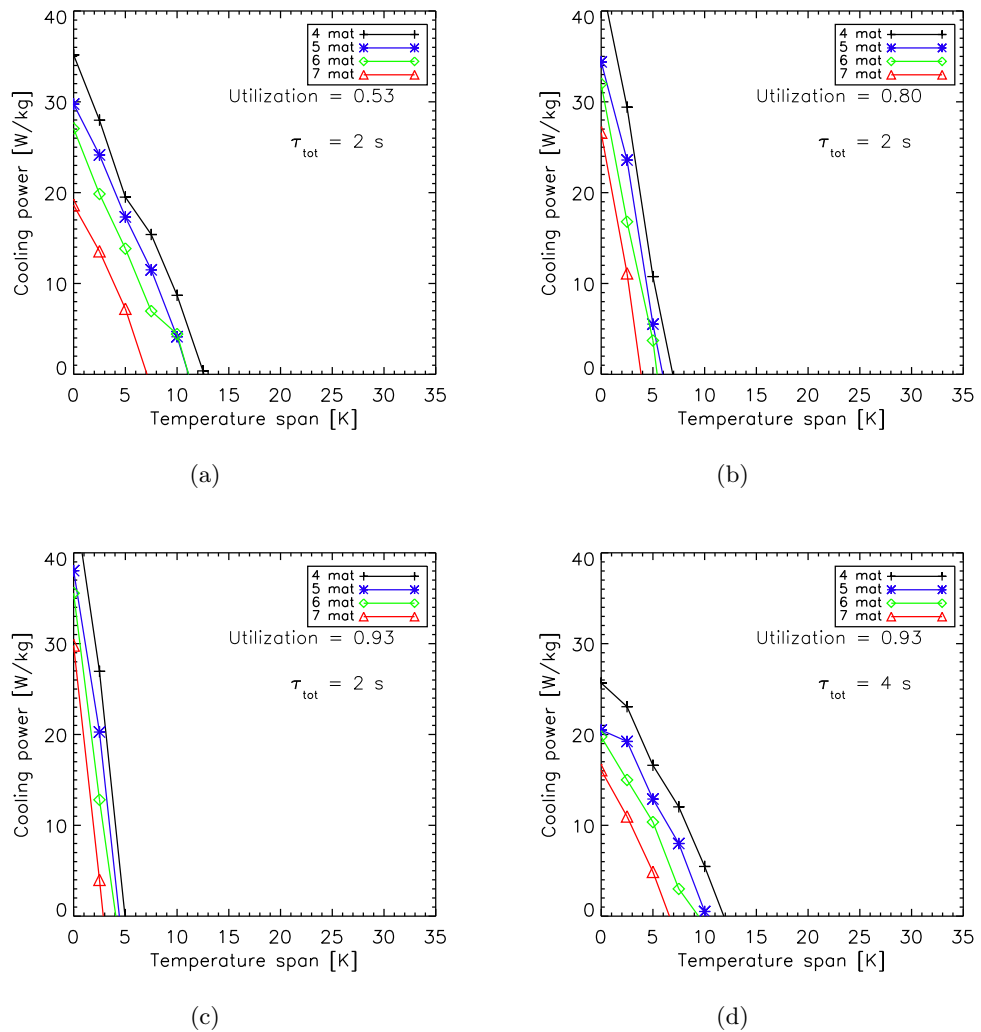


Figure 5.13: Cooling power versus temperature span using the experimental LCSM data. The figures show a selection of utilizations and total AMR cycle times.

other configurations. However, the differences seem to be quite small, especially for some sets of utilization and total cycle timing.

In Tab. 5.4 an “ideal” temperature span is indicated for the respective configurations. This span is the difference between the hot and cold side Curie temperatures and is thus a rough estimate of what can be expected to be optimal. When considering the results presented in Fig. 5.13 it is clear that none of these parameter sets produce a sufficiently effective regenerator such that the temperature range spanned by the Curie temperatures may be exploited. Thus, the more materials the “worse” it gets since even less of the regenerator material is active. This was actually also observed in the idealized modeling using either Gd or LCSM (Sections 5.3–5.4). When the temperature span is too small to sufficiently activate each individual material the regenerator is comprised of fewer materials is better, since more regenerator material will be active.

5.6 Summary

In this chapter modeling multi-material active magnetic regeneration was considered. First, the two-material case using mean field modeled Gd-like materials were analyzed. It was shown that the performance in terms of temperature span, cooling power, exergetic cooling power and coefficient of performance can indeed be enhanced using multi materials. This result is quite in line with the results presented in literature. Second, the more generalized case of n materials (still assuming mean field modeled Gd-like materials) was considered. For the cases studied here it was found that adding more materials to the regenerator indeed enhances the performance, however, depending on how the spacing in terms of the individual Curie temperatures is done, fewer materials may perform equal to more materials if the distance between the Curie temperatures differ between the two cases.

The n -material modeling of Gd lead to modeling of LCSM where the magnetocaloric properties were modeled using the MFT. Here similar trends to those found when considering Gd were observed. However, due to the fact that an LCSM-based regenerator is less effective than a similar Gd-like regenerator because of the large difference in thermal conductivity between the two materials, the LCSM-based regenerators yield smaller temperature spans and cooling powers than those based on Gd.

In order to assess regenerators made of real materials, i.e. materials that have actually been produced and characterized, the LCSM data presented in Chapter 2 were applied. It was observed that only at small values of the utilization and slow AMR cycle timings can the LCSM-based regenerators uphold temperature spans that enable all the individual materials to operate around their Curie temperature.

Chapter 6

Model predictions of an experimental AMR device

This chapter presents a selection of results where the AMR model presented in Chapter 3 has been applied to the conditions of an experimental AMR test machine. This chapter thus serves to provide a comparison with experiments which is essential for the understanding of the AMR.

In Sec. 6.1 the AMR test machine located at Risø DTU is considered. The results from this section are based on papers A.1.6 (Nielsen et al., 2009a), A.3.1 (Nielsen et al., 2008), which was presented at the 8th Gustav Lorentzen Conference on Natural Working Fluids in Copenhagen 2008, A.3.4 (Nielsen et al., 2009b), which was presented at the 7th World Conference on Experimental Heat Transfer, Fluid Mechanics and Thermodynamics 2009 in Krakow, Poland and A.3.6 (Bjørk et al., 2009), which was presented by Dr. R. Bjørk at the SIMS50 conference in Denmark, 2009. In Sec. 6.2 the chapter is summarized.

6.1 The Risø DTU test device

An experimental AMR test machine has been designed and built at Risø DTU. This device is described in thorough detail in Bahl et al. (2008); Nielsen et al. (2008); Engelbrecht et al. (2009). The device is of a reciprocating design. Two stepper motors enable the movement of the regenerator (Fig. 6.1(b)) in and out of the permanent magnet bore and the displacement of pistons so that the heat transfer fluid can be moved independently. The whole machine is shown in the photograph in Fig. 6.1(a). The magnetic field source is a Halbach permanent magnet built of 16 pieces of NdFeB. The Halbach design is discussed in detail in, e.g., Bjørk et al. (2008). In Fig. 6.2(a) the mean magnetic flux density as a function of the distance out of the magnet bore is given. The length and radius of the magnet bore are 50 mm and 21 mm, respectively. A schematic of the AMR devices is depicted in Fig. 6.2(b). The reciprocating design defines certain constraints to the operating parameters so that the maximum operating frequency of the system is about 0.3 Hz. The mass flow rate and the fluid movement, i.e. the utilization, may be varied by controlling the pistons.

The AMR test device is placed in a temperature controlled environment where the ambient temperature may be adjusted between 273 and 298 K. In the hot end

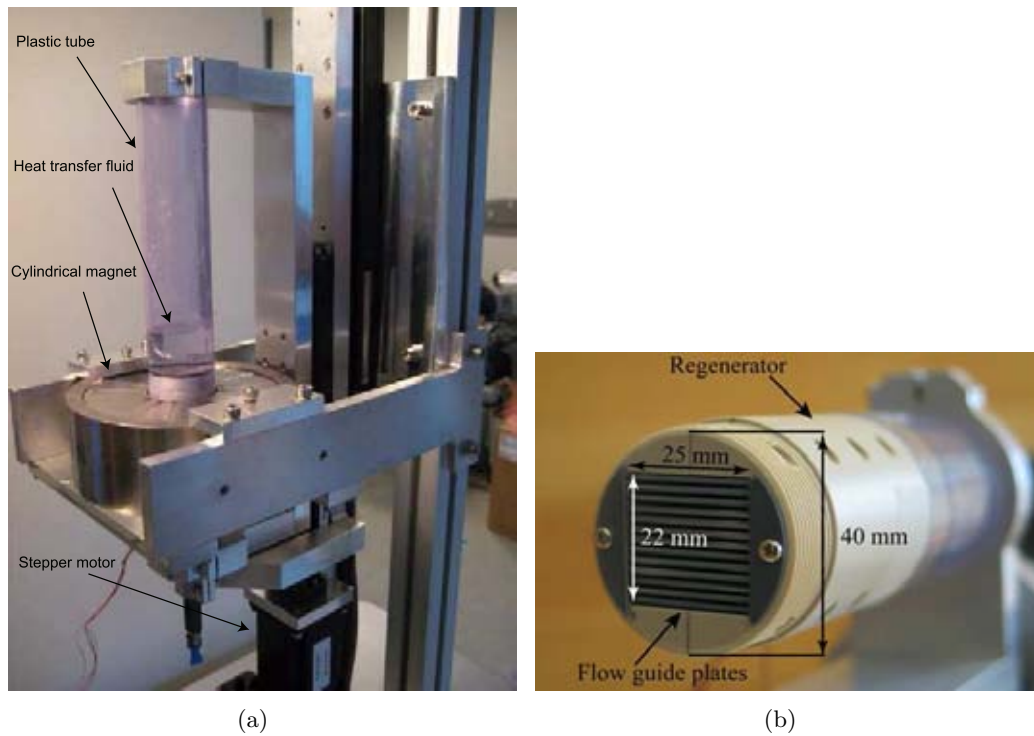


Figure 6.1: In (a) the entire Risø DTU AMR test device is depicted. The regenerator is seen to be situated inside the Halbach magnet bore. The permanent Halbach magnet is also seen. In (b) a close-up picture of a regenerator housing is shown with dimensions.

of the regenerator a heat exchanger is located. This is a coil that is cooled by a secondary water circuit, which exchange heat with the ambient in the cabinet through forced convection.

In the following the various regenerator housings and constructions are briefly discussed. Next, a selection of modeling results of various configurations, both in terms of regenerator geometry, magnetocaloric materials and operating conditions are presented.

6.1.1 Regenerators

A range of housings for the regenerator have been made. The first generation of these were machined in plastic, see Fig. 6.1(b), which limited the channel spacing to 0.8 mm. Through the usage of the poly-jet rapid prototyping technique it was possible in the second generation of these housings to obtain a channel thickness of 0.5 mm as an absolute lower limit. Since both numerical models and basic heat transfer analysis predict that thinner channels and thinner plates perform better (due to the increase of the number of transfer units) techniques were investigated to make third generation regenerators with spacings down to 0.1 mm (see Fig. 6.3). Figure 6.4 shows examples of regenerator blocks. These have been made using various rapid prototyping techniques.

Using a stiff thread of a certain diameter it has been possible to stack plates

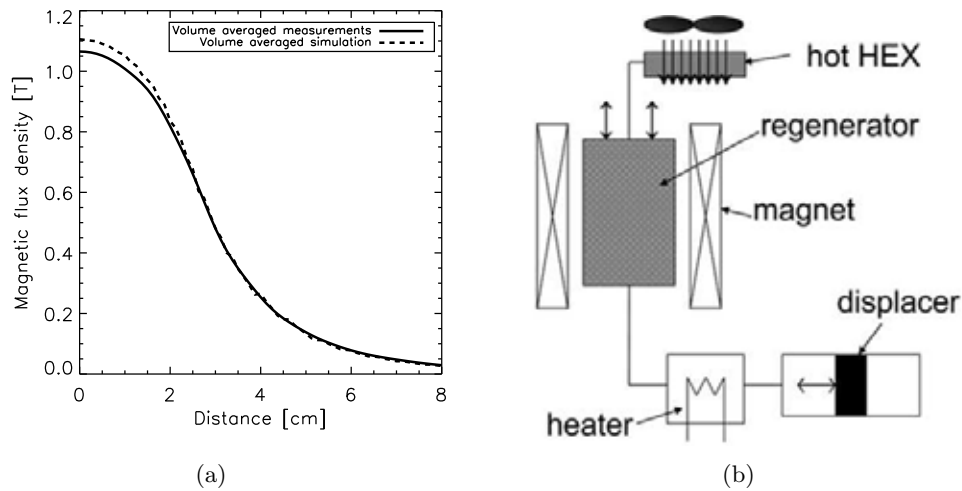


Figure 6.2: (a) The average flux density as a function of the distance out of the magnet bore of the Halbach magnet used in the Risø DTU AMR test device. The simulations were done using Comsol Multiphysics by Dr. R. Bjørk. Reproduced from paper A.1.6 (Nielsen et al., 2009a). (b) A schematic of the AMR test device. The hot heat exchanger, regenerator, magnet, heater and displacer are illustrated. Reproduced from paper A.1.8 (Engelbrecht et al., 2010a).

with a spacing down to 0.1 mm (nominally). However, the variation of the channel spacing is too coarse using this technique. Furthermore, the flatness and uniformity of the used plates needs to be quite high. In Chap. 8 the stacking of parallel plates is discussed in a broader sense.

6.1.2 Single material experiments

In the following a range of experimental AMR results from the AMR device at Risø DTU is investigated and the model presented in Chap. 3 is used to model the experiments.

Cooling load experiment

The AMR test device was configured with 13 plates of Gd of the dimensions $40 \times 25 \times 0.9 \text{ mm}^3$ evenly spaced with 0.8 mm using the regenerator housing pictured in Fig. 6.1(b). The total mass of the regenerator was thus 92 g. The AMR cycle time was approximately 9 s and two values of the utilization were investigated (0.68 and 0.96, respectively). The resulting temperature span was measured as a function of an applied heat load.

The numerical AMR model was configured such that the two heat exchangers had properties equivalent to plastic since the experiment was performed without any heat exchangers (see Bahl et al. (2008); Nielsen et al. (2008) for details). The thermal parasitic loss mechanism was enabled in the model. Since the ambient temperature of the experiment varied between 296 and 300 K during the experiments the model was adjusted to take this into account accordingly.

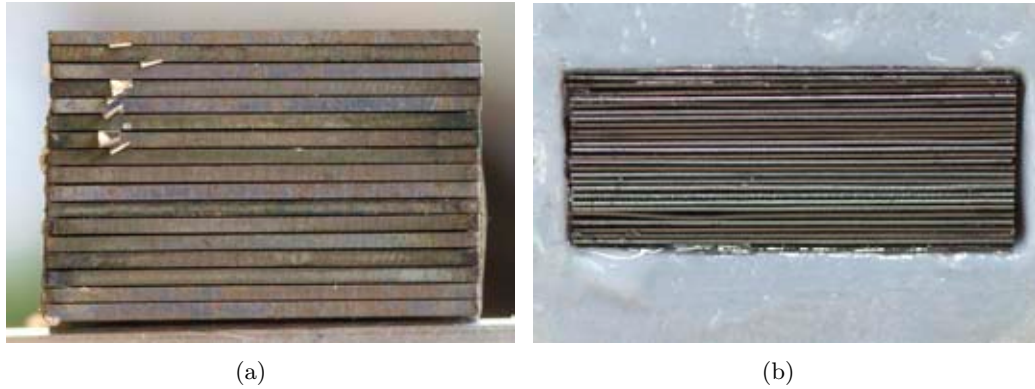


Figure 6.3: A stack of LaFeCoSi plates (a) with a plate thickness of 0.9 mm and a nominal channel thickness of 0.1 mm. In (b) a stack of LCSM plates with a thickness of 0.3 mm and a spacing of 0.1 mm is shown. In both cases it is apparent that the stacks are far from homogeneous. This may be of crucial importance and is discussed further in Chapter 8; see also Jensen et al. (2010).

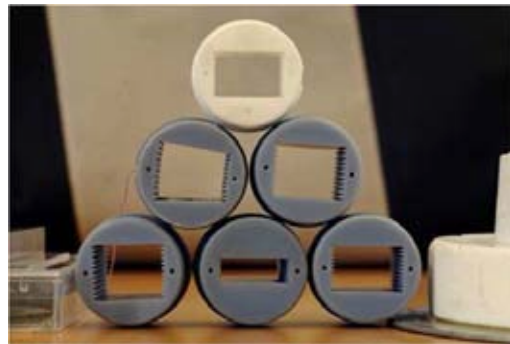


Figure 6.4: Examples of various regenerator blocks with plate thicknesses varied between 0.3 and 1.0 mm and spacings of 0.5 and 0.9 mm, respectively. A housing designed for a regenerator with radially changing spacing is seen. Results from this regenerator structure is not considered in this work, however.

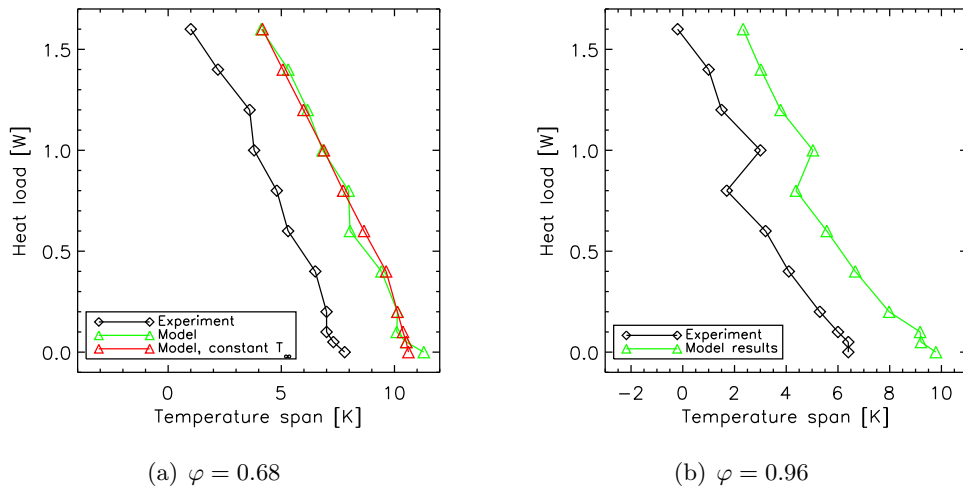


Figure 6.5: Experimental and modeling results expressed as cooling power versus temperature span. In (a) the utilization is 0.68 and in (b) it is 0.96. Since the ambient temperature varied between the individual experiments it was recorded and the model took this into account accordingly, i.e. the ambient temperature at the different temperature spans differ slightly. To show that the cooling power versus temperature span may be assumed linear a cooling power curve modeled at constant ambient temperature (296 K) has been added in (a). Data partially reproduced from paper A.3.1 (Nielsen et al., 2008).

In Fig. 6.5 the results of both the experiment and the model are shown. The cooling power versus temperature span curves are seen to be approximately linear; however, the variation of the ambient temperature between the individual experiments make the curves differ slightly from being linear. In Fig. 6.5(a) an extra cooling curve has been calculated using the model and setting the ambient temperature to be the same for all the cooling loads. This shows that the cooling curve is indeed linear.

It is very interesting that the model follows the trend of the experiment. Furthermore, the approximate slopes of the cooling curves are fairly identical when comparing the experimental and model. The deviations from linearity in the cooling power versus temperature span curves are seen to be captured by the model.

That the model does not predict the exact experimental results is to be expected. Many factors are not taken into account such as the behavior of the internal magnetic field (see Chapter 7), the transient behavior of the parasitic losses to the ambient etc. It may thus be argued that further improvements to numerical AMR models should be done. Suggestions for this are given in, e.g., paper A.1.7 (Nielsen et al., 2010e).

Timing and stroke experiments

In Bahl et al. (2008) a range of experiments are presented and correspondingly modeled using the model published in Petersen et al. (2008b). This model did not

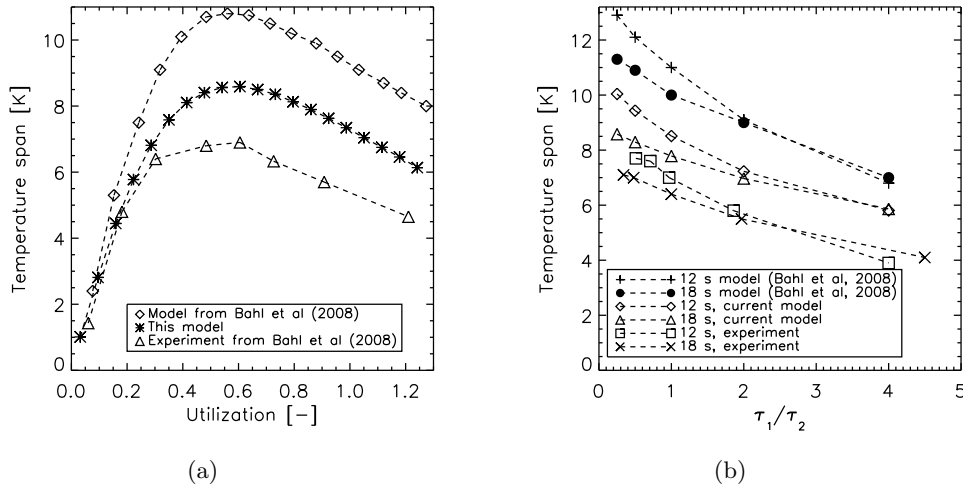


Figure 6.6: Modeling and experimental results presented as zero load temperature span as a function of utilization (a) and timing and fraction of magnetization and flow period durations (b). In both figures the experimental and modeling results presented in Bahl et al. (2008) and the results of the present model with thermal parasitic losses enabled are given. Reproduced from paper A.1.6 (Nielsen et al., 2009a).

have the possibility of enabling thermal parasitic losses. The presented configurations from Bahl et al. (2008) have thus been modeled using the model presented in Chap. 3 with thermal parasitic losses enabled for comparison.

The results show that both models capture the trends of the zero load temperature span both as a function of utilization (Fig. 6.6(a)), cycle frequency and fraction between magnetization and flow duration timings (Fig. 6.6(b)). Considering the dependency of the utilization it may be concluded that the maximum temperature span is achieved at a utilization of approximately 0.5, which is quite in line with the theoretical predictions presented in Chap. 4. It is furthermore observed that when including the thermal parasitic losses the model predictions are closer to the observed experimental results. It may thus be concluded that the parasitic losses are accounted for to some degree; when the regenerator housing is made of an insulating material like plastic in this case the thermal response time of the housing is rather small compared to the transients of the magnetocaloric material and the heat transfer fluid. Thus, the lumped analysis suggested in Sec. 3.2.5 is validated. Alternatively a transient model of the heat transfer in the regenerator housing could be considered. Such a model would add significant complexity to the computational domain, however, for certain regenerator housing materials it might be necessary. If, for instance, the thermal conductivity was very high in the regenerator housing the heat transfer here could probably not be approximated with the lumped analysis.

Another series of experiments was conducted and the model presented in Chap. 6 was applied to the cases. Here, two different series were investigated: one where the mean field model was used to calculate the magnetocaloric data and one where experimental data was used. In Fig. 6.7 the results are given. It is concluded from

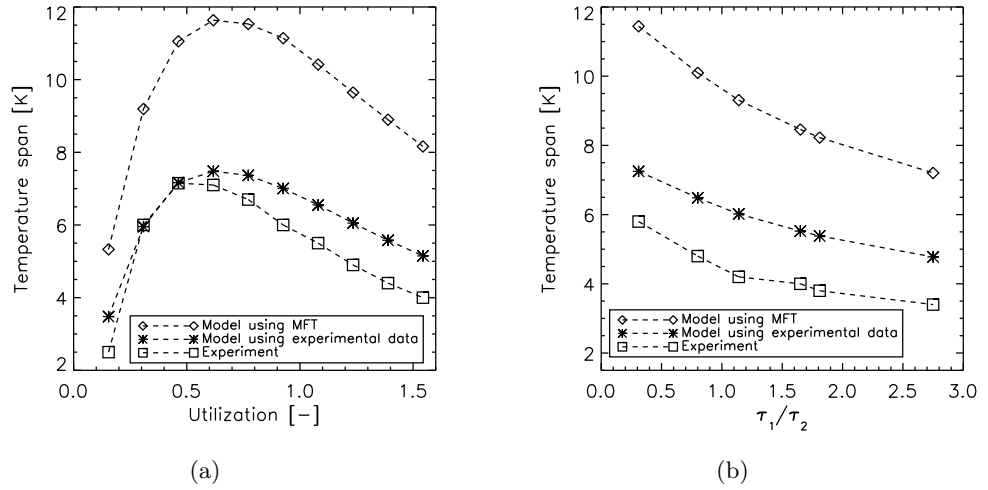


Figure 6.7: The zero heat load temperature span as a function of utilization (a) and as a function of magnetization to flow period duration fraction (b). In either case two sets of modeling configurations have been used: one where the mean field model has been used to provide the magnetocaloric data and one where experimental data for the adiabatic temperature change has been used. Reproduced from paper A.1.6 (Nielsen et al., 2009a).

the figure that using experimental data improves the correspondence between the experiment and the model significantly.

Field variation experiment

As can be seen in Fig. 6.2(a) the magnetic field profile of the permanent Halbach magnet is not zero right outside the magnet bore. Experiments were therefore conducted in order to probe how far out the regenerator should be moved in order to achieve maximized performance. The AMR model was applied to the experimental cases. As can be seen from Fig. 6.8 the model and experimental results agree on the trend as a function of the distance out of field. And again, it may be concluded that enabling thermal losses in the model brings the modeling results closer to the experimental.

6.1.3 Multi-material experiments

The LaFeCoSi material presented in Sec. 2.5 has been kindly supplied in the shape of $20 \times 25 \times 0.9$ mm³ plates by Vacuumschmelze, Germany. It has therefore been possible to perform AMR experiments using the test device at Risø DTU with a layered regenerator. The details of the experiment are available in paper A.1.8 (Engelbrecht et al., 2010a).

The case where two materials with Curie temperatures of 276 and 289 K, respectively, were used is investigated here. In the experiment the utilization and fluid velocity were varied through various configurations of the piston stroke length

Table 6.1: Fluid flow velocity, thermal utilization and resulting cycle timings used in the 2-material LaFeCoSi experiments and the corresponding modeling.

Fluid velocity [mm/s]	$\varphi = 0.33$		$\varphi = 0.54$		$\varphi = 0.76$	
	τ_{tot} [s]	τ_{rel} [-]	τ_{tot} [s]	τ_{rel} [-]	τ_{tot} [s]	τ_{rel} [-]
5.4	9.5	0.15	14.6	0.09	19.9	0.07
7.3	7.4	0.20	11.2	0.12	15.2	0.09
10.9	5.3	0.30	7.9	0.18	10.6	0.13
14.5	4.3	0.39	6.2	0.24	8.2	0.17

and the piston velocity. Table 6.1 summarizes the operating parameters. A total of 11 plates¹ was used. The spacing was 0.5 mm with a resulting (average) porosity of 0.34. The ambient temperature was 287 K.

In Fig. 6.9 results in terms of the zero-load temperature span as a function of the fluid velocity (in the channels) are provided. Two sets of corresponding modeling results are given: one where the thermal parasitic losses are enabled and one without. The experimental data presented in Sec. 2.5 are used as magnetocaloric material properties.

The trend, both from the experiments and the modeling results, is quite clear. The temperature span decreases as a function of fluid velocity. The model predictions

¹Of each material resulting in a total of 11 times $40 \times 25 \times 0.9$ mm plates when butted together

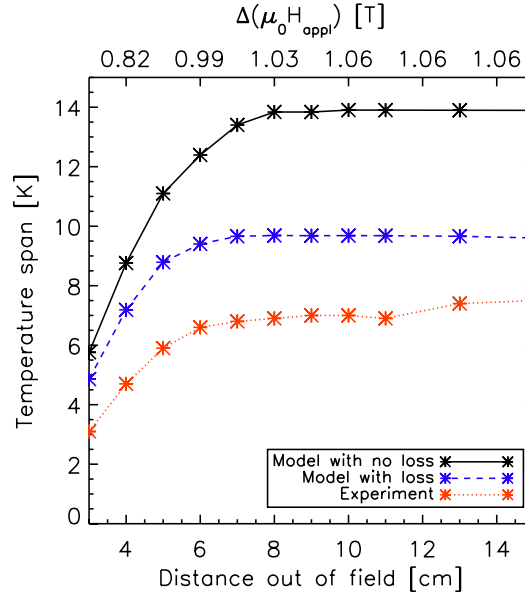


Figure 6.8: The zero heat load temperature span as a function of the distance the regenerator is moved out of the magnetic field. Modeling results with and without thermal losses are given. On the upper x -axis the difference in applied between the high and low field regions is given (corresponding to the centre of the plate). Data reproduced from paper A.3.1 (Nielsen et al., 2008).

(including losses) and the experimental results at a utilization of 0.33 and 0.54 seem, however, to have a maximum at a fluid velocity slightly higher than the minimum velocity considered. In order to investigate the decrease in temperature span with increased fluid velocity the number of transfer units, NTU, has been added to the x -axis in the plot. Recalling the definition of the NTU

$$\text{NTU} = \frac{hA}{\dot{m}c_f}, \quad (6.1)$$

where the heat transfer coefficient is h , the heat transfer area is A and the mass flow rate is \dot{m} . In Sec. 4.1.1 the Nusselt number was introduced and through this the heat transfer coefficient may be found

$$\text{Nu}_m \equiv \frac{hD_H}{k_f}. \quad (6.2)$$

The heat transfer area and the mass flow rate for a parallel plate regenerator are

$$A = 2L_r W_f \quad (6.3)$$

$$\dot{m} = \rho_f \tilde{u} W_f H_f, \quad (6.4)$$

where L_r and W_f are the length and width of the regenerator and fluid channel, respectively. Combining Eqs. 6.2–6.4 an expression for the NTU may be obtained

$$\text{NTU} = \frac{\alpha_f \text{Nu}_m L_r}{H_f^2 \tilde{u}}. \quad (6.5)$$

From Eq. 6.5 it is seen that the NTU is inversely proportional to the fluid velocity. Considering Fig. 6.9 the temperature span is indeed seen to decrease with decreasing NTU. This may not be surprising bearing Eq. 6.5 in mind, however, as it was found in Chap. 4 the NTU of the regenerator should be at least 20–50 in value for the regenerator to be effective, and this is in great accordance with the experimentally found values presented here. Furthermore, it was not only found that the value of the NTU should be in the interval 20–50 but also that values lower than 20 decreases the performance significantly.

The fastest fluid flow velocities applied here, about 14 mm/s, yield total cycle timings of down to 4.3 s (see Tab. 6.1). For the general performance of the AMR the cycle frequency should be significantly increased (see Chap. 4 and Rowe (2009)). In this case the NTU will not be sufficient. Thus, thinner fluid channels (and therefore also thinner plates) are needed for this to be realized (see Fig. 4.1 for reference).

6.2 Summary

The experimental AMR test device located at Risø DTU was presented. Various configurations of the device were experimentally investigated and numerical modeling was applied so that comparison between experiment and model was possible. In general, it was found that the model over-predicts the experiment in terms of temperature span and cooling power. However, this was partially accounted for through including thermal parasitic losses to the ambient and using proper magnetocaloric data rather than mean field based data. There is room for improvements in terms

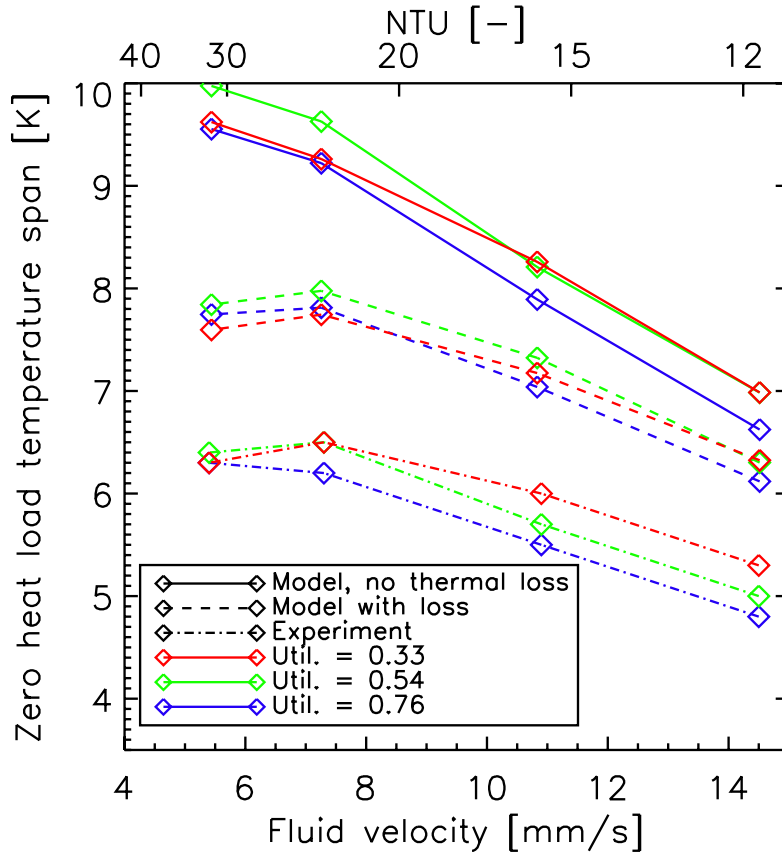


Figure 6.9: Zero heat load temperature span as a function of fluid velocity and number of transfer units. The regenerator is made of LaFeCoSi plates with dimensions $20 \times 25 \times 0.9$ mm. Two different compositions were used, one with a Curie temperature of about 275 and 289 K, respectively. The two sets of plates are butted together so the regenerator is effectively made of two materials with a total length of 40 mm. The plot shows the results from the experiment and the model both with and without thermal parasitic losses for three different values of the utilization. The experimental results have previously been partially published in paper A.1.8 (Engelbrecht et al., 2010a) and Engelbrecht et al. (2009). The experiments were conducted at Risø DTU by Dr. K. Engelbrecht.

of predicting the AMR performance using the numerical model. The spatial domain on which the model is solved could be extended to three dimensions, the internal magnetic field (thoroughly discussed in the next section) could be accounted for and imperfections in the experimental regenerators could be improved.

The AMR model may over-predict the performance to some extent, however, the trends as a function of several operating parameters are clearly represented in the model. Considering, e.g., the temperature span as a function of utilization the trends is obviously that the span has a maximum around 0.3-0.5 both in the model and the experiment. Considering the timing experiments and the magnetic field variation the trends were also clearly the same in the model and the experiment. A significant amount of trust may therefore be put into the model predictions.

Chapter 7

Modeling the demagnetizing field

The internal magnetic field, \mathbf{H} , is a quantity useful, e.g., when comparing experimental magnetic measurements between various experimental setups, sample sizes etc. The calculation of \mathbf{H} is in principle straightforward, however, it often becomes quite involved due to non-homogeneities in, e.g., the temperature distribution of the sample as well as the sample geometry and applied magnetic field orientation. It is most often impossible to measure \mathbf{H} directly. This chapter is concerned with the calculation of the 3-dimensional spatially resolved internal magnetic field of a rectangular flat prism and a stack of such prisms as well as a simple way of using a different observable to probe the magnitude of the internal magnetic field experimentally.

Some of the results in this chapter are known in literature, however, the majority are published in papers as a part of this thesis and some of the results are in preparation for publication. Thus, this chapter is mainly based on the results presented in papers A.1.1 (Bahl & Nielsen, 2009), A.1.3 (Smith et al., 2010), A.1.4 (Christensen et al., 2010a) and A.2.1 (Christensen et al., 2010b). Since the MCE is a strong monotonous function of the internal magnetic field strength, it is essential to have detailed information on this quantity in a non-homogeneous regenerator geometry. The effect of demagnetization is both of a geometrical nature (aspect ratio of the rectangular prism, stack and so forth), the temperature distribution of the system and the possible grading of the materials comprising the prism. Thus, it is of great relevance for magnetic refrigeration to obtain detailed knowledge of this effect on geometries used for this application such that the internal magnetic field may be maximized in order to maximized the magnetocaloric effect and in order to minimize irreversible losses due to gradients in the internal field in the regenerator.

This chapter is organized such that in Sec. 7.1 magnetic fields are briefly introduced with general focus on the demagnetizing field of a magnetized body. In Sec. 7.2 the demagnetizing field of a single rectangular prism is discussed in detail. In Sec. 7.3 the demagnetizing field of a stack of rectangular prisms is discussed with emphasis on magnetic refrigeration as an application. In Sec. 7.4 the more generalized stacks of rectangular prisms are discussed with focus on the overall governing physics of such systems. In Sec. 7.5 the results from the demagnetization model are compared with experiments where the adiabatic temperature change is used to probe the geometrical extent of the internal magnetic field strength. Finally

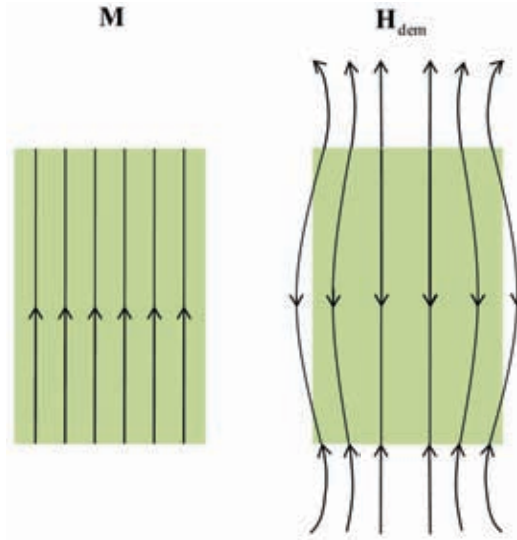


Figure 7.1: A simple illustration of the magnetization, \mathbf{M} , and the demagnetizing field, \mathbf{H}_{dem} , of a homogeneously magnetized body. The demagnetizing field is a consequence of the magnetization of the body and as it is illustrated the demagnetizing field is opposing the magnetization *inside* the body thus reducing the resulting internal field. It is noted that the density of the lines is not intended to accurately show a realistic case.

in Sec. 7.6 the chapter is summarized.

7.1 Magnetic fields

This section gives a brief discussion about magnetic fields. This is a classical topic that is much more thoroughly handled in textbooks like, e.g., Coey (2010); Griffiths (1999); Blundell (2001). However, it is important for the results and analysis of the remainder of this chapter to keep a few fundamental concepts in mind.

Now, here \mathbf{B} will be denoted the magnetic flux density and \mathbf{H} the magnetic field. This is simply a convention and the author is aware that other conventions exists. In any case, the relation between the magnetic flux density and the magnetic field is

$$\mathbf{B} = \mu_0 (\mathbf{M} + \mathbf{H}), \quad (7.1)$$

where the vacuum permability, μ_0 , and the magnetization, \mathbf{M} , have been introduced. It follows immediately that

$$\nabla \cdot \mathbf{H} = - \nabla \cdot \mathbf{M} \quad (7.2)$$

due to the non-existence of magnetic monopoles. Considering a magnetic body with zero applied field, such as illustrated in Fig. 7.1, and assuming the body to be homogeneously magnetized \mathbf{H} inside the body is opposite \mathbf{M} . This is what is known as the demagnetizing field, \mathbf{H}_{dem} . This field is thus a function of the magnetization, which in turn is a function of both temperature and the total internal field, \mathbf{H} . The demagnetizing field is also a strong function of the geometry of the body and this is the issue considered in the following sections.

Table 7.1: The boundary conditions of \mathbf{H} and \mathbf{B} on boundaries between two different materials. The total surface current density is denoted \mathbf{K} and the free surface current density is \mathbf{K}_f . For the cases considered here \mathbf{K}_f is zero thus making the parallel components of \mathbf{H} continuous. The roman numerals indicate the two materials (I and II, respectively). $\hat{\mathbf{n}}$ denotes the unit vector normal to the surface.

	\mathbf{H}	\mathbf{B}
	$\mathbf{H}_{\parallel}^{\text{II}} - \mathbf{H}_{\parallel}^{\text{I}} = \mathbf{K}_f \times \hat{\mathbf{n}}$	$\mathbf{B}_{\parallel}^{\text{II}} - \mathbf{B}_{\parallel}^{\text{I}} = \mu_0 \mathbf{K} \times \hat{\mathbf{n}}$
	$(\mathbf{H}^{\text{II}} - \mathbf{H}^{\text{I}}) \cdot \hat{\mathbf{n}} = -(\mathbf{M}^{\text{II}} - \mathbf{M}^{\text{I}}) \cdot \hat{\mathbf{n}}$	$(\mathbf{B}^{\text{II}} - \mathbf{B}^{\text{I}}) \cdot \hat{\mathbf{n}} = 0$

When describing some of the results presented later in this chapter the boundary conditions applying for \mathbf{H} and \mathbf{B} are used for interpretation. These boundary conditions are therefore summarized in Table 7.1 for convenience (their derivation may be found in any textbook on magnetostatics).

7.2 A single rectangular prism

The internal magnetic field may generally be expressed as

$$\mathbf{H} = \mathbf{H}_{\text{appl}} + \mathbf{H}_{\text{dem}}, \quad (7.3)$$

with the applied and demagnetizing fields denoted \mathbf{H}_{appl} and \mathbf{H}_{dem} , respectively. The real-world situation usually allows the control and detailed knowledge of the applied field. The demagnetizing field is a consequence of the magnetization, \mathbf{M} , of the sample due to the applied field. Since, in turn, the magnetization is a function of both \mathbf{H} and temperature, T , the calculation of \mathbf{H}_{dem} is rather involved for any case but the simplest with constant properties assumed. Even in that case, where the temperature and internal field are assumed homogeneous throughout the sample, the geometry of the sample may pose a difficult task of calculating the demagnetizing field. Generally, using basic magnetostatics and somewhat tedious, however straightforward, math the demagnetizing field may be expressed as (see Appendix A of paper A.1.3 for further details)

$$\mathbf{H}_{\text{dem}}(\mathbf{r}, T) = \frac{1}{4\pi} \int_{\Omega} d\mathbf{r}' \mathbb{D}(\mathbf{r} - \mathbf{r}') \cdot \mathbf{M}[\mathbf{H}(\mathbf{r}', T), \mathbf{r}', T], \quad (7.4)$$

with \mathbf{r} denoting the position vector of the point at which the demagnetizing field is sought and \mathbb{D} denotes a 3×3 symmetric tensor, with the components given in Eqs. A5-6 in paper A.1.3. The spatial domain over which the integral is performed is denoted Ω .

For a rectangular prism with homogeneous magnetization, \mathbf{M}_0 , Eq. 7.4 becomes

$$\mathbf{H}_{\text{dem}}(\mathbf{r}) = -\mathbb{N}(\mathbf{r}) \cdot \mathbf{M}_0. \quad (7.5)$$

Here, the symmetric 3×3 demagnetization tensor, \mathbb{N} , has been introduced. The components of \mathbb{N} are given in paper A.1.3 Eqs. A8 and A12. Considering the rectangular prism shown in Fig. 7.2 the origin is at the centre of the prism, which has the

dimensions $2a$, $2b$ and $2c$. The prism may be divided into $n_x \times n_y \times n_z$ prisms, each with the dimensions $a' = a/n_x$, $b' = b/n_y$ and $c' = c/n_z$. Assuming each prism to have homogeneous properties, Eq. 7.5 is valid for the individual prism. Applying the superposition principle the resulting demagnetizing field at the position \mathbf{r} becomes

$$\mathbf{H}_{\text{dem}}(\mathbf{r}) \approx - \sum_{i=1}^{n_x} \sum_{j=1}^{n_y} \sum_{k=1}^{n_z} \mathbf{N}(\mathbf{r} - \mathbf{r}'_{i,j,k}) \cdot \mathbf{M}_0 [\mathbf{H}(\mathbf{r}'_{i,j,k}, T_{i,j,k}), \mathbf{r}'_{i,j,k}, T_{i,j,k}], \quad (7.6)$$

where the subscripts i, j, k refer to the cell with indices i, j, k . The solution is, of course, an approximation since it was assumed that each individual rectangular prism had homogeneous properties. Equation 7.6 is the basis for the demagnetization model. However, in order to complete the model two additional components are needed. A state function giving the magnitude of the magnetization, M , as a function of internal field strength, H , and T . This may be the mean field equation of state, given in Eq. 2.13, or from a table of experimental values. In the latter case it is important to make sure that the table gives the magnetization as a function of the internal magnetic field strength and thus the experimental data has to have been corrected for the demagnetization. This may be done if the experimental measurements were performed under circumstances that validate the assumption of homogeneity and constant properties, and the geometry of the sample makes a simple characterization of the demagnetization factor possible.

The remaining component comes from the fact that the demagnetizing field is a function of \mathbf{H} . Thus, Eqs. 7.3 and 7.6 should be combined to provide the total solution. In this way, the problem of calculating the internal magnetic field becomes an iterative task. In Smith et al. (2010) the numerical validation of the demagnetization model is provided. It is furthermore assumed that \mathbf{M} and \mathbf{H} are parallel (Brug & Wolf, 1985).

7.2.1 Results relevant to magnetic refrigeration

Solving Eqs. 7.3 and 7.6 in order to obtain the internal magnetic field is highly relevant for many applications. In the following, situations relevant to magnetic refrigeration are investigated. Generally, the physical situation for a flat prism of a magnetic material used in magnetic refrigeration is that a temperature profile is present along one of the principal axes of the prism (the direction of the fluid flow). Ideally, the remaining two directions have negligible temperature gradients. At the same time, the operating temperature will usually be around the Curie temperature of the material (see Sec. 2.2 for details). Furthermore, the magnetocaloric prism may be made of several magnetic materials each with a different Curie temperature. These situations are all investigated in the remainder of this section. For simplicity,

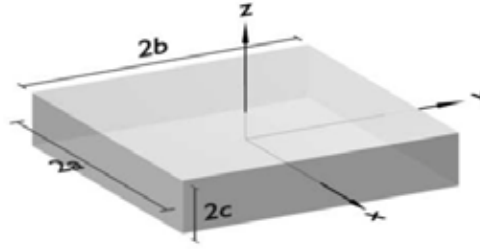


Figure 7.2: The coordinate system of the rectangular prism considered. The relative dimensions of the prism are $a = b = 20c$. Reproduced from paper A.1.4 (Christensen et al., 2010a).

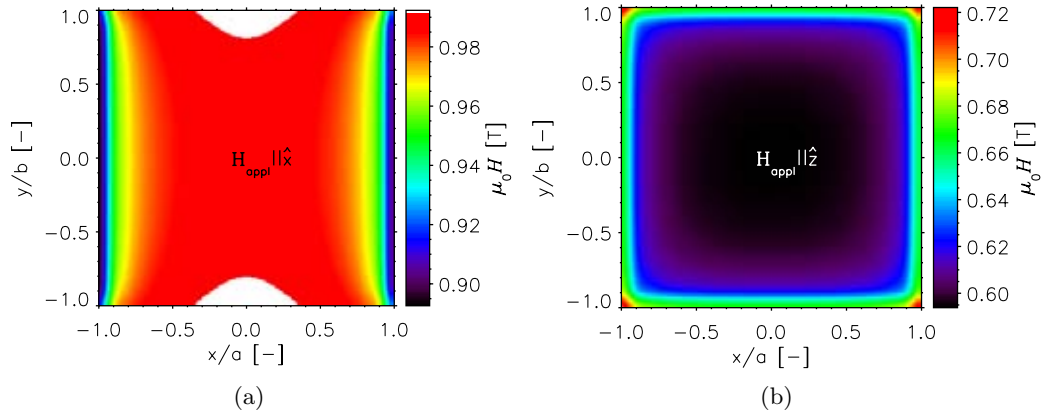


Figure 7.3: The magnetic field strength, H , in the xy -plane and averaged in the z -direction. The applied flux density is homogeneous and equal to 1.0 T and the temperature of the prism set to the Curie temperature, i.e. 293 K. a) The applied field is along the x -direction. b) The applied field is along the z -direction.

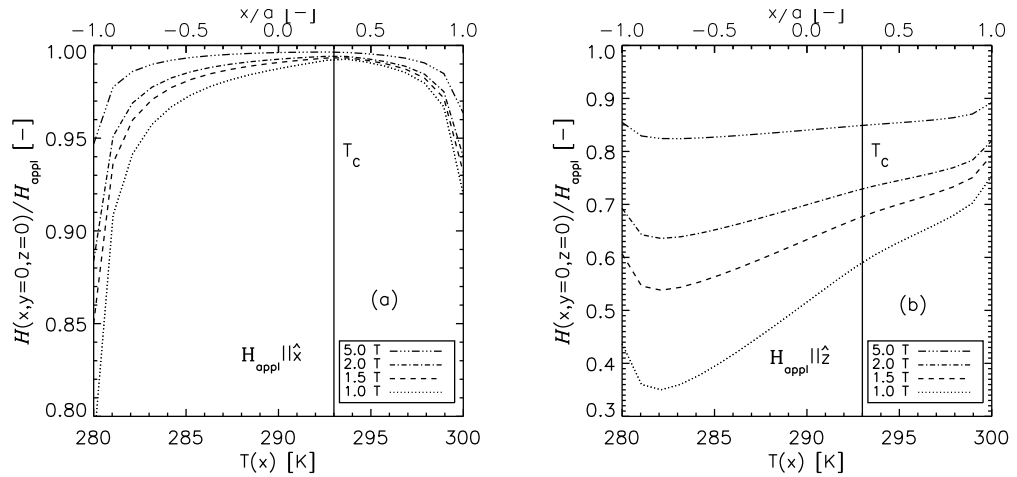


Figure 7.4: The internal magnetic field strength along the line defined as $-a \leq x \leq a$ and $b = c = 0$ for four different applied fields. The prism considered is rectangular and consists of a single magnetic material, i.e. mean field modeled Gd with a $T_C = 293$ K. A linear temperature profile ranging from 280 to 300 K is imposed along the x -direction. a) The applied field is along the x -direction. b) The applied field is along the z -direction. Reproduced from paper A.1.3 (Smith et al., 2010).

mean field modeled gadolinium is used for the magnetic equation of state (see the relevant properties in Table 2.1).

Single material prism

First, the well-known situation with a single material prism having a constant temperature and a homogeneous applied field is investigated. Fig. 7.3 shows H in the xy -plane of a square prism with the relative dimensions $a = b = 20c$; see Fig. 7.2 for details. In Fig. 7.3a the applied field is along the x -direction and in Fig. 7.3b it is

along the z -direction, i.e. perpendicular to the largest face of the prism. It is quite apparent that a large difference exists between applying the field along the two directions. Applying the field along the former direction produces an internal magnetic field close, on average, to the applied field whereas applying the field perpendicular to the largest face of the prism significantly decreases the internal field compared to the applied field. This is completely in accordance with the well-known results of e.g. Aharoni (1998). However, the novelty in this case is the complete spatial resolution of the internal field.

Considering the case of a single material prism with an imposed linear temperature profile, over a temperature range including the Curie temperature of the material, the situation becomes so involved that \mathbf{H} has to be spatially resolved; a simple scalar value representing the geometric demagnetization is no longer a valid approximation. This is apparent from Fig. 7.4. Here the linear temperature profile ranges from 280 K to 300 K along the x -direction.

Now, considering the application of the magnetic field along the x -direction, Fig. 7.4a shows the resulting H along the line defined as $-a \leq x \leq a$, $y = z = 0$ normalized with respect to the applied field. For four different applied magnetic fields (1 to 5 T) the same trends are apparent; the internal field is more affected by the demagnetizing field at lower temperatures and the internal field drops at the boundaries. The latter result is explained simply from the fact that the demagnetizing field is more profound on the boundary faces perpendicular to the applied field, i.e. those where $x = -a$ and $x = a$, respectively. That the demagnetizing field is more profound at temperatures below the Curie temperature is due to the fact that the material is ferromagnetic here and thus has a higher magnetization. Since the demagnetizing field essentially is a product between the demagnetization tensor and the magnetization it is thus more profound here.

Applying the field along the z -direction (Fig. 7.4b) shows that the magnitude of the resulting internal field along z varies almost linearly with x -position throughout most of the prism increasing as a function of temperature. This is explained using the same argument as was valid in Fig. 7.4a, namely that the material is ferromagnetic at the lower temperatures and thus has a larger magnetization. Two other quite interesting effects are also observed. First, the internal field increases towards either end. That is due to the fact that the geometric demagnetization is actually smaller on the edges compared to the centre of the prism; yet again a fact that confirms the need for a spatially resolved demagnetization tensor and the insufficiency of a single scalar representation. Second, the resulting internal magnetic field is seen to increase significantly with the applied field.

This is due to the absolute nature of the demagnetizing field; the demagnetizing tensor is not a function of the applied field and the magnetization is only

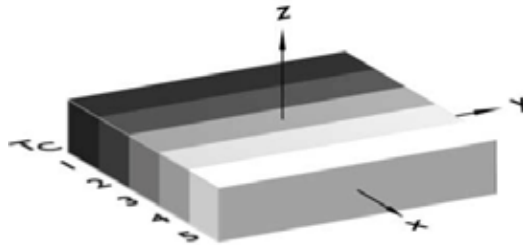


Figure 7.5: *Conceptual drawing of a graded rectangular prism. The coordinate system is the same as in Fig. 7.2. The grading is along the x -direction and the Curie temperatures are chosen to be 280 to 300 K in steps of five degrees. Reproduced from paper A.1.3 (Smith et al., 2010).*

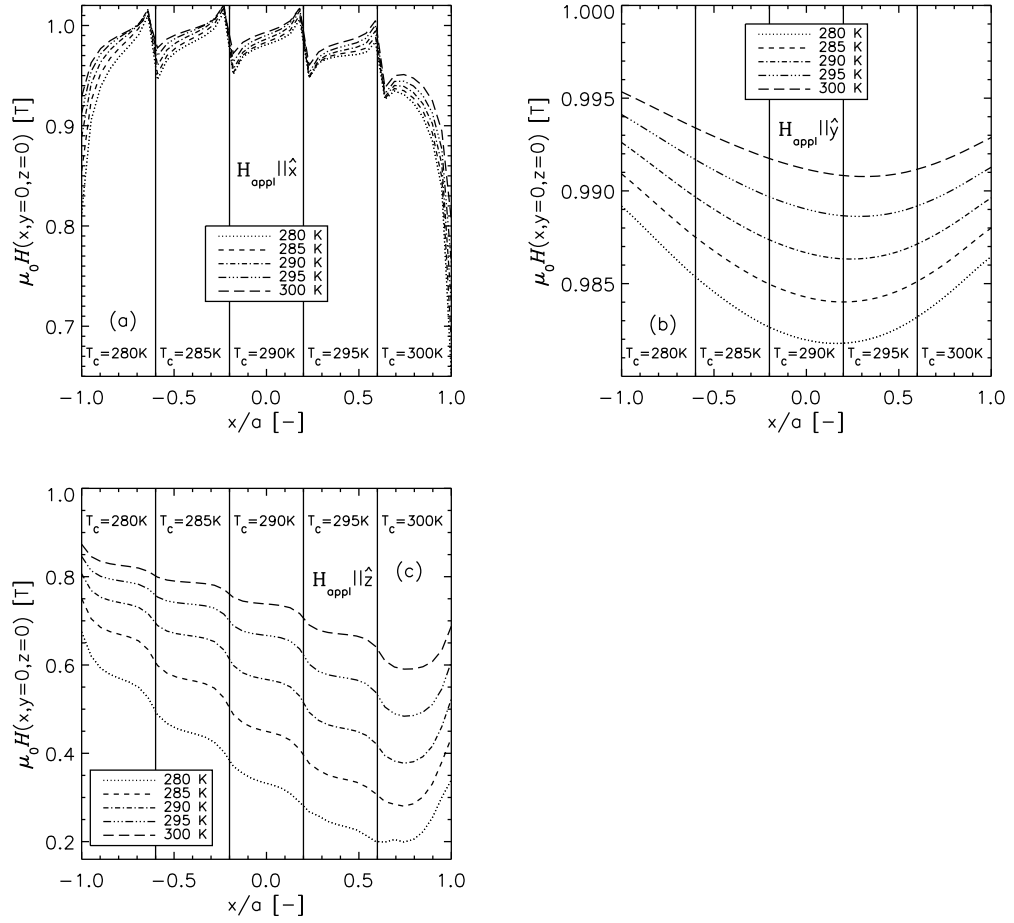


Figure 7.6: H as a function of x along the same line as in Fig. 7.4 for a constant and homogeneous temperature throughout the prism. The temperature has been varied between 280 and 300 K in steps of five degrees. The applied flux density is 1 T. The grading of the prism is indicated in each plot with vertical lines and the respective Curie temperatures annotated. a) The applied field is along the x -direction. b) The applied field is along the y -direction. c) The applied field is along the z -direction. Reproduced from paper A.1.3 (Smith et al., 2010).

little sensitive to the magnetic field at temperatures below the Curie temperature due to saturation. At temperatures greater than the Curie temperature, i.e. in the paramagnetic phase, the magnetization is proportional to the magnetic field (the Curie-Weiss law). It is apparent in this case that the demagnetizing field is almost relatively the same for all the applied fields (the resulting normalized internal fields approach each other; see Fig. 7.4b).

Multi-material prism

As was discussed in detail in Chapter 5, grading the magnetocaloric material for use in the active magnetic regenerator significantly enhances the performance of the magnetic refrigerator. Thus, it is of great interest to investigate the internal

magnetic field under circumstances where multiple ferromagnets, each with different Curie temperatures, are aligned.

Figure 7.5 shows a drawing of how the grading is done in this case. The figure shows how five ferromagnets with the respective Curie temperatures $T_{C,1-5}$ are arranged with the relevant coordinate system defined similar to that presented in Fig. 7.2. The Curie temperatures of the prism are chosen to be 280, 285, 290, 295 and 300 K, respectively. Each material has a volume fraction of 20 percent of the total prism.

In Fig. 7.6 H is plotted along the same line as in Fig. 7.4; $-a \leq x \leq a$ and $y = z = 0$. The applied flux density has been kept constant at 1 T and the temperature of the prism has been assumed homogeneous but various values of the temperature have been used.

Applying the field along the three principal axes has been investigated (Figs. 7.6 a through c, respectively) and a significant variation is observed. The effect on the magnetic field strength, H , is seen to be largest when applying the field along the z -direction, i.e. perpendicular to the largest face of the prism. That is the same conclusion as for the single-material prism and not surprising since the demagnetization tensor is invariant to anything but the geometry of the prism. However, the spatial variation of H depends on the grading of the prism.

Considering Fig. 7.6a it is seen that across each boundary between two consecutive materials that H is discontinuous. This is to be expected since the main component of \mathbf{H} is parallel to the applied field and thus perpendicular to the material boundary. This component has to be discontinuous across material boundaries, i.e. where there is a discontinuity in the permeability, due to the general continuity rules applying for \mathbf{H} (see Tab. 7.1). In the other two cases, i.e. where the applied field is along the y - and z -directions, respectively, no discontinuities are seen, which is also expected per the boundary conditions.

Another interesting effect is seen in Fig. 7.6c where H decreases as a function of x , which is opposite what was seen in Fig. 7.4b. This is explained from the fact that as x increases the prism is closer to its ferromagnetic phase, e.g. the material with the Curie temperature equal to 300 K is almost completely ferromagnetic for all the temperature cases studied here. Thus, the demagnetizing field is greater here than in the rest of the prism.

In Fig. 7.7 B is plotted along the same line as H in Fig. 7.6 and also for the cases of applying the field along the three principal axes. It is clearly seen that in the two cases where H is continuous (applying the field along the y and z axes, respectively) B is discontinuous and in the case where H is discontinuous B is continuous.

Another interesting effect is observed in Fig. 7.7b, where the applied field is along the y -axis. Here, a staircase-like B is observed as a function of x . This is explained from the choice of the individual Curie temperatures and the different constant temperature cases. This may be understood by considering, e.g., the parts of the prism which have Curie temperatures of 285 K and 290 K, respectively. When the overall temperature of the prism is, say, 280 K the magnetization in the 285 K part of the prism is virtually identical to that in the 290 K part of the prism when the temperature is 285 K and so on. Since H is quite homogeneous, as seen in Fig. 7.6b, M will dominate the spatial variation of B as per Eq. 7.1 and B in the 285 K part at a temperature of 280 K will be almost entirely equal to B in the 290 K part

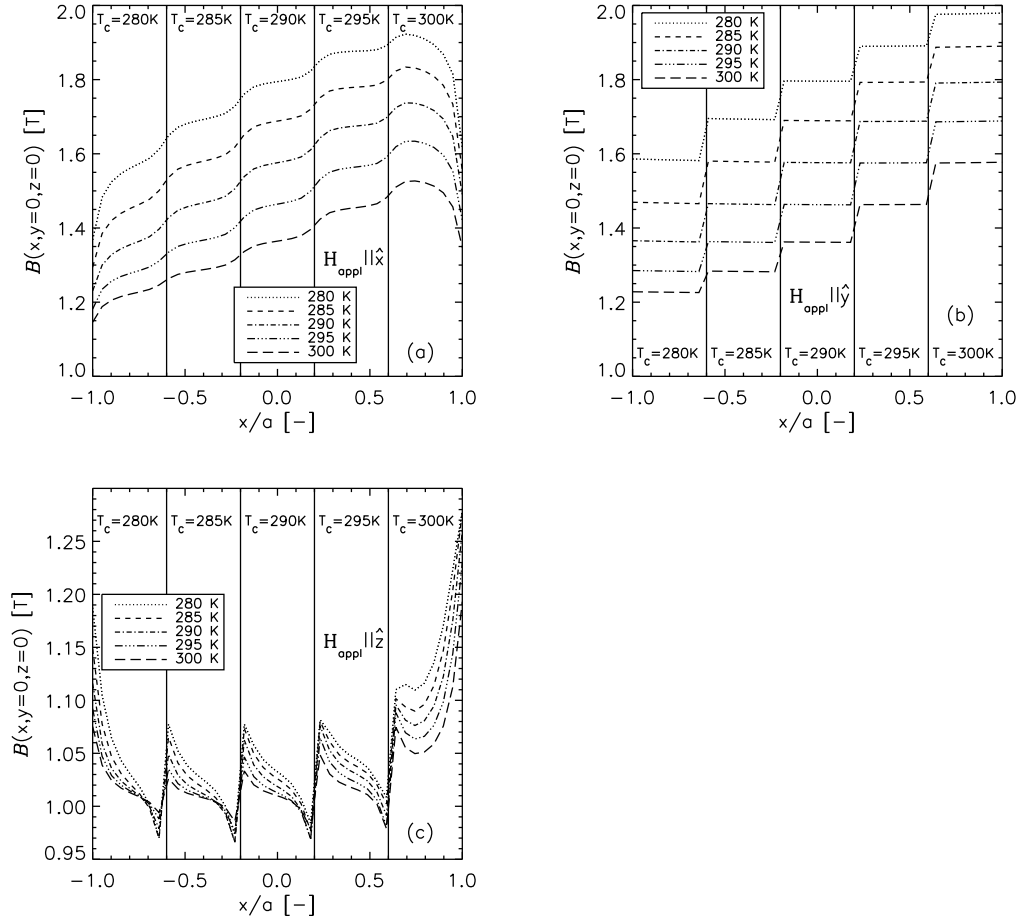


Figure 7.7: The magnitude of the magnetic flux density, B , along the line defined as $-a \leq x \leq a$ and $y = z = 0$. The lines show the different cases where the temperature is kept constant at different values (280 to 300 K, respectively). The applied field is in all cases 1 T. a) The applied field is along the x -direction. b) The applied field is along the y -direction. c) The applied field is along the z -direction. Reproduced from paper A.1.3 (Smith et al., 2010).

when the temperature is 285 K. In this way the staircase-like behavior is explained.

Finally, the case of a graded prism with a linear temperature profile is considered. In Fig. 7.8 H is plotted as a function of x along the same line as in Figs. 7.4 and 7.6–7.7. The temperature is varied linearly from 280 to 300 K. It is observed that the trend is somewhat similar to that in Fig. 7.6, however, the discontinuities across the material boundaries in Fig. 7.8a are much more profound than in Fig. 7.6a. Also, it is observed that the internal magnetic field strength can actually attain a greater value than the applied field. This is explained by flux shimming as was also observed by Peksoy & Rowe (2005). When a discontinuity in the permeability is present the magnetic field lines are “forced” together on the boundary and this enhances the flux density.

When applying the field along the y -direction, Fig. 7.8b, the trend is virtually

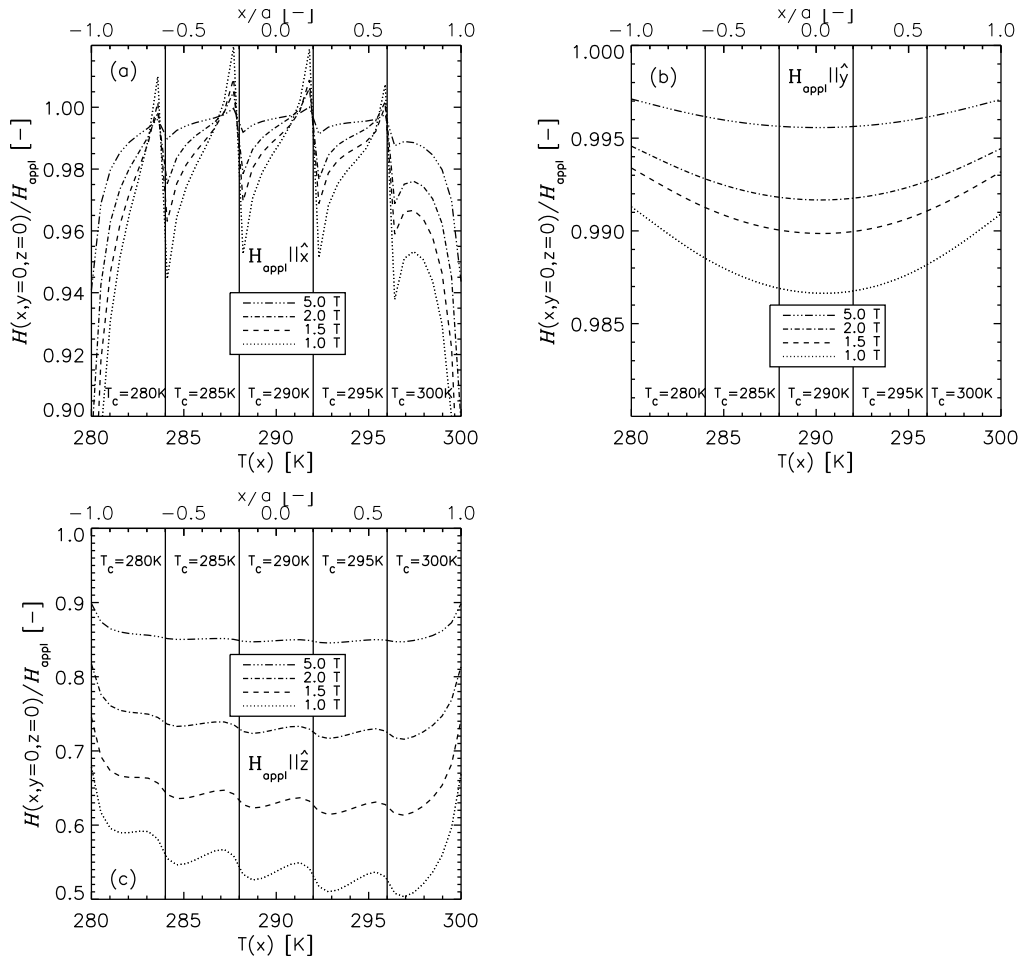


Figure 7.8: H as a function of x through the point where $y = z = 0$. The rectangular prism considered is constructed of five ferromagnets each with an individual Curie temperature. The temperature is linearly varying from 280 to 300 K along the x -direction and the lines show the cases where the applied field is varied from 1 to 5 T. a) The applied field is along the x -direction. b) The applied field is along the y -direction. c) The applied field is along the z -direction. Reproduced from paper A.1.3 (Smith et al., 2010).

identical to the case of constant temperature (Fig. 7.6b). Finally, when the field is applied along the z -direction, the resulting internal magnetic field strength is seen to be more homogeneous than in the constant temperature case (compare Figs. 7.6c and 7.8c).

It is concluded that applying the magnetic field such that the field lines are parallel to the material boundaries and in the plane of the plate, i.e. as in Fig. 7.8b is preferable if the configuration should yield the most homogeneous and greatest magnetic field strength as is preferred in magnetic refrigeration applications.

7.3 A stack of rectangular prisms

The previous section dealt with the details of the demagnetizing field in a single rectangular prism. Now the focus will turn to the natural extension: a stack of such prisms. Such a stack may be created in many ways, however, when considering magnetic refrigeration as an application the general stack will be made of identical rectangular prisms that are “flat” and “long” in the sense that the $a \times c$ and the $b \times c$ faces are much smaller than the $a \times b$ face; see Fig. 7.9. These prisms are then stacked along the direction perpendicular to the large face; again, see Fig. 7.9. In this way a heat transfer fluid can move in an oscillating flow between the plates. This application is described in detail in Chapters 3–6.

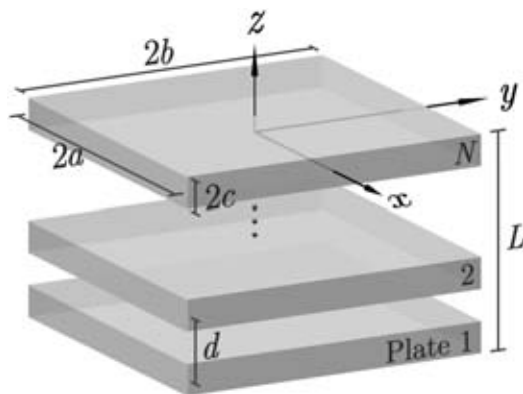


Figure 7.9: *The coordinate system of the stack of rectangular prisms. The relative dimensions of the individual prism are $a = b = 20c$. Reproduced from paper A.2.1 (Christensen et al., 2010b).*

Now, it is relevant to investigate how the resulting, spatially resolved internal magnetic field is as a function of the number of prisms (or plates), the distance between two consecutive plates, the aspect ratio of the individual plate, the orientation of the applied field, the temperature (distribution) of the stack and the composition in terms of which materials each individual plate is made of.

This enables a rather large range of parameter variations. However, the purpose of this section is not to optimize the configuration nor is it to provide a detailed mapping of the influence of each individual parameter. The purpose is simply to investigate situations relevant for magnetic refrigeration. Thus, the number of plates and their spacing have been kept fixed at 20 plates and 1.54 mm, respectively. Also, the dimensions of each individual plate are kept at $20 \times 20 \times 1$ mm, as was the case in the previous section (7.2). The thickness in the z -direction and the spacing between the plates ensures a porosity of the stack of 0.35.¹

7.3.1 Single material results

Physically, each plate will influence the other plates with its magnetic field and so it is expected that the resulting internal magnetic field in either prism cannot generally be assumed to be equal. In Fig. 7.10 different configurations of stacks and applied field orientations are illustrated.

Figure 7.11 shows the resulting magnitude of the internal field as a function of x in the ten plates from the end of the stack to the centre for three different applied field directions. The internal field is observed to behave similarly in all the

¹It may be argued that the porosity of a stack of parallel flat plates is inherently anisotropic. In this case the porosity is meant as the fraction of the entire void space in the stack and the total volume of the stack.

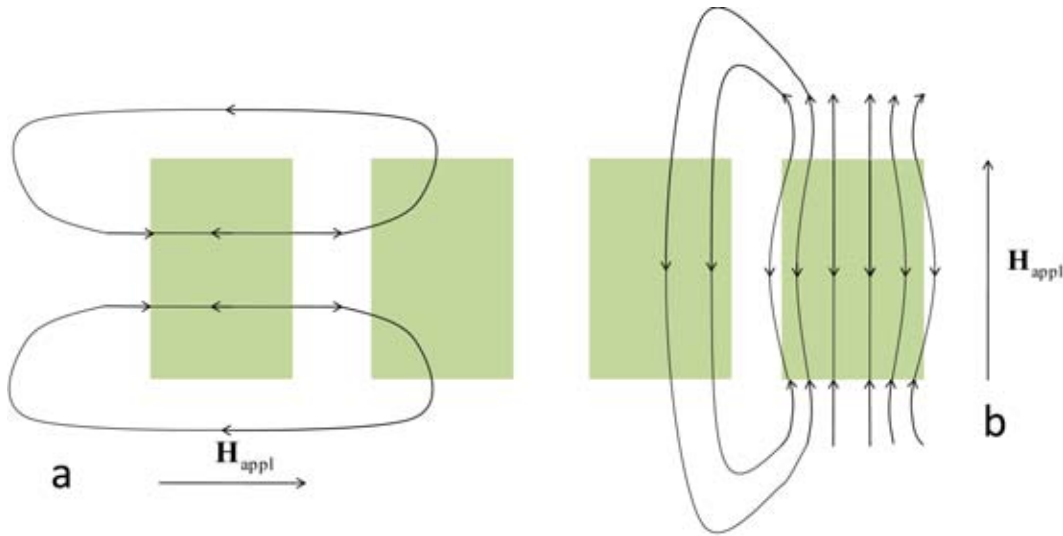


Figure 7.10: Illustration of the demagnetizing field in a stack of rectangular prisms when the applied field is along two different directions. In (a) the field in the rightmost rectangle is increased due to the demagnetizing field of the leftmost plate. In (b) the field in the leftmost plate is decreased due to the demagnetizing field in the rightmost plate. The figure provides an example only. This serves to show how the concept of the demagnetizing field in a stack of prisms behaves qualitatively. It is also stressed that the lines only serve to show the direction of the local field – the density of the lines does not correspond to the magnitude of the local field.

plates, however, the magnitude is either monotonously increasing or decreasing as a function of the plate number depending on the direction of the applied field.

In the case of applying the field along the x -direction it is observed that the internal field is smaller in the centre plate (#10 in Fig. 7.11(a)) than in the outer plate (#1 in the figure) and that it increases monotonously outward. This is to be expected since the demagnetizing field from each individual plate will tend to decrease the internal field in the other plates, (see Fig. 7.10), and since the outer plate naturally is furthest from the centre and thus least affected by the demagnetizing fields from the other plates it has the smallest demagnetizing field.

The same argument is valid when applying the field along the y -direction since the demagnetization form factor is the same as in the x -direction case. However, the x -dependence is different in the two cases (Figs. 7.11(a)-(b)). The magnitude of the internal field is maximized at the centre of the plates when applying the field along the x -direction and minimized when applying along the y -direction. This is due to the fact that the demagnetization tensor is greater on the face on which the applied field is perpendicular to.

Considering the application of the field along the z -direction, Fig. 7.11(c), it is observed that the centre plate has the largest internal field magnitude, the outer the smallest and that the internal field magnitude decreases monotonously outwards, i.e. the opposite situation of the application along the x - or y -directions. Now, this is due to the fact that the demagnetizing field from each individual plate in this case tends to align with the applied field outside the plate (see Fig. 7.10) and thus decreases the resulting demagnetizing field inside the other plates. Again, the centre

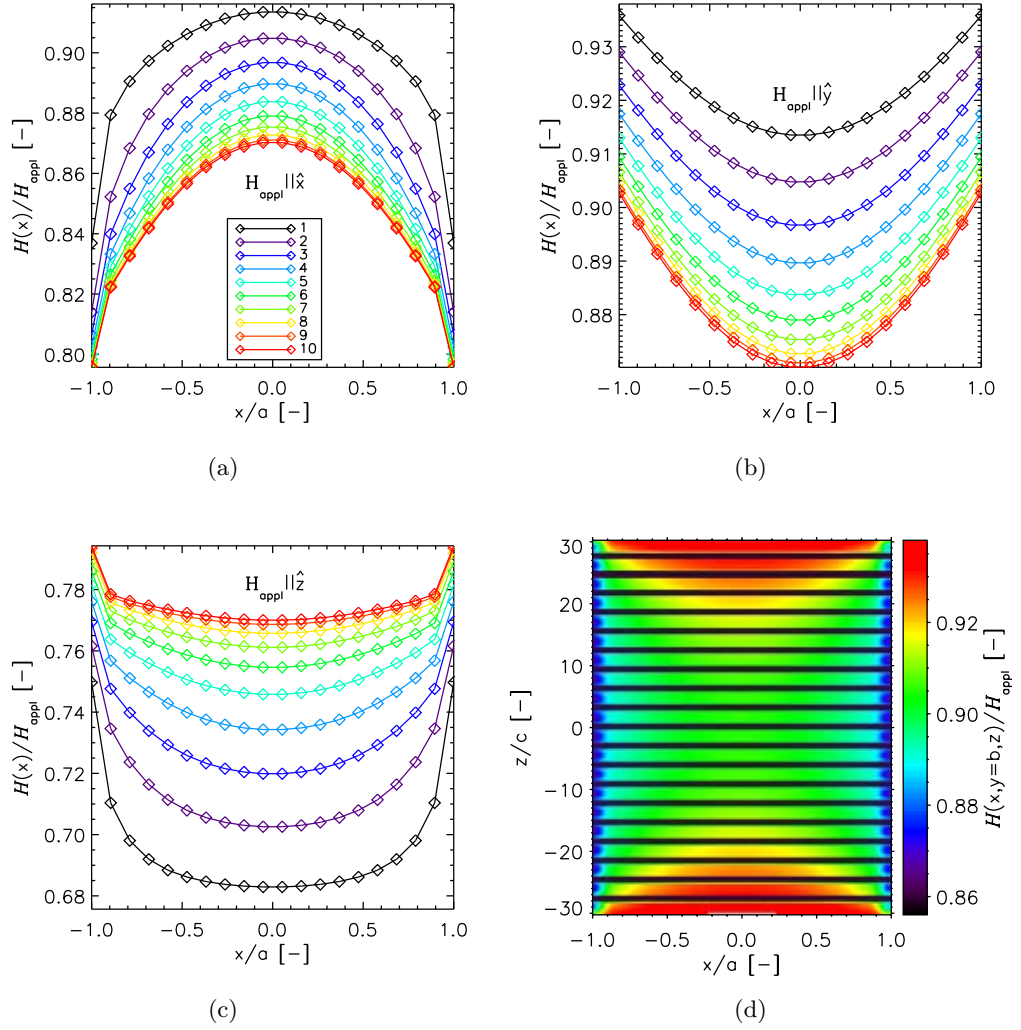


Figure 7.11: The internal magnetic field along the x -axis in each of the stacked prisms going through their respective origins. The temperature is fixed at 295 K and the prisms are single-material Gd modeled using the mean field model. The legend refers to the prism index where 1 is the outmost prism and 10 is the central prism. The direction of the applied field is indicated in the figures and is thus the only difference between (a)–(c). In (d) the xz -plane at $y = b$ of the entire stack is mapped in the case when the applied field is in the x -direction.

plate will experience the biggest effect since it is surrounded by other plates whereas the outer plate will experience the smallest effect since it has fewer neighbors.

The fact that the application along the z -direction results in a significantly smaller internal field, on average, than in the case of applying the field along the x - or y -directions is due to the generally much greater demagnetization factor in this case. However, adding more plates to the stack may decrease the effective demagnetizing field and thus compensate somewhat for the “loss” of internal field as compared to the single prism case. This is investigated in more detail in Sec. 7.4.

Finally, the surface map of the internal magnetic field strength in the xz -

plane at $y = b$ is given in Fig. 7.11(d). It is clear that the resulting internal field is inherently multi-dimensional (a 3D-rendering would reveal that the field is certainly varying in the y -direction as well; compare Figs. 7.11(a)-(b)).

7.3.2 Multi-material results

This subsection deals with the, for magnetic refrigeration as an application, relevant cases of grading a stack of rectangular prisms and imposing a linear temperature profile on such a stack in terms of the effect of geometric demagnetization.

The constant temperature case

In Sec. 7.2 the single prism case was investigated and the focus was on the influence of grading the prism with five different ferromagnets distinguished by their Curie temperature as well as imposing a temperature profile. The same configuration is now considered for a stack of plates otherwise identical to that investigated in the previous section, 7.3.1. Now, for the case where the temperature is constant (in this case 295 K), $H(x)$ is plotted for the three cases of applying the field along the principal axes in Fig. 7.12. The results show that the centre plate has the smallest internal field and the outer plate the greatest when the field is applied along the x - or y -direction exactly as was the case for the single material case in Fig. 7.11. Also, not surprisingly, the situation is reversed when the field is applied along the z -direction (Fig. 7.12(c)). However, the topology of $H(x)$ is not like that in Fig. 7.11, but much rather like the case in Fig. 7.6. These two results are not too surprising since the situation investigated here may be considered as a hybrid between the single-plate situation with a graded plate and the stack of plates consisting of a single material.

These are, however, results that are based on a very typical situation for an active magnetic regenerator (AMR) that is based on a stack of parallel plates. In other words: it is now possible to fully analyze the impact of the effect of geometric demagnetization on the parallel-plate based AMR.

The linear temperature profile case

In the steady-state operation of an AMR the temperature profile along the flow direction, here equal to the x -direction, is typically quite linear. The effect of demagnetization under such circumstances is thus relevant to probe. Now, the stack of plates is identical to that investigated in the previous section as is the material composition. A linear temperature profile is imposed ranging from 280 to 300 K, completely identical to the case investigated in Fig. 7.8 for the single-plate situation.

Figure 7.13 shows the resulting internal field strength along the x -direction for the three cases of applying the field along the principal axes (Fig. 7.13(a)-(c)) and $H(x, y = b, z)$ in Fig. 7.13(d). Again, the results are not surprising in the sense that they resemble a hybrid between the single-prism case with five materials and a linear temperature profile and then the stacked parallel-plate case where the centre plate has the smallest internal field strength when applying the field along the x - or y -direction etc. What is different from the single-plate case is the fact that the internal field strength is lowered with 14 percent in the centre plate compared to the applied field – for the single plate case this decrease was only about 2 percent (Fig.

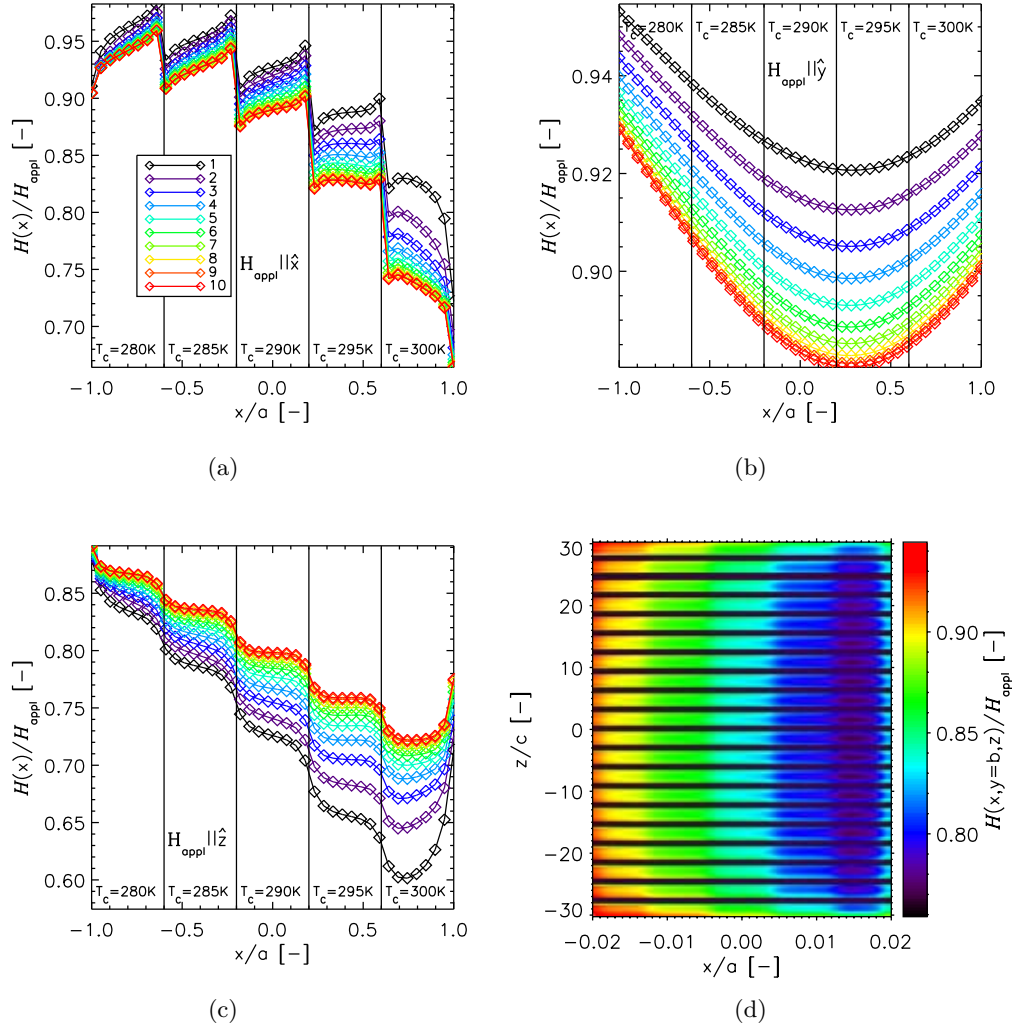


Figure 7.12: The internal magnetic field strength as a function of x for an applied field along the three principal axes. As indicated in each subfigure, the plates are made of five different magnetic materials with their respective Curie temperatures indicated. The applied field strength is 1 T and the temperature is 295 K. In (d) the internal magnetic field strength is mapped in the xz -plane at $y = b$ and the applied field along the y -direction. The legend in (a)–(c) shows the plate number where one is the outer plate and 10 is the centre plate.

7.8b) – when the field is applied along the y -direction. Furthermore, the internal field of the outer plate is lowered up to about 9 percent in this case, which again is somewhat more than for the single plate case. It may thus be concluded that the stacking of the plates has a significant impact on the resulting internal field and that this trend is generally towards a decrease in the field strength – when the field is applied along the x - or y -direction. It was expected that the resulting field should be smaller, however, a decrease of up to 14 percent is quite significant.

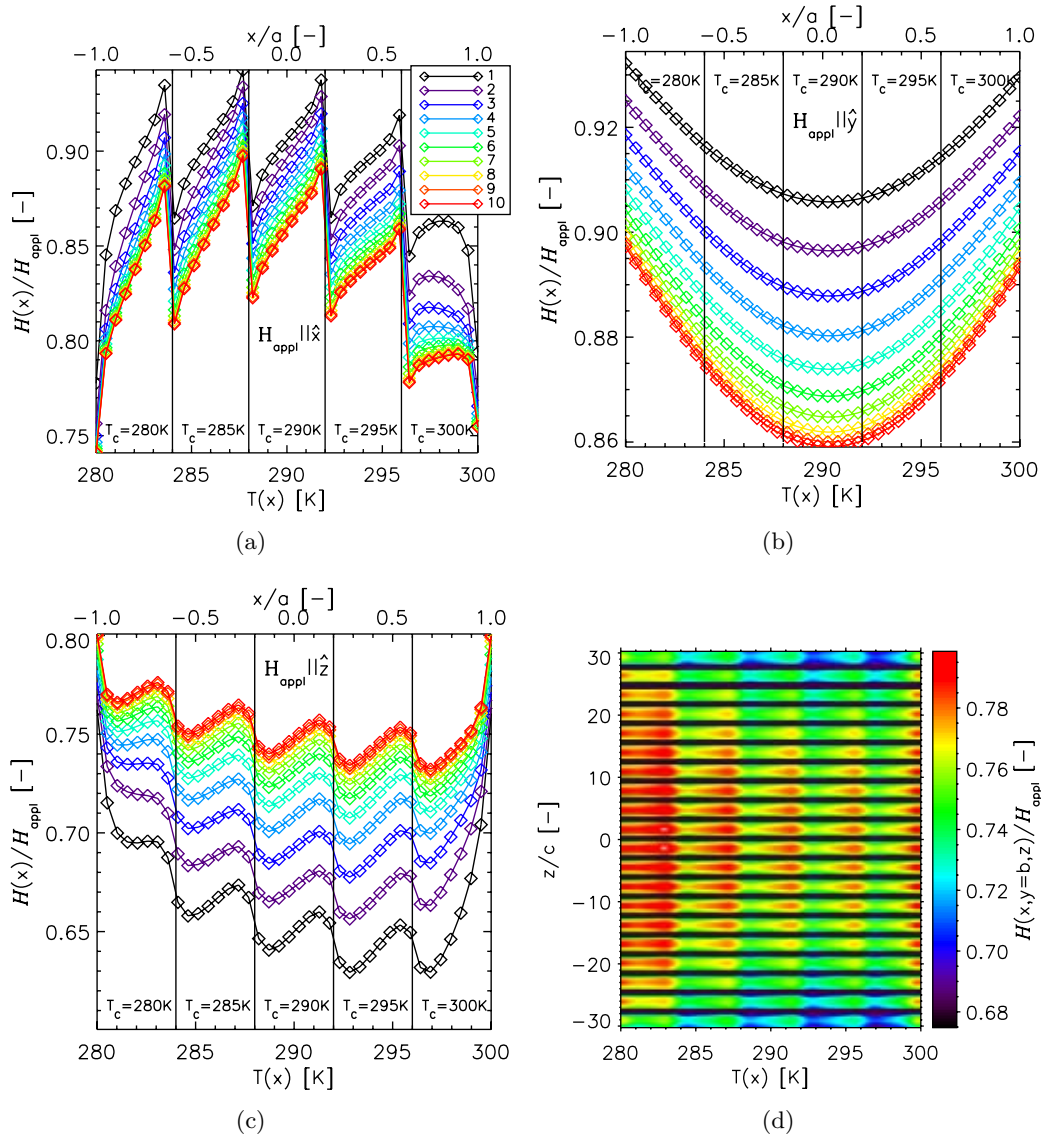


Figure 7.13: The internal magnetic field strength as a function of x for the three cases of applying the field along the principal axes. The stack is made of parallel plates, where each is made of five different materials distinguished by their Curie temperature. A linear temperature profile is applied along the x -axis in order to give a resemblance of the typical situation encountered in magnetic refrigeration. Fig. (d) shows $H(x, y = b, z)$ when the field is applied along the z -direction.

7.3.3 The effect of demagnetization in selected materials

The following section serves to provide an overview of the resulting internal field magnitude, H , in stacks of rectangular plates made of real magnetic materials. This is done in order to give an idea about the impact the demagnetizing field has in a realistic scenario. Magnetization data for two series of materials have been used. The first is the $\text{LaFe}_{13-x-y}\text{Co}_x\text{Si}_y$. This material is characterized in terms of its magnetocaloric properties in Sec. 2.5. This material series is referred to as “LaFeCoSi”

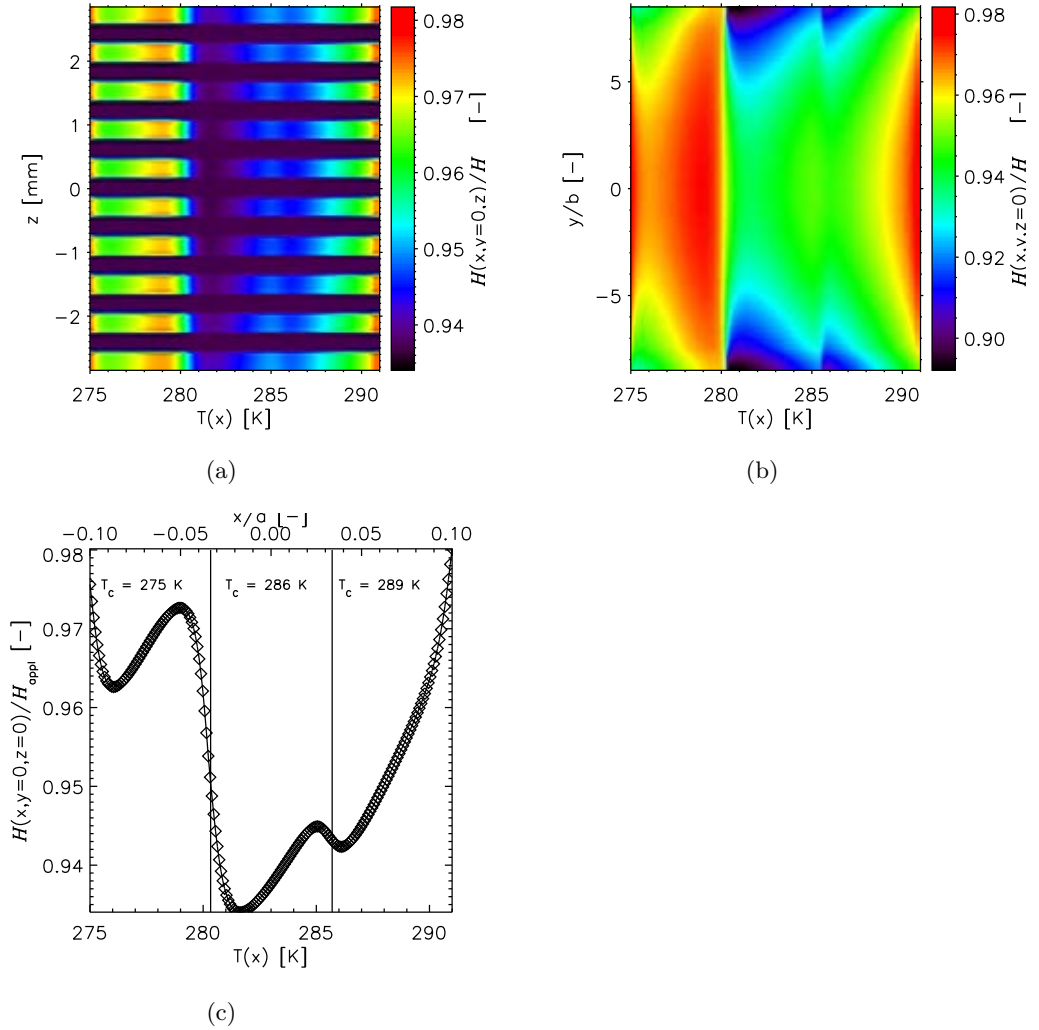


Figure 7.14: H in a stack of plates of LaFeCoSi made of three different materials having different magnetic properties. In (a) the xz -plane at $y = 0$ is shown, in (b) the xy -plane at $z = 0$ and in (c) the field along the x -direction at $y = z = 0$ is shown.

and three materials are considered having Curie temperatures at 275, 286 and 289 K, respectively.² The other material series is $\text{La}_{0.67}\text{Ca}_{0.33-x}\text{Sr}_x\text{Mn}_{1.05}\text{O}_3$, where a total of four materials are considered having Curie temperatures at 270, 275, 284 and 290 K, respectively. This material series is denoted “LCSM” and the data were presented in Sec. 2.5.

The dimensions of the stack are defined such that there is a total of ten plates each with a thickness of 0.3 mm and the distance between each plate is 0.3 mm as well. The total dimensions of each individual plate are $200 \times 17 \times 0.3$ mm³. These dimensions are chosen such that the resulting stack resembles those used in the magnetic refrigeration prototype located at Risø DTU. For this reason, the applied

² T_C is here defined as the inflection point of the magnetization as a function of temperature in a small field; see Sec. 2.5 for further details.

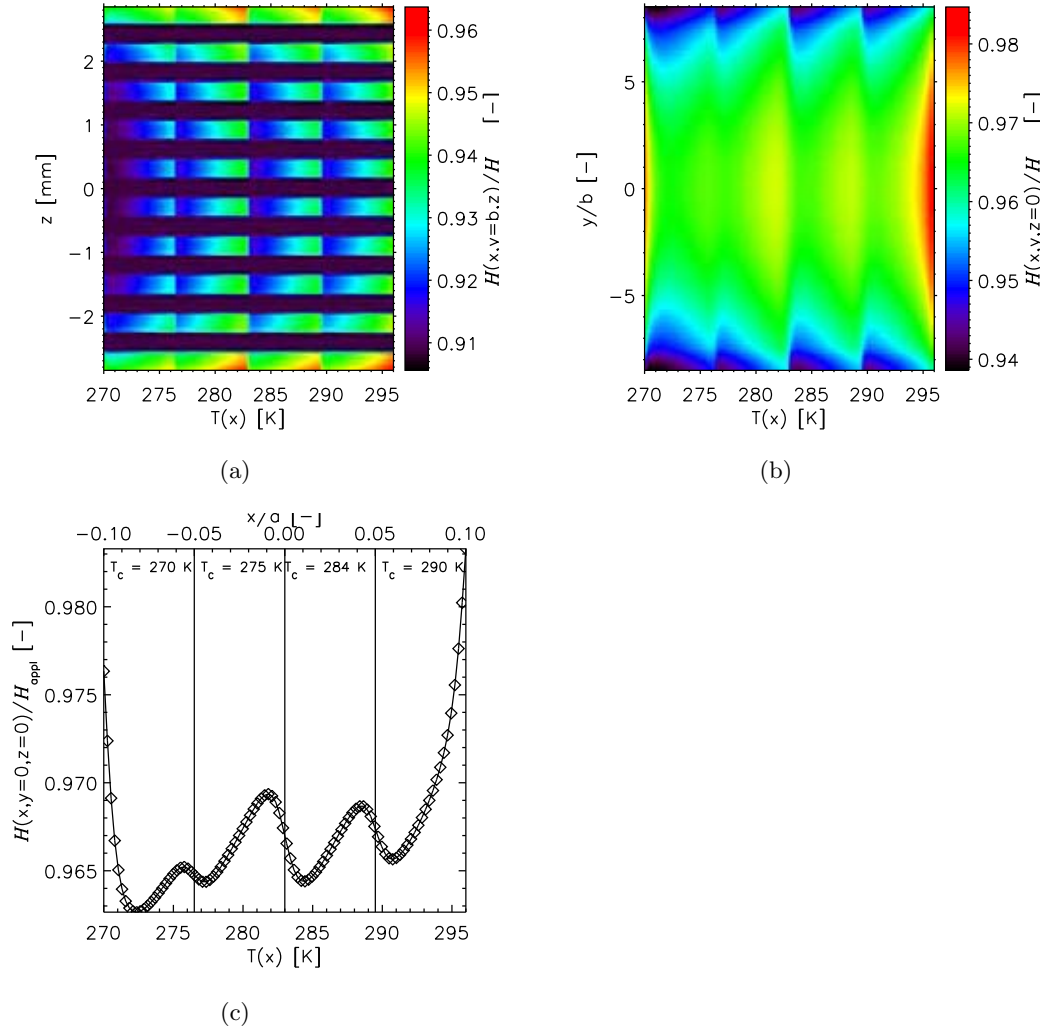


Figure 7.15: The norm of the internal magnetic field in the xz -plane at $y = 0$ (a), the xy -plane at $z = 0$ (b) and as a function of x at $y = z = 0$ (c).

field is along the y -direction, i.e. the 17 mm direction. The design of this device is partially described in Bjørk (2010); Bahl et al. (2010).

In Fig. 7.14 H is plotted in the xz - and xy - planes and along the x -direction at $y = z = 0$ for the case of using the LaFeCoSi materials. A linear temperature profile has been imposed ranging from 275 to 291 K, such that the Curie temperatures are all within this range.

From Fig. 7.14 it may be concluded that the two materials with Curie temperatures at 286 and 289 K have little boundary effects between each other in the sense that the field across their shared boundary is fairly constant. Comparing with the boundary between the materials at 275 and 286 K, it is observed that this boundary implies a much sharper gradient in $H(x)$. The reason for this is that the 275 K material is almost only in its paramagnetic phase whereas the material at 286 K is almost only ferromagnetic. In this way the demagnetizing field of the former is relatively small whereas it is relatively large for the latter. The material at 289

K is somewhat evenly split in terms of its magnetic phases such that half of it is ferro- and the other half is para-magnetic. In this way it “connects” well with the material at 286 K as opposed to the “connection” between the materials at 275 and 286 K.³ The behavior of these “connections” or boundary “layers”⁴ may be crucial for the performance of a magnetic refrigerator. If large gradients of H exist inside the regenerator material during operation parasitic entropy generation may occur.

In Fig. 7.15 H of the LCSM stack is considered. It is clear from the figure that variations in the internal field compared to the applied field certainly exist, however, the magnitude of these is quite small. This is due to the fact that the magnetization of the LCSM is roughly half as large as that of LaFeCoSi (and Gd) and the demagnetizing field is thus smaller. This is, in other words, an advantage for the LCSM material series when evaluated as a potential magnetocaloric material for usage in a magnetic refrigerator.

7.4 Demagnetizing effects in generalized stacks of parallel plates

In the following the demagnetizing field of a stack of rectangular plates where the stack configuration has been varied is considered. The model presented previously in this chapter is applied to three cases where

- the distance between the plates is varied
- the porosity of the stack is varied
- the number of plates is varied

The mean field equation of state, Eq. 2.13, is used and the dimensions of each plate are $2a \times 2b \times 2c = 20 \times 20 \times 1 \text{ mm}^3$. The distance, d , denotes the distance between the *centre* of two consecutive plates. See Fig. 7.9 for clarity. It is noted that when $2c = d$ then the stack has no void space. The temperature is set to 293 K and Gd is used as magnetic material. It is finally noted that in the following an “infinite” stack is mentioned. This actually means a stack with 99 plates, which has been found to be sufficient to be considered as infinite.

7.4.1 Influence of the number of plates

Figure 7.16 shows the average internal field in the stack as a function of the number of plates. The spacing between the plates is 2 mm, corresponding to $d = 3 \text{ mm}$ and a porosity of 0.67. The trend is similar to that found in, e.g., Fig. 7.11. When only a single plate is considered the demagnetizing field when the applied field is along the x -direction is very little whereas the opposite is true when the field is applied along the z -direction. As the number of plates increases the average field decreases when the field is applied along the x -direction and increases when it is along the z -direction.

³By “connection” is meant the behavior of H close to the boundary between the two materials.

⁴Of course, these are purely imaginary layers and should only be understood as a way of expression – not a physically meaningful entity.

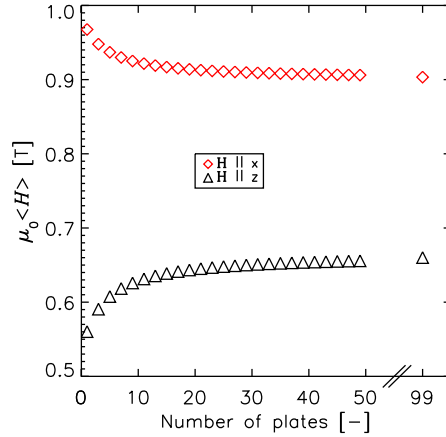


Figure 7.16: The average internal field in a stack where the number of plates is varied. The spacing between the plates is 2 mm, i.e. $d = 3$ mm. The cases where the applied field is along the x - and z -direction are presented. The data is reproduced from paper A.2.1 (Christensen et al., 2010b).

This behavior is to be expected since when the field is along the x -direction the stray field from each plate will tend to oppose the applied field in the other prisms (see Fig. 7.10 for an illustration). It is interesting, though, that the mean internal field seems to have an asymptotic behavior as a function of the number of plates. In the case considered here this means that applying the field along the x -direction will always result in a larger internal field than applying the field along the z -direction.

7.4.2 Spacing of the plates

In the following two stack configurations are considered. One with 19 plates and one is “infinite” (i.e. has 99 plates). The results of varying the distance between the centre of the plates, d , are given in Fig. 7.17. When the distance is minimal, i.e. the ratio $d/2c$ is small, a very interesting and quite non-linear effect dominates the internal field. In this case when the field is applied along the z -direction, the stray field from each individual plate enhances the internal field of the neighboring plate so strongly such that the resulting average field in the stack comes very close to be equal to the applied field (for the infinite stack). When $d/2c = 1$ there is no void space in the stack and it is clear from the figure that a large difference exists between the values $d/2c = 1$ and $d/2c = 2$ for the average internal field. These two values correspond to porosities of 0 and 0.5, respectively.

When considering magnetic refrigeration as an application this is roughly the interval that is relevant to consider. If the geometry of the setup allows for the application of the field along the z -direction, as it is defined here, and at the same time the stack may be considered infinite then this direction of the applied field may be preferable. However, due to the quite strong non-linearity of the behavior of $\langle H \rangle$ at small values of $d/2c$, care should be taken when considering this.

When considering the application of the field along the x -direction, the aver-

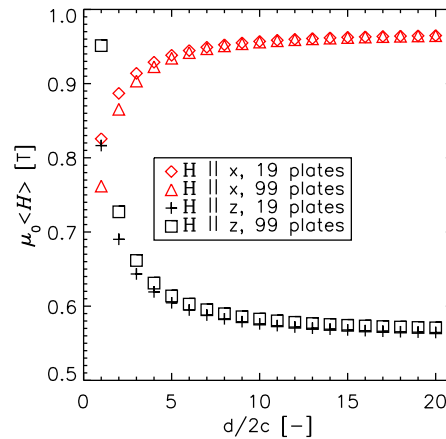


Figure 7.17: The average internal field of the stack as a function of the ratio between the distance between the centres of two plates, d , and the plate thickness, $2c$. The data is reproduced from paper A.2.1 (Christensen et al., 2010b).

age field is seen to be rather small for low values of $d/2c$. The explanation is the same, however, the stray field from each plate is opposing the internal field of the neighboring plates (see Fig. 7.10 for reference).

When the ratio $d/2c$ increases the plates are moved farther away from each other. This results in little influence from the stray fields of neighboring plates and the situation becomes more like a single-prism case. The average field increases as a function of $d/2c$ when the field is applied along the x -direction and decreases when it is applied along the z -direction.

7.4.3 Porosity of the stack

In order to vary the porosity of a stack the total volume is kept constant and plates are added one by one to the stack. Figure 7.18 shows the resulting average internal magnetic field as a function of porosity.

The results show that the average internal field increases (decreases) as a function of the space filled when the field is applied along x -direction (z -direction). The trend is close to being linear. The same argument as used in the previous section applies here as well. When the stack becomes more dense the stray field from neighboring plates becomes more significant. Since these fields oppose the applied field when it is along the x -direction and are aligned with the applied field when it is along the z -direction, the average internal field decreases and increases in the two cases, respectively, for small values of the porosity. A cross-over is observed at a porosity of about 0.1. Below this value applying the field along the z -direction is preferable and above the field should be applied along the x -direction.

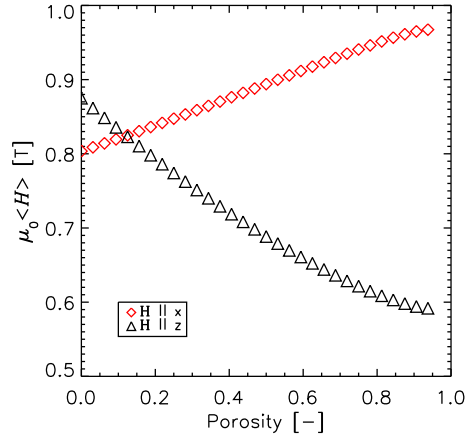


Figure 7.18: The average internal field of the stack as a function of the porosity of the stack. The data is reproduced from paper A.2.1 (Christensen et al., 2010b).

7.5 Experimental predictions

The remainder of this chapter is concerned with an experiment where the adiabatic temperature change is used as a probe for the internal magnetic field. In this way the model presented in this chapter may be compared to experimental measurements even though the internal field of a magnetized material is impossible to measure directly.

7.5.1 The single prism case

A Halbach permanent magnet was used as a magnetic field source (the same as described in Sec. 6.1). Such a design is a cylindrical shape, with a hole in the centre, where the direction of the magnetization varies such that a concentrated (large) flux density is present in the magnet bore. The mean magnetic flux density as a function of distance z from the magnet bore is given in Fig. 7.19. In the figure the extent of a single flat plate of Gd is illustrated as it is symmetrically placed inside the magnet. The dimensions of the plate are $40 \times 25 \times 0.9 \text{ mm}^3$. As described in detail in Christensen et al. (2010a) (paper A.1.4) an infra-red camera was used to measure the spatially resolved temperature of the plate as it was taken out of the magnetic field. This was done from a constant starting temperature of 295 K and for three different angles with respect to the applied magnetic field. In Fig. 7.20 the coordinate system of the Halbach magnet and the Gd plate are illustrated.

Figure 7.21 shows the spatial resolution of the adiabatic temperature change of the Gd plate measured experimentally with the IR camera and modeled using the demagnetization model presented in this chapter. The equation of state used in the model is an experimentally measured magnetization data set published in Bjørk et al. (2010). Recalling Eq. 2.7, it is emphasized that the adiabatic temperature change is a monotonous function of the initial and final internal magnetic field strength for a given initial temperature. Thus, it is possible to make a one-to-one mapping of the internal magnetic field and the adiabatic temperature change, if the initial state is

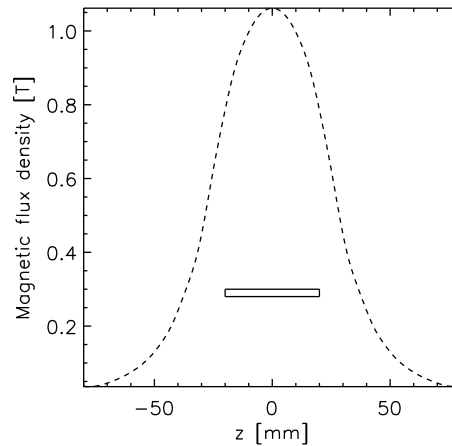


Figure 7.19: The magnetic flux density produced by the Halbach permanent magnet applied in the adiabatic temperature change measurements. A rectangle with the length of a single Gd sheet used in the experiment is illustrated in the figure corresponding to when it is placed in the magnetic field.

known⁵, and thereby use the directly measured adiabatic temperature change as a probe for the internal magnetic field strength. In these experiments the Gd plate was moved from the symmetrical position (see Fig. 7.19) in the Halbach magnet and into zero field. The experimental results presented in Fig. 7.21 thus shows both the observed adiabatic temperature change and the internal magnetic field strength spatially resolved throughout the surface of the Gd plate.

Considering the modeling it is observed that the demagnetization model certainly captures what is experimentally observed. The difference between the values predicted by the model and the experimental results is no more than 0.2 K overall. The topology of the indirectly measured internal field is, though, slightly different than that predicted by the model. This is most apparent when the angle is 45° . Here it is observed that the variation in the x -direction (see Fig. 7.21) differs between the modeled and the observed data. The main reason for this is expected to be the inhomogeneity of the Halbach magnetic field. An inhomogeneity of just 0.1 T will give a difference in adiabatic temperature change of roughly 0.35 K around room temperature in Gd. The discrepancy is clearly less than this; see Fig. 7.21; and the used magnetic field profile (Fig. 7.19) is the averaged flux density measured in the Halbach magnet. At this time a more precise mapping of the field in the Halbach magnet bore is not available; such a mapping would definitely improve the results of the demagnetization model when comparing to the experimentally measured data.

7.6 Summary

In this chapter the internal magnetic field of a magnetic material was considered. Since it is assumed that the internal field magnitude, H , is the quantity that the

⁵This, in the case of a soft ferromagnet, is fulfilled when the applied field is zero

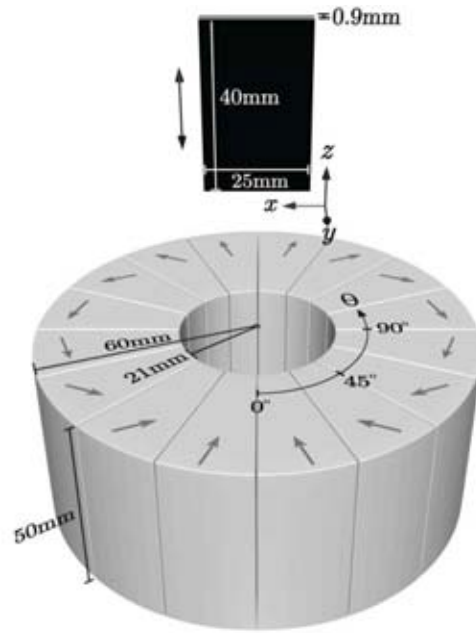


Figure 7.20: The coordinate system of the Halbach magnet and the Gd plate illustrated. When the angle is zero degrees the magnetic field lines are perpendicular to the 40×25 face. Reproduced from paper A.1.4 (Christensen et al., 2010a).

MCE is dependent on, it is of the most high relevance to have detailed knowledge of the behavior of this quantity inside relevant geometries and under parameter configurations relevant to the AMR such as temperature distribution and material composition. A numerical model that is able to calculate \mathbf{H} in a rectangular prism was developed and verified.⁶ The internal field of such a prism under various conditions including an imposed linear temperature profile and grading the prism with a range of magnetic materials with individual Curie temperatures was investigated. The results reveal that H is highly dependent on the direction and magnitude of the applied field, temperature and the composition of the material. It is concluded that for a graded prism the field should be parallel to the lines of the grading and in the large plane of such a prism. In this way the demagnetization factor is minimized and the resulting H is smooth and homogeneous due to the fundamental boundary conditions always applying for \mathbf{H} .

This geometry may be considered as a stepping stone towards more complex and relevant geometries. The model was therefore generalized to a stack of identical prisms⁷ The internal field in such a stack was investigated under similar conditions to the single prism case. It was found that the behavior of the two systems is very similar, however, the demagnetization factor generally increases with the number of plates in the stack when the demagnetization factor of an individual prism is small and vice versa.

In order to probe the effect of demagnetization even further the prism-stack

⁶In close collaboration between Mr. D.V. Christensen, Risø DTU and the author of this thesis.

⁷The model can in principle easily handle prisms of different shapes; the mathematical formulation needed is straightforward.

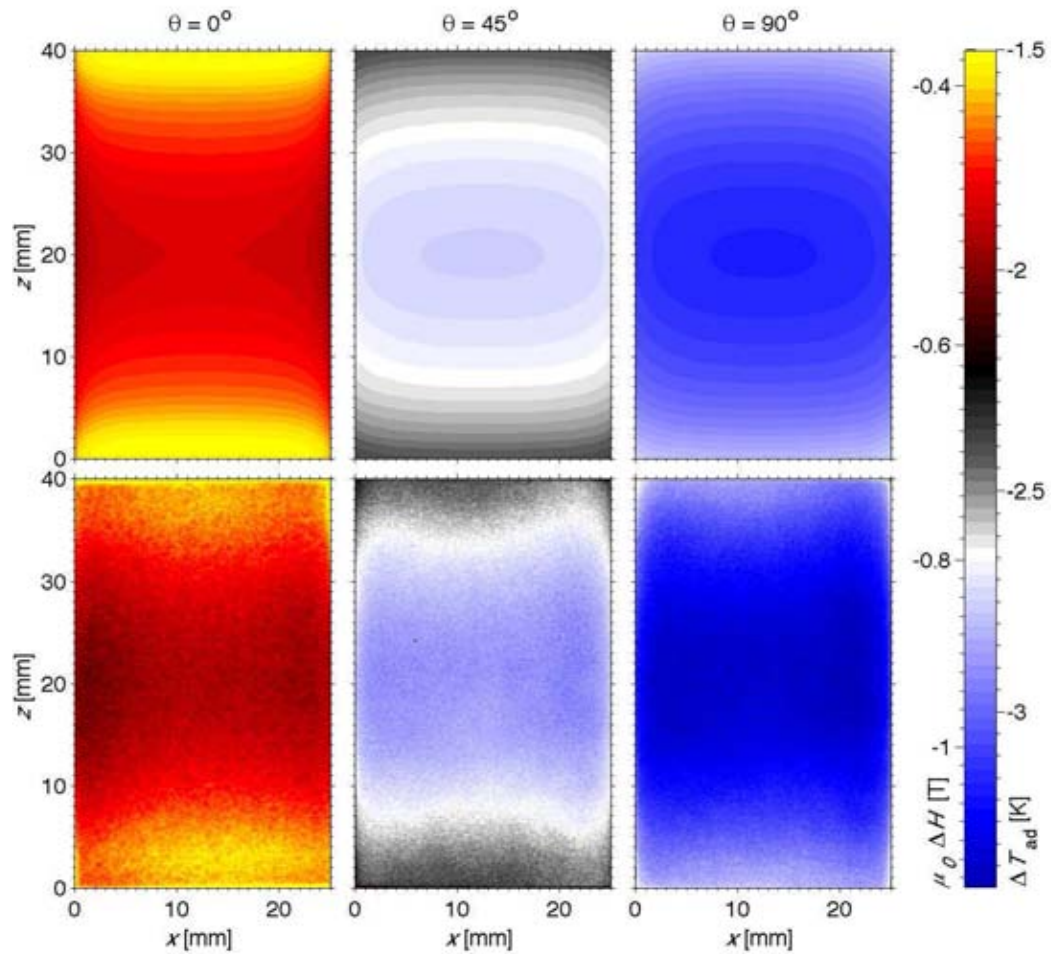


Figure 7.21: Modeling and experimental results of the spatially resolved adiabatic temperature change of a single plate of Gd as a function of the orientation of the applied magnetic field. The color scale shows both the adiabatic temperature change and the mapped internal magnetic field strength. Reproduced from paper A.1.4 (Christensen et al., 2010a).

model was applied to realistic cases using actual materials data. This was done for the two material series LCSM and LaFeCoSi. It was concluded that a stack of LCSM is significantly less affected by the demagnetization due to the quite smaller inherent magnetization of this material compared to e.g. LaFeCoSi and Gd.

After having considered the theoretical behavior of the resulting internal field of a single rectangular prism and a stack of such prisms the model results were compared to experiments. The magnetocaloric effect expressed as the adiabatic temperature change was used as the probe for this comparison. In this way an indirect measurement of the internal field strength was possible and the comparison could be made. It was found using thermography in order to obtain the spatial resolution of the MCE on a single prism that the model not only captures the trends of the behavior of the internal field as a function of parameters such as direction of the applied field etc. but in fact also captures the absolute values to a high level.

Chapter 8

Perspectives and future challenges

In this chapter the work presented in this thesis is put into perspective and suggestions for further work are provided. In Sec. 8.1 other geometries than parallel plates are considered as candidates for application in the AMR. This is a section where discussions of the applicability of various geometries are provided. A range of elements enter this discussion such as the effect of demagnetization, how grading of the regenerator material is possible etc. In Sec. 8.2 suggestions for how to link the demagnetization and AMR models are provided. Finally, in Sec. 8.3 the impact of various physical effects are considered. These have not been included in the work presented so far and are thus included as suggestions for future work.

This chapter is partially based on paper A.3.7 (Engelbrecht et al., 2010b), which was presented at the Fourth International Conference on Magnetic Refrigeration at Room Temperature in Baotou, China 2010 by Dr. K. Engelbrecht and on paper A.1.9 (Pryds et al., 2010).

8.1 Suggestions for candidate regenerator geometries

In magnetic refrigeration the geometries for the AMR itself have so far mainly been limited to parallel-plate regenerators and packed spheres / crushed particles. See, e.g., Gschneidner & Pecharsky (2008) for a review. These geometries have certain advantages and disadvantages. In this thesis the parallel plates have been covered extensively and it may be concluded that spacing such plates precisely enough is probably the greatest problem of this geometry. The spacing needed for the plates to perform adequately (in theory) is between 50 and 100 μm . A spacing of 50 micrometers is equivalent to packed spheres with a diameter of 0.3 mm in terms of heat transfer area and hydraulic diameter. Considering the number of transfer units, see Fig. 8.1, an NTU of approximately 50 is not reached at greater spacings than 50 micrometers at a cycle frequency of 4 Hz. This means that in order for parallel plates to reach a performance similar to that of packed spheres the demands on the constructability are quite high.

Packed spheres have proven to yield the largest temperature spans and cooling powers produced in any AMR device so far. They are both easier to manufacture (of course depending on which material is used) and provide superior heat transfer

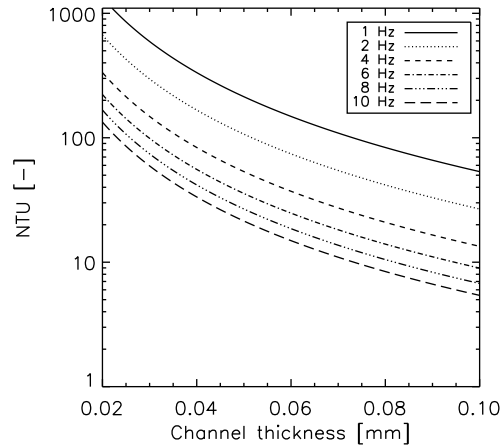


Figure 8.1: The number of transfer units as a function of channel thickness for a parallel plate regenerator. The cycle frequency is indicated in the figure legend. The NTU was calculated using Eqs. 4.1 and 4.2.

characteristics. However, they also provide a too large pressure drop which is so significant that it is difficult to see how this hurdle may be overcome.

Other geometries should thus be considered. Of course, this has happened to some extent in other areas where regenerators are used (Stirling engines, pulse-tubes etc.). However, these applications use compressible gasses and quite different solids than used in a magnetic refrigeration device. Furthermore, they do not have the magnetostatic issues and largely varying specific heats as are present in the AMR. A latent need for further investigation of the influence of the AMR geometry on the performance is thus needed for this particular topic.

In Fig. 8.2 examples of possible regenerator geometries are given. In the following the properties of the suggested geometries are briefly discussed.

Elliptically shaped needle-pins

Rühlich & Quack (1998) suggested the elliptically shaped needle-pin geometry (left-most in Fig. 8.2). They showed that the heat transfer properties of this geometry are superior to parallel plates whereas the pressure drop is larger, however, still much less than for packed spheres. The geometry provides a controlled mixing of the heat transfer fluid. Such a mixing increases the heat transfer and is not present (theoretically) in a parallel-plate regenerator and is, perhaps, too large in a packed sphere bed. The elliptically shaped needle-pins force the mixing to occur in one direction only and the pressure drop is thus significantly smaller than for the packed spheres.

This geometry may furthermore provide excellent demagnetization properties, if the field is applied along the long direction, i.e. perpendicular to the elliptical face. However, the details of this remain still to be investigated.

Finally, on a practical level, the grading of this geometry should be straightforward (on the same level as for packed spheres). Each pin is, in principle, independent and may thus be made of any material. The big issue with this geometry may, how-

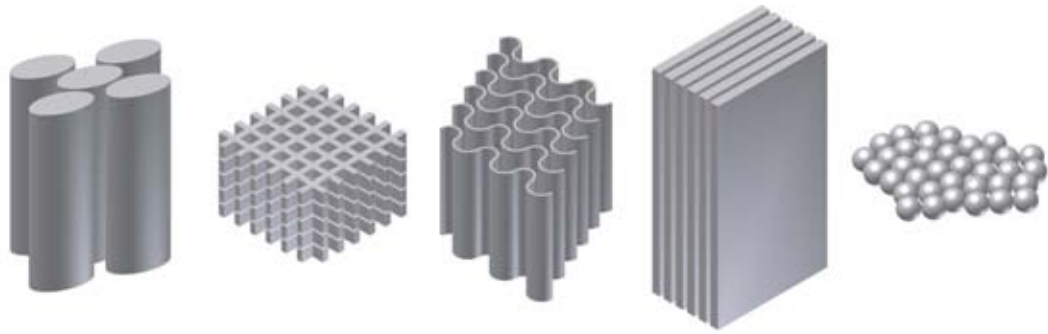


Figure 8.2: Examples of potential regenerator geometries for usage in the AMR. Courtesy of Mr. F. Saxild, Risø DTU.

ever, be the constructability.

Stacked wire mesh screens

This geometry has been widely used in passive regenerators for decades (Organ, 1994). It provides a good compromise between the superior heat transfer characteristics of packed spheres and the low pressure drop of, e.g., parallel plates. However, for the application in magnetic refrigeration the manufacturability seems to be quite a challenge. Either thin threads of the magnetocaloric material need to be spun and woven (which may be possible for metals) or the structure could, e.g., be extruded. This was considered in paper A.1.9 (Pryds et al., 2010). The material considered was LCSM. A monolithic structure resembling the stacked screens was extruded. However, in order to extrude LCSM the process is done when the magnetocaloric powder is partially dissolved in a viscous, non-newtonian liquid. This needs to be sintered after extrusion to yield a structure of pure LCSM. The sintering was not possible and testing of the geometry could only be performed in a state with roughly 60 percent LCSM and 40 percent fluid. This resulted in a rather poor AMR performance. Further research into this is ongoing at Risø DTU.

Corrugated Chevron-plates

Corrugated, or Chevron, plates have several promising properties. A stack of such plates is made of embossed plates where the corrugation pattern varies such that every second plate is identical. The angle between the corrugations may vary and studies of this may be found in, e.g., Focke et al. (1985); Ciofalo et al. (2000); Hessami (2003); Dovic & Svaic (2007).

The chevron plates have the advantage that they are easy to stack since the structure of the plate itself takes care of the spacing. It is thus “only” a question of embossing flat plates with the proper pattern. This could be done by, e.g., rolling. Metals like Gd are quite ductile and therefore easy to emboss. The ceramic LCSM cannot be embossed in its final state (it is much too brittle). However, after tapecasting and before sintering the material is in a very flexible state and here it has been experimentally shown at Risø DTU that it is possible to emboss some pattern that

remains in the material after sintering. From a production and stacking point of view the corrugated plates thus have quite the advantage.

The heat transfer and pressure drop characteristics in the regime of magnetic refrigeration remain to be investigated thoroughly (initial investigations were conducted in paper A.3.7 (Engelbrecht et al., 2010b)). This is thus work to be done both modeling wise and experimentally. No reports in literature that consider the demagnetizing field of such a geometry are known to the author.

8.2 Demagnetization

The effect of demagnetization on the performance of the AMR has not been mapped out yet. In Chap. 7 various static situations concerned with parallel plate regenerators of one or several magnetic materials were investigated. It was concluded that the effect may be severe and that the internal field may be significantly degraded compared to the applied field. However, the dynamical effect on the AMR and especially the influence on the resulting cooling power and temperature span has not been investigated yet. This is exciting work that should be done. Bouchard et al. (2009) did include the effect of demagnetization into their 3-dimensional AMR model, however, the results showing the effect of the demagnetization on the performance of the AMR cycle are not published. They furthermore assume a linear magnetic material, i.e. $M = \xi H$, which is certainly questionable for ferromagnets.

There is, however, a fair number of parameters to consider. The geometry of the regenerator poses a great challenge for the modeling of the demagnetizing field. In this thesis the framework for modeling a stack of plates has been developed. For other geometries, such as packed spheres, a framework like this is not available at present. The physics of the problem are, in principle, quite straightforward. It is, however, a rather involved computation that is needed and book-keeping when considering a geometry like (tens of) thousands of spheres may pose some challenge.

Apart from the actual computation of the demagnetizing field the model has to be combined with an AMR model that can then use the real internal field for the evaluation of the magnetocaloric effect. Since the effect of demagnetization is inherently of a 3-dimensional nature a question of how to represent it in a 1D or 2D numerical AMR model arises. The computational time of an AMR model is several orders of magnitude smaller than for the demagnetization model. Optimization is thus needed, but it seems that a different approach for calculating the demagnetizing field should be considered as well. Such an approach could be through Fourier-space transformations as presented in, e.g., Tandon et al. (2004) or perhaps through tabulated average demagnetization factors.

8.3 Impact of other physical effects

In the following section physical effects not considered when evaluating the AMR performance are discussed. These effects could be considered to be implemented to enhance the current level of AMR modeling and their impact on the AMR performance is certainly of great interest and relevance.

8.3.1 Hysteresis

Magnetocaloric materials with a first order structural transition at or close to the Curie temperature show hysteresis effects to some degree, which is highly material dependent. This is not an attempt to account in detail for the effect of hysteresis, however, some of the key characteristics are discussed. Associated with hysteresis are irreversible losses. The magnitude of these may vary greatly from material to material also depending on the operating frequency of the material.

Certain approaches to model the hysteresis in magnetocaloric system are published already. Papers like Sasso et al. (2006); Basso et al. (2005a,b, 2006b,a) provide the theoretical basis for evaluation of the influence of hysteresis on magnetic refrigeration cycles. There are, however, no published AMR models where the hysteresis is incorporated such that the direct influence on the AMR performance may be found. This is a task that may prove difficult since the use of proper state functions for finding the MCE are challenging to obtain. It is, though, highly relevant to do AMR modeling including the effect of hysteresis since many good candidate magnetocaloric materials have first order transitions and their actual performance in an AMR is still not mapped out.

8.3.2 Specific heat and asymmetrical flow periods

It is well known that the specific heat of a magnetocaloric material may change its peak temperature significantly as a function of applied field. This effect is quite pronounced in materials with a first order transition where the change in peak temperature may be several degrees per tesla (Palacios et al., 2010; Tocado et al., 2009). Furthermore, when considering these first order materials the peak value of the specific heat is usually quite large compared to the base level as opposed to the specific heat of a material with a second order transition.

In operation, the AMR has a temperature profile across it and the magnetic field changes periodically. The specific heat may thus vary significantly across the regenerator (spatially) as well as temporally during the AMR cycle. This may certainly result in asymmetry between the hot and cold blow periods. During the hot blow the field is usually higher and during the cold blow it is usually lower. The specific heat may thus be significantly different in these two periods, which results in effective utilizations of the two periods that may differ remarkably. This is an effect that has not yet been published to the knowledge of the author of this thesis. It is, however, an important effect that is somewhat inherent to the AMR system.

8.3.3 Channeling effects

As mentioned earlier the construction of the regenerator matrix may be troublesome. When precision is wanted and the features are about 0.1 mm or less it becomes relevant to consider the impact on the performance from non-homogeneity in the construction. For instance when considering a parallel-plate regenerator the spacing between the plates will probably always vary somewhat. The plates may always be slightly un-even and stacking plates is no easy task. This results in different channel spacings and that means that the fluid flow will prefer paths with less pressure drop, i.e. the largest channels. This results in several effects that are difficult to control and completely map out. However, at the ends of the regenerator the fluid

will always mix somehow. Since the fluid flow is more or less out of phase the outlet temperatures may vary significantly resulting in a non-ideal situation.

Another and probably equally important effect is the transverse thermal gradients that must arise when the flow is out of phase between the respective channels. One plate may see its upper channel as having a completely different temperature than its lower channel and so forth, which certainly will result in unwanted entropy generation and degradation of the temperature gradient along the flow direction. Initial investigations of these effects have been commenced at Risø DTU and so far one publication deals with this problem (Jensen et al., 2010). It is a problem that is essential to solve (if possible) should parallel plate regenerators be able to produce the theoretical performance that somewhat ideal models (like the one presented in this thesis) predict.

Chapter 9

Conclusion

The work presented in this thesis covered a range of aspects of the active magnetic regenerator. The emphasis was on the numerical modeling of the AMR using a 2-dimensional model. The basic thermodynamics of the MCE were briefly discussed, a range of experimental magnetocaloric data were presented and a constraint on the adiabatic temperature change was derived from first principles. In order to investigate the internal field of the geometries investigated here a demagnetization model was developed that enables the calculations of \mathbf{H} given the dimension of a rectangular prism, the spacing between such prisms, the number of prisms, relevant magnetization data and a temperature profile. In the following the main conclusions from these topics are provided.

Constraint on the adiabatic temperature change

In Chapter 2 the magnetocaloric effect was presented and magnetocaloric properties of various materials were presented. This may be considered background material that enables a framework for this thesis to work within. What is more relevant to consider in terms of new findings is the constraint on the derivative of the adiabatic temperature, which states for second order materials that

$$\frac{d\Delta T_{\text{ad}}}{dT} > -1 \quad T \quad (9.1)$$

and for first order materials

$$\frac{d\Delta T_{\text{ad}}}{dT} \geq -1 \quad T \quad (9.2)$$

for a fixed change in field from H_i to H_f .

This constraint provides some information of the behavior of the magnetocaloric effect. Whether this result will provide further insights into the MCE in conjunction with other fundamental results is at this time impossible to answer.

Parameter study conclusions

Using the AMR model investigations of the influence of the operating and geometric parameters of the AMR were conducted using a single magnetocaloric material. The fluid channel and solid plate thicknesses were varied as were the fluid stroke length and AMR cycle timings. This resulted in a variation of the porosity, utilization and

number of transfer units. The cooling power versus temperature span was mapped as a function of these parameters and certain intervals of the parameters were suggested as yielding the best performance of the AMR.

The utilization should be on the interval 0.2 to 1.0, since values above this result in too small temperature spans to be of any interest. It was found that a small porosity is generally better. However, just having a small porosity is not equivalent to a good performance. Considering the number of transfer units it was found that the NTU should at least be above 20 for acceptable performance. On the other hand, the behavior of the performance is similar to being asymptotic when the NTU is greater than about 50. It may thus be concluded that too large values of the NTU do not add any value to the regenerator performance.

Grading the AMR with several magnetocaloric materials

In Chapter 5 grading the regenerator with several materials with individual Curie temperatures was investigated. The cases studied there included gadolinium-like regenerators with the magnetocaloric properties modeled using the mean field model. This approach allows for studies of the general behavior of the AMR as a function of the number of materials and their individual spacing. The results show that graded regenerators generally perform better than single-material regenerators, however, when too many materials are appended to the regenerator some regions of temperature spans make the AMR be too far from the ideal operating conditions thus actually lowering the performance. It is therefore concluded that it is quite important to specify the operating conditions under which the device will be operating. It is also noted that a potential concern is the inadequacy of a graded AMR to perform sufficiently if the ambient is too far from the intended and/or the cooling load required is too big such that the temperature span is forced down to a region where the graded AMR is performing significantly worse than had it been a single material regenerator.

When considering the potentially varying operating conditions it is also worth considering that an AMR device is tuneable as per its construction in terms of the utilization and operating frequency. In fact, when the material needing refrigeration is at the wanted temperature span the operating frequency could be lowered to save power and just maintain the current span. On the other hand, when the material is far from the wanted temperature the AMR could be accelerated in terms of the frequency and perhaps also boosting the utilization. What is, on the other hand, impossible to imagine is the dynamic changing of the regenerator matrix. First, there are considerable engineering challenges with this concept. Secondly, the “new” regenerator would have to have the temperature span of the previous one when installed for operation. These two reasons seem sufficient for not even considering this possibility.

The LCSM was also considered in terms of its applicability as a gradable material in an AMR. The performance is generally significantly lower for this material than for Gd-based regenerators, however, it was shown that the performance can be significantly enhanced when grading the regenerator with LCSM. The LCSM has a magnetocaloric effect that is somewhat lower than that of Gd (about a factor of four in terms of the peak adiabatic temperature change). Furthermore, the thermal conductivity is roughly ten times lower of the LCSM than of Gd. The performance

advantage of Gd is thus fairly clear.

Modeling an experimental AMR device

The modeling of the Risø DTU experimental test device was presented in Chapter 6. Comparisons were made to previously published experimental (and modeling) results and it was concluded that when accounting for the thermal parasitic losses the AMR model predictions are closer to the experimental results. A similar conclusion was found when experimentally obtained magnetocaloric data were used compared to using the mean field model.

These two conclusions are quite straightforward, though AMR modeling is still not at a level where really precise predictions can be made of the experimental results. Obviously, it cannot be expected that any transient numerical model should predict exactly what the experiments show. Many factors are impossible to account for or at least to quantify satisfyingly. The actual internal field in the regenerator has not been taken into consideration yet, for example, and numerical AMR models exploit several postulated symmetries in order to work on a computational domain that yields reasonable computation times. Also, as mentioned earlier, the homogeneity of the regenerator (both in the transversal and axial directions) is questionable and illuminating the effect of such inhomogeneities may be very important. In this regard it is not a question about predicting the exact AMR performance but rather obtaining an understanding of the behavior as the regenerator is inhomogeneous in various ways.

The experimental testing of passive regenerators resembling AMRs but lacking the magnetic part (either running an AMR without the magnet or choosing a completely different material) is a way of probing various effects that may be partially hidden when the magnetic field is present. This was done in paper A.3.7 (Engelbrecht et al., 2010b) where the regenerator material considered was aluminum. This is a way of isolating the various effects and to study the trends of the regenerative response to similar Reynolds numbers and regenerator geometries.

Development of a demagnetization model

The development of a model that enables the calculation of the internal field of a stack of rectangular prisms was presented in Chap. 7. The results show that the internal field may vary significantly compared to the applied field under different circumstances. The internal field is a function of both temperature and the geometry of the regenerator. Also, the grading, if present, has a significant impact on the topology of the internal field. The regenerator will, in this case, be separated into several regions which are either para- or ferromagnetic and this results in discontinuities in the field (dependent on the boundary conditions) or large variations of the local field. These are all findings that are most important for magnetic refrigeration since the generation of the magnetic field may be considered as the most expensive part of the system (Rowe, 2009). If a system is designed such that the applied field is utilized relatively badly due to the demagnetization a significant amount of the efficiency per cost may not be gained.

So far it has not been possible to investigate the direct influence of the demagnetizing field on the performance of the AMR. Coupling the AMR model and the

demagnetization model is difficult since the demagnetization model takes, perhaps, several minutes or maybe an hour to iteratively find the internal field given a certain temperature distribution and applied field. This is several orders of magnitude more than the AMR model needs per cycle and since the internal field is, in principle, needed at every timestep in the AMR model it is simply not possible to combine the two models directly.

A few techniques could be applied, though, in order to decrease the amount of computational time. One is to apply the demagnetization model at only, perhaps, every 10th timestep or whatever may be found to be sufficient. In the AMR model the timestep is usually about 1 ms and the change in internal field may not be significant on this scale. However, the specific setup should be investigated in detail for this concept to work.

Another way one could imagine this to be implemented is by deriving average, or representative, demagnetization factors. Using the demagnetization model one could possibly extract a single scalar, N , that adequately describes the overall demagnetization of the current situation. In this way one could, by using the applied field, temperature and a magnetization look-up table, find $H(\mathbf{r})$ in the regenerator by applying this expression

$$H(\mathbf{r}) = H_{\text{appl}} - NM(\mathbf{r}). \quad (9.3)$$

It is, at this time, not possible to conclude whether this approach could work. It would require a dataset of N as a function of the geometry, orientation of applied field and a clever representation of the temperature distribution.

Outlook and final remarks

The work presented here provides a basis for understanding some of the governing physics of the AMR and tools for detailed evaluation of specific properties. Obviously, many things could (and should!) be done as an extension of this work and as a completely new way of approaching magnetic refrigeration. Examples are

- the further development of the research into inhomogeneities of the regenerator structure
- combining the demagnetization model and the AMR model
- evaluating various regenerator geometries such as corrugated plates, needle-shaped pins etc.
- improve the magnetocaloric data sets
- further mining of the vast parameter space of graded regenerators such as asymmetrical distribution of the regenerator materials, sensitivity to operating conditions etc.
- consider the impact of physical effects such as hysteresis, channeling etc.

It is finally noted that from a commercial point of view magnetic refrigeration is not viable yet. A range of improvements are needed, however, this could be argued to be fairly obvious; if it were easy then it would probably have been done already.

It is the belief of the author that if the regenerator performance may be enhanced to a level where the operation frequency is at least 10 Hz, using about 100 grams of active magnetic material and a temperature span of 30-40 K, then realization of magnetic refrigeration will certainly be within reach (using permanent magnet magnetic field sources). The amount of material and the temperature span noted are not grasped out of the clear blue sky; the best performing devices currently operating are reaching similar values. The operating frequency, however, is still only wishful thinking to the knowledge of the author. It is crucial that the regenerator efficiency becomes better – both in terms of heat transfer properties and pressure drop. Other considerations, such as how to grade the regenerator with different magnetocaloric materials, optimize the geometry / magnetic field with respect to the issue of demagnetization and general engineering challenges are, of course, also present. However, the tools for solving these problems are fairly developed and they may therefore be considered to be somewhat more under control than the creation of the proper regenerator geometry currently is.

Appendix A

Papers

A.1 Papers published in peer-reviewed international scientific journals

A.1.1 The effect of demagnetization on the magnetocaloric properties of gadolinium; published in Journal of Applied Physics

The effect of demagnetization on the magnetocaloric properties of gadolinium

C. R. H. Bahl^{1,a)} and K. K. Nielsen^{1,2}

¹Fuel Cells and Solid State Chemistry Division, Risø National Laboratory for Sustainable Energy, Technical University of Denmark, DK-4000 Roskilde, Denmark

²DTU Mechanical Engineering, Building 402, Technical University of Denmark, DK-2800 Lyngby, Denmark

(Received 4 September 2008; accepted 18 November 2008; published online 9 January 2009)

Gadolinium displays a strong magnetocaloric effect at temperatures close to room temperature making it useful in the field of room temperature magnetic refrigeration. We discuss the importance of including the effects of the demagnetization field when considering the magnetocaloric properties of gadolinium. The adiabatic temperature change ΔT_{ad} of gadolinium sheets upon application of a magnetic field has been measured at a range of applied magnetic fields and sample orientations. A significant dependence of ΔT_{ad} on the sample orientation is observed. This can be accounted for by the demagnetization factor. Also, the temperature dependence of ΔT_{ad} has been measured experimentally and modeled by mean field theory. Corrections to mean field theory modeling due to the demagnetization field are proposed and discussed. © 2009 American Institute of Physics.

[DOI: 10.1063/1.3056220]

I. INTRODUCTION

Gadolinium has been the benchmark magnetocaloric material for room temperature magnetic refrigeration since the pioneering work of Brown¹ in 1976. Gadolinium is readily available and has a relatively high magnetocaloric effect and a Curie temperature around room temperature. However, gadolinium easily corrodes and is rather expensive. Recently, other materials displaying a magnetocaloric effect similar in magnitude have been demonstrated.² Many of these allow for a tuning of the Curie temperature to a desired value by chemical doping. Although the implementation of gadolinium in commercial magnetic refrigeration devices is not expected, it remains a useful material for testing magnetic refrigeration devices due to the relatively large magnetocaloric effect close to room temperature.

A number of numerical models have been developed to predict and optimize the output of magnetic refrigeration devices. These models are in general configured to calculate the performance using gadolinium as the magnetocaloric material, relying either on mean field theory (MFT) calculations^{3,4} or experimental measurements of the gadolinium properties^{5,6} generally from extremely pure samples. In the following the difference between results obtained from such pure samples or MFT will be compared to those obtained from commercially available gadolinium, which is generally used in actual magnetic refrigeration devices. For a review of such devices, see Ref. 7.

The effect of demagnetization due to the morphology of the gadolinium samples has not previously been reported. This paper presents a study of the adiabatic temperature change ΔT_{ad} measured by a direct method on commercially obtained gadolinium sheets. The importance of considering the demagnetization field when studying the magnetocaloric properties will be shown in the following and the manner in

which this demagnetization affects the temperature and field dependence of ΔT_{ad} is discussed. Also, it will be discussed in the following how the magnetocaloric properties of Gd published in the literature are affected by the level of impurities. Thus, when using gadolinium as a benchmark material for a magnetic refrigeration device care must be taken to ensure that similar purities of gadolinium are used and that the shape of the Gd is taken into account.

Fueled by the increasing interest in room temperature refrigeration and the widespread use of Gd for this a large number of papers have been published on the magnetocaloric properties of Gd. A seminal and broadly quoted work is that of Dan'kov *et al.*⁸ in which a wide range of measurements on a number of samples is presented. A value of $\Delta T_{\text{ad}}=3.8$ K was measured at the Curie temperature T_C in an applied field of 1 T from an extremely pure (99.90 at. %/99.99 wt %) polycrystalline sample of gadolinium prepared by the Materials Preparation Center at the Ames Laboratory. This is similar to the value of 3.6 K previously reported.⁹ A significant lowering of the directly measured adiabatic temperature change was observed in less pure samples.⁸ The lowering seems to depend on the degree and more importantly on the type of impurities present in the sample. A similar lowering of the magnetocaloric effect when comparing a very pure single crystal Gd sample (made from a polycrystalline starting material of 99.85 at. %/99.98 wt %) prepared at Ames to a commercially obtained sample (99.9%) has been observed.¹⁰ Here a value of $\Delta T_{\text{ad}}=3.5$ K was measured in an applied field of 1 T and a temperature of 295 K from the single crystal and $\Delta T_{\text{ad}}=2.8$ K was measured from the commercial sample in the same conditions. Measurements of a 98.0% pure Gd sample at 293 K yielded $\Delta T_{\text{ad}}=3.5$ K, but in a field of 1.3 T.²⁵ Generally it has been shown that even small amounts of impurities can have a significant effect on the physical properties of rare earth elements and compounds.¹¹ An example of this is the change in magneto-

^{a)}Electronic mail: christian.bahl@risoe.dk.

caloric properties of the giant magnetocaloric material $\text{Gd}_5\text{Si}_2\text{Ge}_2$ when prepared from Gd from different sources.¹² Using commercial Gd from two different locations in China, the first order phase transition, characteristic of the giant magnetocaloric material and present when using pure Gd, disappeared.

MFT has previously been successfully used to model the magnetic properties of Gd.^{3,9,13–15} The model employed to find ΔT_{ad} is a combination of the Weiss mean field model for the magnetic properties, the Debye model for the lattice entropy, and the Sommerfeld model for the conduction electron entropy. The modeled profiles for the adiabatic temperature change closely resemble those measured experimentally.^{3,9,13–15} However, the absolute magnitude of ΔT_{ad} is slightly higher than that measured in purified Gd samples, as the calculated values for a 1 T applied field are around 4.0 K.^{3,9} Recently, a Monte Carlo method has been employed to predict a heat capacity in Gd that resembles the experimental data more closely than that predicted by conventional MFT.¹⁶

II. EXPERIMENTAL

Sheets of gadolinium with dimensions of $x=40$ mm, $y=25$ mm, and $z=0.9$ mm were obtained commercially from Metall Rare Earth Ltd. with a claimed purity of 99.4 wt % Gd.

The magnetic properties of the gadolinium were measured using a Lake Shore 7407 vibrating sample magnetometer. Magnetization measurements were conducted in applied fields of $\mu_0 H_{\text{appl}}=0$ T to 1.6 T at temperatures ranging from 240 to 330 K with a $2 \times 2 \times 1$ mm³ (33.8 μg) sample.

A magnetic refrigeration device consisting of a plastic cylinder with a rectangular hole has previously been described in Ref. 17. The hole has grooves into which 13 of the above mentioned sheets of gadolinium can be held at a separation of 0.8 mm between each sheet. The cylinder is held in place in the gap of a Lake Shore EM7 electromagnet with 2 in. diameter pole pieces capable of producing $\mu_0 H_{\text{appl}}=1.3$ T. By rotating the cylinder within the magnetic field the sheets may be magnetized in any direction within the yz -plane. A small groove has been cut in the center of the central plate. In this a 0.13 mm type E thermocouple (chromel constantan) is mounted with thermally conducting epoxy. The temperature increase in the gadolinium is measured when a magnetic field is applied. The field is ramped from zero to between 0.1 and 1.3 T at 0.08 T/s.

Four experimental series were performed. In the first and second, a single sheet of gadolinium is placed in the center of the cylinder. This is magnetized in a range of applied fields along both the y and the z directions, i.e., parallel and perpendicular to the plate. In the third and fourth, the cylinder is filled with 13 sheets and again magnetized along the y and the z directions while measuring the temperature change in the central sheet.

In a different experiment the cylinder with 13 plates is placed in a drive mechanism designed to move it in and out of the bore of a permanent magnet assembly. This permanent

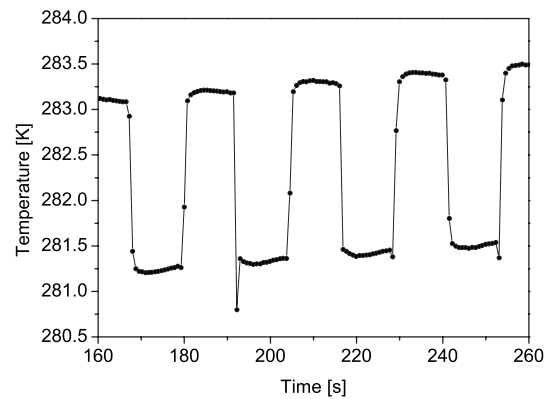


FIG. 1. Sample of the raw data measured by a thermocouple embedded in the center of the 13 Gd sheets. Application and removal of the $\mu_0 H_{\text{appl}}=1.1$ T field from the permanent magnet assembly is clearly seen to result in a change in temperature.

magnet assembly is of the Halbach-type with a 40 mm diameter and 50 mm long bore, supplying a maximum flux density of around 1.1 T.

The cylinder is precooled by dry ice and allowed to warm to room temperature while repeatedly being moved in and out of the magnet bore. The cylinder is held in and out of the magnetic field for 10 s respectively and the movement in and out of field takes approximately 1 s. The sampling frequency of the temperature measurements is roughly 1.3 Hz. A raw sample of the data measured by the thermocouple is shown in Fig. 1. The magnetocaloric temperature change is determined by averaging the measured temperature in the respective situations (in or out of field) and defining these regions with a tolerance of 0.1 K. The occasional spikes observed in the data are due to induction in the thermocouples during the movement. These do not affect the temperature measurements¹⁸ and are ignored in the calculation of ΔT_{ad} . The adiabatic temperature change is quite evident and it is also seen that the temperature of the Gd sheet does not increase significantly during each 10 s period. When the measured temperature approaches room temperature the Gd sheets are heated and allowed to cool to room temperature in order to measure at the hot side of room temperature. The gap in the temperature measurements, visible in Fig. 1, is due to the very slow approach toward room temperature both from above and below.

III. RESULTS AND DISCUSSION

A. Curie temperature

From the magnetization data the Curie temperature T_C can be determined by the inverse susceptibility method of the mean field Curie–Weiss law. Calculating the inverse susceptibility at each temperature and extrapolating the linear part gives $T_C=297(2)$ K, see Fig. 2(a). Alternatively the Curie temperature may be found by fitting the susceptibility to an expression with a critical exponent $\chi \propto (T-T_C)^{-\gamma}$. This results in a Curie temperature of $T_C=295.0(2)$ K, see Fig. 2(b). The critical exponent is found to be $\gamma=1.19(2)$ in correspondence to the published values of around 1.2.¹⁹ In both approaches the data have been corrected for the demagneti-

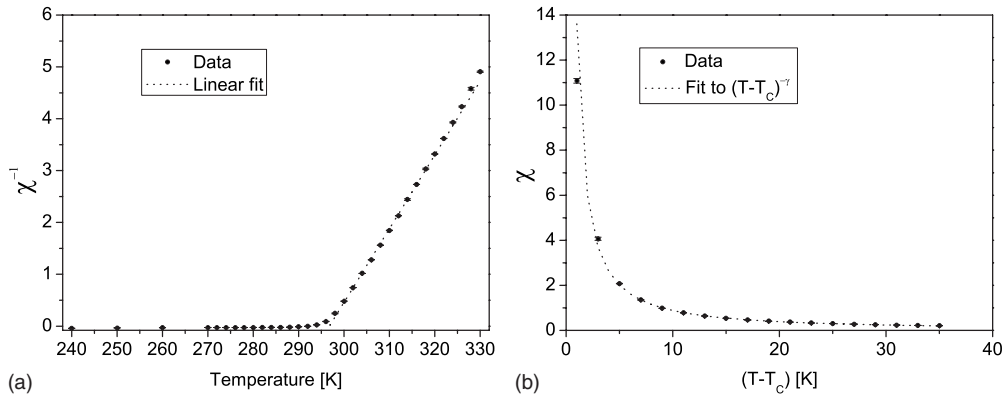


FIG. 2. Determination of the Curie temperature T_C (a) by the mean field inverse susceptibility method and (b) by the critical exponent method.

zation field as will be discussed below. It has previously been found that the ordering temperature of Gd is strongly dependent on both the experimental technique employed and the purity of the sample.^{8,20} Values in the range 290–297 K have been published for low magnetic fields.

B. Field dependence

The measured adiabatic temperature change in the gadolinium as a function of applied field is shown in Fig. 3. As the Gd sheets are held in the plastic cylinder and not isolated in a vacuum chamber the temperature change is not truly adiabatic. However, as the temperature change in the sheets is isotropic and the thermal conductivity of the surroundings is relatively low, heat loss to the surroundings will not be significant on a short time scale¹⁸ and the term adiabatic temperature change will be used in the following. Each data point in Fig. 3 was obtained from an initial temperature of 294 K. It is observed that magnetizing the sheets along the z direction results in a significantly lower temperature change than when magnetizing along the y direction. This is, as expected, due to an increased demagnetization factor N_D^{sheet} of the sheets when the magnetization direction is normal to these, as compared to when it is parallel to the sheets.

The average demagnetization factor of a single sheet can be approximated by a relatively simple analytical expression.²¹ However for a stack of sheets the calculations

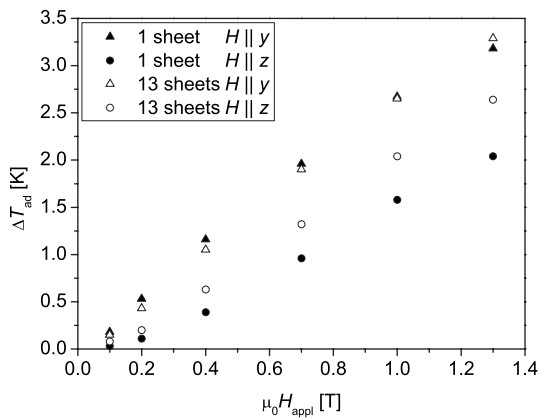


FIG. 3. The temperature change in the Gd sheets measured in the electromagnet at the applied field H_{appl} at an initial temperature of 294 K.

become more involved. We have calculated the average demagnetization factor in a single plate and in a stack of 13 plates by a three-dimensional finite element method using the software package COMSOL MULTIPHYSICS.²²

The calculated average demagnetization factors of the sheets along with those obtained from the analytical expression for a single sheet are given in Table I. Good correspondence is observed between the results of the analytical expression and the numerical calculations.

The magnetization measurements were performed with the $2 \times 2 \times 1$ mm³ sample oriented such that the field is parallel to one of the 2 mm directions. This results in an average demagnetization factor of $N_D^{sample} = 0.25$ by both the analytical expression and numerical calculations. Taking this into account the average internal field H_{int} of the sample can be calculated as

$$H_{int} = H_{appl} - N_D^{sample} M. \tag{1}$$

This gives the pure dependence of the magnetization on the internal magnetic field independent of the size or shape of the sample. Now, the relation between the actual average internal field of the gadolinium sheets H_{int} , the equivalent applied field of the sheets in the various orientations \tilde{H}_{appl} , and the magnetization of the sheets may be written as

$$\tilde{H}_{appl} = H_{int} + N_D^{sheet} M. \tag{2}$$

Figure 4 shows the temperature change data from Fig. 3 plotted versus the internal field in the sheets. The similarity of the data from each of the four experiments when plotted versus H_{int} indicates the validity of the demagnetization factor approach. The effect of a change in the demagnetization factor when the sheets are stacked compared to that from a single sheet is clearly seen when comparing Figs. 3 and 4.

TABLE I. Demagnetization factors N_D^{sheet} of the Gd sheets calculated by numerical simulations using COMSOL and the analytical expression given in Ref. 21.

Number of sheets	Field orientation	COMSOL N_D^{sheet}	Analytical N_D^{sheet}
1	$H \parallel y$	0.05	0.05
1	$H \parallel z$	0.93	0.92
13	$H \parallel y$	0.16	...
13	$H \parallel z$	0.63	...

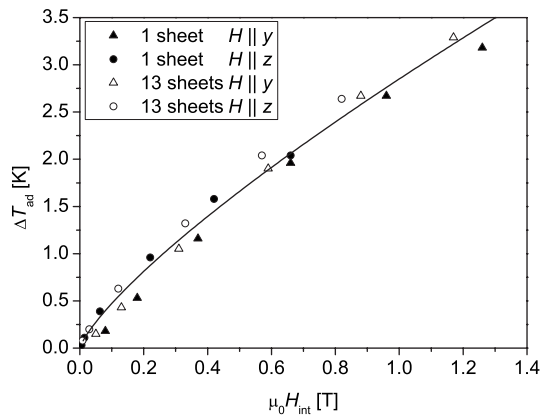


FIG. 4. The temperature change in the Gd sheets vs the internal magnetic field H_{int} at an initial temperature of 294 K. The data have been corrected for the demagnetization field using magnetization data measured from the same Gd. The solid line is a fit to the data as described above.

Thus, when using Gd in any magnetocaloric application it is important to take into account the demagnetization factor of the actual configuration of the Gd.

In Fig. 4 the data are observed to pass through the origin as would be expected. MFT calculations predict that near the Curie temperature T_C , the adiabatic temperature change ΔT_{ad} in Gd upon magnetization or demagnetization is proportional to $H^{2/3}$ (Ref. 23). Compiling a range of experimental data from the literature Pecharsky and Gschneidner² find the relation $\Delta T_{\text{ad}}[\text{K}] = 3.675(\mu_0 H[\text{T}])^{0.7}$ in good accordance with the MFT result.⁹ These data were mainly collected from very pure samples and high field experiments.

Fitting the same type of expression to the data presented in Fig. 4 gives the relation $\Delta T_{\text{ad}}[\text{K}] = 2.85(5)(\mu_0 H[\text{T}])^{0.78(3)}$, as indicated by the solid line in Fig. 4. Thus the exponent is close to the ones found both by MFT and in Ref. 2 while the prefactor is somewhat less.

C. Temperature dependence

The magnetocaloric temperature change in the gadolinium sheets was measured as a function of initial temperature in the applied field of 1.1 T supplied by the permanent magnet assembly. The temperature increase and decrease in response to the movement of the gadolinium sheets into and out of the magnetic field region are shown in Fig. 5; for convenience the sign of the temperature decrease has been changed, such that both data sets appear positive.

The data show a peak in the temperature change in the data recorded during magnetization at about 293 K, which is slightly below the Curie temperature determined above. A difference in the transition temperature depending on the method of measurement has previously been reported in Refs. 8 and 24. The peak in the data recorded during field removal is at a higher temperature, 296 K. This is expected due to the reversibility of the magnetocaloric effect, which requires the distance between the peaks to be the same as the peak adiabatic temperature change.

As the magnetization of the Gd sheets decreases with an increase in temperature, the internal magnetic field of the sheets at a fixed applied field increases as the temperature is

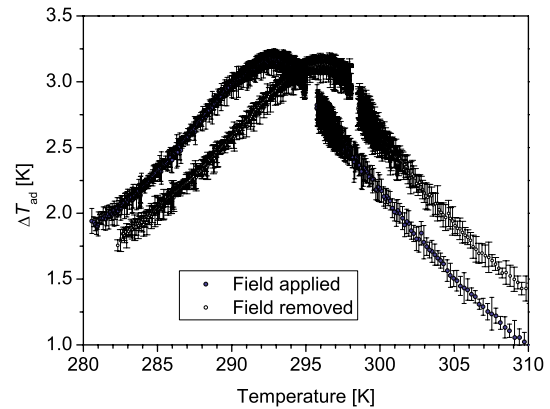


FIG. 5. (Color online) The temperature change in Gd upon application (filled symbols) and removal (open symbols) of the field from the permanent magnet assembly yielding $\mu_0 H_{\text{appl}} = 1.1$ T. Thirteen sheets were used in the orientation with the field in the plane of the sheets, $H \parallel y$. The error bars indicate the standard deviations of the data used to calculate ΔT_{ad} , see Fig. 1.

increased, see Eq. (2). Thus ΔT_{ad} cannot be plotted at a fixed internal field. The temperature dependence of the internal field of Gd sheets at an applied field of $\mu_0 H_{\text{int}} = 1.1$ T is shown in Fig. 6 for a number of different demagnetization factors. Even a modest value of the demagnetization constant leads to a significant temperature dependence of the internal field.

A temperature increase of around 3.1 K is observed upon magnetization at 294 K. This is larger than around 2.8 K increase that may be interpolated from the data in Fig. 3. This difference is presumably due to a difference in the ramping rate of the magnetic field. The slower field ramping of the electromagnet will allow the Gd to lose heat before the ramp is finished. This is not the case for the permanent magnet device, as the field is ramped fast compared to the rate of heat loss. An equivalent difference in the measured magnetocaloric effect due to the ramping rate of the magnetic field is reported in Ref. 10. Here, changing the ramp rate of the magnet from 0.05 to 0.5 T/s also resulted in an increase in the measured temperature change of about 0.3 K.

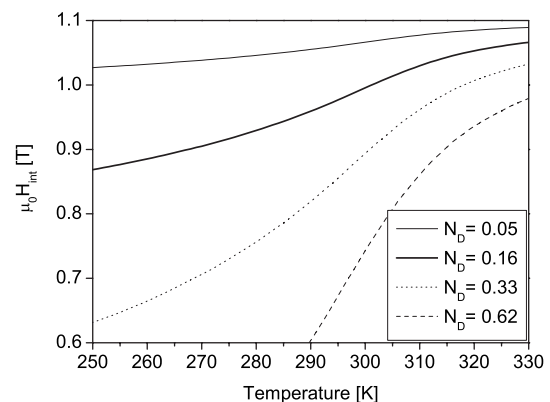


FIG. 6. The temperature dependence of the internal field of the Gd sheets in an applied field of $\mu_0 H_{\text{appl}} = 1.1$ T determined from the magnetization data. The demagnetization factor $N_D = 0.16$ (the broad solid line) is equivalent to the 13 sheet situations with the field in the plane of the sheets, $H \parallel y$.

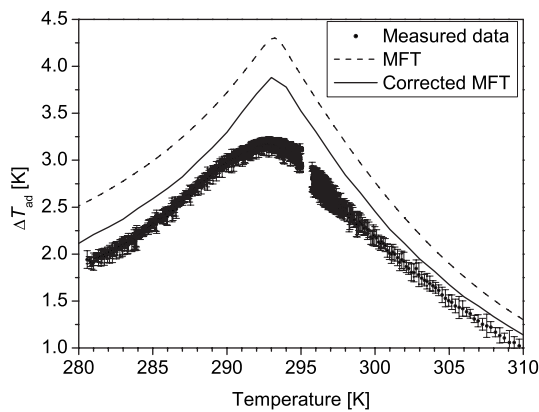


FIG. 7. The temperature change in Gd upon application of the field from Fig. 5 compared to the equivalent MFT results using $\mu_0 H = 1.1$ T as the input (dashed line) and the corrected MFT results, where the internal field, calculated by the demagnetization, is used at each temperature to calculate (solid line).

The adiabatic temperature change in Gd has been calculated by the MFT, as detailed in Ref. 3. The results of this calculation performed in an applied field of 1.1 T are shown in Fig. 7 by a dashed line. However, the input to MFT is the internal magnetic field. To correct for this the MFT value of ΔT_{ad} has been calculated at each temperature using the internal magnetic field given in Fig. 6, resulting in the solid line in Fig. 7. For clarity only the data associated with the application of the field are shown. It is seen that the corrected MFT approach yields a temperature dependence of ΔT_{ad} that closely resembles the experimentally measured one. The experimental data have a less pronounced peak around T_C and are generally below the corrected MFT data. A 10% reduction in the corrected MFT data set results in a profile that, except close to the peak, closely resembles the experimentally measured one. This reduction in the experimental data may be explained by impurities in the commercial grade Gd used for the experiments as discussed above.

IV. SUMMARY AND CONCLUSION

The dependence of the measured magnetocaloric effect on the demagnetization factor of a number of thin sheets of gadolinium has been studied. The demagnetization factor was varied by changing the orientation and number of sheets used in the experiments. The average internal field in the Gd sheets is calculated for each of the experiments. When correcting for the effect of demagnetization in this way, consistent values for the adiabatic temperature change ΔT_{ad} are found for each of the experiments.

The measured peak value of ΔT_{ad} in the present commercial grade Gd is somewhat below that reported for purified samples and that predicted by conventional MFT. Some of this lowering may be explained by demagnetization and indeed a corrected MFT calculation has been shown to model the data more closely. However, the major contribution to the lowering seems to be due to impurities in the commercial Gd, as has previously been reported in the literature.

ACKNOWLEDGMENTS

The authors would like to thank Dr. A. Smith and Dr. N. Pryds for fruitful discussions. Also, the authors would like to acknowledge the support of the Programme Commission on Energy and Environment (EnMi) (Contract No. 2104-06-0032), which is part of the Danish Council for Strategic Research.

- ¹G. V. Brown, *J. Alloys Compd.* **47**, 3673 (1976).
- ²V. K. Pecharsky and K. A. Gschneidner, Jr., *Int. J. Refrig.* **29**, 1239 (2006).
- ³T. F. Petersen, N. Pryds, A. Smith, J. Hattel, H. Schmidt, and H.-J. H. Knudsen, *Int. J. Refrig.* **31**, 432 (2008).
- ⁴P. Li, M. Gong, G. Yao, and J. Wu, *Int. J. Refrig.* **29**, 1259 (2006).
- ⁵J. Dikeos, A. Rowe, and A. Tura, *AIP Conf. Proc.* **823**, 993 (2006).
- ⁶A. Sarlah, A. Kitanovski, A. Poredos, P. W. Egolf, O. Sari, F. Gendre, and Ch. Besson, *Int. J. Refrig.* **29**, 1332 (2006).
- ⁷K. A. Gschneidner, Jr. and V. K. Pecharsky, *Int. J. Refrig.* **31**, 945 (2008).
- ⁸S. Y. Dan'kov, A. M. Tishin, V. K. Pecharsky, and K. A. Gschneidner, Jr., *Phys. Rev. B* **57**, 3478 (1998).
- ⁹S. M. Benford and G. V. Brown, *J. Appl. Phys.* **52**, 2110 (1981).
- ¹⁰Y. I. Spichkin, A. V. Derkach, A. M. Tishin, M. D. Kuz'min, A. S. Chernyshov, K. A. Gschneidner, Jr., and V. K. Pecharsky, *J. Magn. Mater.* **316**, e555 (2007).
- ¹¹K. A. Gschneidner, Jr., *J. Alloys Compd.* **193**, 1 (1993).
- ¹²W. Wu and D. W. Lu, First IIF-IIR International Conference on Magnetic Refrigeration at Room Temperature, Montreux, Switzerland, 2005, p. 127.
- ¹³T. Hashimoto, *Cryogenics* **21**, 647 (1981).
- ¹⁴A. M. Tishin, *Cryogenics* **30**, 127 (1990).
- ¹⁵G. J. Liu, J. R. Sun, J. Z. Wang, T. Y. Zhao, and B. G. Shen, *J. Phys.: Condens. Matter* **19**, 466215 (2007).
- ¹⁶E. P. Nobrega, N. A. de Oliveira, P. J. von Ranke, and A. Troper, *J. Magn. Mater.* **320**, e147 (2008).
- ¹⁷C. R. H. Bahl, T. Petersen, N. Pryds, and A. Smith, *Rev. Sci. Instrum.* **79**, 093906 (2008).
- ¹⁸B. K. Ponomarev, *Instrum. Exp. Tech.* **26**, 659 (1983).
- ¹⁹P. Hargraves, R. A. Dunlap, D. J. W. Geldart, and S. P. Ritcey, *Phys. Rev. B* **38**, 2862 (1988).
- ²⁰L. B. Robinson and F. Milstein, *Solid State Commun.* **13**, 97 (1973).
- ²¹A. Aharoni, *J. Appl. Phys.* **83**, 3432 (1998).
- ²²<http://www.comsol.com>.
- ²³H. Oesterreicher and F. T. Parker, *J. Appl. Phys.* **55**, 4334 (1984).
- ²⁴A. M. Tishin, K. A. Gschneidner, Jr., and V. K. Pecharsky, *Phys. Rev. B* **59**, 503 (1999).
- ²⁵J. H. Huang, J. F. Qiu, J. R. Liu, P. Y. Jin, L. Z. Xu, and J. X. Zhang, First IIF-IIR International Conference on Magnetic Refrigeration at Room Temperature, Montreux, Switzerland, 2005, p. 179.

A.1 Papers published in peer-reviewed international scientific journals **29**

A.1.2 Constraints on the adiabatic temperature change in magnetocaloric materials; published in Physical Review B

Constraints on the adiabatic temperature change in magnetocaloric materials

K. K. Nielsen*

Department of Mechanical Engineering, Technical University of Denmark, Building 425, Niels Koppels Alle, DK-2800 Kongens Lyngby, Denmark

C. R. H. Bahl and A. Smith

Fuel Cells and Solid State Chemistry Division, Risø National Laboratory for Sustainable Energy, Technical University of Denmark, Frederiksborgvej 399, DK-4000 Roskilde, Denmark

(Received 8 July 2009; revised manuscript received 14 December 2009; published 17 February 2010)

The thermodynamics of the magnetocaloric effect implies constraints on the allowed variation in the adiabatic temperature change for a magnetocaloric material. An inequality for the derivative of the adiabatic temperature change with respect to temperature is derived for both first- and second-order materials. For materials with a continuous adiabatic temperature change as a function of temperature, this inequality is shown to hold for all temperatures. However, discontinuous materials may violate the inequality. We compare our results with measured results in the literature and discuss the implications of the result. Similar inequalities hold for barocaloric and electrocaloric materials.

DOI: [10.1103/PhysRevB.81.054423](https://doi.org/10.1103/PhysRevB.81.054423)

PACS number(s): 75.30.Sg, 77.70.+a

I. INTRODUCTION

The magnetocaloric effect is due to the coupling between the magnetic and the lattice degrees of freedom in a solid. That this coupling can induce a field-dependent temperature change in a magnetic sample placed in an external magnetic field may be heuristically understood by an entropy argument.¹ The total entropy of a magnetic solid can often to a good approximation be divided into contributions arising from the lattice degrees of freedom (i.e., from the phonons) and the magnetic degrees of freedom (the spin system). If there are extended electron states occupied, the entropy contribution of these must also be added. This division of the entropy is the basis for the following argument: when a magnetic material is placed in an external field H , the magnetic moments tend to align with the external field, thus decreasing the entropy associated with the magnetic degrees of freedom. Under adiabatic conditions the total entropy is constant, and the decrease in the magnetic part of entropy must be accompanied by an increase in the part of the entropy associated with the lattice degrees of freedom (as long as the electronic entropy can be assumed unchanged). This increase can be observed as a temperature increase in the material. However, it should be noted that in special cases, e.g., where competing phase transitions interact or if one of the phases is ferrimagnetic or antiferromagnetic, the temperature may actually decrease.^{2,3} One way for this to happen is when the change in entropy is due to the entropy difference between different electronic structures in phases separated by a first-order phase transition.⁴

In this way, a magnetocaloric material is characterized thermodynamically by two fundamental materials properties, the isothermal entropy change when a field H is applied, $\Delta S(T, H)$ (which is usually negative), and the adiabatic temperature change upon magnetization, $\Delta T_{\text{mag}}(T, H)$ (which is usually positive). We note in passing that if the starting field is not zero but H_0 , the corresponding entropy and temperature change is $\Delta S(T; H, H_0) = \Delta S(T, H) - \Delta S(T, H_0)$ and $\Delta T_{\text{mag}}(T; H, H_0) = \Delta T_{\text{mag}}(T, H) - \Delta T_{\text{mag}}(T, H_0)$. These quanti-

ties will be a function of both H and H_0 and not just of their difference $H - H_0$.⁵

It is the purpose of this paper to point out that the thermodynamics of the magnetocaloric effect constrains the possible variation in ΔT_{mag} with temperature. Since the argument is independent of the microscopic origin of the temperature change, the analysis is equally relevant for barocaloric or electrocaloric materials (a change in temperature with external pressure or electric field, respectively).

We start out by investigating the consequences of reversibility. Then we consider materials with first-order phase transitions which may possibly have an irreversible magnetocaloric effect, and discuss to what extent the findings are applicable to real materials. We compare our results with selected experimental results from the literature and finally discuss the implications of our analysis.

II. CONSEQUENCES OF REVERSIBILITY

Magnetocaloric materials exhibiting second-order (continuous) phase transitions have a reversible magnetocaloric effect. This amounts to the following: start out with a sample in a state with zero external field at a temperature T_0 . When the sample is magnetized adiabatically, the temperature increases to $T^* = T_0 + \Delta T_{\text{mag}}(T_0, H)$. Now, upon adiabatic demagnetization the temperature drops to $T^{**} = T^* + \Delta T_{\text{demag}}(T^*, H)$. If the process is reversible we must end in the state we started from, i.e., $T_0 = T^{**}$ or

$$T_0 + \Delta T_{\text{mag}}(T_0, H) + \Delta T_{\text{demag}}[T_0 + \Delta T_{\text{mag}}(T_0, H), H] = T_0, \quad (1)$$

that is

$$\Delta T_{\text{mag}}(T_0, H) = -\Delta T_{\text{demag}}[T_0 + \Delta T_{\text{mag}}(T_0, H), H]. \quad (2)$$

Note that ΔT_{demag} is negative (if ΔT_{mag} is positive).

In the following, all H dependence will be suppressed, and to emphasize the fact that ΔT_{mag} and ΔT_{demag} are differ-

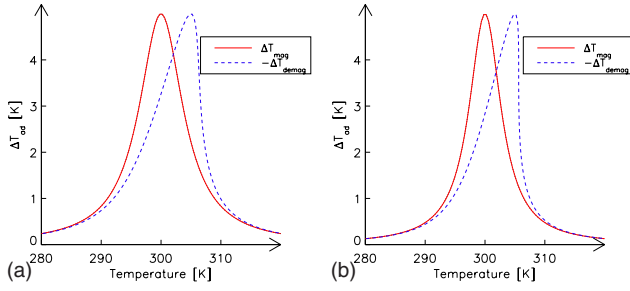


FIG. 1. (Color online) The adiabatic temperature change in a model magnetocaloric material both when magnetizing (full red line) and demagnetizing (dashed blue). (a) The slope of the ΔT_{mag} is greater than -1 for all temperatures. (b) The slope of the ΔT_{mag} curve is exactly -1 at a single temperature above T_* . This results in a demagnetization curve with a vertical tangent at the corresponding temperature.

ent functions of temperature the following notation will be introduced:

$$f(T) \equiv \Delta T_{\text{mag}}(T, H), \quad (3)$$

$$g(T) \equiv \Delta T_{\text{demag}}(T, H). \quad (4)$$

In terms of f and g , the condition of reversibility becomes

$$f(T) = -g[T + f(T)] \quad (5)$$

(where the subscript 0 on the temperature has been dropped). This equation allows the determination of g given the measurement of f (and vice versa). In Fig. 1 is shown corresponding f and g curves. It is clearly apparent that the shape and maximum point of the two curves differ. The general shape of the curves is one appropriate for pure materials (i.e., not containing grains of different composition and Curie temperature) where the adiabatic temperature change upon magnetization for a given H has a single maximum at $T = T_*$, and no other local extrema. This maximum will be close to the Curie temperature T_C but will, in general, not coincide with it;¹ indeed, it will often depend on H .

Read from right to left Eq. (5) states that a material in field at a temperature $T + f(T)$ will, when demagnetized, cool to T . A magnetized material demagnetized from a starting temperature T_s will cool to a unique temperature T_e which obeys $T_s = T_e + f(T_e)$. The uniqueness implies that $T + f(T)$ is one-to-one considered as a function of temperature. Furthermore, the magnetized material may obviously be demagnetized from any starting temperature T_s by connecting it to a heat bath at an appropriate temperature while in field; isolating it thermally; and then removing the field. This means that $T + f(T)$ must also map the entire temperature range $[0, \infty[$ onto itself. Taken together with the fact that it is one-to-one this implies that $T + f(T)$ is an invertible function. If $f(T)$ is continuous a necessary and sufficient condition for this to be the case is that $T + f(T)$ is monotonically increasing in the entire range $[0, \infty[$ (increasing, given that $f(T)$ approaches 0 for $T \rightarrow 0$ and $T \rightarrow \infty$), i.e., that the derivative is greater than zero for all T : $d[T + f(T)]/dT > 0$, or

$$\frac{d[\Delta T_{\text{mag}}(T, H)]}{dT} > -1. \quad (6)$$

This is the main result of the present paper; below we discuss how the inequality is modified for first-order materials. The same inequality will be obeyed by barocaloric materials (with ΔT being the change in temperature as the pressure is changed adiabatically from 0 to p) and electrocaloric materials (with ΔT being the change in temperature as the electric field is changed adiabatically from 0 to E), as long as the temperature change is a continuous function of T .

We note that assuming that f and g are differentiable—which is a reasonable assumption for real materials, at most excepting a finite number of temperatures—we get, using the chain rule,

$$f'(T) = -\frac{1}{1 + g'[T + f(T)]^{-1}}. \quad (7)$$

From this it is seen that if $f'(T)$ approaches -1 at a given temperature T_1 , the demagnetization curve g becomes steeper and steeper, and when $f'(T_1)$ reaches -1 the derivative of g becomes infinite at the corresponding temperature $T_1 + f(T_1)$, i.e., the curve becomes vertical at this point. This is shown on Fig. 1(b).

III. FIRST-ORDER IRREVERSIBLE MATERIALS

For magnetocaloric materials exhibiting a first-order phase transition, the magnetocaloric effect can be irreversible due to hysteretic losses.⁶ In such cases, the equality Eq. (2) is changed into an inequality,

$$\Delta T_{\text{mag}}(T_0, H) > -\Delta T_{\text{demag}}[T_0 + \Delta T_{\text{mag}}(T_0, H), H]. \quad (8)$$

It is important to note that this irreversibility is limited to a temperature interval in the vicinity of the phase transition.⁶ Outside this temperature interval, the magnetocaloric effect is still reversible and the arguments of the previous section still apply, and, in particular, the constraint Eq. (6) applies.

Inside the irreversibility region, it is possible to use the general shape of the T - S diagram for a first-order material to place limits on the variation in ΔT_{mag} .¹ Consider such a material having a first-order phase transition from a low-temperature phase to a high temperature at a temperature $T_{\text{pt},1}$ in zero field. At a field H , the transition temperature will be $T_{\text{pt},2} > T_{\text{pt},1}$. Such a material will in the vicinity of the phase transition have an T - S diagram as shown schematically in Fig. 2. For an ideal first-order transition, the entropy will be discontinuous, i.e., the entropy curves will be vertical at $T_{\text{pt},2}$ and $T_{\text{pt},1}$, respectively. We now define a temperature by the following equation:

$$S(T_m, 0) = S(T_{\text{pt},2}, H). \quad (9)$$

Above T_m , ΔT_{mag} will decrease linearly with T until $T_{\text{pt},2}$ is reached, as can be seen geometrically from the figure. This means that for $T_m < T < T_{\text{pt},2}$ we have the equality,

$$\frac{d[\Delta T_{\text{mag}}(T, H)]}{dT} = -1. \quad (10)$$

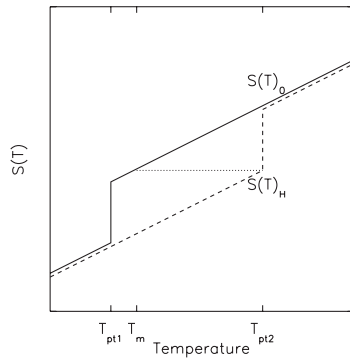


FIG. 2. Schematic T - S diagram for a first-order material (after Ref. 1). Horizontal lines between the two curves with field 0 (full line) and H (dashed line) correspond to the adiabatic temperature change ΔT_{mag} . The adiabatic temperature change has its maximum in the temperature interval between $T_{\text{pt},1}$ and T_m (defined geometrically as shown). For $T_m < T < T_{\text{pt},2}$, the adiabatic temperature change decreases as $\Delta T_{\text{mag}} = T_{\text{pt},2} - T$ due to the vertical entropy curve at $T_{\text{pt},2}$. If the transition is not strictly first order, the entropy curve will have a finite, positive slope at $T_{\text{pt},2}$ and the decrease in ΔT_{mag} will be slower.

In the interval $T_{\text{pt},1} < T < T_m$, the slope of the adiabatic temperature change is strictly greater than -1 . In this interval, the adiabatic temperature change attains its maximum value, which may be at more than one temperature. Indeed, direct measurements show plateau-like maximum adiabatic temperature changes.⁴

Thus, for first-order materials the strict inequality Eq. (6) is replaced by

$$\frac{d[\Delta T_{\text{mag}}(T, H)]}{dT} \geq -1, \quad (11)$$

valid for all T .

IV. COMPARISON TO EXPERIMENTAL RESULTS

The adiabatic temperature change may be measured experimentally in several different ways. Measuring the temperature change in a sample upon changing the field under adiabatic conditions $\Delta T_{\text{mag}} = T(H) - T(H_0)$ is termed a direct method. The temperature change may also be calculated from entropy data using the relation $\Delta T_{\text{mag}} = T^* - T_0$, where $S(T^*, H) = S(T_0, H_0)$. The entropy can be obtained either by integrating heat-capacity data or—using the Maxwell relation $\partial S / \partial H = \partial M / \partial T$ valid for materials with a second-order transition—through magnetization measurements. In the majority of the literature reporting the adiabatic temperature change in magnetocaloric materials, indirect methods are employed as standard equipment such as differential scanning calorimetry and magnetometry may be used for this. Direct measurements require more specialized, often custom built, equipment. Furthermore, even when direct measurements are used, usually only the magnetization results (ΔT_{mag}) are reported. From magnetization results it is, however, straightforward to reconstruct the demagnetization curve from Eq. (2). In Fig. 3, we show a direct measurement

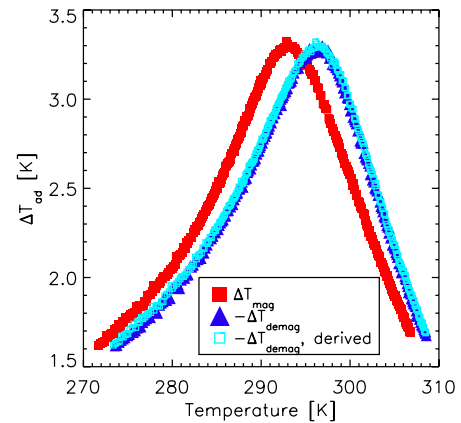


FIG. 3. (Color online) The adiabatic temperature change in gadolinium with a magnetic field change from 0 to 1.1 T. Both ΔT_{mag} and $-\Delta T_{\text{demag}}$ are shown (filled squares and triangles, respectively). The open squares show $-\Delta T_{\text{demag}}$ derived using Eq. (2) and the ΔT_{mag} data. The measurements were performed following a slightly modified procedure from Ref. 7 with the sample and magnet contained in a temperature-controlled environment.

of both ΔT_{mag} and ΔT_{demag} for a plate of 99.9% pure gadolinium (obtained from China Rare Metal Material Co.) together with the reconstructed demagnetization curve, showing the validity of this approach.

In second-order materials, good agreement is observed between ΔT_{mag} results obtained by direct and indirect methods.^{8,9} However, for first-order materials severe discrepancies between the two methods are often observed. This is partly due to the slow kinetics of the structural part of the transition.^{10,11} Fast direct measurements may result in an underestimation of ΔT_{mag} . Also, the latent heat inherent to a first-order transition makes indirect methods relying on entropy results prone to erroneous results.^{12,13}

First-order materials, in general, have a more abrupt change in ΔT_{mag} as a function of temperature, in agreement with the discussion above. When validating the derived constraint against experimental data we choose only to include directly measured temperature dependencies of ΔT_{mag} as any uncertainty in the results due to the kinetics of the transition will tend to underestimate the value of ΔT_{mag} .

A number of studies of first-order materials have shown direct measurements of ΔT_{mag} , where $\partial \Delta T_{\text{mag}} / \partial T$ is close to the constraint of -1 , e.g., MnAs,¹⁴ La(Fe_{0.89}Si_{0.11})₁₃,¹⁵ Mn₁As_{0.9}Sb_{0.1},¹⁶ and Gd₅Si₂Ge₂.¹⁷ It should be noted that the number of data points in the relevant temperature range just above T_* where the slope of the ΔT_{mag} is most negative in all of the cited studies is relatively limited, often consisting of only two to three measurements. As an example, in Fig. 4 the data from Ref. 16 is reproduced. ΔT_{mag} data from field changes of 0–2 and 0–5 T together with reconstructed values of ΔT_{demag} are shown. It is evident that the slopes of the magnetization curves are very close to -1 (corresponding to a vertical section of the demagnetization curves). However, within the experimental uncertainty it is not possible to determine whether the constraint indeed is violated. It would be interesting to resolve this temperature range in higher detail to allow a more stringent test of the constraint.

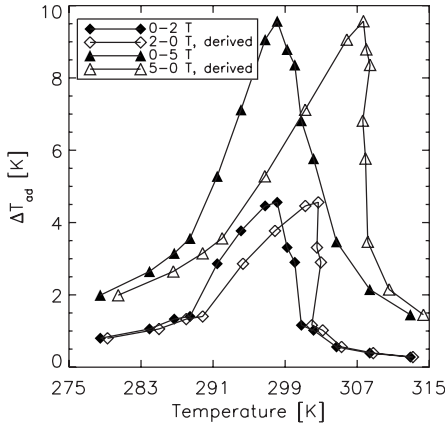


FIG. 4. The adiabatic temperature change in $\text{Mn}_{1.00}\text{As}_{0.9}\text{Sb}_{0.1}$ when magnetizing from 0 to 2 T and from 0 to 5 T. The curves denoted “derived” show the absolute value of the adiabatic temperature change when demagnetizing (changing the field from 2 to 0 T and from 5 to 0 T, respectively) calculated from the ΔT_{mag} data set using Eq. (2). The data is reproduced from Ref. 16 and obtained through private communication with Dr. H. Wada.

V. “DISCONTINUOUS” MATERIALS

As shown above, a sufficient condition for the validity of the constraint, Eq. (6) (reversible materials) or Eq. (11) (irreversible materials), is that $f(T) = \Delta T_{\text{mag}}$ should be a continuous function of temperature. In this section, we show that a discontinuous, reversible ΔT_{mag} can indeed violate the inequality. To do this we construct a model shape of a discontinuous $f(T)$ with $df/dT < -1$ in a given interval. For simplicity we choose a constant slope $\alpha < -1$,

$$f(T) = \begin{cases} \beta_1(T) & \text{for } T < T_1 \\ \Delta T_0 + \alpha(T - T_1) & \text{for } T_1 < T < T_2 \\ \beta_2(T) & \text{for } T > T_2 \end{cases} \quad (12)$$

Here T_1 , T_2 , and ΔT_0 are constants while β_1 and β_2 are arbitrary functions obeying $d\beta_1/dT > -1$ and $d\beta_2/dT > -1$, with the limiting values of $\beta_1(T_1) = \Delta T_0 + (1 + \alpha)(T_2 - T_1)$ and $\beta_2(T_2) = \Delta T_0 - (T_2 - T_1)$. These values are chosen to make $T + f(T)$ invertible and thus ensure that Eq. (5) can be fulfilled for all temperatures. In Fig. 5, we show an example of such a discontinuous f and the corresponding $g(T) = \Delta T_{\text{demag}}$.

It may be asked if such discontinuous materials actually exist. While we are aware of no direct reports in the literature of such magnetocaloric materials it is not completely inconceivable that they could exist. Consider, e.g., a material with competing structural and magnetic transitions. A low-temperature magnetic state with a Curie temperature $T_{C1} > T_0$ (or indeed a nonmagnetic state) is destabilized by a structural phase transition at $T = T_0$ in favor of a second magnetic state with a Curie temperature $T_{C2} \leq T_0$. This second phase does not manifest itself at the low-temperature side of T_0 due to the structural phase transition. At $T = T_1$, the second phase is destroyed due to another structural instability in favor of a third phase with a Curie temperature T_{C3} .

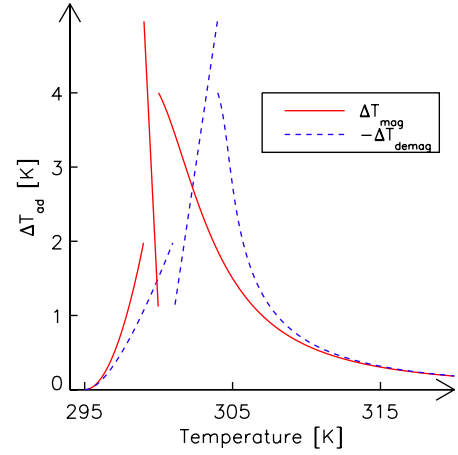


FIG. 5. (Color online) The adiabatic temperature change in a fictitious reversible magnetocaloric material with a discontinuous magnetocaloric effect. The full red line is the magnetization curve whereas the dashed blue line is the demagnetization curve. It is observed that such a material fulfills the reversibility criterion in Eq. (2) even though the slope of ΔT_{mag} is less than -1 over an entire temperature interval. Note that discontinuity is a necessity for the constraint in Eq. (6) to be invalid.

While such an interplay of phases may seem unlikely, the example at least shows that there are no obvious theoretical reasons forbidding a discontinuous variation in ΔT_{mag} with temperature.

VI. DISCUSSION AND CONCLUSION

A general constraint on the possible variation in the adiabatic temperature change at a fixed magnetic field change and as a function of temperature has been derived based on the basic thermodynamics of the magnetocaloric effect together with the assumption of continuity of the adiabatic temperature change as a function of temperature. These assumptions will apply to most real materials and as a result these materials will obey the constraint. This conclusion is in accordance with the literature of experimental data. However, better resolved data of the temperature region just above the maximum temperature change would be useful to be able to test the constraint in more detail.

The derived constraint will be of importance when optimizing graded regenerators for use in an active magnetic regenerative refrigerator device. Indeed it has been suggested that for an ideal performance the magnetocaloric effect of the regenerator should obey just this constraint.¹⁸ The results presented here show that for most materials this is a valid assumption.

ACKNOWLEDGMENTS

The authors thank the support of the Programme Commission on Energy and Environment (EnMi) (Contract No. 2104-06-0032) which is part of the Danish Council for Strategic Research.

*Also at the Fuel Cells and Solid State Chemistry Division, Risø National Laboratory for Sustainable Energy, Technical University of Denmark; kaki@risoe.dtu.dk

¹V. K. Pecharsky, K. A. Gschneidner, Jr., A. O. Pecharsky, and A. M. Tishin, *Phys. Rev. B* **64**, 144406 (2001).

²A. M. Tishin and Y. Spichkin, *The Magnetocaloric Effect and its Applications* (Institute of Physics, Bristol, 2003).

³P. J. von Ranke, N. A. de Oliveira, B. P. Alho, E. J. R. Plaza, V. S. R. de Sousa, L. Caron, and M. S. Reis, *J. Phys.: Condens. Matter* **21**, 056004 (2009).

⁴R. Burriel, L. Tocado, E. Palacios, T. Tohei, and H. Wada, *J. Magn. Magn. Mater.* **290-291**, 715 (2005).

⁵V. Franco, J. Blazquez, and A. Conde, *Appl. Phys. Lett.* **89**, 222512 (2006).

⁶K. Morrison, J. D. Moore, K. G. Sandeman, A. D. Caplin, and L. F. Cohen, *Phys. Rev. B* **79**, 134408 (2009).

⁷C. R. H. Bahl and K. K. Nielsen, *J. Appl. Phys.* **105**, 013916 (2009).

⁸K. A. Gschneidner, Jr., V. K. Pecharsky, and A. O. Tsokol, *Rep. Prog. Phys.* **68**, 1479 (2005).

⁹S. Y. Dan'kov, A. M. Tishin, V. K. Pecharsky, and K. A.

Gschneidner, Jr., *Phys. Rev. B* **57**, 3478 (1998).

¹⁰A. Giguere, M. Foldeaki, B. Ravi Gopal, R. Chahine, T. K. Bose, A. Frydman, and J. A. Barclay, *Phys. Rev. Lett.* **83**, 2262 (1999).

¹¹A. Fujita, S. Fujieda, Y. Hasegawa, and K. Fukamichi, *Phys. Rev. B* **67**, 104416 (2003).

¹²V. K. Pecharsky and K. A. Gschneidner, Jr., *J. Appl. Phys.* **86**, 565 (1999).

¹³L. Tocado, E. Palacios, and R. Burriel, *J. Appl. Phys.* **105**, 093918 (2009).

¹⁴L. Tocado, E. Palacios, and R. Burriel, *J. Therm. Anal. Calorim.* **84**, 213 (2006).

¹⁵A. Fujita and K. Fukamichi, *J. Alloys Compd.* **404-406**, 554 (2005).

¹⁶H. Wada, T. Asano, M. Ilyn, and A. Tishin, *J. Magn. Magn. Mater.* **310**, 2811 (2007).

¹⁷K. A. Gschneidner, V. K. Pecharsky, E. Bruck, H. G. M. Duijn, and E. M. Levin, *Phys. Rev. Lett.* **85**, 4190 (2000).

¹⁸J. L. Hall, C. E. Reid, I. G. Spearing, and J. A. Barclay, *Adv. Cryog. Eng.* **41**, 1653 (1996).

A.1 Papers published in peer-reviewed international scientific journals 135

**A.1.3 The demagnetizing field of a nonuniform rectangular prism;
published in Journal of Applied Physics**

The demagnetizing field of a nonuniform rectangular prism

A. Smith,¹ K. K. Nielsen,^{1,2,a)} D. V. Christensen,^{1,3} C. R. H. Bahl,¹ R. Bjørk,¹ and J. Hattel²

¹*Fuel Cells and Solid State Chemistry Division, Risø National Laboratory for Sustainable Energy, Technical University of Denmark, Frederiksborgvej 399, DK-4000 Roskilde, Denmark*

²*Department of Mechanical Engineering, Technical University of Denmark, Building 425, Niels Koppels Alle, DK-2800 Kongens Lyngby, Denmark*

³*The Niels Bohr Institute, University of Copenhagen, Blegdamsvej 17, DK-2100 Copenhagen, Denmark*

(Received 8 February 2010; accepted 12 March 2010; published online 20 May 2010)

The effect of demagnetization on the magnetic properties of a rectangular ferromagnetic prism under nonuniform conditions is investigated. A numerical model for solving the spatially varying internal magnetic field is developed, validated, and applied to relevant cases. The demagnetizing field is solved by an analytical calculation and the coupling between applied field, the demagnetization tensor field, and spatially varying temperature is solved through iteration. We show that the demagnetizing field is of great importance in many cases and that it is necessary to take into account the nonuniformity of the internal field, especially for nonconstant temperature distributions and composite magnetic materials. © 2010 American Institute of Physics. [doi:10.1063/1.3385387]

I. INTRODUCTION

The importance of demagnetization for the properties of a magnetic body has long been recognized. The long-range nature of the dipolar force acting between individual magnetic moments will give rise to a demagnetizing field inside the body and can give rise to shape dependence of the thermodynamic properties, e.g., the heat capacity, of the body.¹ Only in uniform ellipsoidal samples (and a few other limiting cases such as an infinite sheet or an infinite cylinder) is the demagnetizing field uniform. Even in these cases, calculations of the demagnetizing field can be quite involved.² The results can be expressed in terms of a demagnetization tensor \mathbf{N}

$$\mathbf{H} = \mathbf{H}_{\text{appl}} - \mathbf{N} \cdot \mathbf{M}, \quad (1)$$

where \mathbf{H} is the total internal magnetic field, \mathbf{H}_{appl} is the applied magnetic field, and \mathbf{M} is the constant magnetization. The demagnetization tensor is symmetrical and has a trace equal to one.

If the coordinate axes are chosen to coincide with the principal axes of the ellipsoid, the demagnetization tensor becomes diagonal. Thus, the demagnetizing field is determined by three quantities N_{xx} , N_{yy} , and N_{zz} whose sum is unity. When both the applied field and \mathbf{M} are along a principal axis, Eq. (1) becomes the scalar equation

$$H = H_{\text{appl}} - NM, \quad (2)$$

where N is the relevant demagnetization factor. This equation is often used for other geometries as well. In such cases N should be interpreted as an average demagnetization factor.³ This approach can be sufficient if one is only interested in the average demagnetizing field over the entire sample. Otherwise, it becomes necessary to consider the spatial variation in the demagnetization explicitly. In particular, this is the

case when the relevant physical properties of the material depend nonlinearly on the local field.

In cases where the demagnetizing field is nonuniform, the calculation of it is nontrivial. Since the magnetization of the sample at a given point is dependent on the local field, which in its turn depends on the entire magnetization of the sample, the demagnetizing field has to be calculated self-consistently, e.g., through an iterative approach. Often, the simplifying assumption that the magnetization can be considered as constant and independent of the external field is made. In this case, calculations for a wide range of nonellipsoidal bodies have been carried out.⁴⁻⁷ In Ref. 4 the case of letting the direction (but not the magnitude) of the magnetization vary is considered and analytical expressions for the demagnetizing field to second order are given for a few special geometries.

To go beyond such simple magnetic equations of state requires numerical methods. For thin disks with cylindrical symmetry Ref. 8 calculated the demagnetizing field for homogeneous applied fields and four different magnetic equations of state: constant susceptibility, constant susceptibility with step discontinuity, hyperbolic tangential field-dependent susceptibility and finally the equation of state for a mean field ferromagnet. In Ref. 9 an axisymmetric model was applied to the problem of demagnetization in an active magnetic regeneration (AMR) device.

In this work we present a full three-dimensional modeling of a rectangular prism based only on the assumption of discretizing the prism into a mesh of grid cells each assumed to have a constant temperature and magnetization. A similar approach was followed in Ref. 10 however, only the demagnetization tensor was calculated and not the demagnetizing field.

The model is introduced in Sec. II. Then, in Sec. III the model is applied to the case of a flat prism with the magnetic field aligned along different axes and with different internal temperature distributions. Two main cases are considered: a

^{a)}Electronic mail: kaki@risoe.dtu.dk.

single-material prism with an internal temperature gradient and a multimaterial prism, i.e., a single prism consisting of several materials, uniformly distributed for simplicity, each having an individual Curie temperature. In Sec. IV the model is compared to the average expression given in Ref. 3. The results, and in particular their relevance to the construction and optimization of an AMR magnetic refrigeration system where multiple materials are expected to be crucial for performance, are discussed in Sec. V.

II. DEMAGNETIZATION MODEL OF A RECTANGULAR PRISM

The internal magnetic field can be written in the general form

$$\mathbf{H} = \mathbf{H}_{\text{appl}} + \mathbf{H}_{\text{dem}}, \quad (3)$$

where the difference between the internal and external field is the demagnetizing field \mathbf{H}_{dem} .

The demagnetizing field can be expressed as an integral over the interior Ω of the body in the following manner

$$\mathbf{H}_{\text{dem}}(\mathbf{r}, T) = \frac{1}{4\pi} \int_{\Omega} d\mathbf{r}' D(\mathbf{r} - \mathbf{r}') \cdot \mathbf{M}[\mathbf{H}(\mathbf{r}', T), \mathbf{r}', T], \quad (4)$$

where D is a symmetric 3×3 tensor whose components are given in Appendix A. This expression is valid both for points \mathbf{r} inside and outside the body. The magnetization is in general a function of both the internal field, position and temperature. The explicit position dependence is relevant when, e.g., a multimaterial prism is considered. Due to the appearance of the internal field in \mathbf{M} , Eq. (4) becomes an implicit equation for the demagnetizing field. Only when the magnetization is independent of the internal field, the equation may be evaluated explicitly. For constant magnetization this may be done either by direct integration⁴ or through a Fourier transform approach.^{6,7}

At low applied fields the magnetization within a soft ferromagnetic body will form domains in order to minimize the magnetostatic energy. Upon application of a modest magnetic field the domains will be aligned bringing the ferromagnet into a single-domain, saturated state. This saturated state is always assumed in the following.

To assume that the magnetization will not depend on the internal field will be a fair approximation for ferromagnetic bodies at temperatures far below the Curie temperature. However, close to the Curie temperature the magnetization has a strong field dependence. In the following, we will assume that the mean field equation of state captures the essential aspects of this dependence for the purpose of calculating the demagnetizing field. We do not expect our results to differ markedly for more realistic equations of state.

For concreteness we will only consider rectangular prisms. However, the procedure below may readily be adapted to, e.g., multimaterial spheres or cylinders. Considering now a rectangular prism bounded by the inequalities $-a \leq x \leq a$, $-b \leq y \leq b$, and $-c \leq z \leq c$ (see Fig. 1) the demagnetizing field may be expressed as

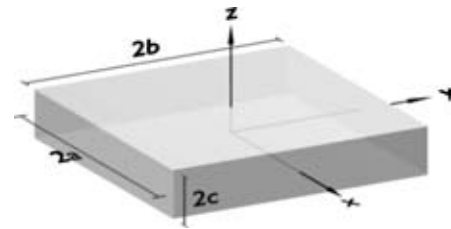


FIG. 1. The coordinate system of the modeled rectangular prism with the coordinate system defined with Origin at the center of the prism. Note that the z -direction is the “thin” direction, i.e., $2c \ll 2a$.

$$\mathbf{H}_{\text{dem}}(\mathbf{r}, T) = \frac{1}{4\pi} \int_{-a}^a dx' \int_{-b}^b dy' \int_{-c}^c dz' D(\mathbf{r} - \mathbf{r}') \cdot \mathbf{M}[\mathbf{H}[\mathbf{r}', T(\mathbf{r}')], \mathbf{r}', T(\mathbf{r}')]. \quad (5)$$

Dividing the prism into $n_x \times n_y \times n_z$ rectangular cells (following Refs. 10 and 11) the integral in Eq. (5) may be written as a sum of integrals over each cell

$$\mathbf{H}_{\text{dem}}(\mathbf{r}, T) = \frac{1}{4\pi} \sum_{i=1}^{n_x} \sum_{j=1}^{n_y} \sum_{k=1}^{n_z} \int_{-a'}^{a'} dx' \int_{-b'}^{b'} dy' \int_{-c'}^{c'} dz' D(\mathbf{r} - \mathbf{r}') \cdot \mathbf{M}[\mathbf{H}[\mathbf{r}', T(\mathbf{r}')], \mathbf{r}', T(\mathbf{r}')]. \quad (6)$$

with $a' = a/n_x$, $b' = b/n_y$, and $c' = c/n_z$. Each cell has the same relative dimensions as the original prism.

Assuming each cell to be sufficiently small to have constant magnetization, $\mathbf{M}_0(\mathbf{r}'_{i,j,k}, T_{i,j,k})$, Eq. (6) may be approximated by

$$\mathbf{H}_{\text{dem}}(\mathbf{r}, T) \approx - \sum_{i=1}^{n_x} \sum_{j=1}^{n_y} \sum_{k=1}^{n_z} \mathbb{N}(\mathbf{r} - \mathbf{r}'_{i,j,k}) \cdot \mathbf{M}_0[\mathbf{H}(\mathbf{r}'_{i,j,k}, T_{i,j,k}), \mathbf{r}'_{i,j,k}, T_{i,j,k}], \quad (7)$$

where \mathbb{N} denotes the symmetric 3×3 demagnetization tensor field with the components given in Eqs. (A8) and (A12) below. The vector $\mathbf{r}'_{i,j,k}$ denotes the center of the cell with index i, j, k .

The magnetization is generally a function of both the magnitude of the internal field, H , and temperature, T . Therefore, Eq. (3) has to be solved by iteration. For simplicity the magnetization is assumed to be aligned with \mathbf{H} , i.e., there is no magnetocrystalline anisotropy.⁴

To obtain the magnitude of the magnetization, M , the mean field equation of state for a ferromagnet is assumed¹²

$$M(T, H) = N_s g J \mu_B \rho B_J(\chi) \quad (8)$$

with N_s denoting the number of magnetic spins per unit mass, g the Landé factor, J the total angular momentum in units of \hbar , μ_B the Bohr magneton, and ρ the mass density. The Brillouin function, B_J , is defined as

$$B_J(\chi) = \frac{2J+1}{2J} \coth\left(\frac{2J+1}{2J} \chi\right) - \frac{1}{2J} \coth\left(\frac{1}{2J} \chi\right), \quad (9)$$

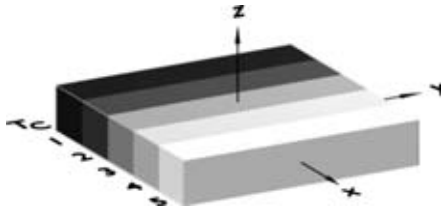


FIG. 2. The concept of grading the prism with different ferromagnets. In this case five materials are illustrated. The Curie temperatures differ from layer to layer as indicated by T_{C1-5} .

$$\chi = \frac{gJ\mu_B\mu_0 H}{k_B T} + \frac{3T_C J}{T(J+1)} B_J(\chi). \quad (10)$$

Here the vacuum permeability, μ_0 , the Boltzmann constant, k_B , and the Curie temperature, T_C , were introduced. Equation (10) is iterated to obtain a self-consistent solution. In Appendix B a numerical model solving the coupled problem in Eqs. (3)–(10) is described in detail.

III. APPLICATION OF THE MODEL

Four different cases are investigated in the following. Two cases with a rectangular prism made of a single magnetic material, i.e., having one Curie temperature, and two cases with a so-called graded material, i.e., a composite material which contains regions with different Curie temperatures. In the latter case, the grading is assumed to be along the x -direction; for concreteness we consider five equal-sized regions each with its own Curie temperature (illustrated in Fig. 2). This is presented in Sec. III B.

Both materials configurations are considered under two different temperature situations: one with a constant temperature and one with an imposed temperature gradient. The latter case is relevant to investigate for, e.g., magnetic refrigeration, or in other cases where a thermal gradient is present in the system. In general, such a gradient may cause the prism to be in different magnetic phases at the same time. This is the typical operation mode of a magnetic material used in magnetic refrigeration, which will be roughly centered around the Curie temperature for optimal utilization of the magnetocaloric effect.¹³

As a magnetic material, gadolinium (Gd) is used since it can be fairly well described by the mean field equation of state, Eq. (8);¹⁴ additionally it acts as a de facto benchmark material in magnetic refrigeration. The Curie temperature of Gd is taken to be 293 K, and the other input parameters for the mean field equation of state are given in Table I. The dimensions of the prism are taken to be $2a=0.02$ m, $2b=0.02$ m, and $2c=0.001$ m in all cases. The coordinate system is illustrated in Fig. 1.

TABLE I. Parameters for the mean field equation of state, Eq. (8), for Gd. Data taken from Refs. 15 and 16.

Parameter	N_s (kg^{-1})	g (–)	J (\hbar)	ρ (kg m^{-3})	T_C (K)
Value	3.83×10^{24}	2	7/2	7900	293

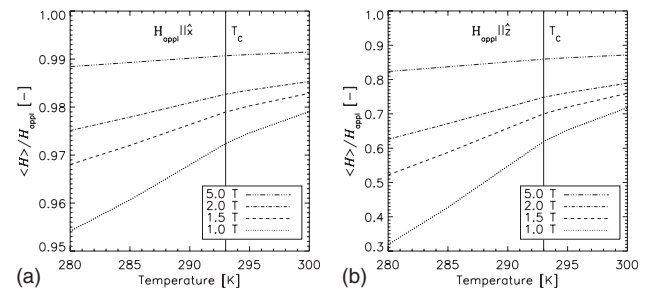


FIG. 3. The normalized mean of the magnetic field as a function of the (spatially constant) temperature for four different applied fields in the case of a rectangular prism consisting of one magnetic material. (a) The applied field is along the x -direction. (b) The applied field is along the z -direction.

A. Single Curie-point flat prism

1. Constant temperature

We first consider the case of a single material with a constant temperature to validate our approach. This is a well-known situation and will only briefly be discussed. In Fig. 3 the normalized mean of the magnitude of the internal field is plotted as a function of the (spatially constant) prism temperature for four different applied fields. It is evident from the figure that the effect of demagnetization decreases at higher applied fields in the ferromagnetic phase. This follows directly from the fact that the magnetization is saturated in the ferromagnetic phase and thus the demagnetizing field becomes constant. However, a field of more than 5 T is needed in order for this to be the case (this field value is material dependent, of course). Furthermore, when applying the field in the xy -plane of the prism, the magnetic field is reduced with a few percent whereas it is reduced with up to 70% in the case of applying the field along the z -direction. The decrease is dependent on temperature and material properties.

2. Linear temperature profile

In the following, the rectangular prism is assumed to have an imposed temperature profile ranging linearly from 280 to 300 K along the x -direction. This will make the magnetic state of the prism depend on x . This is a special case of great importance in, e.g., magnetic refrigeration where a magnetic material acts both as a regenerator material, i.e., upholding a thermal gradient, and as an active magnetic material through the magnetocaloric effect.

Figure 4 shows the two cases where the applied field is along the x -direction and z -direction, (a) and (b), respectively. Four different fields have been applied, namely 1.0, 1.5, 2.0, and 5.0 T. The same trends as in Fig. 3 are observed. The rather large applied magnetic field of 5 T saturates the magnetization (in the ferromagnetic phase) and the effect of demagnetization is thus small here. However, considering the cases of applied fields of 1.0–2.0 T a rather large gradient in the internal field is observed when the applied field is along the z -direction [Fig. 4(b)]. In the case of applying the field along the x -direction [Fig. 4(a)], the internal field is generally not affected greatly by the demagnetizing field. However, on the low temperature edge, i.e., where $x/a=-1$, the field drops rapidly. A similar, though not as large, drop is seen on the

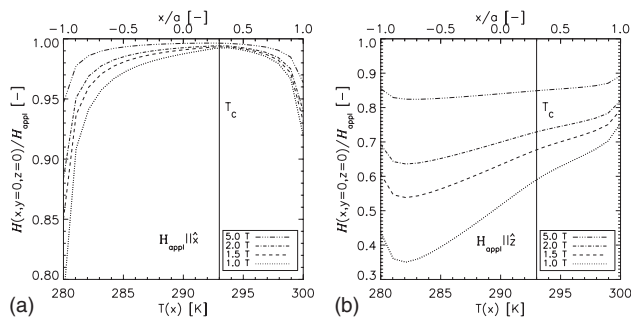


FIG. 4. The magnetic field along the line $y=0, z=0$, and $-1 \leq x/a \leq 1$. The prism has an imposed thermal gradient along the x -direction ranging from 280 to 300 K and consists of one magnetic material with a Curie temperature of 293 K. (a) The applied field is along the x -direction. (b) The applied field is along the z -direction.

high temperature edge (at $x/a=1$). These two drops in the internal field are due to the fact that the demagnetization tensor field is largest on the edges perpendicular to the direction of the applied field. The reason that the lower temperature edge has the somewhat greater drop in internal field is because this part of the prism is in the ferromagnetic phase and thus the magnetization is largest here and consequently the demagnetizing field is greater.

B. Flat prism with multiple Curie temperatures

In the following a rectangular prism consisting of five equally distributed magnetic materials resembling Gd but with Curie temperatures 280 K, 285 K, 290 K, 295 K, and 300 K, respectively, is considered. The grading of the prism is along the x -axis. With the temperature of the prism in the interval 280 to 300 K the individual parts of the prism will be in different magnetic phases but still in the vicinity of their respective Curie temperatures.

1. Constant temperature

Considering the case with the prism having a constant temperature the magnitude of the internal field across the prism in the direction of the grading is plotted in Fig. 5 for five different constant temperatures. The applied field is in all cases equal to 1 T. The magnetic field is seen to be discontinuous in the x -direction when applying the field in this direction [Fig. 5(a)], whereas it is continuous in the x -direction when applying the field along the y -direction and z -direction [Figs. 5(b) and 5(c)]. This is to be expected since in the former case the magnetic field lines are crossing material boundaries and the normal component of \mathbf{H} is discontinuous. In the latter cases the field lines are perpendicular to the materials boundaries and the parallel component of \mathbf{H} across boundaries is continuous as expected. It should be noted that the largest component of \mathbf{H} is along the direction of the applied field. Considering the magnetic flux density,

$$\mathbf{B} = \mu_0(\mathbf{H} + \mathbf{M}), \quad (11)$$

the opposite is true, i.e., the normal component is continuous whereas the parallel component is discontinuous. This is seen in Figs. 6(a) and 6(c). Figure 6(b) shows a plot of the magnitude of the magnetic flux density along the x -axis

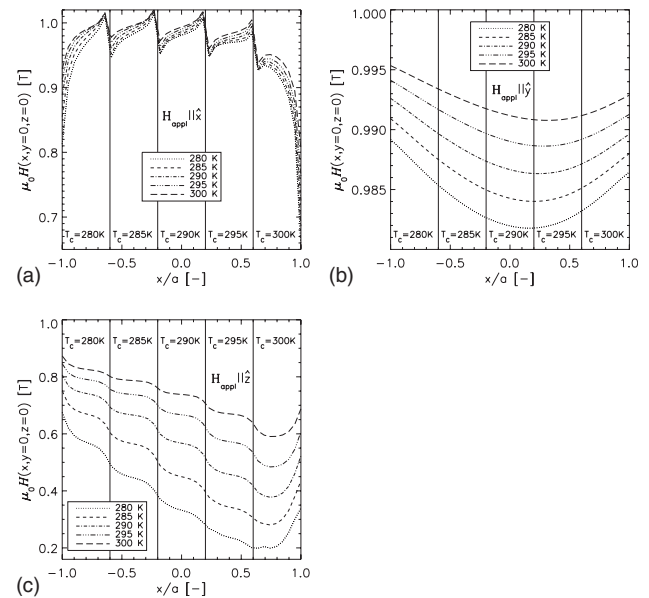


FIG. 5. The magnitude of the magnetic field along the line defined as $-1 \leq x/a \leq 1, y=0$, and $z=0$ through the prism for five different constant temperatures. The prism is divided in five regions each being a magnetic material resembling Gd but with different Curie temperatures (280 K, 285 K, 290 K, 295 K, and 300 K, respectively), as illustrated in Fig. 2. (a) The applied field is along the x -direction. (b) The applied field is along the y -direction. (c) The applied field is along the z -direction. In all cases $\mu_0 H_{\text{appl}} = 1.0$ T.

when the magnetic field is applied along the y -axis. Since H is virtually constant (to within a few per mille; see Fig. 5), the magnetization is dominating the spatial variation in B . This is seen in the staircaselike plot on Fig. 6(b). At, e.g., a constant temperature of 280 K, the value of B in the part of the prism with a Curie temperature of 280 K is equal to B at a temperature of 285 K in the part of the prism with a Curie

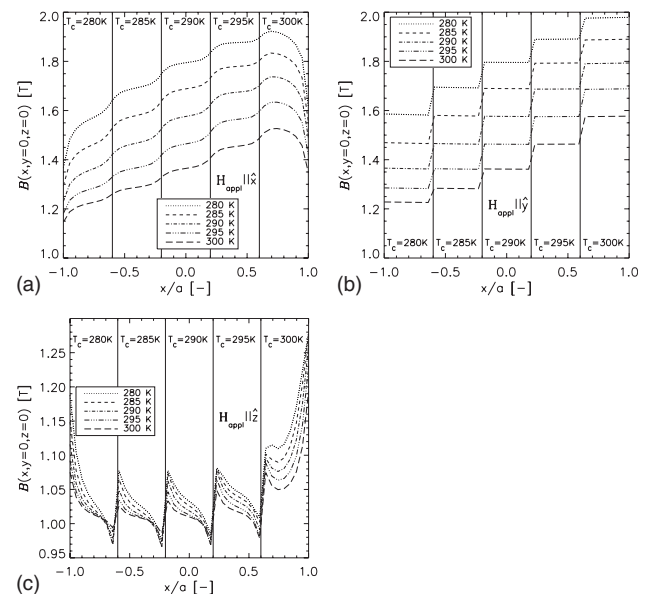


FIG. 6. The magnitude of the magnetic flux density, B , along the same line as in Fig. 5, i.e., $-1 \leq x/a \leq 1, y=0, z=0$ for five different temperatures. The prism is the same as considered in Fig. 5. (a) The applied field is along the x -direction. (b) The applied field is along the y -direction. (c) The applied field is along the z -direction. In all cases $\mu_0 H_{\text{appl}} = 1.0$ T.

point of 285 K, etc. The discontinuities across the internal materials boundaries are expected again due to the boundary conditions.

When applying the magnetic field along the x -direction, which causes minimal demagnetization, it is observed that the variation in the temperature of the prism does not change the internal field significantly. However, when applying the field along the z -direction, Fig. 5(c), a significant difference is observed between the various temperature cases. The lower the temperature of the prism the more of the individual composites are in their ferromagnetic state. This produces higher magnetization values and thus also a larger demagnetizing field. For increasing Curie temperature (along the x -axis) the magnetic field decreases because of the larger magnetization. It should be noted that for a constant temperature of 280 K the average internal field is about 60% of the applied field. The maximum decrease is observed to be around 80% for the cases studied here. The reason for the increase in magnetic field at either ends for all temperature cases is the relatively low demagnetization factor on the boundary. It is noted that the internal field may actually be greater than the applied field locally. This is seen in Fig. 5(a) and can be explained by flux shimming due to the discontinuity in the permeability on the boundary between two different magnetic materials.⁹

Finally, it is noted that applying the field along the y -direction [Fig. 5(b)] yields both a continuous and large internal magnetic field. The difference in this situation between the largest and smallest values of the magnitude of the internal field is only a few percent whereas in the case of applying the field along the x -direction may give a decrease in as much as 30%, though only in relatively small regions.

2. Linear temperature profile

Figure 7 shows the magnetic field in the x -direction of a prism similar to the one considered in Sec. III B 1 but with an imposed linear temperature profile ranging from 280 to 300 K. For the four different applied fields, 1, 1.5, 2.0, and 5.0 T, Figs. 7(a)–7(c) show the case when magnetizing along the x -direction, y -direction, and z -direction, respectively. A magnetic field similar to that obtained in the constant temperature case, Fig. 5, is produced in this case. However, when applying the field along the x -direction the drop in magnetic field at either end is similar to the edge defined as $x=-a$ in Fig. 5(a).

Again, as discussed in Sec. III B 1, applying the field along the y -direction [Fig. 7(b)] yields both a smooth and large internal field. This may be explained by the simple fact that the normal component of \mathbf{H} is continuous across materials boundaries and the demagnetization is low when the field is applied in the y -direction.

Finally, when applying the field along the z -direction the internal field is more smooth than in the constant temperature case [see Figs. 5(c) and 7(c)]. This is due to the fact that each section of the prism having a specific Curie temperature is relatively close to this temperature. Thus, the magnetization across the prism is fairly constant as opposed to the decrease with increasing x in Fig. 5(b). This results in a more constant demagnetizing field. It is also observed in Figs. 7(a)–7(c)

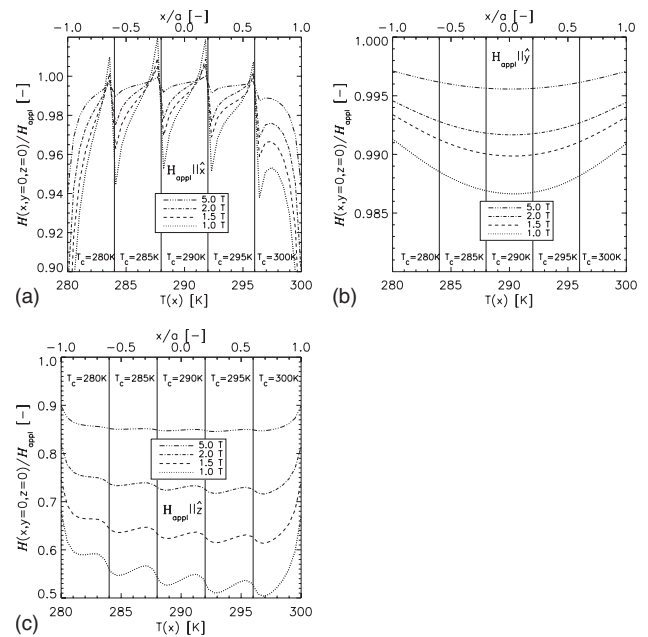


FIG. 7. The magnitude of the internal field along the line $-1 \leq x \leq 1$, $y=0$, and $z=0$ for four different applied fields. The prism is divided into five materials each having a different Curie temperature as in Fig. 5. The prism has an imposed linear temperature profile along the x -direction ranging from 280 K to 300 K. (a) The applied field is along the x -direction. (b) The applied field is along the y -direction. (c) The applied field is along the z -direction.

that lower applied fields induce larger variation along the x -direction, which is due to the fact that the magnetization becomes saturated above a certain field and thus the demagnetizing field becomes constant.

IV. COMPARISON TO THE AVERAGE DEMAGNETIZATION FACTOR

In Ref. 3 the average demagnetization factor, N , of a prism under the assumption that the magnetization and internal field are homogeneous and constant was calculated by Aharoni. In the following a comparison between the results of the model presented here and this average value is performed. Experimentally, the applied field and the mean magnetization along the direction of the applied field may be obtained. This leads to the definition of a representative average demagnetization factor, $N_{0,i}$

$$\langle H_i \rangle = H_{\text{appl},i} - N_{0,i} \langle M_i \rangle \quad (12)$$

with the subscript i denoting the component of the field. It should be noted that with this definition, $N_{0,i}$, is not the average of the demagnetization tensor field given in Eqs. (A8) and (A12). In particular, the sum of $N_{0,x}$, $N_{0,y}$, and $N_{0,z}$ need not be unity. It should rather be interpreted as a simplification of the model results in terms of a single number, which is useful when analyzing experimental data.

Figure 8(a) shows $N_{0,x}$ for the case of a constant temperature, single material rectangular prism with an applied field of 1 T along the x -direction. The prism has a symmetric yz -cross section and the length is varied in the x -direction giving rise to a variation in the aspect ratio. The average demagnetization factor is seen to coincide with the Aharoni

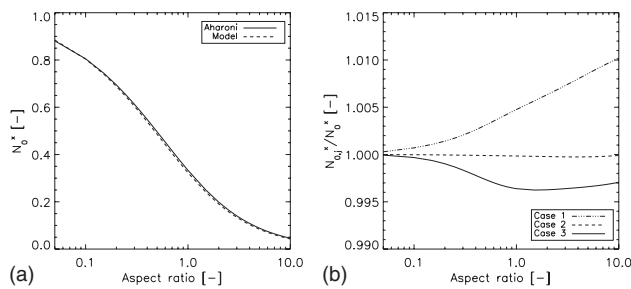


FIG. 8. The representative average demagnetization factor as defined in Eq. (12). (a) Shows this factor as a function of aspect ratio for a rectangular prism with quadratic cross section (in the yz -plane) and varying length (along the x -direction). The applied field is along the x -direction and has a magnitude of 1 T. The temperature is fixed at 293 K, i.e., the Curie temperature. (b) Three specific cases where the temperature and composition of the magnetic material are varied. Case 1 is for a constant temperature of 293 K with five materials, with Curie temperatures 280 K, 285 K, 290 K, 295 K, and 300 K, respectively, spaced evenly along the x -direction. Case 2 is for the same composition as in Case 1 but with a linear temperature profile ranging from 280–300 K. Case 3 is for a single material prism with an imposed linear temperature profile also from 280–300 K. In all cases the graphs show the ratio between the respective average demagnetization factor and the single material, constant temperature average demagnetization factor.

expression almost completely. In the limits where the aspect ratio goes to zero and infinity, respectively, the demagnetization factors are equal. However, for aspect ratios from one to five the Aharoni demagnetization factor is a few percent larger than the representative average defined in Eq. (12). This may be explained from the fact that the corners of the prism have a relative large impact on the demagnetization factor in these cases, i.e., the magnetization and thus internal field deviate mostly from being parallel to the applied field for this range of aspect ratios. Since the Aharoni expression assumes the magnetization to be completely parallel to the applied field, a discrepancy is to be expected.

Figure 8(b) shows the average demagnetization factor for the constant temperature and single material case compared to the three cases: (1) a rectangular prism graded with five materials as discussed in Sec. III B 1, (2) same as in (1) but with an imposed linear temperature profile, i.e., as discussed in Sec. III B 2, and finally (3) a single material prism with an imposed linear temperature profile as discussed in Sec. III A 2. It is clearly evident from the figure that the representative average demagnetization factor is not purely geometric. In the cases investigated here the effect of grading the material or imposing a linear temperature profile is of the order of 1% only. This should be taken as a consequence of the selected cases rather than as a general rule. Indeed, Ref. 8 found their effective demagnetization factor to vary with as much as 10%–20% due to nongeometric factors.

V. CONCLUSIONS AND DISCUSSION

A numerical solution to the fully coupled problem of solving for the internal magnetic field in a three-dimensional rectangular prism with spatially varying temperature, applied magnetic field and magnetization has been derived and implemented. The model was applied to several relevant cases where the orientation of a magnetic material and an applied magnetic field is crucial combined with imposed

temperature gradients. The magnetic material was assumed to be either homogeneous or a multilayered composite.

From the results presented in this paper it can be concluded that detailed knowledge of the demagnetizing field throughout the sample is important in many cases. This includes the situations when the temperature is not spatially constant or the sample is a composite material consisting of several materials each having a distinct Curie temperature. Imposing a temperature gradient across the sample makes the internal magnetic field become spacially asymmetric and especially when the demagnetization tensor field is rather large the internal field may be approximately linear as shown in Fig. 4(b). In this case the largest value of the internal field in the sample may be 50% greater than the smallest, which certainly invalidates any assumption of constant magnetization throughout the sample.

When applying a magnetic field along the direction of the grading of the material (in this case the x -direction) discontinuities on each internal boundary are observed. This is a direct consequence of the boundary conditions that apply generally for \mathbf{H} and \mathbf{B} . This leaves two preferred directions to apply the magnetic field in (the x -direction and y -direction, respectively), in order to minimize the demagnetizing field. However, a large difference is observed in the behavior of the internal magnetic field between these two cases. When the external magnetic field is applied along the x -direction, discontinuities exist at every internal material boundary due to the boundary conditions for \mathbf{H} . In the other case, when the applied magnetic field is along the y -direction, no discontinuities are present. Furthermore, the magnitude of the internal magnetic field is generally seen to be larger in this case. It may therefore be concluded that great care should be taken when deciding along which direction the magnetic field should be applied with respect to both the demagnetizing field and a possible grading of the magnetic material.

In the case of applying the magnetic field in the z -direction to a constant temperature sample a difference between single and multiple material prisms is observed. In the former case the internal field is fairly constant. In the latter case the internal field becomes almost linear in the x -direction for a range of temperatures [see Fig. 5(c)]. However, when imposing a temperature gradient in the x -direction the virtually opposite is the case [compare Figs. 4(b) and 7(c)].

An average demagnetization factor was introduced and compared to the analytical expression calculated in Ref. 3 which is based on the assumptions that the magnetization is constant and completely aligned with the applied field. However, when the prism does not have a constant temperature or is made of a composite of different magnetocaloric materials, the demagnetization factor of Eq. (12) changes slightly.

Finally, it is concluded that the internal magnetic field is far from being constant under realistic circumstances and that it may be a poor approximation to assume so. As expected, when imposing a temperature gradient across the rectangular prism and assuming a composite material the internal field can become highly inhomogeneous, depending on the orientation of the applied field. Such inhomogeneities

are important in any case where a good representation of the internal field is sought. It is noted that the results of this paper are valid for single prisms only. In many situations stacks or arrays of prisms will be relevant. A future paper on this using the model presented here is in preparation.

ACKNOWLEDGMENTS

The authors thank the support of the Programme Commission on Energy and Environment (EnMi) (Contract No. 2104-06-0032) which is part of the Danish Council for Strategic Research.

APPENDIX A: CALCULATING THE D TENSOR FIELD

The vector potential of a single magnetic dipole at \mathbf{r}' is

$$\mathbf{A}_i(\mathbf{r}) = \frac{\mu_0 \mathbf{m}_i \times (\mathbf{r} - \mathbf{r}')}{4\pi |\mathbf{r} - \mathbf{r}'|^3}. \tag{A1}$$

The total vector potential of a magnetic body is obtained by integrating over the interior of the body (with $\mathbf{m}_i = \mathbf{M}dV$):

$$\mathbf{A}(\mathbf{r}) = \frac{\mu_0}{4\pi} \int_{\Omega} d\mathbf{r}' \frac{\mathbf{M}(\mathbf{r}') \times (\mathbf{r} - \mathbf{r}')}{|\mathbf{r} - \mathbf{r}'|^3}. \tag{A2}$$

Note that this gives the vector potential both inside and outside of the prism.

The resulting \mathbf{H} -field is

$$\begin{aligned} \mathbf{H}(\mathbf{r}) &= \frac{1}{\mu_0} \mathbf{B}(\mathbf{r}) - \mathbf{M}(\mathbf{r}) = \frac{1}{\mu_0} \nabla \times \mathbf{A} - \mathbf{M}(\mathbf{r}) \\ &= -\frac{1}{4\pi} \int_{\Omega} d\mathbf{r}' (\mathbf{M}(\mathbf{r}') \cdot \nabla) \frac{\mathbf{r} - \mathbf{r}'}{|\mathbf{r} - \mathbf{r}'|^3}, \end{aligned} \tag{A3}$$

which is the required demagnetizing field, \mathbf{H}_{dem} .

The differentiations can be performed straightforwardly, giving rise to the following equation

$$\mathbf{H}_{\text{dem}}(\mathbf{r}) = \frac{1}{4\pi} \int_{\Omega} d\mathbf{r}' \mathbf{D}(\mathbf{r} - \mathbf{r}') \cdot \mathbf{M}(\mathbf{r}'), \tag{A4}$$

with \mathbf{D} being a symmetrical 3×3 tensor with elements

$$N_{ij}(\mathbf{r}) = -\frac{1}{4\pi} \ln \left[\frac{F_{ij}(\mathbf{r}, a, b, c) F_{ij}(\mathbf{r}, -a, -b, c) F_{ij}(\mathbf{r}, a, -b, -c) F_{ij}(\mathbf{r}, -a, b, -c)}{F_{ij}(\mathbf{r}, a, -b, c) F_{ij}(\mathbf{r}, -a, b, c) F_{ij}(\mathbf{r}, a, b, -c) F_{ij}(\mathbf{r}, -a, -b, -c)} \right], \quad i \neq j \tag{A12}$$

where

$$F_{xy}(\mathbf{r}, a, b, c) = (c - z) + [(a - x)^2 + (b - y)^2 + (c - z)^2]^{1/2} \tag{A13}$$

$$F_{yz}(\mathbf{r}, a, b, c) = (a - x) + [(a - x)^2 + (b - y)^2 + (c - z)^2]^{1/2} \tag{A14}$$

$$D_{ii}(\mathbf{r}) = -\frac{1}{|\mathbf{r}|^3} + \frac{3x_i^2}{|\mathbf{r}|^5} \tag{A5}$$

$$D_{ij}(\mathbf{r}) = \frac{3x_i x_j}{|\mathbf{r}|^5}, \quad i \neq j \tag{A6}$$

Considering a rectangular prism with constant magnetization, $\mathbf{M}(\mathbf{r}) = \mathbf{M}_0$,⁴ the demagnetizing field becomes

$$\begin{aligned} \mathbf{H}_{\text{dem}}(\mathbf{r}) &= \frac{1}{4\pi} \int_{-a}^a dx' \int_{-b}^b dy' \int_{-c}^c dz' \mathbf{D}(\mathbf{r} - \mathbf{r}') \cdot \mathbf{M}_0 \\ &= -\mathbf{N}(\mathbf{r}) \cdot \mathbf{M}_0, \end{aligned} \tag{A7}$$

where the symmetric 3×3 demagnetization tensor $\mathbf{N}(\mathbf{r})$ has the components

$$\begin{aligned} N_{ii}(\mathbf{r}) &= \frac{1}{4\pi} [\arctan f_i(x, y, z) + \arctan f_i(-x, y, z) \\ &\quad + \arctan f_i(x, -y, z) + \arctan f_i(x, y, -z) \\ &\quad + \arctan f_i(-x, -y, z) + \arctan f_i(x, -y, -z) \\ &\quad + \arctan f_i(-x, y, -z) + \arctan f_i(-x, -y, -z)] \end{aligned} \tag{A8}$$

where

$$f_x(x, y, z) = \frac{(b - y)(c - z)}{(a - x)[(a - x)^2 + (b - y)^2 + (c - z)^2]^{1/2}} \tag{A9}$$

$$f_y(x, y, z) = \frac{(a - x)(c - z)}{(b - y)[(a - x)^2 + (b - y)^2 + (c - z)^2]^{1/2}} \tag{A10}$$

$$f_z(x, y, z) = \frac{(b - y)(a - x)}{(c - z)[(a - x)^2 + (b - y)^2 + (c - z)^2]^{1/2}}. \tag{A11}$$

The off-diagonal elements are

$$F_{xz}(\mathbf{r}, a, b, c) = (b - y) + [(a - x)^2 + (b - y)^2 + (c - z)^2]^{1/2}. \tag{A15}$$

APPENDIX B: NUMERICAL IMPLEMENTATION OF THE MODEL

This appendix describes the implementation of a numerical model for solving the demagnetization problem as stated in Eqs. (3) and (7). First a simple scheme for optimized

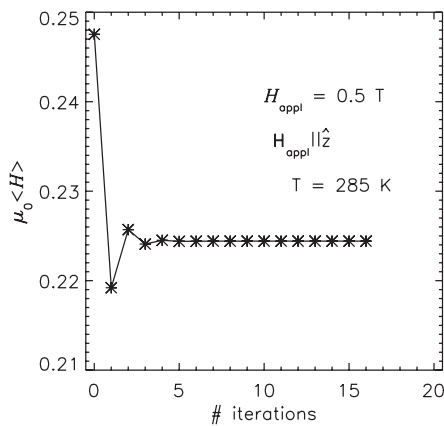


FIG. 9. The mean of the internal magnetic field as a function of number of iterations for the case when applying the magnetic field in the z -direction, setting the temperature to be constant at 285 K (below the Curie temperature) and $\mu_0 H_{\text{appl}} = 0.5 \text{ T}$.

convergence conditions is presented. Second, the resolution of the model is discussed. Finally, symmetry conditions and parallelization are considered since the problem is of order n^2 with $n = n_x \times n_y \times n_z$.

1. Convergence

The criterium for convergence is defined as the maximum difference between the internal magnetic fields in two following iterations should be less than 10^{-8} T . This is a criterium that is very similar to that of Ref. 8. An under-relaxation technique on the magnetization for obtaining convergence *in situations* with small applied fields and/or temperatures below the Curie temperature was applied in Ref. 8. By thorough testing, we found that under-relaxing on the internal field was better for convergence. This may be expressed as

$$\mathbf{H}_{n+1} = \mathbf{H}_n + \lambda_n [\mathbf{H}(M_n) - \mathbf{H}_n], \quad (\text{B1})$$

where n denotes the iteration step, $\mathbf{H}_0 = \mathbf{H}_{\text{appl}}$, $M_n = M(H_n)$ using Eq. (8) and assuming \mathbf{M} to be parallel to \mathbf{H} in the previous step and $\mathbf{H}(M_n)$ is obtained through Eqs. (3) and (7). The under-relaxation parameter for the n th iteration is denoted λ_n , which attains a value in the interval $0 < \lambda_n \leq 1$. Finally, it is noted that Eq. (B1) is used on every mesh point and the convergence is determined from the mesh point where two consecutive iterations yield $\max[\text{abs}(\mathbf{H}_n - \mathbf{H}_{n+1})]$ ensuring the slowest but most precise convergence. Figure 9 shows an example of the under-relaxation technique.

2. Resolution

A variation in resolution is shown in Fig. 10. The resolution of the prism is in all cases, except when comparing to the average demagnetization factor, $(n_x, n_y, n_z) = k(2a, 2b, 10 \times 2c)$ with k being an arbitrary scaling constant. As can be seen from the figure a fairly low resolution is sufficient. This corresponds to $(n_x, n_y, n_z) = (20, 20, 10)$ for the case discussed in this work.

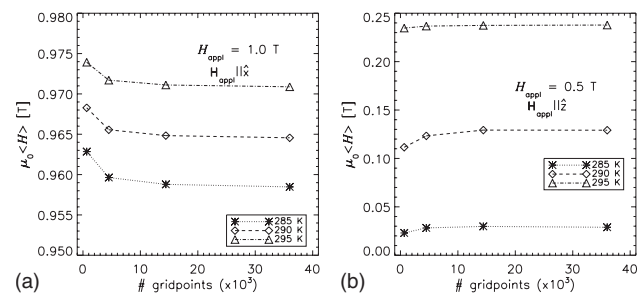


FIG. 10. The mean of the internal magnetic field as a function of the number of grid points for three different constant temperatures and an applied field of 1.0 T applied along the x -direction (a) and an applied field of 0.5 T applied along the z -direction (b).

3. Symmetry and optimization

The solution to the problem stated in Eqs. (3) and (7) both involves iteration of Eq. (3) and an n^2 problem from Eq. (7). Optimization in the form of exploitation of symmetry should be employed. The rectangular prism is symmetric around all three axes meaning that only one octant needs to be considered when calculating the demagnetization tensor field, \mathbb{N} . Obviously, the applied field, temperature and magnetization cannot *a priori* be assumed to be symmetric since realistic scenarios include both temporally and spatially varying magnetic fields and temperatures.

However, the nature of \mathbb{N} is purely geometric and is thus only a function of $\mathbf{r} - \mathbf{r}'_{i,j,k}$, a' , b' , and c' . Since the grid is defined to be homogeneous, the calculation of \mathbb{N} only has to be performed once (at the beginning of the iteration process). Furthermore, \mathbb{N} needs only to be evaluated in one octant and from this result can be mirrored to the remaining part of the coordinate system. Finally, during the calculations needed for one iteration, the value of \mathbf{M} is obtained from the previous iteration (or, in the case of the first iteration, from the initial guess), which means that the evaluations of the dot products between \mathbb{N} and \mathbf{M} needed in Eq. (7) are completely decoupled, which results in the possibility of maximized parallelization.

¹P. M. Levy and D. P. Landau, *J. Appl. Phys.* **39**, 1128 (1968).

²J. A. Osborn, *Phys. Rev.* **67**, 351 (1945).

³A. Aharoni, *J. Appl. Phys.* **83**, 3432 (1998).

⁴R. I. Joseph and E. Schloemann, *J. Appl. Phys.* **36**, 1579 (1965).

⁵M. Beleggia and M. De Graef, *J. Magn. Magn. Mater.* **263**, L1 (2003).

⁶S. Tandon, M. Beleggia, Y. Zhu, and M. De Graef, *J. Magn. Magn. Mater.* **271**, 9 (2004).

⁷S. Tandon, M. Beleggia, Y. Zhu, and M. De Graef, *J. Magn. Magn. Mater.* **271**, 27 (2004).

⁸J. A. Brug and W. P. Wolf, *J. Appl. Phys.* **57**, 4685 (1985).

⁹O. Peksoy and A. Rowe, *J. Magn. Magn. Mater.* **288**, 424 (2005).

¹⁰M. Lu, Z. Yang, and F.-L. Wei, *Int. J. Infrared Millim. Waves* **19**, 1027 (1998).

¹¹M. Schabes and A. Aharoni, *IEEE Trans. Magn.* **23**, 3882 (1987).

¹²A. H. Morrish, *The Physical Principles of Magnetism* (Wiley, New York, 1965).

¹³A. Rowe and A. Tura, *Int. J. Refrig.* **29**, 1286 (2006).

¹⁴G. J. Liu, J. R. Sun, J. Z. Wang, T. Y. Zhao, and B. G. Shen, *J. Phys.: Condens. Matter* **19**, 466215 (2007).

¹⁵D. R. Lide, *CRC Handbook of Chemistry and Physics* (CRC, Boca Raton, FL, 2004).

¹⁶A. M. Tishin and Y. I. Spichkin, *The Magnetocaloric Effect and its Applications* (Institute of Physics, London, 2003).

-
- A.1.4 Spatially resolved measurement of the magnetocaloric effect and the local magnetic field using thermography; published in Journal of Applied Physics

Spatially resolved measurements of the magnetocaloric effect and the local magnetic field using thermography

D. V. Christensen,^{1,2,a)} R. Bjørk,¹ K. K. Nielsen,^{1,3} C. R. H. Bahl,¹ A. Smith,¹ and S. Clausen⁴

¹Fuel Cells and Solid State Chemistry Division, Risø National Laboratory for Sustainable Energy, Technical University of Denmark, Frederiksborgvej 399, DK-4000 Roskilde, Denmark

²The Niels Bohr Institute, University of Copenhagen, Blegdamsvej 17, DK-2100 Copenhagen, Denmark

³Department of Mechanical Engineering, Technical University of Denmark, Building 425, Niels Koppels Alle, DK-2800 Kongens Lyngby, Denmark

⁴Plasma Physics and Technology Division, Risø National Laboratory for Sustainable Energy, Technical University of Denmark, Frederiksborgvej 399, DK-4000 Roskilde, Denmark

(Received 29 March 2010; accepted 9 August 2010; published online 22 September 2010)

The magnetocaloric effect causes a magnetic material to change temperature upon application of a magnetic field. Here, spatially resolved measurements of the adiabatic temperature change are performed on a plate of gadolinium using thermography. The adiabatic temperature change is used to extract the corresponding change in the local magnetic field strength. The measured temperature change and local magnetic field strength are compared to results obtained with a numerical model, which takes demagnetization into account and employs experimental data. © 2010 American Institute of Physics. [doi:10.1063/1.3487943]

I. INTRODUCTION

The applied magnetic field, \mathbf{H}_{appl} , differs from the local magnetic field, \mathbf{H} , in a magnetic material. The difference arises as the magnetization, \mathbf{M} , itself produces a magnetic field, known as the demagnetizing field, \mathbf{H}_{dem} , which tends to decrease the local magnetic field inside the body. In general the demagnetizing field varies spatially and is highly dependent on the geometry and the magnetization of the body. Since the demagnetizing field depends on the magnetization, which in turn generally depends on the local magnetic field, the demagnetizing field can typically only be evaluated analytically in the few cases where both the magnetization and the demagnetizing field are homogeneous. This is fulfilled only in ellipsoidal bodies¹ and a few other cases such as infinite cylinders or infinite sheets.

When the local magnetic field in a finite, nonellipsoidal body is needed, a commonly used approach is to assume a homogeneous magnetization throughout the body. The position dependence of the local magnetic field can then be expressed as

$$\mathbf{H}(\mathbf{r}) = \mathbf{H}_{\text{appl}}(\mathbf{r}) + \mathbf{H}_{\text{dem}}(\mathbf{r}) = \mathbf{H}_{\text{appl}}(\mathbf{r}) - \mathbf{N}(\mathbf{r}) \cdot \mathbf{M}, \quad (1)$$

where the demagnetization tensor field, $\mathbf{N}(\mathbf{r})$, has been evaluated for a range of geometries, see e.g. Refs. 2 and 3, and a general expression has been given using a Fourier space approach.⁴ However, as the local magnetic field varies spatially the assumption of a homogeneous magnetization is often invalid. When this is the case the demagnetizing field can be solved numerically as in, e.g., Refs. 5 and 6.

Another approach is to determine the local magnetic field experimentally. Due to the strong shape dependence of the demagnetizing field this must be done without altering

the shape of the sample. One way of achieving this is to determine the local field indirectly by measuring an observable that depends on the local magnetic field. As shown in Refs. 5 and 7 one such observable is the magnetocaloric effect, which manifests itself as an adiabatic temperature change, ΔT_{ad} , if the local magnetic field in a magnetocaloric material changes in time.

Here, measurements of the adiabatic temperature change in a plate of gadolinium are performed using thermography as described in Sec. II. The measurements are compared to a numerical model introduced in Sec. III, which corrects for the demagnetization and employs measurements of the magnetization and adiabatic temperature change in samples of gadolinium. Finally, the results of the measured and calculated adiabatic temperature change and corresponding local magnetic field changes are discussed in Sec. IV.

II. EXPERIMENTAL

The experiment was carried out using a $40 \times 25 \times 0.9$ mm³ plate of gadolinium with a purity of 99.9% obtained from China Rare Metal Material Co. The relevant dimensions and defined coordinate system are given in the illustration of the experimental setup in Fig. 1. Two layers of black paint were applied to the plate, and the plate was mounted in a plastic cylinder with a hole of the same size as the plate allowing transmission of thermal radiation. To ensure approximately adiabatic conditions the plate was mounted such that only the faces with $x=0$ and $x=25$ mm were in contact with the thermally insulating cylinder. Using a stepper motor the cylinder was moved into the center of a Halbach magnet with a magnetic field profile as seen in Fig. 2. When thermal equilibrium was reached at 295 K, the cylinder was moved out of the magnet in 0.7 s resulting in a negative adiabatic temperature change. During the movement the intensity of the thermal radiation was recorded in

^{a)}Electronic mail: dennischristensen@stud.ku.dk.



FIG. 1. (Color online) The thermographic measurements were performed by moving a plate of gadolinium out of a Halbach magnet, while recording the thermal radiation. The dimensions of the plate and Halbach magnet are given in the figure along with the defined coordinate system of the plate and the angle θ between the applied field and the y -direction (chosen normal to the plate). For the configuration shown here $\theta=0^\circ$. The Halbach magnet consists of 16 segments of permanent magnets each with a magnetization direction given by the arrows.

real-time using an infrared camera of the type Cedip FLIR Titanium SC7000. The camera was calibrated by measuring the intensity of the thermal radiation from a black body at two temperatures and interpolating linearly.

The experimental setup allows for variation in the angle θ in the xy -plane between the direction of the applied field and the y -direction, where the y -direction is chosen to be normal to the plate as illustrated in Fig. 1. Three orientations were investigated: $\theta=0^\circ$ (i.e., \mathbf{H}_{appl} parallel to the y -direction), $\theta=45^\circ$ and $\theta=90^\circ$ (i.e., \mathbf{H}_{appl} parallel to the x -direction).

To confirm that the temperature change in the plate is adiabatic, the plate was moved out of the applied field and the difference between the temperature of the surroundings and the average temperature of the plate was monitored over time. For both $\theta=0^\circ$ and $\theta=90^\circ$ the temperature difference, $|\Delta T|$, was well-described by an exponentially decaying func-

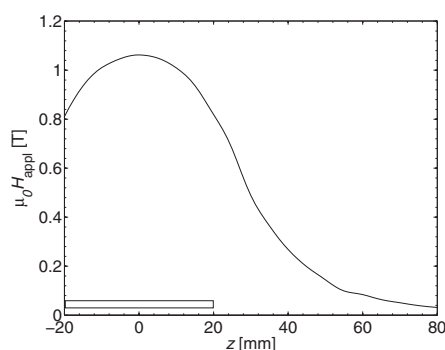


FIG. 2. The experimentally measured magnetic field strength, $\mu_0 H_{\text{appl}}$, of the Halbach magnet as a function of the distance, z , from the center of the magnet (from Ref. 8). The field strength is approximately constant in the xy -plane. The horizontal bar shows the spatial extent of the plate when placed inside the magnet.

tion, $|\Delta T| \propto \exp(-t/\tau)$, with a characteristic time constant, τ , of approximately a minute. Since the characteristic time for the temperature relaxation is almost two orders of magnitude larger than the time it takes to move the plate out of the magnet, the plate can be considered in adiabatic conditions.

Using the measured adiabatic temperature change as a function of the local magnetic field, taken from Ref. 9, the thermographically obtained adiabatic temperature change is converted into the corresponding change in the local magnetic field strength. The measurements in Ref. 9 are obtained using a type E thermocouple and the results have been corrected for demagnetization and thus represent the adiabatic temperature change without shape effects. Hence, the spatially varying adiabatic temperature change is directly measured in real-time using thermography, whereas the local magnetic field strength is determined indirectly.

III. MODEL

To predict the adiabatic temperature change a numerical model was developed, which operates in two steps.

First, the model solves for the spatially varying local magnetic field inside the plate when situated in the center of the Halbach magnet. The local field is calculated using the iterative, magnetostatic demagnetization approach described in Ref. 6 and the experimentally measured magnetization from Ref. 9. Assuming a negligible stray field at a distance of 100 mm from the center of the magnet, the magnetic field change is given directly by the calculated local magnetic field.

Second, the local magnetic field change is converted into the corresponding adiabatic temperature change using the aforementioned measurements of the adiabatic temperature change reported in Ref. 9. It is important to clarify that the measurements in Ref. 9 represent the adiabatic temperature change as a function of the local field, whereas the temperature change obtained using the model described here includes shape effects, which enter via the demagnetizing field.

When developing the model a few simplifying assumptions have been made: As the y -dimension of the plate is only 0.9 mm, heat transfer will, to some degree, smooth out the temperature variations in the y -direction; therefore the model averages the adiabatic temperature change in this direction. During the time it takes to move the plate out of the field (0.7 s), heat transfer is neglected in the x -direction and z -direction and between the plate and the surroundings. Furthermore, the applied magnetic field has been assumed homogeneous in the xy -plane.

IV. RESULTS AND DISCUSSION

The simulated and measured adiabatic temperature change and the corresponding changes in the local magnetic field strength are shown in Fig. 3. Since the stray field of the Halbach magnet is negligible, the change in the local magnetic field strength is also a direct measure of the local field. When the plate is moved out of the Halbach magnet, the center of the plate ($z=20$ mm) is subjected to a 30% higher applied magnetic field change compared to the field at the edges ($z=0$ mm and $z=40$ mm), see Fig. 2. This causes the

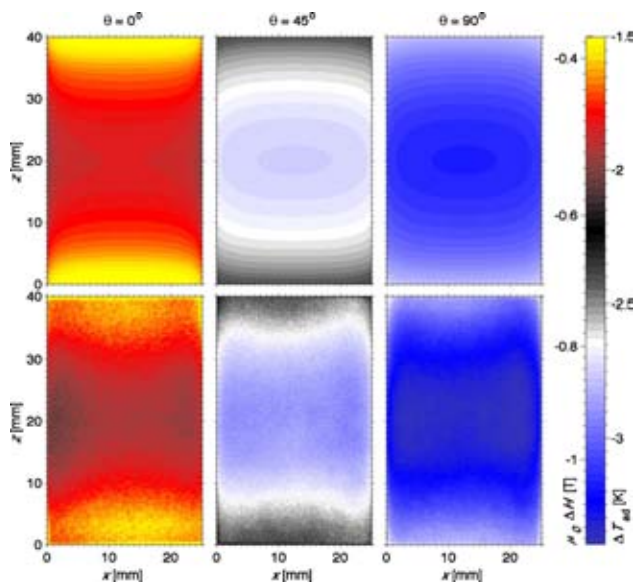


FIG. 3. (Color online) Simulated (first row) and measured (second row) adiabatic temperature change, ΔT_{ad} , and corresponding local magnetic field change, $\mu_0 \Delta H$, resulting from removing a plate of gadolinium from the applied magnetic field of a Halbach magnet. The angle θ between the applied magnetic field and the y -axis is 0° , 45° , and 90° in the first, second and third column, respectively. Note that the color scale is the same for all figures.

plate to experience a varying local magnetic field change and consequently a gradient in the adiabatic temperature change along the z -direction as observed in Fig. 3. In the model the applied magnetic field is assumed homogeneous in the xy -plane, and hence the uneven temperature distribution observed along the x -direction in the first row of Fig. 3 is solely due to the demagnetizing field. For $\theta=45^\circ$ and $\theta=90^\circ$ the applied field is, however, slightly larger at $x=0$ mm and $x=25$ mm compared to $x=12.5$ mm resulting in the largest temperature change near the edges and not at the center as predicted by the model. The difference between the model and the observed data is small and can be attributed to the inhomogeneous applied field. Hence the model is able to reproduce the spatial dependence of the changes in the temperature and local magnetic field strength, thereby validating the demagnetization approach described in Ref. 6.

The average change in the temperature and local magnetic field strength for various applied field orientations is given in Fig. 4. Here, the change in the average local magnetic field strength is increased by 50% when applying the magnetic field along the x -direction compared to the y -direction. The dependence of the sample orientation is a result of the demagnetizing field, since the average local magnetic field strength without taking demagnetization into account is independent of the angle θ assuming a homogeneous applied field in the xy -plane. Reducing the demagnetizing field increases the absolute value of the adiabatic temperature change from 1.8 to 3.2 K clearly showing the importance of taking the demagnetizing field into account as noted in Refs. 5 and 7.

The significant decrease in the absolute temperature change upon removal of a magnetic field oriented perpendicular to the plate has important consequences for magnetic

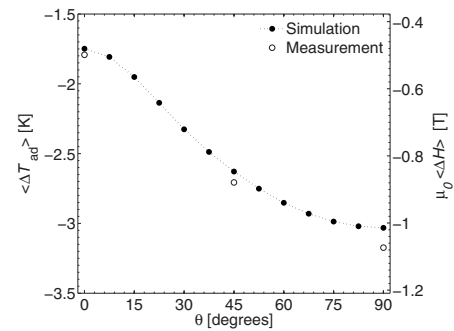


FIG. 4. Average adiabatic temperature change, $\langle \Delta T_{\text{ad}} \rangle$, and corresponding local magnetic field change, $\mu_0 \langle \Delta H \rangle$, as a function of the angle θ between the applied field and the y -axis.

cooling. Here, the temperature increase and decrease in a magnetocaloric material caused by application or removal of an applied magnetic field replaces the compression and expansion of a gas used in conventional cooling; for a review of magnetic cooling see Ref. 11. Therefore, increasing the magnitude of the adiabatic temperature change improves the efficiency of the cooling, hence making it important to choose geometries of the magnetocaloric materials and an orientation of the applied field, which minimize the demagnetizing field.

Furthermore, Fig. 3 suggests that a detailed description of the adiabatic temperature change requires a spatial resolution due to the observed inhomogeneities. Here, these inhomogeneities are caused by an inhomogeneous applied magnetic field and the demagnetizing field. In addition, numerical simulations⁶ predict that the local magnetic field, and consequently the adiabatic temperature change, is highly inhomogeneous when the material is subject to an inhomogeneous temperature distribution or when the Curie temperature varies with position inside the material. Both conditions are often met in magnetic refrigeration as the temperature span between the surrounding and the inside of the refrigerator causes the magnetocaloric material to experience a temperature gradient. Since the adiabatic temperature change is maximized at temperatures around the Curie temperature, one often utilizes graded materials where the Curie temperature changes with position in order to match the temperature gradient. The effect of material grading and the temperature gradient can also be investigated experimentally using the thermographic technique presented here if a heat source and sink is placed in either end of a graded material.

Though the thermographic method described here provides a simple way of mapping the spatial dependence of the local magnetic field and adiabatic temperature change in real-time, it is subject to some limitations. First, the thermographic measurements only probe the surface temperature. Second, only the magnitude of the local magnetic field can be determined making it possible to extract the demagnetizing field from Eq. (1) only when the dominant component of the local magnetic field is along the applied field or when the direction can be deduced from symmetry considerations. For example, consider an applied magnetic field oriented along the x -axis, y -axis or z -axis. For these orientations the local magnetic field must be invariant under 180° rotation around

the axis of the applied field, and consequently the mean of the local magnetic field can only have a nonzero component parallel with the applied field. Third, the material of interest must exhibit a measurable adiabatic temperature change. Several such materials have been reviewed in Ref. 10.

V. CONCLUSION

The spatially varying adiabatic temperature change in a plate of gadolinium was measured directly using thermography, and the adiabatic temperature change was converted into the corresponding change in the local magnetic field strength. The measured change in the temperature and local magnetic field strength was compared to the results from a numerical model, which utilizes a magnetostatic demagnetization approach and experimentally measured data. The model is able to predict both the spatial dependence and the magnitude of the measured temperature and local magnetic field change hence validating the demagnetization approach. The adiabatic temperature change and local magnetic field strength are found to be highly dependent on the orientation of the applied field due to the demagnetizing field.

ACKNOWLEDGMENTS

The authors thank the support of the Programme Commission on Energy and Environment (EnMi) (Contract No. 2104-06-0032), which is part of the Danish Council for Strategic Research.

¹J. A. Osborn, *Phys. Rev.* **67**, 351 (1945).

²R. I. Joseph and E. Schloemann, *J. Appl. Phys.* **36**, 1579 (1965).

³K. Tang, H. W. Zhang, Q. Y. Wen, and Z. Y. Zhong, *Physica B* **363**, 96 (2005).

⁴M. Beleggia and M. De Graef, *J. Magn. Magn. Mater.* **263**, L1 (2003).

⁵O. Peksoy and A. Rowe, *J. Magn. Magn. Mater.* **288**, 424 (2005).

⁶A. Smith, K. K. Nielsen, D. V. Christensen, C. R. H. Bahl, R. Bjørk, N. Pryds, and J. Hattel, *J. Appl. Phys.* **107**, 103910 (2010).

⁷C. R. H. Bahl and K. K. Nielsen, *J. Appl. Phys.* **105**, 013916 (2009).

⁸K. K. Nielsen, R. Bjørk, J. B. Jensen, C. R. H. Bahl, N. Pryds, A. Smith, A. Nordentoft, and J. Hattel, Eighth IIR Gustav Lorentzen Conference on Natural Working Fluids, Copenhagen, September 7–10, 2008.

⁹R. Bjørk, C. R. H. Bahl, and M. Katter, *J. Magn. Magn. Mater.* **322**, 3882 (2010).

¹⁰K. A. Gschneidner, Jr., V. K. Pecharsky, and A. O. Tsokol, *Rep. Prog. Phys.* **68**, 1479 (2005).

¹¹K. A. Gschneidner, Jr. and V. K. Pecharsky, *Int. J. Refrig.* **31**, 945 (2008).

A.1 Papers published in peer-reviewed international scientific journals

A.1.5 A comprehensive parameter study of an active magnetic re-generator using a 2D numerical model; published in International Journal of Refrigeration

available at www.sciencedirect.comjournal homepage: www.elsevier.com/locate/ijrefrig

A comprehensive parameter study of an active magnetic regenerator using a 2D numerical model

K.K. Nielsen^{a,b,*}, C.R.H. Bahl^b, A. Smith^b, N. Pryds^b, J. Hattel^a

^a Department of Mechanical Engineering, Technical University of Denmark, Building 425, Niels Koppels Alle, DK-2800 Kgs. Lyngby, Denmark

^b Fuel Cells and Solid State Chemistry Division, Risø National Laboratory for Sustainable Energy, Technical University of Denmark, Frederiksborgvej 399, DK-4000 Roskilde, Denmark

ARTICLE INFO

Article history:

Received 7 August 2009

Received in revised form

14 December 2009

Accepted 28 December 2009

Available online 14 January 2010

Keywords:

Magnetic refrigerator

Simulation

Performance

Heat transfer

Heat exchange

Regenerator

Gadolinium

ABSTRACT

A two-dimensional numerical heat transfer model is used to investigate an active magnetic regenerator (AMR) based on parallel plates of magnetocaloric material. A large range of parameter variations are performed to study the optimal AMR. The parameters varied are the plate and channel thicknesses, cycle frequency and fluid movement. These are cast into the non-dimensional units utilization, porosity and number of transfer units (NTU). The cooling capacity vs. temperature span is mapped as a function of these parameters and each configuration is evaluated through the maximum temperature span and exergy. The results show that the optimal AMR should have a utilization in the range 0.2–1 and an NTU higher than 10 and not necessarily more than 30. It is concluded that parallel plate-based regenerators face significant challenges in terms of manufacturability. However, the benefit of parallel plate regenerators is a very low pressure drop, which is needed for high performance.

© 2010 Elsevier Ltd and IIR. All rights reserved.

Etude approfondie sur les paramètres des régénérateurs magnétiques actifs à l'aide d'un modèle numérique bidimensionnel

Mots clés : Réfrigérateur magnétique ; Simulation ; Performance ; Transfert de chaleur ; Échange de chaleur ; Régénérateur ; Gadolinium

* Corresponding author at: Fuel Cells and Solid State Chemistry Division, Risø National Laboratory for Sustainable Energy, Technical University of Denmark, Frederiksborgvej 399, DK-4000 Roskilde, Denmark. Tel.: +45 4677 4758.

E-mail address: kaki@risoe.dtu.dk (K.K. Nielsen).

0140-7007/\$ – see front matter © 2010 Elsevier Ltd and IIR. All rights reserved.

doi:10.1016/j.ijrefrig.2009.12.024

Nomenclature*Variables*

T	Temperature [K]
T_C	Curie temperature [K]
T_∞	Ambient temperature [K]
c_p	Specific heat capacity [J/kg K]
ρ	Mass density [kg/m ³]
k	Thermal conductivity [W/m K]
h	Convective heat transfer coefficient [W/m ² K]
τ_1	Timing of magnetization part of the AMR cycle [s]
τ_2	Timing of hot blow part of the AMR cycle [s]
τ_3	Timing of demagnetization part of the AMR cycle [s]
τ_4	Timing of cold blow part of the AMR cycle [s]
τ_{rel}	Equal to $\tau_1/\tau_2 = \tau_3/\tau_4$ [-]
τ_{tot}	Equal to $2(\tau_1 + \tau_2)$ [s]
μ_0	Vacuum permeability equal to $4\pi \cdot 10^{-7}$ N/A ²
$\mu_0 H$	Magnetic field [T]
H	Height [mm]
L	Length [m]
W	Width [m]
V	Volume [m ³]
D_H	Hydraulic diameter [m]
\dot{m}	Mass flow rate [kg s ⁻¹]
f	Frequency [Hz]
Δx	Fluid stroke length as fraction of total plate length [-]
ϕ	Utilization [-]
ε	Porosity [-]
Q_c	Cooling power [W/kg]

α	Slope of cooling power vs. temperature span [W/kg K]
β	Zero temperature span cooling power [W/kg]
Q_{max}	Maximum cooling power [W/kg]
Ex_Q	Exergy [W/kg]
Ex_{max}	Maximum exergy [W/kg]
\dot{q}''	Boundary surface heat flux [W/m ²]
Δp	Pressure drop [Pa]
μ_f	Dynamic viscosity [Pa s]
\dot{w}_{pump}	Pump work [W/kg]

Abbreviations

AMR	Active Magnetic Regenerator
MCE	Magnetocaloric effect
MCM	Magnetocaloric material
MFT	Mean field theory
HHEX	Hot heat exchanger
CHEX	Cold heat exchanger
Gd	Gadolinium
NTU	Number of Transfer Units

Parameters

Nu_m	Mean Nusselt number
Gz_L	Graetz number
Bi	Biot number
Re	Reynolds' number

Sub- and superscripts

f	Fluid
r	Regenerator

1. Introduction**1.1. Background**

Magnetic refrigeration at room temperature is a promising technology for obtaining higher energy efficiency and a lower environmental impact due to the possible usage of non-toxic solid refrigerants in comparison with conventional vapour-compression based refrigeration (Gschneidner and Pecharsky, 2008).

So far a range of experimental Active Magnetic Regeneration (AMR) devices have been constructed that demonstrate the applicability of magnetic refrigeration (Tura and Rowe, 2007; Rowe et al., 2006; Okamura et al., 2006; Zimm et al., 2006; Bahl et al., 2008). Some optimization has also been conducted in terms of operating parameters and regenerator geometry. However, a mapping of how the various parameters influence the performance of active magnetic regenerative refrigerators has not been published in large scale so far. This work contributes with such a mapping.

The outline of this paper is the following: in the remainder of the current section the design and operating parameters are presented and they are cast into standard non-dimensional variables for making comparison across various experimental designs straightforward. In Section 2 the results are presented

in their non-dimensional form and discussed. Finally, in Section 3 the work is concluded and put into perspective.

1.2. Design and parameters

In this work the theoretical cooling capacity of an AMR device based on a regenerator with parallel plates of gadolinium (Gd) modeled via the mean field theory (MFT) as described in e.g. Morrish (1965) is addressed. The magnetic field change has been set to be from 0 to 1 tesla (T) and the input parameters for the MFT are equivalent to those for Gd given in Petersen et al. (2008b). The specific heat of the magnetocaloric material is modeled through the MFT (for the magnetic part) and using the Debye and Sommerfeld models (Ashcroft and Mermin (1976)) for the structural and electron contributions to the specific heat. The specific heat is updated in each time step of the numerical solution.

The reason for choosing Gd is that it can be fairly well described via the MFT and Gd is the material of choice for many AMR test devices. However, it is not claimed that the MFT perfectly reproduces the magnetocaloric effect (MCE) of Gd but it does provide a good basis for comparison and does not lack the typically insufficient parameter coverage of MCE data sets found through experiments. The reason why the magnetic field change is chosen to be from 0 to 1 T is that this

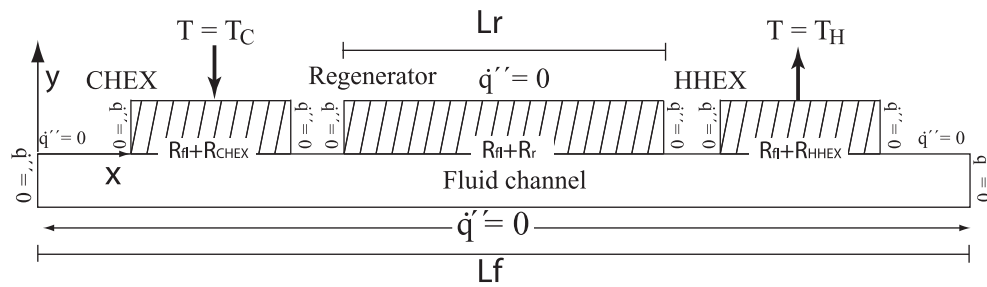


Fig. 1 – The geometry of the model. Shown are half a fluid channel, half an MCM plate, half a cold heat exchanger (CHEX) and half a hot heat exchanger (HHEX). Also the thermal boundary conditions are indicated. The figure is reproduced in revised form from Nielsen et al. (2009).

is roughly what is expected to be feasible for permanent magnets in large scale devices to produce. Permanent magnets may be designed to produce up to 2 T in field change, however, the cost of such magnets and the rather small volume available for the regenerator make this unrealistic in a large scale device (Bjørk et al., 2008).

The geometry of the model is 2-dimensional with the resolved dimensions being parallel to the flow (denoted the x-direction) and orthogonal to the plane of the magnetocaloric plates, denoted the y-direction. Fig. 1 shows the modeled geometry. Symmetry is used and thus only half an MCM plate and half a fluid channel are modeled.

The lengths of the regenerator L_r and fluid domains L_f were kept constant at 0.05 m and 0.16 m respectively in all the simulations.

So far an investigation of the cooling capacity as a function of temperature span has not been reported in the literature in large detail. This work is focused on varying a range of the most common parameters in the AMR system by modeling and thus to extract important information on the performance of the generic AMR system.

The model used to simulate the AMR is described in detail in Nielsen et al. (2009). The parameters varied are the regenerator plate thickness H_r , the fluid channel thickness H_f , the fluid stroke length Δx expressed as fraction of regenerator length L_r , the total cycle time τ_{tot} and the ratio τ_{rel} between the duration of the magnetization period and the duration of the blow period. The simulated cycle with the duration τ_{tot} consists of four substeps, namely the magnetization (duration τ_1), fluid flow from cold to hot end called the hot blow (duration τ_2), the demagnetization period (duration τ_3) and finally the cold blow period where the heat transfer fluid is moved from the hot towards the cold end (duration τ_4). The cycle is symmetric

meaning that $\tau_1 = \tau_3$ and $\tau_2 = \tau_4$. Furthermore, the fraction between the magnetization process timing and the flow process timing is $\tau_{rel} = \tau_1/\tau_2 = \tau_3/\tau_4$. The cycle frequency is $f = 1/\tau_{tot}$. Table 1 provides an overview of the parameter space covered.

This parameter space is based on estimates of realistic geometrical and operating conditions for a parallel plate AMR. The minimum flow channel and plate thicknesses are estimated from realistic manufacturability. The timings, or frequencies, are chosen from a practical viewpoint. The stroke lengths are chosen from experimental experience (e.g. Bahl et al., 2008).

1.3. Non-dimensionalizing the parameters

The process and geometrical parameters are to a certain extent fixed in terms of the specific regenerator system modeled. Therefore they are cast into a non-dimensional form through the three parameters utilization, ϕ , porosity, ϵ , and number of transfer units, NTU. The ranges of the non-dimensional parameters included in this study are given in Table 2.

The utilization is defined as

$$\phi = \frac{\rho_f V_f c_{p,f}}{\rho_r V_r c_{p,r} (\mu_0 H = 0, T = T_c)} \quad (1)$$

Table 2 – The range of the three non-dimensional units used to plot the results in a meaningful and generic way.

Non-dimensional unit	Range
ϕ	0.14–6.4
ϵ	0.17–0.8
NTU	0.16–74.8

Table 1 – The system-specific parameters covered in this survey. The total number of AMR simulations amounts to all combinations of this table multiplied by seven for the number of different temperature spans.

Parameter	Values
Δx [%]	40, 50, 60, 70, 80, 90
τ_{tot} [s]	0.25, 0.5, 1.0, 2.0, 3.0, 4.0, 5.0, 6.0, 7.0
τ_{rel} [-]	0.25, 0.5
H_f [mm]	0.2, 0.3, 0.4, 0.5, 0.6, 0.7, 0.8, 0.9, 1.0
H_r [mm]	0.25, 0.5, 0.75, 1.0

Table 3 – The thermal properties of the MCM and the heat transfer fluid (water).

Parameter	Value
ρ_f	1000 kg/m ³
ρ_r	7900 kg/m ³
$c_{p,f}$	4200 J/kg K
$c_{p,r}(\mu_0 H = 0, T = T_c)$	300 J/kg K

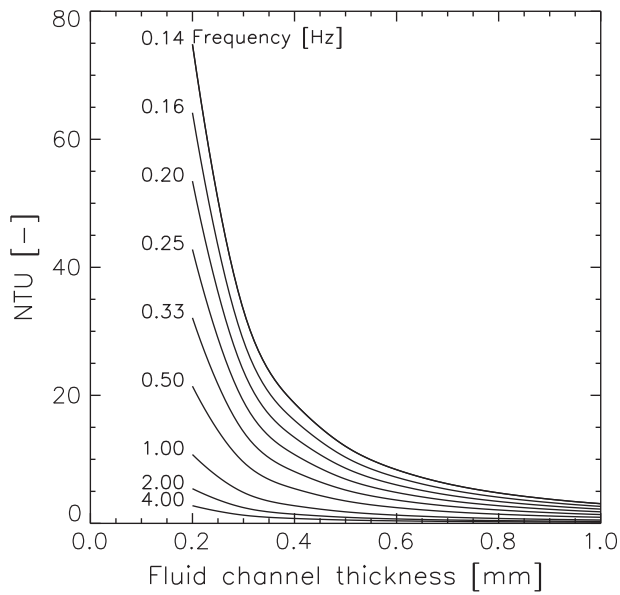


Fig. 2 – The number of transfer units (NTU) as a function of fluid channel thickness for the operating frequencies covered.

Subscripts f and r denote fluid and regenerator respectively. The mass density is denoted by ρ and the specific heat capacity as c_p . The specific heat of the regenerator material is evaluated at the transition, or Curie, temperature at zero magnetic field following Tura and Rowe (2009). The values of these parameters are given in Table 3. V_r denotes the total volume of the regenerator material per repeating unit and is thus equal to $H_r \times L_r \times W_r$, where W_r denotes the width of the regenerator. V_f denotes the volume of the fluid per repeating unit moved during either blow period and is thus

$$V_f = \frac{\dot{m}}{\rho_f} \tau_2 = H_f W_r L_r \Delta x, \quad (2)$$

with \dot{m} denoting the mass flow rate. The utilization expresses physically the ratio of thermal mass of the moved fluid to the total thermal mass of the regenerator.

The porosity is simply expressed as

$$\varepsilon = \frac{H_f}{H_f + H_r}, \quad (3)$$

and thus denotes the ratio between the fluid volume and the total volume.

An expression for the number of transfer units for laminar flow between parallel plates found in Nickolay and Martin (2002) is

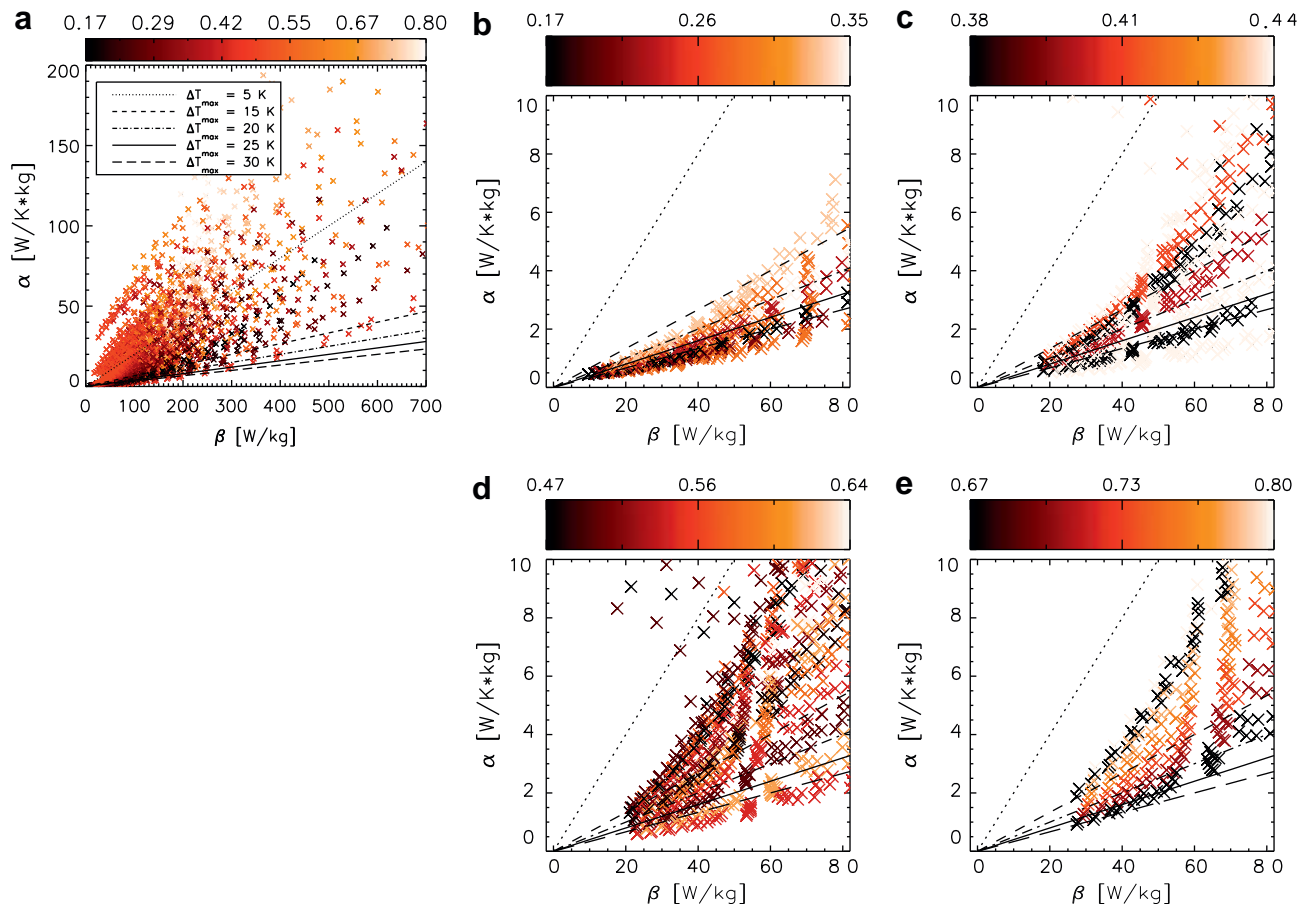


Fig. 3 – The slope of the cooling capacity vs. temperature span curve (α) as a function of zero temperature span cooling power (β). The color mapping indicates the porosity, ε . The straight lines indicate iso maximum temperature span curves. Points below a given line are configurations able to yield a higher temperature span than indicated. (a) shows the total parameter space covered. (b)–(e) show a magnified area of the most data-point dense region divided into four ranges of values of the porosity for clarity.

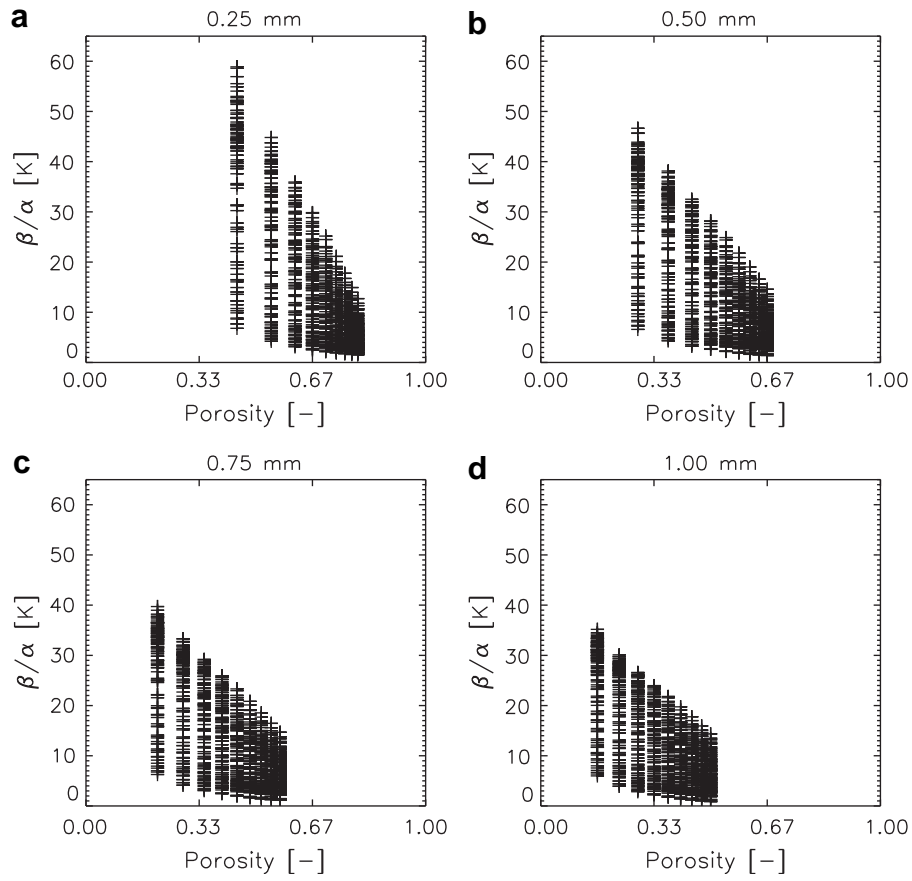


Fig. 4 – The maximum temperature span, β/α , as a function of porosity. Each subfigure, (a)–(d), shows the results for a specific plate thickness (0.25–1.0 mm respectively).

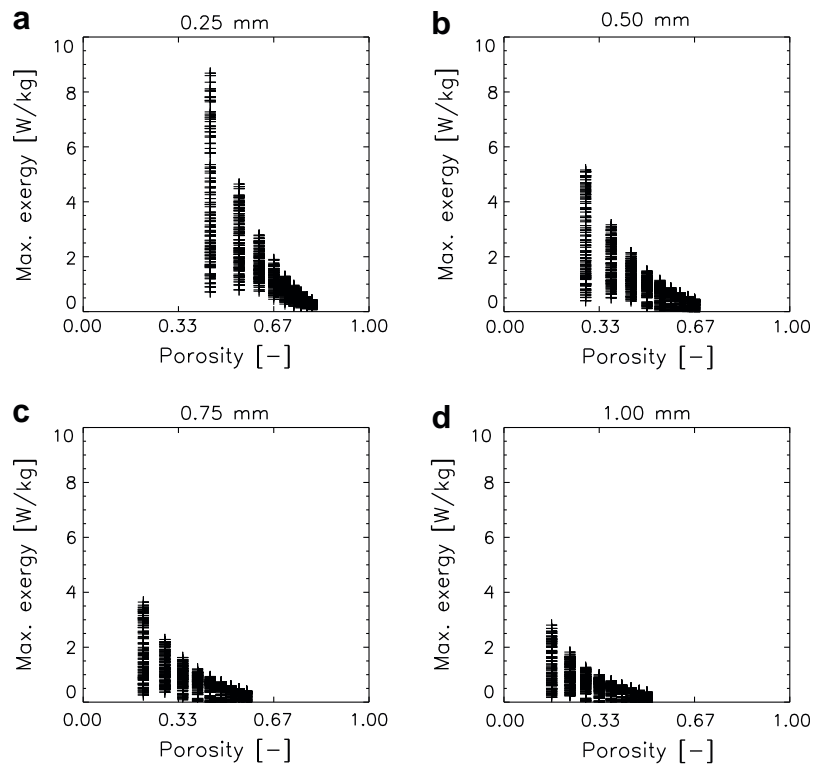


Fig. 5 – The maximum exergy as defined in Eq. (9) as a function of porosity. Each subfigure, (a)–(d), shows the results for a specific plate thickness (0.25–1.0 mm respectively).

$$NTU = 4 \frac{Nu_m}{Gz_L}, \quad (4)$$

where also the mean Nusselt number, $Nu_m \equiv hD_H/k_f$ for a blow of length L is found. The convective heat transfer coefficient, h , and the hydraulic diameter, $D_H = 2H_f$ have been introduced. The NTU expresses how fast the temperature in the fluid and the solid equalize during a blow period (this goes as $\exp(-NTU)$). The mean Nusselt number and the Graetz number are defined as Nickolay and Martin (2002)

$$\begin{aligned} Nu_m &= (Nu_1^n + Nu_2^n)^{1/n} \\ Nu_1 &= 7.541 \quad Nu_2 = 1.841Gz_L^{1/3} \quad n = 3.592 \\ Gz_L &= 4 \frac{H_f^2}{\alpha_f \tau_2}. \end{aligned} \quad (5)$$

The expression for the Graetz number has been rewritten to the form given in Petersen et al. (2008a); $\alpha_f = k_f/c_p \rho_f$ is the thermal diffusivity of the fluid. The diffusivity is constant for this case and thus the NTU is a function of blow period timing and channel thickness only. In Fig. 2 the NTU is plotted as a function of fluid channel thickness for each cycle frequency simulated. As expected it is observed that the faster an AMR cycle is, the thinner the fluid channel should be in order to

keep a high value of the NTU. In Li et al. (2006) (their Fig. 2) it is found that the value of the NTU should be above 10 for obtaining the maximum possible efficiency of the regenerator (dependent on the utilization). Therefore it may be expected from Fig. 2 that the simulation results obtained with total cycle frequencies of 1.0 Hz or greater are significantly less optimal than those at smaller frequencies for the otherwise same operating parameters.

The Biot number can be written as

$$Bi \equiv \frac{hH_f}{k_r} = Nu_m \frac{k_f}{k_r} \frac{H_f}{2H_f}. \quad (6)$$

Where the definition of the Nusselt number has been used.

If the Biot number is less than one the heat transfer from the interior of the regenerator plate to the boundary interface between the plate and the fluid is faster than the heat transfer across the boundary. Thus, in this case, the plate is essentially able to supply the heat transfer fluid with heat at all times. In the opposite case, if the Biot number is greater than one, the heat transfer within the plate is too slow and the performance may therefore be expected to decrease. The range of the Biot numbers in the present modeled parameter survey is 0.05–1.11.

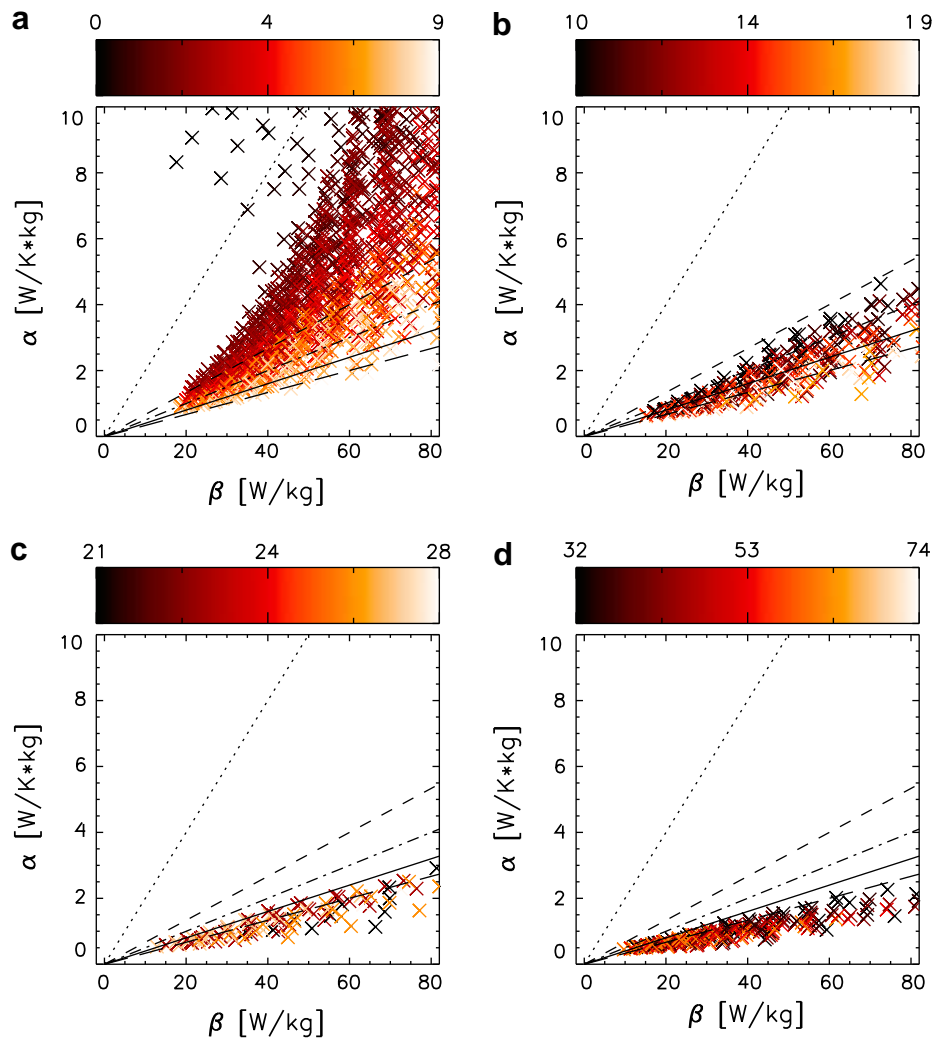


Fig. 6 – The slopes of the cooling curves (α) as a function of maximum cooling power (β) color mapped with NTU divided into four ranges in subfigures (a)–(d). The lines indicate, as in Fig. 3, iso maximum temperature span curves.

1.4. Obtaining the cooling capacity

For each parameter configuration seven simulations were run. The temperature span between the hot heat exchanger (HHEX) and the cold heat exchanger (CHEX) was set to vary from 0 to 30 K in increments of 5 K and thus the cooling power, Q_c , in steady-state was found as a function of imposed temperature span. A total of 27,216 simulations were carried out in order to obtain cooling curves for each parameter configuration (i.e. all combinations possible from Table 1 for seven different temperature spans). In all experiments the ambient temperature experienced by the HHEX was set to $T_\infty = 298$ K.

For each parameter configuration the following expression was fitted to obtain the cooling power

$$Q_c = -\alpha\Delta T + \beta, \quad (7)$$

assuming a linear relation between the cooling power and the temperature span ΔT . The assumption of linearity is justified through both the modeling results and experimental experience (Zimm et al., 2006; Nielsen et al., 2008; Oliveira et al., 2009; Tura and Rowe, 2009). The standard error on the fitted

values of α and β are all within 5%. The offset of the cooling curve, β , expresses the zero temperature span cooling power $Q_{c,\max}$ and the ratio between the offset and the slope, β/α , expresses the zero cooling load temperature span ΔT_{\max} . It should be noted that in the case of a negative temperature span Eq. (7) is also valid. This is seen both from the model results (not all configurations included in this survey can sustain temperature spans up to 30 K) and through experiments (e.g. Nielsen et al., 2008).

2. Results and discussion

Considering the slope of the cooling curve, α , and the offset, β , it is somewhat complicated to define what their optimal values are. The two parameters are tightly connected and together they provide information on the cooling capacity and obtainable temperature span. It is expected that the maximum temperature span is a function of regenerator efficiency only (obviously at a fixed magnetic field change) whereas the cooling power is expected also to be proportional

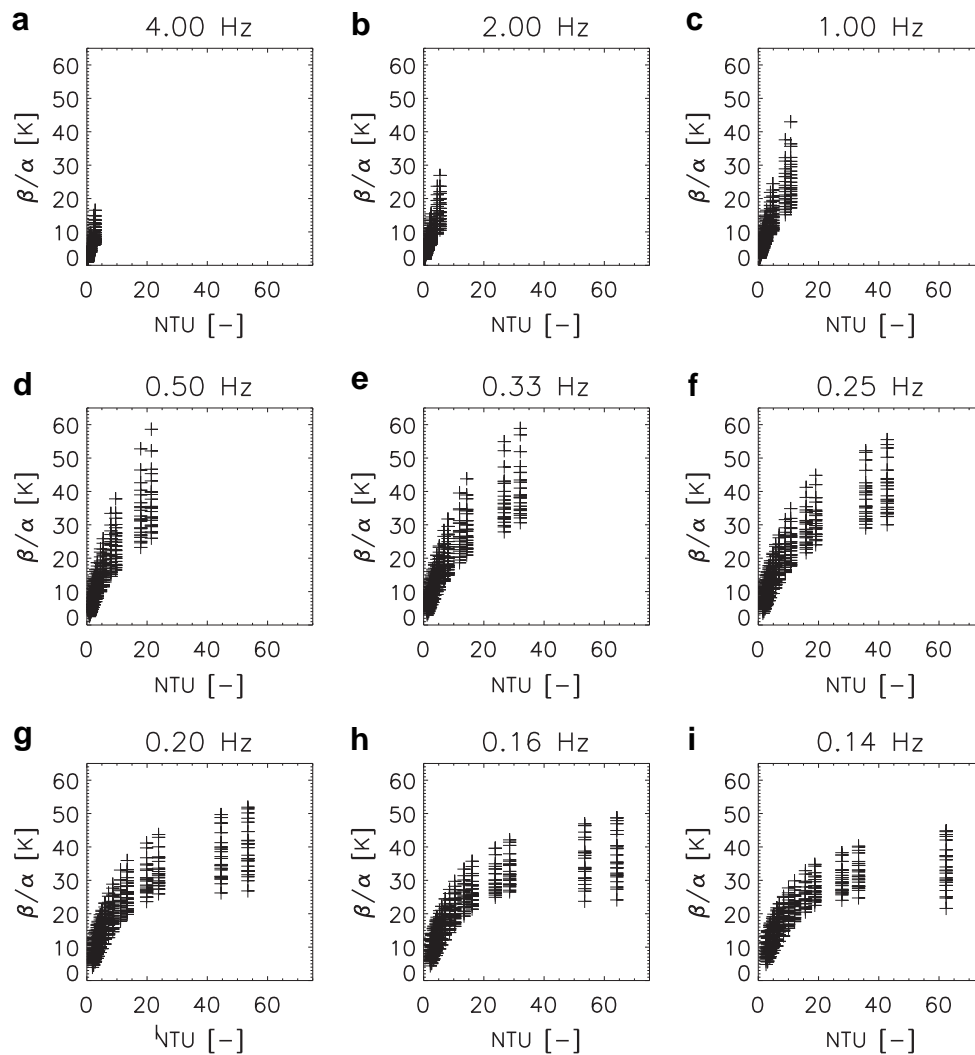


Fig. 7 – The maximum temperature span, β/α , as a function of NTU. Each subfigure, (a)–(i), shows a specific operating frequency, 4–0.14 Hz respectively.

to the operating frequency and the amount of active material in the regenerator. Therefore the probing parameters have been normalized in units of mass of magnetocaloric material.

In order to evaluate the performance of the individual configuration a third parameter, the exergy or available cooling power, is introduced:

$$\text{Ex}_Q(Q_c) = \frac{Q_c(Q_{\max} - Q_c)}{Q_{\max}(T_\infty/\Delta T_{\max}) - (Q_{\max} - Q_c)} = \frac{Q_c(\beta - Q_c)}{\alpha T_\infty - (\beta - Q_c)} \quad (8)$$

as defined in Rowe (2009). The maximum cooling capacity Q_{\max} and the maximum temperature span ΔT_{\max} have been expressed in terms of α and β . The maximum exergy is obtained at approximately $Q_c = Q_{\max}/2$ (Rowe, 2009), thus

$$\text{Ex}_{\max} = \text{Ex}_Q(Q_{\max}/2) = \frac{\beta/4}{\alpha T_\infty/\beta - 1/2}. \quad (9)$$

2.1. Dependence on porosity

In Fig. 3 the porosity is mapped as a function of α and β . From the plots it is evident that the porosity should be minimized in order to get the best values of ΔT_{\max} . Higher values generally

seem to yield too low temperature spans to be usable. The general trend seems to be that a lower porosity is better. It is noted, however, that not all configurations with a low porosity are automatically optimal. As can be seen from Fig. 3 some of these configurations are quite far from optimal, which only confirms that the porosity is not the only important parameter for the performance of the AMR.

Fig. 4 shows the maximum temperature span as a function of porosity for each plate thickness included in this survey. From the figure the trend seems to be a monotonical decrease in the maximum temperature span as a function of porosity. Furthermore, the thinner the plate the higher the maximum temperature span can be achieved.

The plot of the maximum exergy (Fig. 5) as defined in Eq. (9) as a function of porosity is seen to have the same trends as for the maximum temperature span. Nevertheless, the decrease in maximum exergy as a function of porosity is somewhat more steep than the decrease in maximum temperature span (as seen in Fig. 4).

It is concluded that the porosity and the plate thickness should be minimized when considering the maximization of exergy and temperature span. Furthermore, the present

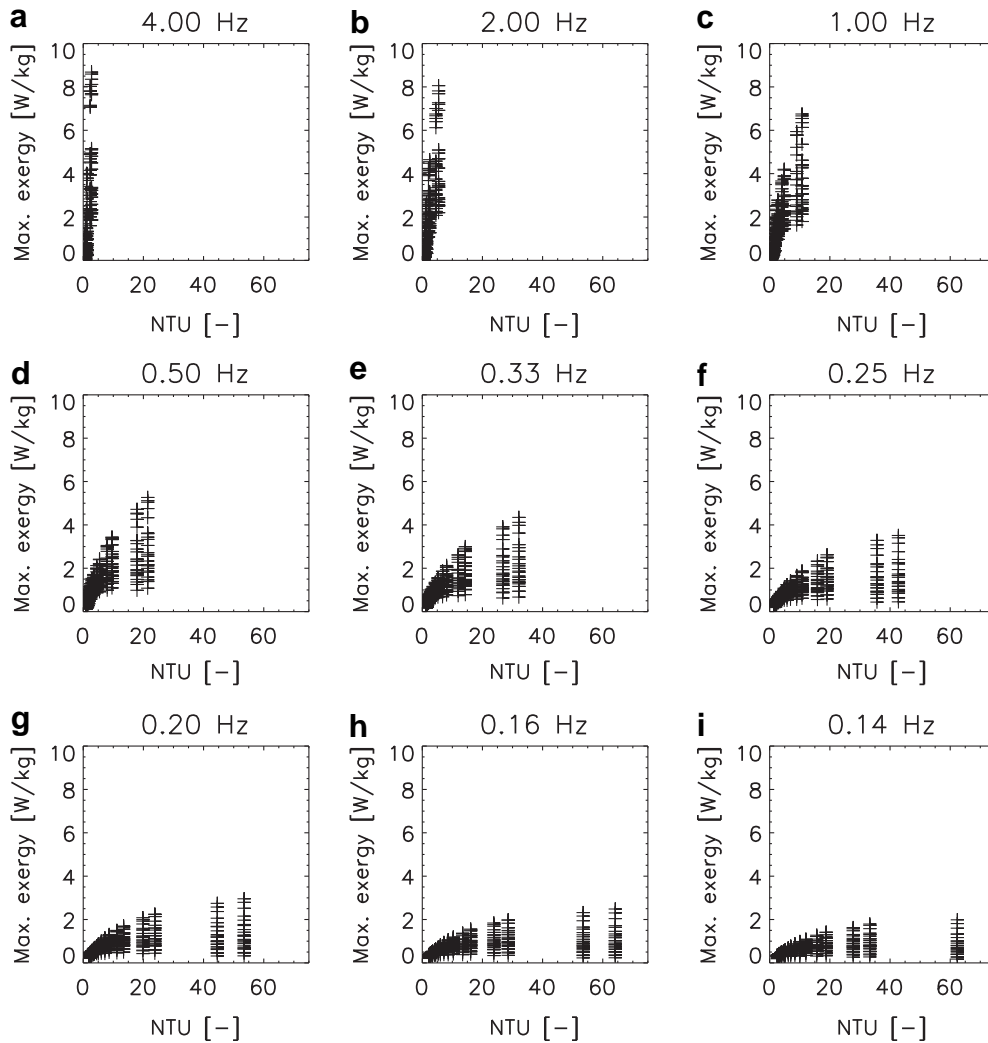


Fig. 8 – The maximum exergy as defined in Eq. (9) as a function of NTU. The subfigures (a)–(i) each show the results for a specific frequency, 4–0.14 Hz respectively.

survey is limited to a minimum porosity of 0.17 and it can therefore not be determined whether an optimum porosity value exists below a value of 0.17.

2.2. Dependence on NTU

Fig. 6 maps the number of transfer units as a function of α and β . A clear trend is observed, namely that the larger the value of the NTU the higher the maximum achievable temperature span. The color scale of Fig. 6 shows that the configuration with a value of the NTU between 5 and 10 is situated between the lines denoting maximum temperature spans of 15 K and 20 K, respectively. Between the lines denoting maximum temperature spans of 20 K and 25 K respectively the value of the NTU lies in the range of approximately 10 and 15. The trend continues for higher maximum temperature spans.

Considering Fig. 7 it is seen that within the parameter space covered here the high values of NTU are at the lowest frequency. This was expected from Fig. 2 as well. However, the largest temperature span is obtained at values of the NTU less than half the maximum spanned by the present parameter

space, i.e. between 20 and 30 but at higher cycle frequencies (in the range 0.3–0.5 Hz).

Fig. 8 shows that for a given frequency the higher the value of the NTU the higher the maximum exergy. However, the frequency of the cycle has a significant impact. It is evident from the figure that a higher frequency yields a higher maximum exergy at a lower value of the NTU. Therefore the cycle frequency may compensate somewhat for a lower value of the NTU.

Combining the results from Figs. 7 and 8 it is concluded that the geometrical constraints on the regenerator pose quite a firm upper limit in terms of the NTU, namely a value of roughly 30. This leaves room for operating at higher frequencies, which evidently yields the most optimal performance considering the maximization of the exergy.

2.3. Dependence on the utilization

The utilization is mapped as a function of α and β in Fig. 9. Not surprisingly, the largest temperature spans are obtained for the smallest values of the utilization. More interestingly, it is observed that values of the utilization up to about 1 seem

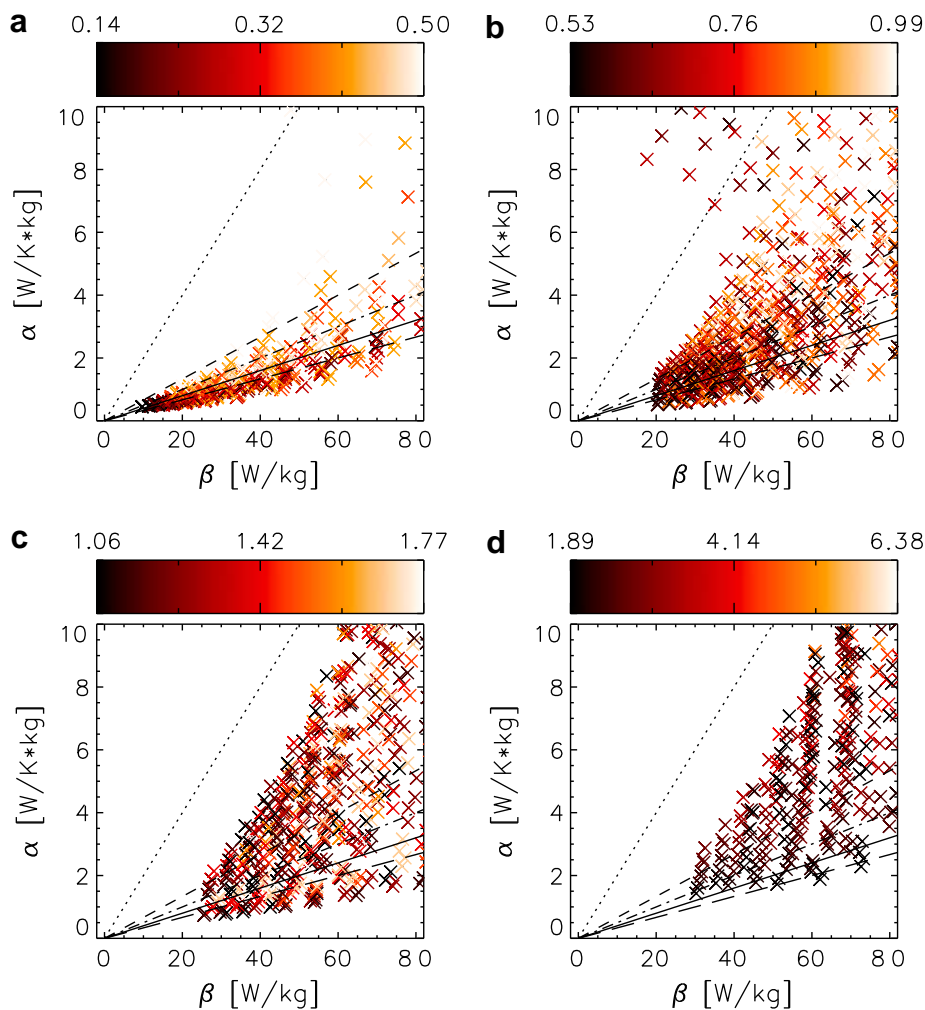


Fig. 9 – The cooling curve slope, α , as a function of the zero temperature span cooling capacity, β , color mapped with utilization. The straight lines indicate the same as in Fig. 3. The utilization has been divided into four intervals as indicated in subfigures (a)–(d) for clarity.

feasible in terms of obtaining a high maximum temperature span and at the same time maintaining a reasonable cooling power. This is in good accordance with the results of e.g. Li et al. (2006) and Tura and Rowe (2009).

Fig. 10 shows that the maximum temperature span is obtained at the lowest values of the utilization independently of the cycle frequency. Fig. 11 shows that the maximum exergy is optimized at values of the utilization around one independent of the frequency. However, the figure also shows that the utilization is not the only parameter characterizing the optimal maximum exergy.

2.4. Influence of the cycle timing

The total cycle time, τ_{tot} , should generally be minimized in order to increase the cooling capacity and maximize the exergy. This poses a problem since the regenerator geometry puts a tight constraint on how fast the AMR device can be operated. The NTU should be in the range 10–30 as previously mentioned and since the NTU decreases with increasing frequency (Fig. 2), a faster operating AMR device demands a smaller geometry, i.e. thinner plates and closer spacing.

At the same time the fraction τ_{rel} between the time of magnetization (τ_1) and the blow period (τ_2) should be minimized. This is both observed in the present simulated parameter space and can also be argued logically in the following way: the time used for magnetization/demagnetization is a period where no cooling power is generated (the fluid is stationary) and is thus practically wasted time.

2.5. Influence of pressure drop

Even though the model does not take pressure drop directly into account – it is, of course, implicitly included through the flow profile – it is possible to estimate the pressure drop and pumping power required. The pressure drop for a channel pipe may be expressed as (Incropera and DeWitt, 1996)

$$\Delta p = \frac{96}{\text{Re}} \frac{L_f}{D_H} \frac{u^2}{2}, \quad (10)$$

where u is the mean fluid velocity and the Reynolds' number is $\text{Re} = \rho_f u D_H / \mu_f$ with μ_f denoting the dynamic viscosity of the fluid. The pump work per mass of the regenerator, \dot{w}_{pump} , is

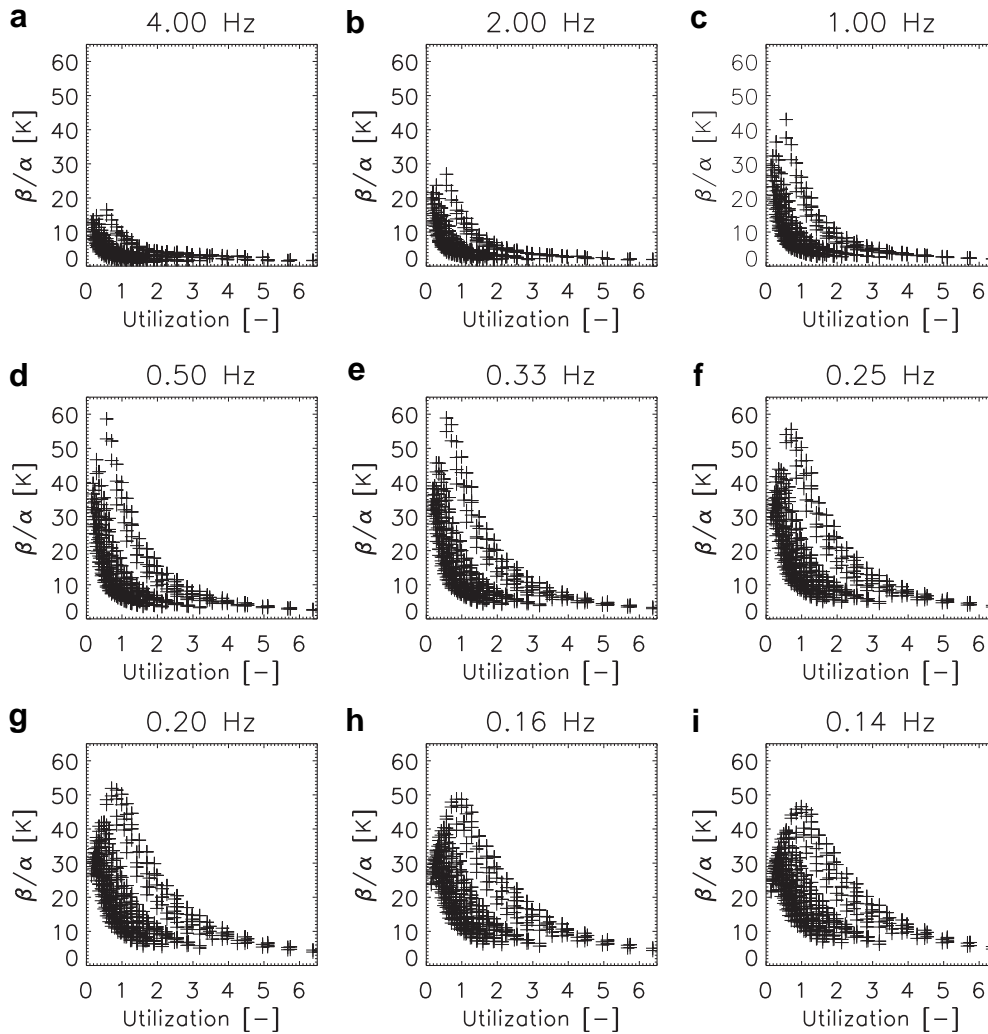


Fig. 10 – The maximum temperature span, β/α , as a function of utilization. The nine subfigures (a)–(i) each show a specific operating frequency, 4–0.14 Hz respectively.

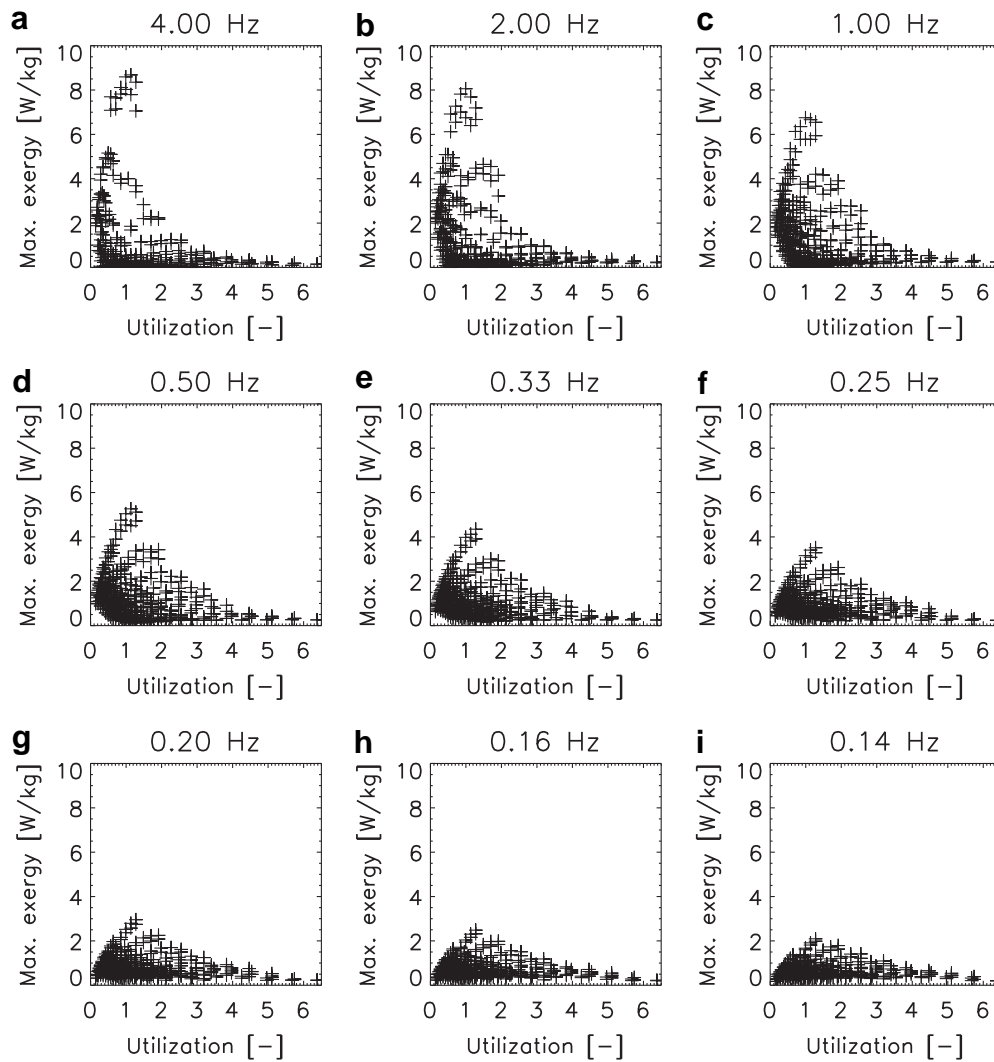


Fig. 11 – The maximum exergy as defined in Eq. (9) as a function of utilization. Each subfigure, (a)–(i), shows a specific frequency, 4–0.14 Hz respectively.

then expressed as the pressure drop multiplied with the volume flow

$$\dot{w}_{\text{pump}} = 2 \frac{\Delta p u H_f}{\rho_f L_f H_r} = 24 \frac{\mu_f u^2}{\rho_f} \frac{1}{H_f H_r} \quad (11)$$

Now, from Table 1 the two parameter configurations with the largest and smallest pressure drops and pump works can be found. The smallest pressure drop is found when the fluid channel is largest and the flow velocity minimal, i.e. at the shortest stroke length and the lowest cycle frequency. The greatest value of the pressure drops when the situation is reversed, i.e. when the flow channel and cycle frequency are minimal and the stroke length maximum.

The pump work is maximized when the flow velocity is maximum and the flow and plate heights are minimal. In the reverse situation, when the flow velocity is minimum and the flow and plate heights are maximized, the pump work is minimized.

The respective values are

$$\begin{aligned} \Delta p_{\min} &= 3.7 \text{ Pa} \\ \Delta p_{\max} &= 6014 \text{ Pa} \\ \Delta \dot{w}_{\text{pump},\min} &= 0.001 \text{ W/kg} \\ \Delta \dot{w}_{\text{pump},\max} &= 87 \text{ W/kg} \end{aligned} \quad (12)$$

It is seen that the span of values is large and care must therefore be taken when designing a device. However these values are, as expected, all significantly lower than those found in spherical particle beds (e.g. Tura and Rowe, 2009).

3. Summary and conclusion

Through an extensive coverage of the relevant parameter space (consisting of 27,216 simulations) of parallel plate-based active magnetic regenerative refrigeration utilizing a 2-dimensional numerical model the key parameters for the optimal design and operation of an AMR device have been investigated. It was shown that the optimal range of the utilization is roughly

constant when maximization of the exergy and temperature span are sought. The values should be in the range 0.2–1.

The maximum exergy and temperature span were seen to decrease with increasing porosity and generally increase with decreasing plate thickness.

It was also shown that the maximum exergy is linearly increasing with cycle frequency, which leads to the conclusion that higher frequency will generally increase the available cooling power. This conclusion is by itself neither surprising nor new, but combined with the results of the maximum temperature span obtainable, an optimized compromise (for a given geometry) was found to be possible.

The primary reason for the peak in maximum temperature span at fairly low frequencies (0.3–0.5 Hz) was seen to be too low values of the NTU at higher frequencies. It is concluded that the value of the NTU should be in the region 10–30. Lower values will yield too small temperature spans and higher values achieved by smaller values of H_f and H_r will result in enhanced heat transfer but at the cost of increased pressure drops, thus increasing losses and cost unnecessarily.

It is concluded that the success of parallel plate-based AMR refrigerators depends partially on whether sufficiently thin channels and plates can be manufactured. At least 0.2 mm channel spacing, and thus plates of thickness 0.3 mm are needed to obtain reasonable performance compared to packed sphere regenerators with sphere diameter of 0.6 mm. To further improve the parallel plates either even thinner channels and plates or more than one MCM (i.e. a multi-material regenerator) are needed. The thinner the plates and fluid channels the more costly the system will be both in terms of manufacturing and assembly but also in terms of increased pressure drop (which scales quadratically with the inverse fluid channel thickness). Alternatively, modified parallel plates may be considered, e.g. dimpled or perforated plates. The main reason why parallel plates are interesting, even though they have obvious obstacles to overcome, is their inherent low pressure drops in operation. The problem inherent to too high pressure drops, as seen in particle beds, is an increase in the work input to the fluid pump and thus a lowering of the coefficient of performance (COP). This also adds unwanted heating in the system due to viscous dissipation in the regenerator.

Acknowledgements

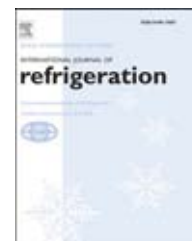
The authors thank the support of the Programme Commission on Energy and Environment (EnMi) (Contract no. 2104-06-0032) which is part of the Danish Council for Strategic Research.

REFERENCES

- Ashcroft, Neil W., Mermin, David, 1976. *Solid State Physics*. Saunders College.
- Bahl, C.R.H., Petersen, T., Pryds, N., Smith, A., 2008. A versatile magnetic refrigeration test device. *Review of Scientific Instruments* 79 (9), 093906.
- Bjørk, R., Bahl, C.R.H., Smith, A., Pryds, N., 2008. Optimization and improvement of Halbach cylinder design. *Journal of Applied Physics* 104 (1), 013910.

- Gschneidner, K., Pecharsky, V., 2008. Thirty years of near room temperature magnetic cooling: where we are today and future prospects. *International Journal of Refrigeration* 31 (6), 945–961.
- Incropera, F.P., DeWitt, D.P., 1996. *Introduction to Heat Transfer*, third ed. John Wiley & Sons, Inc.
- Li, P., Gong, M., Yao, G., Wu, J., 2006. A practical model for analysis of active magnetic regenerative refrigerators for room temperature applications. *International Journal of Refrigeration* 29, 1259–1266.
- Morrish, A.H., 1965. *The Physical Principles of Magnetism*. John Wiley & Sons, Inc..
- Nickolay, M., Martin, H., 2002. Improved approximation for the Nusselt number for hydrodynamically developed laminar flow between parallel plates. *International Journal of Heat and Mass Transfer* 45 (15), 3263–3266.
- Nielsen, K.K., Bahl, C.R.H., Bjørk, R., Pryds, N., Smith, A., Hattel, J., 2009. Detailed numerical modeling of a linear parallel-plate active magnetic regenerator. *International Journal of Refrigeration* 32, 1478–1486.
- Nielsen, K.K., Bjørk, R., Jensen, J.B., Bahl, C.R.H., Pryds, N., Smith, A., Nordentoft, A., Hattel, J., 2008. Magnetic cooling at Risø DTU. In: Hansen, S., Paul, J. (Eds.), *Eighth IIF/IIR Gustav Lorentzen Conference on Natural Working Fluids*. International Institute of Refrigeration, Copenhagen, Denmark.
- Okamura, T., Yamada, K., Hirano, N., Nagaya, S., 2006. Performance of a room-temperature rotary magnetic refrigerator. *International Journal of Refrigeration* 29, 1327–1331.
- Oliveira, P.A., Trevizoli, P.V., Barbosa, J.R., Prata, A.T., 2009. Numerical analysis of a reciprocating active magnetic regenerator – part I: fluid flow and heat transfer modeling. In: Egolf, P.W. (Ed.), *Third International Conference on Magnetic Refrigeration at Room Temperature*. International Institute of Refrigeration, Des Moines, Iowa, USA, pp. 283–288.
- Petersen, T.F., Engelbrecht, K., Bahl, C.R.H., Elmegaard, B., Pryds, N., Smith, A., 2008a. Comparison between a 1d and a 2d numerical model of an active magnetic regenerative refrigerator. *Journal of Physics D: Applied Physics* 41 (10), 105002.
- Petersen, T.F., Pryds, N., Smith, A., Hattel, J., Schmidt, H., Knudsen, H., 2008b. Two-dimensional mathematical model of a reciprocating room-temperature active magnetic regenerator. *International Journal of Refrigeration* 31, 432–443.
- Rowe, A., 2009. Performance metrics for active magnetic refrigerators. In: Egolf, P. (Ed.), *Third International Conference on Magnetic Refrigeration at Room Temperature*. International Institute of Refrigeration, Des Moines, Iowa, USA, pp. 195–205.
- Rowe, A., Dikeos, J., Tura, A., 2006. Experimental studies of near room-temperature magnetic refrigeration. In: Egolf, P.W. (Ed.), *First International Conference on Magnetic Refrigeration at Room Temperature*. International Institute of Refrigeration, pp. 325–333.
- Tura, A., Rowe, A., 2007. Design and testing of a permanent magnet magnetic refrigerator. In: Poredos, A., Sarlah, A. (Eds.), *Second International Conference on Magnetic Refrigeration at Room Temperature*. International Institute of Refrigeration, Portoroz, Slovenia, pp. 289–297.
- Tura, A., Rowe, A., 2009. Progress in the characterization and optimization of a permanent magnet magnetic refrigerator. In: Egolf, P.W. (Ed.), *Third International Conference on Magnetic Refrigeration at Room Temperature*. International Institute of Refrigeration, Des Moines, Iowa, USA, pp. 387–392.
- Zimm, C., Boeder, A., Chell, J., Sternberg, A., Fujita, A., Fujieda, S., Fukamichi, K., 2006. Design and performance of a permanent-magnet rotary refrigerator. *International Journal of Refrigeration* 29 (8), 1302–1306.

- A.1.6 Detailed numerical modeling of a linear parallel-plate active magnetic regenerator; published in International Journal of Refrigeration

available at www.sciencedirect.comjournal homepage: www.elsevier.com/locate/ijrefrig

Detailed numerical modeling of a linear parallel-plate Active Magnetic Regenerator

K.K. Nielsen^{a,b,*}, C.R.H. Bahl^b, A. Smith^b, R. Bjørk^b, N. Pryds^b, J. Hattel^a

^aDepartment of Mechanical Engineering, Technical University of Denmark, Building 425, Niels Koppels Allé, DK-2800 Kgs. Lyngby, Denmark

^bFuel Cells and Solid State Chemistry Division, Risø National Laboratory for Sustainable Energy, Technical University of Denmark, Frederiksborgvej 399, DK-4000, Denmark

ARTICLE INFO

Article history:

Received 10 December 2008

Received in revised form

2 March 2009

Accepted 16 March 2009

Published online 24 March 2009

Keywords:

Magnetic refrigerator

Modelling

Simulation

Magnetic field

Heat

Loss

ABSTRACT

A numerical model simulating Active Magnetic Regeneration (AMR) is presented and compared to a selection of experiments. The model is an extension and re-implementation of a previous two-dimensional model. The new model is extended to 2.5D, meaning that parasitic thermal losses are included in the spatially not-resolved direction.

The implementation of the magnetocaloric effect (MCE) is made possible through a source term in the heat equation for the magnetocaloric material (MCM). This adds the possibility to model a continuously varying magnetic field.

The adiabatic temperature change of the used gadolinium has been measured and is used as an alternative MCE than mean field modeling. The results show that using the 2.5D formulation brings the model significantly closer to the experiment. Good agreement between the experimental results and the modeling was obtained when using the 2.5D formulation in combination with the measured adiabatic temperature change.

© 2009 Elsevier Ltd and IIR. All rights reserved.

Modélisation numérique d'un régénérateur magnétique linéaire à plaques parallèles

Mots clés : Réfrigérateur magnétique ; Modélisation ; Simulation ; Champ magnétique ; Chaleur ; Perte

1. Introduction

Magnetic refrigeration at room temperature is a topic that spans several research areas. These include the optimal design of permanent magnet assemblies, focused research into

relevant magnetocaloric materials and system/regenerator designs (e.g. Bjørk et al., 2008; Pecharsky and Gschneidner, 2006; Rowe and Barclay, 2003; Rowe and Tura, 2008).

The theoretical advantages of magnetic refrigeration compared to conventional gas vaporization based refrigeration

Abbreviations: AMR, Active Magnetic Regeneration; MCE, Magnetocaloric effect; MCM, Magnetocaloric material; MFT, Mean field theory; HHEX, Hot heat exchanger; CHEX, Cold heat exchanger; PDE, Partial Differential Equation; FEM, Finite Element Method; ADI, Alternate Direction Implicit; TDMA, Tri-diagonal Matrix Algorithm; Gd, Gadolinium.

* Corresponding author. Tel.: +45 4677 4758.

E-mail address: kaspar.kirstein.nielsen@risoe.dk (K.K. Nielsen).

0140-7007/\$ – see front matter © 2009 Elsevier Ltd and IIR. All rights reserved.

doi:10.1016/j.ijrefrig.2009.03.003

Nomenclature*Variables*

ΔT_{ad}	Adiabatic temperature change [K]
T	Temperature [K]
T_{∞}	Ambient temperature [K]
c_p	Specific heat capacity [J/kg K]
ρ	Mass density [kg/m ³]
k	Thermal conductivity [W/m K]
h	Convective heat transfer coefficient [W/m ² K]
t	Time [s]
Δt	Timestep [s]
τ_1	Timing of magnetization part of the AMR cycle [s]
τ_2	Timing of hot blow part of the AMR cycle [s]
τ_3	Timing of demagnetization part of the AMR cycle [s]
τ_4	Timing of cold blow part of the AMR cycle [s]
τ_{rel}	Equal to $\tau_1/\tau_2 = \tau_3/\tau_4$ [-]
τ_{tot}	Equal to $2(\tau_1 + \tau_2)$ [s]
μ_0	Vacuum permeability equal to $4\pi \cdot 10^{-7}$ (N/A ²)
$\mu_0 H$	Magnetic field [T]
B	Magnetic flux density [T]
m	Magnetization [Am ² /kg]
\mathbf{u}	Velocity vector [m/s]
u	x-direction velocity component [m/s]
v	y-direction velocity component [m/s]
\tilde{u}	Inlet fluid velocity [m/s]

μ	Dynamic viscosity [kg/m s]
Re	Reynolds number [-]
H	Height [m]
L	Regenerator length [m]
p	Absolute pressure [N/m ²]
Δp	Pressure drop [N/m ²]
Δx	Finite difference length in the x-direction [m]
Δy	Finite difference length in the y-direction [m]
Δz	Finite difference length in the z-direction [m]
R	Thermal resistance [K/W]
Q	Thermal source term [W]

Sub- and super-scripts

f	Fluid
s	Solid
r	Regenerator
m	Material (solid or fluid)
l	Summation dummy index
pl	Plate
$conv$	Convection
i	x-direction index
j	y-direction index
0	Value at time t
$*$	Value at time $t + 1/2\Delta t$
$**$	Value at time $t + \Delta t$

are: significantly higher energy efficiency, low-noise operation and non-toxic magnetocaloric materials and heat transfer fluids.

So far numerous experiments have been done that are based on the Active Magnetic Regenerator (AMR) cycle (e.g. Rowe et al., 2004; Gao et al., 2006; Okamura et al., 2006; Bahl et al., 2008). These experiments show in general that it is certainly possible to utilize the magnetocaloric effect (MCE), which manifests itself as an adiabatic temperature change (ΔT_{ad}), inherent in the magnetocaloric material (MCM), to lift the temperature span of the AMR device to several times that of ΔT_{ad} of the used material. The experiments differ mainly in the basic design of the regenerator; some use porous packed beds and some parallel plates (of MCM). The optimal geometrical configuration of the regenerator is not obvious and since building experiments that span a sufficient number of configurations is both time-consuming and demands a great amount of resources, the need for fast and in particular accurate modeling is great.

The AMR models previously published have been one-dimensional (e.g. Dikeos et al., 2006; Li et al., 2006; Engelbrecht et al., 2005; Shir et al., 2005; Allab et al., 2005) with the exception of one, published in Petersen et al. (2008), which is a two-dimensional model of a parallel-plate design. In the one-dimensional models the regenerator is discretized with a sufficient number of grid cells in the x-direction (parallel to the flow) and thus a lumped analysis needs to be employed in order to describe the heat transfer between the active MCM and the heat transfer fluid. This description is the main simplification compared to a two-dimensional model that also resolves the thickness of both the fluid channels and MCM-plates. The model is developed for a parallel-plate based

design; it would be much more tedious to develop a consistent 2D model of a porous bed-based design.

This work presents a 2.5-dimensional model that is a further development and re-implementation of the model presented in Petersen et al. (2008). This new model was developed in order to decrease computation time, make it much more versatile in terms of geometrical and operational configurations and to include parasitic thermal losses in a physically realistic way in order to resemble the current experimental AMR device situated at Risø DTU in Denmark (see Bahl et al., 2008).

The outline of this paper is the following: In Section 2 the model is presented. In Section 3 the conditions of the experimental setup are implemented into the model. The model is validated in various geometrical and operational configurations. Finally in Section 4 the conclusions are drawn and future work is presented and proposed.

2. The numerical model

The model is designed to resemble a reciprocating linear parallel-plate based AMR design. The basic model is thoroughly discussed in Petersen et al. (2008). The following subsection is a short summary of that model and in Subsections 2.2–2.4 new additions are presented.

2.1. Summary of the original model

Fig. 1 shows the geometry and boundary conditions in detail. The plates are stacked with an equal spacing that defines the

fluid channel thickness. The plates can be made of any MCM and the heat transfer fluid can be any liquid of interest. The x -direction is defined to be parallel to the flow. The y -direction is perpendicular to the plane of the MCM-plates. The z -direction, which is not resolved in the basic model denotes the width of the fluid channel and MCM-plate. Placed at either end in the x -direction are a cold and a hot heat exchanger, respectively. The model includes half a plate and half a fluid channel in the y -direction in a so-called replicating cell thus exploiting the symmetry of both the fluid channel and plate.

When the fluid displacement is modeled the fluid-domain is kept stationary and the solid domains (i.e. heat exchangers (HEXs) and the MCM-plate) are subject to a movement correspondingly and an appropriate fluid-flow profile is applied to the fluid-domain. The heat exchangers at either end ensure a smooth way of measuring the temperature span for a no heat-load modeling situation. In the case of a heat-load modeling situation the cold heat exchanger (CHEX) is kept at a fixed temperature via its upper boundary. The hot heat exchanger (HHEX) is at all times kept at the ambient temperature T_∞ via its upper boundary condition.

The AMR cycle simulated includes four steps. The total cycle time is denoted by τ_{tot} and the timings of the four sub-steps are denoted by τ_1 , τ_2 , τ_3 and τ_4 respectively. The cycle is symmetric meaning that $\tau_1 = \tau_3$ and $\tau_2 = \tau_4$. The first step is the magnetization of the MCM. The second step is the so-called “hot blow”, i.e. where the fluid is moved from the cold towards the hot end. In the third step the MCM is demagnetized. The fourth step is called the “cold blow” and during this step the fluid is moved from the hot end towards the cold end. The timing fraction of the magnetization periods to the blow periods is defined as $\tau_{\text{re}} \equiv \tau_1/\tau_2 = \tau_3/\tau_4$.

The MCE is modeled via mean field theory (MFT) (see Petersen et al., 2008) and the resulting ΔT_{ad} is directly applied as a discrete temperature increase/decrease in the control volume under consideration. The specific heat capacity $c_p(H, T)$ is also calculated (as a function of both temperature and field) from MFT and is updated in every timestep. The MCE is highly sensitive to impurities and variations in the MCM, which are not modeled by MFT. It is therefore imperative that experimental data are used when available.

The equation system solved consists of four partial differential equations (PDEs) coupled via inner boundaries. For the solid domains (subscript s) the equations are all unsteady diffusion equations (for convenience subscript s has been adopted for all three solid domains, though the material properties ρ , k and c_p are not the same):

$$\rho_s c_{p,s} \frac{\partial T_s}{\partial t} = k_s \nabla^2 T_s. \quad (1)$$

Here, the mass density is ρ , the temperature is T , time is t and the thermal conductivity is k . The PDE describing the transient thermal behaviour of the fluid-domain, subscript f , includes an extra term, namely the convective heat transfer:

$$\rho_f c_{p,f} \left(\frac{\partial T_f}{\partial t} + (\mathbf{u} \cdot \nabla) T_f \right) = k_f \nabla^2 T_f. \quad (2)$$

The fluid velocity is denoted by $\mathbf{u} = (u, v)$. Thus, all the thermal properties except c_p for the MCM are assumed constant.

2.1.1. Velocity profile

The applied velocity field is a steady, incompressible, fully developed and laminar flow de-coupled from the thermal system. The boundary conditions are non-slip on the boundary between the fluid-domain and the solid domains and slip on the symmetry boundary.

The assumption of incompressible flow is certainly valid since water (or a water + ethanol mixture) is used as the heat transfer fluid. Since the thermal properties (ρ , c_p and k) of water do not change significantly under the present working conditions, these are safely assumed to be constant and thus de-coupled from the thermal system.

The Reynolds number of the system is given by

$$Re = \frac{2H_f \bar{u} \rho_f}{\mu}, \quad (3)$$

where \bar{u} is the inlet velocity, H_f the fluid channel thickness and μ the dynamic viscosity of the fluid. The mass density and viscosity are constant ($\rho_f = 997 \text{ kg/m}^3$ and $\mu = 8.91 \times 10^{-4} \text{ kg/m s}$) and the most extreme (i.e. in this case maximum) values of \bar{u} and H_f are 0.01 m/s and $0.8 \times 10^{-3} \text{ m}$, respectively. This yields a maximum value of the Reynolds number to be ≈ 24 . This value is well within the range of laminar flows justifying our assumption.

Balancing the convective and viscous terms in the incompressible Navier–Stokes equations the entrance length, L , of a laminar pipe-flow can be found to be $L = 0.06 H_f Re$ (e.g. Lautrup, 2005). For the extreme case where \bar{u} and H_f attain their maximum values the entrance length is about 0.001 m and thus compared to the length of the flow channel ($L_f = 0.16 \text{ m}$) the assumption of fully developed flow is valid.

The only non-zero velocity component is the x -direction velocity u . The steady incompressible Navier–Stokes equations for laminar flows can thus be reduced to

$$\mu \frac{\partial^2 u}{\partial y^2} = \frac{\partial p}{\partial x}, \quad (4)$$

where the pressure gradient in the flow-direction is given by $\partial p / \partial x = \Delta p / L_f$. We assume the pressure drop to be constant,

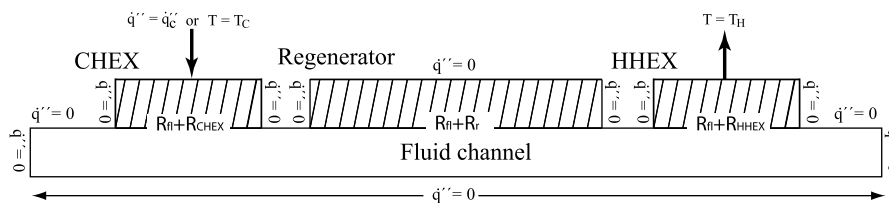


Fig. 1 – Two-dimensional slice of the original model. Half a fluid channel, MCM-plate and HEXs are seen. The thermal boundary conditions are indicated.

given by $\Delta p = 12L_f\mu\bar{u}/H_f^2$ (Fox and McDonald, 1994). Integration of Eq. (4) and utilization of the boundary conditions $u(y = 1/2H_f) = \bar{u}$ and $\partial U/\partial y|_{y=0} = 0$, where $y = 0$ is defined as the middle of the flow channel and $y = 1/2H_f$ is the upper boundary between the fluid channel and solid domain, gives the well-known velocity profile

$$u(y) = \bar{u} \left(\frac{6y^2}{H_f^2} - 1/2 \right). \quad (5)$$

2.2. The numerical scheme

In the original model Eqs. (1) and (2) were solved using the commercial software package Comsol (Comsol, 2005). The numerical discretization was based on the Finite Element Method (FEM) and the temporal integration was done fully implicit. The current model has been re-written using finite differences of second order and the Alternate Direction Implicit (ADI) temporal integration method. The code is written by the authors and is currently available in generic Fortran.

The reason for choosing finite differences is that total energy conservation across boundaries is guaranteed at all times due to the nature of that formalism as opposed to the FEM where the conservation of energy has to rely on interpolation methods between node points. The reason why strict energy conservation is crucial in this work is the nature of the moving boundaries. It is very important that the thermal energy exchange between the subdomains is fully conserved at all times. This can be achieved by the FEM (see Petersen et al., 2008). But the cost is a large computational time. The original Comsol model uses around 50 h to complete a simulation of 600 AMR cycles whereas this new code uses around 30 min, in both cases on an Intel Core 2 Duo 2.0 GHz Windows-based PC.

The reason for using the ADI method (see e.g. Patankar, 1980) is that the benefit from the implicit solution of each timestep is achieved and the speed of the explicit integration method is almost reached. The ADI scheme for two-dimensional problems is split into two sub-timesteps. In the first sub-timestep one direction is determined implicitly and the other is used explicitly. In the second sub-timestep the situation is reversed. The term “explicitly used” means that the variable solved for (e.g. temperature T) is known at the beginning of the timestep. Likewise, the term “implicitly determined” means that the variable is solved for at the new point in time.

If the index-pair (i, j) defines the position in the x - and y -direction and T_{ij}^0, T_{ij}^* and T_{ij}^{**} are chosen to denote the temperatures at times $t, t + 1/2\Delta t$ and $t + \Delta t$, respectively, for the grid cell centered at (i, j) the unsteady discretized equation for the thermal conduction becomes:

$$\rho c_p \Delta x \Delta y \Delta z \frac{T_{ij}^* - T_{ij}^0}{1/2\Delta t} = \frac{k \Delta y \Delta z}{\Delta x} \left[(T_{i+1j}^* - T_{ij}^*) - (T_{ij}^* - T_{i-1j}^*) \right] + \frac{k \Delta x \Delta z}{\Delta y} \left[(T_{ij+1}^0 - T_{ij}^0) - (T_{ij}^0 - T_{ij-1}^0) \right], \quad (6)$$

$$\rho c_p \Delta x \Delta y \Delta z \frac{T_{ij}^{**} - T_{ij}^*}{1/2\Delta t} = \frac{k \Delta y \Delta z}{\Delta x} \left[(T_{i+1j}^{**} - T_{ij}^{**}) - (T_{ij}^{**} - T_{i-1j}^{**}) \right] + \frac{k \Delta x \Delta z}{\Delta y} \left[(T_{ij+1}^{**} - T_{ij}^{**}) - (T_{ij}^{**} - T_{ij-1}^{**}) \right], \quad (7)$$

when applying Fourier’s law of heat conduction and using the formalism of the ADI method. The numerical grid cell size is denoted $\Delta x \times \Delta y \times \Delta z$. The x -direction has – arbitrarily – been chosen to be the implicit direction in the first sub-timestep (where super-scripts 0 and * mean explicit and implicit, respectively) and explicit in the second (where super-scripts * and ** mean explicit and implicit, respectively). The inclusion of Δz in Eqs. (6) and (7) is done in order to emphasize the importance of using the correct control volume when including the loss terms defined below in Eq. (12).

Eqs. (6) and (7) can be re-written in the form

$$a_{ij} T_{ij}^* = b_{ij} T_{i+1j}^* + c_{ij} T_{i-1j}^* + d \left(T_{ij}^0; T_{ij+1}^0; T_{ij-1}^0 \right), \quad (8)$$

$$a_{ij} T_{ij}^{**} = b_{ij} T_{ij+1}^{**} + c_{ij} T_{ij-1}^{**} + d \left(T_{ij}^*; T_{i+1j}^*; T_{i-1j}^* \right), \quad (9)$$

where a_{ij} , b_{ij} and c_{ij} are assumed constant throughout the timestep and d includes the explicit and other additive terms. This function may be spatially dependent. Solving Eqs. (8) and (9) is equivalent to inverting a tri-diagonal matrix. Such an inversion is linearly time-consuming in the number of mesh points and can be done using the well-known Tri-Diagonal Matrix Algorithm (TDMA) given in, e.g., Patankar (1980).

The coupling between the four domains is done using Fourier’s law of heat conduction formulated through the use of thermal resistances (see the schematic in Fig. 2).

The heat capacity of the MCM is typically a strong function of both temperature and magnetic field. It is calculated from MFT and in this implementation a large dataset of c_p values has been tabulated with a sufficient range in both temperature and field. The value of c_p needed for every sub-timestep is then spline-interpolated in this dataset using a natural cubic spline (Press et al., 1992).

The forced convection term, due to the fluid movement, is implemented following the “up-wind scheme” (see Patankar, 1980). This ensures that the thermal energy of the up-wind cell influences the convection term rather than using the centered difference.

The boundary conditions are given in Figs. 1 and 4. The initial condition was for all experiments set to be a uniform temperature of 298 K throughout the domains.

In Petersen et al. (2008) the original numerical model is thoroughly validated. The new implementation has been exposed to the same tests and is equally numerically valid and in some cases (especially when heat conservation is crucial) the new implementation is more accurate.

2.3. The magnetocaloric effect as a source term

Previously the change in magnetic field was modeled as an abrupt or discrete change as described in Petersen et al. (2008). This approach is obviously not physically correct, but may be sufficient to a certain extent. In order to improve this aspect of the modeling, the change in magnetic field could be implemented to happen through a number of timesteps. One approach would be a simple ramping of the field through an appropriate function, e.g. linear, sinusoidal or hyperbolic tangent. An even more realistic solution is to model the physical movement of the regenerator in and out of the magnetic field from a specific magnet configuration. If the

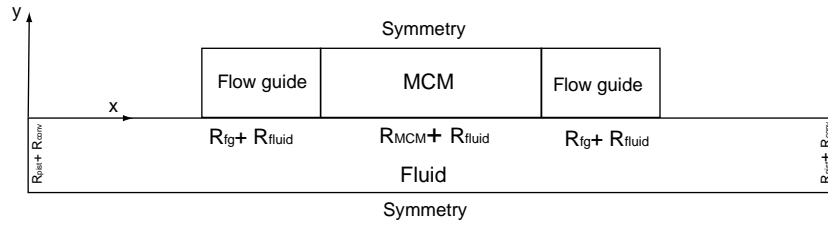


Fig. 2 – The xy-plane of the replicating cell (half a fluid channel and half a plate of MCM and flow guides). The two boundaries marked “symmetry” are symmetric, or adiabatic, due to the nature of the representation using half a replicating cell. The internal boundaries are marked with their respective thermal resistances.

field profile is known then the magnetic flux density as a function of time (and space) is trivial to derive.

Whichever method is used for modeling the magnetic field change in a continuous way, the MCE has to be formulated as a source term in the thermal equation for the MCM. Assuming adiabatic magnetization through each timestep, the heat energy released from the change in magnetic field from time t to $t + \Delta t$ is calculated on basis of the known, or explicit, temperature (i.e. $T_{i,j}(t)$). The differential adiabatic temperature change can be written as

$$\frac{d\Delta T_{ad}}{dt} \Big|_t = -\mu_0 \frac{T(t) \partial m}{c_p(t) \partial T} \Big|_t \frac{dH}{dt} \Big|_t \quad (10)$$

Here indices i, j have been omitted for simplicity and μ_0 is the vacuum permeability, m is the specific magnetization and H is the magnetic field. Multiplying by $\Delta x \Delta y \Delta z \rho c_p$ on both sides of Eq. (10) the MCE source term Q_{MCE} becomes

$$Q_{MCE} = -\mu_0 \rho T(t) \frac{\partial m}{\partial T} \Big|_t \frac{dH}{dt} \Big|_t \Delta x \Delta y \Delta z. \quad (11)$$

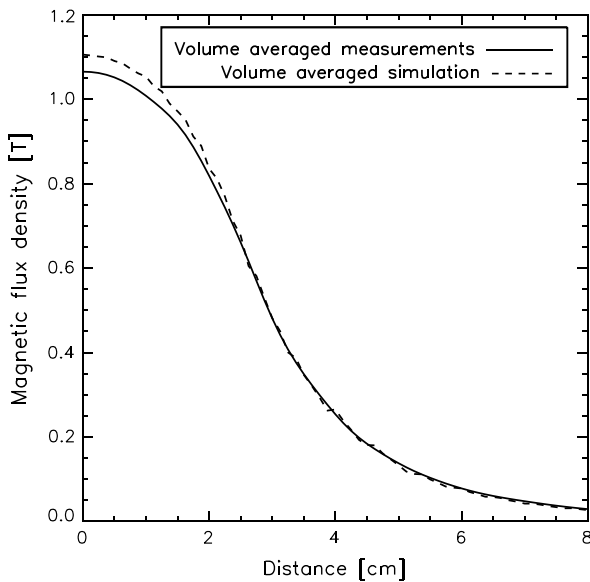


Fig. 3 – The profile of the magnetic flux density of the permanent Halbach magnet used in the experiments. Shown are both the measured data values and the corresponding model results.

Eq. (11) can be inserted directly on the right hand side of Eqs. (6) and (7) as a source term.

The temporal rate of change of the magnetic field dH/dt is derived from the field profile of the used magnet system. In Fig. 3 the flux density of the permanent Halbach magnet system used in the AMR experiments is given as a function of distance from the centre of the bore of the Halbach cylinder. The figure shows both the measured flux density and modeling data using the model from Bjørk et al. (2008).

2.4. The 2.5D heat loss formulation

The experimental setup (Bahl et al., 2008) does not include heat exchangers but does of course leak heat to the surroundings. These are two major differences between the model and the experiment. It is expected that the performance in general will be over-estimated by the model since it is somewhat ideal without losses and that the trends in performance (both in load and no-load situations) will be reproduced fairly well by the model. This is due to the fact that the model actually resolves the important parts of the experimental geometry well and the geometrical parameters are expected to be crucial for the trends of a parallel-plate AMR device.

However, to improve the model, heat losses have been implemented as an alternative to the original HEXs modeled as copper plates. The heat loss is implemented through a lumped analysis and under the assumption that the replicating cell under consideration loses most of its heat in the not-resolved z -direction. The loss can then be implemented as an additional term in Eqs. (6) and (7) using the formalism of thermal resistance:

$$Q_{loss} = \frac{T_{\infty} - T_{ij}}{\sum_l R_l}, \quad (12)$$

where the total thermal resistance from the centre of the cell (in terms of the z -direction) to the ambient is denoted by $\sum_l R_l$. There are three terms in this sum. First the thermal resistance through the material within the regenerator R_m (fluid or solid). Second, the housing of the regenerator block R_{pl} (made of a plastic material) and finally loss via natural convection to the ambient R_{conv}

$$\sum_l R_l = R_m + R_{pl} + R_{conv} = \frac{1/2\Delta z}{k_m \Delta x \Delta y} + \frac{1/2\Delta z}{k_{pl} \Delta x \Delta y} + \frac{1}{h_{conv} \Delta x \Delta y} \quad (13)$$

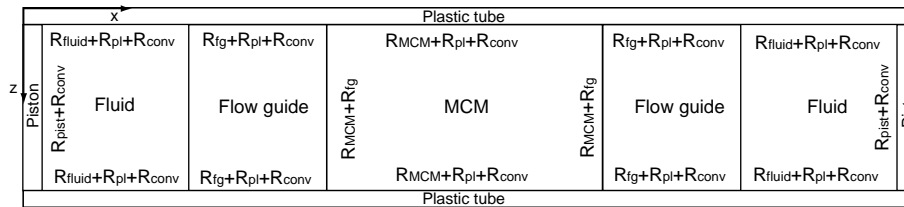


Fig. 4 – The xz -plane of the system. The z -direction is not resolved, however, the 2.5D model takes the distance from the centre of the control volumes to the ambient into account when calculating the thermal losses, as indicated in the figure.

This 2.5D thermal loss formulation is schematically visualized in Fig. 4. The loss to the ambient through natural convection is characterized by the parameter h_{conv} . Textbook values suggest that h_{conv} lies in the range 5–20 W/K m² (Holman, 1987). The thermal properties of the plastic housing are given in Table 1.

3. Results and discussion

In this section the numerical model is compared to various experiments performed with the experimental AMR device located at Risø DTU (Bahl et al., 2008). The model is able to operate in different configurations (2D ideal with no thermal losses, 2.5D with thermal losses, discrete or continuous magnetic field, etc.). Therefore various situations have been picked out for investigation. First, in Section 3.1 variation of the fluid displacement is investigated and compared to the experimental and original model data. Second, in Section 3.2 variation in the timing of the AMR cycle is explored. Third, in Section 3.3 the variation in the application of the magnetic field is compared between the ideal model, the 2.5D loss model and the experiment.

Table 2 gives the specifications of each experiment/model. All experiments were carried out with 0.9 mm thick plates of pure Gd (obtained from China Rare Earth Materials Co.) with a spacing of 0.8 mm. The experiments were all equipped with 13 plates. For further details on the experimental setup see Bahl et al. (2008).

3.1. Fluid displacement experiments

The fluid displacement, δx , is one of the key process parameters for an AMR. In Bahl et al. (2008) the dependency of the AMR performance on this parameter is studied using the experimental device and a slightly changed version of the numerical model of Petersen et al. (2008). However, the

model did not include losses in the z -direction and the plastic flow guides were lumped to represent the entire loss of the plastic tube and regenerator housing. The geometric and operational parameters in the 2.5D loss model were set to resemble the configuration of the original experiment and to use MFT for modeling the MCE. The results are seen in Fig. 5.

The directly measured adiabatic temperature change of the Gd plates when using the Halbach magnet assembly is taken from Bahl and Nielsen (2008). A new experiment series was performed varying the fluid displacement. The model was adjusted to use MFT for calculating the MCE and also to use the directly measured ΔT_{ad} values. The heat capacity was in both cases determined from MFT. The results are seen in Fig. 6.

The fluid displacement experiments show a clearly asymmetric bell-shaped curve (Figs. 5 and 6). This shape is reproduced fairly well by the model. The peak in the curve is situated at a fluid movement around 40%. There is a significant improvement when the experimentally determined values for the adiabatic temperature change are used instead of the mean field model.

3.2. Timing experiments

The timing of the AMR cycle is important for the performance of the system. There are two critical questions that need answering. First of all how long the entire cycle (τ_{tot}) should be. Secondly, the amount of time used for magnetizing/demagnetizing and afterwards reaching thermal equilibrium (τ_1 and τ_3) compared to the time spent moving the fluid during the blow periods (τ_2 and τ_4). In Bahl et al. (2008) experimental and model results are given for AMR setups where τ_{rel} and τ_{tot} are

Table 1 – Values of the various thermal properties of the materials used

Material/property	k [W/m K]	ρ [kg/m ³]	c_p [J/kg K]
Copper	401	8933	385
Water	0.595	997	4183
Gadolinium	10.5	7900	170–300 (temperature and field dependent)
Plastic	0.2	800	1250

Table 2 – An overview of the experiments conducted in this work. The process parameters (fluid movement, timing and magnet assembly) are presented. The parameters apply both for the experiment and the corresponding modeling

Model	δx %	τ_{tot} [s]	τ_{rel}	Magnet
Stroke, (Bahl et al., 2008)	5–95	12	1	Electro
Stroke, new experiments	5–95	8.2	0.51	Halbach
Timing, (Bahl et al., 2008)	50	12–18	0.25–4.5	Electro
Timing, new experiments	50	9	0.25–3.0	Halbach
Varying magnetic flux density	40	11.8	1.03	Halbach

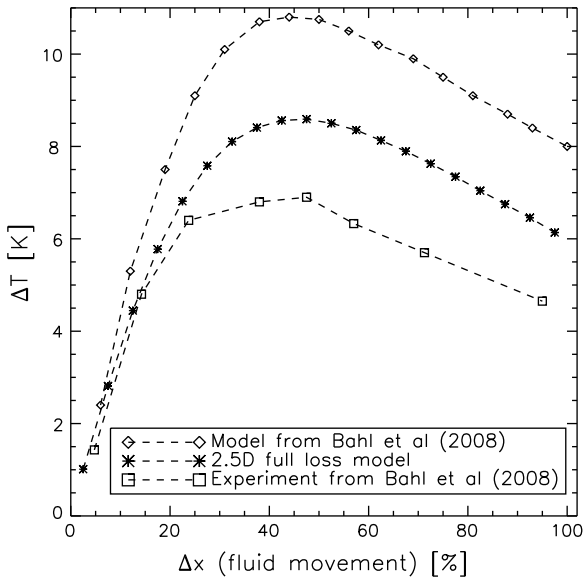


Fig. 5 – Fluid movement experiment from Bahl et al. (2008) with modeling results from both the original paper and this work. The model from this work used MFT to calculate the MCE, since it is not possible to translate the measured ΔT_{ad} values to a different magnetic field profile (the original experiment used an electromagnet).

varied. The 2.5D loss model was setup to the same geometrical and process parametric configuration. The results are given in Fig. 7.

A new experiment series, again using the Halbach magnet was performed varying τ_{rel} and the input parameters to the 2.5D loss model were set accordingly. Both the MFT and the directly measured ΔT_{ad} were used for modeling the MCE. The results are given in Fig. 8.

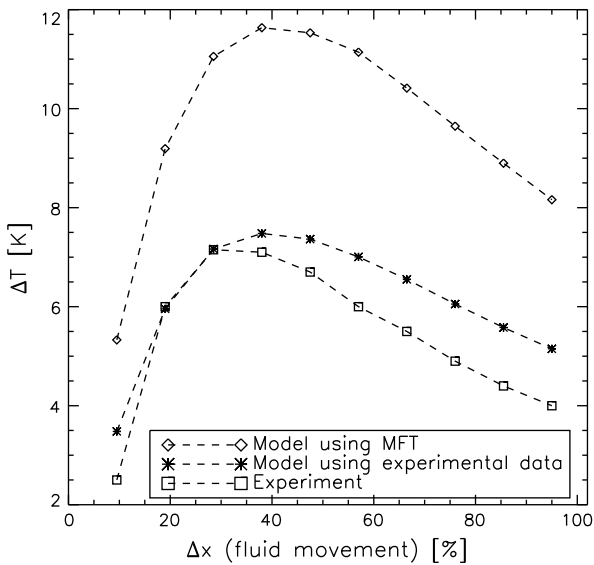


Fig. 6 – A new fluid movement experiment performed using the permanent Halbach magnet and modeled both using MFT and the measured adiabatic temperature changes.

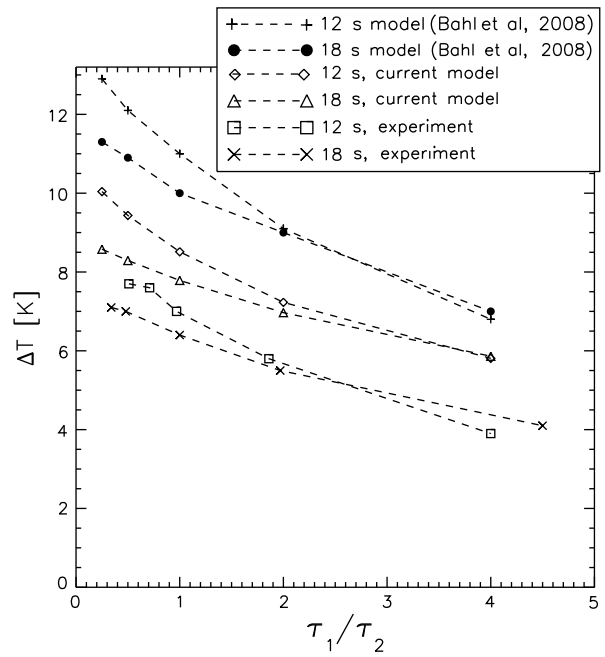


Fig. 7 – Timing experiment and corresponding modeling from Bahl et al. (2008) with the MFT-based 2.5D loss model from this work overlotted.

The timing experiments, presented in Figs. 7 and 8, show that the no-load temperature span decreases as a function of the fraction τ_{rel} . This behaviour is also well reproduced by all the models. In Fig. 7 a cross-over is seen between the curves for $\tau_{tot} = 12$ and 18 s at large τ_{rel} . This is also a feature that the models reproduce.

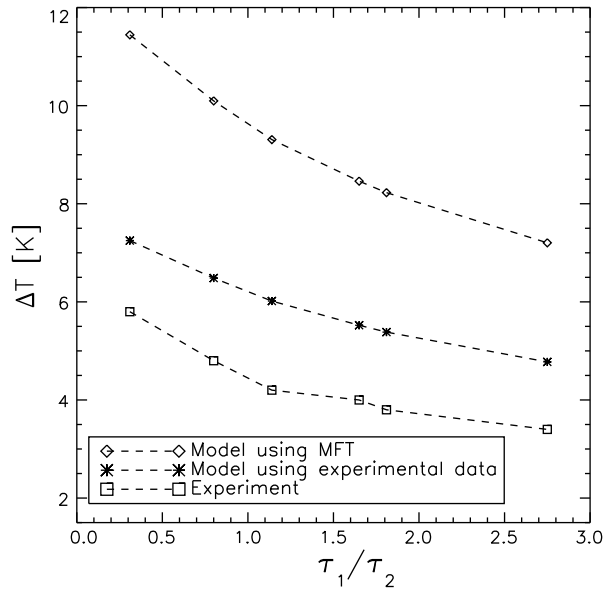


Fig. 8 – New timing experiment performed using the permanent Halbach magnet. The corresponding modeling has been performed for two cases, one using MFT and one using the measured ΔT_{ad} values. Both were done using the 2.5D loss formulation.

However, all the models using MFT for calculating ΔT_{ad} over-estimate the temperature span significantly. Using the measured ΔT_{ad} values the model is seen to reproduce the absolute temperature spans to a higher degree. This is the same conclusion as for the fluid displacement experiments.

3.3. Varying the magnetic flux density

The magnetic flux density of the Halbach cylinder as a function of distance from the centre of the bore is given in Fig. 3. An experiment has been conducted where the regenerator was moved from the centre of the Halbach magnet out to various distances in an otherwise identical experiment. It is seen from the results in Fig. 9 that at a certain distance (approximately 7 cm) the magnetic flux density is low enough that moving the regenerator further out does not increase the temperature span.

The modeling of the varying magnetic flux density was done in two ways, both using the MCE described as a source term (see Subsection 2.3). One model-series was performed with the ideal (no heat loss) setup and the other with the 2.5D loss formulation. The results are shown in Fig. 9.

The experimental and modeling investigations of the sensitivity towards the change in field result in two interesting conclusions. First, the need for moving the regenerator far out of the field is limited to roughly 7 cm for the present system configuration. This fact is important. The timing of the experiment is to a certain degree dependent on how much time is spent moving the regenerator in and out of field. As seen from the timing experiments the time spent during this process should be as short as possible. Second, in Fig. 9 it is seen that including thermal parasitic losses in the model

significantly improves the results of the model compared to the experiment. In both cases the MFT was used to model the MCE. Thus, only the inclusion of thermal parasitic losses can explain the clear improvement of the modeling results. It should be emphasized that the remaining difference between the model and the experiments is probably due to the additional heat losses in the experimental setup which have not been included in the model due to the lack of knowledge for the origin of these losses.

3.4. Overall discussion

The three different no heat-load situations experimentally investigated and numerically modeled here all point in the same direction. When keeping all parameters except one fixed the tendency in no-load temperature span is well described by the models. However, there is a tendency for the models to over-estimate the absolute values of the temperature span. The reason for this is primarily that the MFT is too idealized and that real experimental data should be used instead. This is supported by the results from the modeling when using the measured values of the adiabatic temperature change.

Furthermore, passive regeneration in the plastic housing may be significant for the performance of the AMR. Generally, the thermal losses to the ambient may be more tightly dependent temporarily (through the cycle). This cannot be investigated in the present model and full three-dimensional modeling is needed to investigate this.

4. Conclusion

A re-definition, re-implementation and feature-upgrade of the numerical 2D AMR model (Petersen et al., 2008) were presented. The computation time has been reduced by a factor of 100. This allows for large parameter space surveys which are under preparation for future publication.

The current state of the 2D AMR model has been investigated and presented. It is concluded that the 2.5D loss model is a significant improvement in terms of reproducing the experimental results. The continuous description of the change in magnetic flux density is recognized as an important improvement of the model in terms of operating the experiment and confidence that the model is well-represented using the discrete change if needed.

Including the measured adiabatic temperature change in the experimental setup with the Halbach magnet has enabled the model to reproduce all aspects of the no heat-load experiments reasonably well.

On the basis of the results presented in this paper it is concluded that the ideal 2D model can be used to explore the performance of a linear reciprocating parallel-plate based AMR design. Once the optimal configuration settings have been found, the 2.5D full loss model can be used to explore the expected experimental performance in more detail. The reason for not only using the loss model is that the ideal AMR work is independent of experimental shortcomings and choices. The results from such an ideal AMR study can thus be used by other experiments and provide a more general understanding of the details and theory of AMR.

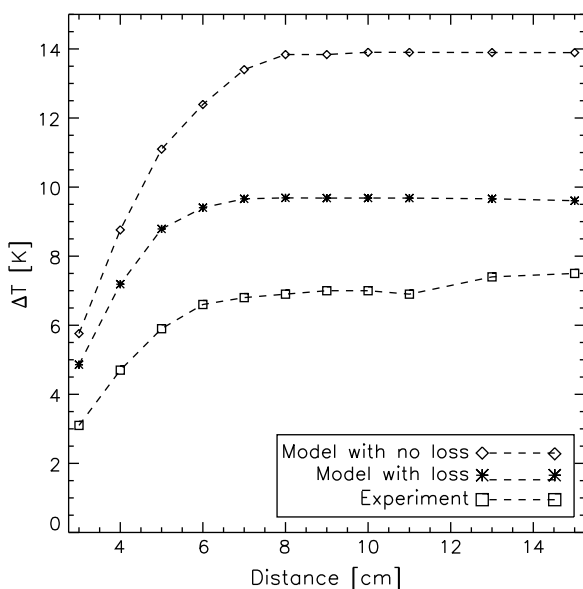


Fig. 9 – Experiment performed by altering the distance from the centre of the magnet bore that the regenerator is moved out to. Two modeling cases are seen. One with the ideal (not including 2.5D losses) and one with the 2.5D loss formulation. The trends are clearly seen to be reproduced, though the absolute values are not quite the same in the models as in the experiment.

Acknowledgements

The authors thank Jørgen Geyti for technical assistance. Furthermore the authors would like to acknowledge the support of the Programme Commission on Energy and Environment (EnMi) (Contract no. 2104-06-0032) which is part of the Danish Council for Strategic Research.

REFERENCES

- Allab, F., Kedous-Lebouc, A., Fournier, J., Yonnet, J., 2005. Numerical modeling for active magnetic regenerative refrigeration. *IEEE Transactions on Magnetics* 41 (10), 3757–3759.
- Bahl, C., Nielsen, K., 2008. The effect of demagnetization on the magnetocaloric properties of gadolinium. *Journal of Applied Physics* 105, 013916.
- Bahl, C., Petersen, T., Pryds, N., Smith, A., 2008. A versatile magnetic refrigeration test device. *Review of Scientific Instruments* 79 (9), 093906.
- Bjørk, R., Bahl, C.R.H., Smith, A., Pryds, N., 2008. Optimization and improvement of Halbach cylinder design. *Journal of Applied Physics* 104 (1), 013910.
- Comsol, 2005. In: *Comsol Multiphysics Model Library*, third ed. COMSOL AB, Chalmers Teknikpark 412 88 G.
- Dikeos, J., Rowe, A., Tura, A., 2006. Numerical analysis of an active magnetic regenerator (amr) refrigeration cycle. *AIP Conference Proceedings* 823 (1), 993–1000.
- Engelbrecht, K., Nellis, G., Klein, S., Boeder, A., 2005. Modeling active magnetic regenerative refrigeration systems. In: Egolf, P.W. (Ed.), *First International Conference on Magnetic Refrigeration at Room Temperature*. Refrigeration Science and Technology Proceedings, vol. 1, pp. 265–274.
- Fox, R.W., McDonald, A.T., 1994. *Introduction to Fluid Mechanics*. John Wiley and Sons, Inc.
- Gao, Q., Yu, B., Wang, C., Zhang, B., Yang, D., Zhang, Y., 2006. Experimental investigation on refrigeration performance of a reciprocating active magnetic regenerator of room temperature magnetic refrigeration. *International Journal of Refrigeration* 29, 1274–1285.
- Holman, J., 1987. In: *Heat Transfer*, first ed. McGraw-Hill.
- Lautrup, B., 2005. *Physics of continuous matter. Exotic and Everyday Phenomena in the Macroscopic World*. Institute of Physics.
- Li, P., Gong, M., Yao, G., Wu, J., 2006. A practical model for analysis of active magnetic regenerative refrigerators for room temperature applications. *International Journal of Refrigeration* 29, 1259–1266.
- Okamura, T., Yamada, K., Hirano, N., Nagaya, S., 2006. Performance of a room-temperature rotary magnetic refrigerator. *International Journal of Refrigeration* 29, 1327–1331.
- Patankar, S.V., 1980. *Numerical Heat Transfer and Fluid Flow*. Taylor & Francis.
- Pecharsky, V.K., Gschneidner, K., 2006. Advanced magnetocaloric materials: what does the future hold? *International Journal of Refrigeration* 29, 1239–1249.
- Petersen, T.F., Pryds, N., Smith, A., Hattel, J., Schmidt, H., Knudsen, H., 2008. Two-dimensional mathematical model of a reciprocating room-temperature active magnetic regenerator. *International Journal of Refrigeration* 31, 432–443.
- Press, W.H., Teukolsky, S.A., Vetterling, W.T., Flannery, B.P., 1992. *Numerical recipes in FORTRAN*. In: *The Art of Scientific Computing*, second ed. University Press, Cambridge.
- Rowe, A., Barclay, J., 2003. Ideal magnetocaloric effect for active magnetic regenerators. *Journal of Applied Physics* 93 (3), 1672–1676.
- Rowe, A., Tura, A., 2008. Active magnetic regenerator performance enhancement using passive magnetic materials. *Journal of Magnetism and Magnetic Materials* 320 (7), 1357–1363.
- Rowe, A., Tura, A., Richard, M.-A., Chahine, R., Barclay, J., 2004. Magnetic refrigeration – an overview of operating experience using the amr test apparatus. *Advances in Cryogenic Engineering* 49 (B), 1721.
- Shir, F., Mavriplis, C., Benneth, L., Torre, E., 2005. Analysis of room temperature magnetic regenerative refrigeration. *International Journal of Refrigeration* 28, 616–627.

-
- A.1.7 Review on numerical modeling of active magnetic regenerators; accepted for publication in International Journal of Refrigeration

Review on numerical modeling of active magnetic regenerators for room temperature applications

K.K. Nielsen^{a,b}, J. Tusek^c, K. Engelbrecht^b, S. Schopfer^d, A. Kitanovski^c,
C.R.H. Bahl^b, A. Smith^b, N. Pryds^b, A. Poredos^c

^a*Department of Mechanical Engineering, Technical University of Denmark
Building 425, Niels Koppels Alle, DK-2800 Kgs. Lyngby, Denmark*

^b*Fuel Cells and Solid State Chemistry Division
Risø National Laboratory for Sustainable Energy*

Technical University of Denmark, Frederiksborgvej 399, DK-4000 Roskilde, Denmark

^c*University of Ljubljana*

*Faculty of Mechanical Engineering
Askerceva c. 6, 1000 Ljubljana, Slovenia*

^d*University of Victoria*

*Institute of Integrated Energy Systems
ELW B126, PO Box 3055 STN CSC
Victoria BC, V8W 3P6, Canada*

Abstract

The active magnetic regenerator (AMR) is an alternative refrigeration cycle with a potential gain of energy efficiency compared to conventional refrigeration techniques. The AMR poses a complex problem of heat transfer, fluid dynamics and magnetic field, which requires detailed and robust modeling. This paper reviews the existing numerical modeling of room temperature AMR to date. The governing equations, implementation of the magnetocaloric effect (MCE), fluid flow and magnetic field profiles, thermal conduction etc. are discussed in detail as is their impact on the AMR cycle. Flow channeling effects, hysteresis, thermal losses and demagnetizing

Email address: e-mail: kaki@risoe.dtu.dk (K.K. Nielsen)

fields are discussed and it is concluded that more detailed modeling of these phenomena is required to obtain a better understanding of the AMR cycle.

Keywords: Magnetic refrigerator, Gadolinium, Regeneration, Modelling

Nomenclature

<i>Variables</i>	
T	Temperature [K]
T_C	Curie temperature [K]
T_∞	Ambient temperature [K]
ΔT_{ad}	Adiabatic temperature change [K]
$\mathbf{u} = (u_x, u_y, u_z)$	Velocity vector [ms^{-1}]
A_{HT}	Wetted area per unit cell [m^2m^{-3}]
c	Specific heat capacity [$\text{Jkg}^{-1}\text{K}^{-1}$]
ρ	Mass density [kgm^{-3}]
k	Thermal conductivity [$\text{Wm}^{-1}\text{K}^{-1}$]
h	Convective heat transfer coefficient [$\text{Wm}^{-2}\text{K}^{-1}$]
τ_1	Timing of magnetization part of the AMR cycle [s]
τ_2	Timing of hot blow part of the AMR cycle [s]
τ_3	Timing of demagnetization part of the AMR cycle [s]
τ_4	Timing of cold blow part of the AMR cycle [s]
τ_{rel}	Equal to $\tau_1/\tau_2 = \tau_3/\tau_4$ [-]
τ_{tot}	Equal to $2(\tau_1 + \tau_2)$ [s]
μ_0	Vacuum permeability equal to $4\pi 10^{-7}\text{NA}^{-2}$
$\mu_0 H$	Magnetic field [T]
M	Magnetization [Am^{-1}]
D_p	Dispersion coefficient [-]
Pe	Peclet number [-]
d_p	Particle diameter [m]
d_r	Regenerator diameter [m]
L	Length [m]
V	Volume [m^3]
\dot{m}	Mass flow rate [kgs^{-1}]
f	Frequency [Hz]
φ	Utilization [-]
ϵ	Porosity [-]
Q_c	Cooling power [Wkg^{-1}]
Δp	Pressure drop [Pa]
μ_f	Dynamic viscosity [$\text{Pa}\cdot\text{s}$]
$K(r)$	Particle bed permeability [m^2]

Abbreviations

AMR	Active Magnetic Regeneration
MCE	Magnetocaloric effect
MCM	Magnetocaloric material
MFM	Mean field model
HHEX	Hot heat exchanger
CHEX	Cold heat exchanger
HTF	Heat transfer fluid
COP	Coefficient of Performance

Sub- and super scripts

f	Fluid
s	Solid
<i>i</i>	Initial
<i>f</i>	Final
HT	Heat transfer
Cold	Refers to the cold side reservoir
Hot	Refers to the hot side reservoir
Stat	Static
Eff	Effective
Appl	Applied

1. Introduction

For several decades the active magnetic regenerator (AMR) has been a research topic within the magnetic refrigeration community, as it is a potential alternative to vapor compression technology at room temperature. Such an AMR is based on the magnetocaloric effect (MCE), which manifests itself as a temperature change of a magnetocaloric material (MCM) upon adiabatically changing the magnetic field of the material. Since the maximum adiabatic temperature change of any known MCMs is no more than a few degrees in a magnetic field of one tesla (Pecharsky & Gschneidner, 2006), the regenerative cycle has to be applied in order to create temperature spans comparable to e.g. those of vapor-compression based cooling systems (Barclay, 1983). Recently, a range of experimental AMR devices have been built and a review of these can be found in Gschneidner & Pecharsky (2008); Yu et al. (2010). In Yu et al. (2003); Engelbrecht et al. (2007b) general reviews of room temperature magnetic refrigeration are given. Although improvements in AMR performance have been realized, there are currently no commercial devices available, and additional technology development is necessary. Therefore, it is critical to understand the fundamental loss mechanisms, performance limits, and optimal design of AMR systems using detailed models.

Since the AMR involves solid state physics, thermodynamics, fluid dynamics and magnetism a broad range of physical effects influences the performance of such a system. It is therefore quite important to have reliable numerical models such that the performance trends may be mapped out. A range of such models have been made already, however, a review of these models is not available at present. This paper provides such a review, which

not only include a discussion of the various models but also discusses in detail the various components of an AMR model and how they affect the model results.

1.1. The AMR cycle

The AMR cycle consists of four processes, which can overlap. First there is magnetization, where the field applied to the solid regenerator material is increased causing a temperature increase. Magnetization is followed by a fluid flow from the cold fluid reservoir to the hot fluid reservoir, rejecting heat to the ambient. During demagnetization the applied field is then reduced causing the temperature of the regenerator solid to drop and, finally, there is fluid flow from the hot reservoir to the cold, and a cooling load is accepted. The flow processes are governed by the same governing equations as for passive regenerators, which have been studied in detail by, for example, Hausen (1983); Dragutinovic & Baclic (1998); Willmott (1964). The major difference between passive regenerator models and AMR models is the implementation of the MCE and the timing between the magnetic field profile and the fluid flow profile. A range of AMR models exists and they differ in several ways such as number of spatially resolved dimensions, implementation details of flow and magnetic field profiles etc.

Several approaches to the overall AMR modeling are applied. Steady-state models are simple models, which may provide an estimate of the performance in terms of cooling power versus temperature span as a function of e.g. the geometry of the AMR. Time-dependent models provide a more complex description of the AMR. Since the change of the magnetic field and the fluid flow is inherently time dependent and is coupled with heat transfer

between a fluid and a solid, these models capture the physics on a more fundamental level. Both types of models are discussed in the following, although the emphasis is put on the time-dependent models, which are dominant in the more recent literature. In Section 2 the specifics of these models are discussed in detail. The remainder of this section gives an overview of the overall development of AMR models.

1.2. Steady-State AMR Models

There are several time independent models of AMR systems; these models are sometimes referred to as zero-period or steady-state models. The models generally start from an ideal AMR cycle and reduce the performance individually for estimated losses to axial conduction, heat transfer losses, etc. Steady state models are useful for qualitative investigations of AMR cycle characteristics; for example, the evaluation of the magnetocaloric properties of various materials in the context of an AMR cycle or the parametric investigation of the impact of a particular cycle parameter. The major benefit of these steady-state models is their computational efficiency; however, the predictive capability of a steady state model is limited as they are unable to capture interactions between loss mechanisms. Zhang et al. (2000); He et al. (2003); Zhang et al. (1993) and papers by Yan & Chen (1991, 1992) all present steady state models that can be used to understand the characteristics of various AMR cycle configurations. Shir et al. (2003) use a time independent model to show how magnetic nanocomposites may be used to obtain an ideal magnetic refrigerant, one in which the local adiabatic temperature change is proportional to the local absolute temperature. Rowe & Barclay (2003) presents a model based on entropy minimization that predicts

the ideal MCE along the length of the regenerator bed. The major shortcomings of all steady state models are their approach to capturing the effect of material properties and their macroscopic approach to estimating losses.

1.3. Time Dependent AMR Models

Researchers at Astronautics Corp. of America have presented the Finite Reduced Period (FRP) model; this AMR model is one-dimensional and time dependent, but it requires that the heat capacity of the entrained fluid in the regenerator be negligible compared to that of the magnetic material (DeGregoria et al., 1990; DeGregoria, 1991). In this limit, the conventional regenerator equations are solved during the flow portions of the cycle and instantaneous temperature changes are imposed at the conclusion of these processes. These temperature changes represent the magnetization and demagnetization processes, which are assumed to occur reversibly and adiabatically. The pumping loss, axial conduction, and dispersion losses are calculated separately and then subtracted from the predicted refrigeration power (Johnson & Zimm, 1996).

The FRP model has been applied primarily to the design of low temperature AMR systems that use a gas as the heat transfer fluid, as described by Janda et al. (1989), and therefore the assumption of negligible entrained fluid heat capacity is not overly restrictive.

Kirol & Mills (1984) describe a one-dimensional transient model of a magnetic cycle that assumes perfect regeneration. Smaili & Chahine (1998) describe a one dimensional transient model in which only the flow processes are considered; the magnetization and demagnetization processes are assumed to happen instantaneously and reversibly. The heat transfer coefficient is as-

sumed to be constant throughout the regenerator, and the impact of axial conduction and entrained heat capacity is not considered. Hu & Xiao (1995) present an analysis of AMR systems that is based on small perturbation theory; a technique that is used for pulse-tube type refrigeration systems, as described by several researchers including Hooijkaas & Benschop (1999). The governing equations are linearized and the fluctuating parameters are written in complex form, implying a sinusoidal variation of all such quantities.

These models consider regenerator geometries where the heat transfer between the solid and the fluid is described via a Nusselt number, i.e. the physical domain on which the heat transfer takes place is not resolved. Most geometries, such as packed spheres, wire mesh screens etc. make it quite difficult if not impossible to model the physical situation directly. However, a two-dimensional model of a flat plate AMR is described by Petersen et al. (2008b). The model uses a finite element (FEM) approach to solve for fluid flow profiles and temperature gradients in the solid and the liquid. Because of the increased complexity of the model, the computation time is much higher for the two-dimensional model than equivalent one-dimensional models. The geometry is fixed as a flat plate regenerator and modeling other regenerator geometries would require significant modifications to the existing model. See Appendix A for a summary of the published AMR models to date.

The overall goal of an AMR model is to predict the cooling power versus the temperature span, i.e. the difference in temperature between the hot and cold reservoirs. Including the work performed during the AMR cycle the coefficient of performance (COP) is also available. In this way the theoretical performance of an AMR may be mapped out using a numerical model.

2. Components in a numerical AMR model

This section describes the various aspects of an AMR model. These include the basic equations that are solved, how fluid flow and magnetic field profiles are implemented, how the MCE is addressed etc.

2.1. Basic energy balance equations

All numerical models of the AMR are based on a mathematical model describing heat transfer in a solid matrix structure, the MCE in the solid due to the changing magnetic field, and the coupling to the convective heat transfer of a fluid. Thus, the most general energy equation for the regenerator solid may be expressed as

$$\rho_s c_s \frac{\partial T_s}{\partial t} = \nabla \cdot (k_s \nabla T_s) + \dot{Q}_{\text{MCE}} + \dot{Q}_{\text{loss}} + \dot{Q}_{\text{HT}} \quad (1)$$

Here, with the subscript s for solid, the mass density is denoted by ρ_s , the specific heat is c_s , temperature is T_s , time is t , thermal conductivity is k_s , the MCE term \dot{Q}_{MCE} , irreversible losses are denoted by \dot{Q}_{loss} and finally the heat transfer between solid and fluid is denoted \dot{Q}_{HT} . In the case of a 1D model this will be given through a Nusselt-Reynolds correlation whereas for a 2D or 3D model the boundary interface between solid and fluid is usually spatially resolved and the term is thus expressing an internal boundary condition. However, 2D or 3D models may apply Nusselt-Reynolds correlations as well. The energy equation for the heat transfer fluid may be written as

$$\rho_f c_f \left(\frac{\partial T_f}{\partial t} + (\mathbf{u} \cdot \nabla) T_f \right) = \nabla \cdot (k_f \nabla T_f) + \dot{Q}_{\text{loss}} - \dot{Q}_{\text{HT}} \quad (2)$$

Here the subscript f denotes fluid and $\mathbf{u} = (u_x, u_y, u_z)$ is the fluid velocity vector. The energy balance equations are assumed valid over the length scale of the regenerator.

The problem intrinsically also involves fluid dynamics and thus the Navier-Stokes equations must also be solved

$$\frac{\partial \mathbf{u}}{\partial t} + (\mathbf{u} \cdot \nabla) \mathbf{u} = \frac{\mu_f}{\rho_f} \nabla^2 \mathbf{u} - \frac{1}{\rho_f} \nabla p \quad (3)$$

$$\nabla \cdot \mathbf{u} = 0, \quad (4)$$

where μ_f is the dynamic viscosity and p is pressure. Now, Eqs. 3-4 represent a Newtonian incompressible flow. If, e.g., a gas is used as heat transfer fluid (HTF), the more involved compressible Navier-Stokes equations may be necessary. In most cases Eqs. 3-4 are simplified into analytical expressions, which is the case in the 1D and 2D models (e.g. Nielsen et al. (2009a)) or solved numerically (e.g. Petersen et al. (2008b)).

In general, AMR mathematical models include the following assumptions, also used for passive heat regenerator analysis (Shah & Sekulic, 2003)

- No phase change in the fluid occurs. As long as water with anti-freeze is used as HTF, this is a fully valid assumption.
- The fluid is incompressible and thus no compression/expansion of the fluid and no pressure oscillations occur during the flow periods. Again, when a water/anti-freeze HTF is used this is valid.
- No flow leakage or flow bypassing occurs. This is definitely a simplifying assumption. Experimentally it may be very difficult to control flow

bypassing properly.

- Heat transfer caused by radiation within the regenerator is negligible compared to the convective and conductive heat transfer. For near room-temperature applications this is a good approximation since very little heat transfer occurs through radiation.
- The solid within the regenerator is uniformly distributed with no edge effects. This is a simplifying assumption that is notoriously difficult to control in experiments.

2.2. One-dimensional models

Many AMR models are one-dimensional and thus assume a Nusselt number correlation as a function of the Reynolds number in order to describe the convective heat transfer between the solid and the fluid. Expressing Eqs. 1–2 in one dimension, the equations for the solid and the fluid in the 1D case can be defined as:

$$\rho_s c_s \frac{\partial T_s}{\partial t} = \frac{\partial}{\partial x} \left(k_s \frac{\partial T_s}{\partial x} \right) + \dot{Q}_{\text{MCE}} + \dot{Q}_{\text{loss}} + \dot{Q}_{\text{HT}} \quad (5)$$

$$\rho_f c_f \left(\frac{\partial T_f}{\partial t} + u_x \frac{\partial T_f}{\partial x} \right) = \frac{\partial}{\partial x} \left(k_f \frac{\partial T_f}{\partial x} \right) + \dot{Q}_{\text{loss}} - \dot{Q}_{\text{HT}} \quad (6)$$

2.3. Implementation of the heat transfer between the fluid and the solid

In all 1D models a heat transfer coefficient, h , describing the heat transfer between the fluid and the solid must be used. The heat transfer rate can be written as

$$\dot{Q}_{\text{HT}}(x) = h A_{\text{HT}} (T_s(x) - T_f(x)) \quad (7)$$

where the wetted area per unit cell of the solid material is denoted A_{HT} . Perhaps the most crucial parameter in a 1D model is the heat transfer coefficient. This parameter presents a correlation for the convective heat transfer between the solid and the fluid and the most crucial part of the AMR model thus relies on it. In general, correlations for h are presented in literature (Nusselt-Reynolds correlations). However, often the correlations do not cover the total operational range in terms of the Reynolds number and various correlations exist making it difficult to decide which is the “most correct” to use in a given situation. According to Sarlah & Poredos (2010) a 10 percent higher heat transfer coefficient yields about 4 percent higher temperature span of the AMR.

The equations for the fluid and the solid in 2D models are usually not coupled through a heat transfer coefficient, but rather an internal boundary condition, which defines thermal contact between the fluid and the solid (Petersen et al., 2008b; Nielsen et al., 2009a; Oliveira et al., 2009). As expected, and as was shown in Petersen et al. (2008a) 1D models may in fact yield very similar results to 2D models given certain circumstances; especially when the fluid channels and solid plates are thin and thus the internal thermal gradients perpendicular to the direction of the flow are negligible.

Sarlah & Poredos (2005) developed a partial 2D model of the AMR based on parallel plates. They used a one-dimensional equation for the heat transfer in the fluid and a two-dimensional heat transfer equation for the solid. Thus, they calculated the temperature distribution in the solid (in the flow direction and a perpendicular direction), but they used a correlation for the heat transfer coefficient for the heat transfer between the fluid and solid (very

similar to the regular 1D approach) on the form:

$$k_s \left. \frac{\partial T_s}{\partial y} \right|_{y=H} (x) = h (T_s(x, y = H) - T_f(x, y = H)) \quad (8)$$

where the position in the y -direction denoted H refers to the contact point between the solid and fluid.

Since 1D models do not directly account for temperature gradients in the solid material, it has been suggested to reduce the heat transfer coefficient between solid and fluid to account for the losses (Jeffreson, 1972; Engelbrecht et al., 2006). Both Engelbrecht (2008) and Sarlah (2008) used a correction factor for the heat transfer coefficient making it into an effective heat transfer coefficient and thus, to a certain extent, took into account the effect of a non-uniform temperature distribution in the solid perpendicular to the flow direction.

2.4. Two-dimensional models

Petersen et al. (2008b) were the first to implement a complete 2D model of a parallel-plate based AMR at room temperature. In their model the spatially resolved dimensions are the x - and y -directions, i.e. the direction along the flow and the direction perpendicular to the flow and along the thickness of the solid plate. The equations for the solid and fluid used in the Petersen et al. 2D model may be written as

$$\rho_s c_s \frac{\partial T_s}{\partial t} = k_s \left(\frac{\partial^2 T_s}{\partial x^2} + \frac{\partial^2 T_s}{\partial y^2} \right) \quad (9)$$

$$\rho_f c_f \left(\frac{\partial T_f}{\partial t} + u \frac{\partial T_f}{\partial x} \right) = k_f \left(\frac{\partial^2 T_f}{\partial x^2} + \frac{\partial^2 T_f}{\partial y^2} \right) \quad (10)$$

$$\rho_f \left(\frac{\partial \mathbf{u}}{\partial t} + (\mathbf{u} \cdot \nabla) \mathbf{u} \right) = \mu_f \nabla^2 \mathbf{u} - \nabla p \quad (11)$$

$$\nabla \cdot \mathbf{u} = 0 \quad (12)$$

assuming constant thermal conductivity and that $\mathbf{u} = (u_x, u_y, 0)$. The heat transfer between the solid and fluid domains is modeled through an internal boundary condition, which can be expressed as

$$k_s \frac{\partial T_s}{\partial y} = k_f \frac{\partial T_f}{\partial y} \quad (13)$$

which is valid on the boundary between the two domains only. Oliveira et al. (2009) formulated the 2D AMR problem in a very similar way, albeit using non-dimensional variables.

Very recently, Liu & Yu (2010) presented a 2D model of a porous structure. The authors show that it is possible to track the 2-dimensional temperature distribution in the regenerator bed. In this way internal temperature gradients orthogonal to the flow direction may be resolved.

The equations presented above (1 and 2) (for both 1D and 2D models) include the effect of thermal conduction in the solid and the fluid, convective heat transfer, viscous losses, heat losses to the surroundings and, of course, the MCE. These effects have varying influence on the operation of an AMR and different models thus include various effects, which are discussed below in detail.

2.5. Three-dimensional models

Bouchard et al. (2009) presented a three-dimensional model of the AMR with a regenerator comprised of particles of spherical and elliptical nature.

Their model solves the fully coupled problem with the governing equations including Eqs. 1-2, the incompressible Navier-Stokes equations and the relevant magnetostatic equations describing the coupling between the applied magnetic field, magnetization and internal magnetic field. The model of Bouchard et al. (2009) is of great interest since it is the first (published) attempt to model the full geometry of an AMR including magnetostatics. Such a model may provide deeper insights into the actual ongoing physics in the regenerator. The results are so far of a limited nature, however, improvements and further results are expected.

2.6. Other mathematical models

Kitanovski et al. (2005) developed a numerical steady state model for a rotary AMR. The model was described in cylindrical coordinates. The radial dimension was neglected. Because of the higher frequency the longitudinal heat conduction was neglected as well. Results of the analysis provided a 2D map of temperature gradients in the solid and fluid, respectively.

2.7. Boundary conditions

Initial and boundary conditions have to be specified in order for any AMR model to be solved. These conditions include hot and cold side fluid inlet temperatures and boundary conditions towards the ambient. The common way of defining the boundary conditions is given in Tab. A.1.

TABLE 1

In the 2D and 3D cases an internal boundary condition similar to that given in Eq. 13 is needed to describe heat transfer between the fluid and the solid. Steady state operation is specified by setting the temperature of the

fluid and solid at the beginning of the cycle to the temperature at the end of the previous cycle.

2.8. Implementation of the magnetocaloric effect

In order to analyze the operation of the AMR, magnetic properties need to be included in the model. The adiabatic temperature change, ΔT_{ad} , and specific heat of the solid is generally a function of both temperature and magnetic field and appropriate look-up tables should be applied. The MCE is generally implemented in one of two ways.

The simplest and most straightforward way of including the MCE in the model is to apply the adiabatic temperature change to the solid during the processes of magnetization or demagnetization directly. This may be formulated mathematically as

$$T = T_i + \Delta T_{\text{ad}}(T_i, \mu_0 H_i, \mu_0 H_f) \quad (14)$$

where the initial temperature is denoted T_i , the initial magnetic field H_i and the final magnetic field is H_f .

The adiabatic temperature change as a function of temperature, initial and final magnetic field can be derived from experimental data tables or using the mean field model (MFM) (Morrish, 1965) and many authors have used the MFM in their AMR numerical models (Petersen et al., 2008b; Nielsen et al., 2009a; Smaili & Chahine, 1998; Li et al., 2006; Allab et al., 2005; Siddikov et al., 2005; Oliveira et al., 2009; Aprea et al., 2009; Tagliafico et al., 2010; Sarlah & Poredos, 2005; Kitanovski et al., 2005).

The following equation may be used to describe the energy release in

the magnetocaloric material during magnetization or demagnetization over a period of time

$$\dot{Q}_{\text{MCE}} = -T_s \frac{\partial M}{\partial T} \mu_0 \frac{\partial H}{\partial t} \quad (15)$$

with the volumetric magnetization denoted M . This equation is simply derived from the basic thermodynamics of the MCE using the Maxwell relation between the derivative with respect to magnetic field of the entropy and the derivative of the magnetization with respect to temperature. This expression was employed in the models published by e.g. Shir et al. (2004); Engelbrecht et al. (2007a); Nielsen et al. (2009a). This way of implementing the MCE is a so-called built-in method.

The built-in method for including the MCE in the model presupposes a continuous change of the magnetic field, which will certainly always be the case in an experiment. However, this method requires detailed, and numerically differentiable data sets of the magnetization and specific heat as functions of both temperature and magnetic field. These may not always be available from experimentally obtained data for MCMs.

The processes of magnetization and demagnetization in an AMR can be simulated by both methods. However, the selection of the most suitable method in general depends on the purpose of the simulations. If the main goal of the numerical model is to simulate actual experimental AMRs with high accuracy, it is crucial to use the experimentally obtained magnetocaloric properties of the chosen magnetocaloric material. However, in the case that sufficient experimental data is not available, the direct application of the adiabatic temperature change may be the best method of applying the MCE.

2.9. Effect of longitudinal thermal conduction

Longitudinal thermal conduction is included in most models. It has a large influence on the operation of the AMR under certain geometric and operational circumstances, especially for regenerators with a relatively short length and a structure continuously connected along the flow direction (e.g. parallel plates) and/or for small values of the utilization, where the fluid is, of course, moved a short distance. The utilization is defined as the ratio of the thermal mass of the HTF moved to the total thermal mass of the regenerator solid

$$\varphi = \frac{\dot{m}_f c_f \tau_2}{m_s c_s}, \quad (16)$$

where the mass flow rate is denoted \dot{m}_f and the duration of the blow period is τ_2 . This is also related to the frequency of the operation. A lower frequency means a larger influence of the longitudinal thermal conduction.

Figure A.1 shows the impact of the longitudinal thermal conduction at different mass flow rates and at two different operating frequencies. It should be noted that the thermal conduction is extremely important to consider at low mass flow rates (low utilizations) and low cycle frequency, since under these conditions the convective heat transfer due to fluid movement is of the same order as the thermal conduction of the fluid and does thus not dominate the heat transfer of the fluid as it does for larger mass flow rates.

FIGURE 1

Among the published AMR numerical models, some include longitudinal thermal conduction in the solid as well as in the fluid (Petersen et al., 2008b; Nielsen et al., 2009a; Kawanami et al., 2006; Siddikov et al., 2005; Tagliafico et al., 2010; Legait et al., 2009; Dikeos et al., 2006), which is physically

the most correct. Engelbrecht (2008); Sarlah (2008); Dikeos et al. (2006) included longitudinal thermal conduction in the system through an effective longitudinal thermal conduction. In porous media, such as a packed sphere regenerator, the conduction path through the solid and fluid is complex and difficult to separate and model independently. Therefore, the fluid/solid matrix is modeled as a single entity regarding longitudinal thermal conduction, which is expressed in the parameter k_{eff} . Such a measure not only simplifies the equation for the fluid, but may also improve the stability of the numerical simulation (Sarlah, 2008). The effective longitudinal thermal conduction of the solid and the fluid may be expressed as

$$k_{\text{eff}} = k_{\text{stat}} + k_f D_p(\text{Pe}) \quad (17)$$

where D_p is the dispersion coefficient, which is a function of the Peclet number, Pe . Correlations for the static conduction, k_{stat} , and the dispersion coefficient may be found in e.g. Hadley (1986).

Thermal dispersion is a complex phenomenon and may be understood as thermal conduction due to hydrodynamic mixing in the fluid. This mixing occurs due to the geometry of the solid structure and is thus much more complicated to derive in a packed sphere based regenerator than in, e.g., parallel-plate based regenerators. A continuously connected solid as, e.g., parallel plates may have a significant dispersion due to higher longitudinal thermal conductivity.

2.10. Effect of viscous dissipation

Viscous dissipation in the fluid is the irreversible degradation of mechanical energy into heat and may have a large impact on the thermal analysis of the regenerator. The impact of the viscous losses is included in most models using a friction factor correlation as presented in e.g. Engelbrecht (2008); Sarlah (2008); Dikeos et al. (2006). Viscous dissipation is generally low for most prototype AMRs and is often neglected in models of AMRs and other regenerators. However, as regenerator geometries reduce in size and AMRs operate at higher frequency, which requires higher fluid flow to maintain an equal utilization, viscous dissipation will increase and may become significant for future AMR configurations or operating conditions.

Figure A.2 shows the impact of the pressure drop on the COP of packed spheres AMR with water as a heat transfer fluid at different mass flow rates. Note that pressure drop (viscous losses) affects the COP through irreversible viscous losses as well as through the work needed to pump the fluid through the AMR. The impact on the COP is seen to be most profound at higher mass flow rates (higher utilizations) as expected.

FIGURE 2

2.11. Heat losses

Most AMR models assume perfect insulation to the ambient and ignore thermal interactions with the regenerator housing. That means that parasitic losses due to inevitable temperature gradients between the regenerator and the surroundings are neglected. As far as we know, only one model has included a formulation of the parasitic losses to ambient through the concept

of an extra “half” dimension (Nielsen et al., 2009a). This extra spatial dimension is not numerically resolved but a lumped heat loss term is applied and found through analyzing the thermal resistance from the regenerator core to the ambient. Results show that this effect may have a significant impact on the AMR performance (Nielsen et al., 2009a,c). Figure A.3 shows an example of including the thermal losses in a numerical AMR model.

Frischmann et al. (2009) present a model that considers the thermal interaction between the fluid and regenerator housing using a dispersion model that considers radial temperature gradients within the regenerator. Experimental single blow data showed that the regenerator housing significantly reduced the apparent heat transfer in the regenerator, especially at low Reynolds numbers (Frischmann et al., 2009). Thermal interactions with the regenerator housing and with the ambient can be a significant loss mechanism for AMRs. However, the authors are not aware of work that studies these losses in detail.

FIGURE 3

2.12. Magnetic field change

In general, the magnetic field change can be distinguished between discrete “on-off” and a continuous change (Fig. A.4). If the discrete magnetic field change is assumed, the inclusion of the MCE is limited to the application of the adiabatic temperature change directly since the built-in method is meaningful only with continuous magnetic field changes. However, if the purpose of the numerical model is to simulate the experimental operation of an AMR, it may be important to implement the time-dependent change of the magnetic field as the magnetic field change and fluid flow processes

often overlap in real AMR devices. The time-dependent change of the magnetic field can generally be handled with both methods of including the MCE presented in Sec. 2.8.

FIGURE 4

Most AMR models neglect spatial-dependent magnetic field changes and assume that each piece of magnetocaloric material in the AMR is subject to the same magnetic field change at a given point in time. In Nielsen et al. (2009a) an experimental AMR device was modeled with a spatially resolved applied magnetic field. Bjørk & Engelbrecht (2011) show that the synchronization and width of the magnetic field can be of great importance to the AMR performance. The effect of the demagnetizing field, presented in Sec. 2.8, may have a strong influence on the spatial variation of the internal magnetic field in an AMR. The demagnetizing field is generally a function of geometry, temperature and the material properties of the MCM (Smith et al., 2010; Brug & Wolf, 1985).

2.13. Materials properties

The physical properties of the fluid and the solid are important to include in a physically realistic way. The heat transfer fluid most commonly assumed when modeling AMRs is water perhaps with added anti-corrosives and anti-freeze (Engelbrecht, 2008; Aprea et al., 2009; Tagliafico et al., 2010; Petersen et al., 2008b; Nielsen et al., 2009a). In this case the fluid may safely be assumed to be incompressible and most authors also assume constant fluid properties, i.e. viscosity, mass density and specific heat (Petersen et al., 2008b; Nielsen et al., 2009a; Li et al., 2006; Allab et al., 2005; Oliveira et al., 2009; Aprea et al., 2009; Dikeos et al., 2006), whereas a few have imple-

mented models with temperature-dependent properties (Engelbrecht, 2008; Engelbrecht et al., 2007a; Siddikov et al., 2005). When the temperature of water is changed, for example, from 0 to 40 °C the mass density and specific heat are consequently changed by less than 1 percent, while the dynamic viscosity may depend on temperature but has less effect on the performance of the AMR. If, for example, a gas is used as the heat transfer fluid, the assumption of constant physical properties would lead to a much greater error since mass density, specific heat, thermal conductivity and dynamic viscosity of gasses depend significantly on temperature and pressure. Also, an equation of state is needed if the flow cannot be considered incompressible. However, the effect on the AMR performance due to temperature-dependent fluid properties has not been investigated in great detail yet.

Many authors assume temperature independence of mass density and thermal conductivity of the MCM (see Table A.2). This assumption depends highly on the MCM considered. Considering e.g. gadolinium the thermal conductivity and the mass density do not change significantly around room temperature (see e.g. Jacobsson & Sundqvist (1989) for details) whereas at both lower and higher temperatures the thermal conductivity is dependent on temperature. The specific heat of the MCM varies significantly with temperature and magnetic field – especially around the magnetic transition temperature of the material – and should thus not be assumed to be constant. Also, some materials (usually exhibiting a 1st order transition) have a structural transition close to the magnetic phase transition temperature. This often induces changes in the volume of the material and thus also the mass density and perhaps even the thermal conductivity.

It is important that the thermodynamic MCM properties are consistent. If care is not taken when determining specific heat and the corresponding entropy change with magnetization or adiabatic temperature change, model predictions can become unrealistic. An example of inconsistent thermodynamic properties is the assumption of a specific heat that is independent of magnetic field combined with a constant adiabatic temperature change with magnetization. If the specific heat of the material is used to calculate the entropy curves for zero field and a high magnetic field, the two will be equal because the specific heat is constant. This means that the entropy change with magnetization, and therefore adiabatic temperature change, is zero, which contradicts the assumption of a constant non-zero adiabatic temperature change. Using a material with constant specific heat with an assumed adiabatic temperature change will result in an over prediction of cooling power, and a cycle that does not obey the 2nd law of thermodynamics.

2.14. Flow conditions

A periodic fluid flow is present in all numerical AMR models. It is of great importance to implement the fluid flow correctly and several approaches for this have been made. Two main considerations should be done carefully.

- The assumptions about the actual flow include whether the flow is laminar, incompressible, fully developed, temperature dependent etc.
- The representations of the change in input velocity can be a discrete step function, following a sinusoidal curve or whichever profile an experimental AMR device uses.

In models where the flow is transversally resolved (in one or two dimensions perpendicular to the flow direction) a flow-profile is needed. If the geometry is simple the profile may be derived analytically as is the case for models of parallel plate regenerators (Nielsen et al., 2009a) or in more advanced cases a numerical solution to the Navier-Stokes equation for the fluid velocity profile may be needed (Bouchard et al., 2009).

The determination of the mean fluid velocity is usually done through a fixed mass flow rate or similar; however, the temporal change of the mean fluid velocity is implemented differently. Some authors assume a discrete velocity profile as a function of time such that the flow is either on or off (Li et al., 2006; Allab et al., 2005; Siddikov et al., 2005; Aprea et al., 2009; Petersen et al., 2008a; Nielsen et al., 2009a), perhaps through a ramping method (Petersen et al., 2008b; Nielsen et al., 2009a) and some models assume a more realistic continuous flow curve as a function of time (Dikeos et al., 2006; Nielsen et al., 2009a; Engelbrecht, 2008; Oliveira et al., 2009). It was argued in Nielsen et al. (2010) that for the general purpose of theoretical evaluation of the AMR performance discrete velocity profiles may be the best option since it removes the possible impact of specific experimental devices. In Nielsen et al. (2009a) and Nielsen et al. (2010) it was argued that when modeling experimental devices it is of great importance to actually make the flow profile in the numerical model resemble that of the experiment, which may seem obvious but is not necessarily always how models are implemented.

2.15. Channeling effects

Flow channelling is caused by a non uniform porosity distribution in the transverse bed direction. For a packed particle bed the porosity at the wall

is typically greater than the porosity at the center position of the regenerator. As a consequence, the pore velocity near the wall will be larger than the center velocity due to the lower pressure drop close to the wall (Kaviany, 1995; Achenbach, 1995). Flow channelling will result in cold or hot bypasses that will lower the effectiveness of the regenerator (Chang & Chen, 1998). The amount of flow channeling depends greatly on the ratio of regenerator diameter, d_r , to particle diameter, d_p . The flow channeling becomes more important with decreasing ratio d_r/d_p (Nemec & Levec, 2005). In order to resolve the radial velocity distribution the volume averaged transport equations for the momentum transport may be used (Hsu, 2005).

$$\epsilon(r) \frac{dp}{dz} = \mu \left(\frac{d^2 u_z}{dr^2} + \frac{1}{r} \frac{du_z}{dr} \right) - \frac{\mu u_z}{K(r)} - F \rho \frac{|u_z| u_z}{\sqrt{K(r)}} \quad (18)$$

Here u_z is understood as the superficial velocity, i.e. the velocity the flow would have if the bed was empty, in the axial direction. The permeability for a particle bed is $K = \epsilon^3 d_p^2 / (a(1-\epsilon)^2)$ and the Forchheimer factor $F = b / \sqrt{a\epsilon^3}$ with $a = 150$, $b = 1.75$ and ϵ being the porosity. In this sense the regenerator is understood as a continuum described by a radial porosity distribution. An extensive review on porosity distributions for packed beds can be found in du Toit (2008). They strongly recommend the use of the following correlation for the porosity

$$\epsilon(r) = \epsilon_\infty + (1 - \epsilon_\infty) \exp \left[-\frac{N}{d_p} r \right] \quad (19)$$

with $N = 6000$ and $\epsilon_\infty = V_f / (V_f + V_s)$ being the bulk porosity. Equation (18) can be solved with standard solvers in, e.g., Matlab using the boundary conditions $dv_z(r=0)/dr = 0$ and $v_z(r=R) = 0$. The pressure gradient is

assumed to be constant (i.e. obtained from experiments).

FIGURE 5

Figure A.5 shows the radial velocity profile close to the wall. A significant departure of the radial velocity adjacent to the wall from the center velocity is observable. There are two ways to resolve flow channeling in an actual model for a magnetic refrigerator device: resolve the regenerator on a 2D computational domain or account for a modified pressure drop and heat transfer correlation that takes flow channeling (and therewith the ratio d_r/d_p) into account (Achenbach, 1995). So far the channeling effect has not been studied in detail in terms of its impact on the AMR cycle. This may certainly pose a significant issue to address.

2.16. Modeling of graded AMRs

It has been experimentally shown that grading the regenerator along the flow direction with a range of MCMs each with a different Curie temperature increases the AMR performance (Rowe & Tura, 2006). This is an area of the magnetic refrigeration research where numerical models may prove to have the most significant impact. The optimal performance of the AMR as a function of multiple MCMs, i.e. through a variation of the Curie temperatures of each material, the number of materials and perhaps even the amount of each material, pose a very large problem due to the many free parameters. In this area only a few models have been applied (Jacobs, 2009; Engelbrecht et al., 2007b; Nielsen et al., 2009b). Layered regenerators are generally modeled by assigning solid material properties as a function of position in the regenerator. Several problems arise when considering the modeling of graded regenerators. Apart from the vast parameter space, magnetocaloric data for

each of the individual materials may not yet be available to such a degree that it is usable for this kind of modeling. Also, the interface between each material should be considered. This could demand spatially varying thermal conductivity, mass density etc. It is noted that knowledge of whether the amount of each individual MCM should be the same for optimal performance of the AMR or if it could be beneficial to have an asymmetrical distribution of the materials. The definition of the problem inherently also includes the intended application. Figure A.6 shows a schematic of the concept of layering an AMR bed.

FIGURE 6

2.17. Implementing the effect of demagnetization

It is well-known that the internal magnetic field of a magnetic material in a homogeneously applied magnetic field can be highly inhomogeneous, an effect known as geometric demagnetization (Bouchard et al., 2005, 2009; Smith et al., 2010; Joseph & Schloemann, 1965; Brug & Wolf, 1985; Peksoy & Rowe, 2005). In fact, the internal magnetic field may be reduced to as little as a few percent of the applied field dependent on the temperature of the sample, the sample's geometry, and direction and magnitude of the applied magnetic field (Smith et al., 2010). This effect may be understood through the demagnetizing field, which is generally dependent on the geometry of the magnetic material and the orientation of the applied magnetic field as well as the spatially non-constant magnetization, which is a function of both the internal magnetic field and temperature in turn. This emphasizes the highly non-linear nature of the demagnetization problem and it is basically impossible to simplify it into e.g. an extra source term in the energy equation

of the solid. A fully coupled numerical model for calculating the internal magnetic field is thus needed and should be solved simultaneously with the heat transfer model.

It is emphasized that the MCE, whether expressed as the isothermal entropy change or the adiabatic temperature change, should be considered as a function of the internal magnetic field. Of course, measurements may be reported as a function of applied magnetic field, but in order to compare materials properties of different materials between different experimental setups the internal magnetic field is the proper independent variable (and, of course, so is also the temperature).

So far only a few published numerical AMR models have included this effect (Bouchard et al., 2005, 2009; Nielsen et al., 2010; Peksoy & Rowe, 2005). In Bouchard et al. (2005, 2009) the effect of demagnetization was included as an extra coupled equation to be solved together with the thermal equations. However, the results were not discussed in detail in terms of the impact of this on the AMR cycle. It was shown, however, that the adiabatic temperature change may be considerably affected when accounting for demagnetization (Bouchard et al., 2005), which is consistent with the recent results from Christensen et al. (2010) and Bahl & Nielsen (2009).

In Peksoy & Rowe (2005) the demagnetization was investigated for a symmetric regenerator setup and the resulting magnetization showed as a function of position in the regenerator under various conditions. The results showed that care should indeed be taken when deciding how to align the applied magnetic field with respect to the regenerator material when considering thermal gradients in the system etc.

In other extreme cases, such as described in Bahl & Nielsen (2009), the effect may be significant. An example of the resulting internal magnetic field is shown in Fig. A.7. It is apparent that there is a vast difference between the resulting internal magnetic field dependent on the orientation of the applied magnetic field and the temperature of the MCM. The more ferromagnetic the material is the more significant the effect is. In the case of applying the field perpendicular to the largest surface of the plate (Fig. A.7b) the internal field may be decreased with up to 80 percent for the cases considered here.

FIGURE 7

2.18. Hysteresis effect in AMR modeling

In literature it is often argued that with a 1st order magnetic transition MCMs are among the most promising candidates as refrigerants in an AMR device due to their large MCE. However, at least three very important aspects of this assumption have not yet to our knowledge been investigated in detail. Firstly, the MCE is usually confined to a quite narrow temperature interval for 1st order materials compared to 2nd order materials. Secondly, the specific heat usually has a high but narrow peak around the Curie temperature and the peak temperature changes as a function of magnetic field (e.g. Palacios et al. (2010)). Thirdly, the inherent hysteretic effects present in most 1st order materials (e.g. Pecharsky & Gschneidner (2006) and Tocado et al. (2009)) have not yet been considered in any published AMR model.

In Basso et al. (2005, 2006) the fundamentals of hysteresis were considered for magnetic materials and to some extent that analysis covered initial steps to evaluate the impact on the AMR cycle. In Kitanovski & Egolf (2009) the hysteretic losses were implemented as a scalar quantity expressing

a degradation of the efficiency of an AMR device. However, this efficiency was estimated and not found through a rigorous analysis. At present the hysteresis effect has not been implemented in any AMR model and that is thus a quite relevant task to be done. Generally, an analysis of the impact of the special behavior of the magnetocaloric properties of 1st order materials should certainly be performed. The operating frequency of the AMR cycle may be limited by e.g. the inherently slower 1st order transition (Gschneidner et al., 2005). See Kuz'min (2007) for other examples of limiting factors to the AMR frequency.

3. Conclusion

A large range of numerical AMR models were discussed. The individual components of a general AMR model were described in detail and their impacts were discussed. The rank, or dimensionality, of the individual AMR models ranges from 1D to 3D. Most models published are 1D of nature and thus include a heat transfer correlation to describe the heat transfer between the solid regenerator matrix and the heat transfer fluid. It was also argued, on the other hand, that 2- or 3D models are difficult to realistically implement to model complex structures different from e.g. parallel plates, even though a first attempt of full 3D-modeling of a particle bed has been published. It is therefore concluded that each kind of model is relevant to consider and that the requirements of the particular case modeled should be carefully analyzed when choosing which kind of model to use.

The various components of an AMR model, such as the implementation of the MCE, flow profiles etc., were discussed in detail. It may generally be

concluded that it is important to ensure that the 2nd law of thermodynamics is not violated. Furthermore, each component should be implemented as detailed as possible, which includes the use of proper experimental data, consideration of the resulting internal magnetic field, proper applied magnetic field and flow profiles in accordance with any experiment modeled etc. It should be stressed, however, that simpler models are usually much easier to interpret and, especially, to ensure to be numerically well-behaved. It may therefore be recommended to use a simple model to try to identify the most important physical processes of a given geometry and configuration, and to build on that to implement more sophisticated models.

The modeling of AMR cannot be said to be sufficient as is. Several very interesting physical aspects have not been considered yet, at least not in detail. The hysteresis inherent in most 1st order materials should be the topic of detailed future investigations as should the special specific heat curves that such materials exhibit. The effect of demagnetization on the performance of the AMR should also be the topic of detailed future investigations.

Appendix A. Summary of published AMR models

TABLE A.1

Acknowledgements

K.K. Nielsen, K. Engelbrecht, C.R.H. Bahl, A. Smith and N. Pryds thank the support of the Programme Commission on Energy and Environment (EnMi) (Contract no. 2104-06-0032) which is part of the Danish Council for Strategic Research. K. K. Nielsen also thanks the Danish Agency for

Science, Technology and Innovation under the Danish Ministry for Science, Technology and Innovation.

References

- Achenbach, E. (1995). Heat and flow characteristics of packed beds. *Experimental Thermal and Fluid Science*, 10(1):17–27.
- Allab, F., Kedous-Lebouc, A., Fournier, J., and Yonnet, J. (2005). Numerical modeling for active magnetic regenerative refrigeration. *IEEE Transactions on Magnetics*, 41(10):3757–3759.
- Aprea, C., Greco, A., and Maiorino, A. (2009). A numerical analysis of an active magnetic regenerative cascade system. In Egolf, P. W., editor, *Third International Conference on Magnetic Refrigeration at Room Temperature*, pages 259–265. International Institute of Refrigeration.
- Bahl, C. R. H. and Nielsen, K. K. (2009). The effect of demagnetization on the magnetocaloric properties of gadolinium. *Journal of Applied Physics*, 105(1):013916 (5 pp.).
- Bahl, C. R. H., Petersen, T. F., Pryds, N., and Smith, A. (2008). A versatile magnetic refrigeration test device. *Review of Scientific Instruments*, 79(9):093906.
- Barclay, J. A. (1983). Theory of an active magnetic regenerative refrigerator. *NASA Conference Publication*, pages 375–387.

- Basso, V., Bertotti, G., LoBue, M., and Sasso, C. (2005). Theoretical approach to the magnetocaloric effect with hysteresis. *Journal of Magnetism and Magnetic Materials*, 290-291(Part 1):654–657.
- Basso, V., Sasso, C. P., Bertotti, G., and LoBue, M. (2006). Effect of material hysteresis in magnetic refrigeration cycles. *International Journal of Refrigeration*, 29(8):1358–1365.
- Bjørk, R. and Engelbrecht, K. (2011). The influence of the magnetic field on the performance of an active magnetic regenerator (AMR). *International Journal of Refrigeration*, 34:192–203.
- Bouchard, J., Nesreddine, H., and Chahine, R. (2005). Impact of demagnetization on magnetocaloric effect in pure gadolinium. *1st International Conference on Magnetic Refrigeration at Room Temperature*, pages 93–101.
- Bouchard, J., Nesreddine, H., and Galanis, N. (2009). Model of a porous regenerator used for magnetic refrigeration at room temperature. *International Journal of Heat and Mass Transfer*, 52(5-6):1223–1229.
- Brug, J. and Wolf, W. (1985). Demagnetizing fields in magnetic measurements i. thin discs. *Journal of Applied Physics*, 57(10):4685–4694.
- Chang, Z.-C. and Chen, P.-H. (1998). Flow channeling effect on a regenerator’s thermal performance. *Cryogenics*, 38(2):191–196.
- Christensen, D. V., Bjørk, R., Nielsen, K. K., Bahl, C. R. H., Smith, A., and Clausen, S. (2010). Spatially resolved measurements of the magnetocaloric

- effect and the local magnetic field using thermography. *Journal of Applied Physics*, 108(6):063913.
- DeGregoria, A. (1991). Modeling the active magnetic regenerator. *Advances in Cryogenic Engineering*, 37(pt B):867–873.
- DeGregoria, A. J., Barclay, J. A., Claybaker, P. J., Jaeger, S. R., Kral, S. F., Pax, R. A., Rowe, R., and Zimm, C. B. (1990). Preliminary design of a 100 w 1.8 k to 4.7 k regenerative magnetic refrigerator. *Advances in Cryogenic Engineering*, 35:1125–1131.
- Dikeos, J., Rowe, A., and Tura, A. (2006). Numerical Analysis of an Active Magnetic Regenerator (AMR) Refrigeration Cycle. *AIP Conference Proceedings*, 823(1):993 – 1000.
- Dragutinovic, G. D. and Baclic, B. S. (1998). *Operation of Counterflow Regenerators*. Computational Mechanics Inc., Billerica, MA.
- du Toit, C. (2008). Radial variation in porosity in annular packed beds. *Nuclear Engineering and Design*, 238(11):3073–3079.
- Engelbrecht, K. (2008). *A Numerical Model of an Active Magnetic Regenerator Refrigerator with Experimental Validation*. PhD thesis, University of Wisconsin, Madison.
- Engelbrecht, K., Nellis, G. F., and Klein, S. A. (2007a). Comparing modeling predictions to experimental data for active magnetic regenerative refrigeration systems. In Egolf, P. W., editor, *Second International Conference on Magnetic Refrigeration at Room Temperature*, pages 349–357. International Institute of Refrigeration.

- Engelbrecht, K. L., Nellis, G. F., and Klein, S. A. (2006). The effect of internal temperature gradients on regenerator matrix performance. *Journal of Heat Transfer*, 128(10):1060–1069.
- Engelbrecht, K. L., Nellis, G. F., Klein, S. A., and Zimm, C. H. (2007b). Review article: Recent developments in room temperature active magnetic regenerative refrigeration. *HVAC and R Research*, 13(4):525.
- Frischmann, M., Jacobs, S., Nellis, G., and Klein, S. (2009). Measuring nusselt number using a single-blow regenerator facility. In Egolf, P. W., editor, *Third International Conference on Magnetic Refrigeration at Room*, pages 443–448. International Institute of Refrigeration.
- Gschneidner, K A, J., Pecharsky, V. K., and Tsokol, A. O. (2005). Recent developments in magnetocaloric materials. *Reports on Progress in Physics*, 68(6):1479–1539.
- Gschneidner, K. and Pecharsky, V. (2008). Thirty years of near room temperature magnetic cooling: Where we are today and future prospects. *International Journal of Refrigeration*, 31:945–961.
- Hadley, G. R. (1986). Thermal conductivity of packed metal powders. *International Journal of Heat and Mass Transfer*, 29(6):909–919.
- Hausen, H. (1983). *Heat Transfer in Counterflow, Parallel-Flow and Cross-flow*. McGraw-Hill Co.
- He, J., Chen, J., and Wu, C. (2003). The influence of heat-transfer laws on the performance of a magnetic stirling refrigeration cycle. *International Journal of Ambient Energy*, 24(2):75–82.

- Hooijkaas, H. W. G. and Benschop, A. A. J. (1999). Pulse tube development using harmonic. In Ross, R. G., editor, *Simulations, Proc. 10th Int. Cryocooler Conf.*, pages 359–367, New York, NY. Kluwer Academic/Plenum Publishers.
- Hsu, C. H. (2005). *Dynamic Modeling of Convective Heat Transfer in Porous Media*. Taylor&Francis, New York.
- Hu, J. and Xiao, J. (1995). New method for analysis of active magnetic regenerator in magnetic refrigeration at room temperature. *Cryogenics*, 35:10–104.
- Jacobs, S. (2009). Modeling and optimal design of a multiplayer active magnetic refrigeration system. In Egolf, P. W., editor, *Third International Conference on Magnetic Refrigeration at Room Temperature*. International Institute of Refrigeration.
- Jacobsson, P. and Sundqvist, B. (1989). Thermal conductivity and electrical resistivity of gadolinium as functions of pressure and temperature. *Physical Review B*, 40(14):9541–9551.
- Janda, D., DeGregoria, A. J., Johnson, J., and Kral, S. (1989). Design of an active magnetic regenerative hydrogen liquefier. *Advances in Cryogenic Engineering*, 37:891–898.
- Jeffreson, C. P. (1972). Prediction of breakthrough curves in packed beds. *American Institute of Chemical Engineers*, 18(2):409–20.
- Johnson, J. W. and Zimm, C. B. (1996). Performance modeling of a 4 k active

- magnetic regenerative refrigerator. *Journal of Applied Physics*, 79:2171–2175.
- Joseph, R. and Schloemann, E. (1965). Demagnetizing field in nonellipsoidal bodies. *Journal of Applied Physics*, 36(5):1579–1593.
- Kaviany, M. (1995). *Principles of Heat Transfer in Porous Media*. Springer, New York, 2nd edition.
- Kawanami, T., Chiba, K., Sakurai, K., and Ikegawa, M. (2006). Optimization of a magnetic refrigerator at room temperature for air cooling systems. *International Journal of Refrigeration*, 29(8):1294–1301.
- Kirol, L. D. and Mills, J. I. (1984). Numerical analysis of thermomagnetic generators. *Journal of Applied Physics*, 56(3):824–828.
- Kitanovski, A. and Egolf, P. (2009). Application of magnetic refrigeration and its assessment. *Journal of Magnetism and Magnetic Materials*, 321(7):777–781.
- Kitanovski, A., Egolf, P. W., Gendre, F., Sari, O., and Besson, C. (2005). A rotary heat exchanger magnetic refrigerator. In Egolf, P. W., editor, *First International Conference on Magnetic Refrigeration at Room Temperature, International Institute of Refrigeration*, pages 297–307. International Institute of Refrigeration.
- Kuz'min, M. D. (2007). Factors limiting the operation frequency of magnetic refrigerators. *Applied Physics Letters*, 90:251916 (3pp).

- Legait, I., Kedous-Lebouc, A., and Rondot, L. (2009). Numerical simulation and analysis of the refrigerant bed behavior using fluent software. In Egolf, P. W., editor, *Third International Conference on Magnetic Refrigeration at Room Temperature*, pages 295–302. International Institute of Refrigeration.
- Li, P., Gong, M., Yao, G., and Wu, J. (2006). A practical model for analysis of active magnetic regenerative refrigerators for room temperature applications. *International Journal of Refrigeration*, 29:1259–1266.
- Liu, M. and Yu, B. (2010). Two-dimension porous medium model for reciprocating active magnetic regenerator of room temperature magnetic refrigeration. In Egolf, P. W., editor, *Fourth International Conference on Magnetic Refrigeration at Room Temperature*. International Institute of Refrigeration.
- Morrish, A. H. (1965). *The Physical Principles of Magnetism*. John Wiley & Sons, Inc.
- Nemec, D. and Levec, J. (2005). Flow through packed bed reactors: 1. single-phase flow. *Chemical Engineering Science*, 60(24):6947–6957.
- Nielsen, K. K., Bahl, C. R. H., Smith, A., Bjørk, R., Pryds, N., and Hattel, J. (2009a). Detailed numerical modeling of a linear parallel-plate active magnetic regenerator. *International Journal of Refrigeration*, 32(6):1478–1486.
- Nielsen, K. K., Bahl, C. R. H., Smith, A., Pryds, N., and Hattel, J. (2010). A comprehensive parameter study of an active magnetic regenerator using a 2d numerical model. *International Journal of Refrigeration*, 33(4):753–764.

- Nielsen, K. K., Engelbrecht, K., Bahl, C. R. H., Smith, A., Pryds, N., and Hattel, J. (2009b). Numerical modeling of multi-material active magnetic regeneration. In *7th World Conference on Experimental Heat Transfer, Fluid Mechanics and Thermodynamics*.
- Nielsen, K. K., Pryds, N., Smith, A., Bahl, C. R. H., and Hattel, J. (2009c). 2-dimensional numerical modeling of active magnetic regeneration. In Egolf, P., editor, *Third International Conference on Magnetic Refrigeration at Room Temperature*, pages 251–258. International Institute of Refrigeration.
- Oliveira, P. A., Trevizoli, P., Jr., J. R. B., and Prata, A. T. (2009). Numerical analysis of a reciprocating active magnetic regenerator - part I. In Egolf, P. W., editor, *Third International Conference on Magnetic Refrigeration at Room Temperature*, pages 283–288. International Institute of Refrigeration.
- Palacios, E., Wang, G. F., Burriel, R., Provenzano, V., and Shull, R. D. (2010). Direct measurement of the magnetocaloric effect in $\text{Gd}_5\text{Si}_2\text{Ge}_{1.9}\text{Ga}_{0.1}$. *Journal of Physics: Conference Series*, 200(9):092011.
- Pecharsky, V. K. and Gschneidner, K. (2006). Advanced magnetocaloric materials: What does the future hold? *International Journal of Refrigeration*, 29:1239–1249.
- Peksoy, O. and Rowe, A. (2005). Demagnetizing effects in active magnetic regenerators. *Journal of Magnetism and Magnetic Materials*, 288:424–432.
- Petersen, T. F., Engelbrecht, K., Bahl, C. R. H., Elmegaard, B., Pryds, N., and Smith, A. (2008a). Comparison between a 1d and a 2d numerical

- model of an active magnetic regenerative refrigerator. *Journal of Physics D: Applied Physics*, 41(10):105002.
- Petersen, T. F., Pryds, N., Smith, A., Hattel, J., Schmidt, H., and Knudsen, H. (2008b). Two-dimensional mathematical model of a reciprocating room-temperature active magnetic regenerator. *International Journal of Refrigeration*, 31:432–443.
- Risser, M., Vasile, C., Engel, T., Keith, B., and Muller, C. (2010). Numerical simulation of magnetocaloric system behavior for an industrial application. *International Journal of Refrigeration*, 33(5):973–981.
- Rowe, A. and Barclay, J. (2003). Ideal magnetocaloric effect for active magnetic regenerators. *Journal of Applied Physics*, 93(3):1672–1676.
- Rowe, A. and Tura, A. (2006). Experimental investigation of a three-material layered active magnetic regenerator. *International Journal of Refrigeration*, 29:1286–1293.
- Sarlah, A. (2008). *Thermohydraulic properties of heat regenerators in magnetic refrigerators*. PhD thesis, University of Ljubljana, Slovenia.
- Sarlah, A. and Poredos, A. (2005). Regenerator for magnetic cooling in shape of honeycomb. In Egolf, P. W., editor, *First International Conference on Magnetic Refrigeration at Room Temperature*, International Institute of Refrigeration, pages 283–290. International Institute of Refrigeration.
- Sarlah, A. and Poredos, A. (2010). Dimensionless numerical model for simulation of active magnetic regenerator refrigerator. *International Journal of Refrigeration*, 33 (6):1061–1067.

- Shah, R. K. and Sekulic, D. P. (2003). *Fundamentals of Heat Exchanger Design*. John Wiley & Sons, Inc., Hoboken, New Jersey.
- Shir, F., Della Torre, E., Bennett, L. H., Della Torre, E., Bennett, L. H., Shull, R. D., and Mavriplis, C. (2004). Modeling of magnetization and demagnetization in magnetic regenerative refrigeration. *IEEE Transactions on Magnetics*, 40(4):2098–2100.
- Shir, F., Yanik, L., Bennet, L. H., Torre, E. D., and Shull, R. D. (2003). Room temperature active regenerative magnetic refrigeration: Magnetic nanocomposites. *Journal of Applied Physics*, 93(10):8295–8297.
- Siddikov, B., Wade, B., and Schultz, D. (2005). Numerical simulation of the active magnetic regenerator. *Computers and Mathematics with Applications*, 49:1525–1538.
- Smailli, A. and Chahine, R. (1998). Thermodynamic investigations of optimum active magnetic regenerators. *Cryogenics*, 38:247–252.
- Smith, A., Nielsen, K. K., Christensen, D. V., Bahl, C. R. H., Bjørk, R., and Hattel, J. (2010). The demagnetizing field of a nonuniform rectangular prism. *Journal of Applied Physics*, 107(10):103910.
- Tagliafico, G., Scarpa, F., and Canepa, F. (2010). A dynamic 1-d model for a reciprocating active magnetic regenerator; influence of the main working parameters. *International Journal of Refrigeration*, 33(2):286–293.
- Tocado, L., Palacios, E., and Burriel, R. (2009). Entropy determinations and magnetocaloric parameters in systems with first-order transitions: Study of MnAs. *Journal of Applied Physics*, 105(9):093918.

- Tusek, J., Sarla, A., Zupan, S., Prebil, I., Kitanovski, A., and Poredos, A. (2010a). A numerical optimization of a packed bed AMR. In Egolf, P. W., editor, *Fourth International Conference on Magnetic Refrigeration at Room Temperature*. International Institute of Refrigeration.
- Tusek, J., Zupan, S., Sarlah, A., Prebil, I., and Poredos, A. (2010b). Development of a rotary magnetic refrigerator. *International Journal of Refrigeration*, 33(2):294–300.
- Willmott, A. J. (1964). Digital computer simulation of a thermal regenerator. *International Journal of Heat and Mass Transfer*, 7(11):1291–1302.
- Yan, Z. and Chen, J. (1991). The characteristics of polytropic magnetic refrigeration cycles. *Journal of Applied Physics*, 70(4):1911–1914.
- Yan, Z. and Chen, J. (1992). The effect of field-dependent heat capacity on the characteristics of the ferromagnetic Ericsson refrigeration cycle. *Journal of Applied Physics*, 72(1):1–5.
- Yu, B., Gao, Q., Zhang, B., Meng, X., and Chen, Z. (2003). Review on research of room temperature magnetic refrigeration. *International Journal of Refrigeration*, 26:622–636.
- Yu, B., Liu, M., Egolf, P. W., and Kitanovski, A. (2010). A review of magnetic refrigerator and heat pump prototypes built before the year 2010. *International Journal of Refrigeration*, 33(6):1029–1060.
- Zhang, L., Sherif, S. A., DeGregoria, A. J., Zimm, C. B., and Veziroglu, T. N. (2000). Design and optimization of a 0.1 ton/day active magnetic regenerative hydrogen liquifier. *Cryogenics*, 40:269–278.

Zhang, L., Sherif, S. A., Veziroglu, T. N., and Sheffield, J. W. (1993). Second law analysis of active magnetic regenerative hydrogen liquefier. *Cryogenics*, 33(7):667–674.

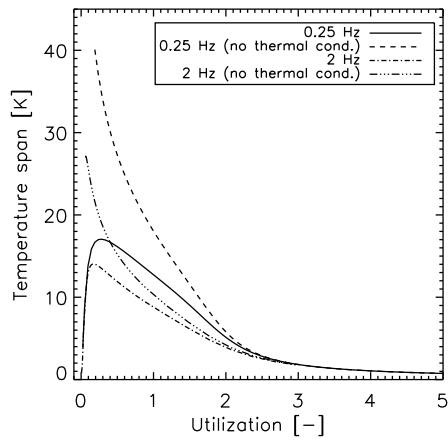


Figure A.1: The impact of the longitudinal thermal conduction on the predicted temperature span of the AMR at two different operating frequencies. The operating conditions in this case were an ambient temperature of 293 K and a regenerator of packed spheres with a diameter of 1 mm. The model is published in Tusek et al. (2010a).

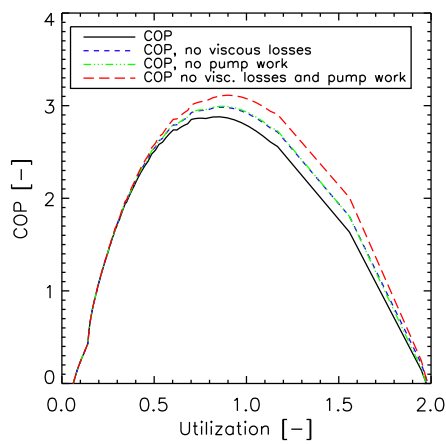


Figure A.2: The impact of the viscous losses on the COP of a packed spheres-based AMR. The model configuration was the same as that used for the results in Fig. A.1. The hot and cold side temperatures were set to 296 and 290 K, respectively.

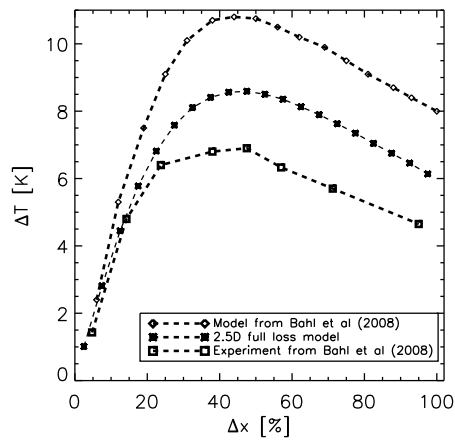


Figure A.3: Example of the impact of including the parasitic thermal losses. The two curves denoted “Model from Bahl et al. (2008)” and “Experiment from Bahl et al. (2008)” are based on data published in Bahl et al. (2008). The curve denoted “2.5D full loss model” is the model published in Nielsen et al. (2009a) with the parasitic losses enabled. The abscissa shows the fluid movement as a percentage of the total length of the regenerator and the ordinate shows the zero heat load temperature span of the regenerator. The figure is reproduced from Nielsen et al. (2009a).

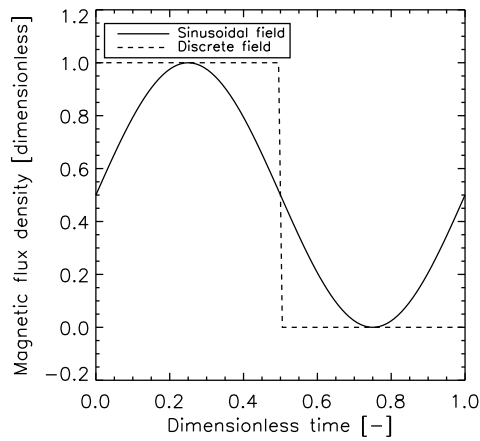


Figure A.4: Example of discrete on-off and continuous changing magnetic fields.

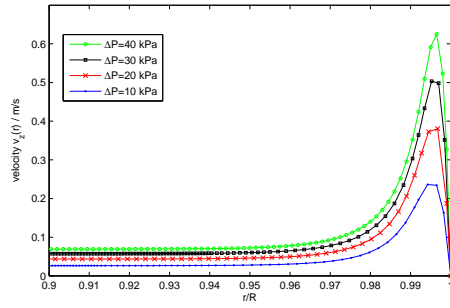


Figure A.5: Radial velocity distribution with $d_r = 3\text{cm}$, $d_p = 1\text{mm}$, $d_r/d_p = 30$, regenerator length $L = 7\text{cm}$

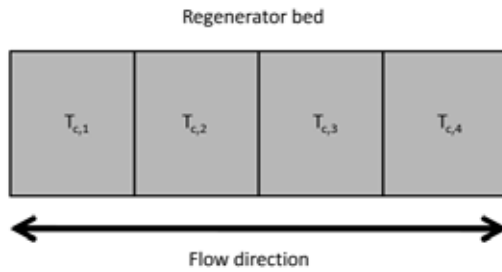


Figure A.6: Schematic of a layered regenerator. This case shows four different MCMs each with a specific Curie temperature denoted on the drawing. It is as yet not fully understood whether the optimum is an equal amount of each material, as shown here, or if the distribution of the materials should be asymmetric.

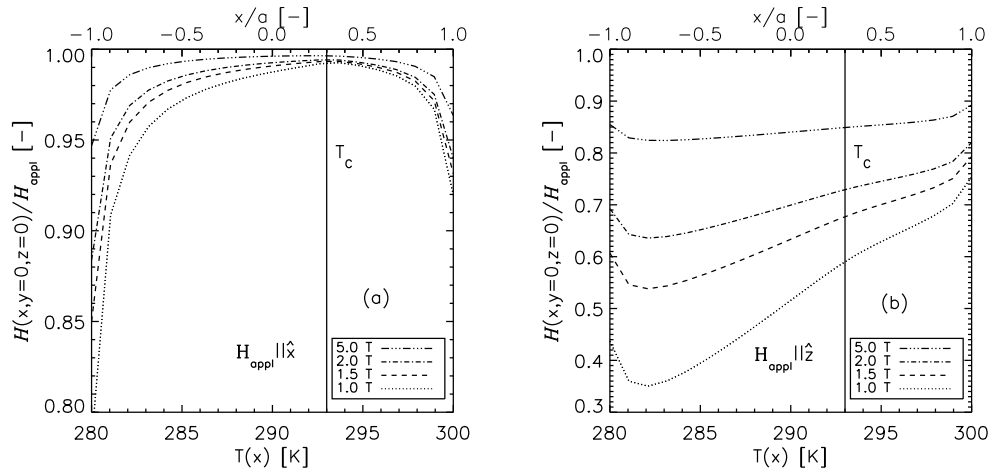


Figure A.7: Example of the internal magnetic field in a single-material magnetocaloric flat plate. A linear temperature profile is imposed from the cold end (280 K) to the hot end (300 K) and the internal magnetic field is calculated using the model from Smith et al. (2010). Left: the applied field is along the x -direction, i.e. the direction of the flow. Right: the applied field is along the z -direction, which is perpendicular to the flat plate. Four different applied fields are considered and the resulting internal magnetic field is plotted along the x -direction normalized to the applied field. The material used is Gd with a Curie temperature of 293 K (indicated on the figures). Reproduced from Smith et al. (2010).

Table A.1: The boundary conditions during AMR operation.

Period	Cold side	Hot side
Hot blow	$T_f = T_{\text{cold}}$	$\partial T_f / \partial x = 0$
Cold blow	$\partial T_f / \partial x = 0$	$T_f = T_{\text{hot}}$

Table A.2: Summary of the numerical AMR models published to date. The columns represent the following. The reference to the paper is given in Ref. The type of heat transfer fluid in HTF. Flow profile in F. prof. Flow properties in F. prop. Magnetic field profile in Mag. prof. Method for implementing the magnetocaloric effect in MCE. The rank or dimensionality in Rank. Whether the demagnetizing field is implemented in Dem. The functional dependency of the specific heat in c . Whether axial conduction is included in the model in Ax. cond. Whether thermal conduction is included in the solid in Sol. ther. cond. Whether the pressure drop / viscous losses is included in the model in Pres. drop. And finally, whether thermal dispersion is included in Ther. disp.

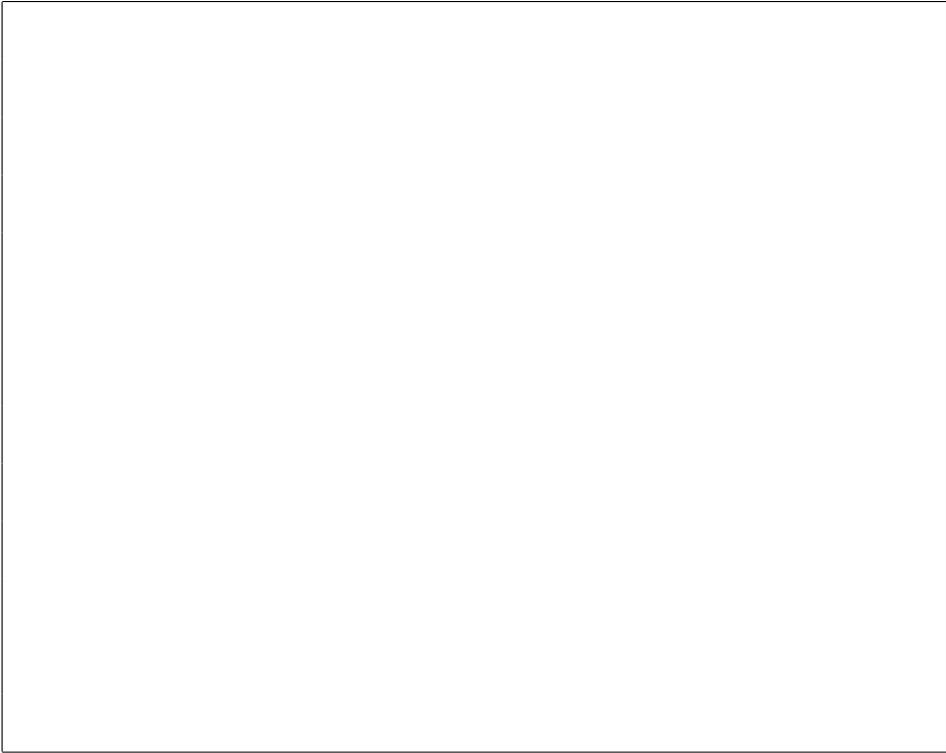
Ref.	HTF	F. prof.	F. prop.	Mag. prof.	MCE	Rank	Dem.	c	Ax. cond.	Sol. ther. cond.	Pres. drop	Ther. disp.
Smailli												
& Chahine (1998)	-	-	Cst.	Discr.	-	1D	No	T, H dep.	No	No	No	No
Shir et al. (2004)	He	Discr.	Cst.	Discr.	Built-in	1D	No	Cst.	No	No	No	No
Siddikov et al. (2005)	-	Discr.	T -dep.	Discr.	Built-in	1D	No	T, H dep.	Yes	Yes	Yes	Yes
Sarlah & Pore-dos (2005)	He	Discr.	Cst.	Time-dep.	Built-in	2D	No	T, H dep.	No	Yes	No	No

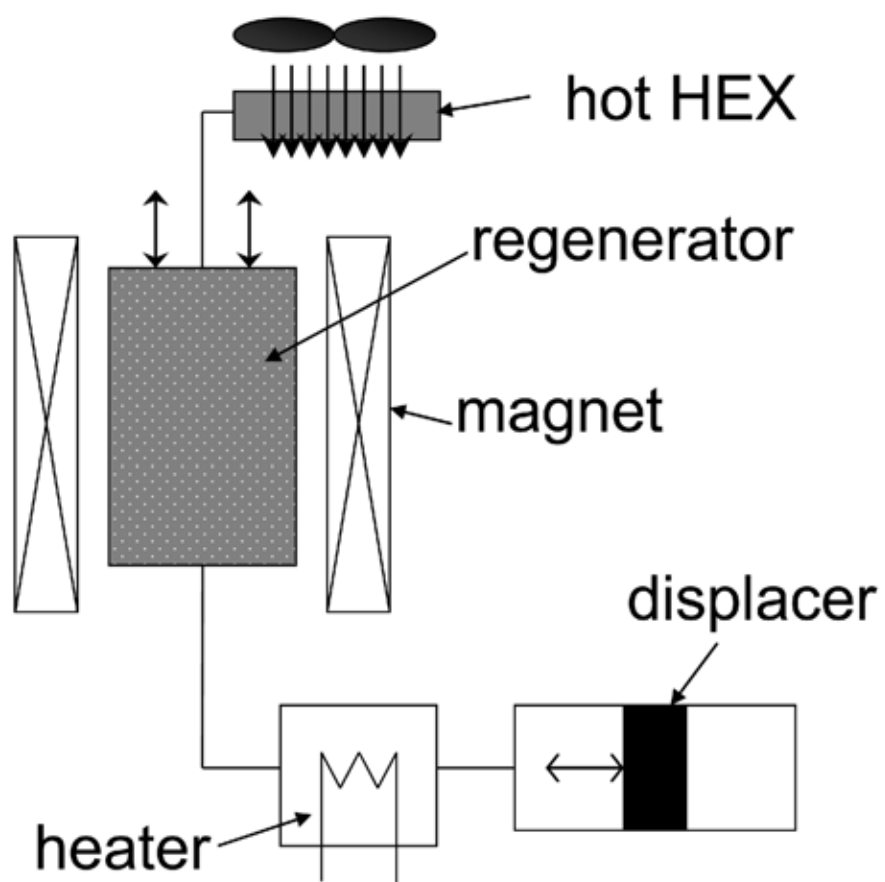
Kitanovski										
et al.	Air	Discr.	Cst.	Discr.	1D	No	-	No	No	No
(2005)										
Dikeos										
et al.	He	Sin.	Cst.	Sin.	1D	No	T, H dep.	Yes	No	Yes
(2006)										
Li et al.										
(2006)	Discr.	Cst.	Discr.	Built- in	1D	-	No	No	No	No
Water Allab										
et al.	Water	Discr.	Cst.	Discr.	1D	No	-	No	-	-
(2005)										
Kawanami										
et al.	Air/Water	-	-	-	1D	No	-	Yes	No	No
(2006)										
Engelbrecht	Sine	Built-								
(2008)	Water	T -dep.	in	1D	No	Yes	Yes	Yes	Yes	Yes
				T, H dep.						

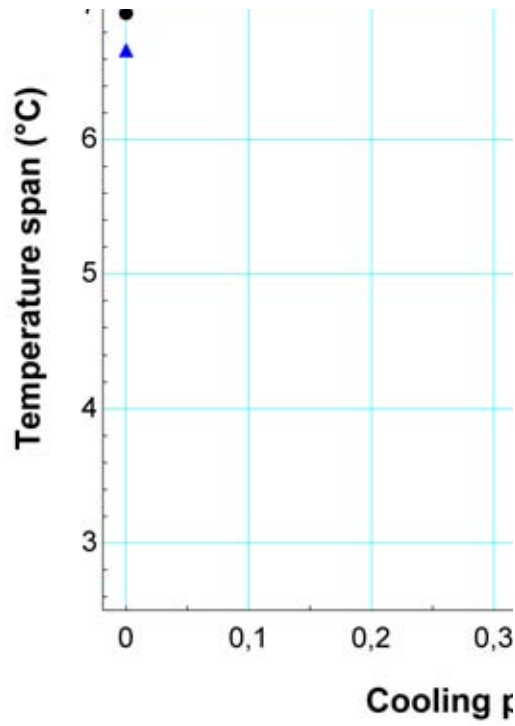
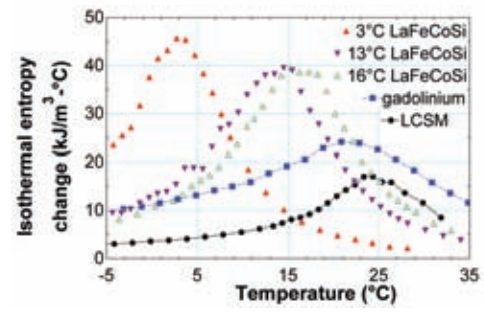
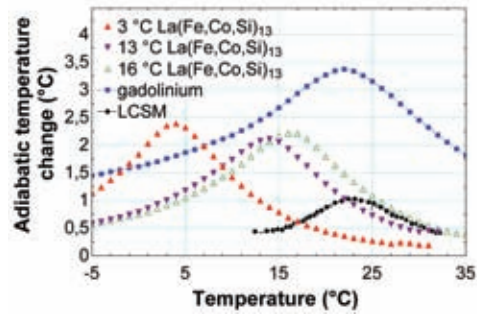
Petersen et al. (2008b)	Water	Discr.	Cst.	Discr.	Discr.	2D	No	T, H dep.	Yes	Yes	Yes	No
Nielsen et al. (2009a)	Water	Discr./sin	Est.	Discr./prof in	Discr./Built- 2.5D	2.5D	Yes	T, H dep.	Yes	Yes	Yes	No
Oliveira et al. (2009)	Water	Sine	Cst.	Discr.	Discr.	2D	No	T, H dep.	Yes	Yes	No	No
Aprea et al. (2009)	Water+g	Discr.	Discr.	Discr.	Discr.	1D	No	-	No	No	No	No
Jacobs (2009)	Water	-	-	-	-	1D	-	T, H dep.	Yes	Yes	Yes	Yes
Bouchard et al. (2009)	Water	-	Cst	Discr.	Built- in	3D	Yes	T, H dep.	Yes	-	-	-

Legait et al. (2009)	Water	-	-	-	Discr.	2D	No	Cst.	Yes	Yes	Yes	Yes
Tagliafico et al. (2010)	Water	-	-	Discr.	Discr.	1D	No	T, H dep.	Yes	Yes	No	Yes
Risser et al. (2010)	Zitrec S-10	Time dep.	Cst.	Time- dep.	Discr.	1D	No	T, H dep.	Yes	Yes	Yes	No
Liu & Yu (2010)	Water	Discr.	T -dep.	Discr.	Built- in	2D	No	T, H dep.	Yes	Yes	Yes	Yes
Tusek et al. (2010b)	Water	Discr.	Cst.	Discr.	Discr.	1D	No	T, H dep.	Yes	Yes	Yes	Yes

-
- A.1.8 Experimental results for a magnetic refrigerator using three different types of magnetocaloric material regenerators; accepted for publication in International Journal of Refrigeration







A.1.9 Monolithic Perovskite for magnetic regenerator; accepted for publication in Journal of American Ceramic Society

A Monolithic Perovskite structure for use as a Magnetic Regenerator

Nini Pryds^{}, Frank Clemenc^{**}, Mohan Menon^{*}, Pernille H. Nielsen^{*}, Karen Brodersen^{*}, Rasmus Bjørk^{*}, Christian R. H. Bahl^{*}, Kurt Engelbrecht^{*}, Kaspar K. Nielsen,^{#*}, Anders Smith^{*}*

^{*}Fuel Cells and Solid state Chemistry Division, Risø DTU, Technical University of Denmark, DK-4000, Roskilde, Denmark, ^{**}EMPA Dübendorf, Laboratory for High Performance Ceramics, Überlandstrasse 129, 8600 Dübendorf, Switzerland, [#]Technical University of Denmark, Department of Mechanical Engineering, Produktionstorvet, building 425, 2800 Kgs. Lyngby, Denmark

ABSTRACT: A $\text{La}_{0.67}\text{Ca}_{0.26}\text{Sr}_{0.07}\text{Mn}_{1.05}\text{O}_3$ (LCSM) perovskite was prepared for the first time as a ceramic monolithic regenerator used in a regenerative magnetic refrigeration device. The parameters influencing the extrusion process and the performance of the regenerator, such as the nature of the monolith paste and the influence of the sintering on the adiabatic temperature change, were investigated. Comparisons between the extruded monolithic structure before and after the sintering showed that an increase of the adiabatic temperature change was seen after the sintering. Furthermore, calculations show that the performance of the monolithic structure is potentially superior to a parallel plate regenerator, indicating the potential cost and structural benefit of using such structure, i.e. a mechanically stable ceramic thin wall structure which can be produced in one processing step.

^{*}Author to whom correspondence should be addressed. E-mail: nipr@risoe.dtu.dk

Introduction

Magnetic refrigeration is a promising technology for energy efficient and environmentally friendly space cooling and refrigeration. The technology uses magnetic materials as the active components and non-volatile fluids, e.g. water, for heat transfer¹. The temperature of magnetic materials changes when they are subjected to a change in magnetic field. This so-called magnetocaloric effect is due to interaction of the spin and lattice degrees of freedom of the magnetic material. The magnetic field aligns the spins, lowering their entropy; which, under adiabatic conditions, leads to higher lattice entropy resulting in an increase of the temperature of the material. The adiabatic magnetisation/demagnetisation cycle is reversible for LCSM, and the theoretical efficiency of the entire cooling cycle may be as much as 60% greater than for conventional compressor based refrigerators².

A wide range of different types of materials, from metals to ceramics, exhibit the magnetocaloric effect³. Generally, the magnetocaloric effect manifests itself as a reversible increase in temperature when the magnetic material is placed in a magnetic field, and the maximum magnetocaloric effect occurs near the Curie temperature. The process of choosing a magnetocaloric material for a specific magnetic refrigeration application is complex. A large magnetocaloric effect, corrosion resistance, the ability to adjust the Curie temperature, ease of fabrication, and cost are important in nearly every practical application. Magnetic ceramics materials are very stable at room temperature, can be compositionally tuned to adjust the Curie temperature, and do not corrode in water. This makes them an attractive option for use as regenerators for magnetic refrigeration systems. Families of functional materials with a large magnetocaloric effect (MCE) have been found in several perovskite-type manganese oxides such as Ca- and Sr-doped lanthanum manganites, $\text{La}_{0.67}\text{Ca}_{0.33-x}\text{Sr}_x\text{MnO}_{3\pm\delta}$ ($0 \leq x \leq 0.33$)⁴. These samples show a substantial magnetocaloric effect (e.g. $\Delta T \sim 0.5\text{-}1.4\text{K}$ depending on the exact composition) in a temperature range around their respective Curie temperature which makes the

compounds suitable for air-conditioning and refrigeration applications. By varying the composition parameter x the Curie temperature can be adjusted between 267 K ($x = 0$) and 369 K ($x = 0.33$)⁴,

The performance of the magnetic refrigeration system is strongly affected by the heat transfer and magnetocaloric characteristics of the regenerator and its geometry^{5,6}. Perovskite-type oxides can be processed into different geometries such as parallel plates and monolithic perforated cylinders which may have much lower pressure losses than typical magnetic regenerator geometries such as packed particles. For a regenerator consisting of magnetocaloric plates, reducing the regenerator plate thickness as well as the gap distances between the plates can improve the regenerator performance^{5,7}. However, a reduction of wall thickness causes a reduction of the mechanical strength and makes the fabrication of such a regenerator very difficult, especially when it must be assembled with hundreds of plates separated by small distances of 0.1-0.5 mm. In order to overcome this problem, a single monolithic structure is suggested. Achieving the goal of producing a one-piece magnetic regenerator can be a breakthrough in the manufacturability and commercialization of a magnetic cooling device. Monolithic structures can be viewed as two-dimensional assemblies of long, parallel channels through which the heat transfer fluid may flow. Fine monolithic structures have the following benefits: (1) the surface area is increased and thereby the heat transfer to and from the fluid medium, (2) the channels are straight and parallel so that the flow is not obstructed and the pressure drop across the monolith is low and (3) a complete complex monolithic structure is made as a single part. Monolithic structures are often produced through the process of extrusion. These complex structures have been used so far almost exclusively for catalytic systems in power plant and automotive emission control systems⁸.

In the present work, the fabrication of a monolithic regenerator for magnetic refrigeration, made of a perovskite type ceramic material using a thermoplastic extrusion process, was investigated. The fabrication of such a magnetic refrigeration regenerator made of complex

ceramic powders has not previously been reported and it is the main topic of this work. To optimize the extrusion process the different process parameters are investigated, including the effect of mixing ratios (vol% binder/vol% powder) on the homogeneity of the feedstock and the pressure drop during extrusion. The fabricated monolithic regenerator is tested and evaluated in a magnetic cooling device from which preliminary results are presented.

Experimental procedure

Powders with the composition of $\text{La}_{0.67}\text{Ca}_{0.26}\text{Sr}_{0.07}\text{Mn}_{1.05}\text{O}_3$ (LCSM) were prepared by the solid-state reaction (SSR) method with the starting materials Calcium oxide (CaO, 99.9%), Lanthanum oxide (La_2O_3 , 99.99%), Manganese oxide (MnO_2 , 99.9%) and Strontium carbonate (SrCO_3 , 99.9%). The powder was then calcined at an elevated temperature of 1473 K (heating and cooling rate of 100 K/h) for 16 h followed by additional heat treatment at 1573 K (heating and cooling rate of 100 K/h) for additionally 6 h. After calcination and ball milling, the powder was coated with stearic acid (97% pure stearic acid, Fluka Chemie AG). The coating method procedure has been described previously⁹. Before the coating process the specific surface area and the density of the powder were measured using BET (SA3100, Beckman-Coulter Inc) and a helium pycnometer (Micromeritics, AccuPyc 1330), respectively. To achieve sufficient plasticity for the honeycomb production, a thermoplastic binder system based on low density polyethylene (PEBD 1700MN 18C – Lacqtene Elf Atochem S.A.) was used. The two main advantages in using thermoplastic binder systems and not the conventional water based feedstocks are (1) possible formation of carbonates is avoided and (2) phase separation due to the high extrusion pressure can be eliminated easily. In a first series, blends with three different contents of stearic acid coated LCSM powder were mixed (HAAKE PolyLab Rheomix 600, Thermo Fisher Scientific) and the viscosity was evaluated using a capillary rheometer (RH7-2 Flowmaster, Rosand Precision Limited, Malvern) with a 1 mm capillary die configuration. Based on the results from these investigations, a 58 vol.% LCSM compound was prepared with a high shear mixer (HAAKE

PolyLab Rheomix 3000, Thermo Fisher Scientific). To achieve a homogenous ceramic-polymer blend, the composition was mixed with roller blade rotors and a frequency of 10 rpm until the torque reached equilibrium. The extrusion was performed in a pilot-scale piston extruder with a cylinder diameter of 45 mm and heating option up to 523 K at EMPA, Switzerland. The die head honeycombed structures (36 mm in diameter, 0.5 mm wall thickness and 1 mm channel width) were first extruded with a SiC (Silicon Carbide) paste in order to polish the die head channels. In order to keep the flows of the feedstock continuous without blocking the extruder head during the process, the whole setup was preheated to a temperature between 423 K and 473 K for about 30-40 min. before and during the extrusion process. The speed of the piston varies between 5 and 50 mm/min. Following the extrusion, sintering took place under the following conditions: (1) heating the sample to 473 K at a rate of 60 K/h, (2) heating to 593 K at 10 K/h and holding the sample for 2 h, (3) heating to 973 K at 5 K/h and finally (4) heating to 1523 K at 30 K/h for 0.5 h and cooling down to room temperature at 50 K/h. The powders and the sintered samples were checked by X-ray diffraction using a STOE diffractometer with Cu-K α radiation and differential scanning calorimetry (DSC) using a Netzsch DSC 200F3 Maia for phase purity and their magnetic transition temperatures. The Curie temperatures were defined as the position of the maximum peak heights of the phase transition peaks.

Results

Preparation of the powder and the feedstocks

Before preparation of the feedstock, the powder was ball milled to an average grain size of approximately 2 μm as confirmed by laser scattering particle analysis and XRD patterns were then taken from the LCSM sample after the calcination. The observed peaks in XRD patterns after the calcinations confirmed that the sample remained single phase without any secondary phase. All the observed peaks were assigned to the formation of a crystalline perovskite phase (based on JCPDS data). The heat capacity and the transition temperature of the LCSM were

measured from the DSC at zero magnetic field, see Fig. 1. From the DSC measurement the transition temperature was found to be 290 K, as was expected for this composition⁹. One of the main parameters in the preparation of the feedstock is to maximize the powder volume fraction in the compound in order to ensure extrudability and to ensure that there is no contamination after kneading and extrusion. Maximizing the amount of powder has another important outcome as the cooling capacity of a magnetic refrigeration device is directly related to the amount of magnetocaloric material. To achieve this, LCSM powder and polyethylene were mixed in different volume ratios to get a stable and reproducible mixing process and to reach a homogeneous distribution of the ceramic particles in the thermoplastic matrix. The density and surface area of the uncoated powder were 5.68 g/cm³ and 4.21 m²/g, respectively. Figure 2 shows the pressure versus the extrusion speed for powder content between 52 and 58 vol.%, measured in front of a capillary die with a diameter of 1 mm and a length of 16 mm. These results confirmed high viscosity of the mixture where 58 vol% ceramic powder was used, compared to the other mixtures with lower powder content. Fig. 2b presents apparent viscosity curves depending on shear rate and ceramic powder portion.

A general challenge in extrusion is the dimensional control, i.e. maintaining uniform shrinkage during drying and sintering. The shrinkage of these mixtures measured for different volume fraction of the ceramic feedstock show that, for the investigated ratios, the variation in the shrinkage of the volume contraction is approx. 40-45% regardless of the fraction of powder/binder. The highest volume fraction that was therefore used 58 vol% of LCSM and 42 vol% binder, giving a ratio of 1.38.

Extrusion and sintering of the monolithic structure

A die head with the dimensions that give an extruded part, which fits the magnetic refrigeration test device has been designed, taking into account the experimentally determined shrinkage. Based on the obtained results and the pressure limitation of the die head, a mixture of 650 g

LCSM powder, 19 g stearic acid and 74 g polyethylene binder was used to extrude the honeycomb structure in this study, which is equal to the 58 vol.% powder content (ratio of 1.38). The wall thickness (for each channel) and channel width of the extruded honeycomb were designed to be 0.5 and 1.0 mm, respectively.

Prior to the final extrusion experiment, tests were performed at different temperatures and piston velocities. Extruding the monolithic structures at 423 K with a piston speed of 5 mm/min resulted in stable structures that were able to sustain usability in the magnetic refrigeration device. A piston force of 4 kN, corresponding to a pressure of 2.5 MPa, was necessary to extrude the 58 vol.% LCSM compound through the orifice of the honeycomb die. Increasing the piston speed from 5 to 50 mm/min, the corresponding pressure increased up to 22 MPa which is significantly over the maximum allowed pressure of the honeycomb die (10 MPa). Decreasing the temperature to 403 K, the pressure reached a maximum of 13 MPa when using a piston speed of 5 mm/min.

A monolithic squared microchannel structure with a wall thickness of approx. 0.5 mm was fabricated and is shown in Figure 3. Spatial variations in the mold seem to have induced localized unevenly spaced channels. It is at this point not possible to assess this in detail; however, it is an issue that is being pursued. After cooling the monolith was cut to a length of 4 cm corresponding to the length of the regenerator. Due to the fact that the fraction volume of the binder was relatively high, the monolith could not maintain its shape upon sintering. Furthermore, the binder burnout has not been optimized with respect to heating rates and holding temperatures which resulted in the sagging of the monolith. Thus, for the present implementation of the monolith in the magnetic refrigeration test device we have chosen to use the unsintered monolith as a regenerator. Hence, the total weight of the monolith contains both the LCSM and the binder, thus lowering the magnetocaloric effect.

Measurement of the magnetocaloric effect and the performance of the monolith

The adiabatic temperature change, ΔT_{ad} , is the temperature increase or decrease of a magnetocaloric material upon application or removal of a magnetic field under adiabatic conditions. Samples taken from the monolith before and after sintering have been measured in a ΔT_{ad} measurement device at Risø DTU¹⁰. The results are shown in Fig. 4. Measurements were done with an applied magnetic field change of 1 T, as this is in the range of practical magnetic fields for a commercial magnetic refrigerator. Demagnetization effects due to the shape of the sample have been taken into account and the internal fields of the samples during the measurements is indicated in the upper scale of Fig.4.

As expected, there is a significant difference between ΔT_{ad} in the two measurements. The lower value for the sample prior to sintering is partly due to the dilution of the thermal mass of the magnetocaloric material with the thermal mass of the binder material. Also, the LCSM powder prior to sintering may be of a more nano-crystalline nature. In similar materials, this has previously been observed to lead to a reduction of the magnetocaloric effect along with a broadening of the phase transition^{11,12}.

Differential scanning calorimetry was performed using a device built at Risø DTU in which samples can also be subjected to an applied magnetic field¹⁷. The samples in zero applied magnetic field shows a peak at the Curie temperature of the sintered sample with a value close to the expected⁴. In a magnetic field of 1 T the peak in heat capacity is broadened, as expected. However, in the unsintered sample at zero magnetic field there is no distinct clear peak (see Fig. 5). This may be due to a broadening of the transition, due to nano-crystallinity or a non-uniform composition. The increased level of the measured heat capacity is due to the high heat capacity of the binder (about 2000 J/ kg K) compared to LCSM (Fig. 5). Table 1 summarizes the results of these investigations.

A reciprocating active magnetic regenerator test machine has been used to test the monolith. The magnetic field is provided by a Halbach cylinder type permanent magnet with an average flux density in the bore of 1.03 T. The magnet, which is described by Bjørk et al.¹³, has a bore of 42 mm and a height of 50 mm. Magnetisation and demagnetisation of the regenerator is achieved by moving the regenerator vertically relative to the stationary magnet by means of a stepper motor. The test device is described in more detail by Bahl et al.¹. In order to determine the best operating parameters, preliminary tests of the monolithic regenerator (81.7 g) were carried out for a range of experiments where the fluid flow rates, piston stroke lengths and cycle times were varied. In these preliminary results, a maximum temperature span of 0.9 K for the non-sintered regenerator was found for a piston stroke of 9 mm, fluid velocity of 1 mm/s and a cycle time of 21 s. The heat rejection temperature was set to be 298 K. For comparison with the performance of other magnetic refrigeration devices the value of the utilization was calculated using the following equation

$$\varphi = \frac{\dot{m}c_{p,f}P}{m_s c_{p,s}} \quad (1)$$

where the mass flow rate of the heat transfer fluid is denoted \dot{m} , the flow period of either blow is P and the mass of the regenerator is m_s . Subscripts f and s denote fluid and solid, respectively. The utilization is a dimensionless number, which describes the amount of moved thermal fluid mass to the amount of thermal mass in the regenerator. For the optimal operating conditions presented here the value of the utilization is 0.18.

Passive regenerator experiments

Regardless whether the regenerator is operated as an Active Magnetic Regenerator (AMR) or as a passive regenerator the regenerator geometry has a large impact on the device performance.

A highly effective passive regenerator will in general also perform well when operated actively.

In the following experiments the extruded monolithic structured regenerator was therefore tested as a passive regenerator. In devices using passive magnetic or nonmagnetic materials, a thermal wave-front propagates back and forth within the regenerator. In this mode the applied magnetic field remains zero throughout all experiments. One end of the regenerator exchanges heat with the ambient through a secondary heat exchanger thus maintaining the ambient temperature at that end at all times. At the other end of the regenerator an electric heater is situated. In this way a temperature difference between the two ends may be obtained and maintained by the regenerative process. The effectiveness of such a passive regenerator is given by¹⁴

$$\text{Eff} = 1 - \frac{\int_0^\tau (T_{hot} - T_{f,exit}) dt}{\tau (T_{hot} - T_{cold})} \quad (2)$$

where T_{hot} is the temperature at the end of the regenerator with the heater, T_{cold} is the temperature at the end of the regenerator thermally connected to the ambient and $T_{f,exit}$ is the temperature of the fluid exiting the regenerator. Finally, the total cycle time is denoted τ . Equation 2 can be interpreted as one minus the heater power necessary to maintain a reservoir temperature divided by the maximum energy required to heat the fluid from the cold reservoir temperature to the hot temperature. For the experiments considered here, the heater power in the hot reservoir is held constant and the cold reservoir temperature is fixed. Therefore, the temperature span achieved in each experiment is a direct measurement of the regenerator effectiveness. Thus, the passive regenerator performance is reported as the temperature span in this work.

Numerical model

In order to evaluate the experimental results obtained from operating the monolithic structure passively, a well-established numerical model was used to predict the regenerator performance in terms of expected temperature spans. The model is one-dimensional and it solves the governing regenerator equations for the coupled heat transfer between a solid and a fluid in counter-flow

operation. The model is presented in detail in ref. 15 and it is available for public usage. The governing equations solved are

$$A\epsilon\rho_f c_f \frac{\partial T_f}{\partial t} = -\dot{m}c_f \frac{\partial T_f}{\partial x} - \frac{Nuk_f}{D_h} aA(T_f - T_s) \quad (3)$$

$$A(1 - \epsilon)\rho_s c_s \frac{\partial T_s}{\partial t} = \frac{Nuk_f}{D_h} aA(T_f - T_s) \quad (4)$$

where A , ϵ , ρ_f , c_f , \dot{m} , T_f , Nu , k_f , D_h , a , T_s are the cross sectional area, porosity of the structure, mass density of the heat transfer fluid, specific heat of the heat transfer fluid, mass flow rate, temperature of the fluid, the Nusselt number describing the heat transfer between the solid and fluid, thermal conductivity of the fluid, hydraulic diameter of the regenerator, specific surface area of the regenerator and temperature of the solid, respectively. The equations are solved in time and space along the direction of the flow.

Several parameters are needed for the model. The specific surface area is found as the wetted perimeter of one channel divided by the unit cross section of a channel, which in this case corresponds to $a = 4 \times 1 \text{ mm} / (1.5 \text{ mm})^2 = 1778 \text{ m}^{-1}$. The porosity is given by the void cross section fraction of the unit cross section of a channel, i.e. $\epsilon = (1 \text{ mm})^2 / (1.5 \text{ mm})^2 = 0.44$. Finally, the hydraulic diameter is given by four times the flow cross sectional area divided by the wetted perimeter of one channel, i.e. $D_h = 4(1 \text{ mm})^2 / 4 \times 1 \text{ mm} = 1 \text{ mm}$.

For square channels, as considered here, the Nusselt number has been found¹⁶ to be 2.98.

Experimental and modeling results

The thermal utilization, as defined in Eq. (1), and the mass flow rate were varied for different values of the heater power. In this way the temperature span of the regenerator, when operating passively, could be obtained throughout a relevant parameter space. The results presented in Fig. 6 were obtained with a heater power of 0.4 W and those in Fig. 7 at a heater power of 1.7 W. The

regenerator cycle timings are given as a function of utilization and mass flow rate in Table 2. In both figures the temperature span, i.e. the difference between the hot and cold side temperatures, is given as a function of the thermal utilization and at different mass flow rates.

The model predictions are seen to be in qualitatively good agreement with the experimental results. The trend as a function of the utilization is clear. At higher utilizations the temperature span decreases and thus the effectiveness of the regenerator is degraded. It is also evident from the results that at larger mass flow rates the regenerator is less efficient than at the smaller mass flow rate. This is explained from the fact that as the mass flow rate increases the fluid velocity will increase also. The time for local heat transfer between the solid and the fluid is thus decreased and is therefore less efficient resulting in an overall less efficient regenerator. The model is based on a single perfect channel of the monolith. Although, as mentioned before, some of the channels seem to be slightly skewed the model was able to capture correctly the behavior of the regenerator. These results indicate indirectly that the overall geometry of the monolithic regenerator after extrusion is as expected on average without major distortion of the shape which could affect the performance.

Discussion

Much of the effort to improve the performance of magnetic refrigeration is centered on the search for new magnetic materials with a large magnetocaloric effect and new designs of permanent magnet systems producing strong magnetic fields. However, the geometry of the regenerator has an equally large impact on the device performance. Even so, the question of the processability of candidate magnetocaloric materials into a relevant geometry has hitherto not been experimentally investigated in much detail. In this study, we have succeeded in fabricating for the first time a monolithic ceramic regenerator made of LCSM.

The key to the fabrication of high quality monolithic structure lies in the quality of the extrusion dies and in achieving a lower viscosity with a higher solid loading of the LCSM material. As

discussed above, polymeric additives are necessary to provide sufficient plasticity for the material to be extruded. The demand to provide sufficient plasticity for the material introduces other difficulties, such as diluting the magnetocaloric effect and the lack of rigidity of the structure during sintering if the ratio powder/binder is low. The amount and type of plasticizers added is determined by empirical evaluation rather than by scientific approach. Indeed, this remains one of the most poorly understood areas of ceramic processing. Sintering is an essential step in producing a dense and structurally stable ceramic microstructure. In the present investigation, a tendency of the structure to collapse was observed during sintering for the extruded material with the high powder volume fraction content. The tendency to collapse is associated with the presence of excess polymer between the oxide particles, which accounts for the viscoplastic creep which makes the structure too soft to retain its shape. Water based paste might be a promising route in the future to avoid this problem.

Taking into consideration the fact that the monolith was not sintered, i.e. the ΔT_{ad} is only 0.26 K, the results indicate that during the testing of the monolith, the measured temperature span was found to be almost four times larger than the adiabatic temperature change suggesting the possibility for good future performance of such a structure providing that the binder is removed. For a better monolith performance, the external parameter such as the channel dimension, i.e. the wall thickness, needs to be optimized for high kinetic performance balanced against low pressure drop regardless of whether the monolith in a non-sintered or sintered state.

Parallel plate regenerators with small plate spacings (1 mm or less) received a huge interest owing to their theoretically high thermal performance (i.e., high heat transfer coefficient due to a large specific surface area) with low pressure drops. However, a novel manufacturing technique offers the possibility to obtain a monolithic ceramic structure which overcomes some of the limitations of producing parallel plate regenerator by increasing the surface area while maintaining a high amount of material and structural rigidity of the structure. Figure 8 shows a comparison between a parallel plate and monolithic regenerator. The plate regenerator

performance was predicted using the model for a regenerator with 1 mm plate spacing and a plate thickness of 1.27 mm, resulting in porosity equal to the monolithic regenerator. As seen from this figure the characteristics provided by the monolithic design seem to be similar to parallel plate. However, the monolithic structure provide a larger surface area for heat transfer of the MCM and more importantly the intrinsic brittle character of the ceramic materials is overcome by making the regenerator monolithic leading to a stable structure which can be produced by one processing step. Although the passive regenerator performance could not be compared directly to an active regenerator the present results indicate that the monolithic regenerator perform well as a passive regenerator. These results indicated that if we are able to sinter the monolith, and by that obviously removing the binder, we can achieve a high performance of the active regenerator.

Further work on understanding the parameters influencing the extrudability of magnetic regenerators as well as the parameters influencing the sintering of the monolith is needed. It will also be crucial to understand the impact of the mal distribution of the flow channels on the resulting heat transfer properties of the structure. This effect, known as flow channeling, is beyond the scope of the present work; however, it may be of crucial importance for the optimization of regenerators and will thus have a significant impact on the required tolerances of the extrusion process.

Conclusion

$\text{La}_{0.67}\text{Ca}_{0.26}\text{Sr}_{0.07}\text{Mn}_{1.05}\text{O}_3$ (LCSM) perovskite was prepared for the first time as a ceramic monolith for use as a magnetic regenerator. The parameters influencing the extrusion process and the performance of the regenerator, such as the nature of the monolith paste and the influence of sintering on the adiabatic temperature change, were investigated. A tendency of the structure to collapse was observed during sintering due to the high ratio of binder to powder.

The present results indicate that the monolithic regenerator perform well as a passive regenerator suggesting that if we are able to sinter the monolith while maintain its shape we can

achieve a high performance of the active regenerator. Further comparison between a parallel plate regenerator and monolith structure show similar performance indicating the potential financial and structural benefits of using such a structure, i.e. a stable ceramic thin wall structure which can be produced by a one-step processing technique.

Acknowledgements

The authors thank Mr. Jørgen Geyti for his technical help as well as Dr. Carlos Eugenio Ancona-Torres for helping with the DSC measurements. This project is supported by the Programme Commission on Energy and Environment (EnMi) (Contract no. 2104-06-0032) which is part of the Danish Council for Strategic Research.

References

¹C. R. H. Bahl, T. F. Petersen, N. Pryds, A. Smith, A versatile magnetic refrigeration test device, *Review of Scientific Instruments*, **79** [9] 093906 (2008).

²C. R. H. Bahl, A. Smith, N. Pryds, S. Linderøth, Magnetic Refrigeration – an Energy Efficient Technology for the Future, Presented at: Risø International Energy Conference 2009. Risø (DK), 14 – 16 Sep., 2009, In: Energy solutions for CO2 emission peak and subsequent decline: Proceedings, p. 107-115-Roskilde : Risø National Laboratory for Sustainable Energy, 2009

- ³K. Gschneidner, V. Pecharsky, A. Tsokol,. Recent developments in magnetocaloric materials. Rep. Prog. Phys., **68** 1479–1539 (2005)
- ⁴Dinesen A R, Linderoth S and Mørup S, Direct and indirect measurement of the magnetocaloric effect in $\text{La}_{0.67}\text{Ca}_{0.33-x}\text{Sr}_x\text{MnO}_{3+\delta}$ (x is an element of [0; 0.33]). J. Phys.: Condens. Matter, **17** 6257-6269 (2005)
- ⁵L. Peng, G. Maoqiong and W.Jianfeng, Geometric optimization of an active magnetic regenerative refrigerator via second-law analysis, J. Appl. Phys., **104** 103536 (2008)
- ⁶K.K. Nielsen, C.R.H. Bahl, A. Smith, N. Pryds, J. Hattel, A comprehensive parameter study of an Active Magnetic Regenerator using a 2D numerical model, Int. J. Refrig. **33** 753-764 (2010)
- ⁷P. Li, M. Gong, G. Yao and J. Wu, “A practical model for analysis of active magnetic regenerative refrigerators for room temperature applications”, International Journal of Refrigeration, **29** 1259-1266 (2006),
- ⁸P. Avila, M. Montes and E. E. Miró, Monolithic reactors for environmental applications A review on preparation technologies, Chemical Engineering Journal, **109** 11–36 (2005)
- ⁹P. Bardhan, Ceramic honeycomb filters and catalysts, Current Opinion in Solid State and Materials Science, **2** [5] 577-583 (1997)
- ⁹Heiber, J., Clemens, F., Graule, T. and Hülsenberg, D., Thermoplastic extrusion to highly-loaded thin green fibres containing $\text{Pb}(\text{Zr},\text{Ti})\text{O}_3$. Adv. Eng. Mater., **7** 404–408 (2005)
- ¹⁰R. Bjørk, C. R. H. Bahl and M. Katter, Magnetocaloric properties of $\text{LaFe}_{13-x-y}\text{Co}_x\text{Si}_y$ and commercial grade Gd, Journal of Magnetism and Magnetic Materials, **322**, 3882-3888 (2010).
- ¹¹M. Pėkala and V. Drozd, Magnetocaloric effect in nano- and polycrystalline $\text{La}_{0.8}\text{Sr}_{0.2}\text{MnO}_3$ manganites, Journal of Non-Crystalline Solids, **354** 5308–5314 (2008)

- ¹²M. Pękała, V. Drozd, J.F. Fagnard, P. Vanderbemden and M. Ausloos, Magnetocaloric effect in nano- and polycrystalline manganite $\text{La}_{0.7}\text{Ca}_{0.3}\text{MnO}_3$. *Appl. Phys. A*, **90** 237–241 (2008)
- ¹³R. Bjørk, C. R. H. Bahl, A. Smith, N. Pryds, Review and comparison of magnet designs for magnetic refrigeration, In: *International Journal of Refrigeration*, 33 [3] 437-448 (2010)
- ¹⁴G. D. Dragutinovic, and B. S. Baclic, 1998, *Operation of Counterflow Regenerators*, Computational Mechanics Inc., Billerica, MA.
- ¹⁵K. Engelbrecht, 2008, PhD thesis, University of Wisconsin, Madison.
- ¹⁶Kays, W. M. and M. E. Crawford, 1980, *Convective Heat and Mass Transfer*, McGraw-Hill, New York.
- ¹⁷S. Jeppesen, S. Linderøth, N. Pryds, L. T. Kuhn, and J. B. Jensen, Indirect measurement of the magnetocaloric effect using a novel differential scanning calorimeter with magnetic field, *Review of Scientific Instruments*, **79**, 083901 (2008)

Figure Caption

Figure 1. DSC scan of the powder at zero field after calcination at 1573K.

Figure 2. Rheological results of the three different ceramic blends (52, 54, 58 vol.-% LCSM). The experiment was done with a 1 mm die at 413 K. (a) pressure vs. piston speed and (b) shear rate vs. apparent shear viscosity (the lines are linear fits to the data points).

Figure 3. 58 vol.-% LCSM extruded honeycomb structure. The compound was extruded at 423 K with a piston speed of 5 mm/min.

Figure 4. The adiabatic temperature change (a) before and (b) after sintering. The top x-axis indicates the internal magnetic field of the sample.

Figure 5. The heat capacity measured for sintered and non sintered samples at zero and 1 T field.

Figure 6. Temperature span as a function of utilization as defined in Eq. (1) at a constant heat load of 0.4 W. See Table 2 for the corresponding regenerator cycle timings.

Figure 7. Temperature span as a function of utilization as defined in Eq. (1) at a constant heat load of 1.7 W. See Table 2 for the corresponding regenerator cycle timings.

Figure 8. Comparison between a parallel and monolithic regenerator. The temperature span for these two structures is plotted as a function of utilization

Tables

Table 1. Summary of the magnetocaloric measurements.

Materials/properties	Measurements of the adiabatic temperature			Measurements of the heat capacity		
	ΔT_{ad} (K)	T_c (K)	$\mu_0 H_{int}$ (T)	Peak C_p (J/kgK)	T_c (K)	$\mu_0 H_{int}$ (T)
LCSM – non-sintered	0.26	298	0.96	750.	292	0.94
LSCM – sintered	0.78	300	0.96	600	292	0.94

Table 2. Total cycle time of the passive regenerator experiments as a function of utilization (Eq. 1) and mass flow rate of the heat transfer fluid.

Mass flow rate [g/s]	Utilization [-]			
	0.13	0.19	0.32	0.64
2.7	2	2.4	3.2	5.2
4.5	2.6	3.2	4.6	7.9

A.2 Papers submitted to peer-reviewed international scientific journals

- A.2.1 Demagnetizing effects in stacked, rectangular prisms; submitted to Journal of Applied Physics

Demagnetizing effects in stacked, rectangular prisms

D.V. Christensen^{1,2}, K.K. Nielsen^{1,3}, C.R.H. Bahl¹ and A. Smith¹

¹Fuel Cells and Solid State Chemistry Division

Risø National Laboratory for Sustainable Energy, Technical University of Denmark

Frederiksborgvej 399, DK-4000 Roskilde, Denmark

² The Niels Bohr Institute, University of Copenhagen

Blegdamsvej 17, DK-2100 Copenhagen, Denmark

E-mail: dechr@risoe.dtu.dk

³ Department of Mechanical Engineering, Technical University of Denmark

Building 425, Niels Koppels Alle, DK-2800 Kongens Lyngby, Denmark

(Dated: November 28, 2010)

Abstract

A numerical, magnetostatic model of the internal magnetic field of a rectangular prism is extended to the case of a stack of rectangular prisms. The model enables the calculation of the spatially resolved, three-dimensional internal field in such a stack given any magnetic equation of state, stack configuration, temperature distribution and applied magnetic field. In this paper the model is applied to the case of a stack of parallel, ferromagnetic rectangular prisms and the resulting internal field is found as a function of the orientation of the applied field, the number of prisms in the stack, the spacing between the prisms and the packing density of the stack. The results show that the resulting internal field is far from being equal to the applied field and that the various stack configurations investigated affect the resulting internal field significantly and non-linearly. The results have a direct impact on the design of, e.g., active magnetic regenerators made of stacks of rectangular prisms in terms of optimizing the internal field of such stacks.

PACS numbers: 75.30.Sg,75.30.-m,75.60.Ej,41.20.Gz

I. INTRODUCTION

The total magnetic field, \mathbf{H} , in the vicinity of one or several magnetized bodies is of general interest. In particular, when concerned with, e.g., magnetic refrigeration the local magnetic field of the magnetic material is of great importance.^{1,2} The magnetostatic calculation of \mathbf{H} is in principle straightforward and can in certain cases, e.g. ellipsoids, be found analytically.³⁻⁵ However, this is only true for homogeneously magnetized bodies. When the magnetization of the body is varying spatially, numerical methods are usually required.^{1,6-8}

In the presence of magnetized bodies the total magnetic field at a certain point in space, \mathbf{r} , can be found as the superposition of the applied magnetic field, \mathbf{H}_{appl} , and the magnetic field created by the magnetized bodies. The magnetic field from a single, magnetic body is typically called the demagnetizing field inside the body and the stray or interaction field outside. Since the source of these fields is the same, the remainder of this paper will adopt the concept of the magnetic field of the body, $\mathbf{H}_{\text{body}}(\mathbf{r})$, at any given point in space. The resulting total magnetic field may thus be written as

$$\mathbf{H}(\mathbf{r}) = \mathbf{H}_{\text{appl}}(\mathbf{r}) + \sum_{i=1}^N \mathbf{H}_{\text{body},i}(\mathbf{r}), \quad (1)$$

where the index i represents the i th body out of a total of N bodies. Usually, the solution to the magnetic field from a single, homogeneously magnetized body with magnetization, \mathbf{M} , is written as

$$\mathbf{H}_{\text{body}}(\mathbf{r}) = -\mathbf{N}(\mathbf{r}) \cdot \mathbf{M}, \quad (2)$$

where the demagnetizing tensor field, $\mathbf{N}(\mathbf{r})$, only depends on the geometry of the body.

Under inhomogeneous conditions iterative methods are typically required to determine the internal magnetic field of a magnetized body.^{4,6} Furthermore, even in a homogeneous applied magnetic field, the field of a magnetized body is generally inhomogeneous. In non-saturated conditions the magnetization thus becomes a non-trivial function of position thereby making evaluation of the magnetic field due to the magnetization of the body possible only using numerical methods.

Here, the numerical solution to the total magnetic field of a configuration of multiple bodies with inhomogeneous and field-dependent magnetization is reported. The numerical model is applied to a stack of rectangular prisms as this configuration is important in,

e.g., magnetic refrigeration.⁹ However, the discretization underpinning the model can in principle be applied to any shape. The implementation is described in Sec. II and the results of different stack configurations are presented and discussed in Sec. III. In Sec. IV the implications of the model are considered. Finally, in Sec. V, the conclusions are provided.

II. MAGNETOSTATIC MODEL OF STACKED RECTANGULAR PRISMS

In the following a numerical model capable of calculating the total magnetic field in a configuration of N stacked rectangular prisms, as depicted in Fig. 1, is presented. The model is an extension of the single prism solution presented in Ref. 8 and its predictions are compared to an experiment in Ref. 10. The single prism model uses iteration to solve the two coupled equations

$$\mathbf{M}(\mathbf{r}) = \begin{cases} f(T(\mathbf{r}), H(\mathbf{r})) \frac{\mathbf{H}(\mathbf{r})}{H(\mathbf{r})} & \text{inside the prism} \\ 0 & \text{outside the prism} \end{cases} \quad (3)$$

and

$$\mathbf{H}(\mathbf{r}) = \mathbf{H}_{\text{appl}}(\mathbf{r}) + \mathbf{H}_{\text{body}}(\mathbf{r}). \quad (4)$$

Note that the magnetization is taken to be along the direction of the internal magnetic field thereby assuming the material to be isotropic.⁶ To solve Eqs. 3–4 iteratively expressions for the magnetic equation of state, f , and the magnetic field produced by the magnetic body, \mathbf{H}_{body} , need to be established. The magnetic equation of state is chosen to be the mean field equation of state describing a ferromagnet¹¹

$$f(T, H) = N_s g J \mu_B \rho B_J(\chi) \quad (5)$$

where the Brillouin function

$$B_J(\chi) = \frac{2J+1}{2J} \coth\left(\frac{2J+1}{2J}\chi\right) - \frac{1}{2J} \coth\left(\frac{1}{2J}\chi\right) \quad (6)$$

$$\chi = \frac{gJ\mu_B\mu_0 H}{k_B T} + \frac{3T_C J}{T(J+1)} B_J(\chi), \quad (7)$$

TABLE I: Parameters for the mean field equation of state, Eq. 5, for gadolinium. Data are taken from Refs. 12,13.

Parameter	N_s [kg^{-1}]	g [-]	J [\hbar]	ρ [kgm^{-3}]	T_C [K]
Value	3.83×10^{24}	2	7/2	7900	293

is itself found through iteration. The parameters are the number of spins per unit mass, N_s , the Landé factor, g , the total angular momentum, J , the Bohr magneton, μ_B , the mass density ρ , the Curie temperature, T_C , the Boltzmann constant, k_B , and the permeability of free space, μ_0 . The input parameters to the mean field equation of state are given in Table I and correspond to the rare earth metal gadolinium frequently used in magnetic refrigeration. The temperature is chosen to be 293 K, which is also the Curie temperature of gadolinium. The model may straightforwardly be extended to handle temperature and material variations across the prisms, however, for simplicity this is not done in the present study; see Ref. 8 for further details.

The magnetic field of the magnetized rectangular prism is found by dividing the prism into k cells each shaped as a rectangular prism small enough to be approximately homogeneously magnetized, whereas both the magnitude and direction of the magnetization may vary from cell to cell. The magnetic field of each homogeneously magnetized cell can be expressed analytically⁴ and hence the total magnetic field due to the magnetization can be obtained by superimposing the contributions from each cell⁸

$$\mathbf{H}_{\text{body}}(\mathbf{r}) \approx - \sum_{j=1}^k \mathbb{N}(\mathbf{r} - \mathbf{r}_j) \cdot \mathbf{M}_j \quad (8)$$

where \mathbf{r}_j denotes the center of the j 'th cell, \mathbf{M}_j is the magnetization of the j th cell and \mathbb{N} is the symmetric 3×3 tensor field with components given in Appendix A. Note that the expression given in Eq. 8 is an approximation that relies on the discretization of the rectangular prism into small cells; see Ref. 8 for details on sufficient grid size and the numerical implementation.

The extension to a configuration of multiple prisms is done by extending the sum in Eq. 8 to include each individual prism, i.e. by combining Eqs. 1 and 8. The total magnetic field

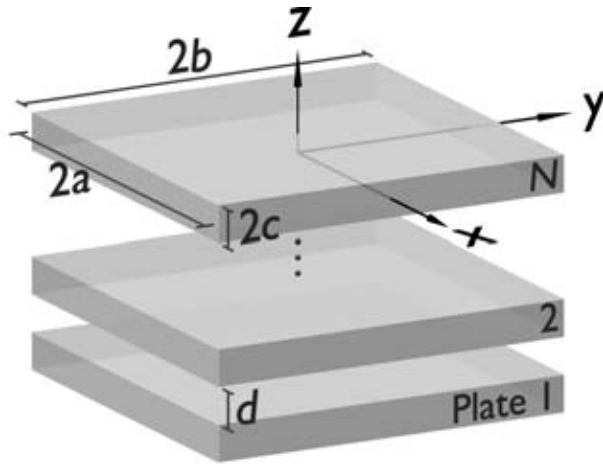


FIG. 1: The coordinate system of a stack composed of rectangular prisms each with dimensions $2a \times 2b \times 2c$. The stacking of the prisms is in the z -direction where the prisms are thinnest. The total height of the stack is denoted L and the distance between two adjacent prisms is d .

therefore becomes

$$\mathbf{H}(\mathbf{r}) \approx \mathbf{H}_{\text{appl}}(\mathbf{r}) - \sum_{i=1}^N \sum_{j=1}^k \mathbb{N}(\mathbf{r} - \mathbf{r}_{i,j}) \cdot \mathbf{M}_{i,j}, \quad (9)$$

where N is the number of prisms and i is used to index the prisms. Thus, the extension to multiple prisms is obtained by dividing each prism into a set of cells and superimposing the contributions from all cells. This approach can readily be extended to cover the case of a two- or three-dimensional array of rectangular prisms. In addition, any other shape can be divided into cells and solved using the method described here.

III. RESULTS AND DISCUSSION

The model is applied to the case of N prisms equally spaced with a distance d between adjacent prisms resulting in a spatial extent $L = N2c + (N - 1)d$ of the stack in the z -direction as shown in Fig. 1. Following Ref. 8 the dimensions of each prism have been chosen to be $2a \times 2b \times 2c = 20 \times 20 \times 1 \text{ mm}^3$ and an applied magnetic field of 1 T is oriented along either the x - or the z -direction. Three sets of parameter variations are considered. Firstly, the number of prisms in the stack is varied while the distance between two adjacent prisms is kept constant. Secondly, a stack of a fixed number of prisms is considered in which the distance between the prisms is varied. Thirdly, the overall spatial extent of the stack in the direction of the stacking is kept constant (i.e. L is a fixed number). The number

of prisms, the distance and the thickness of the prisms are then varied within this space in order to probe the effect of the packing density of the stack on the internal magnetic field of the stack.

A. Number of prisms

The number of prisms in the stack, N , is varied from 1 to 99 and the spacing between two adjacent prisms is kept fixed at $d = c$ or $d = 4c$. In the former case the spacing between two adjacent prisms is equal to half the thickness of a single prism whereas in the latter it is equal to the thickness of two prisms. These two cases result in packing densities of $2/3$ and $1/3$, respectively, where the packing density, α , is given by

$$\alpha = \frac{2c}{d + 2c}. \quad (10)$$

The volume average of the internal magnetic field strength in all the prisms is given in Fig. 2 for an applied magnetic field oriented along either the x - or z -direction. For a single prism the volume average of the internal magnetic field strength attains its lowest value when the applied field is along the z -direction as the demagnetizing field is maximized for this orientation. The opposite is true when the applied field is in the x -direction. These results follow from the well-known single prism solution that may be found in, e.g., Ref. 5.

Increasing the number of prisms when the applied magnetic field is perpendicular to the direction of the stacking (i.e. $\mathbf{H}_{\text{appl}} \parallel \mathbf{x}$) reduces the total average internal field of the stack. Oppositely, the total average internal field increases when the applied field is along the stacking direction ($\mathbf{H}_{\text{appl}} \parallel \mathbf{z}$). This is to be expected and simply explained by considering Fig. 3. When the stacking direction is parallel with the applied field the stray field due to the magnetization of each individual magnetized body will tend to enhance the applied field in neighboring prisms, whereas the stray field tends to reduce it when the stacking is perpendicular to the applied field. Note that this entails that the largest internal field is experienced by the center prism for $\mathbf{H}_{\text{appl}} \parallel \mathbf{z}$ and the outermost prisms for $\mathbf{H}_{\text{appl}} \parallel \mathbf{x}$, whereas the minimum internal field is found at the outer prisms and the center prism for $\mathbf{H}_{\text{appl}} \parallel \mathbf{z}$ and $\mathbf{H}_{\text{appl}} \parallel \mathbf{x}$, respectively. The minimum and maximum values for the individual prisms are represented by the shaded areas in Fig. 2.

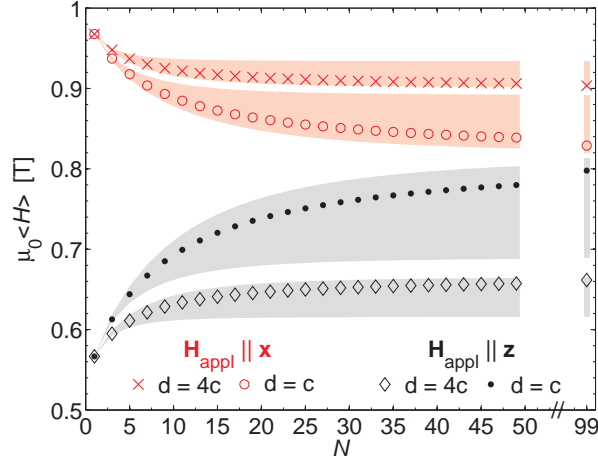


FIG. 2: The average internal magnetic field strength in stacks composed of N prisms. The prisms are stacked with a distance of $d = c$ or $d = 4c$ and subjected to two orientations of the applied field. The shaded areas cover the area between the lowest and highest values of the average internal field of the individual prisms instead of the entire stack.

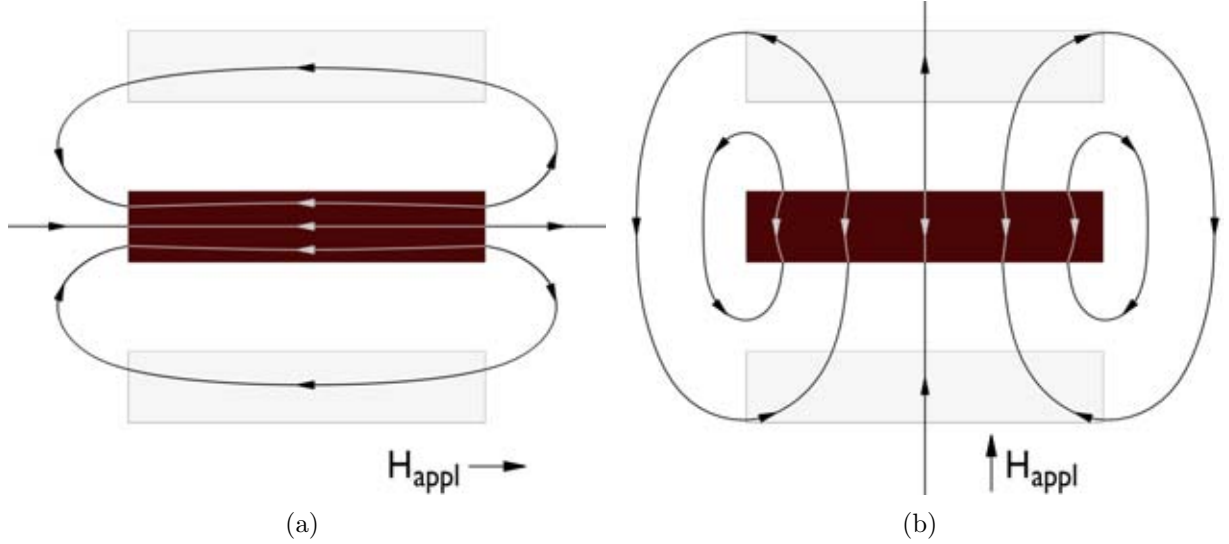


FIG. 3: Schematic illustration of the magnetic field from a single rectangular prism positioned in a stack. The prism is magnetized along either the x -direction (a) or the z -direction (b). In both cases the magnetic field from the prism opposes the applied field inside the prism as seen by the white field lines. Stacking the prisms perpendicular to the magnetization direction results in a decrease in the internal magnetic field, whereas parallel stacking enhances the internal field. Note that the \mathbf{H} -field is discontinuous across the surfaces effectively containing magnetic charges.

As the number of magnetized bodies increases the field enhancing or reducing effect is enlarged steadily reaching a level where the stack of prisms tends to behave as an infinite stack. In this case the outer boundaries become virtually negligible. This is clearly apparent

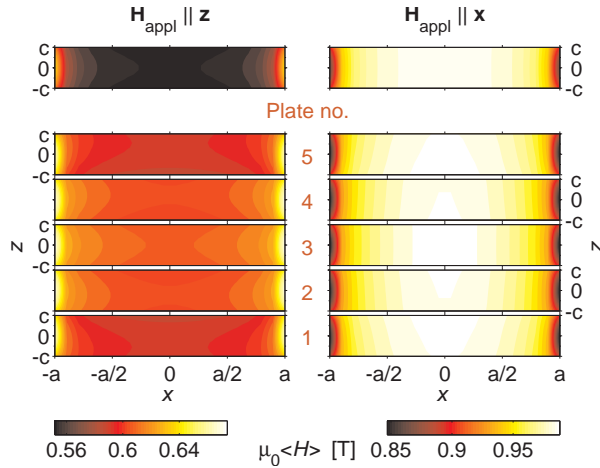


FIG. 4: The internal magnetic field strength of a single rectangular prism (top) and a configuration of 5 prisms displaced with $d = 4c$ (bottom; not drawn to scale) for two different orientations of the applied magnetic field. The internal magnetic field strength is averaged in the y -direction.

from Fig. 2 for $d = 4c$ where increasing the number of prisms from $N = 49$ to 99 only changes the average internal field by 0.3% and 0.6% when the applied field is along the x - and z -direction, respectively. In addition the average internal field of the whole stack almost coincides with the average internal field of the center prism thereby indicating that the boundaries are indeed of minor importance. In the case where $d = c$ the average of the total internal field in the stack is also seen to behave asymptotically, however, the convergence is less pronounced. A better description of the infinite stack is found by only considering the center prism instead as convergence is essentially reached at $N = 99$ and consequently the influence of the boundaries is negligible. In the remainder of this paper the internal field of the center prism in a stack of 99 prisms will therefore be used when referring to an infinite stack. Note that this assumption improves with increasing distance between the prisms.

Figure 4 shows an example of the spatial variations in the magnitude of the internal field in a single prism and a stack of five prisms spaced with $d = 4c$. Here, it is observed that the internal field is significantly affected when the number of prisms in the stack is greater than one. The difference between a single prism and the stack of five prisms is most pronounced in the case where the applied field is along the z -direction.

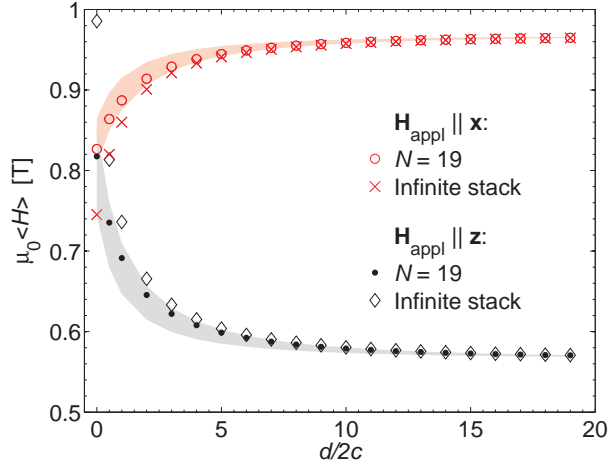


FIG. 5: The average internal field strength in stacks composed of rectangular prisms as a function of the distance between two adjacent prisms normalized to the thickness of a single prism. Two orientations of the applied field are provided (along the x - and the z -direction). Furthermore, an infinite stack and a stack composed of 19 prisms are considered. As in Fig. 2 the shaded areas mark the maximum and minimum average internal field strengths of the individual prisms in the given configuration.

B. Distance between each prism

For an infinite stack and a stack containing 19 prisms the average, internal magnetic field strength is plotted in Fig. 5 as a function of the distance between the prisms given in units of the prism thickness, $d/2c$. As in the previous section the shaded areas in Fig. 5 mark the maximum and minimum values of the average internal field strength in each individual prism for a given stack configuration. An increase in the distance is observed to result in an asymptotical approach towards a value of 0.96 and 0.57 T for an applied field along the x - and z -direction, respectively. This behavior is almost identical for the two stacks considered. When the distance between adjacent prisms increases the stray field from each magnetized prism has less influence on neighboring prisms and the number of prisms in the individual stacks becomes less important. The asymptotic values are therefore equal to the single prism solutions seen in Fig. 2.

Interestingly, the results from the two stack configurations differ considerably at low values of the ratio $d/2c$. Here, the stray fields from the magnetized prisms have a much larger influence on neighboring prisms, as expected, which is also clearly manifested in a great response of the internal magnetic field strength when varying the distance. In addition, when the applied magnetic field is along the z -axis and $d/2c$ is close to zero the average

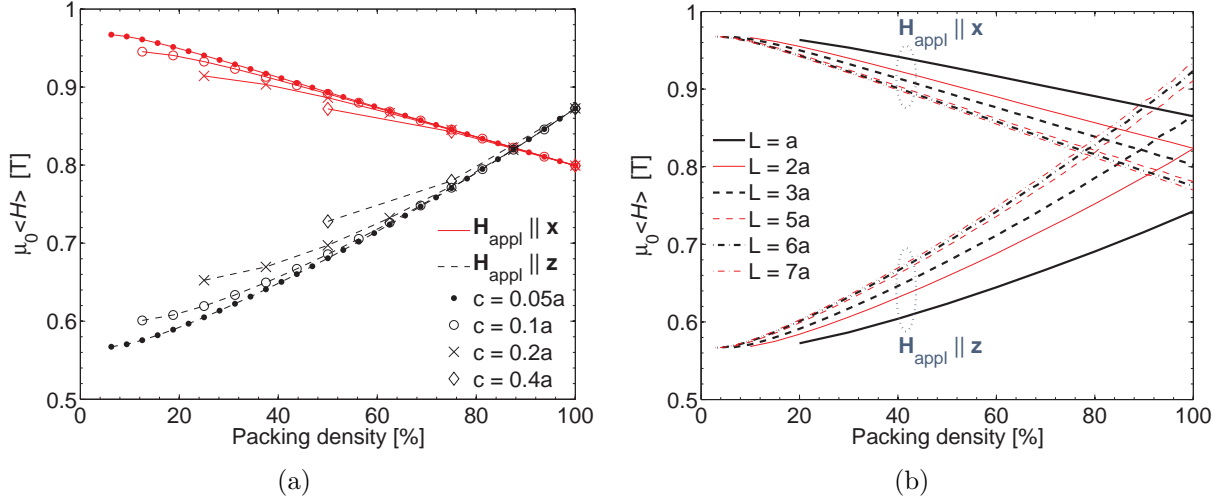


FIG. 6: The average internal field strength in stacks composed of rectangular prisms as a function of the packing density. a) The packing density is varied by changing the number of equally spaced prisms while keeping the total height of the stack fixed at $L = 3.2a = 32$ mm. Furthermore, four different prism thicknesses are provided, $c = 0.05a$, $c = 0.1a$, $c = 0.2a$ and $c = 0.4a$, and the applied field is oriented along either the x - or the z -direction. b) The thickness of the prisms is kept fixed at $c = 0.05a$ whereas the total height of the stack is varied from $L = a$ to $L = 7a$. Note that for a packing density of one the stack becomes a single prism; in particular, when $L = 2a$ the stack is a cube.

internal field strength is actually significantly larger than in the case where the applied field is along the x -direction. This is not surprising considering the limit where $d/2c$ is zero since the stack is then effectively a single prism with dimensions $2a \times 2b \times 2cN$; here, the single prism solution dictates that the average internal field should be greater when applying the external magnetic field along the direction where the prism is thickest.⁵ In particular for the infinite stack the magnetic field from the magnetization vanishes if $d/2c = 0$ and the applied field is oriented along the direction of stacking. This is observed in Fig. 2 by the strength of the internal magnetic field almost being equal to the applied field (1 T). The small discrepancy is solely due to the fact that the infinite stack is represented by a prism surrounded by a large, albeit finite number of prisms.

C. Packing density

Recalling the definition of the packing density, Eq. 10, maintaining a constant total stack height, L , and adding prisms such that the distance between adjacent prisms for a given number of prisms is constant, the packing density of the stack may be varied consistently.

In addition the packing density can be varied by changing the thickness of the prisms along the direction of stacking.

In Fig. 6a the average internal field strength of the stack is given as a function of the packing density for four different prism thicknesses. For all thicknesses it is observed that values of the packing density greater than about 90% yield the largest average internal field when the applied is along the z -direction, whereas applying the field in the x -direction results in the maximum average internal field of the stack for packing densities less than 90%. As the packing density increases the stack approaches a single prism with dimensions $2a \times 2b \times L = 20 \times 20 \times 32 \text{ mm}^3$. Applying the field along the z -direction thus yields the strongest internal magnetic field in agreement with the single prism solution from Ref. 5. On the other hand thin prisms located in a stack with a low packing density are almost isolated and the strongest internal field is therefore found when applying the external field along the x -direction in agreement with the results of, e.g., Fig. 2.

By comparing the results from different prism thicknesses the same trends are seen. Increasing the packing density for a given prism thickness the internal field of the stack is decreased for an applied field along the x -direction and increased when applying the field in the z -direction. The trends are due to the field reducing ($\mathbf{H}_{\text{appl}} \parallel \mathbf{x}$) or enhancing ($\mathbf{H}_{\text{appl}} \parallel \mathbf{z}$) effects of both adding more prisms and decreasing the distance between adjacent prisms. Interestingly, at any packing density the strongest internal field is found when the stack is composed of thin prisms for the case of an external magnetic field applied parallel to the x -direction, whereas thicker prisms result in the highest internal field when the applied field is along the z -direction.

The effect of varying the total height of the stack while maintaining a fixed thickness of the prisms is shown in Fig. 6b. Consistent with the single prism solution increasing the height of the stack for a packing density of one increases the internal magnetic if the applied magnetic field is along the z -direction and decreases the field for the applied field oriented along the x -direction. For a packing density of one and a stack height of $L = 2a$, the stack is a cube in which case applying the external field along any of the principal axes results in identical average internal fields. For smaller stack heights the largest internal field is obtained by applying the external magnetic field along the x -direction for all packing densities. At greater stack heights the optimal orientation of the applied field is less trivial as it is dependent on the actual stack configuration. For a stack height of, e.g., $L = 3.2a$ a

value of around 90% was observed at which the applied field orientation that optimizes the internal field is changed. This value decreases non-linearly as the stack height is increased seemingly reaching a packing density of around 70% asymptotically. This limit can be deduced by noting that the stack in this case effectively becomes an infinite stack with an *a priori* unknown distance d' between neighboring prisms. Varying the packing density is thus equivalent to varying the distance between the prisms in an infinite stack. The distance $d' \approx c$ can therefore be determined by reference to Fig. 5. Recalling the definition of the packing density, Eq. 10, the packing density, at which the optimal direction of the applied field changes, is approximately $2/3$.

IV. IMPLICATIONS OF THE MODEL

As we have seen, the magnetic field of the stack can differ significantly from the magnetic field of a single prism. This makes the optimization of the internal magnetic field non-trivial even for the simple stack configurations considered here. A direct implication of this is seen when considering magnetic refrigeration. Typically, stacks of parallel, ferromagnetic plates are used with the extent of the stack often determined by the spatial extent of the applied magnetic field. To increase heat transfer between the magnetic plates and the heat transfer fluid the plates are generally thin, whereas the number of plates is high in order to increase the volume of the active material. An important factor in determining the exact stack configuration and the orientation of the applied magnetic field is optimizing the internal magnetic field in the entire stack. However, considering Fig. 6a a large number of closely spaced, thin prisms results in significant magnetostatic interactions between the plates making a numerical model a valuable tool for predicting and maximizing the internal magnetic field. In addition Fig. 6b reveals that especially the packing density and the total height of the stack can highly influence the optimal orientation of the applied magnetic field. Extending the presented model to cover conditions relevant for magnetic refrigeration, such as having a temperature gradient along the plates, which may be comprised of several materials, can readily be implemented by allowing temperature and material variations in the magnetic equation of state, Eq. 5. For a single prism the implementation of these conditions has been reported previously,⁸ but in the light of the results presented here extending this to a stack of plates may yield an internal magnetic field significantly different from that

of a single plate. In addition, applying the model to two- and three-dimensional arrays of rectangular prism is likewise of great interest.

Application of the presented model could also be imagined when considering electronic circuits where the local magnetic field may have some influence in certain cases.^{14,15}

V. CONCLUSION

A numerical model capable of determining the spatially resolved, three-dimensional internal magnetic field in a configuration of multiple bodies with inhomogeneous and field-dependent magnetization is presented. The model is applied to a stack of equally spaced, rectangular prisms. The number of prisms, the separation between the prisms and the packing density are varied and the features of the resulting internal magnetic field explained qualitatively.

Generally, it is found that the stray field created by the magnetization of each prism can have a significant impact on the resulting internal magnetic field thus making it important to consider the full geometry of all magnetic bodies present to accurately describe the internal field. In particular it is concluded that the orientation of the applied field, which optimizes the internal field in the stack, may differ considerably from the optimal direction of the applied field for a single prism.

Acknowledgements

The authors thank the support of the Programme Commission on Energy and Environment (EnMi) (Contract no. 2104-06-0032), which is part of the Danish Council for Strategic Research.

APPENDIX A: COMPONENTS OF THE DEMAGNETIZATION TENSOR FIELD, \mathbb{N}

Consider a rectangular prism with a homogeneous magnetization and dimensions of $2a$, $2b$ and $2c$ in the x -, y - and z -direction, respectively. Defining the origin of the coordinate system in the center of the prism the diagonal elements of the demagnetization tensor field,

$\mathbb{N}(\mathbf{r})$, can be written as^{4,8}

$$N_{ii}(\mathbf{r}) = \frac{1}{4\pi} \left(\begin{aligned} &\text{Arctan } f_i(x, y, z) + \text{Arctan } f_i(-x, y, z) + \text{Arctan } f_i(x, -y, z) \\ &+ \text{Arctan } f_i(x, y, -z) + \text{Arctan } f_i(-x, -y, z) + \text{Arctan } f_i(x, -y, -z) \\ &+ \text{Arctan } f_i(-x, y, -z) + \text{Arctan } f_i(-x, -y, -z) \end{aligned} \right) \quad (\text{A1})$$

where

$$f_x(x, y, z) = \frac{(b-y)(c-z)}{(a-x)((a-x)^2 + (b-y)^2 + (c-z)^2)^{1/2}} \quad (\text{A2})$$

$$f_y(x, y, z) = \frac{(a-x)(c-z)}{(b-y)((a-x)^2 + (b-y)^2 + (c-z)^2)^{1/2}} \quad (\text{A3})$$

$$f_z(x, y, z) = \frac{(b-y)(a-x)}{(c-z)((a-x)^2 + (b-y)^2 + (c-z)^2)^{1/2}}. \quad (\text{A4})$$

The off-diagonal elements are

$$N_{ij}(\mathbf{r}) = -\frac{1}{4\pi} \ln \left(\frac{F_{ij}(\mathbf{r}, a, b, c)F_{ij}(\mathbf{r}, -a, -b, c)F_{ij}(\mathbf{r}, a, -b, -c)F_{ij}(\mathbf{r}, -a, b, -c)}{F_{ij}(\mathbf{r}, a, -b, c)F_{ij}(\mathbf{r}, -a, b, c)F_{ij}(\mathbf{r}, a, b, -c)F_{ij}(\mathbf{r}, -a, -b, -c)} \right), \quad i \neq j \quad (\text{A5})$$

where

$$F_{xy}(\mathbf{r}, a, b, c) = (c-z) + [(a-x)^2 + (b-y)^2 + (c-z)^2]^{1/2} \quad (\text{A6})$$

$$F_{yz}(\mathbf{r}, a, b, c) = (a-x) + [(a-x)^2 + (b-y)^2 + (c-z)^2]^{1/2} \quad (\text{A7})$$

$$F_{xz}(\mathbf{r}, a, b, c) = (b-y) + [(a-x)^2 + (b-y)^2 + (c-z)^2]^{1/2}. \quad (\text{A8})$$

The remaining off-diagonal elements can be found by exploiting that the demagnetization tensor field is symmetric.

¹ O. Peksoy and A. Rowe. Demagnetizing effects in active magnetic regenerators. *Journal of Magnetism and Magnetic Materials*, 288:424–432, 2005.

² R. Bjørk and K. Engelbrecht. The influence of the magnetic field on the performance of an

- active magnetic regenerator (AMR). *International Journal of Refrigeration*, Accepted, 2010.
- ³ J.A. Osborn. Demagnetizing factors of the general ellipsoid. *Physical Review*, 67:351–357, 1945.
- ⁴ R.I. Joseph and E. Schloemann. Demagnetizing field in nonellipsoidal bodies. *Journal of Applied Physics*, 36(5):1579–1593, 1965.
- ⁵ A. Aharoni. Demagnetizing factors for rectangular ferromagnetic prisms. *Journal of Applied Physics*, 83(6):3432–3434, 1998.
- ⁶ J.A. Brug and W.P. Wolf. Demagnetizing fields in magnetic measurements i. thin discs. *Journal of Applied Physics*, 57(10):4685–4694, 1985.
- ⁷ M. Beleggia and M. De Graef. On the computation of the demagnetization tensor field for an arbitrary particle shape using a fourier space approach. *Journal of Magnetism and Magnetic Materials*, 263(1-2):L1–L9, 2003.
- ⁸ A. Smith, K. K. Nielsen, D. V. Christensen, C. R. H. Bahl, R. Bjørk, and J. Hattel. The demagnetizing field of a nonuniform rectangular prism. *Journal of Applied Physics*, 107(10):103910, 2010.
- ⁹ C. R. H. Bahl, T. F. Petersen, N. Pryds, and A. Smith. A versatile magnetic refrigeration test device. *Review of Scientific Instruments*, 79(9):093906, 2008.
- ¹⁰ D. V. Christensen, R. Bjørk, K. K. Nielsen, C. R. H. Bahl, A. Smith, and S. Clausen. Spatially resolved measurement of the magnetocaloric effect and the local magnetic field using thermography. *Journal of Applied Physics*, 108:063913, 2010.
- ¹¹ A. H. Morrish. *The Physical Principles of Magnetism*. John Wiley & Sons, Inc., 1965.
- ¹² D.R. Lide. *CRC Handbook of Chemistry and Physics*. CRC Press, 2004.
- ¹³ A.M. Tishin and Y.I. Spichkin. *The Magnetocaloric Effect and its Applications*. Institute of Physics Publishing, 2003.
- ¹⁴ W. Andra, H. Danan, and U. Ropke. Model for perpendicular hysteresis of thin magnetic films. *IEEE Transactions on Magnetics*, 20(1):102–104, 1984.
- ¹⁵ A.N. Bogdanov, I.E. Dragunov, and U.K. Roszler. Reorientation, multidomain states and domain walls in diluted magnetic semiconductors. *Journal of Magnetism and Magnetic Materials*, 316(2):225–228, 2007.

-
- A.2.2 Measuring the effect of demagnetization in stacks of rectangular gadolinium plates using the magnetocaloric effect; submitted to Journal of Magnetism and Magnetic Materials

Measuring the effect of demagnetization in stacks of gadolinium plates using the magnetocaloric effect

K.W. Lipsø¹, K.K. Nielsen^{2,3}, D.V. Christensen^{2,4}, C.R.H. Bahl²,
K. Engelbrecht², L.Theil Kuhn² and A. Smith²

¹ Department of Physics, Technical University of Denmark
DK-2800 Kgs. Lyngby, Denmark

² Fuel Cells and Solid State Chemistry Division
Risø National Laboratory for Sustainable Energy, Technical University of Denmark
Frederiksborgvej 399, DK-4000 Roskilde, Denmark

³ Department of Mechanical Engineering, Technical University of Denmark
Building 425, Niels Koppels Alle, DK-2800 Kgs. Lyngby, Denmark

⁴ The Niels Bohr Institute, University of Copenhagen
Blegdamsvej 17, DK-2100 Copenhagen, Denmark

e-mail: kaki@risoe.dtu.dk

(Dated: December 8, 2010)

Abstract

The effect of demagnetization in a stack of gadolinium plates is determined experimentally by using spatially resolved measurements of the adiabatic temperature change due to the magnetocaloric effect. The number of plates in the stack, the spacing between them and the position of the plate on which the temperature is measured are varied. The orientation of the magnetic field is also varied. The measurements are compared to a magnetostatic model previously described. The results show that the internal field, and thus the magnetocaloric effect, is sensitive to the stack configuration and the orientation of the applied field. This may have significant implications for the construction of a magnetic cooling device.

PACS numbers: 75.30.Sg,07.55.Ge,75.50.Cc,75.60.Ej,41.20.Gz

I. INTRODUCTION

Magnetic materials exhibit the magnetocaloric effect (MCE), which manifests itself as a change in temperature, ΔT_{ad} , when adiabatically changing the magnetic field applied to the material.

The MCE has been used since the 1930s as a tool to reach temperatures close to absolute zero.¹ It was later suggested to utilize it at near-room temperature by using thermal regeneration to increase the temperature span in a so-called active magnetic regenerator (AMR).^{2,3} In Refs. 4–7 extensive reviews of the application of the MCE in AMR devices are given.

One of the main components of a magnetic refrigerator based on the AMR is a regenerator made of one or multiple porous magnetic materials. This component acts as a thermal regenerator that stores/releases heat and supports a temperature gradient in the flow direction, thus upholding a cold and a hot end, in close interaction with a heat transfer fluid (which is typically aqueous for room temperature applications). While working as a regenerator the AMR is exposed to a periodic change in applied magnetic field, H_{appl} . In this way the MCE in terms of the adiabatic temperature change provides the active work input to the refrigeration cycle.³

The geometry of the regenerator may vary and typically either packed spheres^{8,9} or parallel plates^{10,11} are used. When numerical models of the AMR are considered the magnetic field is most often considered to be equal to the applied field, H_{appl} .^{12–17} Recent material studies on a single rectangular prism subjected to conditions relevant for magnetic refrigeration show, however, that the internal magnetic field can differ significantly from the applied magnetic field.^{18,19} This is due to the demagnetizing field created by the magnetization of the structure. This field is a function of the magnetization and the geometry of the regenerator.^{18,20,21} The magnetization is in itself a function of the local field and temperature and given that the AMR is operating around the magnetic transition temperature of the material²² the magnetization is generally far from being homogeneous in the material.

In this paper we consider stacks of parallel plates where the plates are identical and made of gadolinium. The resulting internal magnetic field of such a stack is found using a magnetostatic model previously published.¹⁸ Experimentally, the adiabatic temperature change is measured directly on the surface of a single plate situated in various stack configurations.

II. MAGNETOSTATIC DEMAGNETIZATION MODEL

It is well known that a magnetized body generates a magnetic field that, inside the body, tends to oppose the applied field. When the body is homogeneously magnetized this demagnetizing field may be expressed through a demagnetization tensor field, $\mathbf{N}(\mathbf{r})$, in the following way

$$\mathbf{H}_{\text{dem}}(\mathbf{r}) = -\mathbf{N}(\mathbf{r}) \cdot \mathbf{M}, \quad (1)$$

where \mathbf{H}_{dem} is the demagnetizing field and \mathbf{M} is the magnetization. In general, \mathbf{N} is a function of the shape of the magnetic body. For certain geometries, such as ellipsoids²³, infinite sheets, cylinders²⁴ and rectangular prisms²⁵ it may be found analytically.

When the magnetic body is not homogeneously magnetized, which is the case if, e.g., a temperature profile is present or the magnitude of \mathbf{M} depends on the internal field, \mathbf{H} , Eq. 1 is not valid. The problem of finding the internal magnetic field given by

$$\mathbf{H} = \mathbf{H}_{\text{appl}} + \mathbf{H}_{\text{dem}}, \quad (2)$$

is then coupled with finding the magnetization, which, in turn, is a function of the local field and temperature.

In Refs. 18,19 a numerical model of the demagnetizing field of rectangular prisms is presented. The model assumes a discretization into small rectangular sub-prisms, where the magnetization, internal field and temperature inside each sub-prism are assumed constant and homogeneous. In this way the analytical solution to Eq. 1 may be applied to each individual sub-prism and the solution of the entire system is then a superposition of the individual solutions. This is formulated mathematically as

$$\mathbf{H}_{\text{dem}}(\mathbf{r}) \approx - \sum_{i=1}^N \mathbf{N}(\mathbf{r} - \mathbf{r}'_i) \cdot \mathbf{M}_0(\mathbf{H}(\mathbf{r}'_i, T_i), \mathbf{r}'_i, T_i), \quad (3)$$

where \mathbf{r} and \mathbf{r}'_i are the position vectors of the point at which the demagnetizing field is evaluated and the point contributing with the magnetization, \mathbf{M}_0 , respectively. The index i denotes the respective sub-prism, or grid cell, and N denotes the number of grid cells. In this way the sum in Eq. 3 is taken over all the contributions to the resulting demagnetizing field at the location \mathbf{r} . The components of $\mathbf{N}(\mathbf{r})$ may be found in Ref. 18. Eqs. 2 and 3 are combined with an appropriate state function for $M(T, H)$ and the direction of the

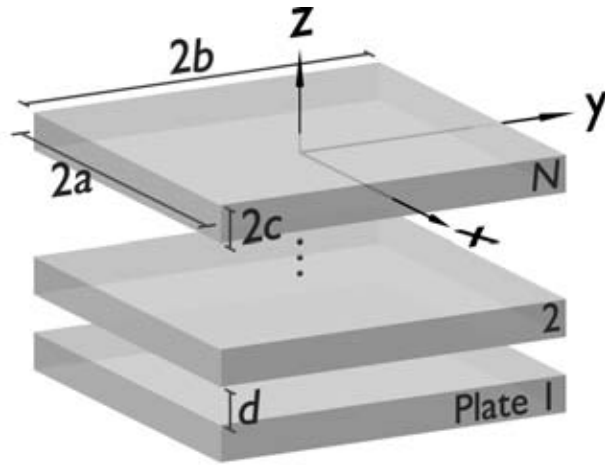


FIG. 1: The coordinate system of the stack of rectangular prisms. The dimensions of each plate, $2a \times 2b \times 2c$, are indicated in the figure as are the number of plates, N , and the distance between adjacent plates, d .

magnetization is assumed to be along \mathbf{H} .²⁰ The model is then solved through iteration until it converges; see Ref. 18 for further details.

Magnetization data is that of commercial grade Gd and are taken from the experimental determination of the magnetization as a function of internal magnetic field and temperature published in Ref. 26. The adiabatic temperature change is found through interpolation from a table where it is a function of the internal magnetic field and temperature also published in Ref. 26.

The coordinate system employed for the stack of rectangular prisms is indicated in Fig. 1. The distance between the prisms is assumed constant and the prisms are assumed flat and uniform. The distance between two adjacent prisms is denoted d and the thickness of a single prism is $2c$. The stacking of rectangular prisms will, in the case of magnetic refrigeration considered as an application, be as depicted in Fig. 1. Considering a single prism, application of a field along the x - or y -direction will thus maximize the internal field due to the resulting minimized demagnetizing field.¹⁸ Application of the field along the z -direction will maximize the demagnetizing field and thus decrease the resulting internal field in a single rectangular prism. It follows qualitatively from Fig. 2 that application of the field along the x - or y -direction will tend to create an opposing magnetic field outside the individual prisms, thus lowering the field in neighboring prisms. In the case of magnetizing along the z -direction, the field external to the individual prism will tend to align with the

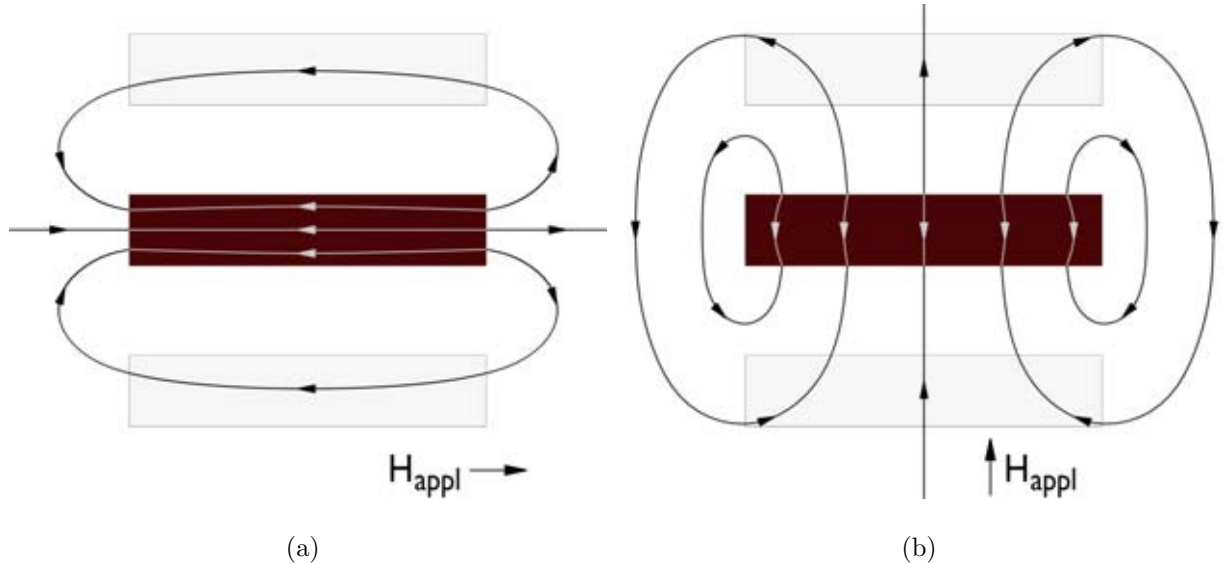


FIG. 2: Illustration of the magnetic field resulting from the magnetization of a single rectangular prism. In (a) the field is along the x -direction and thus parallel to the largest face of the plate. The resulting stray- or interaction field tends to oppose the applied field in the adjacent plates. In (b) the field is along the z -direction. The demagnetizing field inside the body is larger than in (a), however, the stray field tends to enhance the applied field in adjacent plates.

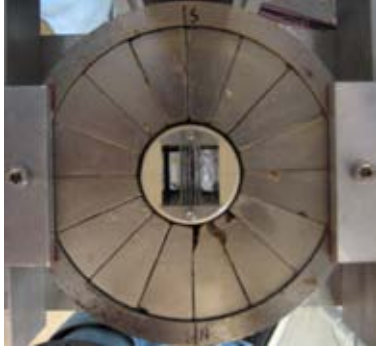
internal field of neighboring plates thus increasing their total internal magnetic field.

It may therefore be concluded that it is not a priori obvious which configuration is optimal. This must be expected to be dependent on the number of prisms in the stack, their relative dimensions and their spacing. It is thus of importance to investigate this in detail, which is the topic of the remainder of this paper.

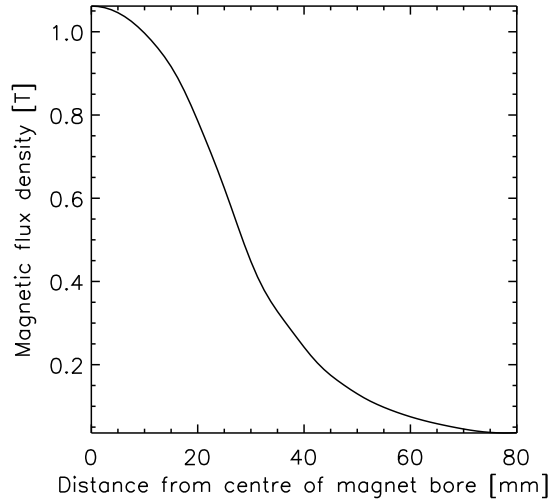
III. EXPERIMENTAL

A plastic housing is used to make the different stack configurations. 13 grooves of 1 mm have been machined with a spacing of 0.8 mm. In this way various combinations of the number of plates and their positioning may be used.

The stacks are situated in and controlled by a device built at Risø National Laboratory for Sustainable Energy, Technical University of Denmark.^{10,28,29} The magnetic field is generated by a cylindrical Halbach magnet assembly, see Fig. 3, which attains its maximum of 1.1 T in the center of the magnet; see Ref. 27 for details. When the stack has attained thermal equilibrium in the center of the magnetic field it is pulled out in around 0.7 s. The



(a)



(b)

FIG. 3: (a) Plates and plastic cylinder fixed in the center of the Halbach magnet. As evident from the picture some of the segments are damaged, resulting in a slightly asymmetric field. (b) the average magnetic flux density as a function of the distance from the centre of the bore of the Halbach magnet (from Ref. 27).

temperature is logged from 5 positions on one plate, see Fig. 4, with a TC-08 Thermocouple Data Logger from Pico Technology with a sampling rate of 10 Hz per thermocouple. It is estimated that the sampling interval and the displacement time are smaller than the time it takes the heat to dissipate significantly.¹⁹

The experiments are conducted at 295 K. This is close to the Curie temperature of gadolinium and thus to the temperature at which the cooling device is expected to function.

The gadolinium plates have the dimensions $40 \times 25 \times 0.9 \text{ mm}^3$. They are obtained from China Rare Metal Material Co. with a stated purity of 99.9%. Thermocouples have been mounted with a non-magnetic heat conducting paste in the center and in the middle of each side of the plates as illustrated in Fig. 4.

Each experiment is repeated five times and the average of the measurements is reported. The maximum observed standard deviation of the average values was 0.05 K. The adiabatic temperature change predicted by the model is found by considering the corresponding locations on the plate with thermocouples in the model.

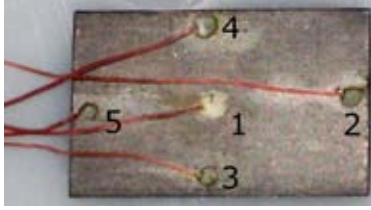


FIG. 4: Gadolinium plate with thermocouples mounted in the center and on the four edges.

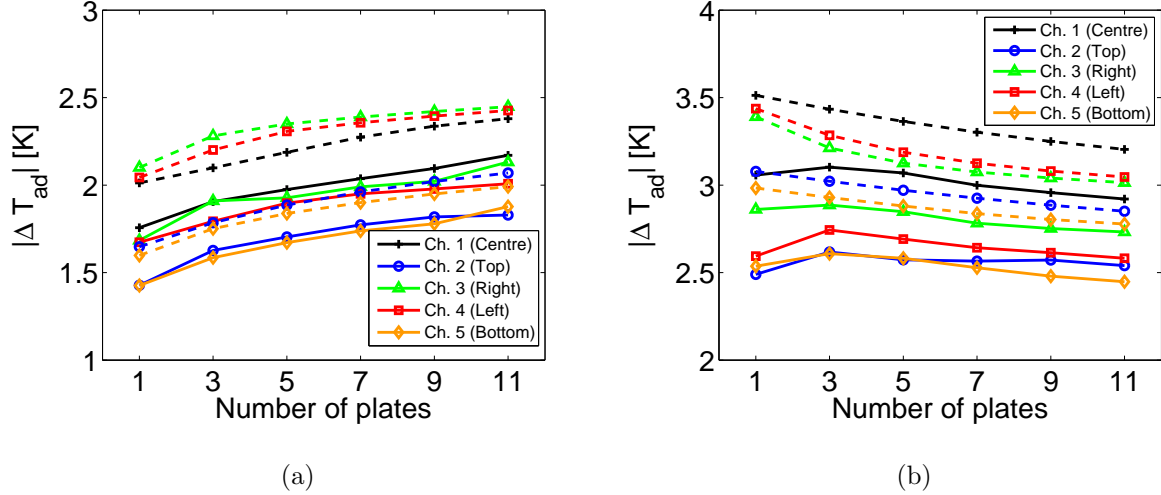


FIG. 5: The adiabatic temperature change of the centre gadolinium plate as a function of the number of plates in the stack. (a) the applied field is along the z -direction, i.e. orthogonal to the $40 \times 25 \text{ mm}^2$ face and thus along the direction of the stacking. (b) the applied field is along the x -direction, i.e. parallel to the $40 \times 25 \text{ mm}^2$ face. The dashed lines show the values predicted by the model.

IV. RESULTS AND DISCUSSION

The experimental results are divided into three groups. Firstly, the number of plates in a stack is varied and the effect on the centre plate is analyzed. Secondly, the number of plates is held constant and the position in the stack of the plate on which the measurements are taken is varied. Finally, the influence of the packing density investigated by keeping the height of the stack fixed, while the number of equally spaced plates and the distance between them are varied.

A. Variation of the number of plates

The adiabatic temperature change as a function of the number of plates is given in Fig. 5 for the centre plate equipped with thermocouples as depicted in Fig. 4. Considering Fig. 5(a), where the applied field is parallel with the z -direction, the trend is clear. As the number of plates increases the magnetocaloric effect also increases. This is clearly observed both experimentally and predicted by the model. Qualitatively it is also to be expected since adding plates to a stack of rectangular plates where the applied field is along the direction of the stacking tends to increase the resulting field in adjacent plates due to the magnetization of each individual plate (see Fig. 2).

The adiabatic temperature change is also seen to be non-uniform across the plate since the thermocouples consistently report different temperature changes, although with a maximum difference across the plate for a given setup of approximately 0.3 K. This is consistent with the fully spatially resolved adiabatic temperature change data obtained by demagnetizing a single plate of gadolinium recently reported in Ref. 19 under identical conditions. The reason for this behavior is a combination of the fact that the applied field is not constant along the 40 mm direction of the plate (see Fig. 3(b) for clarity) and that the demagnetizing field is not homogeneous even if the plate were uniformly magnetized.^{18,20}

Considering Fig. 5(b) it is observed that the trend of the magnetocaloric effect differs from that observed in Fig. 5(a). As the number of plates increases the resulting adiabatic temperature change tends to decrease. This is clear both from the model and the experimental data as well as it is expected from the more qualitative argument given in Sec. II. When the applied field is oriented orthogonally to the direction of the stacking, the field generated external to each individually magnetized plate will tend to oppose the internal field in adjacent plates thus lowering the resulting internal field. The greatest difference is observed at the right thermocouple where an adiabatic temperature change of approximately 3.4, K when a single plate is considered, is lowered to approximately 3 K when considering 11 plates, thus representing a relative difference of about 12 %.

In general, it should be noted that since the positions of the thermocouples (see Fig. 4) are not completely symmetric, both the model and the experiment are expected to deviate slightly. The top and bottom thermocouples are located almost identically on either side of the plate and should therefore, in principle, be exposed to the same change in applied

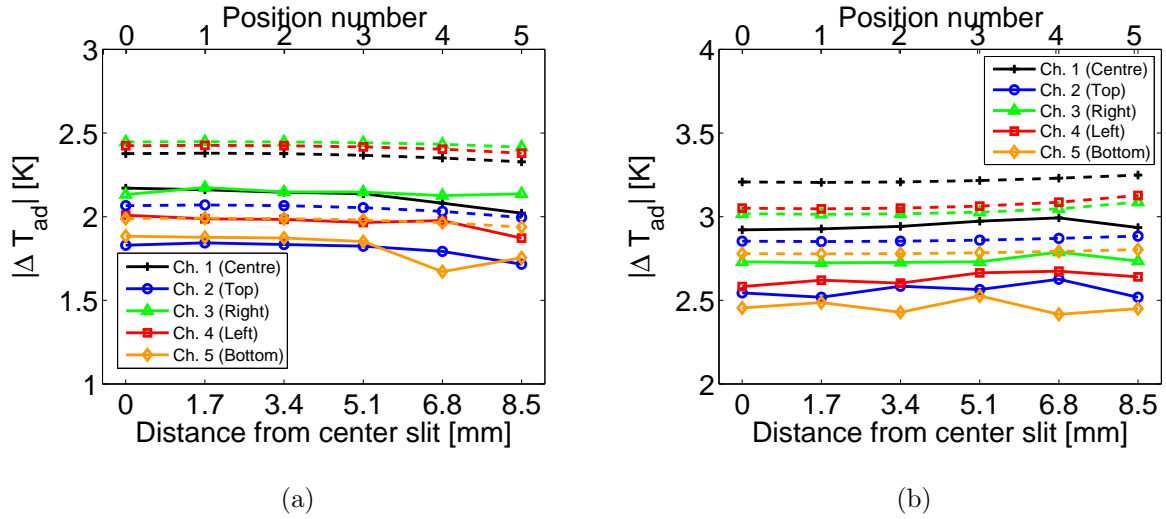


FIG. 6: The adiabatic temperature change when demagnetizing a stack of gadolinium plates as a function of position of a plate in a stack of 11 evenly spaced plates. (a) the applied field is along the z -direction, i.e. orthogonal to the $40 \times 25 \text{ mm}^2$ face. (b) the applied field is along the x -direction, i.e. parallel to the $40 \times 25 \text{ mm}^2$ face. The dashed lines show the corresponding values predicted by the model.

magnetic field. The same is valid for the left and right thermocouples. However, small inhomogeneities in the applied field and uncertainties in the positioning of the thermocouples result in slightly deviating results.

Depending on the number of plates in the stack and the orientation of the applied field the difference in adiabatic temperature change across the plate is observed experimentally to be ranging approximately from 0.3 to 0.8 K equivalent to relative differences of 20 to 33 %, respectively. This is a substantial variation that is supported by the data reported in Ref. 19.

B. Variation of the position in the stack

The adiabatic temperature change as a function of position in a stack of 11 identical plates is given in Fig. 6. The trends from both the model and experiment are the same. Considering the centre position going outwards until the second to last position the adiabatic temperature change is virtually constant in both cases and for both orientations of the applied field. At the outer position the magnetocaloric effect decreases slightly in the case where the field is

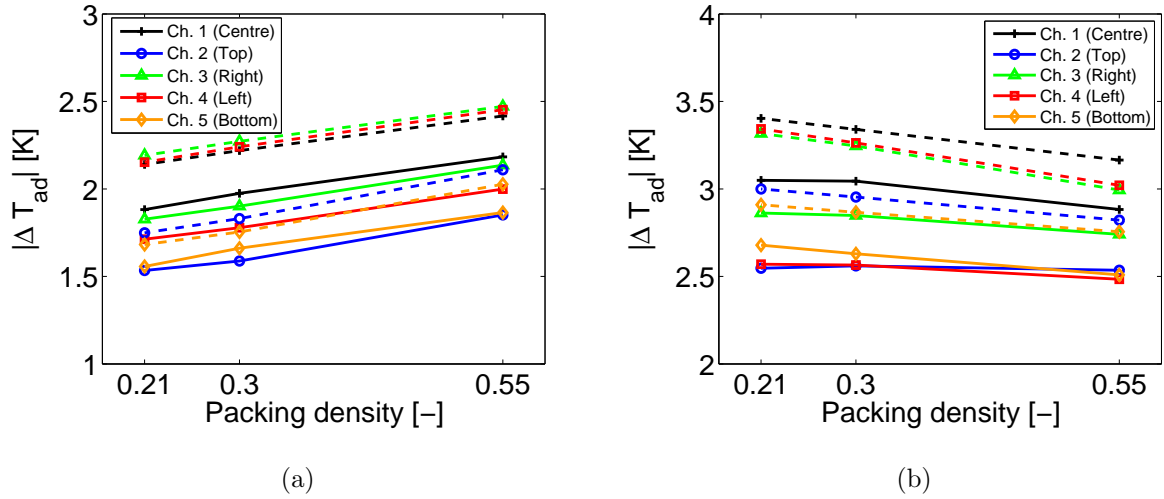


FIG. 7: The adiabatic temperature change when demagnetizing a stack of gadolinium plates as a function of the packing density. The height of the stack is constant (equal to 21.3 mm). For a spacing of 0.8 mm the total number of plates is 13, for a spacing of 2.5 mm it is 7 and finally for a spacing of 4.2 mm the number of plates is 5. (a) the applied field is along the z -direction. (b) the applied field is along the x -direction. The dashed lines show the values predicted by the model.

applied along the z -direction, i.e. along the direction of the stacking. The tendency is a slight increase when the field is along the x -direction, i.e. parallel to the $40 \times 25 \text{ mm}^2$ face. The changes are subtle and it is questionable whether the experimental data sufficiently support the trend. The model predicts a difference in the adiabatic temperature change of no more than 0.1 K in the most pronounced case.

Qualitatively, the predicted trend of the model is easily explained. In the case when the field is along the z -direction, the demagnetizing field is generally largest and on the outer plate the interaction with neighboring plates is minimized. Thus, the internal magnetic field is also minimized and the magnetocaloric effect is decreased. The opposite is the case when the applied field is along the x -direction. Here, the demagnetizing field is minimal on the outer plate, since the interaction from neighboring plates is small, and the magnetocaloric effect tends to increase.

Number of plates	5	7	13
Spacing between plates [mm]	4.2	2.5	0.8
Porosity [-]	0.79	0.70	0.45
Packing density [-]	0.21	0.30	0.55

TABLE I: Summary of the stack configurations used in order to probe the effect of packing density on the resulting magnetic field.

C. Influence of the packing density of the stack

In order to probe the effect of varying spacing between adjacent plates in the stack, a stack with a fixed height of 21.3 mm is considered. One plate is fixed at the centre slit and the remaining plates are distributed in three different modes with 5, 7 and 13 plates, respectively. These modes correspond to spacings between the plates of 4.2, 2.5 and 0.8 mm, respectively. Table I gives a summary of the configurations.

When the applied field is oriented along the z -direction the magnetocaloric effect decreases as the spacing between adjacent plates increases whereas the opposite is true when the applied field is along the x -direction. This is predicted both by the model and clearly observed experimentally; see Fig. 7. Furthermore, the adiabatic temperature change seems to decrease/increase more rapidly between packing densities of 0.55 and 0.3 than it does from 0.3 to 0.21, when the field is applied along the z - and x -direction, respectively. This is an effect that is clearly observed from both the model and the experimental data.

Considering the applied field along the z -direction and the spacing between adjacent plates to increase, the adiabatic temperature change and thus internal field decrease. Increasing the spacing between adjacent plates the stray field from adjacent plates will decrease. The situation may then be considered to approximate the single plate case and when the field is along the z -direction, this case yields the largest demagnetizing field with a smaller internal field as a result. The same explanation is valid for the case where the applied field is along the x -direction, however, here the effect is reversed since the single plate case here results in a larger internal magnetic field.¹⁸

D. Remarks on the experimental data

All of the data points in Figs. 5–7 have small error bars, when these are considered as the standard deviation of the five measured values, i.e. the experiments are highly reproducible. The absolute experimental error has not been estimated. However, a few of the values differ from the overall trend. It was determined from model predictions that a deviation of 2 K in the surrounding temperature should result in a change in ΔT_{ad} of less than 0.1 K. A change of the same order of magnitude is predicted if the stack is misaligned a few degrees with respect to the orientation of the applied field.

Moreover, deviations can be caused by inhomogeneity in the applied field. As seen in Fig. 3 some of the magnetic blocks are damaged in the corners, causing small local perturbations of the field.

The experimental results have been compared to the model predictions in Figs. 5-7. An obvious correspondence between the behavior of the measured and the modeled data may be concluded. However, the adiabatic temperature change tends to be around 0.2 K smaller in the experiment than the model predicts. The consistency of this trend suggests that the thermal mass of the paste that fixes the thermocouples on the plates (Fig. 4) acts to reduce the adiabatic temperature change. This is further supported by comparing with the results in Ref. 19 where the adiabatic temperature change of a single plate of gadolinium is measured using thermography under identical conditions is found to be slightly higher than the experimental data presented here.

V. CONCLUSIONS

A significant change in the magnetocaloric effect expressed as the adiabatic temperature change when altering the magnetic field of a magnetocaloric material may be obtained depending on the overall geometry of the structure considered. In this study various stacks of identical plates of gadolinium were probed with attached thermocouples while the applied magnetic field was changed consistently. In the case of a single plate and applying the field along the largest face of the plate yields the largest internal magnetic field and thus the largest magnetocaloric effect. When the applied field is orthogonal to the largest face the internal field is minimized.

In this paper it was shown that when stacking identical plates the internal field is enhanced if the applied field is along the stacking direction, whereas stacking in a direction perpendicular to the applied field results in a decrease in the internal field. This was investigated using an experimental technique where the surface temperature change of gadolinium plates was measured and modeled through an established fully 3-dimensional magnetostatic numerical model.

Acknowledgements

The authors thank the support of the Programme Commission on Energy and Environment (EnMi) (Contract no. 2104-06-0032) which is part of the Danish Council for Strategic Research. The technical assistance from Mr. Jørgen Geyti, Risø DTU, is gratefully appreciated as are the input and suggestions from Dr. Cathrine Frandsen, DTU Physics.

-
- ¹ W. F. Giauque and D. P. MacDougall. Attainment of Temperatures Below 1 K Absolute by Demagnetization of $\text{Gd}_2(\text{SO}_4)_3 \cdot 8\text{H}_2\text{O}$. *Physical Review*, 43:768, 1933.
 - ² G. V. Brown. Magnetic heat pumping near room temperature. *Journal of Applied Physics*, 47(8):3673–3680, 1976.
 - ³ J. A. Barclay. Theory of an active magnetic regenerative refrigerator. *NASA Conference Publication*, pages 375–387, 1983.
 - ⁴ K.A. Gschneidner and V.K. Pecharsky. Thirty years of near room temperature magnetic cooling: Where we are today and future prospects. *International Journal of Refrigeration*, 31:945–961, 2008.
 - ⁵ K. L. Engelbrecht, G. F. Nellis, S. A. Klein, and C. H. Zimm. Review article: Recent developments in room temperature active magnetic regenerative refrigeration. *HVAC and R Research*, 13(4):525, 2007.
 - ⁶ B. Yu, M. Liu, P. W. Egolf., and A. Kitanovski. A review of magnetic refrigerator and heat pump prototypes built before the year 2010. *International Journal of Refrigeration*, 33(6):1029–1060, 2010.
 - ⁷ K. K. Nielsen, J. Tusek, K. Engelbrecht, S. Schopfer, A. Smith, C. R. H. Bahl, A. Kitanovski,

- N. Pryds, and A. Poredos. Review on numerical modeling of active magnetic regenerators. *International Journal of Refrigeration*, Accepted, 2010.
- ⁸ C. Zimm, A. Boeder, J. Chell, A. Sternberg, A. Fujita, S. Fujieda, and K. Fukamichi. Design and performance of a permanent-magnet rotary refrigerator. *International Journal of Refrigeration*, 29(8):1302–1306, 2006.
- ⁹ A. Tura and A. Rowe. Progress in the characterization and optimization of a permanent magnet magnetic refrigerator. In P. W. Egolf, editor, *Third International Conference on Magnetic Refrigeration at Room Temperature*, pages 387–392. International Institute of Refrigeration, 2009.
- ¹⁰ C. R. H. Bahl, T. F. Petersen, N. Pryds, and A. Smith. A versatile magnetic refrigeration test device. *Review of Scientific Instruments*, 79(9):093906, 2008.
- ¹¹ P. A. Oliveira, P.V. Trevizoli, J. R. Barbosa Jr., and A. T. Prata. Numerical analysis of a reciprocating active magnetic regenerator - part I. In P. W. Egolf, editor, *Third International Conference on Magnetic Refrigeration at Room Temperature*, pages 283–288. International Institute of Refrigeration, 2009.
- ¹² K. Engelbrecht, G. F. Nellis, and S. A. Klein. Comparing modeling predictions to experimental data for active magnetic regenerative refrigeration systems. In P. W. Egolf, editor, *Second International Conference on Magnetic Refrigeration at Room Temperature*, pages 349–357. International Institute of Refrigeration, 2007.
- ¹³ A. Sarlah and A. Poredos. Dimensionless numerical model for simulation of active magnetic regenerator refrigerator. *International Journal of Refrigeration*, 33 (6):1061–1067, 2010.
- ¹⁴ T. F. Petersen, N. Pryds, A. Smith, J. Hattel, H. Schmidt, and H.J.H Knudsen. Two-dimensional mathematical model of a reciprocating room-temperature active magnetic regenerator. *International Journal of Refrigeration*, 31:432–443, 2008.
- ¹⁵ K. K. Nielsen, C. R. H. Bahl, A. Smith, R. Bjørk, N. Pryds, and J. Hattel. Detailed numerical modeling of a linear parallel-plate active magnetic regenerator. *International Journal of Refrigeration*, 32(6):1478–1486, 2009.
- ¹⁶ K. K. Nielsen, C. R. H. Bahl, A. Smith, N. Pryds, and J. Hattel. A comprehensive parameter study of an active magnetic regenerator using a 2d numerical model. *International Journal of Refrigeration*, 33(4):753–764, 2010.
- ¹⁷ R. Bjørk and K. Engelbrecht. The influence of the magnetic field on the performance of an

- active magnetic regenerator (AMR). *International Journal of Refrigeration*, 34:192–203, 2011.
- ¹⁸ A. Smith, K. K. Nielsen, D. V. Christensen, C. R. H. Bahl, R. Bjørk, and J. Hattel. The demagnetizing field of a nonuniform rectangular prism. *Journal of Applied Physics*, 107(10):103910, 2010.
- ¹⁹ D. V. Christensen, R. Bjørk, K. K. Nielsen, C. R. H. Bahl, A. Smith, and S. Clausen. Spatially resolved measurements of the magnetocaloric effect and the local magnetic field using thermography. *Journal of Applied Physics*, 108(6):063913, 2010.
- ²⁰ J.A. Brug and W.P. Wolf. Demagnetizing fields in magnetic measurements i. thin discs. *Journal of Applied Physics*, 57(10):4685–4694, 1985.
- ²¹ O. Peksoy and A. Rowe. Demagnetizing effects in active magnetic regenerators. *Journal of Magnetism and Magnetic Materials*, 288:424–432, 2005.
- ²² A.M. Rowe and J.A. Barclay. Ideal magnetocaloric effect for active magnetic regenerators. *Journal of Applied Physics*, 93(3):1672–1676, 2003.
- ²³ J.A. Osborn. Demagnetizing factors of the general ellipsoid. *Physical Review*, 67:351–357, 1945.
- ²⁴ R.I. Joseph and E. Schloemann. Demagnetizing field in nonellipsoidal bodies. *Journal of Applied Physics*, 36(5):1579–1593, 1965.
- ²⁵ A. Aharoni. Demagnetizing factors for rectangular ferromagnetic prisms. *Journal of Applied Physics*, 83(6):3432–3434, 1998.
- ²⁶ R. Bjørk, C.R.H. Bahl, and M. Katter. Magnetocaloric properties of $\text{LaFe}_{13-x-y}\text{Co}_x\text{Si}_y$ and commercial grade Gd. *Journal of Magnetism and Magnetic Materials*, 322(24):3882–3888, 2010.
- ²⁷ K. K. Nielsen, R. Bjørk, J. B. Jensen, C. R. H Bahl, N. Pryds, A. Smith, A. Nordentoft, and J. Hattel. Magnetic Cooling at Risø DTU. In S. Hansen and J. Paul, editors, *8th IIR Gustav Lorentzen Conference on Natural Working Fluids*. International Institute of Refrigeration, 2008.
- ²⁸ K. Engelbrecht, J.B. Jensen, C.R.H. Bahl, and N. Pryds. Experiments on a modular magnetic refrigeration device. In P.W. Egolf, editor, *3rd International Conference on Magnetic Refrigeration at Room Temperature*, pages 431–436. International Institute of Refrigeration, 2009.
- ²⁹ K. Engelbrecht, C. R. H. Bahl, K. K. Nielsen, and N. Pryds. Experimental results for a magnetic refrigerator using three different types of magnetocaloric material regenerators. *International Journal of Refrigeration*, Accepted, 2010.

A.3 Papers published in conference proceedings

- A.3.1 Magnetic cooling at Risø DTU; published in the proceedings of the 7th Gustav Lorentzen Conference

Magnetic cooling at Risø DTU

K.K. Nielsen^(a,b), R. Bjørk^(b), J.B. Jensen^(b), C.R.H Bahl^(b), N. Pryds^(b), A. Smith^(b), A. Nordentoft^(b), J. Hattel^(a)

^(a) Technical University of Denmark, Department for Mechanical Engineering, Produktionstorvet, building 425 room 024, 2800 Kgs. Lyngby, Denmark, kaspar.kirstein.nielsen@risoe.dk

^(b) Department for Fuel Cells and Solid State Chemistry, Risø National Laboratory for Sustainable Energy, Technical University of Denmark - DTU, building 232, Frederiksborgvej 399, 4000 Roskilde

ABSTRACT

Magnetic refrigeration at room temperature is of great interest due to a long-term goal of making refrigeration more energy-efficient, less noisy and free of any environmentally hostile materials.

A refrigerator utilizing an active magnetic regenerator (AMR) is based on the magnetocaloric effect, which manifests itself as a temperature change in magnetic materials when subjected to a varying magnetic field.

In this work we present the current state of magnetic refrigeration research at Risø DTU with emphasis on the numerical modeling of an existing AMR test machine. A 2D numerical heat-transfer and fluid-flow model that represents the experimental setup is presented. Experimental data of both no-heat load and heat load situations are compared to the model. Moreover, results from the numerical modeling of the permanent magnet design used in the system are presented.

1. INTRODUCTION

The magnetocaloric effect (MCE) was discovered by E. Warburg in 1881. Warburg found that iron got heated up when placed in a magnetic field and when the magnetic field was removed the iron sample cooled down (Warburg 1881). The basic principle of the MCE is that the ordering of the magnetic moments is increased when an external magnetic field is applied to a magnetic material. This means that the spin-entropy decreases. The process is virtually adiabatic if the field is applied rapidly. This means that the total entropy of the system must remain constant and thus the lattice and electron entropies must increase, which is equivalent to an increase in temperature. The process is reversible (for some materials) and thus the opposite will take place when the field is removed again (i.e. the ordering of the magnetic moments decrease and the temperature thus decreases). The MCE is strongest at the phase-transition between the ferromagnetic and the paramagnetic phases. This phase transition takes place at the Curie temperature T_C , which can vary significantly depending on the material. In the past materials have been used mainly for cryogenic applications, but some 30 years ago research into the MCE at room temperature was commenced (Brown 1976).

The MCE yields, for the benchmark magnetocaloric material (MCM) gadolinium (Gd), an adiabatic temperature change of about 3.6 K at room temperature for a 1 tesla (T) magnetic flux density. This rather low temperature change is obviously too small for direct usage in a cooling device. However, if the material is used in an AMR it is possible to achieve, due to regeneration, a higher temperature difference (Brown 1976). In his experiments Brown reached a temperature span of 46 K using Gd with the hot end at 319 K using a 7 T magnetic flux density from a super conducting magnet. The MCE of Gd is proportional to the magnetic flux density to the power of 0.7 (Pecharsky and Gschneidner 2006). Today's state-of-the-art permanent magnets yield a magnetic flux density of about 1.5 T (Tura and Rowe 2007). Therefore it is crucial to develop a high-performing and efficient AMR.

This work is primarily concerned with developing a model describing an existing AMR test machine based on parallel plates, and using a permanent magnet based on the Halbach design yielding around 1.1 T (Halbach 1980). In Section 2 the experimental test machine is described. In Section 3 the corresponding numerical model is presented. In Section 4 results from the test machine and the model are compared both including no-load and load-situations. In Section 5 the results are discussed and the work is concluded with some future aspects briefly discussed.

2. EXPERIMENTAL SETUP

Figure 1 shows photos of the test machine, which consists of a regenerator core in the middle of a plastic tube with outer diameter 40 mm and inner diameter 34 mm. The regenerator core is built up of 13 plates of 99.9 % pure Gd (obtained from China Rare Metal Materials Co). The plates with dimensions 40x0.9x25 mm have a total mass of 92 g. At both ends of the Gd plates (in the flow direction) 20 mm long plastic flow guides are placed to ensure a fully developed laminar flow across the plates. The plates and flow guides are fixed by precision machined grooves and are stacked with a spacing of 0.8 mm, which is then the height of the fluid channel.

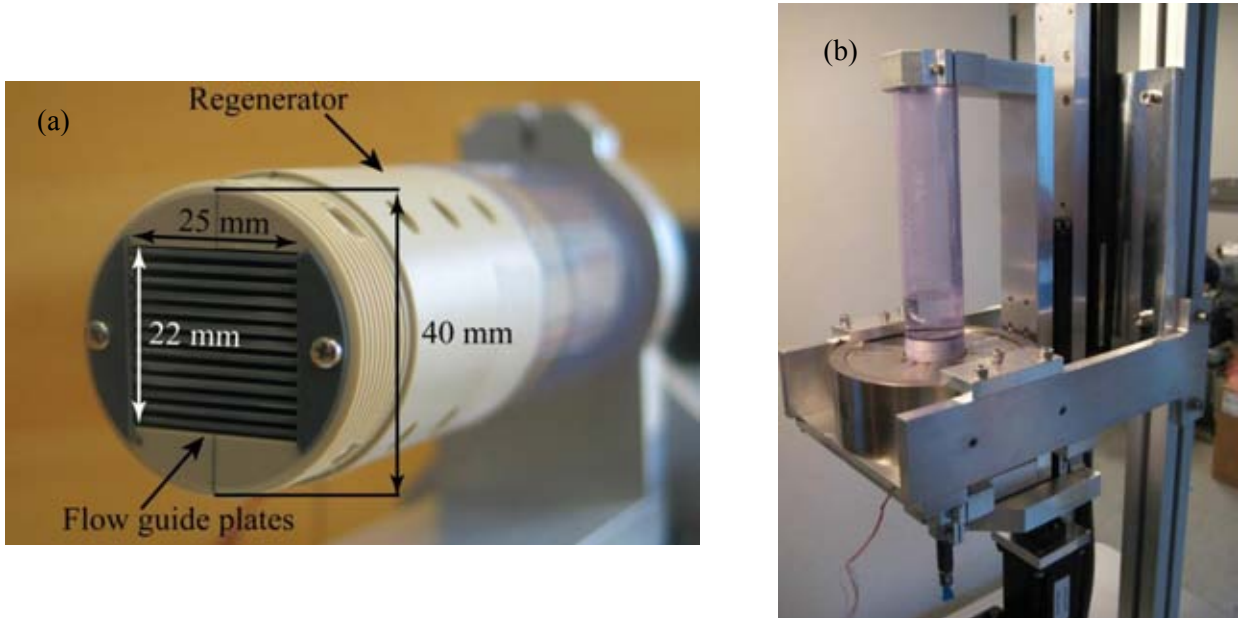


Figure 1: Figure (a) shows a close-up of the experimental AMR test machine where the 13 parallel channels can be seen as well as the plastic tube. Figure (b) is a picture of the machine in its operational environment. The permanent Halbach magnet can be seen with the plastic tube including the regenerator core penetrating it.

The heat transfer fluid is moved by a piston. The regenerator block and its parent plastic tube are suspended vertically in a mounting as shown in Figure 1b and can be moved in and out of the field of the permanent Halbach magnet using stepper motors. This magnet has a maximum magnetic flux density of 1.1 T.

One of the most important results of the experiment – as well as in the model – is to be able to measure the temperature gradient across the regenerator core. This is done via five type E thermo-couples placed equidistantly in the center flow channel as sketched in Figure 2a.

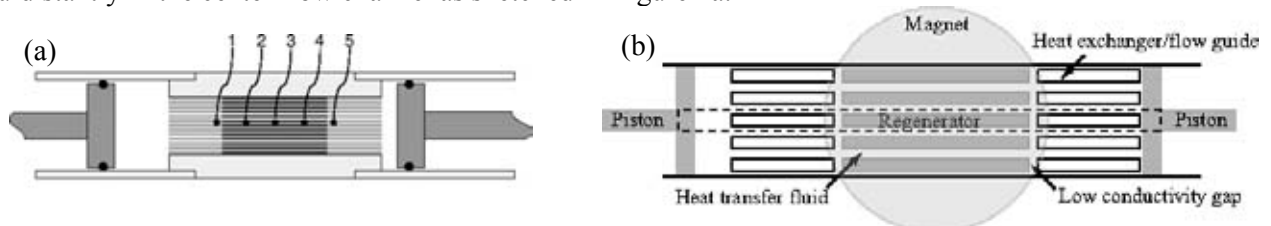


Figure 2: Drawing (a) is a schematic of the regenerator pictured in Figure 1a. The locations of the five thermo-couples are indicated with their appropriate numbers. Thermo-couples 1 and 5 are placed at the cold and hot ends respectively. Figure (b) shows how the numerical model represents the full geometry of the AMR. The model breaks the geometry down into a single replicating cell consisting of one half of a complete flow channel (indicated with a dashed line in the figure and magnified in Figure 3).

The system evolves transiently through a number of AMR cycles until cyclic steady-state has been reached. Each cycle consists of four different steps, which have four different characteristic times τ_1 , τ_2 , τ_3 and τ_4 . The cycle is symmetric meaning that $\tau_1 = \tau_3$ and $\tau_2 = \tau_4$. In the first step the magnetic field is applied thus increasing the temperature of the MCM and at this stage the fluid is stationary. In the second step, the pistons move the fluid for τ_2 seconds towards the hot end of the regenerator to reject heat. At the third step the magnetic field is switched off and thus the temperature in the MCM decreases and again at this stage the fluid is stationary. Finally, the piston pushes the fluid towards the cold end for τ_4 seconds. The total cycle-time is $\tau_{total} = 2(\tau_1 + \tau_2)$. In this way the MCM is used as the active material in a regenerator and a

temperature gradient is built up. The magnitude of this gradient depends mainly on the geometry, material and operational properties, i.e. the piston stroke length, τ_1 and τ_2 , the height of the fluid channel, the MCM, and how strong the magnetic field is. It is therefore quite a challenge to predict the behavior of a certain system for different process parameters.



Figure 3: A close-up of the line of symmetry from the replicating cell marked with a dashed line in Figure 2b.

The geometrical simplicity of such an experimental setup makes it ideal for studies of parallel plate regenerators, facilitating direct comparison to the numerical model. Validating the model against the experiment is crucial since a high-quality model can predict the performance of configurations otherwise not thought of and span a much larger parameter-space than possible with the experiment.

3. NUMERICAL MODELING

3.1 Thermal model of the regenerator

The numerical model is “2.5-dimensional” as illustrated geometrically in Figure 4 and Figure 5. For technical reasons the heat transfer fluid is chosen to be stationary and the solid domains are moved relative to this. Thus, the piston movement is modeled as a coordinate transformation of the solid domains with a suitable convective term in the thermal equation for the fluid. The spatial discretization is the classical 2nd order finite difference scheme with an equidistant grid where $\Delta x = 1$ mm and $\Delta y = 0.05$ mm, and the temporal integration is done using an Alternate Direction Implicit (ADI) solver with a timestep chosen to be 0.001 second. Since the system includes moving boundaries it is extremely important to make sure that there is energy conservation. Therefore the finite difference (FD) formulation is preferred and validation-tests show that the energy-conservation is virtually the precision of the computer. The computational time on a 2.0 GHz Intel Core 2 Duo CPU is roughly 0.7 CPU-seconds pr physical second in the model.

Due to symmetry considerations only half a replicating cell is modeled (as indicated in Figure 3). This is a good assumption at least for the central channels and plates (which have virtually no loss through the top and bottom of the regenerator).

Figure 4a and Figure 5 show a schematic of the boundary conditions of the model in the (x,y)-plane and (x,z)-plane respectively. The various thermal resistances are labeled with their respective names.

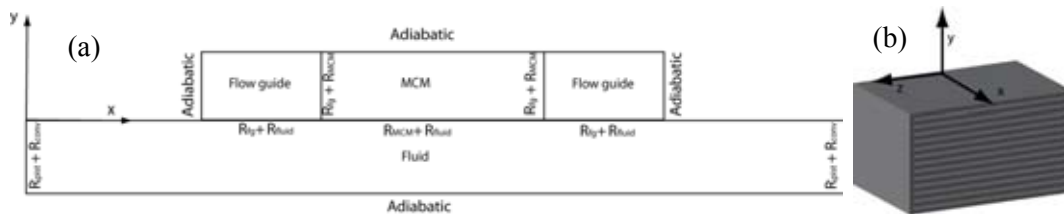


Figure 4 : Figure (a) shows a schematic of the modeled domain in the (x,y)-plane, i.e. half a replicating cell with the boundaries being either adiabatic (symmetry boundaries) or coupled via thermal resistances to the ambient. The x-direction is the direction of the flow and the y-direction is orthogonal to the plates (labeled MCM). The left end is defined as the cold end and the right end as the hot end. Figure (b) shows a 3D sketch of the regenerator block with the coordinate system visualized.

The governing equations for the thermal system are

$$\frac{\partial T_{fl}}{\partial t} = \frac{k_{fl}}{\rho_{fl} c_{p,fl}} \nabla^2 T_{fl} - (\mathbf{u} \cdot \nabla) T_{fl} \quad (1)$$

$$\frac{\partial T_s}{\partial t} = \frac{k_s}{\rho_s c_{p,s}} \nabla^2 T_s \quad (2)$$

where the temperatures of the fluid and solid domains are denoted by T_{fl} and T_s respectively. For simplicity all the solid domains are labeled with an s, although they have different physical properties. The thermal properties, i.e. the thermal conductivities k_{fl} and k_s , the mass densities ρ_{fl} and ρ_s and the heat capacities $c_{p,fl}$ and $c_{p,s}$ are all assumed constant except the heat capacity of Gd, which varies as function of both temperature and magnetic field (see Figure 6). The material properties used are given in Table 1.

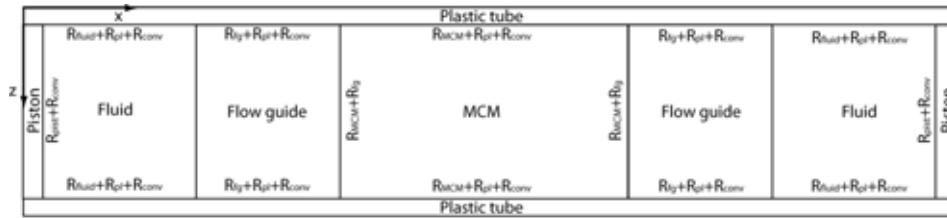


Figure 5 : The model in the (x, z) -plane. The z -direction is only resolved by one grid cell meaning that the model is effectively 2.5-dimensional with the x - and y -dimensions being the two regular dimensions and the finite extension of the z -direction as the half dimension (and most importantly including losses via boundary conditions).

The velocity field in the fluid is denoted by $\mathbf{u} = (u, v)$ and is prescribed by the analytical expression for a parallel-plate laminar flow with piston velocity u_p , see e.g. (T. F. Petersen 2007):

$$u = \frac{H_{fl}^2}{2\mu} \frac{\partial p}{\partial x} \left(1 - \frac{y^2}{H_{fl}^2} \right) + u_p \quad (3)$$

$$v = 0 \quad (4)$$

$$\frac{\partial p}{\partial x} = \frac{96}{Re} \rho_{fl} \frac{1}{4H_{fl}} \frac{u_p^2}{2} \quad (5)$$

The Reynolds' number $Re = u_p 4H_{fl} \rho_{fl} / \mu$, ρ_{fl} is the mass density of the fluid, H_{fl} is half the height of the fluid channel, μ is the viscosity of the fluid and y is the vertical coordinate, i.e. orthogonal to the flow direction.

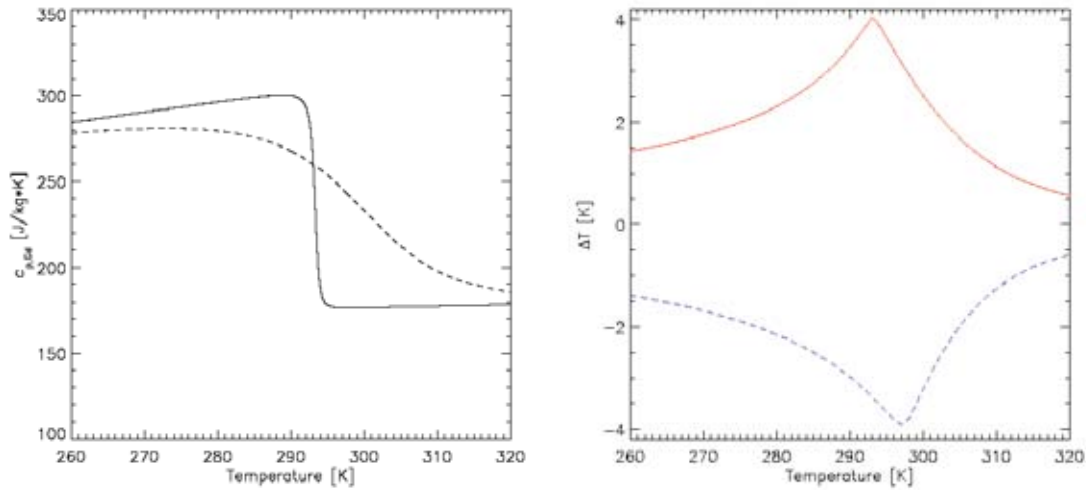


Figure 6 : Left: c_p for Gd as function of temperature in zero field (solid line) and in a 1 T field (dashed line). The change around 293 K is rather significant and is actually the definition of the Curie temperature. Right: The adiabatic temperature change of Gd around room-temperature in a 1 T field. The red/solid line is the temperature increase when the field is applied and the blue/dashed line is the corresponding curve for when the field is removed. The data are calculated from the mean field model of Gd compiled in e.g. (Petersen, et al. 2008).

The internal boundaries between the fluid domain and the solid domains are implemented through thermal resistances in Fourier's law of thermal conduction:

$$q_{bd} = - \frac{T_1 - T_2}{R_1 + R_2}. \quad (6)$$

Here the flux across the boundary between two domains (e.g. fluid and MCM) is denoted by q_{bd} , the temperature of the boundary cells in the two adjacent domains are T_1 and T_2 and their corresponding thermal resistances are R_1 and R_2 respectively. The thermal resistance is simply given by the distance from the grid cell's centre to the boundary face divided by the thermal conductivity of the material multiplied by the area of the face boundary.

Table 1 : Material properties used in the model obtained from (Petersen, et al. 2008) and (Holman 1987).

Material	k [W/m · K]	ρ [kg/m ³]	c_p [J/kg · K]	μ [kg/m · s]
Water/ethanol mixture	0.52	981	4330	$8.91 \cdot 10^{-4}$
Plastic	0.2	1200	840	n/a
Gd	10.5	7900	170-300	n/a

The outer boundaries are either adiabatic, if they are symmetry boundaries, or they simulate heat loss in the z-direction, which is not directly resolved (hence this is what we call a 2.5-dimensional model). These losses are calculated via thermal resistances and they contain the thicknesses and thermal conductivities of the particular domain (fluid or solid) and the insulating material surrounding the entire system. On the outer part of the insulating material there is assumed to be natural convection modeled via the parameter h_{conv} , which has a value in the range 5 – 20 W/Km² and corresponds to free convection of air on a plate (Holman 1987).

3.2 The permanent magnet

The magnetic field that generates the MCE can be produced by an electromagnet or a permanent magnet assembly. For this machine we have chosen the latter as this requires no external power source to produce a strong magnetic field. The requirement of the permanent magnet assembly is that it must produce a strong homogenous magnetic field in a confined region of space and a very weak field elsewhere. The design known as a Halbach cylinder (Mallinson 1973), (Halbach 1980) fulfills these requirements and has therefore been chosen for the test machine. An ideal Halbach cylinder consists of a permanent magnetic material with a bore along the cylinder symmetry axis. The magnetic material is magnetized such that the direction of magnetization varies as shown in Figure 7. This produces a strong homogeneous field in the cylinder bore. In the case of an infinitely long cylinder the flux density in the bore is given by $B = B_r \ln\left(\frac{r_{ex}}{r_{in}}\right)$. An ideal Halbach cylinder is not physically realizable, as it is both necessary to make the Halbach cylinder of a finite length and to

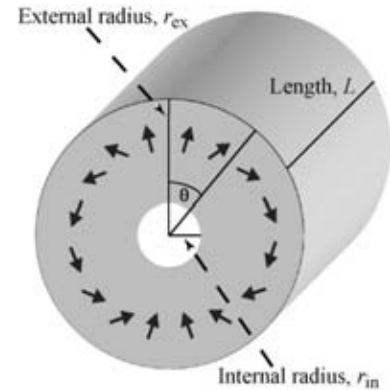


Figure 7: A drawing of a Halbach cylinder showing the internal radius, r_{in} , external radius, r_{ex} , and length, L . Also shown are arrows in the direction of the remanent magnetization of the magnetic material. This varies as 2θ . The figure is from (Björk, et al. 2008)

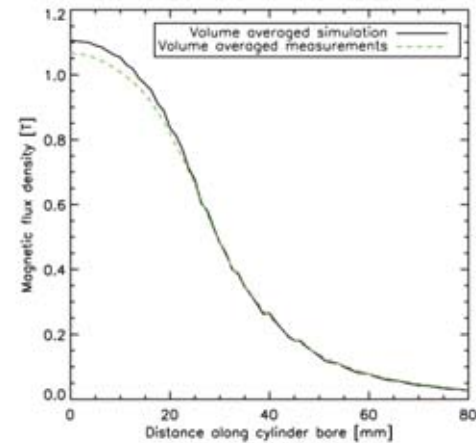


Figure 8: Flux density for the simulated and the physical Halbach cylinder for the test machine. There is good agreement between data.

numerical simulation and the experimental measurements agree, and show that a high flux density is produced in the center of the cylinder bore.

divide the continuously magnetized cylinder into parts consisting of permanent magnets each with their own directions of magnetization. Based on the design of the regenerator the Halbach cylinder for the test machine consists of 16 blocks of permanent magnets and with dimensions $r_{in} = 2.1$ cm, $r_{ex} = 6$ cm, and $L = 5$ cm.

To investigate the magnetic field produced by this Halbach cylinder we have performed numerical simulations using the commercially available finite element multiphysics program, *Comsol Multiphysics* (Comsol 2005), see also (Björk, et al. 2008) for details.

As well as modeling the magnet assembly we have also performed measurements of the flux density of the physical magnet assembly, seen in Figure 1. In Figure 8 the average flux density of the magnetic field as a function of distance from the center of the Halbach cylinder for both simulation and measurement is shown. As can be seen from the figure the

4. RESULTS

The experimental and modeling results are divided in two parts. First a sensitivity analysis of how far the regenerator is taken out of the Halbach's magnetic field is addressed under no-load conditions. Secondly a load-situation is investigated.

4.1 Sensitivity to the magnetic field

Since the magnetic field of the Halbach magnet strays outside of the central bore in the cylinder (see Figure 8), the distance which the regenerator block is moved away from the centre of the Halbach must have some influence on the performance of the regenerator. The experiments were adjusted to move the regenerator out of the magnetic field with a distance varying from 30 mm to 150 mm (see Figure 9). The operating conditions were the same for each experiment, which was allowed to reach steady-state in each case (see Table 2). The model was set with the same parameters and the varying magnetic field was implemented via a volumetric source term in the heat equation for the MCM:

$$\frac{dQ_{MCM}}{dt} = -\rho_{Gd} T_{Gd} \frac{\partial \sigma}{\partial T} \frac{dB}{dt}. \quad (7)$$

This is obtained from the mean field theory of Gd, see e.g. (Petersen, et al. 2008). The change with respect to temperature of the magnetization is denoted by $\partial \sigma / \partial T$ and the magnetic flux density is denoted by B . The magnetic field only varies in the x-direction in the regenerator. The crucial term in this formulation is the time variation of the magnetic field. This is implemented simply using the finite extent of the regenerator block and the velocity of which the regenerator is moved in and out of field.

As seen in Figure 9 there is one series of experimental data and two model series. The data sets show the no-load steady-state temperature span between thermo-couples one and five as function of how far the regenerator is taken out of the magnetic field. It is seen from the experimental data that at distances above 70 mm the temperature span does not increase anymore; hence, the full yield of the magnet is utilized.

The model simulations were done for two cases: One with no loss to the surroundings, i.e. perfect thermal insulation, and one with realistic losses via the boundary conditions described in Section 3.1. The tendencies of all three data sets are virtually the same, which clearly shows that the numerical model catches many of the aspects of the magnetic regeneration. It is not surprising that the ideal adiabatic model overestimates the temperature span somewhat as significant losses to the ambient are expected in the test device. When the losses are included, however, the model comes much closer at the experimental values still showing the exact same tendency.

Table 2 : The operational properties of the two experiment series.

Experiment	Effective piston stroke length (% of plate length)	τ_1 (s)	τ_2 (s)
Magnetic field variation	40 %	3.0	2.9
Heat load experiment	53 %	1.5	2.9

4.2 Load experiment

The piston at the cold end has been equipped with a copper plate connected to a power supply which makes it possible to apply a heat load through ohmic dissipation to the water. An experiment was run with the

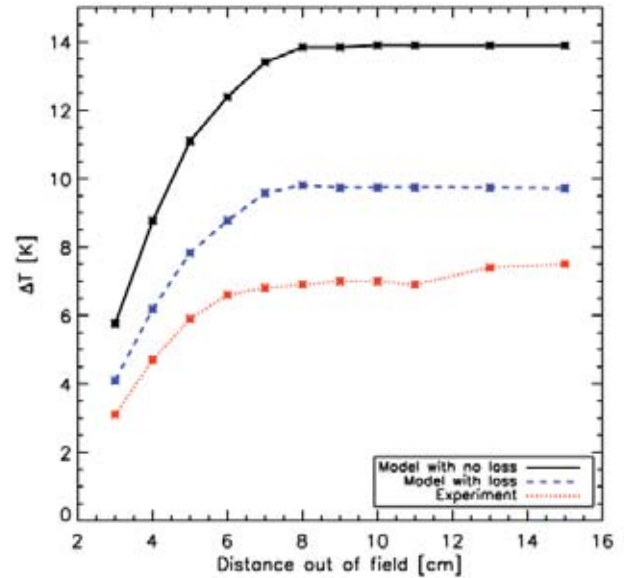


Figure 9: The figure shows how the steady-state and no-load temperature span behaves when the regenerator is not taken completely out of the magnetic field (the red/dotted line). Each asterisk in the graph represents a data point. Also included are the results of two slightly different numerical simulations; one without losses (the black/solid line) and one with ideal losses (blue/dashed line). The tendencies are clearly the same on all three graphs. The absolute values of the temperature spans differ somewhat, however, including losses is seen to improve the correspondence between experiment and model significantly.

parameters given in Table 2 and heat loads from 0 to 1.6 W. The model was set with the same parameters and a spatially constant magnetic flux density of 1 T. Figure 10 shows both an example of the transient evolution of a specific heat load cycles experiment (left-hand) and the results of the heat-load series (right-hand).

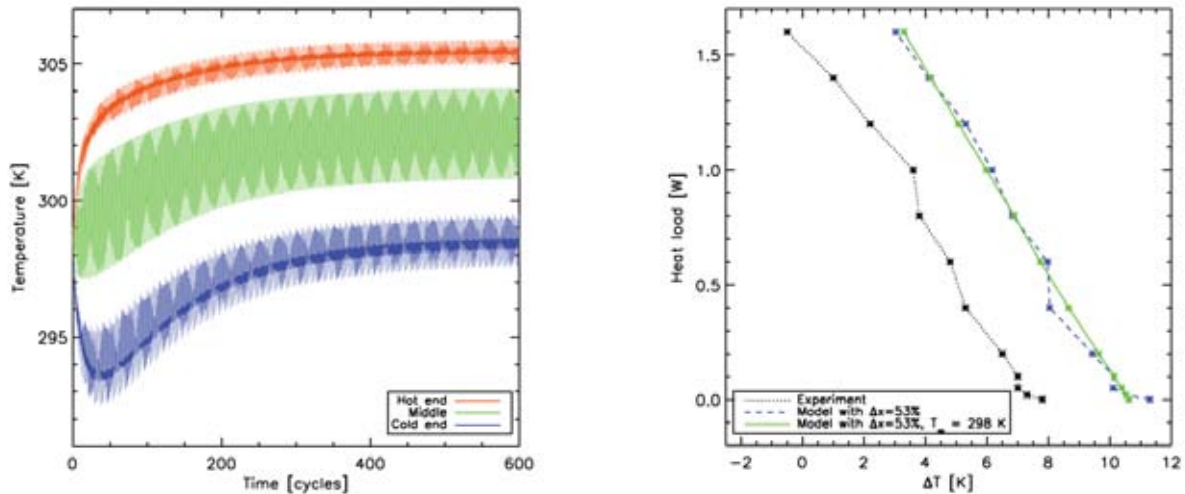


Figure 10: Left: The transient evolution of the cold, middle and hot parts of the regenerator (simulated). The particular example is for a piston stroke (Δx) of 53% with a load of 0.8 W. Right: A load-experiment and the corresponding model results. The model assumed $h_{conv} = 20 \text{ W/m}^2\text{K}$. Note that there are two model-series in the right graph. The green/solid line data set was performed with a constant ambient temperature whereas the blue/dashed line data set corresponds directly to the circumstances during the experimental data acquisition (black line/dotted).

The experimental series was performed over a period of two days since it takes around an hour to reach steady-state for each configuration. Therefore the ambient temperature T_∞ varied slightly (from 296-299 K). This is possible to adjust in the model as well, and therefore the two data sets are directly comparable. The model and the experimental data are very similar in behavior, though the model over-estimates the temperature span. Generally the temperature span decreases linearly with the increasing cooling capacity as one would expect. There are, however, minor fluctuations in the linearity. If the experimental data are considered isolated, the small variations may be regarded as experimental noise. However, when compared to the model data, virtually the same variations are seen. To investigate this, a model-series was performed with the ambient temperature set to the constant value 298 K. This is seen as the green/solid line in the right graph of Figure 10. Thus, the variations away from the linearly decreasing cooling capacity are interpreted as a result of the fluctuations in the ambient temperature. The slopes of each of the three graphs were found by linear regression. The values are all $-0.2 \pm 0.01 \text{ W/K}$.

5. DISCUSSION, CONCLUSIONS AND OUTLOOK

5.1 Discussion

The numerical model has been successfully validated against real experiments in different situations including no-load and load-experiments, varying the magnetic field and some of the operational parameters, namely piston stroke length, τ_1 and τ_2 . The discrepancies between the model and the experiment seen in Figure 9 and Figure 10 are, however, something that should be considered and the model should be improved to minimize these. We have used an ideal model for the behavior of Gd in terms of c_p and ΔT_{ad} . We have independently measured the actual adiabatic temperature change of the Gd used in the test machine and it has turned out that due to impurities the actual adiabatic temperature change is roughly 20 % lower than in the ideal mean field model used in the numerical model. We have chosen not to include this in the present work since we have not yet performed enough measurements of the utilized Gd in order to cover the range in magnetic fields and temperature span needed.

A result of this work is that the model is directly capable of catching the effect of the ambient temperature on the system. This may have been interpreted as an experimental feature (e.g. noise) if the model had not caught it and if not the constant-ambient temperature modeling had resulted in the completely straight line seen in the right part of Figure 10.

5.2 Conclusions and outlook

The experimental AMR at Risø DTU has been demonstrated to be quite versatile in terms of operational parameters and various aspects of the cooling capacity. The corresponding numerical model is to a large extent successful in predicting the behavior of the system. Many interesting aspects still need to be investigated though. They include obtaining more reliable and realistic data of the Gd we actually use in our test machine, testing other potential MCM materials and changing the thickness of the plates and the fluid channels as well as the operating parameters. Having a powerful numerical model that predicts the behavior seen experimentally is crucial for the further development of a new AMR with significantly improved performance. The fact that there is a very strong correspondence between the experimental and modeling results in both series presented in Section 4 strongly indicates that the model indeed captures the general behavior of the parallel-plate AMR system.

ACKNOWLEDGEMENTS

The authors thank Mr. Jørgen Geyti for his technical assistance. Furthermore the authors would like to acknowledge the support of the Programme Commission on Energy and Environment (EnMi) (Contract no. 2104-06-0032) which is part of the Danish Council for Strategic Research.

REFERENCES

- Bjørk, R., C.R.H. Bahl, A. Smith, and N. Pryds. "Optimization and improvement of Halbach cylinder design." *Journal of Applied Physics*, in press, 2008.
- Brown, G. V. "Magnetic heat pumping near room temperature." *Journal of Applied Physics* (AIP) 47 (1976): 3673-3680.
- Comsol. *Comsol Multiphysics Model Library, third ed.* COMSOL AB, Chalmers Teknikpark 412 88 G., 2005.
- Halbach, K. "Design of permanent multipole magnets with oriented rare earth cobalt material." *Nuclear instruments and methods* 169 (1980).
- Holman, J.P. *Heat Transfer*. 6. McGraw-Hill, 1987.
- Mallinson, J. C. "One-sided Fluxes - A Magnetic Curiosity?" *IEEE Transactions on magnetics* 9 (4) (1973): 678-682.
- Pecharsky, V. K., and K.A. Gschneidner. "Advanced magnetocaloric materials: What does the future hold?" *International Journal of Refrigeration* 29 (2006): 1239-1249.
- Petersen, T. F., N. Pryds, A. Smith, J. Hattel, H. Schmidt, and H.J.H Knudsen. "Two-dimensional mathematical model of a reciprocating room-temperature Active Magnetic Regenerator." *International Journal of Refrigeration* 31 (2008): 432-443.
- Petersen, Thomas Frank. "Numerical modelling and analysis of a room temperature magnetic refrigeration system." PhD Thesis, Risø National Laboratory and Technical University of Denmark, 2007.
- Tura, A., and A. Rowe. "Design and Testing of a Permanent Magnet Magnetic Refrigerator." *2nd International Conference on Magnetic Refrigeration at Room Temperature*. 2007. 363-370.
- Warburg, E. "Magnetische untersuchungen." *Ann.Phys (Leipzig)* 13 (1881): 141-164.

- A.3.2 2-dimensional numerical modeling of Active Magnetic Regeneration; published in the proceedings of the 3rd International Conference on Magnetic Refrigeration at room temperature

2-dimensional numerical modeling of Active Magnetic Regeneration

K.K. Nielsen^(a,b), N. Pryds^(b), A. Smith^(b), C.R.H. Bahl^(b), J. Hattel^(a)

^(a) Technical University of Denmark, Department of Mechanical Engineering
Produktionstorvet, building 425, 2800 Kgs. Lyngby, Denmark
kaspar.kirstein.nielsen@risoe.dk

^(b) Risø National Laboratory for Sustainable Energy, Technical University of Denmark
Fuel Cells and Solid State Chemistry Division
Frederiksborgvej 399, 4000 Roskilde, Denmark

ABSTRACT

Various aspects of numerical modeling of Active Magnetic Regeneration (AMR) are presented. Using a 2-dimensional numerical model for solving the unsteady heat transfer equations for the AMR system, a range of physical effects on both idealized and non-idealized AMR are investigated. The modeled system represents a linear, parallel-plate based AMR.

The idealized version of the model is able to predict the theoretical performance of AMR in terms of cooling power and temperature span. This is useful to a certain extent, but a model reproducing experiments to a higher degree is desirable. Therefore physical effects such as thermal parasitic losses have been included. Furthermore, experimentally found magnetocaloric properties are used when available, since the commonly used mean field model can be too idealized and is not always able to determine the magnetocaloric effect accurately.

In the present paper preliminary conclusions on which non-ideal physical effects are thought to be dominating considering the performance of experimental AMR are given. The modeling results are compared to experimental results from the AMR test device situated at Risø DTU, Technical University of Denmark. The experimental validation shows that using the measured magnetocaloric properties significantly improves the modeling results compared to using the mean field model.

1. INTRODUCTION

The magnetocaloric effect (MCE) provides the basic ingredient for magnetic refrigeration. The effect is observed in magnetic materials when exposed to a change in external magnetic field. The MCE is usually either observed as a change in magnetic entropy, ΔS_m (when the field is applied isothermally) or as a change in temperature, ΔT_{ad} (when the field is applied adiabatically). In addition to these two fundamental observations the specific heat, c_p is usually a strong function of both temperature and field. The MCE is typically in the range of 1-5 K / T (in terms of the adiabatic temperature change). This modest change in temperature is obviously not sufficient for applications such as domestic refrigeration etc. Therefore the successful regenerative process, Active Magnetic Regeneration (AMR), is applied for magnetic refrigeration around room temperature. AMR can be thought of as a range of coupled local thermodynamic cycles that differential elements of a regenerator go through (Rowe et al., 2003). The cycle consists of four steps. The first step is the adiabatic magnetization where the magnetocaloric material (MCM) is exposed to a magnetic field under adiabatic conditions. Second, a heat transfer fluid convectively transfers heat from the MCM to the ambient through a hot side heat exchanger – also known as the hot blow. The third step is the adiabatic demagnetization, i.e. the magnetic field is removed. The final step is the so-called cold blow where the heat transfer fluid absorbs heat from a cooling load. These four steps have the durations denoted τ_1, τ_2, τ_3 and τ_4 respectively.

During the AMR cycle a heat transfer fluid and a solid refrigerant (the MCM) exchange heat dynamically and at the same time the material properties of the MCM change as function of both temperature and magnetic field. This makes it impossible to perform an analytical analysis of the entire AMR Refrigeration (AMRR) system in terms of predicting cooling power, comparing material performance and general optimization of the design. Therefore numerical modeling – obviously in close collaboration with extensive experimental studies – is crucial for the development of AMRR.

In this work the focus is on the comparison between the modeling and the experimental results, especially showing the necessity of accurate material data. In Section 2 the model is described. The

governing equations are presented and the emphasis is put on the special features of this model as well as a discussion of how to model the MCE. Results from both modeling and experimental work are presented in Section 3. Finally, in Section 4 the impact on the modeling of the different ways of obtaining the MCE are discussed on the basis of the results presented in this paper.

2. PRESENTATION OF THE MODEL

The basics of the model are summarized in the following. For a detailed description of the model see Nielsen, et al.(2009). The geometry targeted by the model is the parallel-plate based design. The system can be either reciprocating or continuous – that is not significant for the model as such. Four domains are modeled: The heat transfer fluid, MCM plate and cold and hot heat exchangers (HEXs), which can also act as passive flow guides depending on which experiment is modeled. The solid domains are fixed with respect to each other and can be rigidly moved with respect to the fluid (in order to model fluid movement). The AMRR system is thus modeled by solving the coupled heat transfer equations for each domain through a number of timesteps (and AMR cycles) until quasi-steady state is reached. The numerical discretization is done using finite differences of 2nd order and the temporal integration is done using the Alternate Direction Implicit (ADI) method, thoroughly discussed in e.g. (Hattel 2005) or (Patankar 1980). The software for implementing the solver has been written by the authors and is available in generic Fortran.

2.1. Governing equations

The coordinate system is defined so the x -direction is parallel to the flow and the y -direction is perpendicular to the plane of the magnetocaloric plates, i.e. denotes the direction of the height of the MCM plates and the fluid channel. In Figure 1 and Figure 2 the geometry is schematically described. In Bahl et al., (2008) the geometrical details of the system are thoroughly described. The total system of equations can be written as:

$$\frac{\partial T_f}{\partial t} = \frac{k_f}{\rho_f c_{p,f}} \nabla^2 T_f + q_{bd,fc} + q_{bd,fh} + q_{bd,fMCM} + q_{loss,f} - u \frac{\partial T_f}{\partial x} \quad (1)$$

$$\frac{\partial T_{MCM}}{\partial t} = \frac{k_{MCM}}{\rho_{MCM} c_{p,MCM}} \nabla^2 T_{MCM} - q_{bd,fMCM} + q_{loss,MCM} \quad (2)$$

$$\frac{\partial T_c}{\partial t} = \frac{k_c}{\rho_c c_{p,c}} \nabla^2 T_c - q_{bd,fc} + q_{loss,c} \quad (3)$$

$$\frac{\partial T_h}{\partial t} = \frac{k_h}{\rho_h c_{p,h}} \nabla^2 T_h - q_{bd,fh} + q_{loss,h} \quad (4)$$

Subscripts f , c and h denote the fluid, CHEX and HHEX domains respectively. The material properties thermal conductivity, mass density and specific heat (k , ρ and c_p) respectively, are all assumed constant except the specific heat for the MCM, which varies strongly with both temperature and magnetic field. The coupling of Eqs. (1)-(4) is implemented through the boundary heat fluxes denoted by $q_{bd,fMCM}$, $q_{bd,fc}$ and $q_{bd,fh}$ respectively. The heat flux terms with subscript $loss$ are included as parasitic thermal losses to the ambient. These are calculated through the formulation of thermal resistances on the form:

$$q_{loss} = \frac{T - T_\infty}{\sum_i R_i}. \quad (5)$$

Here, the summation is done over the number of thermal resistances R_i experienced by each individual grid cell with temperature T . The ambient temperature is denoted T_∞ . The thermal resistance is calculated on the basis of the thermal properties of the materials considered. For instance, the thermal resistance experienced by the fluid is calculated as:

$$R_{f,total} = \frac{1/2\Delta z_f}{k_f \Delta x \Delta y} + \frac{\Delta z_{pl}}{k_{pl} \Delta x \Delta y} + \frac{1}{h_{conv} \Delta x \Delta y}. \quad (6)$$

The thickness of the fluid channel, Δz_f , and of the plastic housing Δz_{pl} have been introduced. The natural convection that transfers heat from the regenerator to the ambient is modeled through the parameter h_{conv} assumed to attain a value of $10 \text{ W/m}^2 \text{ K}$. The last term in Eq. (1) represents the convective heat transfer. The assumed fluid flow is fully developed, incompressible and laminar. Therefore only the x -component of the fluid velocity is non-zero. An analytical expression for the velocity profile is straightforwardly calculated in e.g. Nielsen et al. (2009):

$$u(y) = \tilde{u} \left(\frac{6y^2}{H_{fl}^2} - 1/2 \right), \quad (7)$$

where \tilde{u} is the inlet velocity and H_{fl} the fluid channel height.

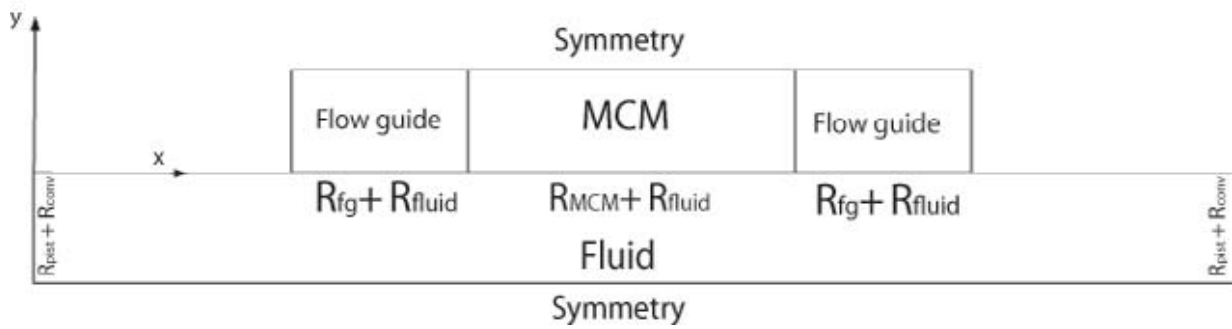


Figure 1 : The xy -plane of the regenerator model. The MCM and flow guides are fixed with respect to each other and can be moved with respect to the fluid in order to model the fluid movement. The internal boundaries are marked with their thermal resistances. The model is half a replicating cell and thus the symmetry boundaries are marked.

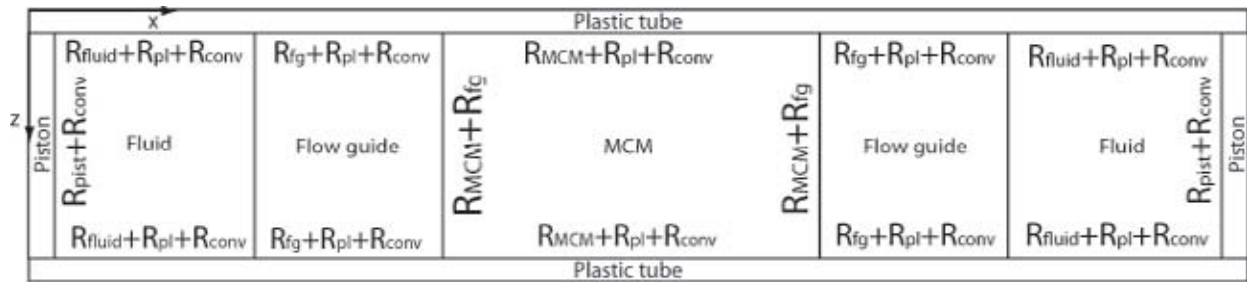


Figure 2 : The xz -plane of the regenerator model. The system should be thought of as seen from above, i.e. the fluid is hidden under the MCM and flow guides. The external boundaries are marked as the thermal resistances to the ambient. It is noted that the z -direction is not resolved by the model, but due to the thermal parasitic losses to the ambient the model can be thought of as 2.5 dimensional.

As indicated in Figure 1 the model utilizes symmetry meaning that only half a flow channel and half a MCM plate are modeled. The symmetry boundaries are by definition set so that both the heat fluxes and the fluid flow across them are zero at all times.

2.2. Obtaining the MCE

Obtaining the magnetocaloric properties of a given MCM can require some work. The well known mean field theory (MFT) (see e.g. Petersen et al. 2008, Kawanami, et al. 2006, Li, et al. 2006) is typically used when considering gadolinium (Gd). From a pure modeling point of view a nice-behaving model like the MFT is good in the sense of minimizing numerical difficulties and having a firm well-resolved data set. However, a critical view on the correspondence between MFT and experimental data should at all times be applied.

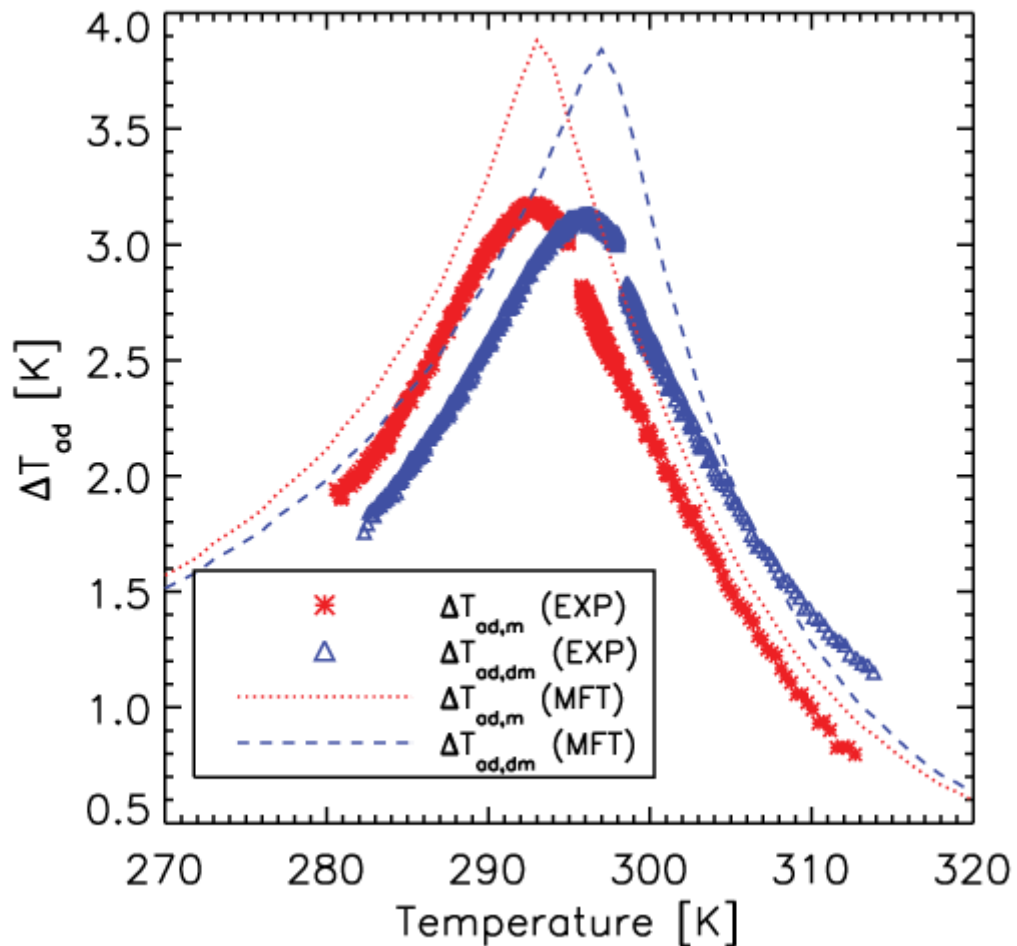


Figure 3 : The red asterisks (magnetization) and blue triangles (demagnetization) mark experimentally obtained ΔT_{ad} values for commercial grade Gd at an applied field of approximately 1.1 T (from Bahl and Nielsen, 2009). The red punctuated line (magnetization) and blue dashed line (demagnetization) mark the corresponding MFT based calculation. The sign of the demagnetization data reversed for clarity.

Two examples of the MFT compared with experimental data are presented in Figure 3 and Figure 4. Here the adiabatic temperature changes for Gd and the ceramic material $(La_{0.67}Ca_{0.26}Sr_{0.07})Mn_{1.05}O_3$ (LCSM) when applying a magnetic field of nearly 1.1 T are plotted. Both as calculated by the MFT and measured (the Gd data are obtained from Bahl and Nielsen (2009) and the LCSM are measured with the same technique). It seems quite evident from the figures that the MFT does not fully catch the actual adiabatic temperature change. For this there may be several explanations, of which only a few will be mentioned here. The purity of the Gd sample seems to have a large impact (Dan'kov et al. 1998). Also, demagnetization effects on the specific experiment may change the actual internal field in the sample (Bahl and Nielsen 2009). The important point is that using the MFT may be misleading if the goal is to model and precisely predict the performance of an *experimental* AMR device.

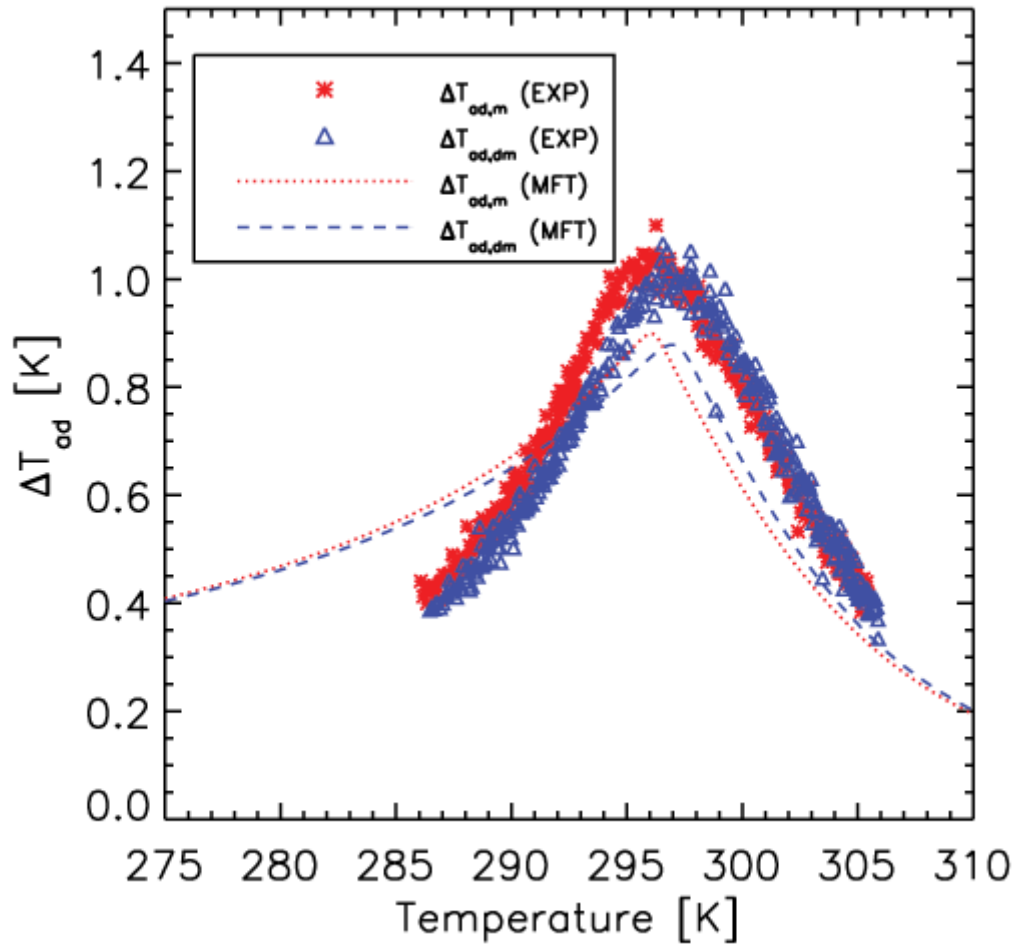


Figure 4 : The adiabatic temperature change of $(La_{0.67}Ca_{0.26}Sr_{0.07})Mn_{1.05}O_3$ both measured (using the same method as with the Gd measurements) and modeled using the MFT. The magnetic flux density of 1.1 T was applied using a Halbach permanent magnet. The input parameters for the MFT were obtained from Dinesen (2004) and are reproduced in Table 1. The sign of the demagnetization data reversed for clarity.

On the other hand, if the modeling is performed in order to predict trends and theoretically based conclusions on the ideal AMR performance, the MFT may be a wise choice. The reasons for this are, among others, that the MFT is well-behaving and thus from a numerical standpoint is easy to handle (compared to most often too insufficient data sets). It is also easier to reproduce and compare modeling across research groups compared to using a specific sample of a MCM. And finally, the MFT predicts values for both the adiabatic temperature change and specific heat capacity that are quite realistic both as function of field and temperature as would be expected of most 2nd order materials.

Table 1 : The input parameters for the mean field model as defined in e.g. Petersen et al. (2008). The parameters are (in order of appearance) number of magnetic spins per unit mass, the Landé factor, the total angular momentum, the Curie temperature, the Debye temperature, the total number of atoms per unit mass and the Sommerfeld constant. The Gd parameters are obtained from Petersen et al. (2008) while the LCSM parameters are from Dinesen (2004). It is noted that the values from Dinesen (2004) are calculated from samples with a little less Mn content (the plates used in the experiment are made of $(La_{0.67}Ca_{0.26}Sr_{0.07})Mn_{1.05}O_3$).

	n_s (kg^{-1})	g (-)	J (-)	T_c (K)	Θ_D (K)	n (kg^{-1})	γ_e ($J/kg \cdot K$)
Gadolinium	$3.83 \cdot 10^{24}$	2	3.5	293	169	$3.83 \cdot 10^{24}$	0.069
$(La_{0.67}Ca_{0.26}Sr_{0.07})Mn_{1.00}O_3$	$2.8 \cdot 10^{24}$	2	1.83	296	353	$1.44 \cdot 10^{25}$	0.025

3. RESULTS

The model described in the previous section can simulate a range of AMR situations. The operating parameters, fluid movement, AMR timing and ambient temperature, are easily set by input parameters. The geometric parameters (flow channel thickness, dimensions of the MCM plate) are set in the same way. The implementation of the MCE can also easily be varied between using MFT or experimental data. Likewise the thermal parameters (thermal conductivity, mass density etc.) are also provided via simple input.

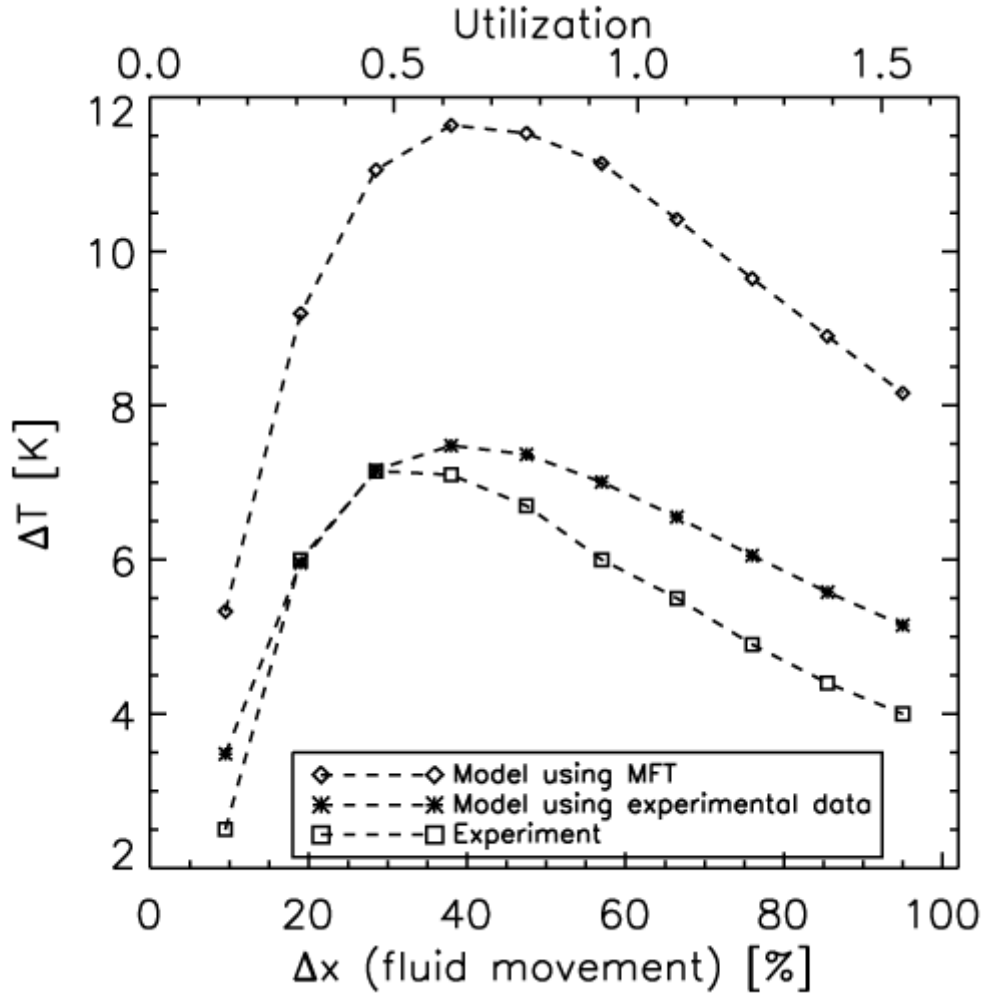


Figure 5 : The no heat load temperature span as function of fluid movement and utilization. The experiment was performed with commercial grade Gd and the parameters for both the model and experiment are given in Table 2.

The model can be set to run for a number of AMR cycles or until a steady-state has been reached. The hot and cold ends can be equipped with ideal heat exchangers (plates made of Cu with perfect contact to the ambient as first described in Petersen et al., 2008) or they can be simple fluid reservoirs in which case the rejection of heat to the ambient is only done through the thermal parasitic losses as described in Eqs. (5) and (6).

As an example we consider the effect of the implementation of the MCE. Two no heat-load experiments have been performed; one with Gd and one with LCSM (see Table 2 for details). The utilization is defined as

$$\varphi = \frac{c_{p,fl} \rho_{fl} H_{fl}}{c_{p,MCM} \rho_{MCM} H_{MCM}} \Delta x, \quad (8)$$

with Δx denoting the fluid movement in percent of the length of the MCM plate and H_{MCM} denoting the thickness of the MCM plate. The utilization can thus be adjusted by varying the amount of fluid moved. The results plotted as steady-state temperature span are given in Figure 5 and Figure 6 as function of both fluid movement and utilization. There are given two modeling situations. One using the MFT to obtain the MCE

and the other using the experimentally determined ΔT_{ad} values (plotted in Figure 3 and Figure 4 respectively). In both cases the specific heat capacity was obtained using the MFT.

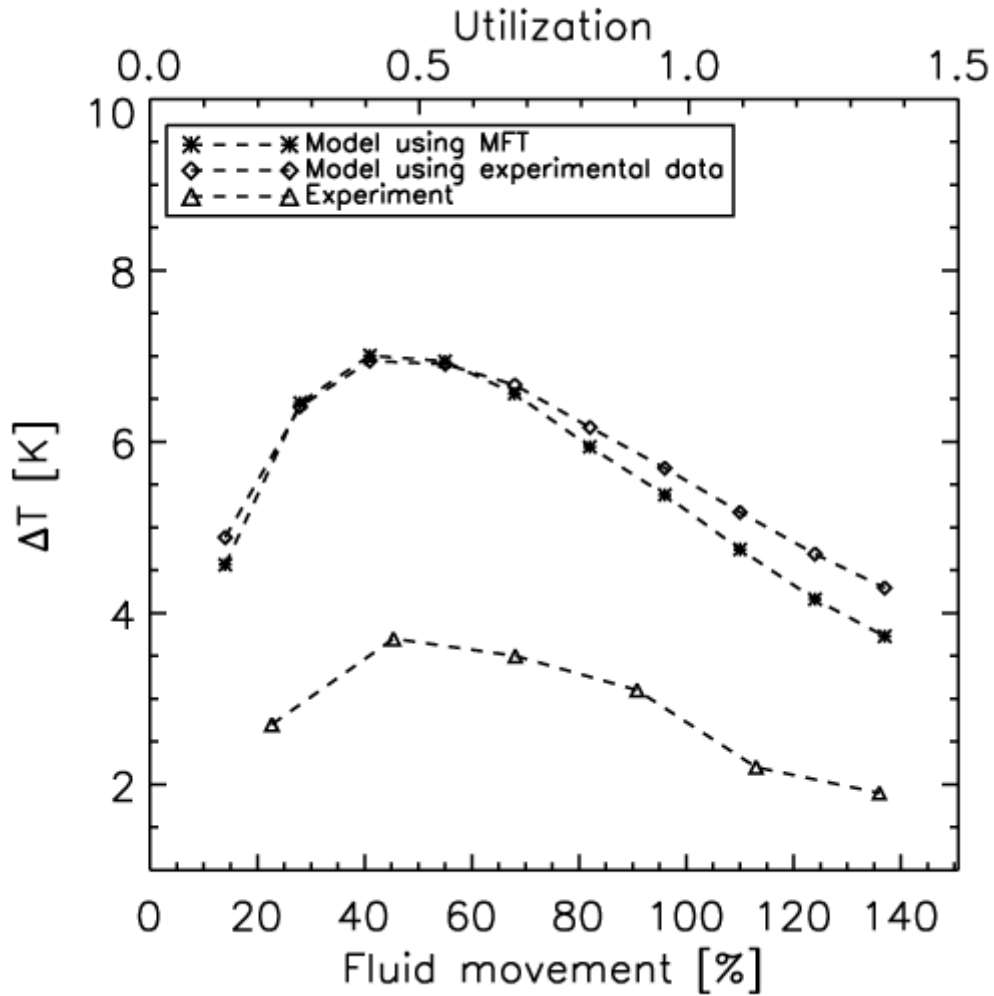


Figure 6 : Experiment with LCSM. The fluid movement has been varied (thus varying the utilization) and the modeling has been performed for two cases (one using MFT and the other experimental data for obtaining the MCE).

The results show that the model, in either case, is able to follow the tendency of the experiment, especially showing a peak value around a utilization of 0.5. It is also observed that using the experimentally determined adiabatic temperature change values significantly improves the absolute temperature span values of the model compared to the experiment when Gd is considered. This is not true for LCSM, which is also apparent from Figure 4.

Table 2 : The basic input parameters for the two experiments (and corresponding modeling). In order of appearance : The flow channel thickness, the thickness of the MCM plate, the timing of the magnetization, the timing of the hot blow and ambient temperature. Both experiments were conducted with a 1.1 T permanent magnet and with a water+ethanol mixture (10% ethanol).

	H_f (mm)	H_{MCM} (mm)	τ_1, τ_3 (s)	τ_2, τ_4 (s)	T_∞ (K)
Gd	0.8	0.9	1.4	2.7	298
LCSM	0.2	0.3	1.5	1.2	296

4. CONCLUSION

An improved version of the original 2-dimensional model by Petersen et al. (2008) was presented and the concept of adding half a modeling dimension was introduced (through thermal parasitic losses to the

ambient). The focus in this work was on the difference between using MFT and experimentally determined values for the MCE (considering only the adiabatic temperature change). Two different MCMs were considered, Gd and LCSM. In the case of Gd it was shown that the experimentally obtained values for the adiabatic temperature change clearly improved the correspondence of the model compared to the experiment. In the case of LCSM the modeling results from the two cases of using MFT and experimental data respectively, were seen to be virtually the same. This was also to be expected from the presented adiabatic temperature change data in Figure 4.

Considering the usability of the MFT for obtaining the MCE as opposed to experimental data it is concluded that each individual material must be considered as a special case. For Gd the MFT may not be the best choice when modeling an actual experiment, but for LCSM the difference between the MFT and the experimentally determined adiabatic temperature change is not significant – at least in the temperature span from 285-305 K as indicated in Figure 4. In this work the specific heat capacity was as mentioned obtained using the MFT in all cases. This leaves quite some work to be done since the specific heat may deviate somewhat experimentally from that calculated using the MFT. The peak temperature may also change as function of field. This is not modeled directly through the MFT (see e.g. Tishin et al, 1999). This is a topic of big interest and therefore near-future work will include an investigation and discussion of the role of the specific heat in terms of AMR modeling – both with respect to the change in peak temperature and absolute values.

REFERENCES

- Bahl, C., & Nielsen, K.K. (2009). The effect of Demagnetization on the Magnetocaloric properties of Gadolinium. *Journal of Applied Physics* . 105,013916
- Bahl, C., Petersen, T., Pryds, N., & Smith, A. (2008). A versatile magnetic refrigeration test device. *Review of Scientific Instruments* , 79, 093906.
- Dinesen, A. R. (2004). *Magnetocaloric and magnetoresistive properties of La_{0.67}Ca_{0.33-x}Sr_xMnO₃*. Ph.D thesis, Technical University of Denmark.
- Hattel, J. (2005). *Fundamentals of Numerical Modelling of Casting Processes*. Polyteknisk Forlag.
- Kawanami, T., Chiba, K., Sakurai, K., & Ikegawa, M. (2006). Optimization of a magnetic refrigerator at room temperature for air cooling systems. *International Journal of Refrigeration* , 29, 1294-1301.
- Li, P., Gong, M., Yao, G., & Wu, J. (2006). A practical model for analysis of active magnetic regenerative refrigerators for room temperature applications. *International Journal of Refrigeration* , 29, 1259-1266.
- Nielsen, K.K., Bjørk, R., Bahl, C., Pryds, N., Smith, A., & Hattel, J. (n.d.). Detailed numerical modeling of a linear parallel-plate Active Magnetic Regenerator. *Submitted for publication in the International Journal of Refrigeration* .
- Patankar, S. V. (1980). *Numerical Heat Transfer and Fluid Flow*. Taylor&Francis.
- Petersen, T. F., Pryds, N., Smith, A., Hattel, J., Schmidt, H., & Knudsen, H. (2008). Two-dimensional mathematical model of a reciprocating room-temperature Active Magnetic Regenerator. *International Journal of Refrigeration* , 31, 432-443.
- Rowe, A., & Barclay, J. (2003). Ideal magnetocaloric effect for active magnetic regenerators. *Journal of Applied Physics* , 93, 1672-1676.
- Siddikov, B., Wade, B., & Schultz, D. (2005). Numerical Simulation of the Active Magnetic Regenerator. *Computers and Mathematics with Applications* , 49, 1525-1538.
- Tishin, A., Gschneidner, K.A., & Pecharsky, V. (1999). Magnetocaloric effect and heat capacity in the phase-transition region. *Physical Review B (Condensed Matter)* , 59, 503-511.

-
- A.3.3** Numerical modeling of graded active magnetic regenerators; published in the proceedings of the 4th International Conference on Magnetic Refrigeration at room temperature

NUMERICAL MODELING OF GRADED ACTIVE MAGNETIC REGENERATORS

K. K. NIELSEN^{1,2}, C.R.H BAH², K. ENGELBRECHT², A. SMITH², N. PRYDS² AND J. HATTEL¹

¹Department of Mechanical Engineering, Technical University of Denmark
Produktionstorvet, building 425, room 020, 2800 Kgs. Lyngby

²Fuel Cells and Solid State Chemistry Divison, Risø National Laboratory for Sustainable Energy, Technical University of Denmark, Frederiksborgvej 399, 4000 Roskilde, Denmark
Email: kaki@risoe.dtu.dk

Abstract: A well-established 2-dimensional numerical model is applied for the case of active magnetic regenerators (AMR) with graded magnetocaloric materials. We examine how the performance of the AMR is affected by using materials with different Curie temperatures and, in general, varying magnetocaloric properties. The performance is benchmarked through the maximum obtainable temperature span, cooling power, exergy, ratio of regeneration and COP. The results show that performance may indeed be enhanced by grading the regenerator as opposed to using a single-material regenerator.

1. Introduction

Magnetic refrigeration faces several challenges in order to realize the goal of becoming a competitive refrigeration technology. One of these challenges is concerned with the design of optimally graded regenerators, i.e. regenerators composed of several magnetocaloric materials distinguished by different Curie temperatures that extend the operational temperature range of the regenerator. It has been shown experimentally that this is feasible (Rowe and Tura, 2006). Even though the grading of active magnetic regenerators (AMR) seems to be generally accepted as a necessity for reaching competitive performances, only a few research papers actually study this. Jacobs proposed a fast scheme for optimizing a graded AMR with interesting results (Jacobs, 2009). Nielsen et al. (2009) showed a good correspondence between experiment and model with a 2-material regenerator based on the $\text{La}(\text{FeCoSi})_{13}$ compounds. Rowe and Barclay (2003) proposed an optimal Curie-temperature composition based on a simplified thermodynamic optimization approach.

2. Model

In this paper we investigate a two-material AMR using a 2-dimensional numerical model of a parallel plate AMR described elsewhere (Nielsen et al. 2009a,b) and varying the Curie temperatures and the fraction of the regenerator occupied by each material. The magnetocaloric material is assumed to be gadolinium with the magnetocaloric effect modeled through the mean field model (MFM) for a ferromagnet combined with the Debye and Sommerfeld models; see (Nielsen et al. 2009a,b and Petersen et al. 2008). The Curie temperature, T_C , is an input parameter to the MFM and may be varied accordingly. The regenerator geometry is kept fixed with dimensions given in Table 1. The operating conditions were also kept fixed for simplicity; see also Table 1.

Table 1: The input parameters for the AMR model and their values. L_r is the length of the regenerator in the flow direction, H_s the thickness of the magnetocaloric plate, H_f the thickness of the fluid channel, Δx the fluid movement in percent of the regenerator length, τ_{tot} the total AMR cycle time, τ_{rel} the percentage of the magnetization or demagnetization processes to the fluid flow time, ϕ the utilization as defined in e.g. [Fejl! Henvisningskilde ikke fundet.] and finally the minimum and maximum applied magnetic fields, H_{min} and H_{max} , respectively.

Property	L_r [m]	H_s [mm]	H_f [mm]	Δx [%]	τ_{tot} [s]	τ_{rel} [-]	ϕ [-]	$\mu_0 H_{max}$ [T]	$\mu_0 H_{min}$ [T]
Value	0.05	0.5	0.2	50	2	0.25	0.28	1.0	0.01

These operating conditions were chosen such that the regenerator when equipped with a single magnetocaloric material would be able to create a temperature span of at least 20 K theoretically (Nielsen et al., 2010). The hot end temperature was assumed to be 298 K in all cases.

The grading of the regenerator is done in the flow direction, and this gives reason to define the plate closest to the cold end as the “cold” material with a Curie temperature denoted $T_{C,cold}$ and the material closest to the hot side as the “hot” material with a Curie temperature denoted $T_{C,hot}$.

3. Results

In the following, a range of resulting parameters from the model are investigated in order to evaluate the grading of the AMR. The cooling power at zero temperature span, the temperature span at zero cooling power, the exergy, the ratio of regeneration and the COP of the system are all investigated as functions of hot and cold side Curie temperatures. Finally, the volume ratio of the two plates is investigated in terms of the maximum cooling power and maximum entropy generation to probe whether the regenerator should be symmetric or benefits could be obtained from adjusting the relative amount of each material.

3.1. Cooling power

The cooling power as a function of varying the two Curie temperatures and keeping the volume ratio of the two plates at 50 percent and the temperature span $\Delta T = 20\text{K}$ is shown in Figure 1. The heat load is normalized in units of power per mass of regenerator material, which is directly comparable to other models and experimental results. The figure clearly shows that the optimum Curie-temperature composition is located such that the hot and cold Curie temperatures are not equal. The hot side optimal Curie point is 295 K, which is three degrees less than the hot end temperature whereas the optimal cold side Curie temperature is 285 K, which is 7 degrees above the imposed cold side temperature. It may also be seen from Figure 1 that the maximum cooling power for a single-material regenerator is some 27 percent less than the maximum cooling power of a two-material regenerator.

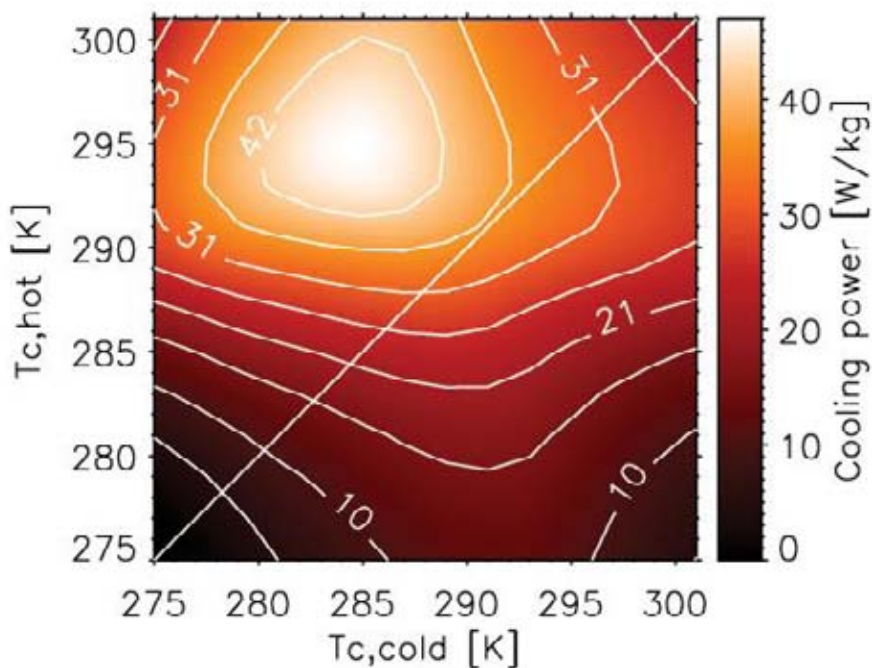


Figure 1: The cooling power at a fixed temperature span of 20 K mapped as a function of the Curie temperatures of the two materials in the regenerator. The contours show lines of equal cooling power. The diagonal line represents a regenerator which effectively is composed of one material, i.e. the Curie temperatures of the two materials are equal. The optimum single-material Curie temperature is equal to 291 K.

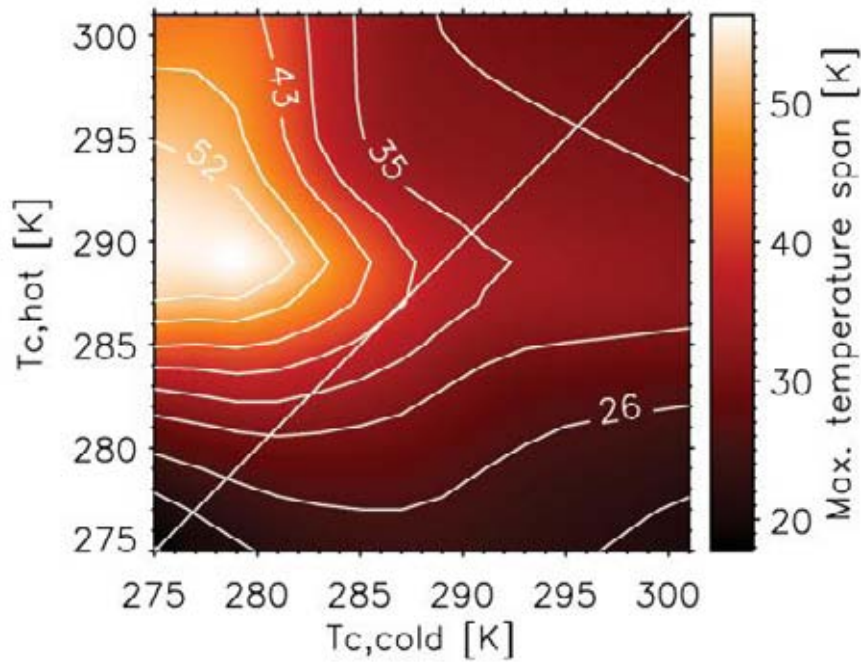


Figure 2: The no-load temperature span as a function of hot and cold side Curie temperatures. The contours show iso-temperature spans. The diagonal line indicates an effective single-material regenerator.

3.2. Maximum temperature span

Figure 2 shows the no-load temperature span as a function of hot and cold Curie temperatures. It is observed that the configuration yielding the maximum temperature span is not coincident with that which maximizes the cooling power. This is an interesting result since it will have a strong influence when deciding how to grade a regenerator because, of course, this is a design choice that cannot be changed during operation. It is furthermore seen that the maximum temperature span of the graded regenerator is around 30 percent greater than the maximum achievable temperature span of a single material regenerator. It should be noted that the maximum achievable temperature span is quite sensitive experimentally, since thermal leaks and imperfections in the regenerator may have a big impact on this parameter. These losses are not included in the current model.

3.3. Exergy

In order to evaluate the performance of a certain AMR configuration (both in terms of geometric and operational parameters) the exergy may be used as suggested in Rowe (2009). The exergy as a function of cooling power is defined as

$$Ex_Q(Q_c) = \frac{Q_c(Q_{\max} - Q_c)}{Q_{\max} \frac{T_{\infty}}{\Delta T_{\max}} - (Q_{\max} - Q_c)} \quad (1)$$

Here the cooling power is denoted Q_c , the maximum cooling power Q_{\max} (at zero temperature span), the ambient temperature T_{∞} and the maximum temperature span is ΔT_{\max} . The maximum exergy may be presumed to represent the optimal performance for a given regenerator configuration from a thermodynamic perspective (Rowe, 2009).

In Figure 3, the maximum exergy is plotted as a function of hot and cold Curie temperatures. Interestingly, the peak is seen to be somewhat halfway between those of the cooling power and maximum temperature span, respectively – both in terms of the hot and cold side Curie temperatures. This indicates that a compromise definitely should be sought between temperature span and cooling power when designing the grading of the AMR, which seems to be a reasonable conclusion.

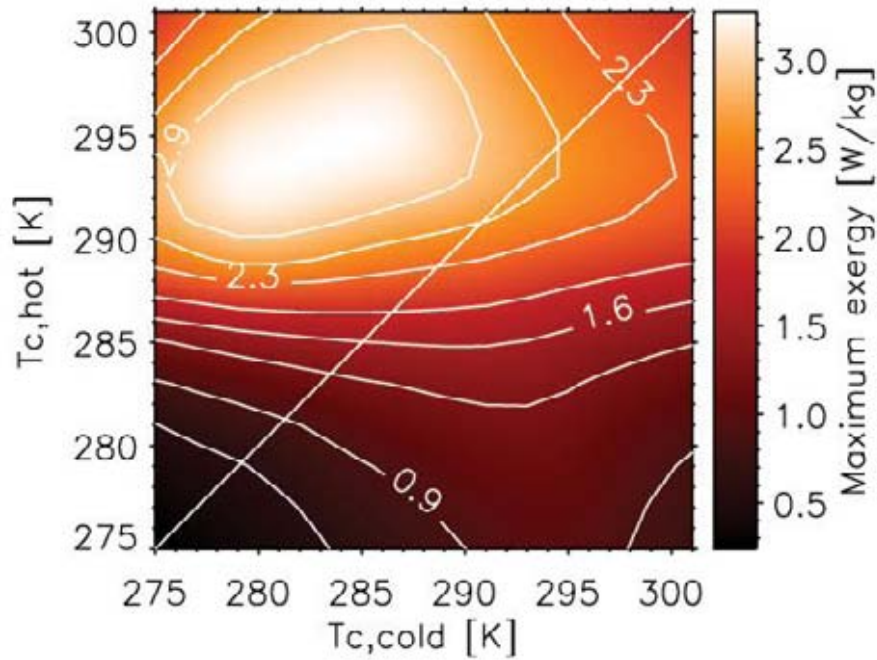


Figure 3: Maximum exergy as a function of hot and cold Curie temperatures. The contours show constant maximum exergy levels.

3.4. Ratio of regeneration

Another way of benchmarking the performance of the AMR as a function of hot and cold Curie temperatures is by using a dimensionless number called the ratio of regeneration. This was introduced in [Fejl! Henvisningskilde ikke fundet.] and later used in [Fejl! Henvisningskilde ikke fundet.]. The ratio of regeneration is defined as:

$$\zeta \equiv \frac{\Delta T}{\Delta T_{ad}} \quad (2)$$

where ΔT is the temperature span over the regenerator and ΔT_{ad} is the average adiabatic temperature change of the magnetocaloric material. This average was calculated given the imposed temperature span and the distribution of the two plates and their magnetocaloric effect, assuming a linear temperature profile from the cold to the hot end. This measure is useful for evaluating the effectiveness of the regenerator since it can be regarded as a measure of the magnification of the adiabatic temperature change intrinsic to the material.

Figure 4 shows the ratio of regeneration as a function of hot and cold Curie temperatures. Not surprisingly, it is maximized around the same values as the zero-load temperature span (Figure 2). It may be concluded that the grading of magnetocaloric materials in the AMR certainly can enhance the performance compared to single-material regenerators, however, highly dependent on how the grading is done. In Figure 4, it may be seen that configurations of the hot and cold Curie temperatures where the cooling capacity is maximized, the ratio of regeneration is actually lower than for single-material AMRs. This was shown experimentally in Engelbrecht et al. 2009.

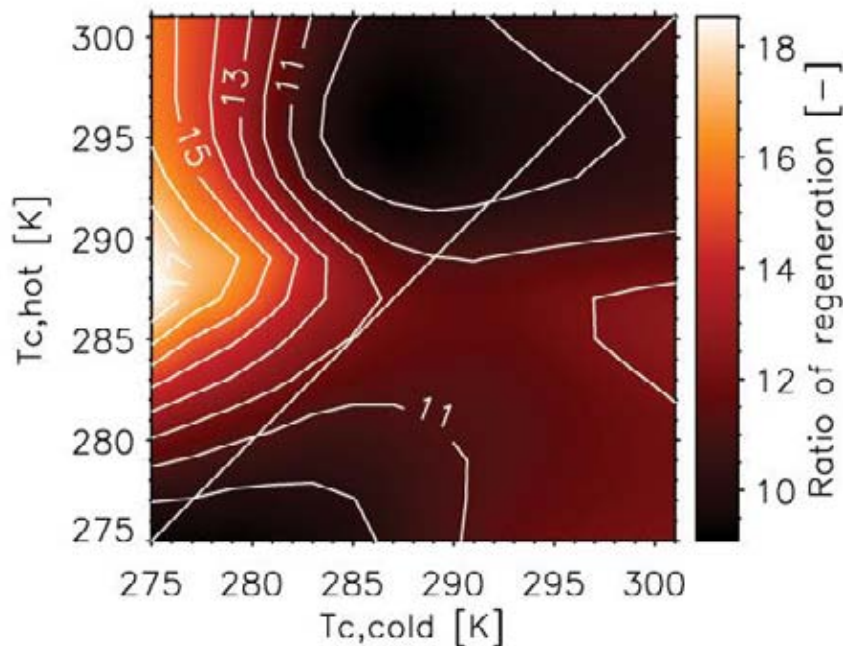


Figure 4: The ratio of regeneration as a function of hot and cold side Curie temperatures. The contours show iso- ζ curves. The diagonal line indicates an effective single-material regenerator.

3.5. Coefficient of performance

The coefficient of performance (COP) provides valuable information on the performance of a refrigeration system. It is defined as

$$\text{COP} = \frac{Q_c}{W} \quad (3)$$

with the total work input denoted by W . In Figure 5, the COP is mapped as a function of the hot and cold Curie temperatures. The maximum value obtained is approximately 4.5 corresponding to a Carnot efficiency of 30 percent and is located where the hot Curie temperature is 291 K and the cold is 279. The COP is furthermore seen to be enhanced from around 3.8 where both Curie temperatures are 291 K (the maximum COP single-material composition), an increase of 16 percent. The maximum region of the COP is not exactly coinciding with the maximum regions of the cooling power, maximum temperature span or ratio regeneration, respectively. From this fact it may be concluded that the COP can be viewed as sort of an independent benchmark parameter.

3.6. Effect of varying the fraction of the materials

So far, the results have been considered with regenerators composed of two magnetocaloric materials distinguished by their respective Curie temperatures and in all cases distributed evenly, i.e. the fraction of each material was 50 percent. Varying this ratio does not change the general form of the plots considered in Figure 1 to Figure 5 significantly, however, the absolute values change somewhat.

For simplicity, characteristic numbers have been selected for characterizing the effect of changing the ratio between the two materials. In Figure 6, the maximum cooling power and maximum COP are plotted as functions of the fraction of the cold Curie temperature material. For each fraction the entire map of hot and cold Curie temperatures was simulated and the respective maxima are thus plotted in Figure 6.

The two curves clearly have their respective maxima at the same fraction, namely 50 percent. Thus, it may be concluded – considering the cooling power and the COP – that the optimal fraction between the two plates corresponds to an equal amount of each material. It may also be concluded that both the cooling power and the COP vary with up to approximately 30 percent as a function of the fraction.

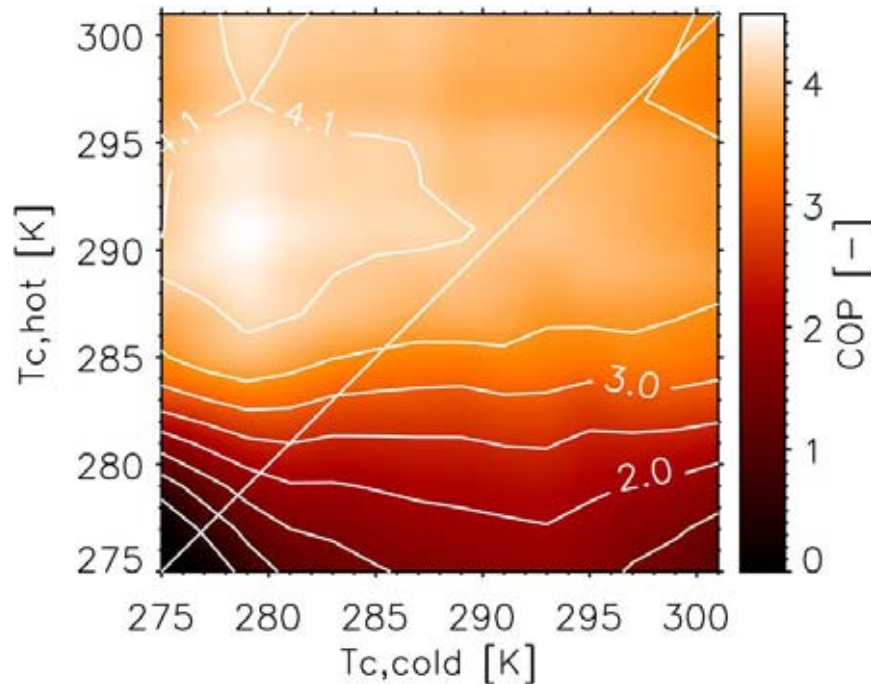


Figure 5: The COP of the regenerator as a function of hot and cold side Curie temperatures.

4. Conclusion

An established 2-dimensional numerical model for parallel-plate active magnetic regenerators was used to investigate the effect of grading the AMR with two magnetocaloric materials. The materials were chosen to be mean field modeled gadolinium for simplicity with their respective Curie temperatures shifted in order to simulate different materials. This approach serves to give insight into the actual effect of grading the AMR and is not biased by experimental data of possible varying quality and is thus not dependent on a specific material.

The results showed that grading may indeed improve the performance of the AMR. However, it does not in all cases seem beneficial to use two rather than one magnetocaloric material. In fact, this is a complicated function of ambient temperature, the two Curie temperatures and also which parameter of the AMR is sought to be optimized. If the zero cooling load temperature span is to be maximized the grading should be quite different from the case where the cooling power at zero temperature span is to be maximized. In between these two extremes the maximization of the exergy is found. This comprises a compromise that may be concluded to be the optimum configuration of the two-material grading of the AMR. It was also seen that the area in the space of Curie temperatures where the exergy is maximized is fairly wide in terms of both the hot and cold end Curie temperatures, which is comforting for the design of the AMR.

The ratio of regeneration was also used as a measure for the performance of the AMR with two materials. Not surprisingly this ratio follows, roughly, the temperature span at zero cooling power map (compare Figure 2 and Figure 4).

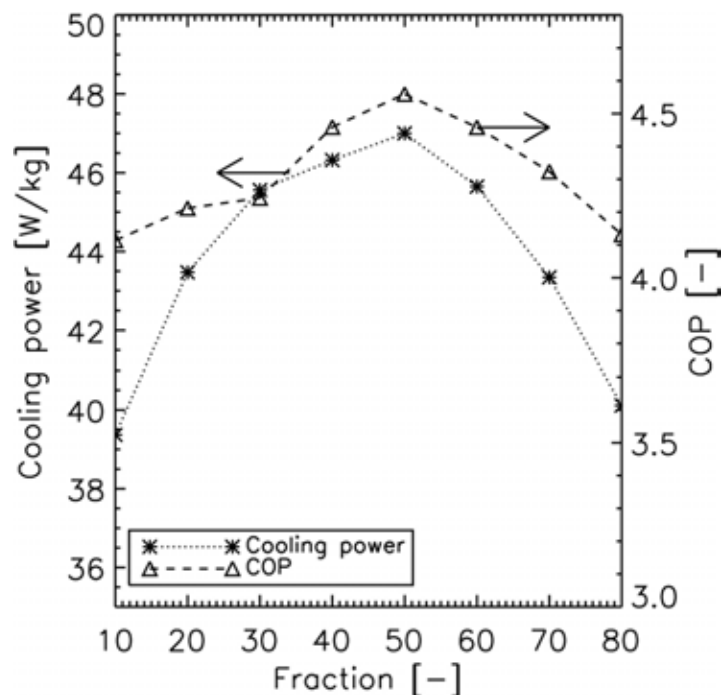


Figure 6: Maximum cooling power and COP as a function of ratio between cold and hot Curie temperature materials.

The total entropy generation of the AMR as a function of the hot and cold Curie temperatures was also discussed. Here it was shown that the entropy generation map follows, roughly, the cooling power map (compare Figure 1 and Figure 5).

Finally, it may be concluded that the ratio between the two materials should, in the cases investigated here, be around 50 percent for optimal performance.

Acknowledgements

The authors thank the support of the Programme Commission on Energy and Environment (EnMi) (Contract no. 2104-06-0032) which is part of the Danish Council for Strategic Research. K. K. Nielsen also thanks the Danish Agency for Science, Technology and Innovation under the Danish Ministry for Science, Technology and Innovation.

References

A. Rowe and A. Tura, "Experimental investigation of a three-material layered active magnetic regenerator", 2006, *Int. J. of Refrig.* 29, 1286-1293.

S. Jacobs, "Modeling and optimal design of a multilayer active magnetic refrigeration system", 2009. In: Egolf, P.W. (ed.), *Third International Conference on Magnetic Refrigeration at Room Temperature*, International Institute of Refrigeration, Des Moines, Iowa, USA, pp. 267-273.

K.K. Nielsen, K. Engelbrecht, C.R.H. Bahl, A. Smith, N. Pryds and J. Hattel, "Numerical modeling of multi-material active magnetic regeneration", 2009. In: J.S. Szmyd, J. Spalek and T.A. Kowalewski (editors), *7th World Conference on Experimental Heat Transfer, Fluid Mechanics and Thermodynamics*, Krakow, Poland, pp. 515-522.

A. Rowe and J. M. Barclay, "Ideal magnetocaloric effect for active magnetic regenerators", 2003, *J. of Appl. Phys.* 93, 3, 1672-1676.

K. K. Nielsen, C.R.H. Bahl, A. Smith, R. Bjørk, N. Pryds and J. Hattel, "Detailed numerical modeling of a linear parallel-plate Active Magnetic Regenerator", 2009a, *Int. J. of Refrig.* 32, 1478-1486.

K. K. Nielsen, N. Pryds, A. Smith, C.R.H. Bahl and J. Hattel, "2-dimensional numerical modeling of active magnetic regeneration", 2009b, In: Egolf, P.W. (ed.), *Third International Conference on Magnetic Refrigeration at Room Temperature*, International Institute of Refrigeration, Des Moines, Iowa, USA, pp. 251-258.

T.F. Petersen, N. Pryds, A. Smith, J. Hattel, H. Schmidt and H.J.H. Knudsen, 2008, *Int. J. of Refrig.* 31, 432-443.

K.K. Nielsen, C.R.H. Bahl, A. Smith, N. Pryds and J. Hattel, "A comprehensive parameter study of an active magnetic regenerator using a 2D numerical model", 2010, *Int. J. of Refrig.* in press.

A. Tura and A. Rowe, "Progress in the characterization and optimization of a permanent magnet magnetic refrigerator", 2009, In: Egolf, P.W. (ed.), *Third International Conference on Magnetic Refrigeration at Room Temperature*, International Institute of Refrigeration, Des Moines, Iowa, USA, pp. 387-392.

A. Rowe, "Performance metrics for active magnetic regenerators", 2009, In: Egolf, P.W. (ed.), *Third International Conference on Magnetic Refrigeration at Room Temperature*, International Institute of Refrigeration, Des Moines, Iowa, USA, pp. 195-205.

C.R.H. Bahl, T.F. Petersen, N. Pryds and A. Smith, "A versatile magnetic refrigeration device", 2008, *Rev. of Scientific Instruments* 79, 093906-1 - 093906-7.

K. Engelbrecht, C.R.H. Bahl, K.K. Nielsen and N. Pryds, "Experimental results for a magnetic refrigerator using three different types of magnetocaloric material regenerators", 2010, submitted to *Int. J. of Refrig.*

- A.3.4 Numerical modeling of multi-material active magnetic regeneration; published in the proceedings of the 7th World Conference on Experimental heat transfer, fluid mechanics and thermodynamics

NUMERICAL MODELING OF MULTI-MATERIAL ACTIVE MAGNETIC REGENERATION

K.K. Nielsen^{1,2,*}, K. Engelbrecht², C.R.H Bahl², A. Smith², N. Pryds², J. Hattel¹

¹Department of Mechanical Engineering, Technical University of Denmark
Building 425, Niels Koppels Allé, DK-2800 Kgs. Lyngby, Denmark

²Fuel Cells and Solid State Chemistry Division
Risø National Laboratory for Sustainable Energy
Technical University of Denmark - DTU, Frederiksborgvej 399, DK-4000, Denmark

ABSTRACT. Magnetic refrigeration is a potentially environmentally-friendly alternative to vapour compression technology that is presented in this paper. The magnetocaloric effect in two magnetocaloric compounds in the La(Fe,Co,Si)₁₃ series is presented in terms of their adiabatic temperature change and the specific heat as a function of temperature at constant magnetic field. A 2.5-dimensional numerical model of an active magnetic regenerative (AMR) refrigerator device is presented. The experimental AMR located at Risø DTU has been equipped with a parallel-plate based regenerator made of the two materials. Experimental zero heat-load temperature spans are presented for different operating conditions and the results are compared to predictions of the numerical model. It is concluded that the model reproduces the experimental tendencies and when including thermal parasitic losses to ambient and the predictions from the model are within 1.5 K of the experimental results.

Keywords: active magnetic regeneration, numerical modeling, magnetocaloric effect

1. INTRODUCTION

1.1. Magnetic refrigeration and some of the challenges

Magnetic refrigeration is a research field covering a wide range of different physical disciplines. The basic physical property on which magnetic refrigeration is based is the magnetocaloric effect (MCE). This effect is exhibited by magnetic materials where increased ordering may be introduced by applying a magnetic field, thus lowering the magnetic entropy. This makes the MCE an inherently fundamental quantum mechanical effect. If the field is applied under adiabatic conditions the temperature of the material will rise. In order to maintain constant total entropy the decrease of the magnetic entropy must be compensated by an increase of the lattice and electron entropies thus increasing the temperature. This makes the MCE observable on the macroscopic level. The MCE is reversible for many magnetocaloric materials of interest but some materials exhibit some magnetic hysteresis [1].

For refrigeration applications the MCE can be used with the magnetocaloric material (MCM) as a refrigerant to accept a cooling load over a temperature span. However, the magnitude of the MCE is rather small – with an adiabatic temperature change with magnetization on the order a few K per tesla of magnetic flux density. This obviously limits the applicability of the MCE as a potential refrigerant.

* Corresponding author: K.K. Nielsen

Phone: + 45 4677 4758

E-mail address: kaki@risoe.dtu.dk

However, by implementing a regenerative, or active magnetic regeneration (AMR), cycle the technology can be used to absorb a cooling load at a temperature span that is higher than the adiabatic temperature change of the MCM. This process exploits the MCM in two ways; by using the MCE as work input to generate cooling and as a regenerator to store heat temporarily and build up a temperature gradient. This makes temperature spans larger than the adiabatic temperature change possible. The AMR process is composed of four sub processes. First the material is magnetized and thus the temperature in the solid regenerator rises. Second, a heat transfer fluid – typically water-based – is pushed through the material (which is designed in some porous configuration) from the cold to the hot end thus lowering the temperature of the material by rejecting heat to the ambient while still magnetized. The third step is demagnetization. This ensures the material to cool below the initial temperature. The fourth and final step is moving fluid towards the cold end, thus absorbing a heat load from the cooled space. Thus, magnetic refrigeration includes the fundamental MCE as well as macroscopic heat transfer and fluid dynamics.

The challenges are many within this area of research; issues like regenerator geometry (particle bed, parallel plates etc.), operating conditions (cycle frequency, fluid movement etc.) and the magnetocaloric properties of the MCM just to mention a few. The MCE is most pronounced over a relatively small temperature span around the Curie temperature (T_C) of the material (where a ferromagnetic material changes to its paramagnetic state). This limits the optimal operating temperature for any given MCM and thus constructing a regenerator of a series of materials each with its own working temperature range tuned to the local regenerator temperature experienced by each material can greatly increase the total MCE in the regenerator. This work is concerned with a first attempt to model an experimental setup with two materials configured in a parallel-plate stack of magnetocaloric plates of sintered $\text{La}(\text{Fe},\text{Co},\text{Si})_{13}$ made by Vacuumschmelze, Germany [2,3]. Using this material, experiments have been performed using the experimental AMR device located at Risø DTU, Technical University of Denmark. The device is a single regenerator reciprocating AMR that is discussed in more detail in [4] and [5]. Results of this and corresponding modeling results are the scope of this paper. Previous AMR modeling including comparisons with experimental results can be found in e.g. [6,7].

1.2. The magnetocaloric effect

The MCE is typically discussed in three different forms: The isothermal magnetic entropy change (ΔS_{mag}) when magnetizing a sample of a MCM, the adiabatic temperature change (ΔT_{ad}), i.e. the temperature change of a MCM when magnetized adiabatically and finally the specific heat capacity, c_H , as function of temperature, T , at constant magnetic field, H . The adiabatic temperature changes of two magnetocaloric materials are given in Figure 1. The materials are two different $\text{La}(\text{Fe},\text{Co},\text{Si})_{13}$ compounds. The Fe/Co ratio has been varied in order to change the Curie temperature [2]. The figure shows the adiabatic temperature change when magnetizing from 0 T to 1.1 T. Some important details should be observed in the figure. Firstly, the clearly visible position of either material's transition temperature (in this case defined as the peak of the (ΔT_{ad}), curves). Secondly, the temperature ranges where each material exhibits a significant MCE overlap somewhat. Whether this overlap is sufficient for utilizing both materials in an effective refrigeration process is to be decided from modeling and experimental studies. In this paper we address some of these issues. It should be noted that the MCE for these materials is reversible. This is important since irreversibility associated with magnetization and demagnetization, known as magnetic hysteresis, is a serious degrading factor when considering the material's application as a refrigerant.

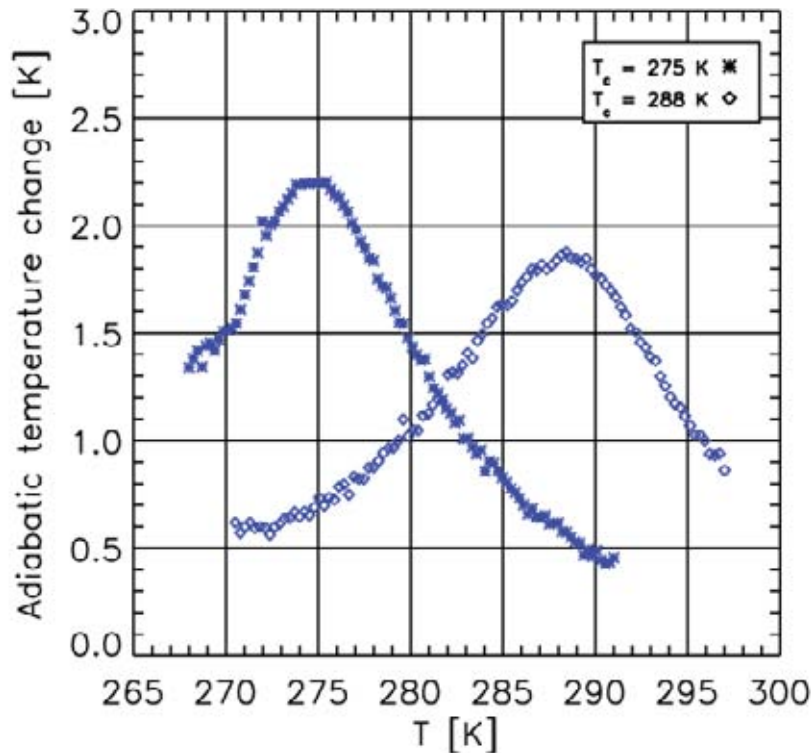


Figure 1: The adiabatic temperature change of two different compositions of La(Fe,Co,Si)₁₃ when magnetized from 0 to 1.1 Tesla. The indicated T_c in the figure legend is the Curie temperature of the materials.

The specific heat in an applied magnetic field has so far only been measured in detail on the compound with the low transition temperature and is given by [3]. Figure 2 shows the temperature dependence of the zero-field and the 1.0 T specific heat. Notice two important factors: First the peak value shifts significantly (3.5 K) between the two applied magnetic fields. Second, the zero-field specific heat has a higher and narrower peak than the 1.0 T specific heat curve has.

2. NUMERICAL AMR MODEL

The experimental device mentioned previously is modeled through a versatile 2.5-dimensional numerical model of a parallel plate AMR. The solution domains consist of a fluid domain and three solid domains; the MCM plate and a hot and cold heat exchanger (HEX). The governing equations are

$$\frac{\partial T_f}{\partial t} = \frac{k_f}{\rho_f c_{p,f}} \nabla^2 T_f + q_{bd,fc} + q_{bd,fh} + q_{bd,fMCM} + q_{loss,f} - u \frac{\partial T_f}{\partial x} \quad (1)$$

$$\frac{\partial T_{MCM}}{\partial t} = \frac{k_{MCM}}{\rho_{MCM} c_{H,MCM}} \nabla^2 T_{MCM} - q_{bd,fMCM} + q_{loss,MCM} \quad (2)$$

$$\frac{\partial T_c}{\partial t} = \frac{k_c}{\rho_c c_{p,c}} \nabla^2 T_c - q_{bd,fc} + q_{loss,c} \quad (3)$$

$$\frac{\partial T_h}{\partial t} = \frac{k_h}{\rho_h c_{p,h}} \nabla^2 T_h - q_{bd,fh} + q_{loss,h} \quad (4)$$

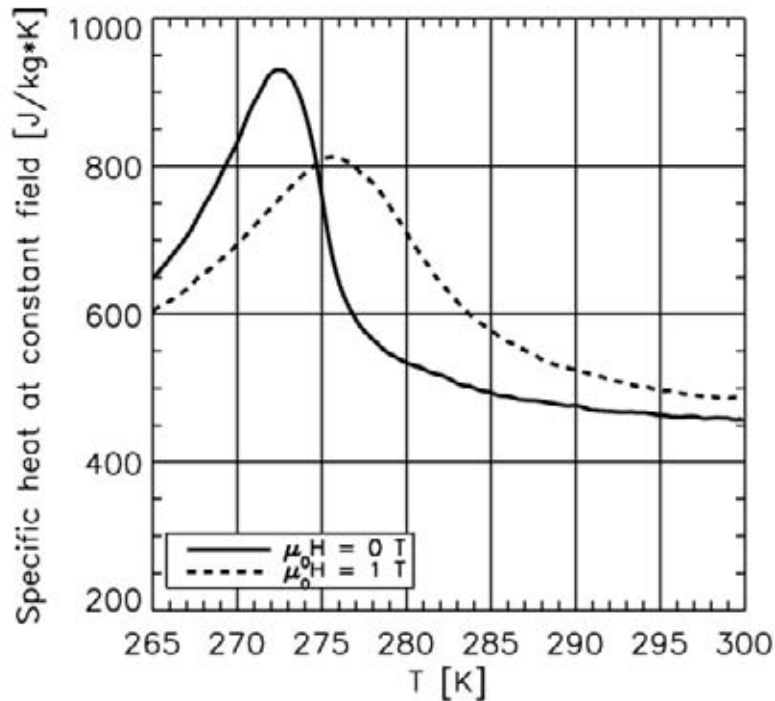


Figure 2: The specific heat capacity at constant magnetic field of the La(Fe,Co,Si)₁₃ sample with $T_c = 275$ K. Notice both the lower peak value as well as the lowering and broadening of the in-field specific heat.

The subscripts f , MCM , c and h indicate fluid, MCM, cold and hot HEX respectively. The thermal properties ρ and k denoting the mass density and the thermal conductivity have been introduced. The domains, as illustrated in Figure 3, are coupled via the boundary heat fluxes with subscripts bd .

The solution to Equations. (1)-(4) is determined for a number of cycles each divided in four sub processes further divided in time steps until cyclic steady-state is reached. The four sub-processes are: Magnetization (duration: τ_1 seconds), fluid flow from cold to hot end (hot blow, duration: τ_2 seconds), demagnetization (duration: τ_3 seconds) and finally flow from hot to cold end (cold blow, duration: τ_4 seconds). The cycle is assumed symmetric and thus $\tau_1 = \tau_3$ and $\tau_2 = \tau_4$. The numerical details can be found in [8]. The thermal properties used in the model are given in

Table 1.

Thermal parasitic losses to the ambient are enabled through the q_{loss} terms in Equations. (1)-(4). These are formulated on the form

$$q_{loss} = \frac{T - T_\infty}{\sum_i R_i} \tag{5}$$

The ambient temperature is denoted by T_∞ and the thermal resistances R_i are to be summed over for each numerical grid cell. An example of such a summation is

$$R_{fl,total} = \frac{1/2\Delta z_f}{k_f \Delta x \Delta y} + \frac{\Delta z_{pl}}{k_{pl} \Delta x \Delta y} + \frac{1}{h_{conv} \Delta x \Delta y}, \tag{6}$$

which is representative for the fluid channel. Here Δx , Δy and Δz denote the dimensions of the grid cell and h_{conv} the passive convective heat transfer coefficient modeling the heat loss on the outside of the generator to the ambient.

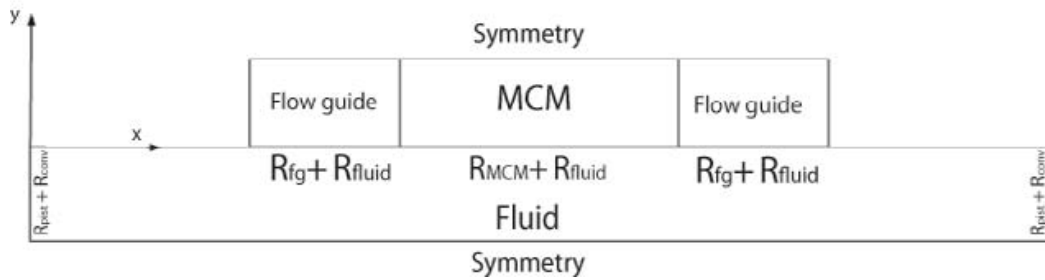


Figure 3: The four solution domains of the numerical AMR model. The domains denoted flow guide, are able to act as either passive plastic flow guides or as HEXs with perfect contact to the ambient (the hot HEX) or to a heat load (cold HEX). The symmetry lines indicate that only half a flow channel and half a solid domain are solved for. The indication of thermal resistances shows the internal thermal boundaries between the domains.

3. RESULTS

In the following results from both modeling and the experimental AMR device located at Risø DTU, are presented. The MCE was modeled discretely in the sense that at the first timestep of the AMR cycle the adiabatic temperature change from magnetizing was applied. Similarly, halfway through the modeled cycle (at the end of the hot blow) the adiabatic temperature change from demagnetizing was applied in one timestep. The specific heat was applied similarly. Here the data set from the 1.0 T measurements was used to temperature-interpolate the specific heat in the first half of the AMR cycle. In the last half of the cycle the zero-field specific-heat table was used. The adiabatic temperature change data is as previously shown in Figure 1. The specific heat is shown in Figure 2. However, since the specific heat of the high transition temperature material is not yet available, the specific heat data of the low-transition temperature material was used but shifted 13 K higher on the temperature scale (matching the difference between the peak values in the adiabatic temperature change values, see Figure 1).

The experimental approach is described thoroughly in both [4,5]. The range of the operating parameters are given in

Table 2. Both experiments were performed with a regenerator using the two materials (each 20 mm long yielding in total a 40 mm long regenerator). The flow channel height was 0.5 mm and the thickness of the plates 0.9 mm. All experiments were performed at an ambient temperature, T_∞ , approximately equal to 287 K, which was also used as the input ambient temperature to the model. A total of 11 plates were used.

The model is able to simulate thermal parasitic losses to the ambient modeled via thermal resistances as described in Equations. (5)-(6). Modeling both with and without this loss has been performed. The results from the two experimental situations are given in Figure 4 and Figure 5. Here it is clearly seen that including the thermal parasitic losses improves the model’s ability to reproduce the experimental results.

Table 1

Thermal properties of the computational domains. Data for copper is used for the HEXs. The thermal conductivity of the MCM was estimated from the results of [9,10].

	ρ [kg/m ³]	c [J/kg·K]	k [W/m·K]
Fluid	1000	4200	0.6
MCM	7100	500-950	9
HEXs	8933	385	401
Housing	N/A	N/A	0.2

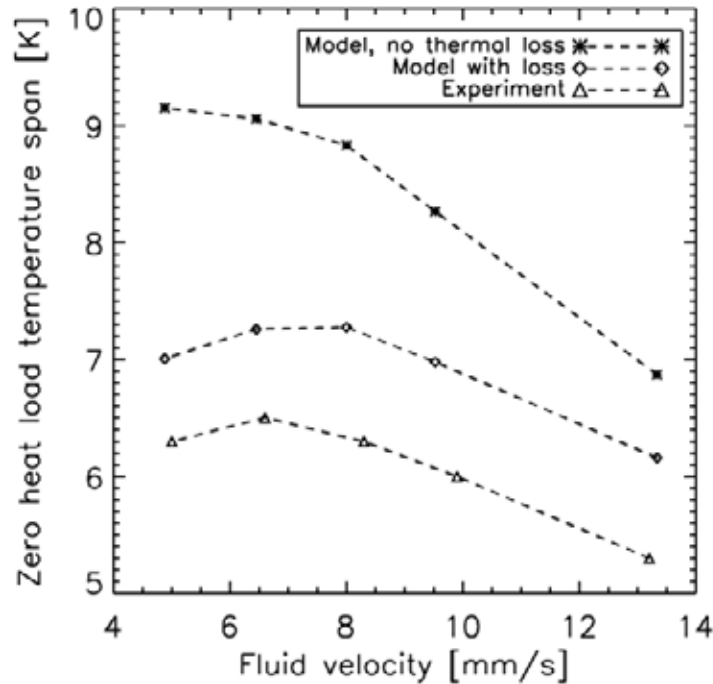


Figure 4: The no heat-load temperature span of experiment #1 (see Table 2 for details).

Overall, the predictions of the thermal loss model overestimate no more than 1.5 K in the worst case and in general about only 1 K, compared to the experimental results. The motivation for performing the two sets of experiments was to change the utilization defined as:

$$U = \frac{\rho_{fl} c_{p,fl} H_{fl} \Delta x}{\rho_{MCM} c_{H,MCM} H_{MCM} L_{MCM}} \tag{7}$$

Where ρ_{fl} is the mass density of the heat transfer fluid, $c_{H,fl}$ is the specific heat of the fluid, H_{fl} is the thickness of the fluid channel, Δx is the stroke length, ρ_{MCM} is the mass density of the MCM, H_{MCM} is the thickness of the MCM plate, $c_{H,MCM}$ is the mean specific heat of the MCM, and L_{MCM} is the length of the MCM plate. Thus, the utilization expresses the fraction of thermal mass of fluid moved compared to the thermal mass of the MCM. The mean specific heat of the MCM was set to 550 J/kgK. Now, the two values of the utilization (which characterize the two experiments respectively) are kept constant by varying the fluid velocity and the timing of the AMR cycle. Thus, a low fluid velocity means a higher cycle time. Therefore, the fact that the model reproduces the experiment at low fluid velocities closer than at high is explained by the fact that thermal losses affect performance more in a slow cycle than a faster cycle. Also, the largest temperature span, and thus the highest conduction loss to the surroundings, is achieved with a relatively slow fluid velocity (not the slowest – the temperature span curves clearly have a peak fluid velocity).

Table 2
The operating parameters of the two experiments.

Experiment	Utilization [-]	Timing range [s]	Fluid velocity range [mm/s]
#1	0.51	5 s – 10.2 s	5.0 – 13.3
#2	0.81	7 s – 15.4 s	5.0 – 13.3

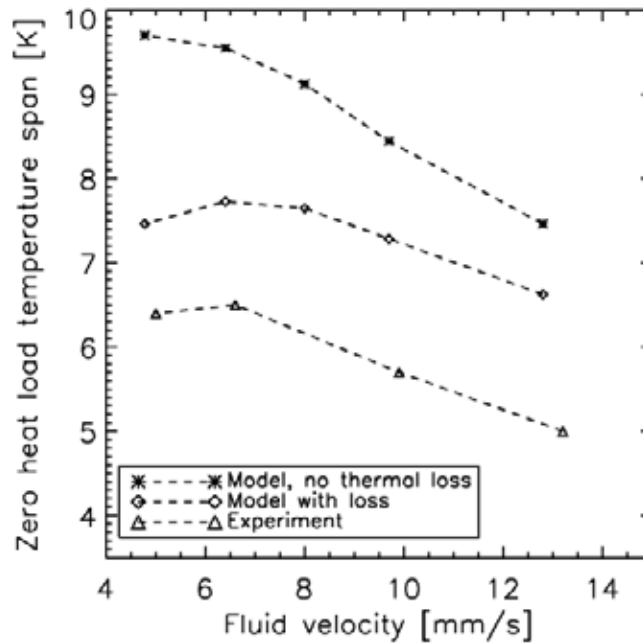


Figure 5: no heat-load temperature span of experiment #2 (see Table 2 for details).

4. DISCUSSION AND CONCLUSION

The comparison between experimental results and modeling of the experiment shows that the numerical AMR model presented here is able to reproduce the tendencies of the experiment. When including thermal losses to the ambient it is furthermore seen that the model results improve significantly in reproducing the experimental values. However, a discrepancy still exists. This may partially be explained by the use of the specific heat of the low-transition temperature material as the specific heat of the high-transition temperature material. Also the internal magnetic field in the MCM is somewhat reduced compared to the external field due to demagnetization [11]. Furthermore, the regenerator is comprised of 11 plates of MCM and will be subject to variation in thermal losses and spatially varying magnetic flux densities, which is not included by the model since the modelled geometry consists only of half a fluid channel and half a solid domain. Future work will include further modeling of the two-material regenerator in order to optimize for future choices of the transition temperatures of each individual material. As the maximum experimentally reached temperature span was about 6.5 K and the ambient was at 287 K the low-transition temperature material was clearly not as active as it could be and was thus not utilized fully.

ACKNOWLEDGEMENT

We thank Mr. Jørgen Geyti for his technical help. Also, we thank Vacuumschmelze GmbH & Co. KG, 63450 Hanau, Germany for supplying the plates of $\text{La}(\text{Fe},\text{Co},\text{Si})_{13}$. The authors further acknowledge the support of the Programme Commission on Energy and Environment (EnMi) (Contract No. 2104-06-0032), which is part of the Danish Council for Strategic Research.

REFERENCES

1. Gschneidner, K. A., V. K. Pecharsky, and A. O. Tsokol. "Recent Developments in Magnetocaloric Materials." *Rep. Prog. Phys.* 68 (2005):1479-1539.
2. Katter M., V. Zellmann, G.W. Reppel, and K. Uestuener. "Magnetocaloric properties of $\text{La}(\text{Fe},\text{Co},\text{Si})_{13}$ bulk material prepared by Powder Metallurgy", *IEEE Trans. Magn.* 44 (2008) 3044.
3. Hansen, B. R., M. Katter, L. Theil Kuhn, C. R. H., A. Smith, and C. Ancona-Torres. "Characterization study of a plate of the magnetocaloric material $\text{La}(\text{Fe},\text{Co},\text{Si})_{13}$." 2009. *Proc. 3rd International Conference on Magnetic Refrigeration at Room Temperature, IIF/IIR.*
4. Bahl, C.R.H., T.F. Petersen, N. Pryds, and A. Smith. "A versatile magnetic refrigeration test device." *Review of Scientific Instruments* 79 (2008): 093906.
5. Engelbrecht, K., J. B. Jensen, C. R. H., and N. Pryds. "Experiments on a modular magnetic Refrigeration Device." 2009. *Proc. 3rd International Conference on Magnetic Refrigeration at Room Temperature, IIF/IIR.*
6. Dikeos, J., A. Rowe, and A. Tura. "Numerical Analysis of an Active Magnetic Regenerator (AMR) Refrigeration Cycle." *AIP Conference Proceedings* 823 (2006): 993-1000.
7. Engelbrecht, K.L., G.F. Nellis, S.A. Klein, and A.M. Boeder. "Modeling active magnetic regenerative refrigeration systems." *Refrigeration Science and Technology Proceedings*, 2005. 265-274.
8. Nielsen, K.K., R. Bjørk, C.R.H. Bahl, N. Pryds, A. Smith, and J. Hattel. "Detailed numerical modeling of a linear parallel-plate Active Magnetic Regenerator." *Accepted for publication in the International Journal of Refrigeration*, 2009.
9. Fujieda, S., Y. Hasegawa, A. Fujita, and K. Fukamichi. "Thermal transport properties of magnetic refrigerants $\text{La}(\text{Fe}_x \text{Si}_{1-x})_{13}$ and their hydrides, and $\text{Gd}_5 \text{Si}_2 \text{Ge}_2$ and MnAs ." *Journal of Applied Physics* (AIP, USA) 95 (2004): 2429-2431.
10. Fukamichi, K., A. Fujita, and S. Fujieda. "Large magnetocaloric effects and thermal transport properties of $\text{La}(\text{FeSi})_{13}$ and their hydrides." *Journal of Alloys and Compounds* (Elsevier, Switzerland) 408-412 (2006): 307-12.
11. Bahl, C.R.H., and K.K. Nielsen. "The effect of demagnetization on the magnetocaloric properties of gadolinium." *Journal of Applied Physics* 105 (2009): 13916.

-
- A.3.5 Numerical analysis of a linear reciprocating active magnetic regenerator; published in the proceedings of the 4th International Conference on Magnetic Refrigeration at Room Temperature

NUMERICAL ANALYSIS OF A LINEAR RECIPROCATING ACTIVE MAGNETIC REGENERATOR

K. K. NIELSEN^{1,2}, J. R. BARBOSA, Jr.³, P.V. TREVIZOLI³

¹Department of Mechanical Engineering, Technical University of Denmark
Produktionstorvet, building 425, room 020
2800 Kgs. Lyngby, Denmark

²Fuel Cells and Solid State Chemistry Division, Risø National Laboratory for Sustainable Energy,
Technical University of Denmark, Frederiksborgvej 399, 4000 Roskilde, Denmark
e-mail: kaki@risoe.dtu.dk

³POLO Research Laboratories for Emerging Technologies in Cooling and Thermophysics
Department of Mechanical Engineering, Federal University of Santa Catarina (UFSC)
Florianópolis, SC, 88040900, Brazil
Phone/Fax: ++ 55 48 3234-5166, e-mail: jrb@polo.ufsc.br

Abstract: The active magnetic regenerative (AMR) refrigeration device developed at the POLO Research Laboratories, Federal University of Santa Catarina, Brazil, presented elsewhere in these proceedings is analyzed using two different numerical models; one for the AMR process and another for analyzing the demagnetizing field present in the regenerator. The results show agreement with the experimental trends presented elsewhere in these proceedings, however, the AMR model predicts a significantly larger zero-load temperature span than experimentally observed. The demagnetization model predicts little impact of the demagnetizing field on the internal field of the magnetocaloric regenerator bed.

1. Introduction

Numerical analysis is often used to predict or understand the behavior of complex physical systems. Considering the active magnetic regenerator a vast range of AMR models have been published (see e.g. Sarlah et al. 2005, Petersen et al. 2008, Nielsen et al. 2009a, Dikeos et al. 2006, Engelbrecht 2008, Oliveira et al. 2009, Jacobs 2009). An AMR model may be used to predict behavior of the system as a function of various operating and geometric parameters. It may also be used to understand the behavior of actual experimental devices. Here we consider the experimental AMR apparatus designed, developed and maintained at the POLO Research Laboratories for Emerging Technologies in Cooling and Thermophysics at the Federal University of Santa Catarina in Brazil. In Trevizoli et al. (2010) the experiment is described in detail and preliminary results are presented. The device is based on 28 flat plates of Gd with dimensions $(x,y,z) = (126,6.9,0.85)$ mm and with the applied magnetic field along the 6.9mm-direction. The magnetic field profile is shown in Figure 1.

The numerical model used for simulating the AMR process is described elsewhere (Nielsen et al. 2009a,b). The two-dimensional heat transfer equations are solved in both the solid and the fluid and half a fluid channel and half a magnetocaloric plate are resolved. The magnetic field change is spatially dependent in the flow-direction (the x -direction in Figure 1) and the applied magnetic field is assumed to be zero everywhere when out of field. The operating parameters are the same as in Trevizoli et al. (2010) and the magnetocaloric properties are assumed to be commercial grade Gd and they are published in Dankov et al. (1998).

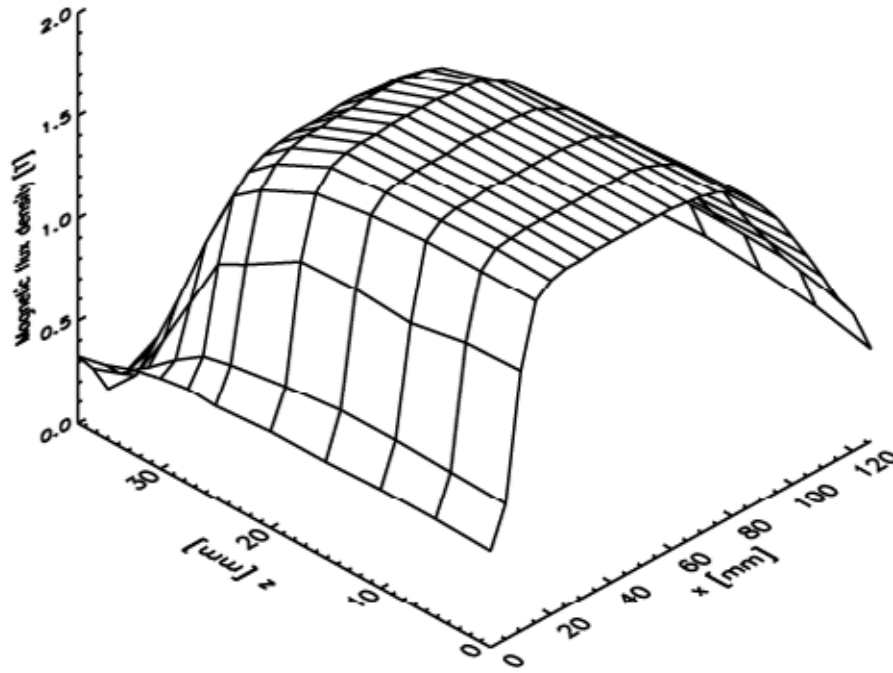


Figure 1: The magnetic flux density spatially resolved. The flow of the AMR device is in the x -direction and the regenerator bed is moved out of the field along the y -direction into a zero field region.

So far little attention has been brought to the effect of demagnetization in the realm of magnetic refrigeration. Only a few research papers discuss this effect to some extent (Rowe & Peksoy 2006, Bouchard et al 2005, 2009, Bahl & Nielsen 2009, Smith et al. 2010 and Christensen et al. 2010). Here, the model presented in Smith et al. (2010) is applied to the applied magnetic field shown in Figure 1 and the magnetocaloric regenerator configuration described in Trevizoli et al. (2010) in order to investigate the effect of demagnetization in the present setup. The demagnetizing field may decrease the internal magnetic field significantly compared to the applied magnetic field under certain circumstances; generally when the temperature is lower than the transition temperature of the magnetocaloric material and/or the geometric demagnetization is large.

Considering a flat plate of a magnetic material the geometric demagnetization will be maximized when the applied field is perpendicular to the largest face and minimized when it is perpendicular to the smallest face (Aharoni 1998, Bahl & Nielsen 2009).

1.1. The numerical demagnetization model

In Smith et al. (2010) a numerical model that is able to calculate the internal magnetic field distribution of a rectangular prism is presented. Here the main components of this model are presented briefly.

When a magnetic material is subjected to an applied field magnetic “surface charge” will accumulate on the edges of the sample perpendicular to the applied field. These create in turn an opposing field, denoted the demagnetizing field, such that the resulting internal magnetic field is smaller than the applied field. The relation between the internal magnetic field, the applied field and the demagnetizing field is

$$\mathbf{H} = \mathbf{H}_{appl} + \mathbf{H}_{dem} \quad (1)$$

The calculation of this field may be done by considering magnetostatics and integrating the magnetization of the interior of the magnetized body. In this way a demagnetization tensor field, \mathbf{N} , is obtained and for the case of a rectangular prism, with constant magnetization, this tensor may be found analytically. The numerical model then assumes a discretization of the total rectangular prism into smaller prisms, in which

the magnetization is assumed constant. In this way the entire prism may have varying temperature, applied field and thus magnetization. The resulting equation to be evaluated for the demagnetizing field at some point \mathbf{r} may be expressed as

$$\mathbf{H}_{dem}(\mathbf{r}) = -\sum_{i=1}^{n_x} \sum_{j=1}^{n_y} \sum_{k=1}^{n_z} \mathbf{N}(\mathbf{r} - \mathbf{r}'_{i,j,k}) \cdot \mathbf{M}_0 [\mathbf{H}(\mathbf{r}'_{i,j,k}, T_{i,j,k}), \mathbf{r}'_{i,j,k}, T_{i,j,k}] \quad (2)$$

where the triple-sum indicates summation over all the discrete prisms, temperature is denoted T , the magnetization of the cell with indices i,j,k is \mathbf{M}_0 and the position vector of the cell with indices i,j,k is $\mathbf{r}'_{i,j,k}$. The demagnetization tensor is given by a quite elaborate expression, which is given in Smith et al. (2010). Now, since Eq. (2) shows that the demagnetizing field is a function of the internal field (and temperature) iteration must be used to solve Eq. (1). The numerical details of this procedure are described in Smith et al. (2010).

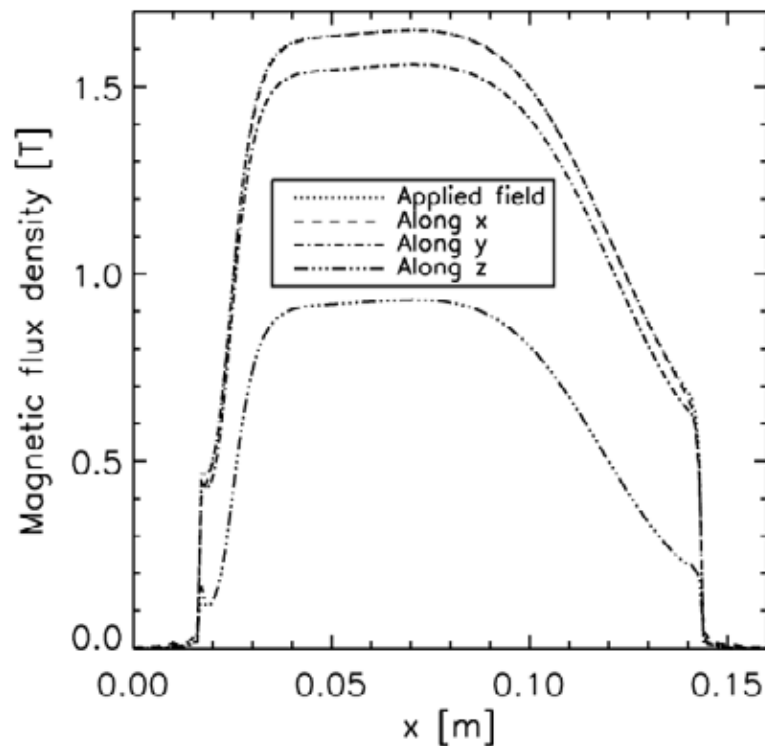


Figure 2: The applied magnetic field strength and the internal magnetic field strength for three different directions of the applied magnetic field. In the experiment the applied direction is the y-direction, i.e. the 6.9mm-direction. The temperature of the plate was set to be equal to the Curie temperature of the magnetocaloric material 293 K. The applied field strength is obtained from experimental measurements (Trevizoli et al. 2009).

2. Results

2.1. The effect of demagnetization

Applying the magnetic field along various directions with respect to the magnetocaloric plate yields quite different internal magnetic fields. In Figure 2 the applied field and the internal magnetic field are shown in three cases; applying the magnetic field along the x-, y- and z-directions respectively. It is clearly apparent that applying the field along the x-direction yields no difference in internal field compared to the applied

field. This is to be expected since the plate is much longer in this direction than in the other two and thus the demagnetization factor is very small (Aharoni, 1998). However, since the plate is also quite large in the y -direction compared to the z -direction, the internal field is fairly close to being equal to the applied field. Applying the magnetic field along the z -direction is seen to produce a quite significant demagnetizing field thus lowering the internal magnetic field significantly compared to the applied field. It should be noted that in the actual experiment the applied field is along the y -direction.

2.2. Model results of the AMR experiment

The AMR model as described in Nielsen et al. (2009a) was applied to the current experimental setup for an AMR cycle of 7 s and a variation in the utilization from 0.2 to 1.0 (see Figure 3). The utilization is defined as

$$\varphi = \frac{\dot{m}_f c_{p,f} P}{m_s c_{p,s} (T = T_C, \mu_0 H = 0)} \quad (3)$$

which follows the definition in Tura & Rowe (2009), Nielsen et al. (2009b) and Nielsen et al. (2010a). The fluid mass flow rate is denoted \dot{m}_f , the specific heat is c_p and the flow period is denoted P . Subscripts f and s denoted fluid and solid, respectively. It is noted that the specific heat of the magnetocaloric material is taken at the Curie temperature and in zero field, which for Gd means a value of 371 J/kg·K.

The results shown in Figure 3 clearly reveal a discrepancy between the predicted values of the model and those observed by the experiment. Even in the case of including parasitic thermal losses, as described in Nielsen et al. (2009a,b), the AMR model seriously over predicts the experimental results. This may be due to one or more of several things. These are

- The numerical model may be inherently inaccurate, i.e. not catching all the relevant physics
- The internal magnetic field may be significantly different from the applied magnetic field
- The magnetocaloric properties may be inadequate
- The regenerator housing / geometry may cause thermal leakage not resolved by the model

These four points are non-trivial to map out. However, the model has previously been fairly successful in predicting the performance of experimental devices (Nielsen et al. 2009a,b,c). As it was shown in Figure 2 the internal magnetic field is very close to the applied field causing the demagnetizing field to have little impact. The magnetocaloric properties are not completely characterized for the specifically used Gd, so in this case it is not currently possible to determine the discrepancy impacted on the model results compared to the experiment. Finally, the regenerator housing may have a significant impact on the performance. As it was applied in the experiment it was made of stainless steel (for technical reasons) and that may influence the AMR performance significantly in several ways. First, the thermal conduction can be quite large in the steel and thus losses to the ambient may be significant. Second, the large thermal conduction may act as a “short-circuit” of the regenerator in the sense that the temperature gradient in the flow direction is partially decreased – which is a significant effect when considering the cycle timing of 7 s. Finally, the stainless steel housing may also induce significant eddy currents from the cyclic change in magnetic field. These will serve to add a parasitic thermal load to the system.

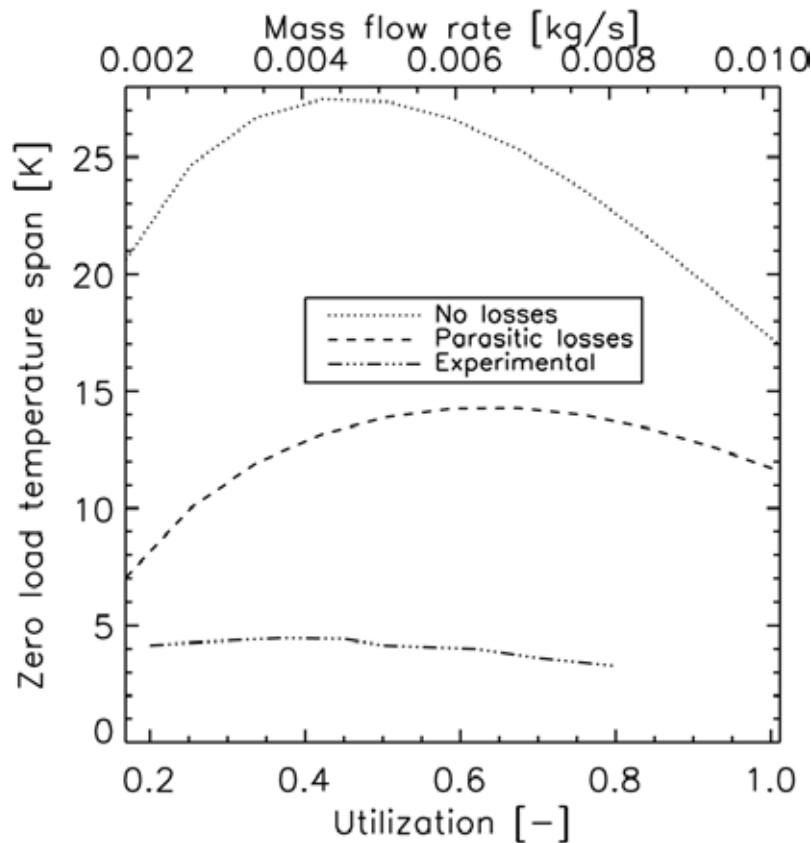


Figure 3: Zero load temperature span of the AMR device as a function of utilization for a 7 second AMR cycle. The two curves showing modeling results are distinguished since one does not include thermal parasitic losses to the ambient whereas the other does. It is seen that the model seriously over-predicts the performance of the experimental device even though including thermal losses to the ambient makes the model and experiment results more similar.

3. Conclusion

A numerical AMR model and a numerical for the demagnetizing field were used to analyze the performance of an experimental AMR device. The spatial variation of the magnetic field was taken into account as was the regenerator geometry. Considering cases with and without thermal parasitic losses it was shown that the numerical AMR model significantly over predicts the zero load temperature span of the experiment. Since the magnetic field change in the experiment is rather high (from zero to 1.65 tesla), the used material is Gd and the fluid channels are quite thin a better performance from the experiment is expected (see e.g. Tura and Rowe 2009, Nielsen et al. 2010). It was justified that the AMR model may over predict the performance by some amount but in this case the discrepancy is at a level where other explanations seem in place. It was investigated whether thermal parasitic losses or the effect of demagnetization could explain the observed discrepancy; however, in both cases the conclusion is that these effects are unlikely to cover most of the difference between model and experiment. It was rather argued that the stainless steel casing acting as regenerator housing would have such a large thermal conductivity that the regenerator in practice is “short-circuited” thermally, i.e. the thermal gradient is partially destroyed by the housing. Further experiments in the future using polymer housings will decide whether this is in fact the explanation.

Acknowledgements

K.K. Nielsen thanks the support of the Programme Commission on Energy and Environment (EnMi) (Contract no. 2104-06-0032), which is part of the Danish Council for Strategic Research, and the Danish

Agency for Science, Technology and Innovation under the Danish Ministry for Science, Technology and Innovation.

References

- Aharoni, A, "Demagnetizing factors for rectangular ferromagnetic prisms", 1998, *Journal of Applied Physics* 83, 6, 3432-3434
- Bahl, C.R.H., Nielsen, K.K., "The effect of demagnetization on the magnetocaloric properties in gadolinium", 2009, *Journal of Applied Physics* 105, 013916
- Bouchard, J., Nesreddine, H., Chahine, R., "Impact of demagnetization on magnetocaloric effect in pure gadolinium", 2005, In: Egolf, P.W. (ed.), *First International Conference on Magnetic Refrigeration at Room Temperature*, International Institute of Refrigeration, Montreux, Switzerland pp. 93-101.
- Bouchard, J., Nesreddine, H., Galanis, N., "Model of a porous regenerator used for magnetic refrigeration at room temperature", 2009, *International Journal of Heat and Mass Transfer* 52, 1223-1229
- Dankov, S. Yu., Tishin, A.M., Pecharsky, V.K. and Gschneidner Jr, K.A., 1998, "Magnetic phase transitions and the magnetothermal properties of gadolinium", *Physical Review B* 57, 6, 3478-3490.
- Dikeos, J., Rowe, A. and Tura, A., "Numerical Analysis of an active magnetic regenerator (AMR) refrigeration cycle", 2006, *AIP proceedings*, 823, 993-1000
- Engelbrecht, K. 2008, PhD thesis, Univ. of Wisconsin, Madison
- Jacobs, S., "Modeling and optimal design of a multilayer active magnetic refrigeration system", 2009, In: Egolf, P.W. (ed.), *Third International Conference on Magnetic Refrigeration at Room Temperature*, International Institute of Refrigeration, Des Moines, Iowa, USA, pp. 267-273.
- Nielsen, K. K., Bahl, C.R.H., Smith, A., Bjørk, R., Pryds, N. and Hattel, J., "Detailed numerical modeling of a linear parallel-plate Active Magnetic Regenerator", 2009a, *Int. J. of Refrig.* 32, 1478-1486.
- Nielsen, K. K., Pryds, N., Smith, A., Bahl, C.R.H. and Hattel, J., "2-dimensional numerical modeling of active magnetic regeneration", 2009b, In: Egolf, P.W. (ed.), *Third International Conference on Magnetic Refrigeration at Room Temperature*, International Institute of Refrigeration, Des Moines, Iowa, USA, pp. 251-258.
- K.K. Nielsen, K. Engelbrecht, C.R.H. Bahl, A. Smith, N. Pryds and J. Hattel, "Numerical modeling of multi-material active magnetic regeneration", 2009c. In: J.S. Szmyd, J. Spalek and T.A. Kowalewski (editors), *7th World Conference on Experimental Heat Transfer, Fluid Mechanics and Thermodynamics*, Krakow, Poland, pp. 515-522.
- Nielsen, K.K., Bahl, C.R.H., Smith, A., Pryds, N. and Hattel, J., "A comprehensive parameter study of an active magnetic regenerator using a 2D numerical model", 2010, *International Journal of Refrigeration*, 33, 753-764.

Oliveira, P.A., Trevizoli, P.V., Barbosa Jr., J.R., Prata, A., 2009, “Numerical analysis of a reciprocative active magnetic regenerator – part I”, 2009, In: Egolf, P.W. (ed.), Third International Conference on Magnetic Refrigeration at Room Temperature, International Institute of Refrigeration, Des Moines, Iowa, USA, pp. 283-288

Peksoy, O. and Rowe, A., “Demagnetizing effects in active magnetic regenerators”, 2005, Journal of Magnetism and Magnetic Materials 288, 424-432

Petersen, T.F., Pryds, N., Smith, A., Hattel, J., Schmidt, H. and Knudsen, H.J.H., “Two-dimensional mathematical model of a reciprocating room-temperature Active Magnetic Regenerator”, 2008b, Int. J. of Refrig. 31, 432-443.

A. Tura and A. Rowe, “Progress in the characterization and optimization of a permanent magnet magnetic refrigerator”, 2009, In: Egolf, P.W. (ed.), Third International Conference on Magnetic Refrigeration at Room Temperature, International Institute of Refrigeration, Des Moines, Iowa, USA, pp. 387-392.

Sarlah, A., Poredos, A., “Regenerator for magnetic cooling in shape of honeycomb”, 2005, In: Egolf, P.W. (ed.), First International Conference on Magnetic Refrigeration at Room Temperature, International Institute of Refrigeration, Montreux, Switzerland pp. 283-290.

Smith, A., Nielsen, K.K., Christensen, D.V., Bahl, C.R.H., Bjørk, R. and Hattel, J., “The demagnetizing field of a rectangular prism”, 2010, Journal of Applied Physics 107, 103910

Trevizoli P. V., Barbosa Jr, J. R., Oliveira P. A., Prata A. T., Ferreira R.T.S. “Direct measurements of the magnetocaloric effect of gadolinium samples at near room temperature”. In: Proceedings of 20th International Congress of Mechanical Engineering (COBEM). Gramado, Brazil, 2009.

Trevizoli, P.V., Barbosa Jr., J.R. and Ferreira, R.T.S., “Design and preliminary results of a Gd-based linear reciprocating active magnetic regenerator test apparatus”, 2010. In: Egolf, P.W. (ed.) Fourth International Conference on Magnetic Refrigeration at Room Temperature, International Institute of Refrigeration, Baotou, Inner Mongolia, China, pp. ???-???

-
- A.3.6 Numerical modeling in magnetic refrigeration; published in the proceedings of the 50th International Conference of Scandinavian Simulation Society, Modelling and Simulation of Energy Technology (SIMS 50)

NUMERICAL MODELING IN MAGNETIC REFRIGERATION

R. Børk, C. R. H. Bahl, A. Smith and N. Pryds,
Technical University of Denmark
Fuel Cells and Solid State Chemistry Division
Risø National Laboratory for Sustainable Energy
DK-4000 Roskilde
Denmark

K. K. Nielsen and J. Hattel
Technical University of Denmark
Department of Mechanical Engineering
DK-2800 Lyngby
Denmark

ABSTRACT

A magnetic refrigeration device built at Risø DTU is presented. For this device there are two important physical systems whose design must be carefully considered. The first is the permanent magnet assembly where the optimal economic values for the magnet design are found based on numerical simulations. A physical magnet was constructed and measurements of the flux density are compared with simulation, showing a good agreement. The second is the design of the so-called Active Magnetic Regenerator (AMR) which is the active core of the refrigeration system. A transient heat transfer 2.5-dimensional numerical model to model AMR is presented. The model is shown to reproduce experimental data from the Risø DTU magnetic refrigeration device.

Keywords: **Magnetic refrigeration, Magnetic field, Heat transfer, Finite element, Finite difference**

INTRODUCTION

Magnetic refrigeration is an evolving technology that has the potential of high energy efficiency and the usage of environmentally friendly refrigerants [1]. Magnetic refrigeration is based on the magnetocaloric effect (MCE). The MCE is observed in magnetic materials when subjected to a change in magnetic field. Under adiabatic conditions, most materials exhibit an increase in temperature when the field change is positive and a decrease when the change is negative. An increase in magnetic field tends to order the magnetic moments and thus lowers the magnetic entropy. Since the total entropy is constant under adiabatic conditions the lattice and electron entropies must increase and thus the temperature of the material rises. If the MCE of the material is reversible, the temperature will decrease

when the field is removed since the direction of the magnetic moments will be randomized when no external field is present. This increase/decrease in temperature is called the adiabatic temperature change, ΔT_{ad} . Magnetocaloric materials exhibit a maximum in the MCE at the transition temperature between a ferromagnetic and a paramagnetic phase, known as the Curie temperature, T_c . Different magnetocaloric materials have different values of T_c [2].

One of the keystones of using magnetocaloric materials (MCMs) as refrigerants is their inherent reversibility (for materials of interest), which allows for an efficient refrigeration process. However, the MCE in the best materials currently available show a temperature change of no more than around 4 K in an magnetic field of around 1 T. Thus a simple reverse thermodynamic cycle will not be able to produce significant refrigeration at reachable magnetic

Corresponding author: E-mail: rab @risoe.dtu.dk

fields from permanent magnets. Therefore the active magnetic regeneration (AMR) cycle is applied. This process combines the MCE of the MCM as work input with the MCM, i.e. the refrigerant, at the same time working as a regenerator. A heat transfer fluid is used to exchange heat between the solid and heat exchangers at the hot and cold ends respectively. Four steps are normally used to characterize the AMR process. These are

1. Adiabatic magnetization, which increases the temperature of the refrigerant.
2. The hot blow period, where the heat transfer fluid is blown from the cold to the hot end, allowing heat from the solid to be rejected at the hot end.
3. Adiabatic demagnetization, which lowers the temperature of the refrigerant.
4. The cold blow where the heat transfer fluid is blown from the hot end to the cold end and thus absorbs a cooling load in the cold end.

The regenerator is a porous structure made of the MCM, with the heat transfer fluid filling the void space. The AMR system cannot be described by a conventional refrigeration cycle since each differential element of the regenerator undergoes its own specific thermodynamic cycle. The scientific problem of magnetic refrigeration consists of a combination of regenerator-effectiveness, the non-linear MCE and an application of an external magnetic field.

In this paper the focus is on the numerical modeling of a magnetic refrigeration test machine constructed at Risø DTU [3, 4]. The test machine is a reciprocating device using parallel plates of magnetocaloric material and using a cylindrical permanent magnet assembly to create the magnetic field.

THE RISØ DTU MAGNETIC REFRIGERATION DEVICE

The test machine, which is pictured in Fig. 1, consists of a regenerator core in the middle of a plastic tube with an outer diameter of 40 mm and an inner diameter of 34 mm. The regenerator core contains 13 precision machined grooves to hold plates of magnetocaloric material with dimensions 40 mm along the flow direction, 0.9 mm thick and 25 mm

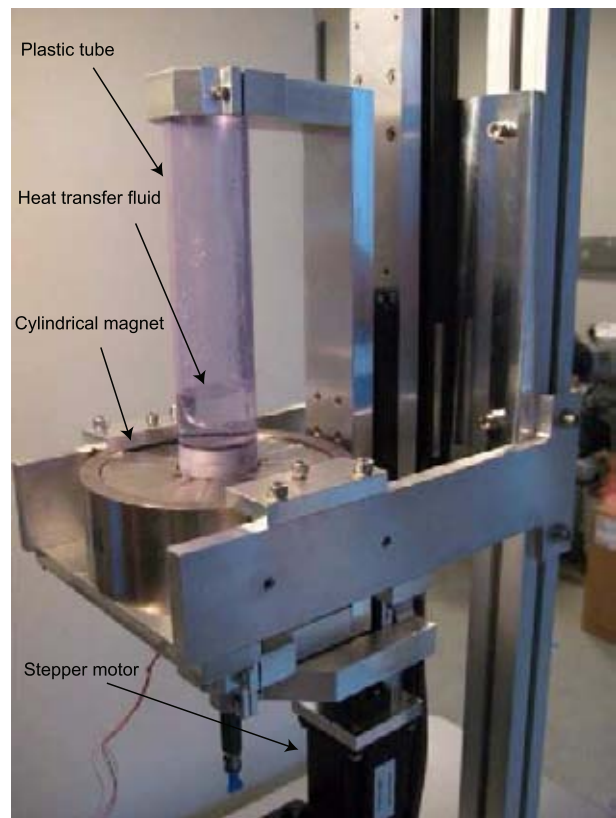


Figure 1: The test machine in its operational environment. The cylindrical permanent magnet assembly can be seen in the center of the picture. Also the plastic tube, filled with water, holding the regenerator core (not visible) can be seen. The regenerator core is inside the magnet. The motor for moving the regenerator core is visible at the bottom of the photo.

wide. The plates are separated by a 0.8 mm spacing which is then the thickness of the fluid channel. A close up photo of the regenerator can be seen in Fig. 2.

The heat transfer fluid is moved using a piston. Five type E thermocouples are placed in the center flow channel of the regenerator so the temperature profile in the AMR can be recorded during an experiment. The permanent magnet assembly that provides the magnetic field can be seen in Fig. 1. This has the shape of a cylinder. The assembly provides a maximum magnetic field of 1.1 T. The regenerator is moved in and out of the magnetic field by a stepper motor.

The total system is compact and is generally easy to handle. The setup allows for easy change of the plates of MCM as well as the heat transfer fluid. Dif-

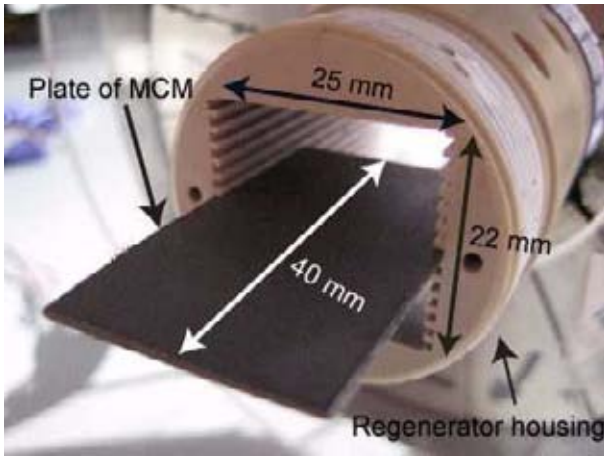


Figure 2: A close-up of the experimental AMR regenerator bed with a plate of MCM material sticking out of the regenerator. The regenerator bed can contain 13 parallel plates.

ferent AMR parameters such as piston stroke length and cycle time are easily adjustable using a custom LabView computer controlled interface.

THE PERMANENT MAGNET ASSEMBLY

In general a magnetic field can be produced by an electromagnet or by a permanent magnet assembly. For the test machine the permanent magnet assembly was chosen as it requires no external power source to produce a magnetic field. The design requirement for the permanent magnet assembly is that it produces a homogenous high flux density magnetic field in a confined region of space and a very weak field elsewhere. The Halbach cylinder design [5, 6] was chosen, because it fulfills the requirements, is compact and relatively simple to assemble.

A Halbach cylinder consists of a permanent magnetic material with a bore along the cylinder symmetry axis in which the magnetic field is concentrated. The magnet is magnetized such that the direction of magnetization varies continuously as, in polar coordinates,

$$\begin{aligned} B_{rem} r &= B_{rem} \cos \theta \\ B_{rem} \theta &= B_{rem} \sin \theta \end{aligned} \quad (1)$$

where B_{rem} is the magnitude of the remanent flux density. An illustration of the Halbach cylinder can be seen in Fig. 3. The Halbach cylinder can be char-

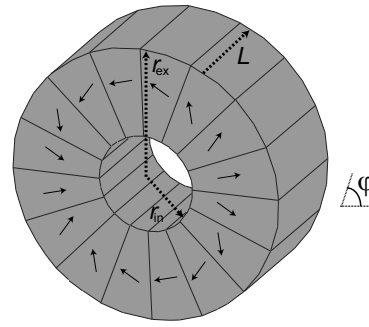


Figure 3: A illustration of a 16 segmented Halbach magnet. Shown as arrows is the direction of magnetization. The internal and external radii, r_{in} and r_{ex} , respectively, and the length, L are also shown.

acterized by three parameters: the internal and external radii, r_{in} and r_{ex} , respectively, and the length, L . For practical applications the Halbach cylinder is built up from segments each with their own direction of magnetization. The Halbach cylinder used for the test machine consists of 16 blocks of permanent magnets. This configuration yields 95% of the flux density of an unsegmented continuous Halbach cylinder [7].

Dimensioning the magnet

As the magnet is the single most expensive part of a magnetic refrigeration device the magnet must be dimensioned such that it uses the minimum amount of magnetic material while at the same time producing a homogenous high flux density over as large a volume as possible. Based on these requirements a magnet assembly can be characterized by three parameters. The first is the volume in which the magnetic field is created, in this case the volume of the cylinder bore. The second is the volume of magnet used to create the magnetic field, in this case the volume of the Halbach cylinder. The third is the flux density of the created magnetic field.

To find the optimal dimensions of the Halbach cylinder for the test machine we have conducted a series of parameter variation simulations using the commercially available finite element multiphysics program, *Comsol Multiphysics*[8]. The Comsol Multiphysics code has previously been validated through a number of NAFEMS (National Agency for Finite Element Methods and Standards) benchmark studies [9].

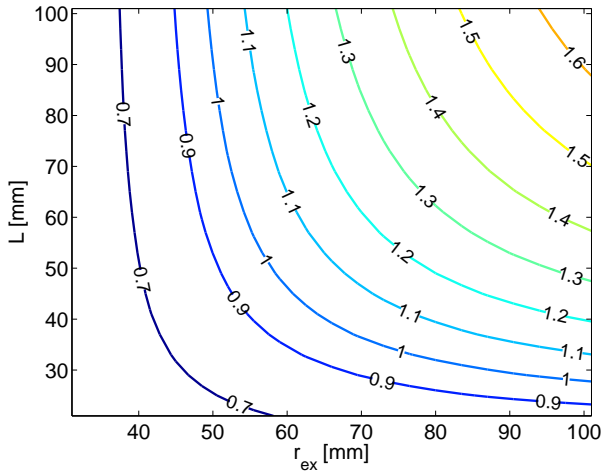


Figure 4: Contours of the mean flux density as a function of external radius and length. Each contour is labeled by its mean flux density. The maximum flux density is obtained by maximizing both r_{ex} and L .

The equation solved in the simulations is the magnetic vector potential equation,

$$\nabla \cdot \left(\frac{1}{\mu_r} \nabla \mathbf{A} \right) + \mathbf{B}_{\text{rem}} = 0 \quad (2)$$

where \mathbf{A} is the magnetic vector potential, \mathbf{B}_{rem} is the remanent flux density, μ_0 is the permeability of free space and μ_r is the relative permeability assumed to be isotropic. A finite element mesh is used as this provides high resolution near geometric connections, e.g. corners. The solver used to solve Eq. 2 on the simulation mesh is *Pardiso* which is a parallel sparse direct linear solver [10, 11]. Boundary conditions are chosen such that the boundaries of the computational volume, which is many times larger than the Halbach cylinder, are magnetically insulating, while all other (internal) boundaries are continuous.

The parameters that were varied were the external radius and the length of the Halbach cylinder. The internal radius of the Halbach cylinder was fixed at $r_{\text{in}} = 21$ mm to fit the regenerator bed. The external radius was varied in the range $r_{\text{ex}} = 31 - 101$ mm in steps of 1 mm while the length was varied in the range $L = 21 - 101$ mm in steps of 1 mm. All in all 5751 simulations were performed. For all simulations a remanent magnetization of the individual magnet of 1.4 T was used.

Shown in Fig. 4 are contours of equal mean flux density in the cylinder bore as a function of external

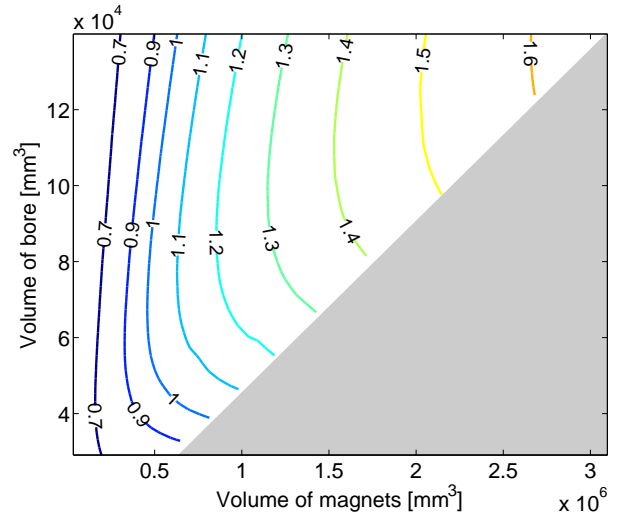


Figure 5: Contours of the mean flux density as a function of the volume of magnets used and the volume of the cylinder bore. It is seen that there is a minimum amount of magnet for each mean flux density contour. Also the volume of the bore can be significantly increased by slightly increasing the volume of the magnets.

radius and length. From this figure it can be seen that increasing the external radius or the length will increase the mean flux density in the cylinder bore. However it cannot be seen which parameters produce the largest flux density over the biggest volume with the minimum amount of magnetic material.

In Fig. 5 contours of equal mean flux density are plotted as a function of the volume of the magnet and the volume of the bore. Using these variables it can be seen that for each flux density there is a minimum value of the volume of the magnet. This is the most economic design as it uses the minimum amount of magnetic material to produce a given mean flux density. However it can also be seen that by increasing the amount of magnetic material slightly the volume of the bore can be significantly increased.

The data points in Fig. 5 (not shown) can be mapped to a specific value of the external radius and length. By finding the minimum value of the volume of the magnet for a range of mean flux densities and recording the external radius and length for this configuration the optimal economic values for r_{ex} and L are found. These are shown in Fig. 6.

From this figure one can get the external radius and length of the Halbach cylinder with the minimum volume of the magnet that produces a given mean

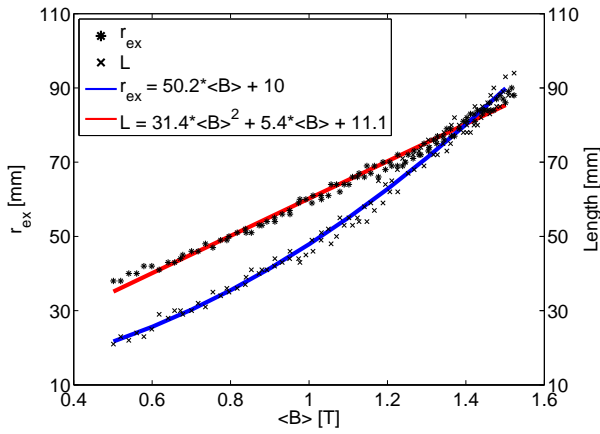


Figure 6: The optimal r_{ex} and L as functions of the mean flux density. Polynomials have been fitted to the data to ease interpolation. Building a Halbach cylinder with an internal radius of 21 mm with dimensions different from the dimensions given here means that more magnetic material is used than need be, if one does not care about the volume of the bore.

flux density. A first order polynomial has been fitted to the external radius data points while a second order polynomial has been fitted to the length data points.

Based on Fig. 6 and a design requirement that the magnet for the test machine should provide a mean flux density of around 1 T, an external radius of the Halbach cylinder of 60 mm and a length of 50 mm was chosen.

The physical magnet

Having found the dimensions of the ideal Halbach cylinder for the test machine a magnet was constructed. The actual Halbach cylinder, part of which can be seen on Fig. 1, has an inner radius of 21 mm, an outer radius of 60 mm and a length of 50 mm. The volume of the magnet is 0.50 L and the volume of the cylinder bore is 0.07 L. We have measured the flux density along the central axis of the Halbach cylinder using a Hall probe and the result is shown in Figure 7. Also shown is the flux density obtained from simulation. As can be seen from the figure the numerical simulation and the experimental measurements agree, and show that a high flux density is produced in the center of the cylinder bore. The small difference between simulation and measurement can be due to uncertainty in the

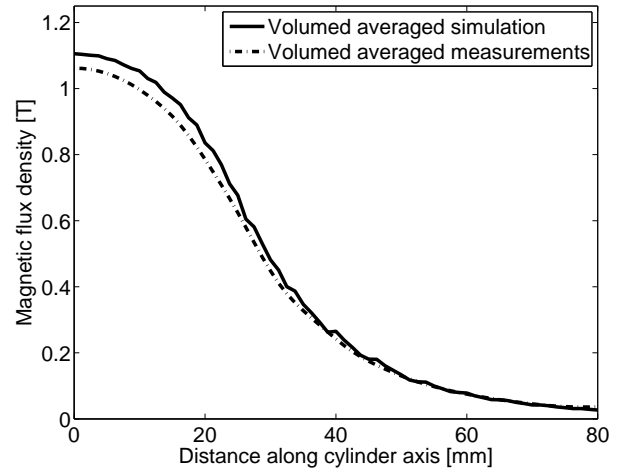


Figure 7: The measured and simulated flux density for the Halbach cylinder for the test machine.

magnet specifications and manufacturing processes as well as measuring uncertainty.

THE AMR MODEL

As the coupling between magnetic field, MCE, fluid-solid heat transfer and the thermal properties of the MCM is highly non-linear, numerical modeling is needed to understand the physics and response of the AMR system to changes in geometry, operating parameters and material composition. Such a model has developed at Risø DTU [12, 14]. The model is 2-dimensional, resolving the flow-direction (parallel to the MCM plates) and the direction perpendicular to the flow and the plane of the plates. Thus the internal gradients are resolved, while the plates are assumed wide enough that boundary effects are negligible. However, the model features an option to model the ambient temperature in the not-resolved dimension through a simple thermal resistive formulation. The governing equations are for the fluid

$$c_p \rho_f \frac{\partial T_f}{\partial t} + \mathbf{u} \cdot \nabla T_f = k_f \nabla^2 T_f \quad (3)$$

and solid

$$c_p \rho_s \frac{\partial T_s}{\partial t} = k_s \nabla^2 T_s \quad (4)$$

respectively. Subscripts f and s stand for fluid and solid respectively. The thermal properties are mass density, ρ , and thermal conductivity k , both assumed constant, and specific heat capacity, c_p , which is a

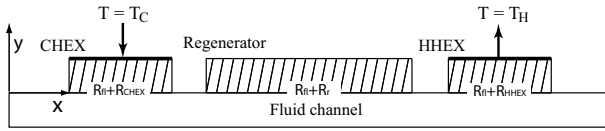


Figure 8: The 2-dimensional geometry of the AMR model. The model exploits symmetry and thus only half a fluid channel and half the solid domains are modeled. All thermal boundary conditions are isolating except those otherwise indicated.

function of temperature and magnetic field. Temperature is denoted T and time is t . Finally, the velocity of the fluid is denoted \mathbf{u} . The solid and fluid domains are coupled via inner boundaries. These slide to simulate the fluid movement and the resulting velocity profile is

$$u_y = \tilde{u} \frac{6y^2}{H_f^2} \quad (5)$$

Here the y direction is perpendicular to the flow and the plane of the MCM-plates. The velocity profile only has a component in the x direction (parallel to the flow) since it is assumed to be fully developed, laminar and incompressible. The mean fluid velocity is denoted \tilde{u} and the thickness of the fluid channel is H_f .

The geometry of the model is displayed in Fig. 8. The model exploits symmetry and thus only half a fluid channel and half a solid domain are modeled. The model is solved using a spatial discretization based on finite differences of 2nd order and the alternate direction implicit (ADI) method for the temporal integration. The code is written by the authors and maintained at Risø DTU and available in generic Fortran. A detailed description of the model is available in [12].

The magnetocaloric effect (MCE) can be modeled either using the mean field theory (MFT) [13] or using experimental data when available).

Thermal parasitic losses

The model is able to include thermal parasitic losses to the ambient in the z -direction, i.e. the dimension not resolved spatially. This formulation is straightforwardly written in terms of thermal resistances

$$Q_{\text{loss}} = \frac{T_{\infty} - T}{\sum_i R_i} \quad (6)$$

The ambient temperature is denoted T_{∞} and the thermal resistances are denoted R_i . This expression is applied for each grid cell, which individually has the temperature T . The thermal resistance sum has three main contributors namely the resistance in the domain under consideration (MCM or fluid), the plastic housing and finally natural convection between the housing and the ambient. Thus, the sum becomes

$$\sum R_i = \frac{1}{k_f \Delta x \Delta y} + \frac{2 \Delta z_f}{k_{pl} \Delta x \Delta y} + \frac{\Delta z_{pl}}{h_{\text{conv}} \Delta x \Delta y} \quad (7)$$

in the case of the fluid (the subscript is simply substituted for the appropriate domain). In this expression the thickness of the domain, Δz_f , has been introduced as well as the area of the individual grid cell perpendicular to the z direction, $\Delta x \Delta y$. The subscript pl stands for plastic. Finally, the natural convection parameter is denoted h_{conv} .

The purpose of including the parasitic losses to the ambient is to model in detail the exterior circumstances to a specific AMR experiment. For ideal modeling, i.e. where the optimal performance is sought for the theoretical AMR device, such losses are without meaning. However, when modeling experimental results they can be of great significance. The expression in Eq. 6 is added as a source term in Eqs. 3 and 4.

Results from the AMR modeling

A wide range of results exist from the current AMR model. These range from theoretical AMR modeling, which aims at understanding the basic principles of active magnetic regeneration both in terms of regenerator efficiency and material composition [15], to modeling of the actual test machine located at Risø DTU [16]. In the latter case e.g. the thermal parasitic losses are taken into account. This way of modeling the AMR problem from different perspectives provides a basis for understanding how to obtain the optimal performance as well as understanding the shortcomings of the experiment (e.g. significance of thermal losses, demagnetization effects [17] etc).

Results from a fluid-displacement variation experiment using gadolinium as MCM and water as heat transfer fluid are showed in Fig. 9. The figure shows a clear dependency of the zero heat-load temperature span as function of fluid displacement. Furthermore,

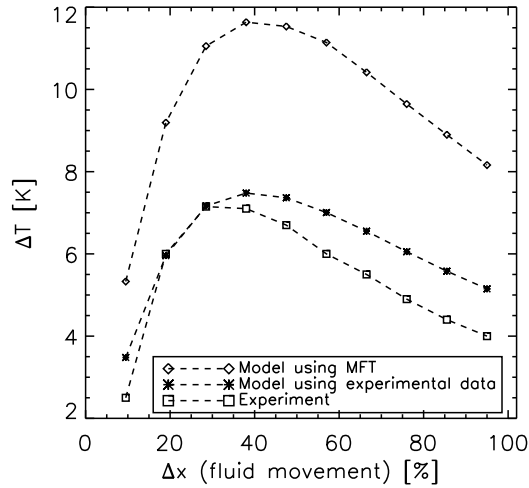


Figure 9: An example of a result from the numerical AMR model compared to the experimental device. The ambient temperature was set to 298 K and gadolinium was used as the MCM and water as the heat transfer fluid. In this figure the no heat-load temperature span is plotted as function of fluid displacement during the AMR process. The two different modeling situations are different in the sense that one uses the mean field theory (MFT) to calculate the MCE and the other uses experimental data from [17]. Reproduced from [12].

it is evident from the figure that the input MCE should be carefully used. The clearly overestimating model-curve is from a modeling series where the mean field theory (MFT) was used to calculate the MCE (see [18] for details on the MFT). The model-curve that is almost overlying with the experimental values uses experimentally obtained data. This shows that the model is quite sensitive to the input MCE, which is important since magnetocaloric data in general are not abundant for most MCMs and thus an effort towards characterizing MCMs in detail is needed.

Figure 10 shows the significance of including the thermal parasitic losses. The experiment was run using gadolinium as MCM and water as heat transfer fluid at a total cycle timing of about 9 seconds, and thus the parasitic losses have plenty of time to destroy the regeneration.

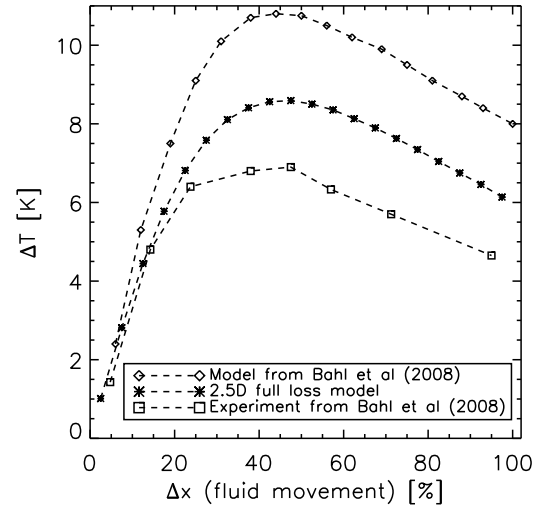


Figure 10: An example of the impact of including the thermal parasitic losses (denoted 2.5D full loss model). The losses are seen to have a significant impact on the experimental results. Reproduced from [12].

CONCLUSION

A magnetic refrigeration test device made at Risø DTU was presented. The Halbach cylinder magnet design for the device was discussed and optimal economic dimensions for the magnet were found. The magnet was constructed and the flux density was measured and compared with simulation and a good agreement was found. Also a numerical AMR model was presented and some results discussed. The modeling shows that the magnetocaloric effect should be carefully implemented, i.e. when modeling experiments real experimental MCE data should be applied when available. Furthermore, it was shown that including the thermal parasitic losses to the ambient greatly improves the resembles of the model and the experiment. Thus, an important point when designing an AMR experiment is to minimize the impact of parasitic losses. This can be done by e.g. increasing the operating frequency.

ACKNOWLEDGEMENTS

We thank Mr. Jørgen Geyti for his technical help. The authors further acknowledge the support of the Programme Commission on Energy and Environment (EnMi) (Contract No. 2104-06-0032), which is part of the Danish Council for Strategic Research.

REFERENCES

- [1] Gschneidner Jr K A and Pecharsky V. *Thirty years of near room temperature magnetic cooling: Where we are today and future prospects*. Int. J. Refrig., 2008;31(6):945.
- [2] Pecharsky V K and Gschneidner K A Jr. *Advanced magnetocaloric materials: What does the future hold* Int. J. Refrig. 2006;29:1239-1249.
- [3] Bahl C R H, Petersen T F, Pryds N and Smith, A. *A versatile magnetic refrigeration test device* Rev. Sci. Inst. 2008;79(9):093906
- [4] Engelbrecht K, Jensen J B, Bahl C R H and Pryds N. 2009. *Experiments on a modular magnetic refrigeration device* Proc. 3rd Int. Conf. on Magn. Refrig. at Room Temp. 2009;IIF/IIR.
- [5] Mallinson J C. *One-sided Fluxes - A Magnetic Curiosity* IEEE Trans. Magn. 1973;9(4):678.
- [6] Halbach K. *Design of permanent multipole magnets with oriented rare earth cobalt material* Nucl. Instrum. Methods 1980;169.
- [7] Bjørk R, Bahl C R H, Smith A and Pryds N. *Optimization and improvement of Halbach cylinder design* J. Appl. Phys. 2008;104:13910.
- [8] COMSOL AB, Tegnergatan 23, SE-111 40 Stockholm, Sweden.
- [9] Comsol, Comsol Multiphysics Model Library, third ed. COMSOL AB, Chalmers Teknikpark 412 88 G (2005).
- [10] Schenk O, Gartner K, Fichtner W and Stricker A., *PARDISO: A High-Performance Serial and Parallel Sparse Linear Solver in Semiconductor Device Simulation* J. of Future Gener. Comput. Syst. 2001;18:69.
- [11] Schenk O and Gartner K. *Two-Level Scheduling in PARDISO: Improved Scalability on Shared Memory Multiprocessing Systems* Parallel Comput. 2002;28
- [12] Nielsen K K, Bahl C R H, Smith A, Pryds N, Bjørk R and Hattel J. *Detailed numerical modeling of a linear parallel-plate active magnetic regenerator* Int. J. Refrig. 2009, doi:10.1016/j.ijrefrig.2009.03.003
- [13] Morrish *The physical principles of magnetism*. New York: John Wiley and Sons Inc., 1965.
- [14] Nielsen K K, Pryds N, Smith A, Bahl C R H and Hattel J. *2-dimensional numerical modeling of active magnetic regeneration* Proc. 3rd Int. Conf. on Magn. Refrig. at Room Temp. 2009;IIF/IIR.
- [15] Nielsen K K, Bahl C R H, Smith A., Pryds N. and Hattel J. *On the ideal cooling capacity of gadolinium in active magnetic regenerative refrigeration 2009*;In prep.
- [16] Nielsen K K, Engelbrecht K, Bahl C R H, Smith A, Pryds N and Hattel J. *Numerical modeling of multi-material active magnetic regeneration* Proc. 7th World Conf. on Exp. Heat Transf., Fluid Mech. and Thermodyn. 2009.
- [17] Bahl, C R H and Nielsen, K K. *The effect of demagnetization on the magnetocaloric properties of gadolinium*. J. Appl. Phys. 2009;105:013916.
- [18] Petersen T F, Pryds N, Smith A, Hattel J, Schmidt H and Knudsen H. *Two-dimensional mathematical model of a reciprocating room-temperature active magnetic regenerator*. Int. J. Refrig. 2008;31:432.
- [19] Rowe A & Barclay J. *Ideal magnetocaloric effect for active magnetic regenerators* J. Appl. Phys. 2003;93:1672

- A.3.7 An experimental study of passive regenerator geometries; published in the proceedings of the 4th International Conference on Magnetic Refrigeration at Room Temperature

AN EXPERIMENTAL STUDY OF PASSIVE REGENERATOR GEOMETRIES

K. Engelbrecht^(a), K. K. Nielsen^(b), N. Pryds^(a)

^(a) Risø National Laboratory for Sustainable Energy, Frederiksborgevej 399,
Roskilde, 4000, Denmark

+45 4677 5649/kuen@risoe.dtu.dk

^(b) Technical University of Denmark - DTU, Produktionstorvet, building 425,
Kgs. Lyngby, 2800, Denmark

ABSTRACT

To optimize the design of an active magnetic regenerative (AMR) system, it is crucial to understand both the regenerator design and magnetocaloric properties of the system. This paper investigates methods of improving the performance of flat-plate regenerators for use in AMR systems. In order to eliminate experimental uncertainty associated with magnetocaloric material properties, all regenerators are made of aluminum. The performance of corrugated, plates and dimpled plates are compared to traditional flat plate regenerators for a range of cycle times and utilizations. Each regenerator is built using 18 aluminum plates with a 0.4 mm thickness, which allows their performance to be compared directly.

1. INTRODUCTION

Heat transfer losses between the fluid and magnetocaloric material are a major loss mechanism in AMR systems. In order to maximize AMR performance, it is critical to understand heat transfer processes in the regenerator. This paper investigates methods of improving the performance of regenerators based on flat plates for use in AMR systems. In order to eliminate experimental uncertainty associated with magnetocaloric material properties, all regenerators are made of aluminum. A simple and flexible passive regenerator test setup has been developed where a heater is applied to the hot reservoir and the steady state reservoir temperatures are measured. The performance of each regenerator is determined by the regenerator effectiveness defined by the heat load and resulting temperature span.

Theoretically, flat plate regenerators offer the best heat transfer to pressure drop ratio (Sarlah, 2008) for common regenerator designs. However, high-performance flat-plate regenerators require a very small plate thickness and plate spacing, making fabrication difficult. This paper investigates the effectiveness of flat plate passive regenerators with varying plate spacing as well as several alternative regenerator geometries based on flat plates. Regenerator geometries that may improve thermal performance including corrugated, or chevron, plates were constructed and compared to flat plate regenerators experimentally. The conclusion of this paper is a suggested geometry for a prototype AMR.

2. EXPERIMENTAL APPARATUS

The experiment is comprised of a single regenerator in contact with hot and cold fluid reservoirs. Fluid flow is provided by a displacer in the hot reservoir, which is also equipped with a heater. The device is the same described for AMR experiments in the past by Engelbrecht et al. (2009) and Bahl et

al. (2008). The device can be used for passive experiments by removing the magnetic field variation from the regenerator and forcing a temperature span across the passive regenerator by adding a heat load to one end. A resistive heater was placed in the hot reservoir and provides a heat load to the hot reservoir. A displacer provides alternating fluid flow through the regenerator and in each experiment, the system is cycled until steady state has been reached. The entire regenerator and both reservoirs are isolated from the environment by foam insulation. The cold reservoir communicates thermally with the environment through a heat exchanger and a secondary heat transfer fluid. The performance of the regenerator is determined by the temperature difference between the hot and cold reservoirs, which is a measure of the regenerator effectiveness.

3. REGENERATOR FABRICATION

Experiments were performed on a total of seven regenerators, each comprised of 18 aluminum plates 0.4 mm in thickness. By holding the mass of regenerator material constant, the utilization is held constant for the same displacer stroke while the porosity varies with the spacing between plates. The plates were laser cut to the desired length and width in order to keep them as flat as possible during the cutting process. Four flat plate regenerators with different plate spacing, two corrugated plate regenerators, and one dimpled plate regenerator were fabricated.

The flat plate regenerator stacks were fabricated using thin wire spacers to regulate the plate spacing. Sections of wire of varying diameter were stretched slightly to produce a straight wire with no sharp bends. The regenerator was stacked with two wires between each plate. After all the plates were stacked, the stack was compressed slightly to reduce the effects of slight bending of the wires and the plates were bonded with epoxy on both sides along the entire length of the plates in the flow direction. The resulting regenerator stack height was measured to determine the average effective plate spacing. Neither the variation in plate spacing nor the non-uniformity of the flow channels are reported for any regenerators in this paper. However, the effective average plate spacing is always slightly larger than the wire spacers, most likely due to non-uniform flatness and thickness of the plates, slight bending in the wire spacers, or possibly from variations introduced when the epoxy was applied.

The corrugated plates were formed by pressing the plate between interspaced cylinders 0.3 mm in diameter. The orientation of the cylinders in relation to the flow direction was controlled. The orientation of alternating plates was reversed, such that troughs in the plates created by the cylinders were never parallel and the plates could not nest on each other. Once all plates were stacked, the stack was compressed and the plates were sealed with epoxy on both sides. The dimpled plates were formed with a special tool consisting of half spheres 1 mm in radius on both halves of the tool. The half spheres are arranged on each half of the tool such that after the plate is formed to a shape similar to an egg crate pattern by the tool. The height of the dimpled pattern can be controlled by how far the halves of the tool are pressed together. Metal stops were placed between the pressing tool halves to yield pressed plates that were approximately 0.65 mm from peak to peak. The regenerator was assembled by alternating flat plates and dimpled plates, which gives an average fluid flow channel that is 0.25 mm.

Each regenerator stack was placed in an acrylic housing and sealed around the periphery of the stack with silicone to prevent heat transfer fluid from bypassing the regenerator stack. A photograph of the dimpled plate regenerator assembled in the housing is shown in Figure 1. A summary of the characteristics of each regenerator tested in this paper is given in Table 1.



Figure 1. The dimpled plate regenerator assembled in the regenerator housing

Table 1. A summary of the passive regenerators that were tested.

Regenerator	Type	Description	Porosity
1	flat plate	0.74 mm spacing	0.64
2	flat plate	0.31 mm spacing	0.43
3	flat plate	0.20 mm spacing	0.33
4	flat plate	0.10 mm spacing	0.20
5	corrugated plate	120 included angle	0.64
6	corrugated plate	90 included angle	0.64
7	dimpled plate	0.23 mm spacing	0.35

4. NUMERICAL MODEL

The experimental data for flat plate regenerators were compared to predictions from a 2D numerical regenerator model (Nielsen et al., 2009). The model treats the regenerator as a repeating cell of a half plate and half channel with an alternating fluid flow. The thermal governing equations solved by the model are given below.

$$\frac{\partial T_f}{\partial t} = \frac{k_f}{\rho_f c_{p,f}} \nabla^2 T_f - u \frac{\partial T_f}{\partial x} \quad (1)$$

$$\frac{\partial T_s}{\partial t} = \frac{k_s}{\rho_s c_{H,s}} \nabla^2 T_s \quad (2)$$

The subscripts f and s indicate fluid and solid, respectively. The thermal properties ρ and k denote the mass density and the thermal conductivity have been introduced. The heat transfer

between the solid and fluid domains is done through an internal boundary condition of the form

$$k_f \frac{\partial T_f}{\partial y} = k_s \frac{\partial T_s}{\partial y} \quad (3)$$

The numerical model converges to a steady state as a function of prescribed temperatures at the cold and hot sides, respectively. Modeling several temperature spans, keeping the hot side fixed, yields a heater power versus temperature span curve. From this, it is possible to intersect with the applied heater load from the experiment in order to find the resulting model temperature span.

5. EXPERIMENTAL RESULTS

Passive regenerators are generally defined by the effectiveness of the regenerator, which is defined below (Dragutinovic and Baclic, 1998).

$$\varepsilon = \frac{\int_0^\tau (T_H - T_{f,exit}) dt}{(T_H - T_C)} \quad (4)$$

Where τ is the blow period and $T_{f,exit}$ is the temperature of the fluid exiting the regenerator. Equation (4) can be interpreted as one minus the heater power necessary to maintain a reservoir temperature divided by the maximum energy required to heat the fluid from the cold reservoir temperature to the hot temperature. For the experiments considered here, the heater power in the hot reservoir is held constant and the cold reservoir temperature is fixed. Therefore, the temperature span achieved by each regenerator is a direct measurement of its effectiveness, and regenerator performance is reported in terms of temperature span in this paper.

In each experiment, a heater power of 1.2 W was applied to the hot reservoir. In one set of experiments, the heat transfer fluid was water and the second set the heat transfer fluid was a mixture of 75% water and 25% ethylene glycol. Therefore, the experiments using different heat transfer fluids are not directly comparable. The dimpled plate regenerator, both corrugated plate regenerators and one flat plate regenerator were all tested with pure water as the heat transfer fluid and selected results are shown in Figure 2.

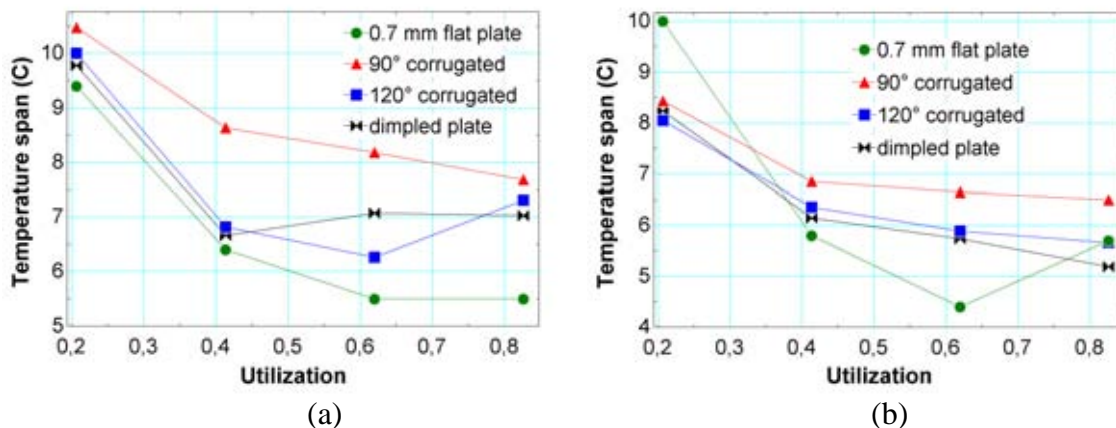


Figure 2. Temperature span as a function of utilization for four different regenerator geometries for a fluid flow rate of 0.7 g/s (a) and 2.7 g/s (b).

Figure 2 shows that the corrugated plates with a 90° included angle generally exhibit the highest effectiveness while the flat plate regenerator generally exhibits the worst regenerator performance. The plate spacing for the flat plate regenerator was chosen to correspond to the average plate spacing for the corrugated plate regenerators. However, the dimpled plate spacing was dictated by the tool used to form the plates and the resulting plate spacing was smaller than the other regenerators shown in Figure 2. Therefore, the dimpled plates have an advantage over the other regenerators, but a significant increase in performance was not measured. These experiments suggest that a corrugated plate regenerator can offer increased performance over a flat plate regenerator and that a 90° included angle relative to the flow direction performs better than plates with a 120° angle of corrugation.

The next set of experiments was performed with a mixture of water and ethylene glycol as the heat transfer fluid for four regenerators with plate spacing of approximately 0.1 mm, 0.2 mm, 0.3 mm and 0.7 mm. The heater power applied to the hot reservoir was 1.2 W. Experiments were run for a range of fluid flow rates and utilizations, and the results for two flow rates are shown in Figure 3.

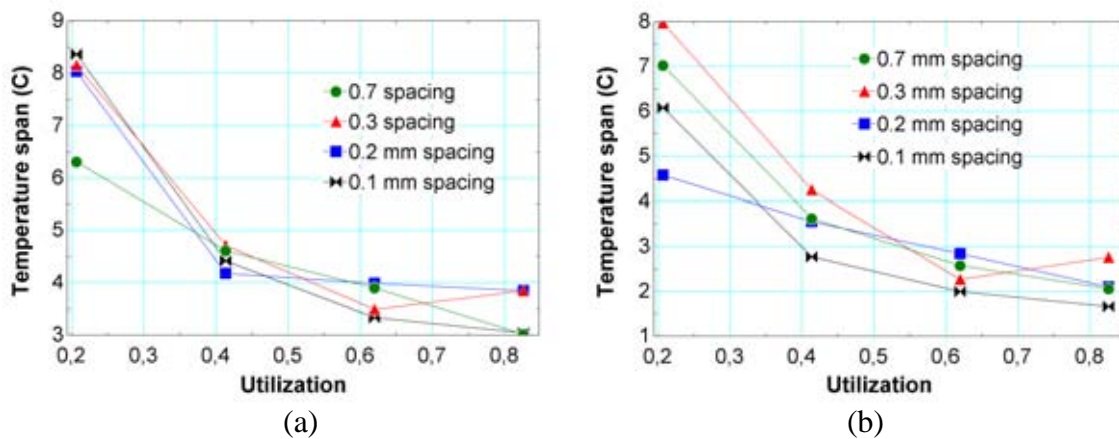


Figure 3. Temperature span as a function of utilization for flat plate regenerators with four different plate spacings for a fluid flow rate of (a) 0.7 g/s and (b) 2.7 g/s.

The temperature span achieved by each regenerator is plotted as a function of plate spacing for two utilizations in Figure 4.

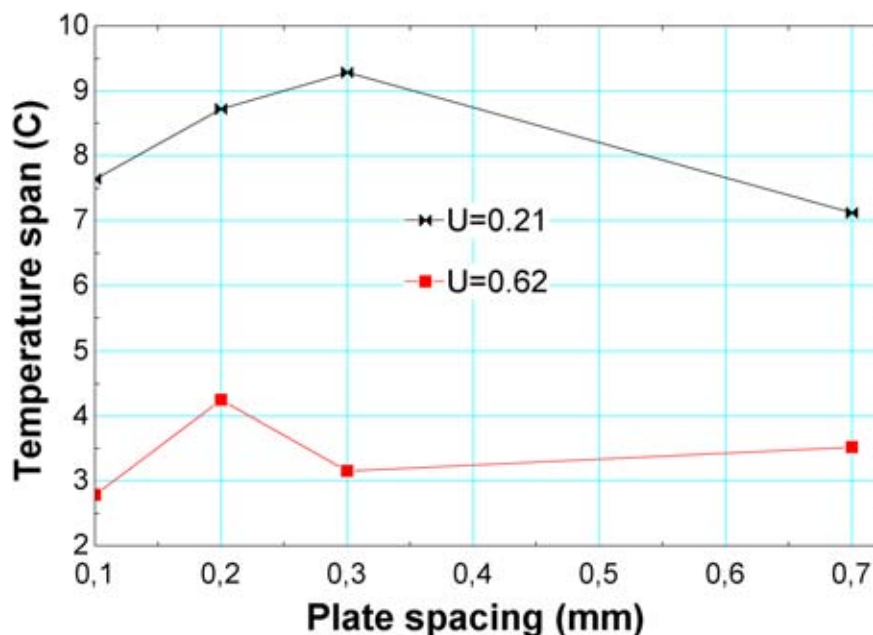


Figure 4. Temperature span as a function of plate spacing for different utilizations and a fluid flow rate of 0.9 g/s

The experimental data were also compared to predicted data from the 2D model. Selected experimental and predicted data are plotted in Figure 5.

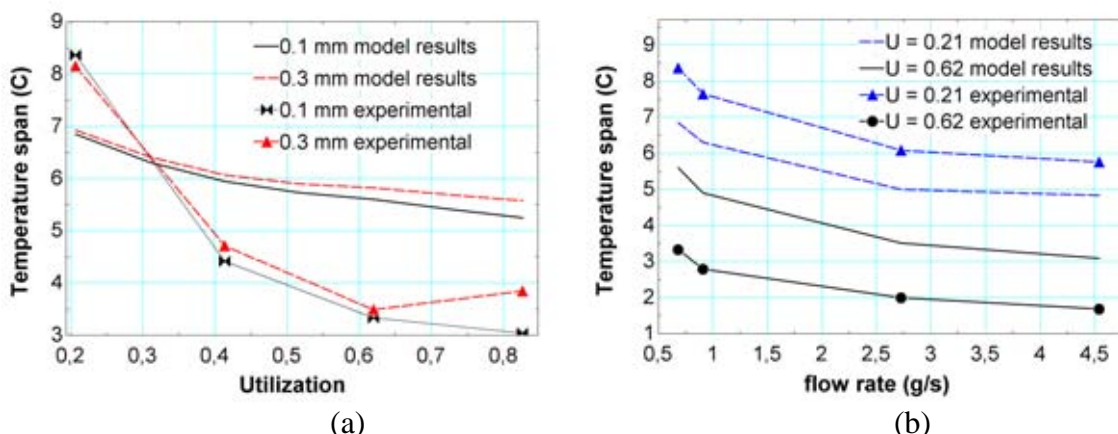


Figure 5. Experimental regenerator temperature span and predicted temperature span as a function of (a) utilization for 0.1 mm and 0.3 mm plate spacings and (b) fluid flow rate for a 0.1 mm plate spacing

6. DISCUSSION

The purpose of the research presented here is to determine the optimum regenerator geometry for a prototype AMR. Flat plate, corrugated plate, and dimpled plate regenerators were tested and compared. The flat plate results were also compared to predictions by a detailed 2D numerical model. Examination of Fig. 2 shows that corrugated plate regenerators show improved heat transfer performance over a flat plate regenerator with approximately the same effective plate spacing. The data presented here suggest that the angle of the corrugation pattern affects regenerator performance, and a 90° included angle pattern outperformed a 120°

corrugation pattern. The dimpled plate regenerator slightly outperformed the flat plate regenerator, but the effective plate spacing of the dimpled plate regenerator was approximately half that of the flat plate regenerator. Therefore, dimpled plate regenerators were not found to be an attractive alternative to flat plate regenerators.

Although the corrugated plate regenerators were shown to have better heat transfer performance than flat plate regenerators with similar plate spacing, the pump losses associated with corrugated plates may be significantly higher than for the flat plates. Dovic and Svaic (2007) report that corrugated plates will have noticeably higher than flat plates, and pump losses may make corrugated plate regenerator less efficient than flat plates in an AMR device. Fabrication of corrugated plates for common magnetocaloric materials may also be a challenge. Gadolinium is a malleable metal and may be well-suited to being formed into corrugated plates, but more brittle materials may pose a challenge. Ceramic materials such as LCsM may be shaped before sintering, but development of the process is necessary.

It was expected that the regenerators with smaller plate spacing would exhibit higher heat transfer coefficients between the fluid and solid and increase regenerator performance. However, results shown in Figures 3 and 4 suggest that the performance of the flat plate regenerators tested for this paper was not highly dependent on plate spacing. Generally, the 0.2 mm or 0.3 mm regenerators performed best, but for some operating conditions the other regenerators produced better experimental results. The reduced dependence on plate spacing may be partly due to variation in plate spacing. Each regenerator was built from the same aluminum plates using the same fabrication technique, and the absolute variation in plate spacing and flatness is likely similar, meaning that the relative variation increases as the plate spacing decreases. The increased variation in the regenerators with smaller plate spacing may erode the performance increase from the enhanced heat transfer between the plate and solid. Based on experimental data generated in this paper, a plate spacing between 0.2 mm and 0.3 mm is optimum for the regenerator fabrication techniques used.

The 2D regenerator model was able to capture general trends in the regenerator performance, but did not show excellent agreement for the range of experiments presented in this paper. In Fig. 5, the model under-predicts the regenerator performance for a utilization of 0.21 but over-predicts the performance when the utilization increases to 0.62. The discrepancy between experiment and model may be caused by the method of measuring the hot reservoir temperature. In this experiment, the heater is placed on the wetted side of the fluid displacer piston and the hot reservoir thermocouple is attached to the piston and measures the fluid temperature very close to the heater surface. The thermocouple may read an artificially high temperature due to its proximity to the heater. This effect is likely maximized for low utilizations because the lower piston stroke reduces mixing between the warm fluid near the heater and the cooler fluid exiting the regenerator. This effect has not been quantified presently.

7. ACKNOWLEDGEMENTS

The authors would like to acknowledge the support of the Programme Commission on Energy and Environment (EnMi) (Contract No. 2104-06-0032) which is part of the Danish Council for Strategic Research. The technical support of Jørgen Geyti is greatly appreciated.

REFERENCES

- Bahl, C.R.H., T.F. Petersen, N. Pryds and A. Smith, 2008, A versatile magnetic refrigeration device, *Rev. of Scientific Instruments* 79, 093906-1 - 093906-7.
- Dovic, D. and S. Svaic, 2007, Influend of Chevron Plates Geometry on Performances of Plate Heat Exchangers, *Technical Gazette* 14(1,2), 37-45.
- Dragutinovic, G. D., and B. S. Baclic, 1998, *Operation of Counterflow Regenerators*, Computational Mechanics Inc., Billerica, MA.
- Engelbrecht, K., Jensen, J. B., Bahl, C. R. H., Pryds, N., 2009, Experiments on a modular magnetic refrigeration device. Proceedings of the 3rd International Conference on Magnetic Refrigeration at Room Temperature, Des Moines, Iowa, USA, 431–436.
- Nielsen, K. K., C.R.H. Bahl, A. Smith, R. Bjørk, N. Pryds and J. Hattel, 2009, Detailed numerical modeling of a linear parallel-plate Active Magnetic Regenerator, *Int. J. of Refrig.* 32, 1478-1486.
- Sarlah, A., 2008, Thermo-hydraulic properties of heat regenerators in magnetic refrigerator. Ph.D. thesis, University of Ljubljana, Slovenia.

References

- Aharoni, A. (1998). Demagnetizing factors for rectangular ferromagnetic prisms. *Journal of Applied Physics*, 83(6):3432–3434.
- Arnold, D. S., Tura, A., and Rowe, A. (2010). Experimental analysis of a two-material active magnetic regenerator. *International Journal of Refrigeration*, Submitted.
- Ashcroft, N. W. and Mermin, D. (1976). *Solid State Physics*. Saunders College.
- Bahl, C. R. H., Engelbrecht, K., Bjørk, R., Eriksen, D., Smith, A., and Pryds, N. (2010). Design concepts for a continuously rotating active magnetic regenerator. In Egolf, P. W., editor, *4th International Conference on Magnetic Refrigeration at Room Temperature*. International Institute of Refrigeration.
- Bahl, C. R. H. and Nielsen, K. K. (2009). The effect of demagnetization on the magnetocaloric properties of gadolinium. *Journal of Applied Physics*, 105(1):013916 (5 pp.).
- Bahl, C. R. H., Petersen, T. F., Pryds, N., and Smith, A. (2008). A versatile magnetic refrigeration test device. *Review of Scientific Instruments*, 79(9):093906.
- Barclay, J. A. (1983). Theory of an active magnetic regenerative refrigerator. *NASA Conference Publication*, pages 375–387.
- Basso, V., Bertotti, G., LoBue, M., and Sasso, C. (2005a). Theoretical approach to the magnetocaloric effect with hysteresis. *Journal of Magnetism and Magnetic Materials*, 290-291(Part 1):654–657.
- Basso, V., Lobue, M., and Bertotti, G. (2005b). Temperature hysteresis and thermal remagnetization in magnetic materials. *Journal of Applied Physics*, 97(10):1–3.
- Basso, V., LoBue, M., Sasso, C., and Bertotti, G. (2006a). Thermodynamic aspects of magnetic-field-driven phase transformations in Gd-Si-Ge alloys. *Journal of Applied Physics*, 99(8):8K907–1–3.
- Basso, V., Sasso, C. P., Bertotti, G., and LoBue, M. (2006b). Effect of material hysteresis in magnetic refrigeration cycles. *International Journal of Refrigeration*, 29(8):1358–1365.
- Bejan, A. (2006). *Advanced Engineering Thermodynamics*. Wiley & Sons, Hoboken, New Jersey.

- Bjørk, R. (2010). *Designing a magnet for magnetic refrigeration*. PhD thesis, Technical University of Denmark, Risø National Laboratory for Sustainable Energy, Frederiksborgvej 399, DK-4000, Roskilde, Denmark.
- Bjørk, R., Bahl, C., and Katter, M. (2010). Magnetocaloric properties of $\text{LaFe}_{13-x-y}\text{Co}_x\text{Si}$ and commercial grade Gd. *Journal of Magnetism and Magnetic Materials*, Submitted.
- Bjørk, R., Bahl, C. R. H., Smith, A., and Pryds, N. (2008). Optimization and improvement of halbach cylinder design. *Journal of Applied Physics*, 104(1):013910.
- Bjørk, R., Nielsen, K. K., Bahl, C. R. H., Smith, A., Pryds, N., and Hattel, J. (2009). Numerical modeling in magnetic refrigeration. In Elmegård, B., editor, *Proceedings of SIMS 50*, pages 323–330.
- Blundell, S. (2001). *Magnetism in Condensed Matter*. Oxford University Press, Great Clarendon Street, Oxford OX2 6DP, 1st edition.
- Bouchard, J., Nesreddine, H., and Galanis, N. (2009). Model of a porous regenerator used for magnetic refrigeration at room temperature. *International Journal of Heat and Mass Transfer*, 52(5-6):1223–1229.
- Brown, G. V. (1976). Magnetic heat pumping near room temperature. *Journal of Applied Physics*, 47(8):3673–3680.
- Brug, J. and Wolf, W. (1985). Demagnetizing fields in magnetic measurements i. thin discs. *Journal of Applied Physics*, 57(10):4685–4694.
- Burriel, R., Tocado, L., Palacios, E., Tohei, T., and Wada, H. (2005). Square-shape magnetocaloric effect in Mn_3GaC . *Journal of Magnetism and Magnetic Materials*, 290-291(Part 1):715–718.
- Chen, D. T., Murphy, R. W., Mei, V. C., Chen, F. C., Lue, J. W., and Lubell, M. S. (1994). Performance analysis of reciprocating regenerative magnetic heat pumping. *Oak Ridge National Laboratory*.
- Christensen, D. V., Bjørk, R., Nielsen, K. K., Bahl, C. R. H. ., Smith, A., and Clausen, S. (2010a). Spatially resolved measurement of the magnetocaloric effect and the local magnetic field using thermography. *Journal of Applied Physics*, Accepted.
- Christensen, D. V., Nielsen, K. K., Bahl, C. R. H., and Smith, A. (2010b). Demagnetizing effects in stacked, rectangular prisms. *Journal of Applied Physics*, In prep.
- Ciofalo, M., Di Piazza, I., and Stasiak, J. A. (2000). Investigation of flow and heat transfer in corrugated-undulated plate heat exchangers. *Heat and Mass Transfer*, 36(5):449–462.
- Coey, J. M. D. (2010). *Magnetism and magnetic materials*. Cambridge University Press, Cambridge CB2 8RU, UK, 1st edition.

- Comsol (2005). *Comsol Multiphysics Model Library, third ed.* COMSOL AB, Chalmers Teknikpark 412 88 G.
- DeGregoria, A. (1991). Modeling the active magnetic regenerator. *Advances in Cryogenic Engineering*, 37(pt B):867–873.
- Dikeos, J., Rowe, A., and Tura, A. (2006). Numerical Analysis of an Active Magnetic Regenerator (AMR) Refrigeration Cycle. *AIP Conference Proceedings*, 823(1):993 – 1000.
- Dinesen, A. R. (2004). *Magnetocaloric and magnetoresistive properties of $\text{La}_{0.67}\text{Ca}_{0.33-x}\text{Sr}_x\text{MnO}_3$* . PhD thesis, Technical University of Denmark.
- Dovic and Svaic (2007). Influence of chevron plates geometry on performances of plate heat exchangers. *Tehnicki Vjesnik*, 14(1-2):37–45.
- Engelbrecht, K. (2008). *A Numerical Model of an Active Magnetic Regenerator Refrigerator with Experimental Validation*. PhD thesis, University of Wisconsin, Madison.
- Engelbrecht, K., Bahl, C. R. H., Nielsen, K. K., and Pryds, N. (2010a). Experimental results for a magnetic refrigerator using three different types of magnetocaloric material regenerators. *International Journal of Refrigeration*, Submitted.
- Engelbrecht, K., Jensen, J., Bahl, C., and Pryds, N. (2009). Experiments on a modular magnetic refrigeration device. In Egolf, P., editor, *3rd International Conference on Magnetic Refrigeration at Room Temperature*, pages 431–436. International Institute of Refrigeration.
- Engelbrecht, K., Nielsen, K. K., and Pryds, N. (2010b). An experimental study of passive regenerator geometries. In Egolf, P. W., editor, *Fourth International Conference on Magnetic Refrigeration at Room Temperature*. International Institute of Refrigeration.
- Focke, W., Zachariades, J., and Olivier, I. (1985). The effect of the corrugation inclination angle on the thermohydraulic performance of plate heat exchangers. *International Journal of Heat and Mass Transfer*, 28(8):1469–1479.
- Fujieda, Hasegawa, Fujita, and Fukamichi (2004). Thermal transport properties of magnetic refrigerants $\text{La}(\text{Fe}_x\text{Si}_{1-x})_{13}$ and their hydrides, and $\text{Gd}_5\text{Si}_2\text{Ge}_2$ and MnAs . *Journal of Applied Physics*, 95(5):2429–2431.
- Fukamichi, K., Fujita, A., and Fujieda, S. (2006). Large magnetocaloric effects and thermal transport properties of $\text{La}(\text{FeSi})_{13}$ and their hydrides. *Journal of Alloys and Compounds*, 408-412:307–312.
- Giauque, W. F. and MacDougall, D. P. (1933). Attainment of Temperatures Below 1 K Absolute by Demagnetization of $\text{Gd}_2(\text{SO}_4)_3 \cdot 8\text{H}_2\text{O}$. *Physical Review*, 43:768.
- Griffiths, D. J. (1999). *Introduction to electrodynamics*. Prentice Hall, Upper Saddle River, New Jersey 07458, 3rd edition.

- Gschneidner, Karl A., J. and Pecharsky, V. K. (2000). The influence of magnetic field on the thermal properties of solids. *Materials Science and Engineering: A*, 287(2):301 – 310.
- Gschneidner, K. and Pecharsky, V. (2008). Thirty years of near room temperature magnetic cooling: Where we are today and future prospects. *International Journal of Refrigeration*, 31:945–961.
- Hargraves, Dunlap, Geldart, and Ritcey (1988). Critical magnetic susceptibility of gadolinium. *Physical Review B (Condensed Matter)*, 38(4):2862–2864.
- Hattel, J. (2005). *Fundamentals of Numerical Modelling of Casting Processes*. Polyteknisk Forlag.
- He, J., Chen, J., and Wu, C. (2003). The influence of heat-transfer laws on the performance of a magnetic stirling refrigeration cycle. *International Journal of Ambient Energy*, 24(2):75–82.
- Hessami, M.-A. (2003). An experimental investigation of the performance of cross-corrugated plate heat exchangers. *Journal of Enhanced Heat Transfer*, 10(4):379–393.
- Holman, J. (1987). *Heat Transfer*. McGraw-Hill, 1 edition.
- Incropera, F. P. and Dewitt, D. P. (1996). *Introduction to heat transfer*. John Wiley and Sons, Inc., 3 edition.
- Jacobs, S. (2009). Modeling and optimal design of a multiplayer active magnetic refrigeration system. In Egolf, P. W., editor, *Third International Conference on Magnetic Refrigeration at Room Temperature*. International Institute of Refrigeration.
- Jacobsson, P. and Sundqvist, B. (1989). Thermal conductivity and electrical resistivity of gadolinium as functions of pressure and temperature. *Physical Review B*, 40(14):9541–9551.
- Jensen, J. B., Engelbrecht, K., Bahl, C. R. H., Pryds, N., Elmegård, B., Nellis, G. F., and Klein, S. A. (2010). Modeling of parallel-plate regenerators with non-uniform plate distributions. *International Journal of Heat and Mass Transfer*, Accepted.
- Jeppesen, S., Linderoth, S., Pryds, N., Kuhn, L. T., and Jensen, J. B. (2008). Indirect measurement of the magnetocaloric effect using a novel differential scanning calorimeter with magnetic field. *Review of Scientific Instruments*, 79(8).
- Kittel, C. (1996). *Introduction to solid state physics*. John Wiley & Sons, Inc., New York, 7 edition.
- Kuz'min, M. D. (2007). Factors limiting the operation frequency of magnetic refrigerators. *Applied Physics Letters*, 90:251916 (3pp).
- Li, P., Gong, M., Yao, G., and Wu, J. (2006). A practical model for analysis of active magnetic regenerative refrigerators for room temperature applications. *International Journal of Refrigeration*, 29:1259–1266.

- Lide, D. (2004). *CRC Handbook of Chemistry and Physics*. CRC Press.
- Matsumoto, K. and Hashimoto, T. (1990). Thermodynamic analysis of magnetically active regenerator from 30 to 70 k with a brayton-like cycle. *Cryogenics*, 30:840–845.
- Morrish, A. H. (1965). *The Physical Principles of Magnetism*. John Wiley & Sons, Inc.
- Morrison, K., Moore, J., Sandeman, K., Caplin, A., and Cohen, L. (2009). Capturing first- and second-order behavior in magnetocaloric $\text{CoMnSi}_{0.92}\text{Ge}_{0.08}$. *Physical Review B (Condensed Matter and Materials Physics)*, 79(13):134408 (5 pp.).
- Nickolay, M. and Martin, H. (2002). Improved approximation for the Nusselt number for hydrodynamically developed laminar flow between parallel plates. *International Journal of Heat and Mass Transfer*, 45(15):3263–3266.
- Nielsen, K. K., Bahl, C. R. H., Engelbrecht, K., Smith, A., Pryds, N., and Hattel, J. (2010a). Numerical modeling of graded active magnetic regenerators. In Egolf, P. W., editor, *Fourth International Conference on Magnetic Refrigeration at Room Temperature*. International Institute of Refrigeration.
- Nielsen, K. K., Bahl, C. R. H., and Smith, A. (2010b). Constraints on the adiabatic temperature change in magnetocaloric materials (5 pages) 054423. *Physical Review B - Condensed Matter*, 81(5).
- Nielsen, K. K., Bahl, C. R. H., Smith, A., Bjørk, R., Pryds, N., and Hattel, J. (2009a). Detailed numerical modeling of a linear parallel-plate active magnetic regenerator. *International Journal of Refrigeration*, 32(6):1478–1486.
- Nielsen, K. K., Bahl, C. R. H., Smith, A., Pryds, N., and Hattel, J. (2010c). A comprehensive parameter study of an active magnetic regenerator using a 2d numerical model. *International Journal of Refrigeration*, 33(4):753–764.
- Nielsen, K. K., Bjørk, R., Jensen, J. B., Bahl, C. R. H., Pryds, N., Smith, A., Nordentoft, A., and Hattel, J. (2008). Magnetic Cooling at Risø DTU. In Hansen, S. and Paul, J., editors, *8th IIR Gustav Lorentzen Conference on Natural Working Fluids*. International Institute of Refrigeration.
- Nielsen, K. K., Engelbrecht, K., Bahl, C. R. H., Smith, A., Pryds, N., and Hattel, J. (2009b). Numerical modeling of multi-material active magnetic regeneration. In *7th World Conference on Experimental Heat Transfer, Fluid Mechanics and Thermodynamics*.
- Nielsen, K. K., Lozano, J., and Barbosa Jr., J. (2010d). The magnetocaloric properties of MnFePAs. *In prep*.
- Nielsen, K. K., Tusek, J., Engelbrecht, K., Schopfer, S., Smith, A., Bahl, C. R. H., Kitanovski, A., Pryds, N., and Poredos, A. (2010e). Review on numerical modeling of active magnetic regenerators. *International Journal of Refrigeration*, Submitted.

- Okamura, T., Yamada, K., Hirano, N., and Nagaya, S. (2006). Performance of a room-temperature rotary magnetic refrigerator. *International Journal of Refrigeration*, 29:1327–1331.
- Oliveira, P. A., Trevizoli, P., Jr., J. R. B., and Prata, A. T. (2009). Numerical analysis of a reciprocating active magnetic regenerator - part I. In Egolf, P. W., editor, *Third International Conference on Magnetic Refrigeration at Room Temperature*, pages 283–288. International Institute of Refrigeration.
- Organ, A. J. (1994). The wire mesh regenerator of the stirling cycle machine. *International Journal of Heat and Mass Transfer*, 37(16):2525–2534.
- Palacios, E., Wang, G. F., Burriel, R., Provenzano, V., and Shull, R. D. (2010). Direct measurement of the magnetocaloric effect in $\text{Gd}_5\text{Si}_2\text{Ge}_{1.9}\text{Ga}_{0.1}$. *Journal of Physics: Conference Series*, 200(9):092011.
- Patankar, S. V. (1980). *Numerical Heat Transfer and Fluid Flow*. Taylor&Francis.
- Pecharsky, V., Gschneidner, K., Pecharsky, A., and Tishin, A. (2001). Thermodynamics of the magnetocaloric effect. *Physical Review B (Condensed Matter and Materials Physics)*, 64(14):144406/1–13.
- Pecharsky, V. K. and Gschneidner, K. (2006). Advanced magnetocaloric materials: What does the future hold? *International Journal of Refrigeration*, 29:1239–1249.
- Peksoy, O. and Rowe, A. (2005). Demagnetizing effects in active magnetic regenerators. *Journal of Magnetism and Magnetic Materials*, 288:424–432.
- Petersen, T. F. (2007). *Numerical modelling and analysis of a room temperature magnetic refrigeration system*. PhD thesis, Risø National Laboratory and Technical University of Denmark.
- Petersen, T. F., Engelbrecht, K., Bahl, C. R. H., Elmegaard, B., Pryds, N., and Smith, A. (2008a). Comparison between a 1d and a 2d numerical model of an active magnetic regenerative refrigerator. *Journal of Physics D: Applied Physics*, 41(10):105002.
- Petersen, T. F., Pryds, N., Smith, A., Hattel, J., Schmidt, H., and Knudsen, H. (2008b). Two-dimensional mathematical model of a reciprocating room-temperature active magnetic regenerator. *International Journal of Refrigeration*, 31:432–443.
- Pryds, N., Clemenc, F., Menon, M., Nielsen, P. H., Brodersen, K., Bjørk, R., Bahl, C. R. H., Engelbrecht, K., Nielsen, K. K., and Smith, A. (2010). Monolithic perovskite for magnetic regenerator. *American Society of Ceramics*, Submitted.
- Rühlich, I. and Quack, H. (1998). New regenerator design for cryocoolers. Technical report, Technische Universität Dresden.
- Rowe, A. (2009). Performance metrics for active magnetic refrigerators. In Egolf, P., editor, *Third International Conference on Magnetic Refrigeration at Room Temperature*, pages 195–205. International Institute of Refrigeration.

- Rowe, A. and Barclay, J. (2003). Ideal magnetocaloric effect for active magnetic regenerators. *Journal of Applied Physics*, 93(3):1672–1676.
- Rowe, A. and Tura, A. (2006). Experimental investigation of a three-material layered active magnetic regenerator. *International Journal of Refrigeration*, 29:1286–1293.
- Rowe, A. M. and Barclay, J. A. (2002). Magnetic refrigerators - design of an active magnetic regenerator test apparatus. *Advances in Cryogenic Engineering*, 47(A):995.
- Sasso, C. P., Basso, V., LoBue, M., and Bertotti, G. (2006). Carnot cycle for magnetic materials: The role of hysteresis. *Physica B: Physics of Condensed Matter*, 372(1-2):9–12.
- Smailli, A. and Chahine, R. (1998). Thermodynamic investigations of optimum active magnetic regenerators. *Cryogenics*, 38:247–252.
- Smith, A., Nielsen, K. K., Christensen, D. V., Bahl, C. R. H., Bjørk, R., and Hattel, J. (2010). The demagnetizing field of a nonuniform rectangular prism. *Journal of Applied Physics*, 107(10):103910.
- Tandon, S., Beleggia, M., Zhu, Y., and De Graef, M. (2004). On the computation of the demagnetization tensor for uniformly magnetized particles of arbitrary shape. part i: Analytical approach. *Journal of Magnetism and Magnetic Materials*, 271(1):9–26.
- Tishin, A. and Spichkin, Y. (2003). *The Magnetocaloric Effect and its Applications*. Institute of Physics Publishing.
- Tocado, L., Palacios, E., and Burriel, R. (2006). Adiabatic measurement of the giant magnetocaloric effect in mnas. *Journal of Thermal Analysis and Calorimetry*, 84(1):213–217.
- Tocado, L., Palacios, E., and Burriel, R. (2009). Entropy determinations and magnetocaloric parameters in systems with first-order transitions: Study of MnAs. *Journal of Applied Physics*, 105(9):093918.
- Tura, A. and Rowe, A. (2007). Design and testing of a permanent magnet magnetic refrigerator. In *2nd Internal Conference on Magnetic Refrigeration at Room Temperature*.
- Tura, A. and Rowe, A. (2009). Progress in the characterization and optimization of a permanent magnet magnetic refrigerator. In Egolf, P. W., editor, *Third International Conference on Magnetic Refrigeration at Room Temperature*, pages 387–392. International Institute of Refrigeration.
- Visser, D. W., Ramirez, A. P., and Subramanian, M. A. (1997). Thermal conductivity of manganite perovskites: Colossal magnetoresistance as a lattice-dynamics transition. *Phys. Rev. Lett.*, 78(20):3947–3950.

- Wada, H., Asano, T., Ilyn, M., and Tishin, A. (2007). Direct measurements of magnetocaloric effects of $\text{Mn}_{1+\delta}\text{As}_{1-x}\text{Sb}_x$. *Journal of Magnetism and Magnetic Materials*, 310(2Part 3):2811–2812.
- Yan, Z. and Chen, J. (1991). The characteristics of polytropic magnetic refrigeration cycles. *Journal of Applied Physics*, 70(4):1911–1914.
- Yan, Z. and Chen, J. (1992). The effect of field-dependent heat capacity on the characteristics of the ferromagnetic Ericsson refrigeration cycle. *Journal of Applied Physics*, 72(1):1–5.
- Yu, B., Liu, M., Egolf, P. W., and Kitanovski, A. (2010). A review of magnetic refrigerator and heat pump prototypes built before the year 2010. *International Journal of Refrigeration*, 33(6):1029–1060.
- Zhang, L., Sherif, S. A., DeGregoria, A. J., Zimm, C. B., and Veziroglu, T. N. (2000). Design and optimization of a 0.1 ton/day active magnetic regenerative hydrogen liquifier. *Cryogenics*, 40:269–278.
- Zhang, L., Sherif, S. A., Veziroglu, T. N., and Sheffield, J. W. (1993). Second law analysis of active magnetic regenerative hydrogen liquefier. *Cryogenics*, 33(7):667–674.
- Zimm, C., Boeder, A., Chell, J., Sternberg, A., Fujita, A., Fujieda, S., and Fukamichi, K. (2006). Design and performance of a permanent-magnet rotary refrigerator. *International Journal of Refrigeration*, 29(8):1302–1306.
- Zimm, C., Jastrab, A., Pecharsky, A. S. V., Gschneidner Jr, K., Osborne, M., and Anderson, I. (1998). Cryocoolers: Regenerative - description and performance of a near-room temperature magnetic refrigerator. *Advances in Cryogenic Engineering*, 43(B):1759.

DTU Mechanical Engineering
Section of Manufacturing Engineering
Technical University of Denmark

Produktionstorvet, Bld. 427S
DK- 2800 Kgs. Lyngby
Denmark
Phone (+45) 45 25 47 63
Fax (+45) 45 93 01 90

www.mek.dtu.dk
ISBN: 978-87-90416-34-8